AVERTISSEMENT

Ce document est le fruit d'un long travail approuvé par le jury de soutenance et mis à disposition de l'ensemble de la communauté universitaire élargie.

Il est soumis à la propriété intellectuelle de l'auteur. Ceci implique une obligation de citation et de référencement lors de l'utilisation de ce document.

D'autre part, toute contrefaçon, plagiat, reproduction illicite encourt une poursuite pénale.

Contact : ddoc-theses-contact@univ-lorraine.fr

LIENS

Code de la Propriété Intellectuelle. articles L 122. 4
Code de la Propriété Intellectuelle. articles L 335.2- L 335.10
http://www.cfcopies.com/V2/leg/leg_droi.php
http://www.culture.gouv.fr/culture/infos-pratiques/droits/protection.htm

LABORATOIRE REACTIONS ET GENIE DES PROCEDES, CNRS
UMR 7274
ECOLE DOCTORALE :
Sciences et Ingénierie des Ressources, Procédés, Produits, Environnement

THESIS

Presented and defended publicly on:
May 26th 2016
for obtaining a:

PhD title from the University of Lorraine
In Process and Product Engineering

by

Carlos MURILLO

Experimental and numerical approaches to particles dispersion in a turbulent flow: application to dust explosions

---

Composition of the Jury:

Referees:	Pr. Pawel KOSINSKI	(University of Bergen)
	Dr. HDR Jérôme MORCHAIN	(LISBP - INSA Toulouse)
Members:	Dr. HDR Jean-Claude LATCHE	(IRSN Cadarache)
	Pr. Jean-Marc COMMENGE	(Université de Lorraine)
	Dr. Nathalie MONNIER	(Université de Lorraine – Thesis Co-Director)
	Pr. Olivier DUFAUD	(Université de Lorraine – Thesis Director)
Guest:	Dr. Felipe MUÑOZ	(Universidad Los Andes Bogotá)

ABSTRACT

EXPERIMENTAL AND NUMERICAL APPROACHES TO PARTICLES DISPERSION IN A TURBULENT FLOW: APPLICATION TO DUST EXPLOSIONS

Keywords: Combustible Dust, Dispersion, Turbulence, Modified Hartmann Tube, 20 L sphere, Computational Fluid Dynamics

The pre-ignition stage of an explosibility test determines the ignitability of a dust cloud as well as the main characteristics of the propagation. For this reason, the dispersion process of a combustible dust that develops inside the explosion chambers of the modified Hartmann tube and the 20 L sphere has been described by two complementary approaches. Initially, an experimental characterization of the evolution of the dust cloud identified the evolution of the turbulence levels of the gas flow along with the main variations of the particle size distribution of the combustible dust. These results were complemented by the identification of the segregation levels of the dispersed powder inside the explosion chambers. Thereafter, a set of CFD simulations based on the Euler-Lagrange formulation was developed to predict the behavior of the combustible dust cloud. This study was accomplished through the characterization of the main interaction mechanisms such as the momentum exchange (two-way coupling) and the dust fragmentation phenomenon. In this manner, the research work constituted for this thesis allowed determining the most appropriate conditions to ignite a dust cloud formed by a metallic (Aluminum micro-Al 42) or organic powders (wheat starch) in a case study. Thus, this research work presents a methodology that can be extended for the analyses of combustible dusts and the further development of the standard test methods.

RÉSUMÉ

APPROCHES EXPERIMENTALE ET NUMERIQUE DE LA DISPERSION DE PARTICULES DANS UN ECOULEMENT TURBULENT : APPLICATION AUX EXPLOSIONS DE POUSSIERES

Mots-clefs : Explosion de Poussières, Dispersion, Turbulence, Tube Hartmann Modifié, Sphère d'Explosion, Mécanique des Fluides Numérique

Les caractéristiques d'un nuage de poussières avant l'activation de la source d'inflammation ont une grande influence sur la sensibilité et la sévérité de son explosion. Pour cette raison, le procédé de dispersion d'une poussière combustible qui se développe à l'intérieur des chambres d'explosion standardisés telles que le tube de Hartmann modifié et la sphère 20 L a été décrit par deux approches complémentaires. Dans un premier temps, une caractérisation expérimentale de l'évolution du nuage de poussière a identifié les niveaux de turbulence de l'écoulement de gaz, ainsi que les principales variations de la distribution de la taille des particules combustibles. Ces résultats ont été complétés par l'identification des niveaux de ségrégation de la poudre dispersée à l'intérieur des chambres d'explosion. Par la suite, une série de simulations CFD basée sur une approche Euler-Lagrange a été développée pour prédire le comportement du nuage. Cette étude a été réalisée grâce à la caractérisation des principaux mécanismes d'interaction tels que le transfert de quantité de mouvement (couplage bidirectionnel) et le phénomène de fragmentation des poudres. Deux types de particules microniques ont été spécifiquement étudiés : une poussière métallique, l'aluminium et un composé organique, l'amidon de blé. Ces résultats ont démontré qu'il est possible de définir ab initio, par simulation numérique, les conditions de tests les plus pertinentes (les plus réalistes ou les plus pénalisantes) en vue de la quantification de ces risques majeurs.

ACKNOWLEDGEMENTS

The development of this PhD thesis has been a fulfilling experience for me. This is due to the great people I have met during this part of my life. They have contributed in so many ways to my personal and professional development during the last few years. For this reason, I want to thank them in a text that I think that remains short because it is not possible to express all my gratitude in some simple words. Nevertheless, I think that this brief passage constitutes a good opportunity to acknowledge some of the people that have supported and accompanied me.

MY FAMILY

My mother (María Rueda) has been the main support for me all my life. Despite the fact that we have been away during these last few years, you have always given me your support for the hard times and have always been there during the good and successful times as well. This encouragement has also come from my grandmother (Inés Buitrago) and my sister (Diana Gómez). Thanks for all the sacrifice you have made and for all your backup.

MY ADVISORS: OLIVIER DUFAUD, NATHALIE BARDIN-MONNIER AND FELIPE MUÑOZ

I would like to express my whole gratitude to you for all your guidance ad motivation. Since the beginning of this thesis, you have shown your great commitment to be not only advisors but also good friends. Your motivation and all the knowledge you have shared with me have been the major basis of this work and will certainly remain during the rest of my professional life. In addition, all your advices have helped me becoming a better person. For this reason, I know that all your students can count on you and vice versa.

You can be sure that we will continue working (and laughing) together… Hala Madrid!

THE MEMBERS OF THE TEAM SAFE AND THE CHEMICAL ENGINEERING DEPARTMENT OF THE UNIVERSITY OF LOS ANDES

I am profoundly grateful with all the members of the team SAFE. Your contribution to this work is quite important and I am gland for spending these years as one of you and participating in all the activities of our research group (and all the sports discussions).

Particularly, I would also like to express my sincere gratitude to Professors André Laurent and Laurent Perrin. During these years, I had the great opportunity to learn several things from you. Thanks for all your kindness and for helping me with different things that have been a little difficult since I was a foreign student.

This thesis was developed in collaboration with the University of Los Andes. The research group of Professor Muñoz constituted the major basis of the computational analyses. For this reason, I want to express all my gratitude to Daniel Vizcaya, Mariangel Amin and Andrés Pinilla. Your work and motivation contributed to the accomplishment of this project.

Moreover, I would like to thank Christian Blanchard and the workshop team of the ENSIC for supporting us in the construction of the 20 L dispersion sphere and the symmetric nozzle. This work was also possible thanks to Denis Funfschilling due to his support for the development of the Particle Image Velocimetry tests.
Furthermore, I also want to express my gratitude to Stéphanie Pacault and Jean-François Remy for their important support during the development of the experimental tests with the standard apparatuses and finally, I also acknowledge my colleagues Miriam D'Amico, David Torrado and Nicolás Cuervo for their hard-work and all the time invested in different experiments, symposiums, congresses and all their contributions to the work presented in this document.

MY FRIENDS:

Being away from your country turns your friends into your family; hence I want to thank all of my friends for your company and support. You certainly do not know how much you have helped me through your messages and all the good moments.

Silvi, your support and company throughout these years have been quite important. We have been so far for a long time but I know that it will be worth it and I hope we can be together soon. Natalia, your friendship has been very important to me. You have always been there. Thanks for all the laughs and your support.

Furthermore, I want to express my gratitude to Alexis Vignes for all his support during all these years. Your motivation really helped me achieving this goal. Finally, I would like to thank all the good friends that I met in Nancy: Alejandra, Andrés, Camilo, David, Deisy, Diana, Edouard, Felipe, François, Guillemette, Johan, Katja, Loïc, Laura, Luis, Miriam, Nicolás, Piña, Quentin, Riadh, Ricardo, Selven, Valentina, and Zineb.

Thanks a lot, I will never forget all the good moments, the discussions about sports and music, the French courses and all your help.

CONTENTS

ABSTRACT i
RÉSUMÉ ii
ACKNOWLEDGEMENTS iii
LIST OF FIGURES viii
LIST OF TABLES xii
INTRODUCTION 1
1 STANDARDIZED METHODS FOR THE QUANTITATIVE EVALUATION OF THE FLAMMABILITY AND EXPLOSIBILITY OF THE COMBUSTIBLE DUSTS 4
1.1 DUST EXPLOSIONS 4
1.2 THE DUST EXPLOSION HEXAGON 5
1.3 MECHANISMS OF DUST EXPLOSIONS 6
1.3.1 Kinetic mechanisms of dust combustion 8
1.3.2 Deflagrations and detonations in dust explosions 10
1.4 EXPERIMENTAL DETERMINATION OF THE DUST IGNITABILITY 11
1.4.1 MINIMUM IGNITION TEMPERATURE (MIT) OF A DUST CLOUD 11
1.4.2 MINIMUM EXPLOSIBLE CONCENTRATION (MEC) AND MINIMUM IGNITION ENERGY (MIE) 12
1.4.3 MINIMUM OXYGEN CONCENTRATION (MOC) 13
1.4.4 INTERNATIONAL STANDARDS 13
1.5 EXPERIMENTAL DETERMINATION OF THE EXPLOSIVITY OF A DUST CLOUD 22
1.5.1 MAXIMUM PRESSURE AND MAXIMUM RATE OF PRESSURE RISE 22
1.5.2 LAMINAR BURNING VELOCITY 23
1.5.3 INTERNATIONAL STANDARDS 25
1.6 INFLUENTIAL PARAMETERS 32
1.6.1 PARTICLE SIZE DISTRIBUTION (PSD) 33
1.6.2 INITIAL TURBULENCE 37
1.6.3 DUST FRAGMENTATION AND AGGLOMERATION 38
1.6.4 MOISTURE CONTENT 45
1.6.5 ADDITIONAL PARAMETERS 46
1.7 CRITICAL ANALYSIS OF THE STANDARDS 49
1.7.1 APPLICABILITY OF THE STANDARDS IN THE CHARACTERIZATION OF MICROMETRIC PARTICLES 51
1.7.2 EMERGING TOPICS: NANOMETRIC PARTICLES AND HYBRID MIXTURES . 52
1.8 CONCLUSIONS 59
1.9 LIST OF VARIABLES 60
1.10 REFERENCES 63
2 NUMERICAL SIMULATIONS OF SOLIDS DISPERSIONS 67

2.1 COMPUTATIONAL STUDY OF A GAS-SOLID FLOW 69
2.1.1 Numerical methods applied for the description of a homogeneous or heterogeneous system 69
2.1.2 Selection criteria for the computational approach 77
2.1.3 Numerical description of the gas flow turbulence 81
2.1.4 Implementation of the DES model in the CFD simulations 86
2.1.5 Lagrangian approach for the description of the dispersion process of the combustible dust 92
2.2 APPLICATION OF THE COMPUTATIONAL FLUID DYNAMICS ON THE DESCRIPTION OF GAS-SOLID MIXTURES 95
2.3 APPLICATION OF THE COMPUTATIONAL FLUID DYNAMICS ON DUST EXPLOSIONS 102
2.3.1 Characterization of the flame velocity 103
2.3.2 Description of dust explosions with the FLACS-DustEx code 104
2.4 SUMMARY 106
2.5 LIST OF VARIABLES 108
2.6 REFERENCES 114
3 EXPERIMENTAL STUDY OF THE DUST DISPERSION AND ITS EFFECTS ON THE EXPLOSIBILITY PARAMETERS 118
3.1 COMBUSTIBLE DUSTS ANALYZED 119
3.1.1 Aluminum 119
3.1.2 Wheat starch 123
3.1.3 Adjustment of the particle size distribution to the Rosin-Rammler equation 125
3.2 GRANULOMETRIC ANALYSES 127
3.3 DIGITAL PARTICLE IMAGE VELOCIMETRY (DPIV) 130
3.3.1 Continuous wave laser 131
3.3.2 Tracer particles 132
3.3.3 Image analysis 134
3.4 DETERMINATION OF THE CHARACTERISTICS OF THE PRESSURIZED GAS INJECTION 137
3.4.1 Mass balance 139
3.4.2 Analysis of the high-speed videos 140
3.4.3 Transient pressure of the vessel 143
3.4.4 Transient pressure of the vessel 144
3.4.5 Gas velocity and Reynolds number 145
3.4.6 Pressure drop of the gas flow 145
3.4.7 Description of the gas injection into the modified Hartmann tube 149
3.5 DETERMINATION OF THE DUST DISPERSION CHARACTERISTICS INSIDE THE MODIFIED HARTMANN TUBE 151

3.5.1 Experimental setup 151
3.5.2 Set of experiments 152
3.6 DETERMINATION OF THE CHARACTERISTICS OF THE DUST DISPERSION INSIDE THE 20 L SPHERE 163
3.6.1 Experimental setup 163
3.6.2 Dispersion nozzles 164
3.6.3 Set of experiments 165
3.6.4 Experimental analyses 167
3.6.5 Determination of the ignition delay 190
3.7 CONCLUSIONS 192
3.8 LIST OF VARIABLES 194
3.9 REFERENCES 197
4 CONFRONTATION OF THE COMPUTATIONAL AND EXPERIMENTAL DESCRIPTION OF THE DUST DISPERSION PROCESS 201
4.1 DESCRIPTION OF THE DUST DISPERSION IN THE MODIFIED HARTMANN TUBE 201
4.1.1 Description of the mesh 203
4.1.2 Boundary and initial conditions 204
4.1.3 Numerical parameters associated to the physics of the gas flow 205
4.1.4 Numerical parameters associated to the physics of the micrometric wheat starch 208
4.1.5 Results and comparison with the experimental approach 210
4.1.6 Application to the determination of the minimum ignition energy of the micrometric aluminum and wheat starch 224
4.2 DESCRIPTION OF THE DUST DISPERSION IN THE 20 L SPHERE 225
4.2.1 Description of the mesh 228
4.2.2 Numerical parameters associated to the physics and the discretization 230
4.2.3 Initial and boundary conditions 231
4.2.4 Results and comparison with the experimental approach 232
4.2.5 Application to the determination of the explosibility parameters of the micrometric wheat starch 253
4.3 LIST OF VARIABLES 255
4.4 REFERENCES 255
CONCLUSION 258
APPENDIX A 261

LIST OF FIGURES

Figure 1.1 Dust explosion hexagon 5
Figure 1.2. Flames developed by 2 combustible compounds of different nature 7
Figure 1.3. Types of dusts involved in dust explosions 8
Figure 1.4. Combustion behaviors of different dusts 9
Figure 1.5. Experimental setups for the determination of the minimum explosible concentration of a dust cloud 17
Figure 1.6. Modified Hartmann tube 20
Figure 1.7. Explosion of micrometric wheat starch in the 20 L sphere 26
Figure 1.8. Standard apparatuses to determine the explosibility of dust clouds 27
Figure 1.9. Schematic of the 20 L sphere 29
Figure 1.10. Influence of the PSD on the flammability parameters of a combustible dust 34
Figure 1.11. Dust explosibility characteristics: effect of particle size on some principal parameters for atomized aluminum 35
Figure 1.12. Flame speed versus dust concentration in unconfined clouds of metal dusts 36
Figure 1.13. Influence of the specific surface area on the maximum pressure rate of aluminum 36
Figure 1.14. Influence of initial turbulence on the flammability parameters of a lycopodium dust cloud 37
Figure 1.15. Influence of the dispersion nozzle on the PSD distribution in the 20 L sphere 39
Figure 1.16. Inertial stress as a mechanism of deagglomeration in fluids 40
Figure 1.17. Rotary stress as a mechanism of deagglomeration in fluids 41
Figure 1.18. Turbulent stresses as mechanisms of deagglomeration in fluids 41
Figure 1.19. Influence of the equilibrium relative humidity of the flammability parameters of magnesium stereate 45
Figure 1.20. Influence of inertant insertion on the maximum explosion pressure of magnesium stearate powders 48
Figure 1.21. Evolution of the maximum explosion pressure and of the maximum rate of pressure rise of magnesium stearate-$NaHCO_3$ explosions as a function of the sodium bicarbonate concentration 49
Figure 1.22. Minimum ignition temperature as a function of particle size diameter 54
Figure 1.23. Dependencies of the MIE versus the particle diameter 54
Figure 1.24. Experimental evolution of explosions of nano-sized aluminum particles 55
Figure 1.25. Contour lines of the P_{max} and the maximum rate of pressure rise of niacin/diisopropyl ether hybrid mixtures 57
Figure 1.26 Effect of methane content on the explosion development of suspensions with cork dust concentrations of 450 g/m^3 58
Figure 1.27. Explosion regimes in the plane methane content/nicotinic acid concentration 58
Figure 2.1. Multiscale characteristics of chemical engineering and its multilevel classification 67
Figure 2.2. Map of flow regimes in particle-laden flows 73
Figure 2.3. Schematic representation depicting scales and various simulators 78
Figure 2.4. Definition of the DES turbulence model in the flow domain 85
Figure 2.5. DDES correction factor 86
Figure 2.6. A single bubble injection in a fluidized bed 96
Figure 2.7. Gas–solid distribution at a simulation time of 5.2 s as a representative case 97
Figure 2.8. The scheme of the computational domain 97
Figure 2.9. Average particle elevation as a function of time for different particle diameters layer thicknesses 98
Figure 2.10. Computational domain 98
Figure 2.11. Ratio between the local dust concentration and the nominal dust concentration 99

Figure 2.12. Temporal trend of the root mean square velocity 99
Figure 2.13. Velocity distribution of the simulated cyclone at different sections 100
Figure 2.14. Temporal stratification of 20 µm particles in a ventilated room 101
Figure 2.15. Flow domain of the wind tunnel and comparisons of the non-dimensional concentrations predicted by the CFD and the Gaussian models of 3 stability classes. 102
Figure 3.1. Scanning electron microscopy of micrometric aluminum 121
Figure 3.2. Adsorption isotherm of aluminum at 25°C 121
Figure 3.3 Initial particle size distribution of the micrometric aluminum samples 122
Figure 3.4. Scanning electron microscopy of micrometric wheat starch 123
Figure 3.5. Initial particle size distribution of the micrometric wheat starch samples 124
Figure 3.6. Geldart classification of the aluminum and the micrometric wheat starch according to their initial PSD 127
Figure 3.7. Experimental arrangement of the granulometric analyses 129
Figure 3.8. Experimental arrangement for a digital particle image velocimetry analysis 131
Figure 3.9. Wheat starch dispersion in the 20 L sphere 134
Figure 3.10. Comparison of between an original and a modified image of starch dispersion 135
Figure 3.11. Comparison of the velocity fluctuations estimated with the DCC method and the multi-pass DFT 137
Figure 3.12. Experimental setup for the characterization of the gas flow in the modified Hartmann tube 138
Figure 3.13. Block diagram of the dynamic analysis of the high-speed videos 141
Figure 3.14. Image analysis of the expansion of the balloon 141
Figure 3.15. Projected surface of the balloon during the gas expansion 142
Figure 3.16. Experimental determination of the variation of the volume of the balloon due to the injection of gas. 142
Figure 3.17. Comparison between the pressure of the vessel and the injection point 147
Figure 3.18. Comparison of the gas pressure inside the two control volumes during the air injection 148
Figure 3.19. Gas velocity at the vessel outlet during the air injection 148
Figure 3.20. Pressure and velocity profiles of the air injection at the entrance of the modified Hartmann tube 150
Figure 3.21. Dispersion tubes 151
Figure 3.22. Injection system used for dust dispersion in the 1 m tube 152
Figure 3.23. Set of experiments with the modified Hartmann tube 153
Figure 3.24. Dispersion of Micro-Al 42 dust within the modified Hartmann tube. 154
Figure 3.25. Evolution of the PSD of aluminum micrometric particles during their dispersion. 156
Figure 3.26. Dispersion of the starch micrometric dust with an injection at 7 barg 157
Figure 3.27. Vertical (left) and horizontal (right) velocities versus time in a square tube for 70 dispersions of 78 mg of wheat starch. 158
Figure 3.28. Sensitivity analysis of the injection pressure 159
Figure 3.29. Radial distribution of micrometric wheat starch with different injection pressures. 160
Figure 3.30. Particles size distributions at 10 cm over the nozzle for the different pressure injections. 161
Figure 3.31. Particles size distributions at different heights for an injection at 7 barg. 162
Figure 3.32. Dispersion sphere 163
Figure 3.33. Dahoe nozzle & half spherical nozzle 165
Figure 3.34. Set of experiments with the 20 L sphere 166
Figure 3.35. Experimental setup established for the granulometric analyses and the recording of high-speed videos in the 20 L sphere 168
Figure 3.36. Injection of a combustible dust developed with the standard rebound nozzle 168
Figure 3.37. Evolution of the combustible dust cloud within the 20 L sphere 170
Figure 3.38. Symmetrical rebound nozzle of the 20 L sphere 171

Figure 3.39. Injection of a combustible dust developed with the symmetrical rebound nozzle..... 171
Figure 3.40. Experimental set-up established for the DPIV analyses of the 20 L sphere 172
Figure 3.41. Evolution of the dust cloud in the geometric center of the 20 L sphere 174
Figure 3.42. Velocity components of the gas flow developed within the 20 L sphere an injection of pressurized air at 20 barg..... 175
Figure 3.43. Mean fluctuations of the horizontal component of the gas velocity 176
Figure 3.44. Mean fluctuations of the vertical component of the gas velocity 176
Figure 3.45. Influence of the injection pressure on the gas velocity at the geometric center of the 20 L sphere 178
Figure 3.46. Root-mean-square velocity of the gas flow 179
Figure 3.47. Determination of the decay exponent (n) for the injections performed at 20 barg 180
Figure 3.48. Particle Size Distributions in the 20 L sphere after the injection with different nozzles 182
Figure 3.49. Diameter d_{50} at the geometric center of the sphere 183
Figure 3.50. Influence of the injection pressure on the flammability parameters of wheat starch determined in the 20 L sphere 185
Figure 3.51. Influence of the injection pressure on the flammability parameters of wheat starch determined in the 20 L sphere 186
Figure 3.52. Influence of the injection pressure on the flammability parameters of wheat starch determined in the 20 L sphere 187
Figure 3.53. Variations of the explosivity parameters 188
Figure 3.54. Influence of the velocity field on the variations of the Particle Size Distribution of a dust cloud formed with an injection at 20 barg..... 191
Figure 4.1 Flow domain defined for the modified Hartmann tube..... 202
Figure 4.2. Mesh of the flow domain of the modified Hartmann tube..... 203
Figure 4.3. Boundary conditions of the CFD simulation of the modified Hartmann tube 204
Figure 4.4. Representation of solid particles for the soft-sphere collision model 210
Figure 4.5 .Velocity magnitude of the dispersion gas at different heights of the dispersion tube..... 211
Figure 4.6. Mean values of the three components of the velocity field with an injection at 7 barg.... 212
Figure 4.7. Absolute pressure of the dispersion gas at different heights of the dispersion tube 214
Figure 4.8. Turbulent kinetic energy of the dispersion gas at different heights of the dispersion tube215
Figure 4.9. Dynamic pressure of the gas flow at 60 ms of dust dispersion..... 217
Figure 4.10 Distribution of the wheat starch dust cloud in the modified Hartmann tube 218
Figure 4.11. Evolution of the turbulent kinetic energy in the modified Hartmann tube at different injection pressures 220
Figure 4.12. Dust concentration in the modified Hartmann tube at different injection pressures..... 222
Figure 4.13. Aluminum concentration at different heights inside the modified Hartmann tube..... 223
Figure 4.14. Mean diameter of 'Micro-Al 42' at the ignition sources location during the dispersion process..... 224
Figure 4.15. Flow domains of the modified 20 L sphere 226
Figure 4.16. Representation of the standard rebound nozzle in the flow domain 227
Figure 4.17. Flow domains of the modified sphere with the symmetric nozzle..... 227
Figure 4.18. Representation of the standard rebound nozzle in the flow domain 228
Figure 4.19. Implementation of the polyhedral cells method on the geometry of the 20 L sphere..... 228
Figure 4.20. Mesh of the flow domain of the 20 L sphere with the standard rebound nozzle 229
Figure 4.21. Mesh of the flow domain of the 20 L sphere with the symmetric nozzle 230
Figure 4.22. Initial and boundary conditions defined for the simulation of the dispersion process in the 20 L sphere..... 232
Figure 4.23. Velocity magnitude of the gas flow with an injection performed with the standard rebound nozzle 234
Figure 4.24. Velocity magnitude of the gas flow with an injection performed with the symmetric nozzle 235

Figure 4.25. Distribution of the combustible dust and the gas flow after 10 ms of dust dispersion ... 237
Figure 4.26. Particle size distribution of the combustible dust injected with the standard rebound nozzle ... 238
Figure 4.27. Particle size distribution of the combustible dust injected with the standard rebound nozzle ... 239
Figure 4.28. Mean velocity magnitude in the canister and the dispersion chamber of the 20 L sphere ... 240
Figure 4.29. Velocity magnitude of the gas flow with an injection performed with the standard rebound nozzle ... 241
Figure 4.30. Velocity magnitude of the gas flow with an injection performed with the symmetric nozzle ... 242
Figure 4.31. Comparison of the pressure profiles determined with the CFD simulations and the experimental data obtained with a test check ... 243
Figure 4.32. Mean values of the three components of the velocity field computed in the 20 L sphere ... 244
Figure 4.33. Evolution of the turbulent kinetic energy during the dispersion process ... 245
Figure 4.34. Turbulent kinetic energy of the gas flow with an injection performed with the standard rebound nozzle ... 246
Figure 4.35. Turbulent kinetic energy of the gas flow with an injection performed with the symmetric nozzle ... 247
Figure 4.36. Variations of the dust concentration in a spherical region (diameter: 3 cm) located at the ignition zone of the 20 L sphere ... 248
Figure 4.37. Comparison of the RMS velocity of the solid particles and the RMS of the gas flow determined by Dahoe et al. (2001) at the ignition zone of the 20 L sphere ... 249
Figure 4.38. Representation of the wheat starch agglomerates ... 250
Figure 4.39. Injection zones of the representative particle clumps ... 251
Figure 4.40. Variations of the PSD of the particle clumps injected in the five analyzed points ... 252

LIST OF TABLES

Table 1.1. Determination and application of the main ignitability parameters of a combustible dust .. 14
Table 1.2. Influential variables for the determination of the minimum ignition energy of a dust cloud19
Table 1.3. Determination and application of the main severity parameters 25
Table 1.4. Main specifications of the standard test apparatus to determine the severity parameters of a combustible dust..... 27
Table 1.5. Repeatability and reproducibility levels recommended by the standard ASTM E1226 − 12a for the explosibility parameters determined with the 20 L sphere 30
Table 1.6. Parameters influencing the ignition sensitivity and explosion violence of dust clouds 33
Table 1.7. Fitting parameters for the turbulent stresses in a particle-laden flow..... 42
Table 1.8. Effect of Temperature on Minimum Ignition Energy 47
Table 1.9. Effect of Temperature on Maximum Explosion Pressure Rise and Maximum Rate of Pressure Rise 47
Table 1.10. Issues generated by the setting of certain operating parameters of the standard test methods 50
Table 2.1. Simulation techniques considered for a fluid-solid mixture..... 68
Table 2.2. General description of the main components of the combustible dust cloud..... 77
Table 2.3. Selection of the computational method for the description of a combustible dust cloud..... 80
Table 2.4. Classification of the RANS turbulence models according to the number of transport equations..... 82
Table 2.5. Subgrid-scale models developed for a LES simulation..... 84
Table 2.6. Summary of some of the physical and chemical processes and properties that may be relevant with regards to dust explosion modeling 104
Table 2.7. Overpressure and maximum rate of pressure rise obtained predicted by a CFD simulation for a maize starch explosion in a silo 105
Table 3.1. Main characteristics of the size distributions of the micrometric aluminum 122
Table 3.2. Technical data sheet of wheat starch..... 124
Table 3.3. Physicochemical properties of wheat starch..... 124
Table 3.4. Comparison of the density values determined experimentally with the values reported in the literature for micrometric wheat starch 125
Table 3.5. Parameters of the Rosin-Rammler size distribution for the analyzed combustible dusts. . 126
Table 3.6. Archimedes number of the combustible dusts 127
Table 3.7. Technical specifications of the Granulometer HELOS/KR 128
Table 3.8. Technical specifications of the continuous wave laser..... 132
Table 3.9. Technical specifications of the 2/2-way Solenoid Valve 146
Table 3.10. Curve fitting of the root-mean-square velocities from 60 to 200 ms in the 20 L sphere.. 180
Table 3.11. Normalization of the factors analyzed in the fractional factorial design..... 185
Table 3.12. Factorial design coefficients determined for the injection nozzle, ignition delay and dust concentration on the wheat starch explosivity parameters 188
Table 3.13. Factorial design coefficients determined for the injection nozzle and ignition delay on the wheat starch explosivity parameters (Fixed nominal concentration: 125 g/m^3)..... 189
Table 3.14. Factorial design coefficients determined for the injection nozzle and ignition delay on the wheat starch explosivity parameters (Fixed nominal concentration: 500 g/m^3)..... 189
Table 4.1. Main features of the mesh of the modified Hartmann tube..... 203
Table 4.2. Control parameters of AMG solver for the CFD simulation..... 208
Table 4.3. Pressure profiles established for the inlet boundary in the sensitivity analysis..... 219
Table 4.4. Commentaries about the modification of the height of the ignition sources..... 225
Table 4.5. Ignition delays recommended for the reduced injection pressures 225

Table 4.6. Parameters of the advancing layer method defined for the meshes of the 20 L sphere 229
Table 4.7. Numerical parameters set to define the solids fragmentation and agglomeration..... 250
Table 4.8. Comparison between the dispersion conditions developed by the standard rebound nozzle and the symmetric injection device 254

INTRODUCTION

The occurrence of dust explosions has become an aspect of major concern in the development of chemical industries that handle different types of solid commodities. For this reason, the storage and manipulation of combustible dusts have envisaged the process safety protocols as one of their priorities. Nevertheless, dust explosions have been an unfortunate part of the continuously growing process industry since 1795 when an explosion in a flour warehouse in Turin, Italy became one of the incidents that generated the first records of this type of incidents (Amyotte & Eckhoff, 2010). Recently, the Chemical Safety Board (CSB) reported that 50 combustible dust accidents led to 29 fatalities and 161 injuries in the United States from 2008 to 2012, the majority of whom has been associated to the food and wood industries. In the same way, the Bureau of Risk Analysis and Industrial Pollution (BARPI in French) registered 110 dust explosions between 1980 and 2005. These major accidents caused 41 deaths and material damage of 37 million of euros approximately (ARIA BARPI).

The protocols of storage, transport and manipulation of fine organic and metallic powders must not only be conceived to avoid their contamination or toxicity effects but also to reduce the eventual risks associated to the generation of ignitable dust-air mixtures. An important contribution for this aspect is accomplished through the determination of the ignitability of combustible dusts and the severity of their explosions at the laboratory scale. In this aspect, the development and standardization of certain flammability tests for the characterization of combustibles dusts have an important role on the definition of the process safety procedures. Therefore, the laboratory-scale representation of a dust cloud produced in a confined environment will allow determining properly the flammability parameters of the solid material.

Previous research studies have shown that the explosibility of a combustible dust differs totally from the explosibility of gases and liquids because of the nature of the solid. In fact the dust-air mixtures are characterized by their heterogeneity and the development of the combustion process by different mechanisms (pyrolysis or surface oxidation) (Gao et al., 2014). Hence, their reproducibility and repeatability are usually considered to be more difficult. This aspect has been evidenced through the variations of the flammability parameters that arise when one of the physical-chemical properties of a dust cloud (e.g. size distribution of the solid phase) is submitted to a significant modification. Nevertheless, the standard flammability tests do not always take into account the changes of the specific properties of a dust sample despite the knowledge of the factors that affect their experimental results. On the contrary, the international normativity has conceived the generation of dust clouds under the same conditions for all types of materials as one of the basis of the standardization of the tests (ASTM E1226 − 12a, 2012).

This fact shows that it is advisable to adapt the operating protocols of the flammability tests according to the characteristics of the sample to accomplish a flammability test that provides the most conservative information about the explosibility of the combustible dust. This condition is necessary due to the remarkable differences of the combustion mechanisms of diverse powders and the development of new materials that are distinguished by their enhanced ignitability (e.g. nanopowders) (Eckhoff, 2012).

The influence of the properties of a combustible dust cloud on the experimental determination of its flammability parameters has been studied with different perspectives. Initially, a literature review showed that some previous studies have focused on the physical and chemical properties of the powder. For instance, the development of a sensitivity analysis on the particle size of a combustible dust established that its ignitability is considerably enhanced when the mean diameter is reduced. This condition is evidenced due to the diminution of the diffusion time in the pyrolysis of organic dusts and the increase of the oxidation surface of metallic dusts. These enhancements of the combustion

mechanisms represent a lower ignition energy for the cloud and also lower dust concentrations to generate its sustained inflammation (Di Benedetto et al., 2010). Similar studies have also considered some additional properties of the combustible dust such as its chemical composition, moisture content, etc. (Abbasi & Abbasi, 2007). These studies have allowed establishing which factors affect positively and negatively the explosibility of a dust.

In the same way, it is possible to find other studies that have focused on the conditions of the dispersion gas that affect the ignitability of the mixture and the propagation of the generated flame. For instance, diverse experimental analyses have described the evolution of the turbulence of a dust cloud by developing anemometry (Dahoe et al, 2001) and high-speed videos (Du et al., 2015). The conclusions of these studies have contributed notably to the standardization of the flammability tests since they have provided an insight into the ascertainment of the most conservative conditions to determine the explosibility of the dust. Likewise, the research work that has focused on the dispersion media has also established how other physical-chemical properties, such as its chemical composition can interact with the dispersed phase. Their results have allowed identifying the case studies that constituted new research areas such as the study of hybrid mixtures (Dufaud et al., 2009; Kosinski et al., 2013) or inerting processes (Eckhoff, 2004) and even recent works focused on the characterization of the dispersion of nanometric powders (Bouillard et al., 2010; Murillo et al., 2013).

In spite of the deeper knowledge about the combustion process of a dust cloud and its mechanisms, there are some limitations in the characterization tests that are applied on combustible dusts. For instance, the ignition delay and the pressurization of the dispersion gas are not always adapted to the specific needs of the assay. This fact sometimes causes an insufficient agreement between the clouds generated for the laboratory tests and those developed inside the industrial units since their conditions do not correspond. For this reason, the flammability parameters that are determined experimentally are considered only as indications for design of process safety measures (Amyotte & Eckhoff, 2010).

In parallel to the studies discussed above, other research areas have delved into the characterization of multiphase flows. The continuous development of new computational resources has provided tools that are capable of representing the interaction mechanisms between a gas and a solid at different scales. This fact has allowed analyzing the behavior of fluid-solid mixtures and their applications in different engineering fields such as rheology, catalysis, chemical process design, etc. These areas have established the influence of the conditions of the cloud on the particle size distribution through the analysis of different phenomena such as fragmentation, agglomeration, sedimentation, among others.

In the particular case of dust explosions, some computational codes have been developed to estimate the consequences associated to an accidental release or explosion of a combustible dust in industrial facilities. Currently these tools represent a good basis for estimation, but do not consider all the mechanisms that affect the explosibility of the dust (Skjold, 2007). This fact poses one of the future trends that will be followed in further studies as the computational resources increase their calculation capabilities.

However, several experimental and computational tools can be considered for the description of the dispersion processes developed at mesoscopic scales. This condition poses the possibility of implementing these approaches on the characterization of the flammability tests in order to reduce their uncertainty levels and envisage their adaptability according to the physical properties the dust cloud. Thereupon, the following question was posed to define the scope of the thesis:

Is it possible to describe the dispersion of a combustible dust within a standard apparatus to define the appropriate operating conditions of a flammability test by taking into account the phenomena that occur in the cloud?

For this purpose, a descriptive study of the dispersion process of a combustible dust is proposed to establish the appropriate operating conditions for the tests in accordance with the interaction

phenomena that cause the variations of the physical properties the dust cloud. Thus, the study presented in this thesis envisages an explanatory analysis directed towards the adaptability of the flammability tests.

The framework of this analysis consists of two complementary approaches, which correspond to the development of a set of descriptive experiments and the subsequent evaluation of the flow variables through Computational Fluid Dynamics (CFD) simulations. For this analysis, the modified Hartmann tube and the 20-L sphere were chosen as case studies because they are two of the most representative explosibility test setups. The dispersion processes evolved within these setups were characterized with two different combustible dusts: aluminum and wheat starch.

This thesis is divided in four different chapters that present the context and scope of this study as well as the descriptive approaches that were considered for this study. Initially, the first chapter presents the experimental parameters and the standardized methods that constitute the quantitative evaluation of the flammability and explosivity of dust clouds. It underlines the factors that determine the results of such test methods and proposes a new approach based on the combination of an experimental description of the dust cloud and a computational characterization of the particle-laden flow developed within the tests apparatuses.

The second chapter is essential to the understanding of the computational approach of this study as it presents the main simulation techniques that can be considered for the description of fluid-solid mixtures. This discussion is defined according to a classification that considers the treatment of the two phases and the length scales of the flow domain. Thereafter, it poses the criteria that were considered to select a simulation technique for this study along with the equations that dictate the behavior of the phases that compose the combustible dust cloud.

Thereafter, the last two chapters of this thesis present the results that were obtained with the two descriptive approaches. The third chapter presents the experimental tests that described the evolution of the dust cloud in the explosion chambers of the standard apparatuses. These tests include the following analyses:

- Visualization of the dispersion process through high-speed videos
- Determination of the variations of the particle size distribution of the combustible dust
- Evaluation of the turbulence levels during the dispersion process

The results obtained with these analyses were complemented with the computational results shown in the fourth chapter. The computational description of the two-phase flow determined the flow variables through the simulation technique that was selected in the second chapter. This representation was also defined according to the operating conditions of the flammability tests in order to predict numerically the trajectories followed by the two phases within the dispersion chambers of the test apparatuses. Thus, this approach established numerically the solids distribution, the velocity fields and the turbulence levels within the test apparatuses in order to determine the influence of the standard operating parameters on the explosibility tests.

Finally, the results obtained with the two approaches were considered to pose a final discussion about the suitability of the parameters fixed by the standards for the characterization of the combustibles dusts considered in these case studies. The results obtained with the two approaches were considered to propose the operating parameters that represent the most favorable conditions (most conservative or relevant with regard to the industrial context) to perform flammability/explosivity tests with the powders that were tested for this study.

REFERENCES

Abbasi, T., & Abbasi, S. A. (2007). Dust explosions–Cases, causes, consequences, and control. *Journal of Hazardous Materials*, *140*(1-2), 7–44.

Amyotte, P. R., & Eckhoff, R. K. (2010). Dust explosion causation, prevention and mitigation: An overview. *Journal of Chemical Health and Safety*, *17*(1), 15–28.

ARIA BARPI. (2006). Base de données du ministère de l'écologie et du développement durable français.

ASTM E1226 − 12a. (2012). Standard Test Method for Pressure and Rate of Pressure Rise for Combustible Dusts. *Annual Book of ASTM Standards*, pp. 1–13.

Bouillard, J., Vignes, A., Dufaud, O., Perrin, L., & Thomas, D. (2010). Ignition and explosion risks of nanopowders. *Journal of Hazardous Materials*, *181*(1-3), 873–880.

Dahoe, A. E., Cant, R. S., Pegg, M. J., & Scarlett, B. (2001). On the transient flow in the 20-liter explosion sphere. *Journal of Loss Prevention in the Process Industries*, *14*(6), 475–487.

Di Benedetto, A., Russo, P., Amyotte, P., & Marchand, N. (2010). Modelling the effect of particle size on dust explosions. *Chemical Engineering Science*, *65*(2), 772–779.

Du, B., Huang, W., Liu, L., Zhang, T., Li, H., Ren, Y., & Wang, H. (2015). Visualization and analysis of dispersion process of combustible dust in a transparent Siwek 20-L chamber. *Journal of Loss Prevention in the Process Industries*, *33*, 213–221.

Dufaud, O., Perrin, L., Traore, M., Chazelet, S., & Thomas, D. (2009). Explosions of vapour/dust hybrid mixtures: A particular class. *Powder Technology*, *190*(1-2), 269–273.

Eckhoff, R. K. (2004). Partial inerting—an additional degree of freedom in dust explosion protection. *Journal of Loss Prevention in the Process Industries*, *17*(3), 187–193.

Eckhoff, R. K. (2012). Does the dust explosion risk increase when moving from μm-particle powders to powders of nm-particles? *Journal of Loss Prevention in the Process Industries*, *25*(3), 448–459.

Gao, W., Mogi, T., Yu, J., Yan, X., Sun, J., & Dobashi, R. (2015). Flame propagation mechanisms in dust explosions. *Journal of Loss Prevention in the Process Industries*, 36, 186–194.

Kosinski, P., Nyheim, R., Asokana, V., & Skjold, T., (2013). Explosions of carbon black and propane hybrid mixtures. *Journal of Loss Prevention in the Process Industries* 26(1), 45–51.

Murillo, C., Dufaud, O., Lopez, O., Perrin, L., Vignes, A., & Muñoz, F., (2013). CFD modelling of nanoparticles dispersion in a dust explosion apparatus, Chemical Engineering Transactions, 31, 889-894.

Skjold, T. (2007). Review of the DESC project. *Journal of Loss Prevention in the Process Industries*, *20*(4-6), 291–302.

CHAPTER I

STANDARDIZED METHODS FOR THE QUANTITATIVE EVALUATION OF THE FLAMMABILITY AND EXPLOSIBILITY OF THE COMBUSTIBLE DUSTS

1.1 DUST EXPLOSIONS

A dust explosion is one of the major hazards that are envisaged in the industrial facilities that handle organic or metallic powders. Indeed, these incidents constitute an aspect of main interest in the development of the process safety protocols in the industry due to the severe consequences that have been associated to this type of incidents. This concern is originated by the presence of several installations that produce, store or process a flammable solid material as a mixture in air (Jaeger, 2001). In fact, the explosion of a combustible dust is a chemical process that is associated to the rapid combustion of flammable particles dispersed in air (Abbasi & Abbasi, 2007). This exothermal process causes a sudden and significant pressure rise when occurring at constant volume (Eckhoff, 2003). The handling procedures of certain grains or metallic powders can represent an explosion hazard if the degree of the subdivision of the dust is high enough to constitute a fast combustion rate and if the dusts are present in such quantities in air that an explosion can occur on ignition. Moreover, some additional elements are also required for the ignition of a combustible dust. These aspects compose the dust explosion hexagon, which will be developed below. The eventual consequences of a dust explosion incident demand the comprehension of the hazards associated to the manipulation of a combustible dust. This procedure can be initially approached by determining the ignitability of the materials and the equipment that are utilized in the industrial plants.

Initially, the term ‘dust’ is commonly attributed to the particulate material that has a particle size distribution under a certain size. This particular size establishes that the particles will settle by sedimentation but they can remain in suspension during a specific time lapse (Petit, 2006). For this reason, the denotation of this word is submitted to diverse interpretations of the threshold values of the particle diameter. For instance, the BS 2955: 1958 defines as ‘powders’ the materials with particle size less than 1000 µm (16 BS mesh size), whereas it refers to particles with a diameter lower than 76 µm (200 BS mesh size) as ‘dust’ (Lees, 2005). On the other hand, the NFPA 68 (2002) establishes that a ‘dust’ is any finely divided solid of 420 µm or less in diameter. This fact constitutes a difference of nearly six orders of magnitude between the two previous references (Abbasi & Abbasi, 2007). This dissimilarity shows the variability on the definition of safety regulations and protocols.

Combustible dusts are characterized through the development of a set of standardized tests that determine their explosibility parameters. These tests envisage the generation and ignition of a dust cloud under fixed conditions. The results obtained with these tests are the basis of the regulations and protocols to manipulate these materials. Moreover, the experimental data of the assays are clearly defined by the mechanisms of the dust explosion, which are determined by the physical and chemical properties of the cloud. The comprehension of the influence of these factors on the experimental results will determine the capability of adapting the standardized tests to the characteristics of the combustible dust.

For this reason, the first chapter of this thesis will present the basic information associated to the characterization of combustible dusts. This review begins with the description of the combustion process of these materials to indicate the elements required for the oxidation of the powder and the dust explosions mechanisms. This fact allows determining the dependency of the chemical reaction on the composition of the powder. Thereafter, the flammability parameters and the standard tests are briefly explained in order to establish the procedures to generate and characterize an explosive gas-solid mixture. Finally, the influence of the physical properties of the cloud on the experimental results of the standardized tests is discussed in order to pose the parameters that will be analyzed in the next chapters.

1.2 THE DUST EXPLOSION HEXAGON

The mixture must satisfy certain conditions to envisage the combustible dust as a hazard besides the degree of subdivision of the particulate material. The conditions shown in Figure 1.1 establish that the dust must be in an environment where the oxidant compound is available in a concentration that is high enough to allow the flame propagation (Eckhoff, 2009a). Additionally, an ignition source is necessary to provide the sufficient energy for the initial combustion of the material. These factors must come together for any combustion process. However, a dust explosion differs from other combustion reactions because it also requires the suspension of the dust in a concentration located in an explosive range. Furthermore, the confinement of the dust cloud is usually considered as a necessary element for the dust explosion. Nevertheless, this characteristic is associated to the severity of the explosion rather than ignitability of the dust. Indeed, an unconfined suspension may ignite but it will only constitute a flash fire whereas a confined explosion may develop a deflagration or even a detonation. It was recently the case in Taiwan, where 498 people were injured by a dust explosion occurred at a recreational water park during an event denominated as “Color Play Asia” (2015). These variations of the dust explosion severity are observed because a partial or complete confinement of the dust/air mixture may result in a rapid development of pressure caused by the heat of combustion of the material. For this reason, Figure 1.1 presents the last element of the fire hexagon in a different way (*).

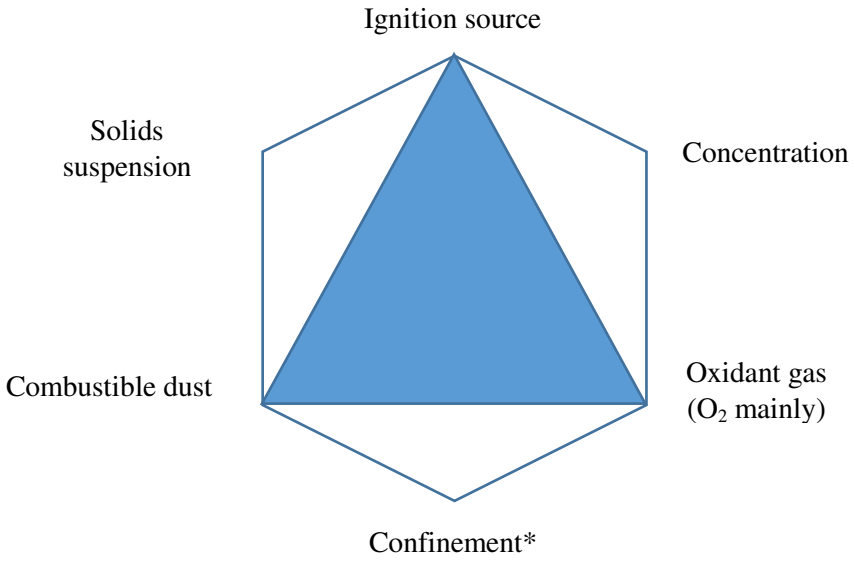

Figure 1.1 Dust explosion hexagon

The fulfillment of the conditions shown in the fire hexagon will establish the flame propagation across the dust cloud and the evolution of large quantities of heat and reaction products (Abbasi & Abbasi, 2007). Thus, the operational conditions and the physicochemical properties of the powder will determine the ignitability of the material and the severity of the explosion.

The development of a dust explosion begins when an appropriate ignition source (hot body, flame, electrical or mechanical spark, etc.) is activated inside the dust-air mixture. Initially, the heat generated by the ignition source provides the energy required to start the combustion process. This is accomplished by the particles located in the vicinity of the ignition point (Proust, 1996). Then, these particles become the ignition source of the adjacent volumes located in the dust cloud. This fact constitutes a combustion zone that propagates in a self-sufficient way as long as the heat generation is greater than the heat losses.

The combustion zone has generally a finite thickness and is called the 'flame'. This region is characterized by the transformation of the 'cold' reactants (dust and air at 300 K for instance) into hot burnt products (1000-1500 K or more). Thus, the fluid that crosses this zone has a drastic change of its specific volume (Proust, 1996). In fact, the expansion of the combustion mixture in the flame front causes a pressure increase that may constitute severe negative effects in the facility where the explosion occurs.

The conditions necessary for the initiation of a combustion process (explosion hexagon) are accomplished in diverse vessels and units such as mills, grinders, and dryers (Amyotte & Eckhoff, 2010). In fact, these incidents are usually defined as primary explosions because they usually result in a subsequent incident which can be external to the process unit. A secondary explosion is initiated due to the lifting of dust layers that is caused by the blast waves arising from a primary explosion. Moreover, Amyotte & Eckhoff (2010) also posed that these explosions might also occur in places where an energetic disturbance disperses the dust that is layered on the floor and the work surfaces. For instance, the coal dust explosions that have been triggered by a previous methane explosion are well-documented in the underground coal mining industry. This fact shows the relevance of considering the amount of combustible that can be dispersed by any aerodynamic disturbance in some industrial installations as well as in test vessels.

1.3 MECHANISMS OF DUST EXPLOSIONS

A multi-phase reactive system that develops a dust explosion is submitted to complex phenomena, which are characterized by the simultaneous momentum, energy, and mass transport. In fact, the characteristics of this combustion process pose certain similarities and differences with respect to the combustion of premixed gases. For this reason, the extent of similarity between these two cases has been discussed to determine if the concepts and tools that are currently considered for studying explosions involving gases can be considered for the characterization of dust explosions as well (Abbasi & Abbasi, 2007).

Eckhoff (2006) has posed the characteristics of the explosive dust clouds that behave in a manner similar to explosive gas mixtures:

- ✓ Existence of flammability/explosibility limits.
- ✓ Links between the laminar burning velocities and quenching distances.
- ✓ The response of the burning velocity to cloud turbulence.
- ✓ Possibility of detonation phenomena.
- ✓ Adiabatic constant-volume explosion pressures of similar magnitudes.
- ✓ Well-defined minimum ignition energies and minimum ignition temperatures for given experimental conditions.

However, the explosions of dusts and gases differ in two general aspects that represent an important variation in the specification of safety standards. Firstly, the physics of generation and suspension of dust clouds and premixed gas/vapor clouds are substantially different (Abbasi & Abbasi, 2007). For this reason, some situations that can produce accidental explosive gas clouds quite readily may not

produce an explosive dust cloud. The second difference lies on the flame propagation in dust/air mixtures. This characteristic is not strictly limited to the flammable dust concentration range of dynamic clouds. In fact, the settled powders will always have some air trapped in the voids between the particles. Thus, the state of stagnant layers/deposits offers an additional discrete ignition possibility. Hence a revision of the existing European Directives 94/9/EC and 1999/92/EC is necessary to clarify important basic differences between dusts and gases/vapors (Eckhoff, 2006).

Evidently, these general dissimilarities are determined by the specific differences that are linked to the dispersion process, the transport phenomena associated to it and the reaction mechanisms. For instance, the inertial forces can produce fuel concentration gradients in the dust/air mixture due to the difference between the densities of the particle and fluid. This fact represents a displacement of particles with respect to the gas phase. Furthermore, the thermal radiation originated during a dust explosion may contribute significantly to the heat transfer from the flame to the unburnt cloud, depending on the type of particle material (e.g. light metals). Additionally, the turbulent combustion of premixed gases and dust clouds also poses a difference in the way their burning rates respond to turbulence. Indeed, flame quenching phenomena can be evidenced when there is a centrifugal separation of dust and air in the turbulent eddies (Rzal & Veyssiere, 1994). Nevertheless, some enhancement mechanisms can also be identified such as the efficient replacement of gaseous reaction products by fresh air round each particle (Abbasi & Abbasi, 2007).

These are just some of the characteristics that constitute the differences between the evolution of the flames developed by a combustible fluid and an explosive dust. Nevertheless, these conditions pose a basis for the description of the flame propagations that correspond to every particular case.

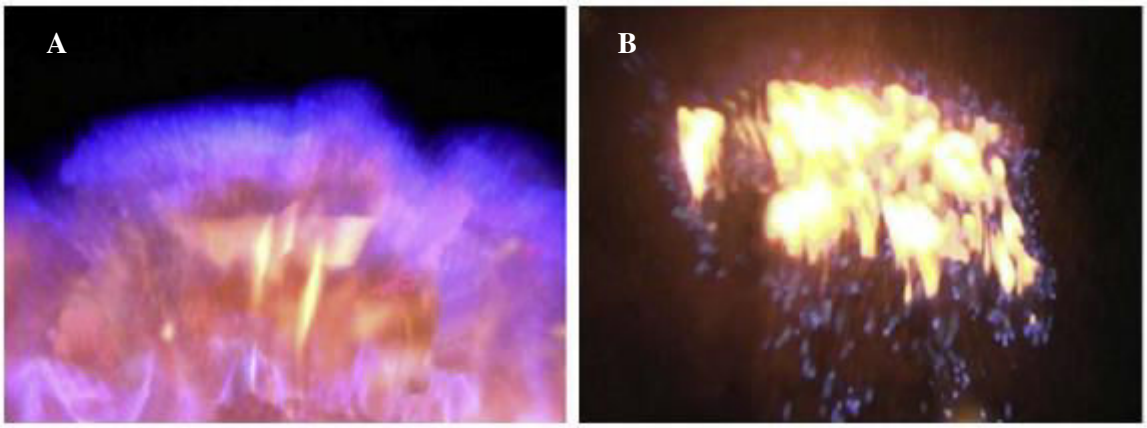

Figure 1.2. Flames developed by 2 combustible compounds of different nature (Gao et al., 2014)
A. Combustible fluid: Methanol (CH_3OH) B. Combustible dust: Eicosanol ($C_{20}H_{41}OH$)

Figure 1.2 poses a direct comparison between the flame fronts constituted by a combustible fluid (methanol) and a combustible dust (eicosanol). The first front is smooth in shape and has a blue profile that can be clearly defined. On the contrary, the structure defined by the flame of a flammable solid is much more complex. The flame front consisted of various zones formed by blue spots at the leading zone and luminous flames behind them. These spots were associated by Gao et al. (2014) to the burning of larger particles or gaseous lumps of materials that were produced by their evaporation/pyrolysis. This condition poses that all the droplets of this alcohol were pyrolyzed or evaporated before the flame front passed through. Therefore, it is possible to identify some variations of the fuel equivalence ratio in the different zones of the flame fronts.

1.3.1 Kinetic mechanisms of dust combustion

The classification of the dust explosions can be associated to the mechanisms that are established by the nature of the dust as well. Indeed, the mechanism of flame propagation for many dusts can be classified in two main different groups. The first category corresponds to the materials that are characterized by the combustion of flammable gases emitted by particles heated to the point of vaporization or pyrolysis (Dufaud et al., 2012; Eckhoff, 2003; Petit, 2006). Additionally, some other dusts can propagate a flame through a direct oxidation process developed at the particle surface (Cashdollar, 2000). The former is commonly associated to the combustion of organic dusts, which are made of vaporizable substances (volatile flames) and the latter is linked to the oxidation of metallic dusts or graphite (Nusselt-type flames).

The majority of the accidents have been associated to the volatile flames due to the widespread use organic compounds in various industries. Figure 1.3 describes the distribution of the events associated to a dust explosion that were reported in North America in 2004 (Stahl, 2004). This chart shows that the activities that are more prone to a dust explosion include notably branches of the food and wood processing industries, paper, synthetics production, and pharmaceuticals production.

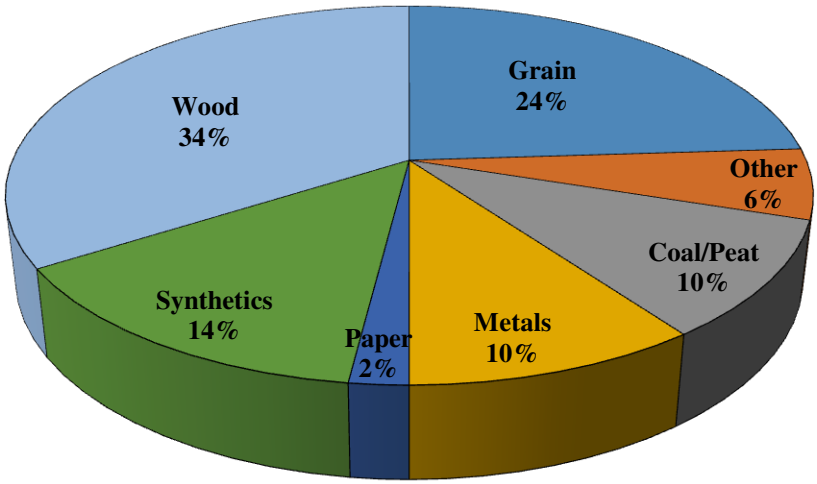

Figure 1.3. Types of dusts involved in dust explosions (Stahl, 2004)

The explosion of an organic dust can be divided into three phases: the particle heating; its devolatilization (pyrolysis) and the oxidation of the pyrolysis gases. In fact, the heating and the pyrolysis steps are very fast for particles having small diameters (generally < 30µm) (Di Benedetto et al., 2010). For these particles, the combustion kinetics can be reduced to the oxidation in the homogeneous gas phase (Dufaud et al., 2012). On the other hand, the devolatilization of the solid particles becomes the rate-controlling factor at high dust loadings, for large particle sizes or for refractory powders.

Previously, Dufaud et al. (2012) established the influence of the pyrolysis step on the kinetics of the combustion of the micrometric starch. For this purpose, their study determined the explosive behavior of the organic powder and a mixture composed by the gases that are released during the pyrolysis phase. The experimental results did not evidence a significant difference between the maximum pressures that were achieved by the two comparative tests. Indeed, the maximum overpressures were 7.5 bar and 8.5 for the gases and the starch respectively. This similarity is attributed to the thermodynamic characteristics of the combustion of each mixture. Nevertheless, a predominance of the pyrolysis phase on the combustion kinetics was observed when the experimental results showed that the value of the maximum rate of pressure rise was 2830 $bar \cdot s^{-1}$ for the pyrolysis gases whereas it was lower than 400 $bar \cdot s^{-1}$ for the starch.

Furthermore, some organic dyes are considered to be more reactive than some organic natural dusts such as the starch and the combustible proteins. This condition is evidenced because the reactivity of these materials depends notably on the products that are yielded during the pyrolysis phase. Eckhoff (2003) established that the combustion rate of dusts that devolatilize unsaturated gaseous compounds, which are more reactive, can be more affected by the presence of fine particles in their size distribution. Further details about this dependence will be discussed in section 1.6.1.

Most of the metallic dusts differ from the organic dusts because they do not volatilize or pyrolyze, but melt and burn as discrete entities. In other words, some metal powders such as magnesium and aluminum may vaporize rapidly when subjected to high temperatures and thus react mainly in gaseous phase. These characteristics were also evidenced experimentally by Gao et al. (2014). These authors identified a more complicated structure in the combustion of organic dusts. The flame zone of these dusts are composed by blue spot flames at the leading zone and luminous flames behind them. This arrangement clearly differs from the one of metallic dust clouds, which is defined by the combustion of every entity. This difference can be observed in Figure 1.4:

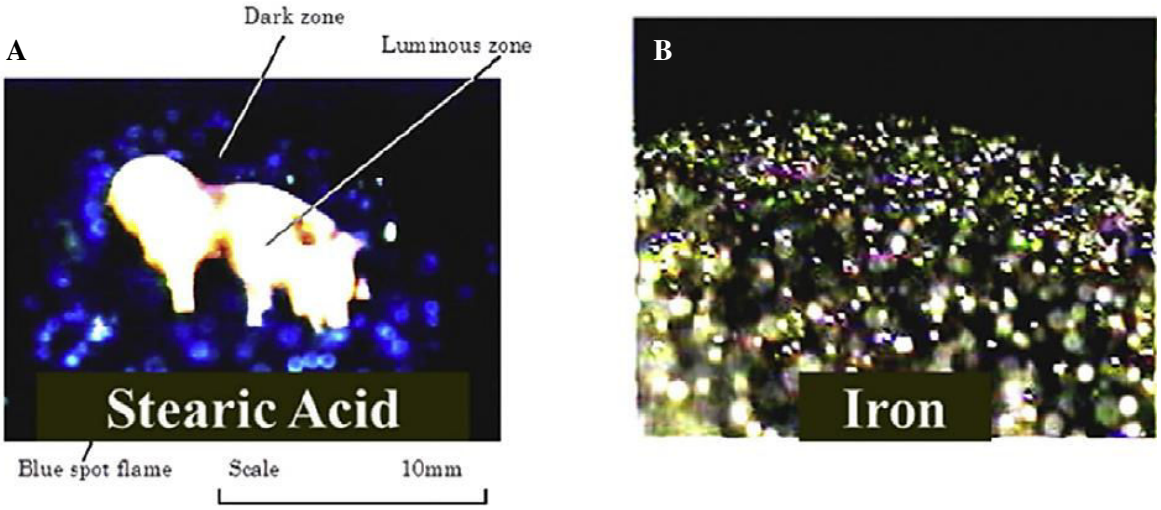

Figure 1.4. Combustion behaviors of different dusts
(Gao et al., 2014)
A) Stearic acid (pyrolysis) B) Iron (Surface oxidation)

Mohan et al. (2009) developed a numerical model for the combustion of aluminum particles that establishes that this chemical process is governed by a combination of heterogeneous and vapor-phase combustion mechanisms. This model determined that there is a critical particle diameter, below which the vapor-phase flame alone cannot be self-sustaining. This condition is attributed to the additional heat that needs to be released by reactions directly on the particle surface to sustain the vapor-phase combustion.

Furthermore, the ignition of most metallic powders requires a spark to remove the oxide surface by causing an electric breakdown on every particle. However, certain metallic dusts do not need it because they have a high surface activity that causes a pyrophoric behavior. This condition defines a rapid oxidation of the dust when exposed to air at room temperature (Murray et al., 1964). For this reason, the ignitability of the solid can be defined as considerably high after considering how the friction of a combustible dust (e.g. zirconium) with the internal walls in a confined flow can result in its ignition at room temperature (Matsuda et al., 2001). This characteristic also explains why some pyrophoric powders can have premature ignitions in the flammability test.

Finally, Eckhoff (2003) posed the variation of the moles of gas in the confined explosion volume as another important difference between the two explosion mechanisms. On the one hand the combustion of a metal dust can cause a greater decrease of the number of total moles of gas in the dust/air mixture than a pyrolysis reaction. This is evidenced because all the reacted oxygen transforms into the corresponding oxide compounds during the chemical reaction. Thus, a reduction of 20% in the number

of moles can be achieved if the gas is air and all the oxygen is consumed. On the other hand, the combustion of organic materials results in an increase of the number of moles of gas due to the generation of some reaction products such as CO_2 (gas) and H_2O (gas) and a lower consumption of the oxygen of the air because a part of it is supplied by the combustible dust. This fact affects the escalation of the adiabatic constant-volume explosion pressure. However, the effect associated to the variation of the number of moles is overshadowed by the temperature augmentation in the burning dust cloud. These elements are highly influenced by the dynamics of the explosive mixture and the segregation of the powder, which also determine the efficiency of the transport phenomena, the formation of char particles and the partial combustion of the dust.

1.3.2 Deflagrations and detonations in dust explosions

Previously it was established that the explosion of a combustible dust can result in a detonation or a deflagration according to the confinement level of the mixture. This condition determines the negative effects according to the characteristics of the flame front developed during the explosion. In fact, the explosion will correspond to a deflagration if the front propagates below the speed of sound in the unreacted gases. On the contrary, when the flame velocity is greater than the speed of sound is known as detonation. This severe explosion is defined by a strong pressure wave, which causes the compression of the unreacted mixture above its autoignition temperature. At this point, the ignition process is defined by the temperature upstream the front flame and not the heat transfer. This process is very rapid and causes an abrupt pressure change or shock in front of the reaction front (Crowl & Louvar, 2011).

The pressure fronts produced by detonations and deflagrations pose some remarkable differences. On the one hand, a detonation is distinguished by a shock front with an abrupt pressure rise that might reach velocities of the order of 2000 – 3000 m/s (Lees, 2005). For this reason, time duration of a detonation is typically less than 1 ms. On the other hand, a deflagration has a wide flat pressure front that reaches subsonic velocities and does not have an abrupt shock front; hence this front can last many milliseconds (Crowl & Louvar, 2011). Besides, a deflagration usually achieves lower values of the maximum pressure than that obtained after a detonation.

The speed of the flame front developed in a dust explosion is usually comparable with that in gas deflagrations (Lees, 2005). Thus, the combustion of solid compounds is commonly associated to deflagrations rather than detonations. For this type of explosions, the energy from the chemical reaction is assumed to be transferred to the unreacted mixture by heat conduction and molecular diffusion. However, Eckhoff (2003) has discussed certain theories that pose that detonations in dust explosions might be developed due to several factors that might increase the flame speed. For instance, the presence of an explosive charge or similar external means of generating the initial shock may increase the strength of the shock wave. Moreover, Proust (1996) also posed that long canalizations or vessels that have a length/diameter ratio greater than 5 can be submitted to an acceleration phenomenon that might result in a detonation as well. In addition, a rising flame can increase the dust concentration in the reactive zone and stretch its front during the propagation process. This fact might also augment the possibility of a detonation. For these reasons, it is possible to establish that the geometry and conditions of the confined volume can determine if a dust explosion can result in a detonation as occurred with gases.

In the same way, some factors determine the impossibility to produce a detonation with a combustible cloud. For instance, a dust/air mixture that is unconfined has ignition delays that can be at least one order magnitude greater than gas/air mixtures. For this reason, the mass of dispersed dust must be extremely high to provide the energy transfer rate that is necessary for the cloud to constitute a detonation. As discussed above, an unconfined mixture will only constitute a flash fire.

1.4 EXPERIMENTAL DETERMINATION OF THE DUST IGNITABILITY

The chemical composition of a combustible dust allows establishing the mechanism associated to its combustion process. This analysis can provide an insight for the estimation of the effects of an eventual dust explosion. Nevertheless, this analysis is just a preliminary characterization of the dust flammability because some aspects associated to the flow dynamics of a dust cloud must also be considered. For this reason, it is necessary to perform a set of laboratory tests that determine the minimum requirements that must be fulfilled to ignite a combustible dust-air mixture. The experimental results of these tests constitute an assessment of the ignitability of the dust by taking into account the elements that compose the fire hexagon.

The sensitivity for dust ignition is an important aspect for the design of the industrial process equipment that is exposed to explosible atmospheres. With regard to the dissimilarities that were described in section 1.3 for the combustion of dust and gases, the interpretation of the flammability parameters must be different from the data of a combustible gas. The significant differences that are found in the heterogeneity of the mixtures and in the mechanisms of combustion demand the acquisition of the flammability data in a different way. They must be acquired according, not only to the procedures that have been standardized, but also according to the physical characteristics of the dust cloud.

This section briefly describes the main flammability parameters that characterize the ignitability of a combustible dust cloud:

- Minimum ignition temperature of a dust cloud
- Minimum explosible concentration
- Minimum ignition energy
- Minimum oxygen concentration

These ignitability parameters are complemented by the determination of the risk parameters associated to dust layers. The main risk that can be associated to dust layers corresponds to the development of secondary explosions. This condition corresponds to the suspension of a combustible dust that is caused by the turbulence generated by a preliminary explosion. This fact represents an escalation of the negative consequences through the development of a domino effect (Yuan et al., 2016). However, the experimental parameter that is considered to characterize the flammability of settled dusts is the minimum ignition temperature of dust layers. This parameter is envisaged as a basis of the determination of the safe operating conditions of locations of material usage and storage. Further information about this parameter and its relevance for the prevention systems of dust deposits is discussed in the international standard ASTM E2021-09.

1.4.1 MINIMUM IGNITION TEMPERATURE (MIT) OF A DUST CLOUD

Various process units are submitted to the presence of hot surfaces (e.g. furnaces or dryers). In addition, the overheating bearings and other mechanical parts can cause the accidental generation of an undesired hot surface (Eckhoff, 2003). This condition constitutes a potential hazard for an explosible dust cloud when it is generated near this surface. These circumstances demand the determination of the minimum temperature at which a given dust cloud will autoignite in a hot environment. This flammability parameter is determined by dispersing the dust in air heated in a furnace at local atmospheric pressure.

However, the minimum ignition temperature is not an intrinsic parameter for a given dust cloud. It depends on the geometry of the hot surface and the dynamic state of the cloud (Eckhoff, 2003). For instance, the increase of the dust concentration of a cloud poses a higher ignition temperature due to

the increase of the effective heat capacity of the mixture. Moreover, it should be noted that this parameter is also strongly related to the initial turbulence of the cloud because the augmentation of the residence time represents a significant decrease of the MIT (Eckhoff, 2003). Indeed the influence of the test parameters is directly linked to the heat transfer phenomenon. The capability of a combustible dust to reach the ignition temperature is defined by the factors that determine the heat transfer rate as well as the balance between the heat generation and the energy loss in the mixture (Vignes, 2008). For this reason, certain physical properties of the powder such as the particle size distribution must also be considered for the determination of this flammability parameter.

1.4.2 MINIMUM EXPLOSIBLE CONCENTRATION (MEC) AND MINIMUM IGNITION ENERGY (MIE)

These ignitability parameters are usually determined with the same test apparatus under very similar procedures. The conditions of the flammability test establish that some characteristics of the system such as the temperature, pressure and humidity do not differ significantly from the environmental conditions that are usually considered as a reference. Thus, the capability of the dust cloud of initiating and propagating an explosion flame depends on the instantaneous condition of the mixture as well as certain physical properties of the combustible dust.

One of the flammability parameters that assess this characteristic of a combustible dust is its minimum explosible concentration (MEC). This limit value determines the lowest quantity of dust per unit volume that is capable of propagating a deflagration through a well dispersed mixture of the dust and air under the specified conditions of test (ASTM E1515 − 14). This parameter is adopted for the design of process equipment and prevention systems. Indeed, the implementation of the necessary procedures to keep a low dust concentration in fluidization and storage units.

The maximum dust concentration is not usually determined for two important reasons. At first, a high concentration in a dust cloud is not stable for long time periods. This fact is attributed to the agglomeration and sedimentation phenomena that is observed for the disperse particles. These occurrences reduce the current concentration and put the dust cloud within the explosible range of the solid material. For this reason, it is not possible to consider a system with a high load of dust as a safe unit. The second reason relies on the high amount of energy that can be stored by a dispersed solid during the explosion. The experimental evidences observed for various combustible powders pose that the energy balance between the energy released by the chemical reaction and the energy absorbed by the biphasic mixture is affected when there is an overload of the dust. This fact represents a diminution of the severity parameters of the dust and a low capability to propagate an explosion flame. Thus, the maximum explosible concentration is not considered as an important factor for the characterization of a combustible dust.

Furthermore, another parameter that assesses the likelihood of ignition of a dust cloud during the processing and handling is the Minimum Ignition Energy (MIE). This parameter is also used in the industry to evaluate the need for precautions such as explosion prevention systems.

The experimental determination of the MIE is performed in a similar way in which the MEC is obtained. These parameters are ascertained by producing a confined dust cloud that is ignited under controlled conditions with an ignitor whose energy release has been established previously. The ignition source can be defined from different systems according to the purpose of the characterization and the available apparatus. In accordance with this statement, one of the suitable sources arises from the electrical energy discharged from a capacitor. The MIE corresponds to the minimum electrical energy that is sufficient to effect ignition of the most easily ignitable concentration of fuel in air under the specific test conditions (ASTM E2019 − 03).

1.4.3 MINIMUM OXYGEN CONCENTRATION (MOC)

This parameter is also known as Limiting Oxygen Concentration (LOC). It corresponds to the oxygen (oxidant) concentration at the limit of flammability for the worst case (most flammable) fuel concentration. In addition, it can also be defined as the minimum concentration of the oxidant gas that can cause the flame propagation in an atmosphere composed by a dust cloud (Amyotte & Eckhoff, 2010). The knowledge of MOC is needed for safe operation of some chemical processes. This information may be needed in order to start up, shut down or operate a process while avoiding the creation of flammable dust-gas atmospheres therein, or to pneumatically transport materials safely. For this purpose, NFPA 69 provides guidance for the practical use of MOC data, including the appropriate safety margin to use.

The minimum oxygen concentration of combustible dust cloud constitutes an important aspect in the determination of the inerting levels that are usually considered for a process unit. Eckhoff (2004) posed the possibility to implement an evacuation system to reduce the concentration of the oxidant gas in the process equipment. Hence, this system can become an integral part of a combined solution to dust explosion protection technique (venting, automatic suppression, full confinement).

The direct influence of the percentage of O_2 on the other flammability parameters has been discussed by Eckhoff (2004). This author affirmed that both the ignition sensitivity and the explosion violence of the dust cloud are reduced when the oxygen content of the atmosphere is reduced by mixing inert gas with the air within the test apparatus. For this purpose, nitrogen is commonly used because other gases (e.g. carbon dioxide) might react with some metals such as aluminum, magnesium, titanium and zirconium (ASTM E2931 − 13).

This advantageous reduction of the severity of a dust explosion allows reducing the vent area of a specific enclosure. This fact is due to the decrease of the maximum pressure that is achieved when the oxygen concentration is diminished. In fact, the experiments discussed by Eckhoff (2004) pose that a diminution of the oxygen content from 21% to 18% and 16% reduced the required vent areas by factors of 0.6 and 0.37 respectively. However, it should be underlined that the efficiency of the inerting process greatly depends on the nature of the gas.

1.4.4 INTERNATIONAL STANDARDS

The standardized methods are envisaged to describe the properties of flammable materials in response to heat and flame under the conditions but not under actual fire conditions. Nevertheless, these standards take into account all the factors associated to the assessment of a fire hazard and can be used as elements of a fire risk assessment. The experimental data obtained with these tests can be of value in determining safe operating conditions in industrial plants, mines, manufacturing processes, locations of material usage and storage and more generally in choosing adequate prevention and protection barriers. Table 1.1 lists the experimental methods that are currently accepted as the standard tests to determine the ignitability parameters of a combustible dust:

Table 1.1. Determination and application of the main ignitability parameters of a combustible dust (Amyotte & Eckhoff, 2010)

PARAMETER	TYPICAL UNITS	DESCRIPTION	EXAMPLE TEST METHODOLOGY	EXAMPLE INDUSTRIAL APPLICATIONS
MIT	K	Minimum autoignition temperature of dust cloud	ASTM E1491-06	Control of process and surface temperatures (dust clouds)
MEC	g/m3	Minimum explosive dust concentration	ASTM E1515-14 EN 14034–3	Control of dust concentrations
MIE	mJ	Minimum ignition energy of dust cloud (electric spark)	ASTM E2019-03 IEC 1241-2-3, 1994	Removal of ignition sources. Grounding and bonding
MOC (LOC)	Volume %	Minimum (or limiting) oxygen concentration in the atmosphere for flame propagation in the dust cloud	ASTM E2931-13 EN 14034–4	Inerting (with inert gas)
MIT OF A DUST LAYER	K	Minimum temperature at which a dust layer will self-heat.	ASTM E2021 – 09 IEC 1241-2-1	Control of process and surface temperatures (dust layers)

The standard test methods suggest performing the flammability tests with as-received samples for the proper characterization of a process dust stream or deposit. The collection of the dust must guarantee the acquisition of a representative sample. This recommendation arises from the wide range of particle sizes and the well-defined specific moisture content that can be found in a sample obtained from a process line.

Unfortunately, the characterization of a sample received from a process stream may be prone to a significant variability of the conditions of the dust. The standards try to counterbalance this issue by setting parameters such as the particle size distribution or the powder humidity. For instance, the standard ASTM E1226 − 12a (2012) requires a dust sample whose size distribution is composed in at least 95 % by particles smaller than 200 mesh (75 μm). For this achievement, various procedures such as pulverization or sieving are recommended. Another example lies on the moisture content, the standard ASTM E1491 – 06 requires humidity levels below 10% on the apparatus in order to avoid a high influence of this variable on the experimental results. This condition is recommended because the dry samples usually provide the most conservative parameters of the combustible dusts. However, this is not the case for the chemical compounds that are reactive with water (e.g. metals, which can generate hydrogen by reduction). There are various methods to determine and/or adjust the moisture content of a weighted sample.

Despite of the recommendations posed for the determination of the flammability parameters, there are still several aspects associated to the dynamics of the dust cloud that can also affect the explosibility of the mixture. This is due to the influence of this variable on the physical properties of the suspension and the transport phenomena associated to the combustion process. For this reason, the recommendations posed by the standards might be insufficient for certain cases and a complete description of the mixture dynamics would be necessary as well.

The influence of the dust cloud conditions on the experimental results of the flammability tests will be discussed in detail in Section 1.6. However, this discussion must be preceded by the definition of the test methods that characterize the explosibility of a combustible dust. Thus, the main representative standards will now be presented in order to describe their procedures to determine the ignitability parameters of a combustible dust. Then, the basic principles that are taken into account in these procedures to generate and ignite a combustible dust cloud to determine a specific ignitability parameter are posed through the presentation of the corresponding standard test method. Moreover,

the discussion of the minimum ignition energy also presents the modified Hartmann tube, which is one of the apparatuses that were considered for the analyses of this thesis.

A. *Standard Test Method for Minimum Autoignition Temperature of Dust Clouds (ASTM E1491-06)*

This test method provides a relative measure of dust cloud autoignition temperatures. The experimental data that are obtained with this test are used in conjunction with minimum spark ignition data to evaluate the hazards of grinding and impact sparks in the presence of dust clouds. The test is based on the measurement of the temperature rise during the ignition of a fairly uniform dust cloud. For this purpose, the method envisages the dispersion of a dust sample into the pre-heated chamber of an oven or furnace. This equipment will provide the energy required for the ignition when the sample is dosed. The experimental results correspond to the observation of a flame propagation at the outlet of the equipment.

PROCEDURE:

The procedure of this test is described as follows:

a) *Description of the dust:* Establish the type of dust, source, code numbers and previous history.
b) *Characterization of the dust:* Determine the particle size distribution, moisture and volatile content of the material received. This step must be repeated with the material tested.
c) *Adaptation of the sample:* The sample must be dried, grinded or sieved to achieve the moisture (<10%) and the particle fineness (<75 μm) that are required for the test.
d) *Inspection of the equipment:* The vessel must be cleaned prior to the development of the test in order to remove the dust associated to previous tests.
e) *Preparation of the test:* Set the temperature of the furnace or oven is set at a predetermined value. The recommended weight of the sample for most dusts constitutes an initial test concentration between 300 and 1000 g/m^3.
f) *Development of the test:* Dust is blown into the heated furnace, which is at ambient pressure.
g) *Data acquisition:* Ignition is determined by visual observation of the flame exiting the furnace. If no ignition occurs, the temperature must be increased from 50 to 100°C and the test the must be repeated with the same concentration.
h) *Parameters variation:* If the ignition of the cloud is achieved, the temperature must be lowered in 25°C increments to determine the lowest temperature at which ignition occurs. Afterwards, the highest temperature at which ignition does not occur for this dust concentration must also be established. For this temperature, the concentration will be varied to determine if the ignition is still possible. If an ignition is evidenced, this temperature must be reduced and the test must be repeated.
i) *Report:* Development of the corresponding documentation about the MIT of the samples tested.

EXPERIMENTAL SETUPS:

The standard ASTM E1491 − 06 establishes that the test is carried out in a heated chamber closed with a frangible diaphragm, or flap vent, or a hole open to the atmosphere. This chamber must be insulated and provided with a thermostatically controlled electric heater. Additionally, the chamber must be composed by an access hole for a 25-μm platinum-rhodium thermocouple that is positioned near the center of the furnace to monitor the rapid increase in temperature as the dust cloud ignites. For this reason this element is connected to a recording system with a fast enough response.

The experimental setups that are widely accepted for determination of the MIT of a dust cloud are the following:

- **Godbert-Greenwald Furnace:** It consists on a vertical ceramic tube with a 3.9 cm diameter and 23 cm height that is connected to a 6.4 m of 18-gage nichrome heater wire. The top of the chamber is connected to a reservoir that contains the combustible dust whereas the bottom is open to the atmosphere. The thermocouples installed in the equipment have a relative error of 1% for the temperatures over 500°C and of 3% for temperatures below 300°C. However, the data determined with this apparatus is usually higher than data acquired with the other three setups.

- **BAM Oven:** The setup consists of a horizontal, heat resistant steel container with a hinged flap at the rear. The test procedure is developed in two stages. The container is heated to 600°C and then the heat source is switched off. Afterwards, the temperature starts to fall and the combustible dust is injected with an air blast. Then, the combustion process will develop a flame that can be observed at the rear of the container.

  The horizontal position of the container might constitute the presence of a post-inflammation phenomenon. This condition might be evidenced due to the sedimentation of the dust inside the oven.

- **Bureau of Mines 1.2-L Furnace:** This apparatus consists of a cylinder with a diameter of 10 cm and a height equal to 33 cm. This dispersion chamber is wrapped with a 9.7-m length of 18-gage nichrome heater wire and is covered with a layer of ceramic braided cloth. The system is also composed of a control thermocouple and a monitoring thermocouple.

  The experimental procedure begins by charging the combustible dust into a dispersion receptacle located at the bottom of the apparatus. Then, a solenoid valve is actuated to create an air blast within the dispersion chamber. The ignition of the dust cloud is reported when there is a rupture of the diaphragm that results in a flame exiting from the top of the chamber within a time period of 3 s.

- **Bureau of Mines 6.8-L Furnace:** This design and operation of this equipment are similar with regard to the 1.2-L furnace. The internal dimensions are 19-cm diameter and 44 cm high. It is wrapped with a 24-m length of 12-gage nichrome heater wire. The ignition of the dust cloud differs from the small apparatus because it is reported for a flame observation within a time period of 6 s.

B. ***Standard Test Method for Minimum Explosible Concentration of Combustible Dusts (ASTM E1515-14)***

EUROPEAN STANDARD: CEN/CENELEC EN 14034–3

This test method covers the determination of the minimum concentration (MEC) of a dust-air mixture that will propagate a dust explosion in a near-spherical closed vessel of 20 L or greater volume. Additionally, the results of this test determine the deflagration characteristics of the dust cloud. The MEC should be considered as a relative rather than absolute measurement because the experimental data vary with the uniformity of the dust dispersion, energy of the ignitor, and the propagation criteria. Therefore, the development of this test usually relies on the homogeneity assumption of the dust cloud.

The test envisages the formation of a dust cloud in a closed combustion chamber by the introduction of a solid sample with air. Then, the ignition of the mixture is attempted by activating an ignition

source located near the center of the explosion chamber. Thereafter, a pressure time curve is recorded to establish if an ignition is produced.

PROCEDURE:

The experimental procedure that is defined by the international standard ASTM E1515 − 14 is described as follows:

a) *Characterization and preparation of the dust sample:* Steps a) to c) of the procedure to determine of the minimum autoignition temperature.
b) *Inspection of the equipment:* The vessel must be cleaned prior to the development of the test in order to remove the dust associated to previous tests.
c) *Preparation of the test:* The material is charged into the closed vessel (combustion chamber). The test is normally made at atmospheric pressure. Afterwards, an ignition source located at the geometrical center of the vessel.
d) *Development of the test:* The dust sample is dispersed and the ignition source is activated after a specific delay to ignite the dust/air mixture.
e) *Data acquisition:* If the ignition of the dust cloud is evidenced, the pressure time curve is recorded on a suitable piece of equipment. Afterwards, the dust concentration is calculated as the mass of dust divided by the volume of the test chamber.
f) *Parameters variation:* The initial concentration of the dust to be tested must be 100 g/m^3. If this concentration produces a deflagration, the weight of the sample must diminished until no deflagration occurs. On the contrary, the negative tests must be repeated by increasing the concentration in steps of 100 g/m^3 until a deflagration is evidenced. Afterwards, these steps must be reduced for the tests near the MEC.
g) *Report:* Development of the corresponding documentation about the MEC of the samples tested.

EXPERIMENTAL SETUPS:

The equipment consists of a closed steel combustion chamber with an internal volume of at least 20 L. The shape of the combustion chamber must be spherical or cylindrical (with a length to diameter ratio between 1.3:1 and 0.7:1). This vessel should be fabricated with maximum allowable working pressure of at least 15 bars in accordance with the ASME Boiler and Pressure Vessel Code, Section VIII.6. The standard setups that are internationally accepted for the development are the Bureau of Mines 20 L Chamber and the 20 L sphere. These apparatuses are shown in Figure 1.5:

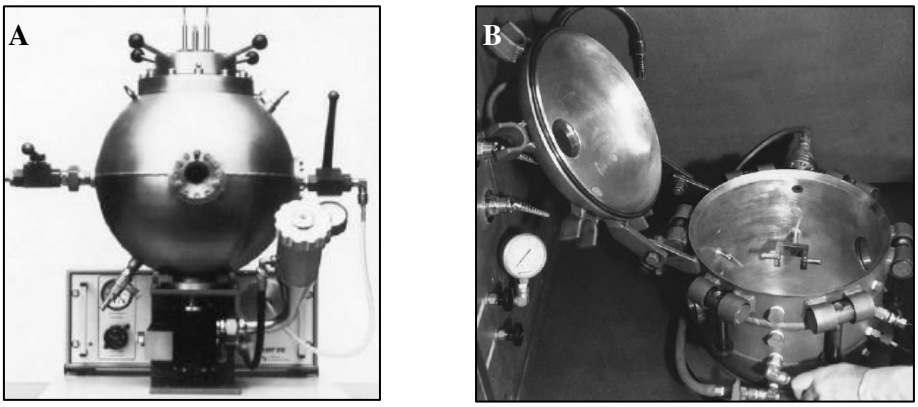

Figure 1.5. Experimental setups for the determination of the minimum explosible concentration of a dust cloud
A) 20 L sphere B) Bureau of Mines 20 L Chamber (ASTM E1515 − 14, 2014; Eckhoff, 2003)

Additionally, each apparatus is composed by the following elements:

- ✓ An injection system that must be capable of dispersing a *fairly uniform dust cloud* of the material. This is usually performed with a perforated nozzle in the 20 L sphere and a spray pipe in the 20 L chamber. However, it is necessary to use special dust dispersers for coarse, voluminous, fibrous or poorly flowing dust samples (prEN 14034, 2004).
- ✓ A pressure transducer and a recording equipment with a combined response rate that is greater than the maximum measured rate of pressure rise.
- ✓ Some optical dust probes are optional. They can be used to monitor the uniformity of the dust dispersion.

C. *Standard Test Method for Minimum Ignition Energy of a Dust Cloud in Air (ASTM E2019-03)*

IEC STANDARD: 1241-2-3, 1994

This test method establishes a procedure for laboratory tests to determine the minimum ignition energy of a dust cloud. The experimental data obtained with this data assess the spark ignitability of a dust cloud. However, this information must not be considered as an intrinsic property of the combustible dust but as a comparison value with regard to the MIE of certain reference dusts. This fact constitutes the comprehension of the relative sensitivity to the spark ignition and represents the basic information required to minimize the probability of explosions caused by an eventual spark.

The experimental apparatus consists of a test chamber, spark electrodes and a spark generation circuit. The test chamber is intended to produce a *uniform, non-turbulent and known density dust cloud* in air at the time of ignition. In accordance with this statement, the assumption of a homogeneous dust cloud is widely considered for the determination of the flammability parameter. There are several dispersion chambers that are currently accepted for the test method. For instance, the clear plastic or glass modified Hartmann tube, typically 0.5 or 1.2 L and the 20 L sphere apparatus have been found suitable for this test method. Moreover, the electrodes are usually constructed in tungsten, stainless steel, brass, or graphite. These elements are installed in a gap of at least 2 mm. This gap is varied according to the ignition energy of the material but it is usually set to 6 mm (ASTM E2019 − 03, 2007).

PROCEDURE:

The experimental procedure that is defined by the international standards is described below:

a) *Characterization and preparation of the dust sample:* Steps a) to c) of the procedure to determine of the minimum autoignition temperature.
b) *Inspection of the equipment:* The vessel must be cleaned prior to the development of the test in order to remove the dust associated to previous tests.
c) *Preparation of the test:* The dust sample is weighted and placed in the reservoir of the test apparatus whereas the ignition sources are placed in the explosion chamber. Then, the system is sealed and evacuated.
d) *Development of the test:* The combustible solid is dispersed with an air injection in the chamber of the laboratory apparatus to form a dust cloud. Then, a spark generated from a charged capacitor after a specific ignition delay. Finally, it is possible to determine if an ignition is produced by visual observation of the flame propagation away from the spark gap.
e) *Data acquisition:* The occurrence and non-occurrence of flame are registered along with the energy discharged by the ignition source (capacitor) into the spark.
f) *Parameters variation:* The procedure is repeated in a sensitivity analysis that varies the dust concentration, the spark discharge energy and optionally the ignition delay to seek the minimum ignition energy.

g) *Report:* Development of the corresponding documentation about the MIT of the samples tested.

Certain factors of the design and operation of the tests apparatus have a direct influence on the experimental determination of the minimum ignition energy. For this reason, the variables that must be considered during the characterization of a combustible dust are listed on Table 1.2:

Table 1.2. Influential variables for the determination of the minimum ignition energy of a dust cloud

CHARACTERISTICS OF THE DUST CLOUD	PARAMETERS SET TO GENERATE THE SPARK
Turbulence and dynamics of the dust cloud **Dust concentration.** **Oxygen concentration**	Voltage to which the capacitor is charged. Capacitance of the discharge circuit capacitor. Inductance of the discharge circuit. Ohmic resistance of the discharge circuit. Materials and dimensions of the electrodes and the gap between the electrodes

The possible fluctuations of the experimental data demand the development of a set of experiments that determines statistically the value of the MIE. This parameter is calculated according to the following expression:

$$MIE = 10^{\left[\log E_2 - I_{[E_2]} \cdot \frac{\log E_2 - \log E_1}{1+(NI+I)_{[E_2]}}\right]} \qquad 1.1$$

Where E_1 is the energy that results in the inflammation of the dust cloud after ten successive tests, E_2 is the lowest ignition energy that produced an inflammation, $I_{[E_2]}$ is the number of tests with an inflammation at E_2 and $(NI+I)_{[E_2]}$ is the total number of tests that were performed at E_2.

EXPERIMENTAL SETUPS:

The setups that are suitable for the determination of the minimum ignition energy are the two apparatuses that were considered for the descriptive analyses of this thesis: the modified Hartmann tube and the 20 L sphere. The first setup is described in this section in order to present its main characteristics whereas the other one will be discussed in Section 1.5.3A because it is also considered to determine the severity parameters of a dust explosion.

The design specifications of the modified Hartmann tube and the procedure of this test method are described in the standards ASTM E789 - 95 and EN 13821. This apparatus consists of a vertical tube with a volume of 1.2 liters coupled to an ignition system. The ignition source installed within the tube can be an electrode with an adaptable inductance on the discharge circuit (1mH – 2mH) or a hot coil (Lees, 2005).

The experimental procedure begins with the placement of a weighted sample of the analyzed material at the bottom of the tube. Afterwards, the sample is dispersed within the vertical tube with the injection of compressed air at 7 barg. Then, the ignition sources are activated after a delay that has been defined prior to the air blast. Finally, the result of occurrence and the ignition energy are registered in order to perform the statistical analysis that was discussed above. The standard ASTM E789 - 95 established that the explosion tests are normally carried out at dust concentrations of 0.1, 0.2, 0.5, 1.0, and 2.0 oz/ft^3 (or kg/m^3).

Figure 1.6. Modified Hartmann tube
(KUHNER Safety, 2015b)

The scheme shown in Figure 1.6 poses the main elements that compose the standardized setup. The pressurized air is stored inside a 50 cm^3 reservoir. Additionally, the system consists of a mushroom-shaped deflector that is installed at the bottom of the vertical tube as the injection nozzle. This device determines the distribution of the gas and the dust within the tube. Although a segregation level is evidenced inside the tube, it is usually assumed that there is a homogeneity condition for the mixture until the activation of the ignition electrodes. This condition may not be valid for all types of dusts due to their different dispersibility levels. For this reason, it is recommended to perform a set of experiments to assess the explosive behavior of the material.

The time elapsed between the initiation of the dispersion procedure and the ignition of the dust cloud (t_v) can be adjusted to take into account the variations attributed to the dust sample. However, this parameter is usually set to 120 milliseconds (ASTM E789 - 95, 2001; KUHNER Safety, 2015b). This parameter can be considered as an important factor for the evolution of the ignition flame; hence it also determines the explosive behavior of the dust and its flammability parameters. This condition arises due to the influence of the initial turbulence of the dust cloud on the physical properties of the mixture and the flame kernel growth. Further details about the influence of this parameter on the explosibility of a dust cloud will be discussed in Section 1.6.2.

D. *Standard Test Method for Limiting Oxygen (Oxidant) Concentration (LOC) of Combustible Dust Clouds (ASTM E2931-13)*

EUROPEAN STANDARD: EN 14034-4

This test method is designed to determine the limiting oxygen concentration of a combustible dust dispersed in a mixture of air and an inert/nonflammable gas. During this test, the proportions of fuel, oxidant gas (oxygen) and inert gas are varied in order to determine the concentrations of the explosibility range of the dust cloud. Then, the LOC is calculated as the average value of the following experimental results:

- ✓ The lower limit is defined as the “worst case” or most flammable fuel concentration range. This value corresponds to the lowest oxygen (oxidant) concentration that causes flame propagation for at least one dust concentration.

- ✓ The upper limit is determined as the highest oxygen (oxidant) concentration for which flame propagation is not possible for the same “worst case” fuel concentration range.

PROCEDURE:

The experimental procedure that is defined by the international standards is described below:

a) *Characterization and preparation of the dust sample:* Steps a) to c) of the procedure to determine of the minimum autoignition temperature.
b) *Inspection of the equipment:* The vessel must be cleaned prior to the development of the test in order to remove the dust associated to previous tests.
c) *Preparation of the test:* The dust sample is weighted and placed in the reservoir of the test apparatus whereas the ignition sources are placed in the explosion chamber. Then, the system is sealed and evacuated.
d) *Development of the test:* The procedure is developed in the same way as the MEC is determined. Moreover, one of the following methods can be implemented to achieve the oxygen concentration specified for the test:

- Pre-Mixed Test Method: The oxidant mixture in the reservoir and the dispersion chamber is preformulated by using different gas cylinders. Thus, the injection of the pressurized gas of the reservoir is only considered for the dust dispersion and for obtaining the desired pressure in the dispersion vessel.

- Test Method with Multiple Volumes of Different Oxidant Concentrations: The oxygen concentration of the dispersion chamber at the time of ignition is calculated from the volume, pressure and oxygen concentration of the residual air volume in the dispersion reservoir, pressurized gas mixture that is added to the dispersion reservoir and the residual air volume in the main test chamber.

e) *Data acquisition:* If the ignition of the dust cloud is evidenced, the pressure time curve is recorded on a suitable piece of equipment. Afterwards, the oxygen concentration is calculated according to the proportions of the gases injected into the chamber.
f) *Parameters variation:* The proportions of dust, oxygen and inert gas are varied until determining the lower and upper limits of oxygen concentration.
g) *Report:* Development of the corresponding documentation about the LOC of the samples tested.

EXPERIMENTAL SETUPS:

The standard ASTM E2931 − 13 establishes that this test is performed at atmospheric pressure and ambient temperature in a nearly spherical closed vessel of 20 L or a greater volume. These apparatuses will be described below for the determination of the minimum explosible concentration in Section 1.5.3.

The determination of the LOC is submitted to the variations of the ignition energy and to the propagation criteria. This condition can be evidenced through the selection of the ignition source. For instance, the utilization of a weak ignitor may result in an overestimation of the LOC that would represent an ignitability limit rather than a flammability limit. For this reason, the ignition energy is increased until the measured LOC is independent of ignition energy. This dependence establishes that the experimental data must be considered a relative rather than an absolute parameter.

Another important aspect that must be considered for this analysis lies on the chemical composition of the diluent gas. For instance, carbon dioxide might react with some metals such as aluminum, magnesium, titanium and zirconium. For this reason, it is advisable to perform the tests of these

materials with nitrogen. Moreover, the presence of impurities such as unburned dust or combustion products of a previous test may affect results as well.

1.5 EXPERIMENTAL DETERMINATION OF THE EXPLOSIVITY OF A DUST CLOUD

The determination of the dust explosibility constitutes an important factor for the design of a process unit that can be subjected to a dust dispersion. Indeed, the information of the severity of a dust explosion constitutes the basis of the design process of the plant equipment and the venting systems. Nevertheless, the vent sizing must envisage the explosibility parameters as a reference and as not absolute parameters. This fact is due to the high influence of the geometric specifications of the unit, which might escalate the explosion pressure or generate quenching effects on the dust explosion. Hence it is possible to find a greater severity in the industrial explosions than that determined as the laboratory test data.

Furthermore, the physical characteristics of the dust-air mixture (particle size distribution, turbulence, etc.) are important factors that define not only the ignitability but also the severity parameters of the dust cloud. This condition is attributed to the influence of these variables on the transport phenomena and the kinetic characteristics of the combustion process. For this reason, the international standards recommend to perform the same procedures that are suggested for the preparation and adaptation of the dust sample in the ignitability test methods.

The equipment that is used to determine of the minimum explosible concentration of a dust cloud is also widely used to establish its severity parameters. Therefore, the operating procedures of these apparatuses are based on the same principles of generation and ignition of a dust cloud. For this reason, the description of the experimental setups of this section is focused on the 20 L sphere, which is one of the test apparatuses that were studied in this thesis. In accordance with this statement, this section presents the specifications of this apparatus along with the following parameters that characterize the severity of a dust explosion:

- Maximum pressure rise.
- Maximum rate of pressure rise.
- Deflagration index

This section is concluded with the presentation of the laminar burning velocity. This property is not considered as a direct severity parameter. However, it is discussed due to the influence of the flame propagation phenomena on the experimental determination of the severity of a combustible dust.

1.5.1 MAXIMUM PRESSURE AND MAXIMUM RATE OF PRESSURE RISE

The deflagration of a combustible dust is characterized at laboratory scale by analyzing the evolution of the pressure that is produced by the ignition of a well-dispersed dust cloud. This analysis evaluates the pressure increase that is produced in a confined test vessel by the impacting shock wave that is generated by an explosion. In this way, it is possible to determine the first two parameters that establish the severity of a dust explosion. The analysis of this information is a deciding factor for the characterization of the performance of its protection system (Bartknecht, 1989) .

Initially, it is possible to determine the maximum pressure (P_{max}) that is achieved by the combustion process. This severity parameter is usually considered for the design of pressure resistant vessels and relief systems such as vents of rupture disks, but it can also be considered for the definition of other

operating parameters such as the equipment isolation or the inerting procedures. This parameter is mainly defined by the thermodynamic properties of the combustible mixture.

The second explosibility parameter that is determined during the course of the flammability test is the maximum rate of pressure rise ($dP/dt_{\max}$). This parameter is mainly associated to the kinetics of the combustion and the evolution of deflagration in the test vessel and is considered for the same purposes than the maximum pressure rise.

Both parameters are defined not only by the physical and chemical properties of the mixture, but also by the other components of the apparatus and the operating conditions of the test (e.g. ignition delay). This condition is due to the balance between the energy that is produced by the chemical reaction and the energy that is transferred by the reactive system to the cooling fluid the test apparatus. Besides, it is also necessary to take into account the effects of the ignition sources in order to correct the experimental results by neglecting the pressure increase that is caused by their activation.

The peak values of the explosion pressure and its rate of increase are obtained for the optimum concentration of the combustible dust. This value is usually unknown; hence the two flammability parameters are determined by a series of tests performed over a large range of concentrations. After determining the maximum rate of pressure increase ($(dP/dt)_{\max}$), this parameter is normalized to a 1.0 m^3 volume with the calculation of a third severity parameter. This additional data is denominated as the deflagration index (K_{St}) and is calculated in accordance with the 'cube-root law'. This law defines a simple relationship that depends on the volume of the vessel to power of 1/3:

$$K_{St} = V_{vessel}^{1/3} \cdot \left(\frac{dP}{dt} \right)_{\max} \qquad 1.2$$

This law is used to scale up the standard test results from laboratory-sized vessels to plant-sized equipment. However, it is continuously controverted because of the inaccuracies that arise when the thickness of the propagation flame is significant with respect to the vessel radius (Dahoe et al., 1996).

1.5.2 LAMINAR BURNING VELOCITY

The analysis of the laminar burning velocity constitutes an important parameter in the characterization of the combustion characteristics of a fuel because it allows predicting the performance and emission of a fuel for a given combustion system (Miao et al., 2014). This property differs from the other severity parameters because it is not considered for the same industrial purposes. However, it constitutes one of the basis to analyze the combustion phenomena. Therefore, it is widely considered to characterize the explosibility of a substance and model its flame propagation in different contexts and scenarios.

The flame speed describes the evolution of the different phases that compose after the ignition of a dust cloud. This description is accomplished by the characterization of the phenomena that constitute the mass and energy transport of the combustion process. Thereupon the comprehension of the flame characteristics and mechanisms at a micrometric scale can pose the direct connection between certain ignitability parameters of the dust cloud and the energy dissipation, which characterizes the severity parameters of the explosion.

The flame propagation can be analyzed from its speed relative to a reference frame (S_f). The flame speed is calculated as the sum of the laminar burning velocity (S_u) and the velocity related to the expansion and buoyancy of the gaseous combustion products (S_g). These two variables are defined by

the specific conditions of the combustible cloud. For instance, the maximum ratio between S_f and S_u is achieved for gases and dusts at the stoichiometric composition under ideal adiabatic conditions (Eckhoff, 2003).

$$S_f = S_u + S_g \tag{1.3}$$

The laminar burning velocity establishes the linear rate at which a laminar combustion wave or reaction zone propagates relative to the unburned gas of a flammable mixture. Thus, it depends on some physical properties of the unburned mixture. The Mallard-le Chatelier theory poses a simple correlation to estimate this velocity according to some physical properties of the gas mixture such as its density (ρ), thermal conductivity (k_g) and specific heat at constant pressure (C_P).

$$S_u = \frac{k_g \left(T_b - T_i\right)}{\rho C_P L \left(T_i - T_u\right)} \tag{1.4}$$

Where T_i is the ignition temperature of the gas mixture, L is the thickness of the reaction zone and T_b and T_u correspond to the temperatures of the burned and unburned zone of the propagation flame. However, this equation only considers the diffusion phenomena. For this reason, more complex approaches have modified this equation to consider the radiation phenomenon and the chemical reaction rate (Eckhoff, 2003).

The flame propagation in a dust cloud differs notably from the one that is observed in a gas explosion. The first difference lies on the Markstein length, which measures the sensitivity of the laminar burning velocity to the influence of flame shape modifications as a deformation parameter. The experimental characterizations of this property determined a more curved profile on the fronts developed by dusts than those generated by gases. For instance, Dahoe et al. (2002) determined experimentally that the Markstein length of cornstarch–air mixtures is much larger than the Markstein length of methane–air mixtures. The non-uniformity of the flame front over its cross section is complemented by the local variations of its burning velocity and thickness. These variables make the characterization of the combustion flame of a dust cloud more difficult since its flames are more difficult to stabilize without causing significant cooling of the flame. (Eckhoff, 2003).

Another distinction lies on the thickness of the reaction zone. This region is considerably thicker in the dust cloud than in the gas. Indeed, it is on the order of at least 10–100 mm according to the combustion mechanisms of the dust. This large span of the thickness is evidenced because the heat transfer by radiation is greater in a Nusselt flame than in a volatile flame. The augmentation of this phenomenon increases the temperature of the unburnt mixture, which might eventually enhance the flame propagation.

This fact poses the influence of the chemical composition of the dust on the transport phenomena in the combustion flame. For instance, metallic powders have a large heat of combustion that establishes a high temperature of the burning particles. For this reason, the heat transfer is clearly defined by the thermal radiation in these particles whereas it is not so relevant for organic particles. This condition causes that a secondary explosion can be induced by the radiation effects of a previously ignited dust cloud of materials such as zirconium and titanium.

Additionally, a Nusselt flame constitutes a heterogeneous reaction, hence it is controlled by diffusion of oxygen to the solid surface. On the contrary, a volatile flame develops a homogeneous reaction that is defined by the rates of gasification, pyrolysis, or devolatilization (Eckhoff, 2003). These facts affect the kinetics of the combustion as well as the diffusion or vaporization rates in the reaction zone. Thus, the influence of the shape and size of the particles must also be considered according to the chemical composition of the dust.

Furthermore, some variations of the burning velocity are due to the heterogeneity of a dust-air mixture and the physical properties of the cloud. The characterization of the combustion process should consider not only the nature of the fuel but also the average size, shape, concentration and distribution of the particles, moisture, oxygen concentration, the initial pressure and the initial turbulence intensity (Gao et al., 2014). These variables become important after considering their effects on the dispersibility of the dust and the heat and mass transport in the different regions that compose the reactive mixture. The aspects discussed above establish that a thorough study of the cloud characteristics is essential to analyze properly dusts flammability. This influence is more important for the severity parameters because they are affected not only by the transient conditions of the cloud prior to the ignition of the cloud but also by the combustion mechanisms developed after it (A. E. Dahoe et al., 2002).

1.5.3 INTERNATIONAL STANDARDS

The test method that determines the explosibility of a dust cloud is widely used to ascertain the degree of explosibility as well. For this reason, these data provide the support information for the specification of prevention systems that are regulated by the norms NFPA 68, NFPA 69, and NFPA 654. The flammability parameters that establish the explosion hazard of dust cloud are characterized by the same standard, which also supports the determination of the minim explosible concentration of the dust cloud. Table 1.3 lists the flammability parameters that establish the severity of a dust explosion as well as their industrial applications:

Table 1.3. Determination and application of the main severity parameters (Amyotte & Eckhoff, 2010)

PARAMETER	TYPICAL UNITS	DESCRIPTION	TEST METHODOLOGY	EXAMPLE APPLICATIONS
Pmax	bar(g)	Maximum explosion pressure in constant volume explosion	ASTM E1226-12a VDI-3673 ISO 6184/1	• Fuel tank venting • Design of pressure resistant vessels • Explosion suppression • Equipment isolation • Partial inerting
$(dP/dt)_{max}$	bar/s	Maximum rate of pressure rise in constant volume explosion	ASTM E1226-12[a] VDI-3673 ISO 6184/1	As per Pmax
Kst	bar·m/s	Volume normalized maximum rate of pressure rise in constant volume explosion	ASTM E1226-12a VDI-3673 ISO 6184/1	As per Pmax
Su	m/s	Rate at which a laminar combustion wave or reaction zone propagates relative to the unburned gas of a flammable mixture	Analysis of stationary and non-stationary flames	• Engine design • Modeling of turbulent combustion • Study of kinetic mechanisms (research)

A. ***Standard Test Method for Explosibility of Dust Clouds (ASTM E1226-12a)***
VDI Standard: VDI-3673
ISO Standard: ISO 6184/1

This test method evaluates the deflagration parameters of dust clouds. The test method envisages the same experimental procedure that was posed for the determination of the minimum explosible concentration of a dust cloud. In accordance with this statement, the formation and ignition of a well-dispersed dust cloud are developed with the same protocol to record the evolution of the pressure of the test apparatus. The only remarkable difference between the two procedures lies on the parameters variation because this method varies the dust concentration in order to determine the maximum pressure and rate of increase. Thus, different notations are defined for the severity parameters determined for a dust concentration and those established for all the concentrations analyzed in the test. For this purpose, the first results are defined with the subscript *m* and the others with the subscript *max.*

The severity parameters of a combustible dust are determined by obtaining a recorded tracing of the pressure of the test vessel (
Figure **1.7**). This profile is characterized by three escalations of the measured variable. The first increase corresponds to the dust dispersion that is initiated by the injection of a pressurized gas. The second pressure augmentation is defined by the combustion of the ignitors and the third one is caused by the dust explosion. The maximum explosion pressure is identified by the maximum peak of the profile, whereas the maximum pressure increase is defined by the maximum slope of the curve in the third escalation. The first and the second increases are separated by the time between the dose of the mixture and the activation of the ignitors (t_v). This time lapse is usually fixed by the international standards and determines the repeatability and reproducibility of the flammability data. The two last augmentations are immediately consecutive and must be differenced to neglect the effects associated to the ignitors.

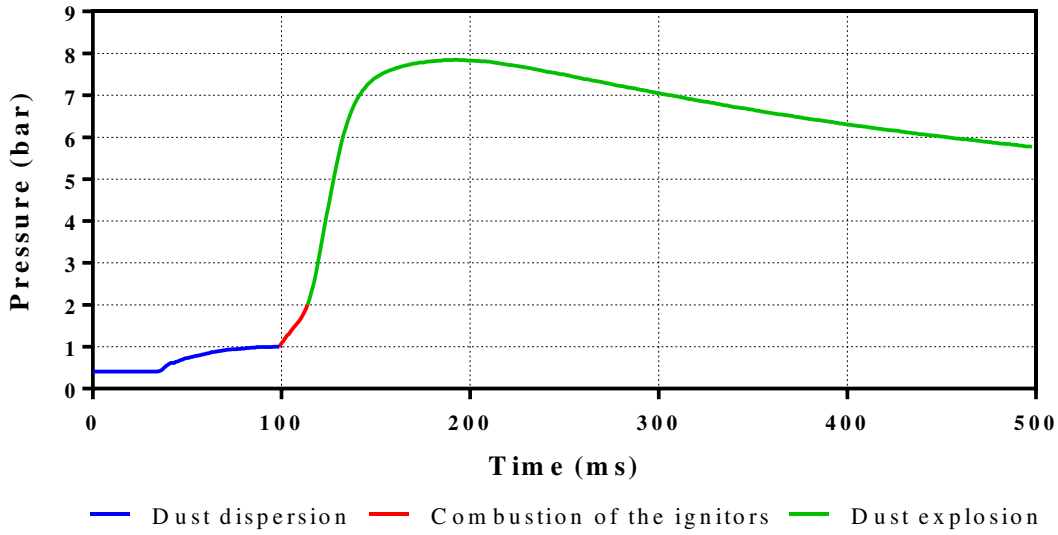

Figure 1.7. Explosion of micrometric wheat starch in the 20 L sphere (Concentration: 500 g/m^3 - t_v: 60 ms)

Furthermore, it is also necessary to determine the dependence of the combustion system on the ignition source. The selection of the energy provided by the ignition source establishes the condition of the flammability test. Thus, the incorrect selection of the ignition source may result in the incorrect estimation of the flammability parameters of the dust. For instance, the utilization of a strong ignitor might associate the severity parameters of a weak deflagration to the energy released by the ignition and not to the dust explosion itself (overdriven system). On the contrary, the implementation of a weak

ignitor may not provide the energy required by the dust cloud and the experimental results would not be representative (under-driven system). The former case is of particular concern with the smaller 20 L vessel whereas the latter is associated to the large test vessels (Going et al., 2000).

EXPERIMENTAL SETUPS:

The equipment recommended for this test method consists of a closed steel combustion chamber with an internal volume of at least 20 L, spherical or cylindrical. The most common apparatuses are the 1 m^3 and the 20 L chambers (Figure 1.8). The 20 L vessel is easier to manipulate because of its dimensions. However, the data obtained with the 1 m^3 vessels are considered to be more representative of industrial scale explosions because they constitute a better reproduction of the phenomena evolved in the industrial units (e.g. stagnant regions) (Going et al., 2000). However, the suitability of the equipment is defined by the dust that is going to be characterized. Indeed, a powder with a low bulk density would require the analysis of solid samples that can occupy a large volume. This fact represents several difficulties to the characterization tests; hence it is more advisable to utilize the 1 m^3 sphere or the 1 m^3 ISO vessel instead of the small apparatus for these particular cases. Nevertheless, some solid materials have a bulk density that is too low even for this equipment.

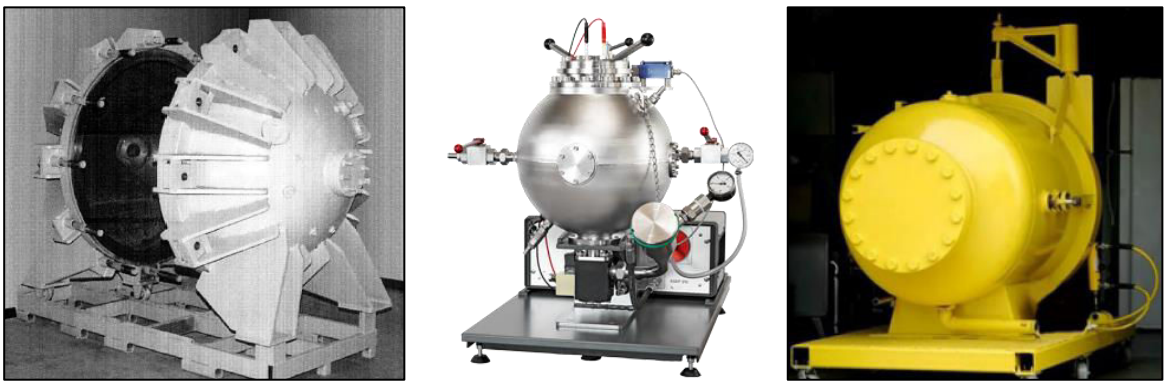

Figure 1.8. Standard apparatuses to determine the explosibility of dust clouds
A) 1-m^3 sphere (Going et al., 2000) B) 20 L apparatus (KUHNER Safety, 2015a)
C) 1 m^3 ISO vessel (Chilworth, 2015)

These standard setups that are used to determine the minimum explosible concentration and the severity parameters of a dust explosion. Therefore, this section presents only the most remarkable differences in the specifications of these apparatuses. These aspects are summarized in Table 1.4:

Table 1.4. Main specifications of the standard test apparatus to determine the severity parameters of a combustible dust
(ASTM E1226 − 12a, 2012; ISO 6184/1, 1985)

PARAMETER	1 m^3 vessels	20 L sphere
Dust storage chamber	5.0 L canister pressurized to 20 barg	0.6 L canister pressurized to 20 barg
Pressurization of the explosion chamber	Atmospheric pressure	0.4 bar
Injection nozzle	Perforated semicircular spray pipe	• Standard rebound nozzle • Perforated annular nozzle
Ignition delay	0.6 s	0.06 s

It is not unusual to find some discrepancies between the flammability parameters determined with the three experimental apparatuses, especially with the 20 L sphere and its equivalent setup of 1 cubic meter. For instance, Proust et al. (2007) established an important conclusion about the behavior of the weakly reactive powders. Indeed, the combustible dusts whose deflagration indexes are determined with a value below 45 bar·m·s^{-1} in the 20 L sphere are totally not explosible in the 1m^3 vessel. This fact remarks an important aspect that was discussed above, which is the preheating of the mixture that is caused by the overdriving effects of the ignitors. Moreover, it is also common to find some dissimilarities in the data scattering of the two test methods. For example, the gap of the maximum pressure rise is usually ±3% in the 20 L sphere and ±5% in the 1 m^3 vessel. This condition is also evidenced with the maximum rate of pressure rise whose gap is ±10% in the small apparatus and ±15% in the large one (Proust et al., 2007). Therefore, it is possible to conclude that the heat and mass transport phenomena are not equivalent in the two apparatuses.

- **Normalization of the experimental data**

The international standards demand the development of a set of experiments to cover a wide range of dust concentrations. This procedure is intended to guarantee the determination of the most severe explosion data. This information must be corrected to take into account the energy transferred with the other elements of the system (ignition sources and cooling jacket). This fact is intended to provide results that can be equivalent to those obtained with the 1 m^3 sphere. For this purpose, the standard ASTM E1226 − 12a poses the corrections of the explosion data that have been obtained with a 20 L apparatus when the measured maximum pressure is superior or inferior to 5.5 bar respectively:

Measured pressure is over 5.5 bar:

$$P_{\max}^{corrected} = 0.775 P_{\max} \tag{1.5}$$

Measured pressure is below 5.5 bar:

$$P_{\max}^{corrected} = 5.5\left(\frac{P_{\max} - E_{ignitors}}{5.5 - E_{ignitors}}\right) \tag{1.6}$$

In spite of these simple relationships, the correspondence between the spherical apparatuses is usually determined by calculating the deflagration index, which is considered as a normalization of the confinement volume. In accordance with this statement, this flammability parameter is widely adopted in the determination of safety protocols. However, the confinement level of explosive mixture affects the speed of the explosion flame. Thus, this simple method might not always be sufficient for the normalization of the volume occupied by the explosive mixture. At this point, it is necessary to remember the influence of the flame propagation on the determination of the flammability data. The validity of the scaling relationship defined by the cube-root law requires the development of the combustion process under two hypothetical circumstances (Skjold, 2003). These conditions are listed below:

- ✓ The mass-burning rate is equal in the test apparatus and the scaled vessel. This is only achieved when both volumes do not have a net flow and are geometrically similar with a small size ratio. This resemblance will establish the same flow conditions and will define the same changes in the pressure, temperature and turbulence in the unburnt mixture.

  In addition, the equality of the burning rates also requires the energy provided by the ignition sources must to be negligible with regard to the energy provided by the dust explosion.

- ✓ The ratio between the flame thickness and the radius of the explosion vessel must be below 1%. A ratio over this value might represents a reduction of the maximum pressure rate due to the geometry of the vessel.

These differences among the test methods show the importance of developing other scaling procedures as well as the necessity of analyzing critically the experimental results that are obtained with every test apparatus. For this reason, the last part of the presentation of the standard test methods is focused only on the description of one of the test apparatuses that were discussed in this section. The setup that was considered for this purpose is the 20 L sphere, which is the equipment that is characterized in the next chapters of this thesis.

- **The 20 L sphere**

The 20 L sphere is a standard setup constructed in stainless steel under a design pressure of 30 bars. This apparatus was designed by Siwek (1988) to characterize the explosibility parameters of combustible dusts and gases. The main components of this setup are shown in Figure 1.9. This vessel is covered with a cooling jacket that dissipates the heat generated by the explosion to maintain a controlled temperature during each test. Besides the 20 L chamber, the system also consists of a dispersion system that is composed by a dust storage canister, a solenoid valve and an injection nozzle. Additionally, two pyrotechnic ignitors (5 kJ each) are located in the geometrical center of the dispersion sphere to constitute the ignition source. These ignitors are activated by a 1-A fuse head and fired in the horizontal plane in opposite directions.

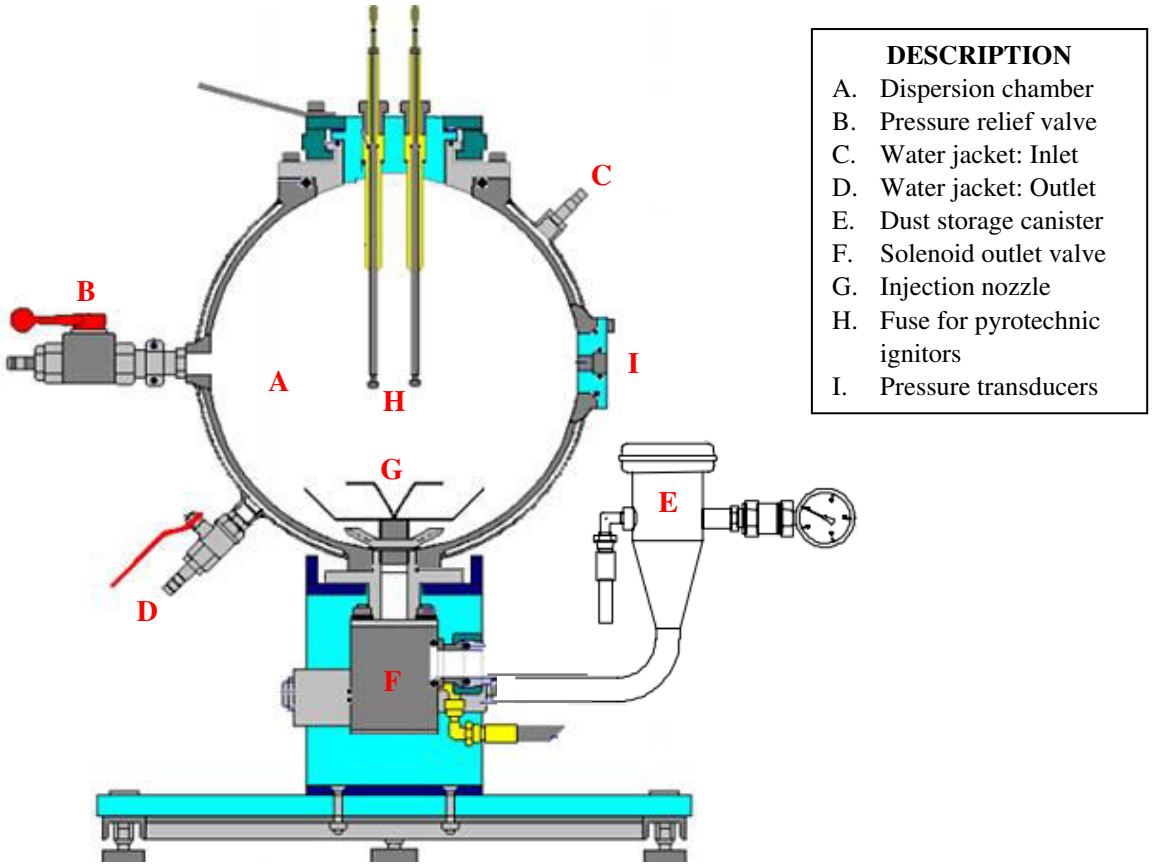

Figure 1.9. Schematic of the 20 L sphere (KUHNER Safety, 2015a)

The internal pressure of the vessel is registered with two pressure transducers that are installed onto the wall of the dispersion chamber. Besides, the sphere is connected to a control unit KSEP 310 12 and a measurement unit KSEP 332. These devices allow controlling the equipment as well as performing

the data acquisition and analysis. These steps are developed with the software KSEP version 6.0f (2003), which is provided by Kühner AG.

The procedure of the test begins with the evacuation of the dispersion chamber down to 0.4 bar absolute. This step is performed in order to achieve a total pressure of 1 bar after the injection of the pressurized gas that is utilized to disperse the combustible dust. Then, the sample of the combustible dust that is going to be characterized is weighted and charged into the storage canister.

Afterwards, the storage canister is pressurized at a total pressure of 20 barg by opening an inlet valve that connects the apparatus to a cylinder that contains the dispersion gas. This gas is usually air, but its composition can be modified for the analysis of the limiting oxygen concentration of the dust cloud. Subsequently, the solenoid valve of the canister is opened to inject the dust-air mixture during a time lapse inferior to 100 milliseconds. This injection produces a two-phase flow that is induced by the pressure gradient between the canister and the dispersion vessel. The flow is distributed within the vessel by a nozzle located at the bottom of the chamber. Further details about the characteristics of the injection nozzle are provided in Sections 1.6.3 and 4.2 of this thesis.

The pressure of the dispersion chamber increases during the injection due to the entry of a finite amount of pressurized gas. This augmentation must range between 0.55 and 0.7 bar. During this period, the conditions of the dust cloud formed by the two-phase flow are submitted to continuous variations that generate different turbulence levels until the activation of the ignition sources. The international standards suggest setting the ignition delay to 60 ± 5 milliseconds. This parameter defines not only the degree of turbulence of the dust cloud but also the local concentration of the powder and some of its physical properties. This condition depends on the confrontation between the turbulence of the cloud and the phenomena of sedimentation and agglomeration that arise when the stresses exerted by the fluid flow are lower than the cohesion forces of the solid phase.

After the dust ignition, the deflagration data are acquired through the analysis of the pressure-time curves that are registered by the transducers installed on the equatorial plane of the vessel. This step is carried out by establishing the peak value of the pressure profile (P_{max}) along with the maximum slope of the curve $(dp/dt)_{max}$ (Figure 1.7).

Finally, the disposal of the gaseous products and the suspended dust and the pressure relief are accomplished by opening an outlet valve. In the meantime, the heat of combustion is dissipated by the double jacket that covers the chamber. Thereafter, the solid dusts that have sedimented or stuck against the walls must be extracted from the apparatus prior to the development of a subsequent test. The test procedure must be repeated several times in order to achieve the reproducibility and repeatability levels that are recommended to report the flammability parameters. The agreement levels suggested for this test are shown in Table 1.5:

Table 1.5. Repeatability and reproducibility levels recommended by the standard ASTM E1226 − 12a for the explosibility parameters determined with the 20 L sphere

PARAMETER	REPRODUCIBILITY	REPEATABILITY
Maximum explosion pressure (P_{max})	10%	5%
Maximum Rate of Pressure Rise ($(dP/dt)_{max}$)	KSt ≤ 50 bar·m/s: 30% KSt ≤ 100 bar·m/s: 20% KSt ≤ 300 bar·m/s: 10%	KSt ≤ 50 bar·m/s: 30% KSt ≤ 100 bar·m/s: 20% KSt ≤ 300 bar·m/s: 10%

The variations that are usually found among the experimental data obtained during the characterization of a combustible dust pose the influence of several parameters of the test. These variables are associated to the design and operation of the apparatus as well the environmental conditions of the laboratory. For this reason, it is necessary to comprehend the evolution of the dust cloud before the activation of the ignition sources. This analysis can envisage the characteristics of the two-phase flow along with the physical properties of the dust. Thus, the influence of the test parameters defined by the international standards on the experimental data of the test methods can be determined.

B. *Experimental determination of the laminar burning velocity*

Andrews & Bradley (1972) discussed the test methods that are widely used for the determination of the laminar burning velocities of combustible dusts. The basic principles that dictate the experimental procedures of these methods are listed in this section in order to present a general overview of the different alternatives.

The following aspects must be considered during the experimental test due to their influence on the burning velocity and reported in the corresponding documentation:

- Experimental procedure
- The chemical composition of the dust and its initial particle size distribution
- Variations of the particle size distribution of the dispersed particles
- Shape variations of irregularly shaped particles
- Fuel concentration
- Oxygen concentration

The experimental procedures can be divided in two categories according to the conditions established to generate a flame (Andrews & Bradley, 1972):

a) Nonstationary flames: These methods consider the movement of the flame through an initially quiescent flame.

- **Tube method:** A combustible mixture is ignited at the end of a tube in order to evaluate the development of the flame along the tube. The burning velocity is determined by tracking the evolving flame by recording high-speed videos in order to identify the variations of the image brightness that are caused by the propagating flame. The flame front formed within the tube is submitted to several changes in its shape due to the influence of the initial turbulence and the internal walls of the tube (Di Benedetto et al., 2011)

- **Contained explosions:** A containing envelope surrounds the explosive mixture. Then, an ignition source is activated at the center of the containment and the propagation of a spherical flame is measured. The tracking methods that can be considered for this flame tracking include, for instance, thermocouples (Sattar et al., 2014), laser Dopper anemometry (Dahoe, 2000) or the inclusion of PIV systems with tracer particles.

  Some interferences are observed near the ignition point due to a reduction of the burning velocity that is caused by curvature of the flame. However, the regions away from the spark are defined by a flame that develops in a one-dimensional plane.

b) Stationary flames: A stream of premixed gas flows into a stationary flame with a velocity equal to the burning velocity. The stability of the flame is achieved by passing the mixture up a tube connected to a burner. Then, the annular space separating the flame from the burner provides a continuous ignition source and anchors the flame.

These methods can determine temperatures lower than the adiabatic flame temperature due to heat losses by radiation and conduction. These losses can be avoided by using burners of large diameters or equipped with walls whose temperature and emissivity profiles match the profiles of the flame (Eckhoff, 2003). The methods available for developing a stationary flame are described as follows:

- **Open circular tube and nozzle methods:** This method defines a conical flame. The geometrical characteristics of the flame are considered to determine the burning velocity of the compound.

- **Flat flame burner methods:** Flow rectification is used to obtain an unburnt gas that flows with a constant velocity profile. The burning velocity is calculated as the ratio between the gas volume flow rate and the flame area.

  The shape of this profile depends on the velocity. Thus, a flat flame develops at short distances above the burner if the velocity is low whereas conical shapes are formed by high gas velocities.

- **Slot burner methods:** This method forms a flat-sided inverted "V" flame by using a long rectangular nozzle. This method increases the probability of wrinkling the flame front but eliminates the effects associated to the flame curvature.

- **Direct measurement of unburnt gas velocity:** These methods consider the same alternatives that were specified for contained explosions.

- **Measurement of flame thrust:** This method envisages the measurement of the pressure drop across a flame. For this purpose, a one-dimensional flow is assumed to develop with no expansion at the outlet of the burner. Thereafter, an estimation of the burning velocity can be obtained from the application of the momentum equation. This method is considered to be highly inaccurate due to its assumptions.

1.6 INFLUENTIAL PARAMETERS

The previous section established that the standard test methods are influenced by several operating factors. These aspects determine not only the applicability of their experimental results but also their correspondence with the flammability data obtained with other standard methods. For this reason, several efforts have been directed to the identification of the main characteristics that must be considered for the development of a flammability test. Table 1.6 presents the main factors that determine the ignitability and severity of a dust explosion (Skjold, 2003). These elements have been classified into two categories according to the nature of their sources, which are associated to the fire hexagon that was discussed above.

Some of these factors are codependent because they constitute the mass and heat transport mechanisms of the combustion process. This fact establishes that there are plenty of combinations that might be observed during the development of a flammability test (Eckhoff, 2003); hence it is necessary to analyze their effects on the experimental results obtained with the standard setups. This section will discuss in detail some of the most relevant characteristics of the dust cloud in order to define the basis of the descriptive analysis that was envisaged for this thesis.

Table 1.6. Parameters influencing the ignition sensitivity and explosion violence of dust clouds (Skjold, 2003)

MATERIAL DEPENDENT PARAMETERS	**COMBUSTIBLE DUST**	Physical properties	-Particle size distribution (Particle surface) -Particle shape and porosity -Oxide layer (metals), fusion enthalpy, vaporization enthalpy, thermal conductivity, density, heat capacity, etc.
		Chemical properties	-Chemical composition and heat of combustion -Inert content -Moisture content -Inert dust content -Volatile components content
	OXIDANT GAS	Physical properties	-Initial pressure and temperature -Transport properties (e.g. viscosity and thermal conductivity)
		Chemical properties	-Chemical composition (inert, oxygen, etc.) -Relative humidity
PROCESS DEPENDENT PARAMETERS	**DUST CLOUD**	Dispersion	-Degree of dispersion -Agglomeration
		Concentration	-Nominal and real dust concentration -Spatial distribution of the particle size in cloud
		Flow conditions	-Turbulence level and velocity field -Temporal and spatial distribution of turbulence
	CONFINEMENT	Degree of confinement	-Explosion developed in a confined volume? -Presence of pressure relief vents (Partially confined)
		Geometry	-Volume and shape -Presence of obstacles (turbulence-generating objects)
		Other factors	-Heat losses through the walls / quenching -Pressure piling -Potential secondary explosions
	INFLAMMATION	Ignition source	-Type of ignition source -Energy (power, duration) -Location and timing of the ignition source

1.6.1 PARTICLE SIZE DISTRIBUTION (PSD)

During the dispersion process, the size distribution of a solid material might present significant variations. This property has a direct effect on the conditions of the dust cloud; hence it can affect the behavior of the mixture during the determination of the explosibility parameters of the dust. This condition is observed because the characteristics of the dust cloud might promote or reduce the presence of fine particles due to the effects of the gas- particle interactions. Therefore, the mass and energy transport phenomena are affected by the dispersion process as well. Evidently, the variations of the transport phenomena that are influenced by the particle size distribution also affect the combustion mechanisms of the solid compounds. For this reason, this parameter becomes a determining factor on the development of the flammability test methods.

This section presents a brief description of the influence of the size distribution on the flammability parameters according to the nature of the combustible dust. The study of this material dependent parameter is usually performed by taking into account the mean size of the dust sample. However, a

detailed analysis should also consider the deviation of PSD in order to consider the different levels of affectation on the flammability parameters.

A. *Influence on organic powders*

An organic powder, which is submitted to a pyrolysis process, will decrease its combustion time when the devolatilization phase is enhanced by a reduction in the particle size. However, this reduction of the combustion time is limited by a critical diameter. The particles with a size below this critical diameter will define the kinetics of the chemical reaction as the determining factor of the combustion rate (Dufaud et al., 2012; Khalili et al., 2012). Thus, a further particle size reduction will not increase the overall combustion rate (Eckhoff, 2009). The size of the critical diameter is defined dust composition and the reactivity of the gaseous pyrolysis products. For instance, the limiting diameter of coal is on the order of 50 µm whereas the starch has a limiting particle size a little smaller than 10 µm (Eckhoff, 2003). This fact is due to the presence of more reactive compounds (e.g. unsaturated gases) that reduce the size of the critical diameter.

An example of this behavior can be considered through the comparison of the MEC of combustible dusts that have different volatiles content. Eckhoff (2003) affirmed that the tendencies of the organic powders show that their minimum explosible concentrations are reduced when the mean particle diameter is smaller. However, the profiles shown in Figure 1.10 also suggest that the reactivity of the pyrolysis products is also defined by the fraction of volatile compounds of the combustible dust. This condition can be illustrated with the comparison of the MEC of polyethylene and coal.

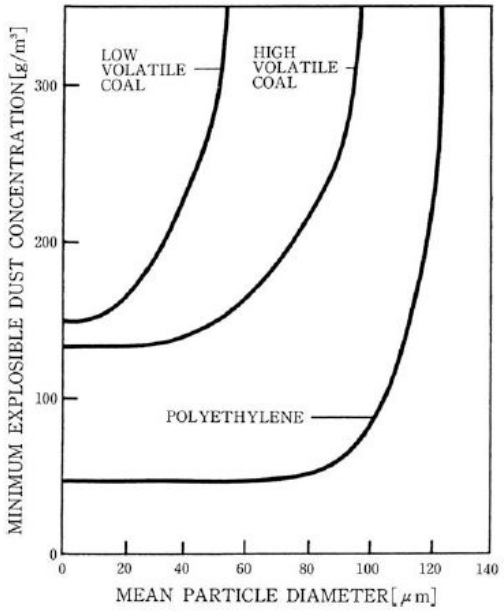

Figure 1.10. Influence of the PSD on the flammability parameters of a combustible dust (Eckhoff, 2003)

The experimental results obtained for polyethylene pose that the ignitability of this dust is higher than that obtained for coal. This condition can be considered because the MEC of the polymer is lower than the MEC of the other combustible dust. A similar comparative analysis between the two compounds shows that the presence of a high volatile content eases the volatilization process. Thus, the restriction of the combustion time that arises when the kinetic rate of the chemical is slower than the devolatilization process is accomplished for a bigger particle diameter. For this reason, the critical diameter of the polymer is bigger than the critical diameter of the other combustible dusts.

B. *Influence on metallic powders*

Many metallic powders such as magnesium and aluminum have a combustion rate enhanced by a particle size decrease. This variation is also limited by a critical diameter. As a matter of fact, the limiting particle size is considerably smaller for metallic dusts than for most organic dusts. This behavior is also evidenced because these materials do not pyrolyze but melt, evaporate, and burn as discrete entities (Dreizin & Hoffmann, 1999). Therefore, the augmentation of their combustion rates is caused by the systematic increase of the surface area (Eckhoff, 2009). The effects of the size distribution on the flammability parameters can be seen in Figure 1.11. This chart presents a comparative study that was posed by Lees (2005) to describe the enhancement of the ignitability and the reduction of the explosion severity of aluminum samples that have smaller size distributions. The experimental results obtained with micrometric aluminum establish that its explosibility is enhanced by the decrease of the particle diameter, except for the minimum explosible concentration. Nevertheless, this behavior also depends on the ratio between the oxide thickness and the particle diameter. For this reason, these tendencies differ from those that are determined for nanometric powders. Further details about these differences will be discussed on Section 1.7.2A.

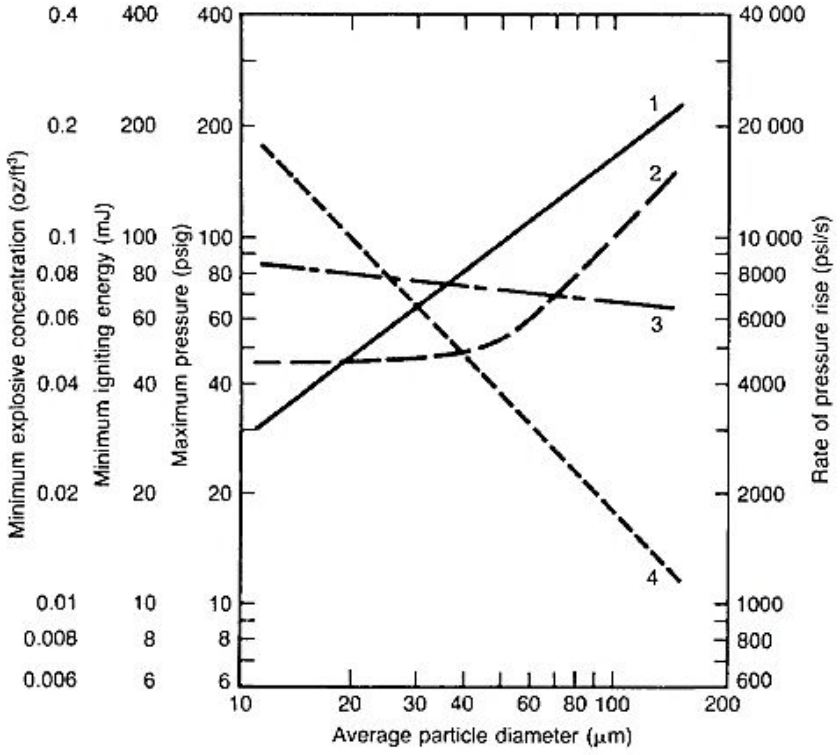

Figure 1.11. Dust explosibility characteristics: effect of particle size on some principal parameters for atomized aluminum
(Lees, 2005)
1) Minimum ignition energy; 2) Minimum explosive concentration;
3) Maximum explosion pressure; 4) Maximum rate of pressure rise

The effects of the chemical composition of the dust can also be illustrated with the augmentation of the flame speed that is caused by a diminution of the particle size. Figure 1.12 shows that the magnesium powder (median particle size of about 33 μm) gave a considerably lower flame speed than the aluminum powder (median particle size of about 9 μm) (Alekseev & Sudakova, 1984). Thereupon the fragmentations levels that can be achieved by a combustible dust during the dispersion process will define the evolution of the reacting mixture.

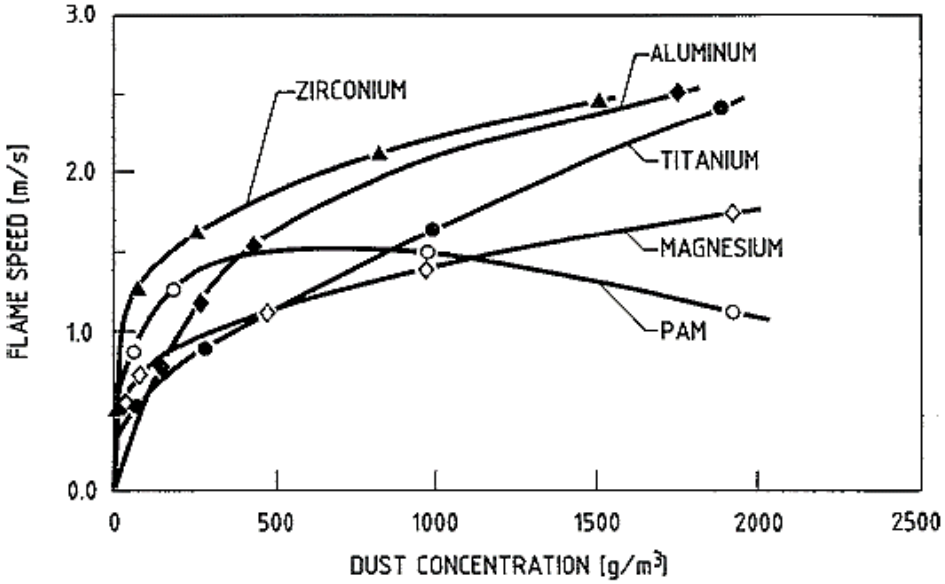

Figure 1.12. Flame speed versus dust concentration in unconfined clouds of metal dusts (Alekseev & Sudakova, 1984)
d_{50} (µm): Zirconium (28.1), aluminum (9.1), titanium (43.6), magnesium (33.2) & PAM (32.0)

Finally, the particle shape and porosity can also have a significant effect on the particle surface area and the reaction rates. Therefore, the dust particle size and shape are of primary importance in regard to dust explosibility characteristics (Cashdollar, 2000). For this reason, the variable considered for different characterization analyses of metallic dusts is the mean surface rather than the corresponding particle size distribution. In accordance with this statement, Figure 1.13 describes the augmentation of the maximum rate of pressure increase that is originated by an increase of the specific surface of aluminum dust.

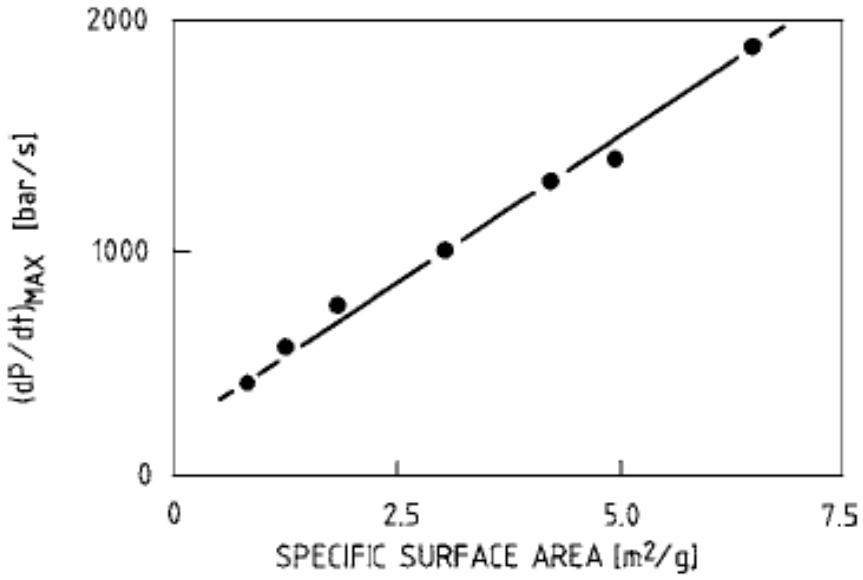

Figure 1.13. Influence of the specific surface area on the maximum pressure rate of aluminum

1.6.2 INITIAL TURBULENCE

The turbulence of the multiphase flow associated to a dust explosion must be considered in two different stages. The first stage envisages the time elapsed between the beginning of the dust dispersion and the ignition of the cloud. The turbulence level of this period is denominated initial or cold turbulence. The second stage considers the flame propagation that occurs after the dust ignition. This period is characterized by the turbulence generated by the explosion itself. During the first stage of turbulence, the flow is characterized by the conditions that are defined for the formation of the dust cloud. In accordance with this statement, the initial turbulence of the flow is defined by the operating parameters of the unit that contains the cloud. Indeed, this variable must be described from the pressurization and arrangement of the injected flow and the geometry of the confinement vessel. This condition is attributed to the influence of the conditions of the fluid flow on the size distribution of the turbulent eddies (Tamanini, 1998).

The effects of the initial turbulence on the flammability parameters of a combustible dust can be evidenced through the analysis of the experimental data obtained at different ignition delays. The test methods carry out the dispersion of the dust with an air blast. This fact creates a two-phase flow from a finite source of kinetic energy. Therefore, the initial turbulence varies for the experiments performed at different ignition delays even if they are carried out in the same vessel with the same dust. Figure 1.14A and Figure 1.14B pose that the explosion violence of a lycopodium explosion decreased as the initial turbulence faded away. The difference observed between the two decreasing profiles can be explained from the different restrictions of the explosibility parameters. The maximum pressure is defined not only by the conditions of the dust cloud but also by the thermodynamic properties of the dust. On the contrary, the rate of pressure rise also depends on the conditions of the mixture but is established according to the kinetics of the chemical reaction and the mass and energy transport as well (Eckhoff, 2003).

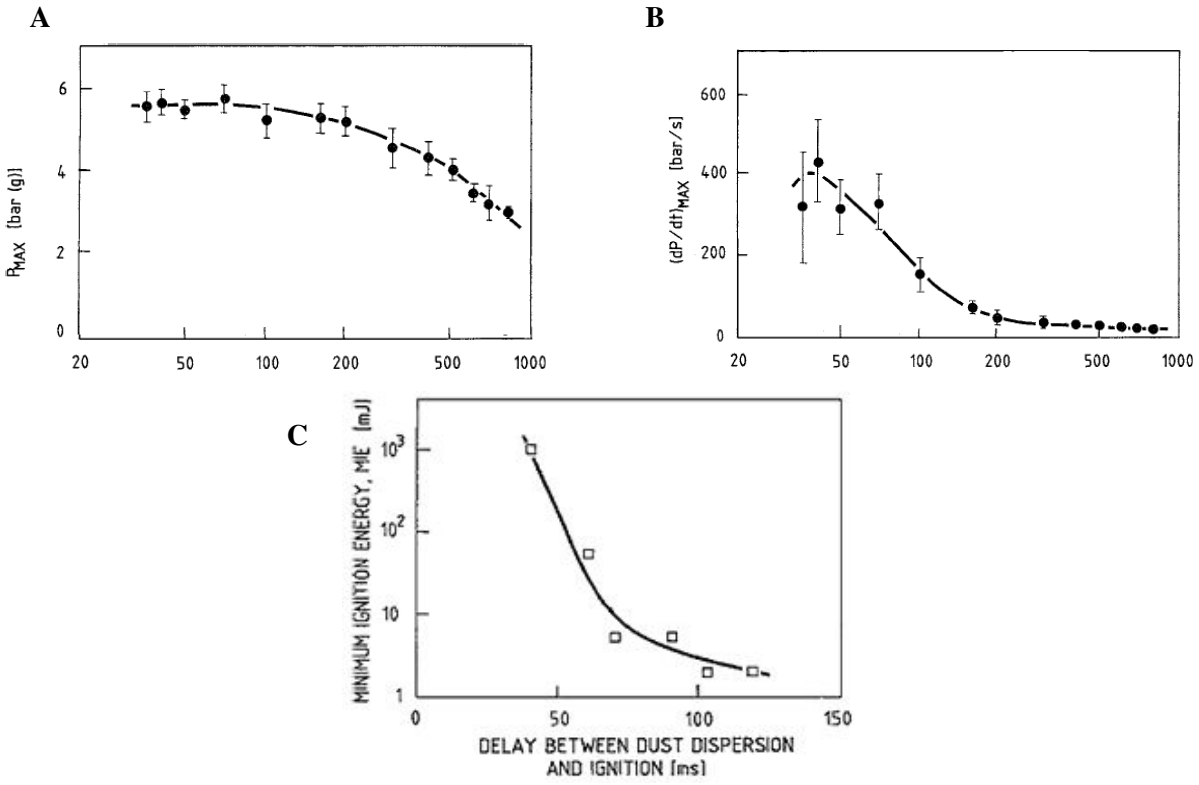

Figure 1.14. Influence of initial turbulence on the flammability parameters of a lycopodium dust cloud (Eckhoff, 2003)
A) Maximum explosion pressure B) Maximum rate of pressure rise C) Minimum ignition energy

Furthermore, a high initial turbulence poses a quenching effect on the ignitability parameters. The ignition of a dust cloud is clearly affected by the flow turbulence because it disturbs the heat transfer by removing heat from the ignition zone (forced convection). In addition, the initial turbulence has a significant effect on the particle size distribution by enhancing the stresses exerted by the fluid flow on the aggregates surface. This variation clearly depends on the physical-chemical properties of the dust sample (e.g. cohesion and particle size distribution). Moreover, eddies formed within the vessel represent a high segregation of the powder in different regions of the containing vessel. This fact calls into question the homogeneity assumption that is considered for the standard test methods. The high levels of the initial turbulence have both enhancing and diminishing effects on the ignitability of the dust cloud. However, the ignition of a turbulent dust cloud generally requires higher energy or temperature than ignition of quiescent clouds (Eckhoff, 2003). An example of this characteristic behavior is shown in Figure 1.14C. This profile poses that the minimum ignition energy of lycopodium must be augmented when the ignition delay is reduced.

These aspects pose the importance of the selection of the ignition delay on the determination of the flammability parameters of the dust. For instance, Dufaud et al. (2012) analyzed the combustion process of starch-air mixtures in the Godbert-Greenwald oven and determined the influence of the ignition delay on the transition from laminar to turbulent flame propagation. Their experimental results determined that for this particular case, the experimental data that were obtained with ignition delays inferior to 250 ms are significantly affected by the initial turbulence intensity.

The second stage of turbulence, which was evoked at the beginning of this section, is considered after the dust ignition. The turbulence level of this stage is established by the explosion itself. The reactive mixture causes the expansion of the unburned dust cloud ahead of the propagating flame. For this reason, the turbulence generation depends on the flow speed and the geometry of the system. Thus, it is necessary to take into account the flame/walls interactions, the existence of obstacles for the flow expansion as well as the presence of long ducts that accelerate the multiphase flow.

During the combustion process, the turbulence favors the mixing of the hot burned and burning parts of the cloud with the unburned parts. This condition constitutes a three-dimensional laminate that alternates the three different zones. As a result of this phenomenon, a turbulent cloud burns much faster than when a single plane flame sheet propagates through a quiescent cloud (Eckhoff, 2003).

The contrary behavior observed between the ignitability and the explosibility parameters establishes the importance of the ignition delay on the experimental results of the flammability tests. Thus, it is necessary to identify the dispersion stage that guarantees the acquisition of the most conservative flammability data. This can be accomplished by considering the aspects and interaction mechanisms that constitute the kinetic energy dissipation of an air blast in a given test method. For this purpose the description of the two-phase flow associated to the dust cloud can be performed by experimental methods as well as computational analyses. In this aspect, a recent research trend has implemented the computational fluid dynamics (CFD) models to take into account the variations of the turbulent field and of the dust concentration through the volume swept by the explosion (Tamanini, 1998).

1.6.3 DUST FRAGMENTATION AND AGGLOMERATION

The previous sections described how the experimental characterization of a combustible dust is affected by the variations of the particle size distribution as well as by the initial turbulence. It appears clearly that both parameters are intertwined and that the influence of the turbulence on the PSD is a subject that has to be addressed before each tests series. Therefore, it is necessary to characterize the constraints that determine the generation and diminution of fine particles in a fluidized powder (Saleh et al., 2014). Moreover, the variations of the velocity field also determine the time periods that favor the lifting and sedimentation of the dust within the vessel.

These variations are produced by the interactions between the phases that compose the two-phase flow. The initial turbulence of the dust cloud determines the segregation level of the dust through the

development of the turbulent eddies. In the same way, it also establishes the solids fragmentation and agglomeration through the collisions and the forces exerted on the surface of the dispersed aggregates. Some of these constraints are discussed in this section in order to pose how the velocity field of the gas flow causes the variations of the number of fine particles in a turbulent dust cloud. The discussion begins with the description of the stresses that are exerted by the fluid phase and concludes with the presentation of the forces that induce the solids agglomeration.

Furthermore, the injection system of the test apparatus is also considered as a determining factor for the variations of the size distribution of the combustible dust that are produced on the powder during the dispersion process. For instance, Sanchirico et al. (2015) developed a comparison test that analyzed the size distributions of different dust samples that were collected from the bottom of the 20 L sphere after being dispersed with the two standard nozzles of the apparatus: the standard rebound nozzle and the perforated ring. A direct comparison of the PSD obtained with the two nozzles with the initial PSD shows that the standard rebound nozzle constitutes a different reduction in the particle size distribution respect to the one that is obtained with the perforated dispersion ring during the dispersion process for several powders. For instance, Figure 1.15A shows that the presence of small particles of ascorbic acid is favored with the rebound nozzle whereas this characteristic is favored with the ring for the nicotinic acid. On the other hand, the behavior of some powders such as the anthraquinone is similar with both nozzles.

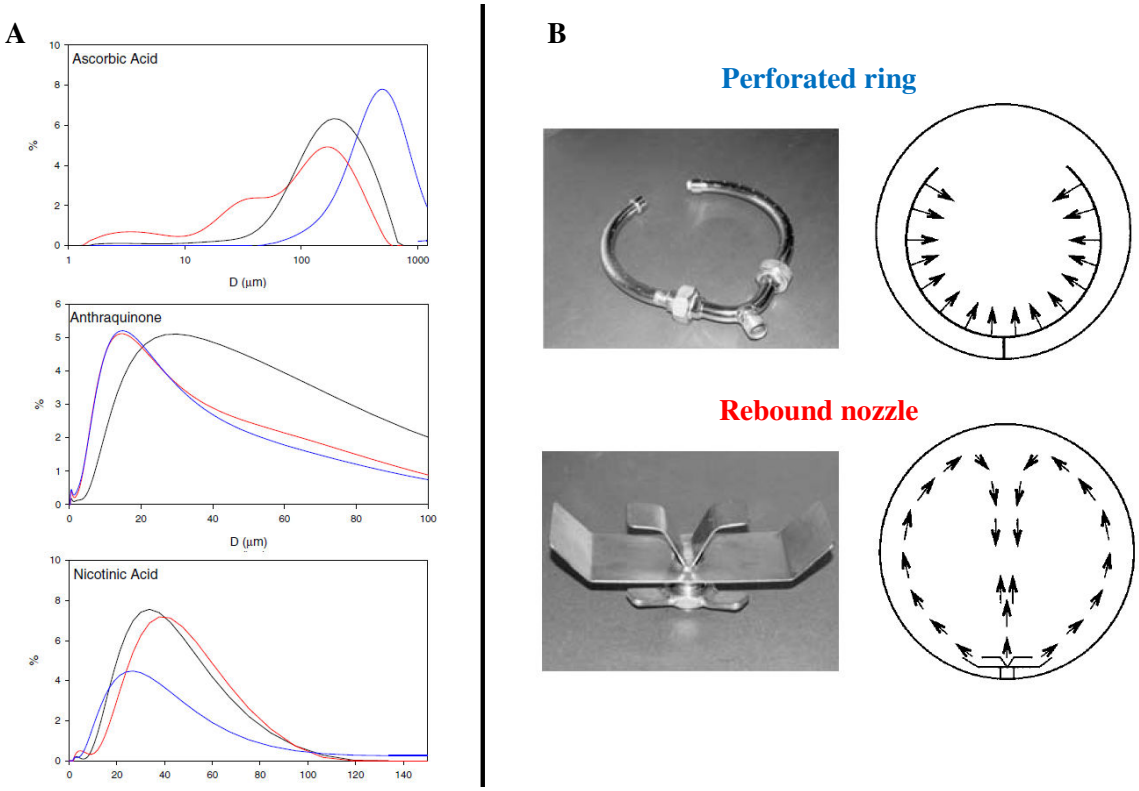

Figure 1.15. Influence of the dispersion nozzle on the PSD distribution in the 20 L sphere
A. Granulometric distribution obtained for three different combustible dusts (Sanchirico et al., 2015) (Black: Initial PSD - Red: Rebound nozzle – Blue: Perforated Ring)
B. Placement and initial flow patterns generated by the two dispersion nozzles (Dahoe et al., 2001)

This condition can be explained by analyzing the flow patterns that are developed within the test apparatus with both injection nozzles. Dahoe et al. (2001) established that the flow patterns and the intensity of the turbulence differ significantly when the injection nozzle is modified. This condition is due to the number of holes and their position in the explosion chamber. A simple description of the pattern developed by the two injection nozzles is shown in Figure 1.15B.

These conditions remark the importance of the characterization of the flow dynamics on the development of a flammability test. This analysis must also consider the nature of the dust because

some fine and cohesive powders must be exposed to very high shear or tensile stresses to generate individual primary particles. This fact means that the effective particle size in dust clouds in practice can be much larger than the size of the primary particles (Eckhoff, 2012). Thus, the variations of the PSD should be determined not only from the collected dust after a dispersion test but also in situ. In this way, it will be possible to establish the direct relation between the ignition delay and the physical properties of the powder as well as their influence on the explosion hazard assessment of the combustible dust.

A. *Deagglomeration aerodynamic stresses*

The deagglomeration mechanisms that cause the disintegration of the dispersed aggregates are defined by velocity of the two phases that compose the gas flow. Therefore, these mechanisms are defined by the velocity gradients and the vorticity of the mean flow. For this reason, this section summarizes the stresses that are exerted by the fluid flow on the particles surface, which depend on the intensity of the turbulent flow:

- **Inertial stress (σ_I):** This stress is caused by aggregated particles accelerations and shifts in the flow direction. It is associated to the resistances per surface area of agglomerate. The maximum inertia stress can be considered when the relative velocity between the fluid and the solid particles reaches a maximum value. This happens especially when the model assumes a resting agglomerate in an air stream (Weiler et al., 2010). During the acceleration process, the relative velocity between the fluid and the particles decreases, reducing the inertia stress too. This fact implies that the stress of inertia acts typically on a short time scales due to the high acceleration rates of small particles. The following figure shows a scheme of this aerodynamic stress:

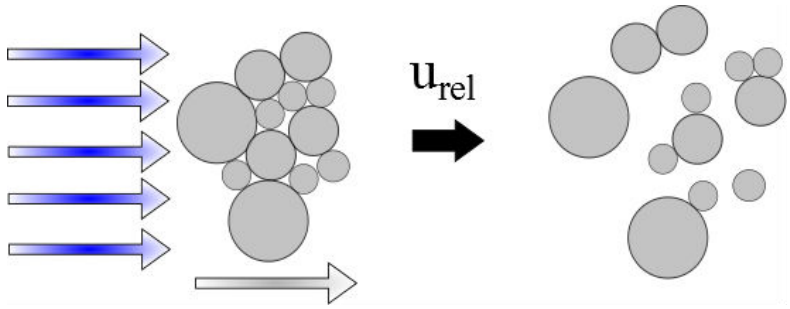

Figure 1.16. Inertial stress as a mechanism of deagglomeration in fluids (Weiler et al., 2010)

The equation that characterizes the inertial stress is defined according to the relative velocity between the two phases ($u-u_p$). In addition, this stress is also defined by the fluid density (ρ) and the contact surface in the outer layer of the agglomerate. These parameters depend on the diameter of a primary particle (d_{pr}) and the one of the agglomerate (d_{Agg}):

$$\sigma_I = \frac{\rho}{8}\left[1-\frac{\arccos\left(\frac{d_{pr}}{d_{Agg}-d_{pr}}\right)}{180°}\right]\left(u-u_p\right)^2\left[\frac{24}{\mathrm{Re}_{rel}}+\frac{4}{\mathrm{Re}_{rel}^{0.5}}+0.4\right] \qquad 1.7$$

The last coefficient on the right side of the equation determines the inertia stress exerted on the solid surface. This parameter is established by the relative Reynolds number defined for the variables mentioned above and the dynamic viscosity of the gas (μ):

$$\mathrm{Re}_{rel} = \frac{\rho d_{Agg}\left(u - u_p\right)}{\mu} \qquad 1.8$$

- **Rotary stress (σ_R):** This stress is introduced by the velocity gradient (du/dz) in a shear flow. It occurs during the transportation of the agglomerate within the shear zone. Weiler et al. (2010) affirmed that this stress decreases according to a power law with an exponent of 2 when the agglomerate size is reduced during a stepwise deagglomeration in a constant shear zone.

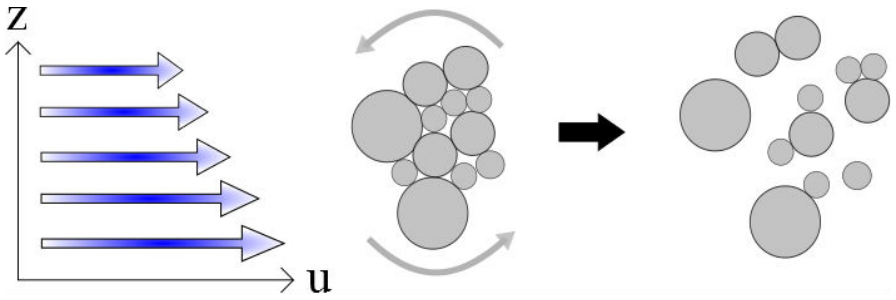

Figure 1.17. Rotary stress as a mechanism of deagglomeration in fluids (Weiler et al., 2010)

The equation used by Weiler et al. (2010) in their model for the dispersion of dry powder agglomerates are based on the aggregate properties and the previous description of the flow profile:

$$\sigma_R = \frac{\rho_p}{40} d_{Agg}^2 \left(\frac{du}{dz}\right)^2 \qquad 1.9$$

- **Turbulent stresses (σ_T):** These stresses are originated by the vortices developed in the velocity field. They can be divided in shear stresses and impaction stresses. The first type is attributed to the vortices of comparable length scale. These fragmentation mechanisms are the most relevant in the characterization of a turbulent particle-laden flow because the disintegration of micron sized agglomerates is mainly ascribed to these stresses. However, the turbulent eddies also promote the agglomerates fragmentation by causing their direct collision at high velocities.

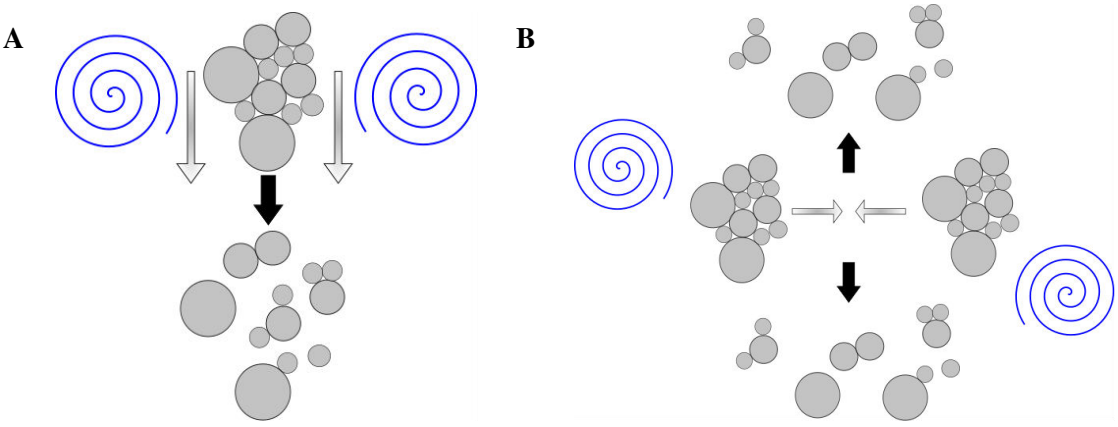

Figure 1.18. Turbulent stresses as mechanisms of deagglomeration in fluids (Weiler et al., 2010)
A) Shear stress B) Impaction stress

The main parameters for the determination of the intensity of the micro-turbulences are the kinematic viscosity of the fluid ν_{kin}, the energy dissipation rate ε and the size of the involved vortices.

The Kolmogorov microscale (l_D) classifies the micro-turbulences according to their size. In fact, the turbulent flows have large sizes vortices (<58 l_D) while the laminar flows are associated to small-size vortices (<3 l_D) (Weiler et al., 2010). The agglomerates sizes are usually in the transitional region located between these two values. The equation to determine the Kolmogorov microscale is:

$$l_D = \left(\frac{\nu_{kin}^3}{\varepsilon} \right)^{0.25} \quad 1.10$$

The turbulent stresses can be calculated according to the following equation which has been adjusted with the respective flow parameters (a_1 to a_4). These constants are listed in Table 1.7.

.

$$\sigma_T = a_1 \rho \left(\frac{\varepsilon^{a_2}}{\nu_{kin}} \right)^{a_3} d_{Agg}^{a_4} \quad 1.11$$

Table 1.7. Fitting parameters for the turbulent stresses in a particle-laden flow

STRESS	KOLMOGOROV LENGTH SCALE	a_1	a_2	a_3	a_4	a_5
Shear stress	$d_{Agg} < 3l_D$	0.260	1.000	0.500	0.000	-1.000
	$d_{Agg} = [3l_D, 7l_D]$	0.068	1.000	1.000	2.000	1.000
	$d_{Agg} = [7l_D, 58l_D]$	0.490	3.000	0.250	1.000	1.000
	$d_{Agg} > 58l_D$	1.900	1.000	0.666	0.666	0.000
Impaction stress	$d_{Agg} = [3l_D, 58l_D]$	0.051	3.000	0.250	1.000	1.000

B. *Adhesion forces*

The agglomerates fragmentation is accomplished when the aerodynamic stress overcome the agglomerate tensile strength (σ_{ATS}). This variable is defined as the total force between particles across the fracture plane divided by the area of fracture (Debrincat et al., 2008). The calculation of σ_{ATS} must take into account the packing arrangement and the inter-particle forces. Some assumptions have been proposed by Debrincat et al. (2008) to simplify the complexities related to these factors. These simplifications consider that the agglomerate consists of spherical particles with a high number of particle contacts in the cross section. Thus, the following expression establishes the required stress the cause the fragmentation of the dispersed agglomerate.

$$\sigma_{ATS} = \frac{9}{8} \left(\frac{1-e}{\pi d_p^2} \right) c F_{IP} \quad 1.12$$

This equation defines the agglomerate tensile strength according to the arrangement of the agglomerate and the inter-particle force per unit contact (F_{IP}). This expression is calculated according to the void fraction of the agglomerate (e), co-ordination number (c) and the primary particle diameter (d_p).

Debrincat et al. (2008) affirmed that the following major adhesive forces define the particle interactions and affect their motion before their collision as well. For this reason, it is necessary to establish the main forces that determine the development of a dust cloud. Some of these forces are described below:

- **Van der Waals force (F_{vdw}):** This is a short-range force that arises when two surfaces are sufficiently close to each other. The atoms that compose the particles spontaneous induce electric and magnetic polarizations. This phenomenon creates a fluctuating electromagnetic field within the medium and the gap between the surfaces involved. Hence the dispersion interaction of two bodies is also affected by the presence of other bodies nearby. This feature is denominated the non-additivity principle of an interaction (Israelachvili, 2011).

  The Van der Waals forces can be calculated for two interacting spheres according to their Hamaker coefficient (H_v) and their separation distance (h):

$$F_{vdw} = \frac{H_v d_p}{12h^2} \tag{1.13}$$

  The difficulties in the estimation of this force rely on the arrangement of particles. This characteristic of the agglomerate causes many variations in the contour of a particle surface as well as irregularities in the contact area. In addition, certain materials have asperities and sub-micron material adhered to their surfaces. This fact defines several issues for the determination of the effective separation distance between particles.

  The Van der Waals forces can be repulsive or attractive as a function of the relative magnitude of the Keesom, London and Debye forces; hence the dispersion force between two molecules or large particles does not follow a simple power law. Moreover, these interactions not only bring molecules together but also tend to align them. However, the effect of this orientation is weak (Israelachvili, 2011).

- **Magnetic force (F_{mag}):** The magnetic forces are long-range forces that must be considered when the interacting surfaces have magnetic dipole moments. These interactions let aggregates of ultra-fines in slurries remain together and can join hetero-aggregations of hematite and magnetite if their sizes are less than 10 μm as well. Debrincat et al. (2008) posed an equation to include the parameters associated to the implementation of the magnetic interactions of the solid particles:

$$F_{mag} = \mu_0 \left(\frac{\pi d_p^3}{6} \right) \left(\kappa_p - \kappa_m \right) \left| H \mathrm{grad}(H)_r \right| \tag{1.14}$$

  where μ_0 is the magnetic permeability of vacuum, H is the intensity of the magnetic field, the gradient function of H in the radial direction is defined by $\mathrm{grad}(H)_r$ and κ_p and κ_m are the volumetric magnetic susceptibility of the particle and medium respectively.

  The combustible dusts that were considered on the characterization tests of this thesis do not pose a behavior that can be associated to the effects of external magnetic fields. Therefore, the analyses discussed in the next chapters will not consider it and is included only

- **Electrostatic force (F_{el}):** This force of attraction is generated by a potential difference between two bodies. These forces characterize the principal inter-particle attractions when the distances between the particles are long enough to neglect the influence of short-range forces. The following equation for the electrostatic force of attraction due to a potential difference between a sphere and a flat plate:

$$F_{el} = \pi \varepsilon_0 \frac{U d_p}{2h^2} \quad 1.15$$

where ε_0 is the permittivity of the air and U is the contact potential difference between the considered surfaces. This variable may range from 0.00 to 0.05 V according to the dispersed material properties.

- **Capillary force (F_{cap}):** Predominant capillary forces can be generated by the water retention in the powder if the relative humidity of the atmosphere and the hygroscopicity of the solid cause a high degree of moisture in the agglomerate. The adsorbed water in equilibrium with the atmospheric humidity affects the inter-particle because it decreases the effective separation distance between particles. Moreover, the water retained between two particles will form capillary bridges that increase the interaction forces.

  The effects of the inter-particle forces depend on the thickness of the moisture layers. In fact a thick layer reduces the distance between the surfaces of two particles and promotes the van der Waals interactions. These characteristics reinforce the cohesion of the units that compose the agglomerate through the formation of bridges. However, Debrincat et al. (2008) affirmed that these forces are negligible at distances in range of 0.005-0.5 d_p. Finally, the calculation of the forces generated by static capillary bridges can be performed with the following equation:

$$F_{cap} = \pi d_p \sigma \cos\alpha \quad 1.16$$

where α corresponds to the angle of contact between the solid and the liquid and defines the degree of wetting of the specified particles, the surface tension of the liquid phase is represented by σ.

  Eckhoff (2012) posed that the augmentation of the humidity level escalates the inter-particle forces. This fact affects the dispersion of the dust aggregates due to the reduction of the effective distance between two touching particles. In addition, the adsorbed liquid layers can adhere firmly to the particle surface and make it smoother. A further increase of the moisture content starts to form liquid bridges between particles and develop a transition range. This range is achieved when the space between the particles is filled with water. At this point, the dust behaves as a cohesive powder due to the high capillary forces. Further details about the influence of the relative humidity of the environment on the flammability of a combustible dust will be discussed in section 1.6.4.

- **Mechanical forces:** Other forces that might contribute in holding the particles together can be related to friction between the particles and the interlocking of the irregular ones. These mechanical forces are defined by the contact area of the particles in the aggregate. For this reason, the principal variables that influence this type of forces are the particle size and its roughness. These forces have not been considered because the particles of the materials tested in this thesis are rather smooth.

The preponderation of a specific type of forces (aerodynamic stresses or agglomerate strength) will determine if the combustible dust cloud is characterized by a fragmentation or agglomeration phenomenon (Wengeler & Nirschl, 2007). For this reason, it is necessary to understand the variations of the initial turbulence of the dust clouds that are characterized in a flammability test. Thus, it will be

possible to comprehend the influence of the operating parameters fixed by the standards and determine the most appropriate conditions for the acquisition of the most experimental data.

1.6.4 MOISTURE CONTENT

The previous section established that the presence of a high moisture content increases the strength of capillary forces and enhances the particles agglomeration. However, this is not the only effect that can be associated to the presence of a high water content in the explosive atmosphere. In fact, this variable also affects the ignition properties of a combustible dust both by changing the ease with which it is dispersed and by altering the way in which it oxidizes in an explosion (Cross & Farrer, 1982). This condition is evidenced because the oxygen diffusion or the growth rate of the oxide layer of metallic dusts pose significant modifications due to the presence of water at the particles surface. For these reasons, it is necessary to determine the water dispersed in the atmosphere as well as the water adsorbed in the particles during the characterization of certain combustible dusts.

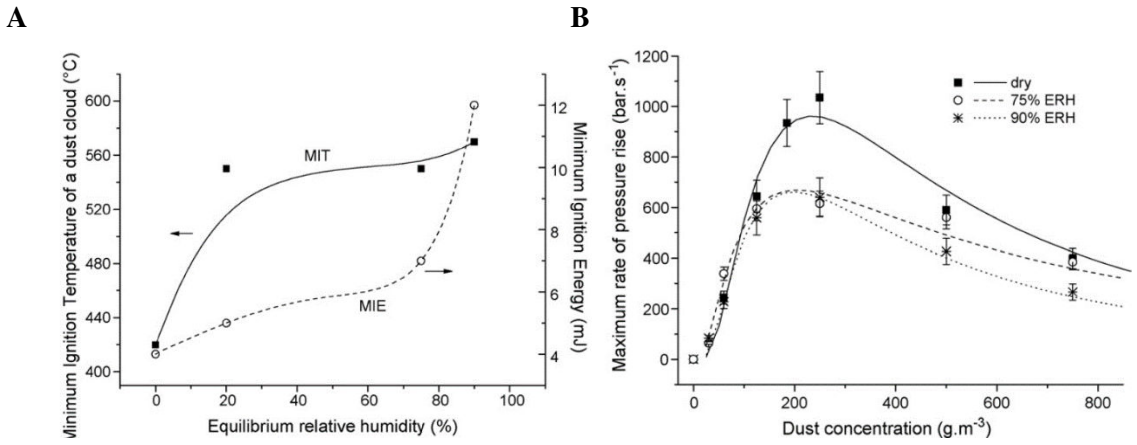

Figure 1.19. Influence of the equilibrium relative humidity of the flammability parameters of magnesium stereate
(Traoré et al., 2009)
A) Evolution of the minimum ignition temperature and minimum ignition energy
B) Influence on the maximum rate of pressure rise

An example of the effects of a high moisture content of the dust cloud is shown in Figure 1.19, which presents the influence of the relative humidity of the explosive atmosphere on flammability parameters of aluminum stereate (Traoré et al., 2009). The experimental results establish that an increase of the moisture content constitutes a reduction of the ignition sensitivity and the explosion violence of a dust cloud (Eckhoff, 2003). Therefore, the moisture content can be considered as a quenching factor for the eventual dust explosion.

In spite of these results, this variable is usually considered to be a determinant factor of the flammability tests only when the environmental humidity is above 30% (Abbasi & Abbasi, 2007; Lees, 2005). Nevertheless, this is not the case for all dusts since some materials like aluminum can react with water to produce not only the corresponding oxide but also hydrogen (Traoré et al., 2009).

Cross & Farrer (1982) and Eckhoff (2003) have listed the main reasons that explain the ignitability reduction and the decrease of the rate of pressure rise of a dust cloud with a high moisture content:

- ✓ Evaporation and heating of water represents an inert heat sink.

- ✓ The pyrolysis of an organic dust is affected by the mixture of the water vapor with the flammable gases in the preheating zone of the combustion wave. This fact diminishes the concentration of the gases and the mixture becomes less reactive.
- ✓ The high moisture content of a dust reduces its electrical resistivity, which limits the ignition by powerful spark discharges. For instance, nylon has a resistivity of 10^{14} Ω in the dry state. This property may diminish to 10^{12} Ω after storage for 48 hours in a humid atmosphere.
- ✓ The presence of water can alter the nature and growth of the oxide layer during the combustion of metallic dusts.
- ✓ Water can react with some metallic dusts to produce hydrogen.
- ✓ The moisture increases the inter-particle cohesion of the dust and prevents its dispersion into primary particles.

1.6.5 ADDITIONAL PARAMETERS

This section briefly describes some additional factors that have an influence on the flammability parameters. The dispersion medium might also have some additional effects on the combustion process if there are more factors that affect the heat and mass phenomena. This is the case of the environmental temperature and the presence of solid inertants. These variables alter the experimental results because they may become another energy source or a heat sink. Therefore, the kinetics of the chemical reaction can be affected by these variables.

A. *Environmental temperature*

Cross & Farrer (1982) discussed the influence of the temperature of the environment on the flammability parameters of a combustible dust. This variable represents an important factor for the implementation of the laboratory data on the process industry. Indeed, the characterization tests are carried out at ambient temperature but this is not always the case for a process unit.

The characterization of a dust explosion in the 20 L sphere implies a temperature rise due to the energy of the chemical ignitors. This augmentation can be of 120°C when the 10 kJ pyrotechnic ignitors are utilized. However, there can be an additional effect when the temperature of the explosive mixture is modified.

The process equipment that operates at temperatures above the ambient temperature is submitted to the variations of the properties of the combustible dust and the increase of the chemical reaction rates. This condition was discussed by Cross & Farrer (1982) from the data obtained in a Hartmann bomb modified to include a pre-heating system for the dust-air mixture. This information is summarized in Table 1.8 and Table 1.9:

:

Table 1.8. Effect of Temperature on Minimum Ignition Energy (Cross & Farrer, 1982)

TEMPERATURE (°C)	MINIMUM IGNITION ENERGY (mJ)	
	Lycopodium	Hydroxypropyl methyl cellulose
Ambient	90.0	160.0
50	50.0	90.0
90	20.0	40.0
180	12.5	-

Table 1.9. Effect of Temperature on Maximum Explosion Pressure Rise and Maximum Rate of Pressure Rise (Cross & Farrer, 1982)

SUBSTANCE	MAXIMUM EXPLOSION PRESSURE RISE (kPa)		MAXIMUM RATE OF PRESSURE RISE ($kPa \cdot s^{-1}$)	
	20°C	100°C	20°C	100°C
Terephthalic acid	653	506	37.9	53.1
Giberilic acid	623	496	66.2	77.2
Lycopodium	707	534	59.3	69.6

The increase of the environmental temperature posed an enhancement of the dust ignitability of the two dusts tested. This condition was evidenced with a decrease of the ignition energy that was observed when the temperature was augmented. However, the severity of the explosion defined a contradictory behavior with increasing temperature. The rate of pressure rise also increased significantly but the maximum pressure rise in the bomb decreased. For these reasons, it is not recommended to consider the laboratory data as the arbitrary parameters for the risk assessment of a process unit.

B. *Solid inertants*

An admixed inert dust can alter the behavior of a combustible dust cloud. For instance, Abbasi & Abbasi (2007) discussed how the presence of certain dusts such as sodium bicarbonate, potassium bicarbonate, monoammonium phosphate and calcium carbonate may affect the flammability curves of different combustible dusts. These curves are usually characterized by a lower flammable limit, an upper flammable limit and a minimum inerting concentration. In addition the deflagration indexes can be significantly reduced in order to achieve a maximum explosion pressure in an acceptable level. The quenching effect of the admixed inertant can be seen in Figure 1.20. The rate of pressure rise of magnesium stereate is significantly reduced when the concentration of a solid inertant such as sodium bicarbonate or silica is augmented (Dufaud et al., 2012).

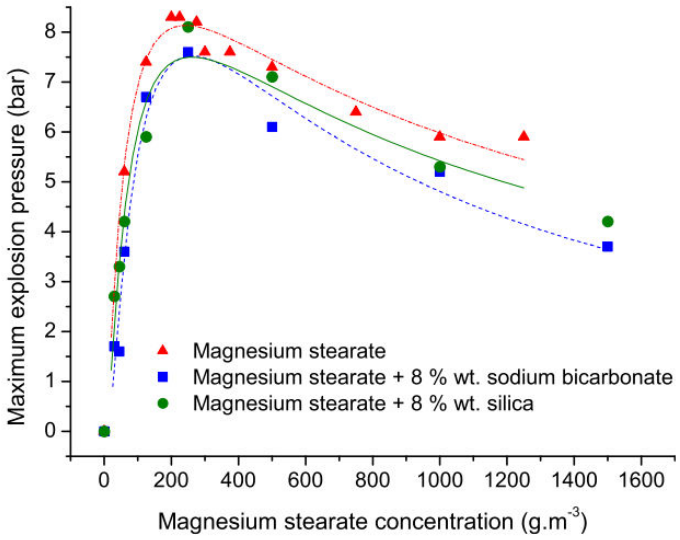

Figure 1.20. Influence of inertant insertion on the maximum explosion pressure of magnesium stearate powders
(Dufaud, et al., 2012)

The effectiveness of the extinguishing agent depends on the compatibility of the fuel dust with the solid inertant. This fact implies that the quantity of suppressant required to mitigate an explosion begins at some initial value at the ignition time and increases rapidly as the explosion fireball increases in size (Amyotte, 2006). In accordance with this statement, the required amount of inertant is defined by the flame temperature, the heat of combustion and certain physical-chemical properties of the admixed material. These properties are listed below:

- **Chemical composition:** The solid inertants have the capacity to absorb the energy released during the dust explosion. Hence they limit the flame propagation through the unburned fuel cloud. This condition arises from the heat capacity, the thermal conductivity and the absorptivity of the admixed material (Abbasi & Abbasi, 2007). In addition, these materials affect the combustion sequence by terminating the branching reactions via free radical capture. This fact constitutes a kinetic interference in the process of flame propagation (Amyotte, 2006).

  Finally, the solid inertants also contribute to the reduction of the severity of the dust explosions by developing a decomposition process. Nevertheless, this additional effect is significant only when the residence time in the flame zone is sufficiently long (Amyotte, 2006). These decomposition effects would include the endothermic heat of reaction as well as dilution of the reaction zone by decomposition products.

- **Concentration:** If the concentration of the inert dust is below a minimum inerting Concentration (MIC), the admixed powder may not mitigate but facilitate the dust ignition. This condition can be evidenced due to several factors. The reasons that have been posed by Janès et al. (2014) for this undesirable behavior include the improvement of the dispersibility of the combustible dust, catalytic effects, variations on the heat transfer mechanisms and the augmentation of the local turbulence levels. Figure 1.21 shows an illustrative example of the different effects that are caused by the addition of an inertant on the explosion according to its concentration. For this particular case, the severity of the dust explosion is increased when the concentration is below 10% (MIC) but decreases when the concentration is above this critical value (Dufaud et al., 2012).

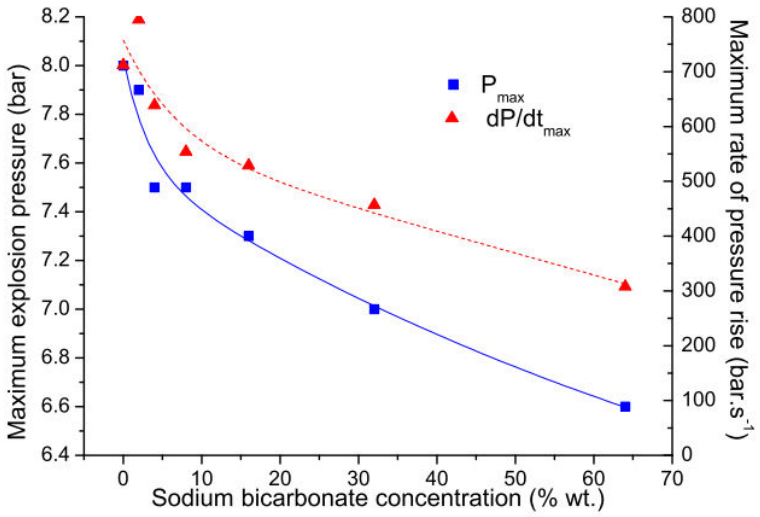

Figure 1.21. Evolution of the maximum explosion pressure and of the maximum rate of pressure rise of magnesium stearate-$NaHCO_3$ explosions as a function of the sodium bicarbonate concentration (Dufaud et al., 2012).

- **Particle size distribution:** The finer sizes are more effective at explosion inerting and suppression than coarser size fractions. Moreover, the probability of decomposition increases as the particle decreases. This fact implies that mechanism is not a rate limiting step in relation to dust devolatilization.

1.7 CRITICAL ANALYSIS OF THE STANDARDS

The meaningfulness of the flammability parameters is usually submitted to the analysis of the correspondence of the laboratory conditions and the environment of an industrial facility. For example, Tamanini (1990) identified a disagreement among the laboratory dust explosibility test method and the large-scale results in the determination of the explosibility parameters of cornstarch. This fact has been discussed by Amyotte (2006), who recommended to perform experimental measurements in chambers larger than laboratory scale to choose a correct inerting level for a combustible dust. In fact, this issue arises from the characteristics of a flammability test, which are intended to represent the generation and development of a combustible dust cloud under the conditions established by the international standards.

This concern has also been considered for the analysis of more complex systems such as the clouds composed by nanometric powders and the hybrid mixtures (Bouillard et al., 2010; Eckhoff, 2012; Khalili et al., 2012; Kosinski et al., 2013). The phases that compose these systems are exposed to different types of interaction mechanisms that might enhance or attenuate their ignitability or explosibility. This fact remarks the relevance of considering the characteristics of every combustible cloud as a particular entity whose physical and chemical properties may differ significantly from other clouds composed by the same substances. For this reason, Table 1.10 presents the main issues that arise due to the setting of certain operating parameters of the flammability tests:

Table 1.10. Issues generated by the setting of certain operating parameters of the standard test methods

	INFLUENTIAL PARAMETER	FLAMMABILITY PARAMETER ASSOCIATED	VALUE FIXED BY THE STANDARD TEST METHOD	ISSUES ASSOCIATED TO THE FIXATION OF THE OPERATING PARAMETER
PRELIMINARY STEPS OF THE TEST METHOD	Physical properties of the dust	MIT, MIT (dust-layer), MIE, MEC, MOC, Pmax, (dP/dt)max	Fixed particle fineness (As-received or sieved to 95% ≤ 200mesh)	Variations of the flammability parameter influenced by the size distribution of the sample.
		MIT, MIT (dust-layer), MIE, MEC, MOC, Pmax, (dP/dt)max	Fixed moisture content (≤10%)	The porosity of some powders might change when the sample is dried.
	Chemical properties of the dust	MIT, MIT (dust-layer), MIE, MEC, MOC, Pmax, (dP/dt)max	Fixed moisture content (≤10%)	Volatile matter content is modified (organic dusts) Integrity of the dust might be affected (sensitivity to heat)
	Physical and chemical properties of the oxidant gas	MIT, MIT (dust-layer), MIE, MEC, Pmax, (dP/dt)max	Test performed with environmental air	Dependence of the flammability on the temperature of the system. The flammability of hygroscopic powders will be affected the air's humidity. Presence of airborne dust (impurities)
		MIT, MIT (dust-layer), MIE, MEC, MOC, Pmax, (dP/dt)max	Test performed with a gaseous mixture of fixed concentration	Possible reactivity of the gas with combustible dust
DUST DISPERSION	Physical conditions of the dust cloud	MIE, MEC, MOC, Pmax, (dP/dt)max	Fixed ignition delay	The dynamics and turbulence of the mixture are a function of the transient conditions of the cloud Fragmentation, agglomeration and sedimentation phenomena on dispersed dust.
		MIT, MIE, MEC, MOC, Pmax, (dP/dt)max	Pressurization and temperature of the explosion chamber and the dispersing gas	The dynamics and turbulence of the mixture are a function of the transient conditions of the cloud Spatial distribution of the dust in the cloud
DUST CLOUD IGNITION	Design specifications of the test apparatus	MIT, MIE, MEC, MOC, Pmax, (dP/dt)max	Geometry of the explosion chamber	Difference between the nominal and real dust concentration. Influence on the evolution of the turbulence of the dust cloud.
		MIT, MIT (dust-layer)		Post-inflammation phenomenon
		MIT, MIT (dust-layer)	Material of construction	Catalytic effects
		MEC, MOC, , Pmax, (dP/dt)max	Cooling jacket	• Quenching effects associated to walls
	Ignition source	MIT, MIT (dust-layer), MIE, MOC, Pmax, (dP/dt)max	Energy provided by the source	• Possible overestimation of the flammability parameter.
		MEC, MOC, Pmax, (dP/dt)max		• Overdriven or under-driven test
		MIE, MEC, MOC, Pmax, (dP/dt)max	Position of the ignition source	Spatial distribution of the dust in the cloud (overestimation of the flammability parameter)

The fixation of the operating parameters constitutes the basis of the repeatability and reproducibility of the tests. Nevertheless, it also affects the certainty levels of the explosibility parameters due to the variations on the properties of the combustible dust and the dust cloud dynamics. A solution for these issues consists on the characterization of these aspects prior to the development of the test. In this way it will be possible to adapt the operating parameters of the test methods and provide a more accurate description of the flammability parameters of a combustible dust. In accordance with this statement, the following aspects must be established in a preliminary stage for every particular case:

- Chemical properties of the combustible dust.
- Fluidization properties of the combustible dust (e.g. density and particle size distribution).
- Variations of the PSD during the dispersion process due to fragmentation, agglomeration or sedimentation of solid particles.
- Hygroscopicity of the dust.
- Environmental conditions (e.g. humidity and temperature).
- Appropriate ignition delay (characterization of the dust cloud dynamics).
- Limitations associated to the test method (e.g. influence of the dispersion conditions and the geometry of the explosion chamber).

1.7.1 APPLICABILITY OF THE STANDARDS IN THE CHARACTERIZATION OF MICROMETRIC PARTICLES

The definition of the appropriate ignition delay and the limitations posed by the test apparatus is the aspect that represents the major difficulties for the development of a flammability test. For this reason, the reproducibility and repeatability of the flammability data have been criticized due to the dissimilarities found among the results obtained with different standardized setups (ASTM E1226 − 12a, 2012; Dahoe et al., 1996; Going et al., 2000; Janes et al., 2008). Thereupon, the flammability parameters are considered with caution for the identification of the safety barriers. This condition has been explained from the experimental comparison of the dust cloud dynamics within different standard setups. These studies have concluded that certain design characteristics of the equipment such as the confinement volume and the injection systems have a direct influence on the evolution of the dust cloud. In accordance with this statement, this section poses a brief discussion of the differences that are observed in the experimental results that are determined from certain apparatuses that are designed to determine the same flammability parameters.

The combustible dust clouds may develop in a different way in the apparatuses designed to establish their ignitability and explosibility characteristics. An example of this situation corresponds to the determination of the minimum ignition energy (MIE) the modified Hartmann tube (MIKE 3). It is usually evidenced that this setup provides MIE results, which are equal or lower to those measured with the original Hartmann apparatus. This dissimilarity is attributed by Janes et al. (2008) to the effects on turbulence in the tube and on dust concentration in spark area that are caused by different injection systems.

Furthermore, the MIKE 3 and the Hartmann apparatus generate different particles concentrations in the spark zone. This condition is also caused by the different dimensions of the dispersion tubes. For instance, the diameters of the original and modified Hartmann tubes are 71 and 68 mm respectively. Hence it is possible to conclude that the optimal concentration of a combustible dust cloud is accomplished at different time intervals. This condition is attributed to the stochastic behavior of the dust cloud, which is clearly influenced by the nature and size distribution of the dispersed dust. For this reason, it is always recommended to perform a strict cleaning protocol during the characterization of a friable or hygroscopic powder (Janes et al., 2008).

This dissimilar behavior can be posed for the equipment considered to determine other flammability parameters. For instance, Section 1.4.4A remarked the influence of the position of the dispersion chamber on the development of a post-inflammation phenomenon during the determination of the minimum ignition temperature of a combustible dust. Moreover, Section 1.5.3A discussed the conditions that generate an under-driven or overdriven characterization of the explosibility of combustible dusts in the 20 L sphere. The analysis presented in that section established that the factors that enhance the combustion mechanisms or the quenching effects were not only the external elements but also the cloud dynamics. These facts establish that these standardized tests demand a great number of assays to achieve the required precision and certainty levels. Thus, it is compulsory to implement some complementary tools on the experimental characterization of combustible dusts. In this way, it could be possible to reduce the experimental effort that is attributed to variations caused by the cloud dynamics.

For this reason, this thesis has proposed the inclusion of experimental tests and CFD simulations on the description of the dust cloud dynamics in the standard test apparatuses. For this purpose, a case study based focused on two of the experimental setups that are used for the characterization of combustible dusts is proposed. This research project has performed a descriptive analysis of the internal conditions of a dust-air mixture in the modified Hartmann tube and the 20 L sphere before the dust ignition. These tools have been widely considered to characterize different fluidization systems among which are the combustible dust-air mixtures (Skjold, 2007).

The evolution of the dust clouds formed in these setups was described with an experimental-computational approach in order to establish the influence of the fluidization properties of different micrometric powders and the design and operating specifications of the tests on the uncertainty levels that are usually found in the flammability tests. The next chapter will present some of the computational alternatives that describe the behavior of fluid-solid mixtures and will pose the main fundaments that were considered for the developed case study and the later chapters will discuss in detail each one of the two approaches.

1.7.2 EMERGING TOPICS: NANOMETRIC PARTICLES AND HYBRID MIXTURES

This chapter concludes with a discussion recent trends in the research field of the dust explosions in process safety. The aspects that have gained more importance are linked to the experimental evidences that have posed significant variations on the combustion mechanisms. These effects are caused when the gas/solid interactions are affected drastically by an additional factor. For this reason, the characterization of the combustion flame and the dispersion mechanisms of new types of mixtures has become an important aspect in the determination of the most conservative conditions to perform a flammability test. The characterization of these mixtures has promoted some modifications in certain safety standards such as the NFPA 68 in order to consider the elements that enhance the ignitability of these combustible clouds.

This section is envisaged as a brief description of two emerging topics that represent the most recent subject in the field of dust explosions: hybrid mixtures and clouds composed by nanometric dusts. These cases are well-known not only because of their presence in different developing process industries but also for their remarkable combustion behavior. Indeed, the combustion process of the following cases defines a clear dissimilarity with regard to the behavior of a typical dust explosion. These differences are originated from changes in the particle size of the dust and the composition of the dust cloud that will be described in detail below.

The remarkable differences found in certain developing mixtures call into question the suitability of the fixation of the operating parameters of a flammability test. For this reason, various studies have delved into these heterogeneous systems in order to describe their characteristic flammability behavior. Some of their results are discussed in this section.

A. *Nanometric particles*

The nanometric materials have become an important aspect in the research field of dust explosions and process safety. This fact is due to the significant variations that have been evidenced in the combustion mechanisms of the nano-sized particles. This fact constitutes an important aspect in the definition the ATEX directives, which specify the regulations for operations in areas that represent a risk due to the presence of an explosive atmosphere. These standards must adapt their risk assessment procedures in order to define properly the protection indexes of the operation areas. This modification of the standard regulations will determine the required modifications of the storage and manipulation protocols of facilities that handle nanometric combustible dusts according to the explosibility characteristics of the material.

Bouillard et al. (2010) extended the study the influence of the particle size to the analysis of nanometric particles. Their results established that the dependency of the combustion rate on the particle size must be classified according to the combustion regimes that are associated to the micrometric and nanometric particles: Diffusion and chemical reaction. As discussed in Section 1.6.1, the combustion of solid particles is mainly controlled by the oxygen diffusion if their size is larger than their critical diameter. On the contrary, the particles whose size is smaller than this critical diameter pose a combustion process in which the kinetics of the reaction is the controlling factor. For this reason, these authors affirmed that the nanopowders are characterized by a higher ignitability, which is determined by their proneness to agglomerate when dispersed in the cloud (Bouillard et al., 2010; Alexis Vignes, 2008).

Furthermore, nanoparticles show different dispersion properties as micron and sub-micron scale particles in flocs (Wengeler & Nirschl, 2007). This fact is evidenced when strong chemical bonds in nanoagglomerates are opposed to attractive Van der Waals forces in flocs. This condition leads to an additional inelasticity in their collisions. Thus, there is a limit in the breakage induced by the aerodynamic stresses and the dispersion level of the primary particles. This result agrees with the conclusions posed by Eckhoff (2012). This author established that the delay between the moment of formation of a well dispersed nano-dust cloud and the moment of ignition of the cloud is decisive for the extent of dust agglomeration. For this reason, Wengeler & Nirschl (2007) affirm that the characterization of nanometric materials necessitates a different design of dispersion processes.

These facts have a direct repercussion of the reaction mechanisms of the dust. The combustion time of the large aluminum micrometric particles and some carbonaceous materials is considered to follow a d_p^n law with n ranging between 1.5 and 2 (Bouillard et al., 2010; Makino & Law, 2009). However, this proportionality has been reported by various studies in a span that ranges between 0.3 and 1.6 for nanometric particles. These values represent a higher reaction rate than that based on the specific effect of the alumina covering layer. Moreover, Bouillard et al. (2010) posed that this relation also establishes a decreasing behavior for the minimum ignition temperature of nanometric dusts when their particle size is reduced. Nevertheless, this behavior is not monotonic for these materials because the smallest particles are affected by their mutual interactions as well. These interactions usually promote the agglomeration/aggregation phenomena in the dust cloud. Additionally, the nm-particle powders have a limited dispersibility (Eckhoff, 2012). These conditions demand an additional amount of energy for the ignition process. Thus, a behavior similar to the profile shown in Figure 1.22 is expected for the minimum ignition energy of micrometric and nanometric particles.

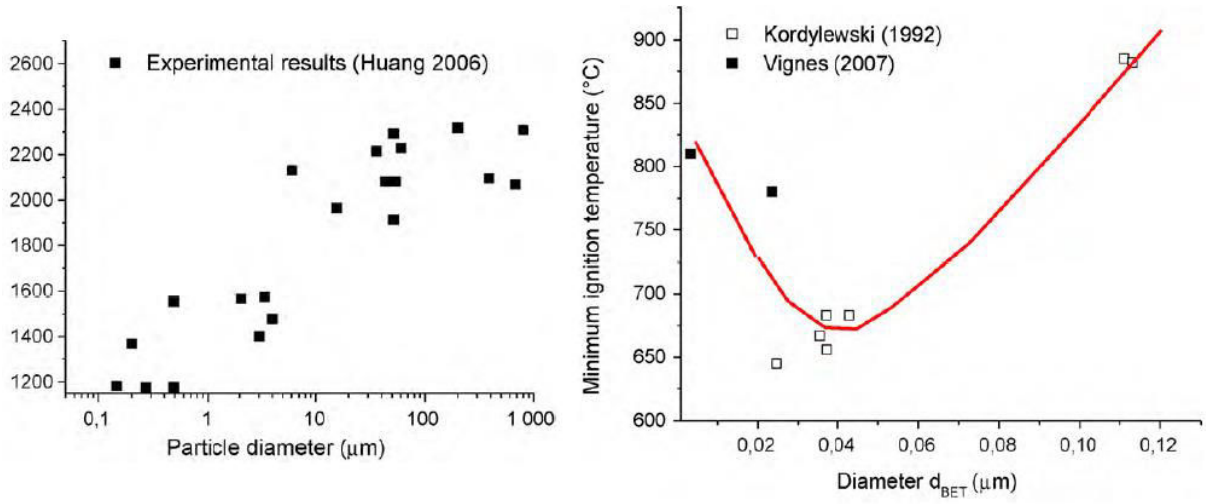

Figure 1.22. Minimum ignition temperature as a function of particle size diameter (Bouillard et al., 2010)
A. Micrometric aluminum B. Nanometric aluminum

A different behavior was observed by Bouillard et al. (2010) during the analysis of the influence of the particle diameter on the minimum ignition energy of the combustible dust. Their experimental results allowed concluding that this flammability parameter has a dependency on the particle size that varies according to the combustion regime. The MIE depends on d_p^3 when the kinetics of the chemical reaction controls the combustion rate whereas it depends on $d_p^{3/2}$ for the diffusion controlled regime. Thus, there is an intermediate region that defines the transition from one regime to another. This characteristic behavior of the flammable material is shown in Figure 1.23. Eckhoff (2012) posed that the temperatures of electric spark plasmas are substantially higher than dust cloud flame temperatures. Therefore, the agglomerates that are located near the ignition source might disintegrate when it induces some thermally induced stresses. The nanometric particles produced after the fragmentation of these agglomerates are well-dispersed in a small cloud zone that can be ignited with a low amount of energy. This first reaction generates a dust flame kernel which is capable of igniting the bulk of the dust cloud.

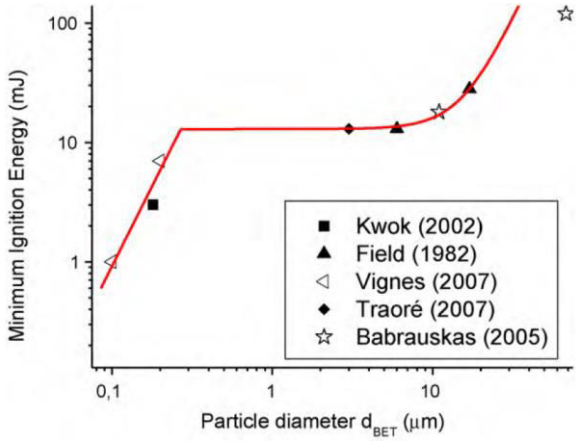

Figure 1.23. Dependencies of the MIE versus the particle diameter (Bouillard et al., 2010)

Furthermore, the maximum pressures and the maximum rates of pressure rise of the explosion of a nanometric dust pose a behavior that differs from the other flammability parameters. The parabolic profiles of severity parameters (Figure 1.24) are characterized by lower maximum values than those obtained after the ignition of a micrometric powder. These flammability parameters are more influenced by other variables of the dust cloud such as the particles concentration and the composition and structure of the compound (Bouillard et al., 2010; Vignes, 2008). Thus, the severity of the nano-sized powder poses a certain degree of passivation. This fact is evidenced due to the contrast between

the enhancement of the combustion rate and the escalation of the particle cohesion forces. Eckhoff (2012) established that the formation of clouds of well-dispersed primary particles from bulk powders consisting of nm-particles is extremely difficult to achieve by dust dispersion processes normally operating in the process industries. This difficulty is originated by the fast agglomeration of the primary particles. This phenomenon turns these particles into much larger agglomerates within fractions of a second.

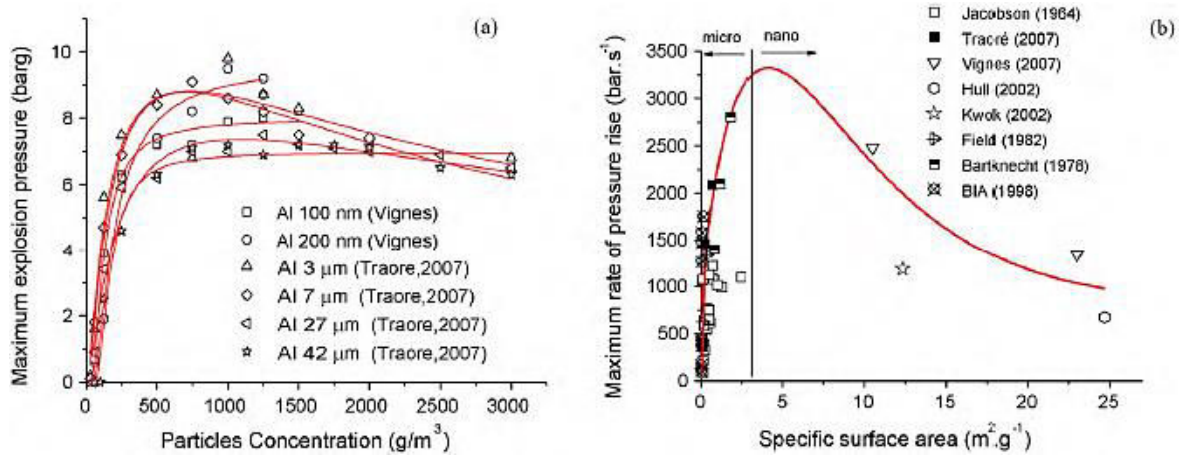

Figure 1.24. Experimental evolution of explosions of nano-sized aluminum particles
A. Maximum Pressure B. Maximum pressure rise
(Bouillard et al., 2010)

The low severity parameters of nanometric dusts establish that the layers of protection associated to the explosion venting, suppression and isolation should be just as feasible with nm primary particles as with primary particles of mm size (Eckhoff, 2012).

This section has presented the influence of the size of the nanometric powders on the interaction mechanisms developed in a combustible dust cloud. These characteristics make them differ from the large-sized micrometric dusts because they determine their dispersibility and ignitability (Bouillard et al., 2010; Eckhoff, 2013). This fact poses a specific flaw of the standard test methods that arises when they establish some sampling criteria. These conditions do not take into account the characteristic behavior of nanometric combustible dusts; hence some materials that reach different fragmentation levels in a dispersion process will have a set of flammability parameters according to their size distribution.

A possible solution for this issue lies on the adaptation of these criteria. For instance, the determination of more than one sieving size for the development of a test series will allow characterizing the explosibility if the dust in three different size ranges: above and below the critical diameter and in the nanometric scale. In accordance with this statement, this suggestion could be also considered for other parameters such as the moisture content of the sample, humidity of the explosive atmosphere, dust concentration and ignition delay. Unfortunately, this modification implies more experimental resources; hence computational tools that allow predicting this behavior will be considerably handy in the reduction of the number of necessary assays.

The explosible behavior of nanometric dusts delineates the potential hazards for the facilities that manufacture such powders. Moreover, it is necessary to take into account that some technical barriers that are efficient to prevent and protect against micrometric powders explosions may be irrelevant in the case of nanometric powders (Vignes et al., 2012). In accordance with this statement, the knowledge of the mechanisms and characteristics of the explosions of ultrafine powders will certainly constitute the basis that is necessary to propose new and proper protection means. Thereupon, the industrial facilities that store and handle these substances will consider the respective protocols and regulations that guarantee the implementation of an appropriate risk analysis method and the best

safety barriers which had to be positioned to ensure the best occupational safety level to all workers (Vignes et al., 2012).

B. *Hybrid mixtures*

The hybrid mixtures consist of a combination of combustible gases and dusts. These mixtures are usually encountered in various facilities that handle fermentation gases and cereals, pigments and solvents, solid active principles or excipients and volatile organic vapors, etc. (Khalili et al., 2012). These mixtures are characterized by an augmentation of the flammable volatile content that is originated by the addition of the combustible gas (Amyotte et al., 1993). A typical case that defines this type of atmospheres is the transfer of powders into flammable solvents. Typically some additives, pigments, catalysts, or any kind of reactants have to be charged in powder form into reactors. Frequently these vessels contain a flammable solvent either already charged in a large amount or as residue from the previous operation or a washing operation (Glor, 2006). Dufaud et al. (2009) refer to the experiments developed by Engler in 1885 as the first tests on hybrid mixtures. The results of these tests provided an insight about the characteristics of the coal dust explosivity in presence of methane, which is widely accepted as one of the major hazards in the mining industry.

The explosions of hybrid mixtures are characterized by some specific behaviors that are defined by the influence of the phase interactions on the aerodynamics of the cloud, the thermal transfer and the combustion kinetics. Khalili et al. (2012) discussed the main features that determine the differences between a hybrid mixture and a combustible cloud that lacks of a solid phase. At first, the initial turbulence and the flame aerodynamics are modified by the presence of a disperse phase. Additionally, the heat absorption of the dispersed solid alters the flame propagation as well as the thickness of the preheated zone. Hence the combustion rates of a hybrid mixture differ notably from the ones of the pure dusts or gases.

The explosibility of a dust cloud can be enhanced by the addition of a combustible fluid. Thus, a hybrid mixture represents a rise in the explosion danger when compared with the dust/air mixtures (Pilão et al., 2006). In accordance with this statement, Khalili et al. (2012) summarized the main characteristics of a combustible gas/dust cloud that have been asserted:

- The ignition sensitivity of a combustible dust is strongly increased by the presence of a few percent of combustible gases or vapors. This effect can be so relevant that some explosions have been observed for mixtures that have concentrations of the two combustible compounds that are inferior to their respective minimum explosible concentrations (MEC). Garcia-Agreda et al. (2011) posed an estimation of the amount of a combustible fluid that is necessary for a flammable condition based on the Le Chatelier's law. This predictive basis is submitted to certain deviations. However, the estimation error is low for the clouds that have a gas and a dust that reach a similar adiabatic flame temperature.

  Furthermore, the minimum ignition energy (MIE) of a dust cloud also poses a drastic decrease with a small addition of a combustible gas (1 to 3% vol.). This decrease of the MEC of the dust is characterized by a non-linearity that is caused by a difference in the ignition energy of the gas and the dust (Pilão et al., 2006). In accordance with this statement, a semi-logarithmic correlation was proposed to estimate the minimum ignition energy of hybrid mixtures (HMIE) from the actual concentration of the gas (C_{gas}), the concentration of the gas that constitutes the lowest MIE (C^*_{gas}) and the respective MIE of each compound. The following relationship is only valid for gas concentrations lower than C^*_{gas}:

$$HMIE = \exp\left[\ln\left(MIE_{dust}\right) - \left(\frac{C_{gas}}{C^{*}_{gas}}\right)\ln\left(\frac{MIE_{dust}}{MIE_{gas}}\right)\right] \qquad 1.17$$

- The severity of a dust explosion is affected by the presence of a combustible gas as well. This condition was attributed by Dufaud et al. (2008) to a promotion effect is especially noticeable on the combustion kinetics for lean mixtures. Synergistic effects have been observed and, under peculiar conditions, the pressure rise rates of hybrid mixtures could even be slightly greater than those of the pure gases/vapors themselves (Khalili et al., 2012). An example of these characteristics is shown in Figure 1.25 for a case study developed by Dufaud et al. (2008). The maximum explosion pressure and the maximum rate of pressure rise were analyzed for a hybrid mixture composed by niacin (pharmaceutical powder) and diisopropyl ether (solvent). The results obtained by Dufaud et al. (2008) posed that the maximum explosion pressure rises from 8.4 and 8.8 barg, respectively, for niacin and diisopropyl ether to 9 bar g for mixtures containing 250 g/m^3 of niacin and less than 2% of diisopropyl ether. For this case, the inclusion of the fluid caused a slight increase of P_{max} that corresponded to a linear tendency. However, this behavior differed from the profile obtained for the maximum rate of pressure rise, which showed a drastic increase that requires a non-linear treatment for its description.

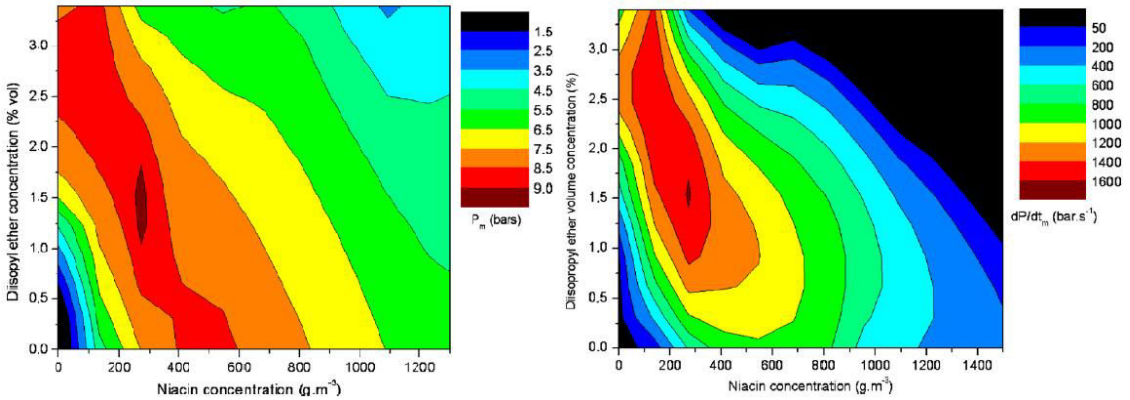

Figure 1.25. Contour lines of the P_{max} and the maximum rate of pressure rise of niacin/diisopropyl ether hybrid mixtures (Dufaud et al., 2008).

However, the influence of the presence of the combustible gas on the severity parameters of the dust is minor when the dust concentration is over its MEC. This fact is evidenced because the combustion of the hybrid mixture during the explosion is dominated by the dust combustion characteristics when the dust concentration is over its minimum explosibility limit (Pilão et al., 2006). The competition of the mechanisms associated to the combustion of the gas and the dust can be observed by comparing the behavior of the system at different concentrations. For instance, Figure 1.26 presents the profiles obtained for a cork dust/methane/air mixture when the concentration of the combustible fluid is varied from 1.98% to 3.50%. The development of the combustion regimes poses an anticipation of the peaks when the gas concentration is increased and its combustion characteristics govern over the characteristics of the dust.

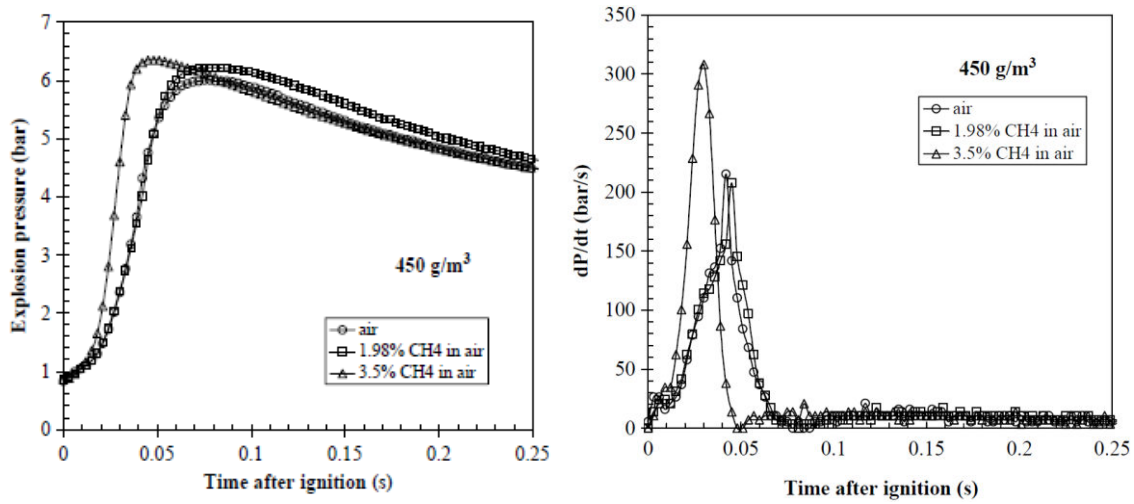

Figure 1.26 Effect of methane content on the explosion development of suspensions with cork dust concentrations of 450 g/m^3 (Pilão et al., 2006)

The distinction of the regimes developed by the hybrid mixtures is important because their physical and chemical characteristics make them differ from the mixtures composed by only a combustible compound. Garcia-Agreda et al. (2011) characterized the five regimes that are defined by the influence of every combustible substance on the severity of the explosion of the hybrid mixture. These regimes are established by the minimum explosible concentration of each compound and the synergic effects associated to the mixture. For this purpose, the variations of the deflagration indexes of the mixture methane/nicotinic are represented in Figure 1.27 with circles whose diameters are proportional to the severity parameters:

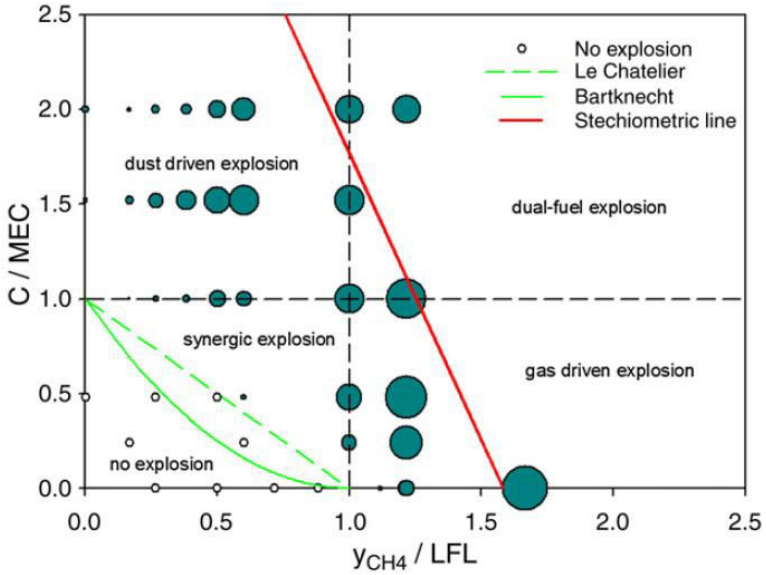

Figure 1.27. Explosion regimes in the plane methane content/nicotinic acid concentration (Garcia-Agreda et al., 2011)

- **No-explosion regime:** The combustible concentrations below the curve defined by the Le Chatelier's law (green line). The dust concentration is below its MEC and the gas concentration is below its lower flammability limit (LFL).
- **Synergic explosion:** The concentration of the dust and the gas is among the Le Chatelier's curve, the MEC line and the LFL line. The explosion is feasible due to the enhancement generated of another combustible compound.
- **Dust driven explosion:** The dust concentration is above the MEC and the gas concentration is below its LFL. The severity of the explosion is mainly defined by the characteristics of the dust. Thus, the combustible gas constitutes an enhancement of the severity.

- **Gas driven explosion:** The dust concentration is below the MEC and the gas concentration is above its LFL. The severity of the explosion is mainly defined by the characteristics of the gas. Thus, the combustible dust constitutes an enhancement of the severity.
- **Dual-fuel explosion:** Both combustible compounds contribute to the explosion severity.

Figure 1.27 shows that the enhancement of the explosion severity is more significant when the dust concentration is increased. This condition is due to the influence of the dispersed solid on the dust cloud dynamics. In accordance with this statement, the turbulence of the two-phase flow is more affected by the addition of the combustible solid. For this reason, the computational tools that are considered for the analysis of combustible dust-clouds could be considered for hybrid mixtures as well.

The determination of the regime that must be associated to a specific hybrid mixture will represent a better comprehension of the combustion mechanisms and the influence of the physical-chemical parameters of the two phases on its flammability parameters. Thereupon, the identification of the likelihood, the severity and the kinetics will provide more representative results in the standardized tests. Thus, the information of the flammability of the hybrid mixtures will lead to the definition of the appropriate preventive and protective barriers.

1.8 CONCLUSIONS

Les nuages des poussières combustibles ont un comportement caractéristique qui constitue certaines dissemblances par rapport au comportement des mélanges composés par les fluides inflammables. Ces différences surgissent à cause des variations des phénomènes associés à la dispersion gaz-solide. Alors, les propriétés d'un mélange hétérogène de ce type affectent notamment les transferts de matière et de chaleur à l'intérieur de la zone réactive et les régions environnantes. Ce fait constitue un facteur d'incertitude pour les paramètres d'inflammabilité qui sont déterminés expérimentalement pour la poudre à partir des tests standardisés. Pour cette raison, plusieurs études ont envisagé la description de l'influence des propriétés physiques et chimiques de la poudre sur le processus de combustion d'un solide inflammable.

Alors, les conclusions apportées par divers études posent que chaque nuage de poussières peut être caractérisé comme une entité particulière. Ce mélange est composé par une poussière dont la distribution des tailles particule et concentration sont définies par les conditions du nuage. De cette manière, le nuage sera envisagé comme un mélange réactif qui est influencé par plusieurs facteurs correspondant aux conditions de l'environnement et au matériel testé. Ainsi le comportement de ce mélange est défini par divers phénomènes interconnectés. Donc les résultats des analyses descriptives réalisés autrefois ont identifié les variables qui affectent la cinétique de combustion et les conditions thermodynamiques ainsi que les effets sur l'explosivité du nuage.

Par exemple, la turbulence initiale de l'écoulement diphasique est un phénomène qui a été étudié à profondeur à cause de son influence sur l'explosivité des nuages combustibles. Cette variable a une grande pertinence sur la vitesse de dispersion des énergies cinétique et calorifique du mélange. De même les champs de vitesse, qui génèrent les régions turbulents du mélange, établissent les variations des tailles de particule et la diffusion du gaz oxydant. Alors les études d'inflammabilité ont montré que toutes les poussières ont de réponses différentes à la turbulence de l'écoulement. Cette condition est observée parce que leur composition chimique et leur distribution des tailles affectent les interactions gaz-solide ainsi que la vitesse des étapes de dévolatilisation et d'oxydation de la surface. Par conséquent, la cinétique de réaction varie d'une manière caractéristique pour chaque poussière combustible.

En plus l'analyse descriptive des mélanges combustibles a envisagé d'autres types de facteurs qui déterminent le comportement des nuages des poussières combustibles. De cette manière, il a été possible de faire une évaluation des effets de la présence d'autres substances sur le taux de réaction de

la poudre ainsi que l'influence des caractéristiques de la poudre (concentration, dispersibilité, hygroscopicité, etc.)

Les paramètres d'inflammabilité de la poudre sont déterminés dans les appareillages standardisés pour la caractérisation des nuages combustibles. Ces équipements permettent d'établir l'explosivité et la sévérité d'une explosion à partir de la génération d'un nuage confiné qui est enflammé en conditions de sécurité. La réalisation de ces tests peut déterminer les conditions qui constituent les majeurs niveaux de risque et d'affectation d'une poussière qui soit mise en suspension. Malheureusement, les caractéristiques spécifiques des poudres testées ont montré certaines variations ou fluctuations des résultats obtenus avec les tests d'inflammabilité.

Les variations observées dans les résultats expérimentaux mettent en question la fixation des conditions d'opération des tests d'explosivité. Normalement, les paramètres d'inflammabilité et d'explosivité sont déterminés sur la base de normes internationales figeant les conditions des tests. Il apparaît que ces conditions ne conduisent pas systématiquement à l'obtention des paramètres les plus reproductibles ou répétables. En plus la variation continue des niveaux de turbulence des nuages testés avec les standards établie que le délai entre l'injection des poudres dans les appareillages et leur inflammation est inadapté pour la plupart des poudres testées. Cet inconvénient est encore plus important pour les mélanges hybrides et les nanoparticules. Pour cette raison, cette thèse a envisagé la description des caractéristiques de la suspension initiale à partir d'une analyse de l'aérodynamique des suspensions. Les résultats de cette thèse fournissent un outil complémentaire aux études basées sur l'explosivité des poussières et la propagation de la flamme de combustion. De cette manière, il serait possible de choisir les conditions les plus pertinentes pour les tests d'inflammabilité.

Le but de cette thèse est donc d'étudier la dispersion des particules micrométriques au sein d'un écoulement turbulent dont les caractéristiques correspondront à celles rencontrées dans les équipements standardisés (tube Hartmann modifié et sphère de 20 litres). Les travaux seront conduits selon deux axes indissociables et complémentaires. D'une part, l'étude expérimentale visera à identifier les paramètres influant sur l'état de la suspension des particules (granulométrie in situ et caractérisation des champs de vitesse). D'autre part, l'étude computationnelle de tels écoulements sera poursuivie à partir des simulations basées sur la mécanique des fluides numérique.

A court terme, les résultats de cette thèse alimenteront les modèles prédictifs d'explosion des poudres. A moyen terme, ces analyses devront permettre d'infléchir les standards existants afin de définir ab initio, par simulation numérique, l'état de la suspension le plus pénalisant en vue de la quantification de ces risques majeurs.

1.9 LIST OF VARIABLES

c	Co-ordination number of the agglomerate	[-]
C_{gas}	Concentration of the gas in a hybrid mixture	[kg·m^3]
C^*_{gas}	Concentration of the gas that constitutes the lowest MIE of a hybrid mixture	[kg·m^3]
C_P	Heat capacity of the gas at constant pressure	[kJ· kmol^{-1}·K $^{-1}$]
d_{Agg}	Diameter of the solid agglomerate	[m]
d_p	Particle diameter	[m]

d_{pr}	Diameter of a primary particle of the solid agglomerate	[m]
$E_{ignitors}$	Energy provided by the ignition sources in the 20 L sphere	[kJ]
e	Void fraction of the agglomerate	[-]
E_1	Energy that results in the inflammation of the dust cloud after ten successive tests	[mJ]
E_2	Lowest ignition energy that produced an inflammation in the modified Hartmann tube	[mJ]
F_{cap}	Capillary force	[N]
F_{IP}	Inter-particle force per unit contact	[N]
F_{vdw}	Van der Waals force	[N]
h	Separation distance between two interacting elements	[m]
H_v	Hamaker coefficient	[J]
$HMIE$	Minimum ignition energy of a hybrid mixture	[mJ]
$I_{[E_2]}$	Number of tests with an inflammation at the energy E_2 in the modified Hartmann tube	[-]
k_g	Thermal conductivity of the combustion gas	[$W \cdot m \cdot K^{-1}$]
K_{St}	Deflagration index of the combustible dust	[$bar \cdot m \cdot s^{-1}$]
L	Thickness of the reaction zone	[m]
l_D	Kolmogorov microscale	[m]
MIE_{dust}	Minimum ignition energy of a combustible dust	[mJ]
MIE_{gas}	Minimum ignition energy of a combustible gas	[mJ]
$(NI+I)_{[E_2]}$	Total number of tests that were performed at the energy E_2 in the modified Hartmann tube	[-]
$P_{\max}$	Maximum pressure determined experimentally with the 20 L sphere	[bar]
$P_{\max}^{corrected}$	Maximum pressure determined with the 20 L sphere	[bar]
Re_{rel}	Relative Reynolds number defined for the solid agglomerate	[-]
S_f	Flame speed	[$m \cdot s^{-1}$]
S_g	Expansion and buoyancy of the gaseous combustion products	[$m \cdot s^{-1}$]
S_u	Laminar burning velocity	[$m \cdot s^{-1}$]

T_b	Temperature of the burned zone of the explosive mixture	[K]
T_i	Ignition temperature of the gas mixture	[K]
T_u	Temperature of the unburned zone of the explosive mixture	[K]
U	Contact potential difference between the considered surfaces	[V]
u	Velocity of the fluid	[m·s^{-1}]
u_p	Particle velocity	[m·s^{-1}]
V_{vessel}	Volume of the vessel where a dust explosion is developed	[m^3]
z	Direction perpendicular to the local gas flow	[-]

Greek symbols

α	Angle of contact between the solid and the liquid	[rad]
ε	Kinetic energy dissipation rate of the gas flow	[m^2·s^{-3}]
ε_0	Permittivity of the air	[F·m^{-1}]
μ	Dynamic viscosity of the gas	[Pa·s]
ν_{kin}	Kinematic viscosity of the gas	[m^2·s^{-1}]
σ	Surface tension of the liquid	[N·m^{-1}]
σ_{ATS}	Agglomerate tensile strength	[Pa]
σ_I	Inertial stress exerted on the aggregates surface	[Pa]
σ_R	Rotary stress exerted on the aggregates surface	[Pa]
σ_T	Turbulent stresses exerted on the aggregates surface	[Pa]
ρ	Fluid density	[kg·m^{-3}]
ρ_p	Particle density	[kg·m^{-3}]

1.10 REFERENCES

Abbasi, T., & Abbasi, S. A. (2007). Dust explosions–Cases, causes, consequences, and control. *Journal of Hazardous Materials*, *140*(1-2), 7–44.

Alekseev, A. G., & Sudakova, I. V. (1984). Flame Propagation Rate in Air Suspensions of Metal Powders. *Combustion, Explosion, and Shock Waves*, 564–566.

Amyotte, P. R. (2006). Solid inertants and their use in dust explosion prevention and mitigation. *Journal of Loss Prevention in the Process Industries*, *19*(2-3), 161–173.

Amyotte, P. R., & Eckhoff, R. K. (2010). Dust explosion causation, prevention and mitigation: An overview. *Journal of Chemical Health and Safety*, *17*(1), 15–28.

Amyotte, P. R., Mintz, K. J., Pegg, M. J., & Sun, Y. H. (1993). The ignitability of coal dust-air and methane-coal dust-air mixtures. *Fuel*, *72*(5), 671–679.

Andrews, G. E., & Bradley, D. (1972). Determination of burning velocities: A critical review. *Combustion and Flame*, *18*(1), 133–153.

ASTM E789 - 95. (2001). Standard Test Method for Dust Explosions in a 1.2-Litre Closed Cylindrical Vessel. *Annual Book of ASTM Standards*, pp. 1–18.

ASTM E1226 − 12a. (2012). Standard Test Method for Pressure and Rate of Pressure Rise for Combustible Dusts. *Annual Book of ASTM Standards*, pp. 1–13.

ASTM E1491 − 06. (2012). Standard Test Method for Minimum Autoignition Temperature of Dust Clouds. *Annual Book of ASTM Standards*, pp. 1–11.

ASTM E1515 − 14. (2014). Standard Test Method for Minimum Explosible Concentration of Combustible Dusts. *Annual Book of ASTM Standards*, pp. 1–9.

ASTM E2019 − 03. (2007). Standard Test Method for Minimum Ignition Energy of a Dust Cloud in Air. *Annual Book of ASTM Standards*, pp. 1–8.

ASTM E2931 − 13. (2013). Standard Test Method for Limiting Oxygen (Oxidant) Concentration of Combustible Dust Clouds. *Annual Book of ASTM Standards*, pp. 1–9.

Bartknecht, W. (1989). *Dust Explosions*. Berlin, Heidelberg: Springer Berlin Heidelberg.

Bouillard, J., Vignes, A., Dufaud, O., Perrin, L., & Thomas, D. (2010). Ignition and explosion risks of nanopowders. *Journal of Hazardous Materials*, *181*(1-3), 873–880.

Cashdollar, K. L. (2000). Overview of dust explosibility characteristics. *Journal of Loss Prevention in the Process Industries*, *13*(3), 183–199.

Chilworth. (2015). THE 1M3 VESSEL FOR DETERMINATION OF EXPLOSION SEVERITY - WHY USE IT? Retrieved from http://www.chilworth.com/wp-content/uploads/2015/06/Focus-Article-The-1M3-Vessel-for-Determination-of-Explosion-Severity-why-use-it.pdf

Cross, J., & Farrer, D. (1982). *Dust Explosions*. Boston, MA: Springer US. Retrieved from http://link.springer.com/10.1007/978-1-4615-6869-8

Crowl, D. A., & Louvar, J. F. (2011). *Chemical process safety: fundamentals with applications*. Upper Saddle River, NJ: Prentice Hall.

Dahoe, A. E. (2000). *Dust Explosions: A Study of Flame Propagation*. TU Delft.

Dahoe, A. E., Cant, R. S., & Scarlett, B. (2001). On the decay of turbulence in the 20-liter explosion sphere. *Flow, Turbulence and Combustion*, *67*(3), 159–184.

Dahoe, A. E., Hanjalic, K., & Scarlett, B. (2002). Determination of the laminar burning velocity and the Markstein length of powder–air flames. *Powder Technology*, *122*(2–3), 222–238.

Dahoe, A. E., Zevenbergen, J. F., Lemkowitz, S. M., & Scarlett, B. (1996). Dust explosions in spherical vessels: The role of flame thickness in the validity of the "cube-root law." *Journal of Loss Prevention in the Process Industries*, *9*(1), 33–44.

Debrincat, D. P., Solnordal, C. B., & Van Deventer, J. S. J. (2008). Characterisation of inter-particle forces within agglomerated metallurgical powders. *Powder Technology*, *182*(3), 388–397.

Di Benedetto, A., Garcia-Agreda, A., Dufaud, O., Khalili, I., Sanchirico, R., Cuervo, N., … Russo, P. (2011). Flame propagation of dust and gas-air mixtures in a tube. In *Proceedings of the 7th Mediterranean Combustion Symposium*. Chia Laguna Cagliari, Sardinia, Italy.

Di Benedetto, A., Russo, P., Amyotte, P., & Marchand, N. (2010). Modelling the effect of particle size on dust explosions. *Chemical Engineering Science*, *65*(2), 772–779.

Dreizin, E. L., & Hoffmann, V. K. (1999). Constant pressure combustion of aerosol of coarse magnesium particles in microgravity. *Combustion and Flame*, *118*(1), 262–280.

Dufaud, O., Perrin, L., Bideau, D., & Laurent, A. (2012). When solids meet solids: A glimpse into dust mixture explosions. *Journal of Loss Prevention in the Process Industries*, *25*(5), 853–861.

Dufaud, O., Perrin, L., & Traoré, M. (2008). Dust/vapour explosions: Hybrid behaviours? *Journal of Loss Prevention in the Process Industries*, *21*(4), 481–484.

Dufaud, O., Perrin, L., Traore, M., Chazelet, S., & Thomas, D. (2009). Explosions of vapour/dust hybrid mixtures: A particular class. *Powder Technology*, *190*(1-2), 269–273.

Dufaud, O., Poupeau, M., Khalili, I., Cuervo, N., Christodoulou, M., Olcese, R., … Perrin, L. (2012). Comparing Pyrolysis Gases and Dusts Explosivities: A Clue to Understanding Hybrid Mixtures Explosions? *Industrial & Engineering Chemistry Research*, *51*(22), 7656–7662.

Eckhoff, R. (2003). *Dust Explosions in the Process Industries, Third Edition: Identification, Assessment and Control of Dust Hazards* (3 edition). Amsterdam ; Boston: Gulf Professional Publishing.

Eckhoff, R. K. (2004). Partial inerting—an additional degree of freedom in dust explosion protection. *Journal of Loss Prevention in the Process Industries*, *17*(3), 187–193.

Eckhoff, R. K. (2006). Differences and similarities of gas and dust explosions: A critical evaluation of the European "ATEX" directives in relation to dusts. *Journal of Loss Prevention in the Process Industries*, *19*(6), 553–560.

Eckhoff, R. K. (2009a). Understanding dust explosions. The role of powder science and technology. *Journal of Loss Prevention in the Process Industries*, *22*(1), 105–116.

Eckhoff, R. K. (2009b). Understanding dust explosions. The role of powder science and technology. *Journal of Loss Prevention in the Process Industries*, *22*(1), 105–116.

Eckhoff, R. K. (2012). Does the dust explosion risk increase when moving from μm-particle powders to powders of nm-particles? *Journal of Loss Prevention in the Process Industries*, *25*(3), 448–459.

Eckhoff, R. K. (2013). Influence of dispersibility and coagulation on the dust explosion risk presented by powders consisting of nm-particles. *Powder Technology*, *239*, 223–230.

Gao, W., Mogi, T., Yu, J., Yan, X., Sun, J., & Dobashi, R. (2014). Flame propagation mechanisms in dust explosions. *Journal of Loss Prevention in the Process Industries*.

Garcia-Agreda, A., Di Benedetto, A., Russo, P., Salzano, E., & Sanchirico, R. (2011). Dust/gas mixtures explosion regimes. *Powder Technology*, *205*(1-3), 81–86.

Glor, M. (2006). Transfer of powders into flammable solvents overview of explosion hazards and preventive measures. *Journal of Loss Prevention in the Process Industries*, *19*(6), 656–663.

Going, J. E., Chatrathi, K., & Cashdollar, K. L. (2000). Flammability limit measurements for dusts in 20-L and 1-m3 vessels. *Journal of Loss Prevention in the Process Industries*, *13*(3–5), 209–219.

ISO 6184/1. (1985). Explosion protection systems — part 1: Determination of explosion indices of combustible dusts in air. *International Standards Organization*, pp. 1–5.

Israelachvili, J. N. (2011). 6 - Van der Waals Forces. In J. N. Israelachvili (Ed.), *Intermolecular and Surface Forces (Third Edition)* (pp. 107–132). San Diego: Academic Press.

Jaeger, N. (2001). Safety strategy against potential hazards due to the handling of powders in a blending unit. *Journal of Loss Prevention in the Process Industries*, *14*(2), 139–151.

Janes, A., Chaineaux, J., Carson, D., & Le Lore, P. A. (2008). MIKE 3 versus HARTMANN apparatus: Comparison of measured minimum ignition energy (MIE). *Journal of Hazardous Materials*, *152*(1), 32–39.

Janès, A., Vignes, A., Dufaud, O., & Carson, D. (2014). Experimental investigation of the influence of inert solids on ignition sensitivity of organic powders. *Process Safety and Environmental Protection*, *92*(4), 311–323.

Khalili, I., Dufaud, O., Poupeau, M., Cuervo-Rodriguez, N., & Perrin, L. (2012). Ignition sensitivity of gas–vapor/dust hybrid mixtures. *Powder Technology*, *217*, 199–206.

Kosinski, P., Nyheim, R., Asokan, V., & Skjold, T. (2013). Explosions of carbon black and propane hybrid mixtures. *Journal of Loss Prevention in the Process Industries*, *26*(1), 45–51.

KUHNER Safety. (2015a). 20-L Apparatus. Retrieved from http://safety.kuhner.com/en/product/apparatuses/safety-testing-devices/id-20-l-apparatus.html

KUHNER Safety. (2015b). Manual Mike 3.4. Retrieved from http://safety.kuhner.com/tl_files/kuhner/product/safety/PDF/B021_071.pdf

Lees, F. P. (2005). *Lees' Loss Prevention in the Process Industries (Partially updated by S. Mannan)* (Vols. 1–1–1–3). Oxford: Elsevier/Butterworth-Heinemann.

Makino, A., & Law, C. K. (2009). An analysis of the transient combustion and burnout time of carbon particles. *Proceedings of the Combustion Institute*, *32*(2), 2067–2074.

Matsuda, T., Yashima, M., Nifuku, M., & Enomoto, H. (2001). Some aspects in testing and assessment of metal dust explosions. *Journal of Loss Prevention in the Process Industries*, *14*(6), 449–453.

Miao, J., Leung, C. W., Huang, Z., Cheung, C. S., Yu, H., & Xie, Y. (2014). Laminar burning velocities, Markstein lengths, and flame thickness of liquefied petroleum gas with hydrogen enrichment. *International Journal of Hydrogen Energy*, *39*(24), 13020–13030.

Mohan, S., Trunov, M. A., & Dreizin, E. L. (2009). On possibility of vapor-phase combustion for fine aluminum particles. *Combustion and Flame*, *156*(11), 2213–2216.

Murray, J., Cooper, A., & Nagy, J. (1964). Explosibility of metal powders. Buraeu of Mines.

NFPA 68. (2002). Guide for Venting of Deflagrations. *National Fire Protection Association*.

Petit, J.-M. (2006). *Les mélanges explosifs. 2. Poussières combustibles* (No. 944). INRS.

Pilão, R., Ramalho, E., & Pinho, C. (2006). Explosibility of cork dust in methane/air mixtures. *Journal of Loss Prevention in the Process Industries*, *19*(1), 17–23.

prEN 14034. (2004). Determination of explosion characteristics of dust clouds. *European Committee for Standardization*, pp. 1–28.

Proust, C. (1996). Dust explosions in pipes: A review. *Journal of Loss Prevention in the Process Industries*, *9*(4), 267–277.

Proust, C., Accorsi, A., & Dupont, L. (2007). Measuring the violence of dust explosions with the "20 l sphere" and with the standard "ISO 1 m3 vessel": Systematic comparison and analysis of the discrepancies. *Journal of Loss Prevention in the Process Industries*, *20*(4–6), 599–606.

Rzal, F., & Veyssiere, B. (1994). Propagation mechanisms of starch particles-air flames. *Proceedings of the Sixth International Colloquium on Dust Explosions*, 186–200.

Saleh, K., Moufarej Abou Jaoude, M.-T., Morgeneyer, M., Lefrancois, E., Le Bihan, O., & Bouillard, J. (2014). Dust generation from powders: A characterization test based on stirred fluidization. *Powder Technology*, *255*, 141–148.

Sanchirico, R., Di Sarli, V., Russo, P., & Di Benedetto, A. (2015). Effect of the nozzle type on the integrity of dust particles in standard explosion tests. *Powder Technology*, *279*, 203–208.

Sattar, H., Andrews, G., Phylaktou, H., & Gibbs, B. (2014). Turbulent Flames Speeds and Laminar Burning Velocities of Dusts using the ISO 1 m3 Dust Explosion Method. *Chemical Engineering Transactions*, *36*, 157–162.

Siwek, R. (1988). Reliable determination of the safety characteristics in 20-l apparatus. In *Proceedings of the Flammable Dust Explosion Conference* (pp. 529–573). St. Louis: Missouri.

Skjold, T. (2003). *Selected Aspects of Turbulence and Combustion in 20-litre Explosion Vessels. Development of Experimental Apparatus and Experimental Investigation*. University of Bergen, Bergen.

Skjold, T. (2007). Review of the DESC project. *Journal of Loss Prevention in the Process Industries*, *20*(4-6), 291–302.

Stahl Schaltgeräte GmbH. (2004). *The basics of dust-explosion protection*. Waldenburg, Germany.

Tamanini, F. (1990). Turbulence effects on dust explosion venting. *Plant/Operations Progress*, *9*(1), 52–60.

Tamanini, F. (1998). The role of turbulence in dust explosions. *Journal of Loss Prevention in the Process Industries*, *11*(1), 1–10.

Traoré, M., Dufaud, O., Perrin, L., Chazelet, S., & Thomas, D. (2009). Dust explosions: How should the influence of humidity be taken into account? *Process Safety and Environmental Protection*, *87*(1), 14–20.

Vignes, A. (2008). *Evaluation de l'inflammabilité et de l'explosivité des nanopoudres : une démarche essentielle pour la maîtrise des risques*. Ecole Nationale Supérieure des Industries Chimiques, Nancy.

Vignes, A., Muñoz, F., Bouillard, J., Dufaud, O., Perrin, L., Laurent, A., & Thomas, D. (2012). Risk assessment of the ignitability and explosivity of aluminum nanopowders. *Process Safety and Environmental Protection*, *90*(4), 304–310.

Weiler, C., Wolkenhauer, M., Trunk, M., & Langguth, P. (2010). New model describing the total dispersion of dry powder agglomerates. *Powder Technology*, *203*(2), 248–253.

Wengeler, R., & Nirschl, H. (2007). Turbulent hydrodynamic stress induced dispersion and fragmentation of nanoscale agglomerates. *Journal of Colloid and Interface Science*, *306*(2), 262–273.

Yuan, Z., Khakzad, N., Khan, F., & Amyotte, P. (2016). Domino effect analysis of dust explosions using Bayesian networks. *Process Safety and Environmental Protection*, *100*, 108–116.

CHAPTER II

NUMERICAL SIMULATIONS OF SOLIDS DISPERSIONS

The computational approach that is envisaged in this study intends to describe the dispersion process of a gas-solid mixture. This analysis must establish how the phenomena associated to the two-phase flow determine the evolution of a combustible dust cloud. Therefore, it must consider the interactions developed by the two phases. For this purpose, this approach must be situated in the context that corresponds to the multi-scale characteristics of the scenario considered. In this manner, the scope of this analysis can be established in accordance with the objectives and limitations of the model proposed for this numerical description. Figure 2.1 describes the multilevel classification that can be posed for a dispersion process according to the scope of the considered analysis.

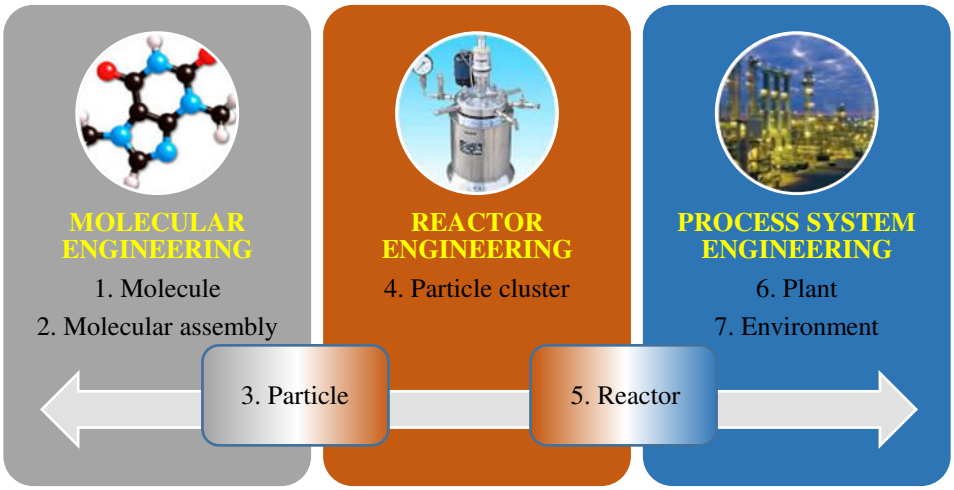

Figure 2.1. Multiscale characteristics of chemical engineering and its multilevel classification (Li et al., 2009)

The dispersion of a micrometric powder in an experimental apparatus, such as the modified Hartmann tube or the 20 L sphere, is located in the intermediate group (see 3. Particle) of the multilevel classification dictated by Li et al (2009). This condition defines the spatiotemporal features of the system between the boundary scales that correspond to a micro and a macro scale. Therefore, the scope of this study is located between the physical characteristics of the flow behavior in the vessels (e.g. turbulence) and the analysis of the interaction phenomena among the solid particles.

Furthermore, this mesoscopic analysis is defined by the length and time scales of the dispersion process. For this particular case, the macroscopic behavior of the dust cloud is established by the evolution of the turbulent eddies within the vessels and the behavior of the bulk of the dust cloud. In addition, the solid phase is characterized by a micrometric size distribution that demands the characterization of the mechanisms that cause the variations of the aggregation levels of the dispersed agglomerates. In accordance with these characteristics, this chapter presents some of the main alternatives that are considered for the computational description of a multiphase system as well as the selection criteria that determined the models that were implemented in the case study.

The description of the trajectories followed by each one of the phases in the dust cloud must define a predictive model to characterize the transport phenomena occurred during the dispersion process. Thus, it will be possible to compute the velocity field and determine the evolution of the turbulence levels of the gas flow as well as the distribution of the combustible dust within the explosion chambers of the tests apparatuses.

The predictive calculation process is defined by the discretization of the flow domain and the physical models that characterize the interaction mechanisms. These parameters are established by the physical properties of the combustible dust cloud and the geometrical specifications of every experimental apparatus. This chapter will present the most representative numerical models that are considered to describe a solid-fluid mixture at a micro or mesoscopic scale. Thereafter, it will pose the selection criteria that were considered to develop the computational approach as well as the numerical scheme of the simulation of the dispersion process. For this purpose, the models that were considered to characterize the behavior of the gas and the dispersed solid are discussed in this chapter in order to determine the main equations that were considered to describe the dispersion phenomena. In this manner, this study constituted the basis of the computational approach that is presented in the fourth chapter of this thesis.

Finally, some particular applications of the selected models on areas associated to fluidization and dust explosions are presented in order to establish the advantages and limitations that may arise on the computational characterization of a combustible dust cloud. Both categories are coupled to present the most representative simulation techniques that can be considered for a fluid-solid mixture, which are listed in Table 2.1:

Table 2.1. Simulation techniques considered for a fluid-solid mixture

APPROACH	SIMULATION SCALE	SIMULATION TECHNIQUE	DESCRIPTION OF THE GAS	DESCRIPTION OF THE COMBUSTIBLE DUST
Particle methods	Microscopic	Molecular Dynamics Monte Carlo simulations	Lagrangian	Lagrangian
Particle methods	Mesoscopic	Dissipative Particle Dynamics Brownian Dynamics Lattice-Boltzmann Methods	Lagrangian	Lagrangian
Particle methods	Macroscopic	Vortex methods Smooth Particle Hydrodynamics	Lagrangian	Lagrangian
Finite-volume method	Mesoscopic and macroscopic	Computational Fluid Dynamics (E-E)	Eulerian	Eulerian
Finite-volume method	Mesoscopic and macroscopic	Computational Fluid Dynamics (E-L)	Eulerian	Lagrangian

2.1 COMPUTATIONAL STUDY OF A GAS-SOLID FLOW

2.1.1 Numerical methods applied for the description of a homogeneous or heterogeneous system

The numerical approaches that will be presented for the description of a multiphase flow are determined by the length and time scales of the system as well as the physics that are going to be described with the computational analysis. For this reason, the techniques that can be employed for a characterization of a given system (homogeneous or heterogeneous) will be classified according to the approach given for every phase (discrete or continuum). The selection of an available technique is an important aspect of the study because it will provide more details and restrictions to the description of certain characteristics of the flow. For this reason, it was necessary to define previously the size scale of the flow domain of this case study.

This section describes briefly some of the most utilized computational techniques that can be adopted to characterize a multiphasic system. The classification that is proposed considers two categories. The first division envisages every phase in a Lagrangian (particle methods) or an Eulerian approach (continuous phase). Afterwards, a second category is proposed in accordance with the size of the simulation scales: microscopic, mesoscopic and macroscopic. The definition of these simulation scales is associated to analyses comprised in the molecular and the reactor engineering

A. *Particle methods for microscopic scales (10^{-9} – 10^{-8} m)*

The particle methods that characterize a discontinuous phase at its minimum scale are the Molecular Dynamics (MD) and the Monte Carlo (MC) simulations. The first method defines a discrete representation of the underlying physics associated to a group of interacting particles. For this reason, it is usually considered for the development of molecular and mesoscopic simulations (Koumoutsakos, 2005). On the contrary, the MC simulations differ from the former method because they are based on a stochastic approach that is not determined by the dynamic analysis of the system but on a criterion defined by the energy minimization (thermodynamic equilibrium). Some details about these techniques are discussed below:

- ***Molecular dynamics (MD):*** This technique describes the motion of a fluid phase in the time and length scales of molecular motion. This model has been considered for the analysis of various issues of fluid mechanics of wetting and hydrophobicity at the nanometric scale (Walther et al., 2004). In addition, it has also been used for the study of thermodynamic equilibrium (Koumoutsakos, 2005). Nevertheless, this method is considered to be more appropriate for investigating the dynamic properties of a system in a non-equilibrium situation. This numerical method establishes the motion of molecules by integrating the Newton's equations of motion in classical theory (Equation 2.1). The motion of the molecule is defined according to the mass of the molecule n (m_n) and the total force exerted on the representative particle (f_n). This force is determined by the contributions of the ambient molecules and an external field (Satoh, 2011).

$$m_n \frac{du_n}{dt} = f_n \qquad 2.1$$

  This approach establishes that the number of equations is equal to the number of molecules. Thus, it requires the development of the Taylor series expansion to constitute an algebraic scheme.

- ***Monte Carlo simulations (MC):*** This method generates a series of microscopic states under a certain stochastic law (Mooney, 1997). This method differs from the techniques discussed above

because its descriptive law does not correspond to the equations of motion of particles. For this reason, it cannot include the concept of explicit time, and thus is only a simulation technique for phenomena in thermodynamic equilibrium. Therefore, this method is not recommended for the predictive analysis of the dynamic properties of a system because of their dependence on the time (Satoh, 2011). In accordance with the basis of this approach, the method minimizes the free energy of a system through the determination of the minimum value of the Helmholtz free energy of a determined number of particles (H_H):

$$H_H = E - TS \tag{2.2}$$

in which E is the potential energy of the system, T is the temperature of the system and S is the entropy. The function is minimized when various stochastic states arise due to the different levels of interaction energy that are developed by the proximity of the particles.

B. *Particle methods for mesoscopic scales (10^{-9} – 10^{-6} m)*

- ***Dissipative Particle dynamics (DPD):*** This method contemplates several groups or clusters of solvent molecules as virtual fluid particles. This alternative allows considering similar characteristic times for the solvent and the dispersed solid particles. For this purpose, the interacting fluid elements are denominated as dissipative particles (Satoh, 2011). In accordance with this statement, they exchange momentum and also exhibit a random motion similar to Brownian particles. The interactions developed by them are defined by the particle-particle potentials.

  This model is usually adopted for the descriptive study of colloidal systems (Phan-Thien et al., 2016) but it has also been considered for the analysis of other phenomena such as natural convection (Abu-Nada, 2015). In fact, they are capable to predict the behavior of this type of mixtures by taking into account the multibody hydrodynamic interactions and the mass of each particle (m_n). For this purpose, the motion of every dissipative particle and its velocity (u_n) are modeled according to the following equation:

$$m_n \frac{du_n}{dt} = \sum_{j(\neq n)} F_{nj}^C + \sum_{n(\neq \mathrm{i})} F_{nj}^D + \sum_{n(\neq \mathrm{i})} F_{nj}^R \tag{2.3}$$

  The total momentum of the system is conserved. Thus, the forces acting on the particle i are exerted by the particles that surround it (j). These forces can be conservative (F_{nj}^C), dissipative (F_{nj}^D) or random (F_{nj}^R). The method is conducted in a similar way that is employed for Brownian dynamics simulations.

- ***Brownian Dynamics (BD):*** This method overcomes the difficulties found in the MD model for the computational cost of the simulation of the dispersion process. The main issue that arises relies on the different characteristic times of the two phases (Pandey et al., 2016). This difference establishes that the MD would represent a quiescent particle surrounded by the moving solvent fluid particles. This problem is solved by considering a continuum medium for the solvent (Satoh, 2011). This fact means that the tracking calculations are restrained to the dispersed phase. Therefore the influence of the molecular motion is combined into the equations of motion of dispersed particles as stochastic random forces.

The continuous phase (solvent) will define a random force (f_B) that will define the motion of every particle with the Langevin equation:

$$m_n \frac{du_n}{dt} = f_B - 3\pi\mu d_p u_n + f_{EF} \quad 2.4$$

In which u_n is the velocity vector, d_p is the particle diameter, μ is the viscosity of a base liquid and f_{EF} is the force exerted by an external field. The Langevin equation is solved for short time intervals as a simple first-order differential equation.

- ***Lattice Boltzmann method (LBM):*** This simulation technique is widely adopted for the analysis of the behavior of polymeric liquids and particle dispersions. This model envisages a simulation region that can be discretized as a lattice, in which the virtual fluid particles move and collide with the adjacent particles. This method differs from the molecular dynamics because it treats the particle distribution function of velocities rather than the positions and the velocities of the fluid particles (Satoh, 2011). In addition, a virtual particle has a limited number of positions in the domain (N_P) for its displacement in the LBM (9 for two-dimensional lattices and 19 for three-dimensional discretizations).

  The basis of the method relies on the calculation of the number density of fluid particles moving in a given direction through a distribution function ($f_{i,LBM}(x,t)$). Thereupon, the macroscopic density of the fluid ($\rho(x,t)$) and the macroscopic velocity ($u(x,t)$) can be determined from the spatiotemporal discretization (Δx , Δt) and the variation of the distribution function.

$$\rho(x,t) = \sum_i^{N_P} f_{i,LBM}(x,t) \quad 2.5$$

$$\rho(x,t)u(x,t) = \sum_i^{N_P} f_{i,LBM}(x,t)\frac{\Delta x}{\Delta t} \quad 2.6$$

C. *Particle methods for macroscopic scales (10^{-6} – 10^{-2} m)*

The Vortex Methods (VM) and the Smooth Particle Hydrodynamics (SPH) constitute a Lagrangian description of the flow of a continuum medium through the numerical analysis of a set of discrete elements. Thereupon, these methods determine the macroscopic properties of a fluid flow in a contributive way. This fact implies that the macroscopic property of the continuous phase in a region is estimated as the sum of the properties of all the representative particles located in it. Koumoutsakos (2005) established that these techniques represent an adaptive, efficient, stable, and accurate computational alternative for simulating continuum flow phenomena and for capturing interfaces such as vortex sheets. Nevertheless, this author also establishes that the VM and the SPH have some difficulties in the accurate treatment of boundary conditions. Moreover, their adaptability may introduce spurious scales arisen from a severe particle distortion; hence several simulations are required to determine which vortex structures represent the fluid flow.

- ***Vortex methods (VM):*** This technique has been used since 1930 to describe the vortical structures in fluid flows. The method is based on the discretization scheme of the Biot-Savart equation. This procedure is accomplished through the regularization of the convecting velocity field and the systematic removal of spurious vortical structures (Koumoutsakos, 2005). For this purpose, a

lagrangian description of the fluid flow is performed with vorticity-carrying particles whose core size is ε.

The locations (x_p) and the vorticity (ω_p) carried by the fluid elements are determined by the sum of the values of the vortex ($u_q \,\&\, \omega_q$) as well as their volumes (v_q). These contributions can be calculated through the development of the following discrete system of differential equations (Toro, 2006):

$$\frac{dx_p}{dt} = \sum_{q=1}^{N_p} v_q K_\varepsilon \left(x_p - x_q\right) \times \omega_q + U_0\left(x_p, t\right) \tag{2.7}$$

$$\frac{d\omega_p}{dt} = \left[\sum_{q=1}^{N_p} v_q \nabla K_\varepsilon \left(x_p - x_q\right) \times \omega_q\right] \omega_q + \frac{\nu_{kin}}{\varepsilon_q^2} \sum_{q=1}^{N_p} v_q \left[\omega_p - \omega_q\right] \eta_{\varepsilon_q}\left(\left|x_p - x_q\right|\right) + F\left(x_p\right) \tag{2.8}$$

These equations are characterized by the Biot-Savart kernel (K_ε) and a solution of the homogeneous Poisson equation ($U_0(x_p, t)$) that satisfies the boundary conditions. In addition the dynamic system considers the viscous effects of the fluid (ν) as well as an even function for the discretization of the Biot-Savart equation (η_ε). Moreover, the vorticity sources located at the solid boundaries ($F\left(x_p\right)$) can also be considered.

- ***Smooth Particle Hydrodynamics (SPH):*** This method is commonly used for grid-free astrophysics simulations. Like the VM, the SPH also requires a mollifier kernel ($W\left(u_p - u_q, h\right)$). This factor must only be positive and have a local support. In addition, the interparticle distance (h) takes the role of the mollifier core size. The SPH model describes the motion of the particles and the continuity and momentum equations according to the following expressions:

$$\frac{dx_p}{dt} = u_p \tag{2.9}$$

$$\frac{d\rho_p}{dt} = \sum_q v_q \left(u_q - u_p\right) \cdot \nabla W\left(u_p - u_q, h\right) \tag{2.10}$$

$$\frac{du_p}{dt} = \frac{1}{\rho_p} \sum_q v_q \left(\underline{\underline{\tau}}_q - \underline{\underline{\tau}}_p\right) \cdot \nabla W\left(u_p - u_q, h\right) + F_{SPH} \tag{2.11}$$

In which $\underline{\underline{\tau}}$ denotes the stress tensor of the flow and F_{SPH} corresponds to external force fields experienced by the particles (Koumoutsakos, 2005). A closure relationship is necessary to express the stress tensor as a function of known variables.

D. *Computational Fluid Dynamics (CFD) (10^{-4} m – Industrial length scales)*

The Navier-Stokes equations are used to describe the behavior of a continuous phase. In accordance with this statement, the characteristics of the flow can be predicted through the conservation of mass,

momentum and energy. The numerical solution of these equations is achieved through the finite-volume method (Wendt, 1992). This method establishes that the conditions of the flow will be determined as the conditions of a discretized domain, in which at least one of the phases is continuous. For this purpose, the flow domain is defined as a polygonal open subset that consists of a set of control volumes. For each one of these volumes, the conservation laws are integrated in the center and its faces (or edges) (Eymard et al., 2007).

The Computational Fluid Dynamics (CFD) codes are based on the description of each flow variable of a continuous phase according to the finite-volume method. Thus, they constitute a very powerful tool that spans over a wide range of industrial and non-industrial applications (Versteeg & Malalasekera, 2007). The computational analysis replaces the governing partial differential equations of the fluid flow with an algebraic equation system. Afterwards, it advances the solutions of the system in space and/or time to obtain a final numerical description of the complete flow field of interest (Wendt, 1992).

Continuity:
$$\frac{\partial \rho}{\partial t} + \nabla \cdot (\rho u) = 0 \qquad 2.12$$

Momentum:
$$\frac{D(\rho u)}{Dt} = -\nabla p - \nabla \cdot \tau + \rho g \qquad 2.13$$

Energy:
$$\rho C_p \frac{DT}{Dt} = -\nabla \cdot q - \left(\frac{\partial \ln \rho}{\partial T} \right)_p \frac{Dp}{Dt} - \nabla \tau : u \qquad 2.14$$

The Computational Fluid Dynamics can be adapted to the description of particle-laden flows. Several researchers such as Alletto & Breuer (2012) and Schellander (2014) have discussed how the CFD can implement a secondary phase in the description of the continuum medium. The selection of the most appropriate CFD approach for the characterization of particle-laden flows relies on the volume fraction of the dispersed phase in the flow domain (Figure 2.2):

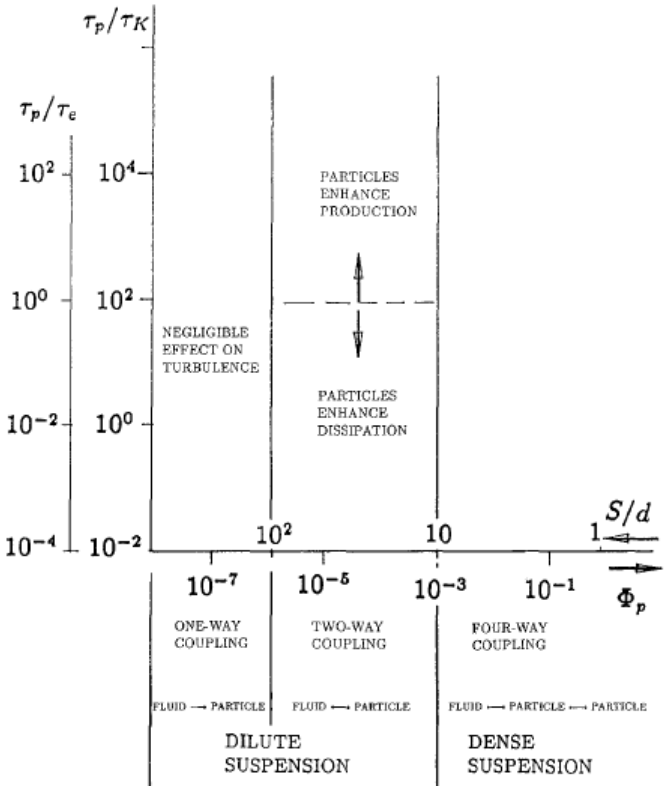

NOTES

Φ_p: Volume fraction of particles

V: Volume occupied by particles and fluid

S: Distance between the centers of two neighboring particles

d: Particle diameter

τ_p: Particle response time for Stokes flow

τ_K: Kolmogorov time scale

τ_e: Turnover time of large eddy

Figure 2.2. Map of flow regimes in particle-laden flows (Elghobashi, 1991)

Indeed, the mixtures whose volume fractions are below 10^{-6} are denominated as dilute flows. These regimes depend only on the behavior of the fluid (one-way coupling). The medium-density flows that range between 10^{-6} and 10^{-3} develop an influence of the particles on the surrounding fluid (two-way coupling). For a given dust concentration, this influence is associated to the particle response time. For instance, a decrease of the particle response time (smaller particle diameter for the same particle material and fluid viscosity) increases the dissipation rate of turbulence energy. On the contrary, an augmentation of this variable increases the Reynolds particle number. This fact enhances the production of turbulence energy if this dimensionless number reaches a value of 400 due to vortex shedding (Elghobashi, 1991).

Furthermore, a greater concentration of particles ($>10^{-3}$) represents numerous particle-particle collisions that have a significant influence of the flow behavior (four-way coupling) (Alletto & Breuer, 2012; Skjold, 2003). These conditions divide the alternatives in two different subcategories or schemes: Eulerian-Lagrangian and Eulerian-Eulerian. The former is recommended for dilute flows whose solids volume fraction below 10% whereas the latter is more suitable for highly concentrated dispersions.

Now, the two main approaches that are established by the finite-volume method for a fluid-solid dispersion will be discussed. The main difference between the simulation techniques relies on the treatment that is posed for the dispersed phase, which can be considered as another continuous phase (Eulerian approach) or as a discrete phase (Lagrangian approach):

- ***Eulerian-Lagrangian approach (E-L):*** This scheme treats the dispersed phase as a discrete entity that can interact with the continuum (Equations 2.12-2.14). Thereupon, the motion of each particle inside the flow is traced according to a momentum balance defined for every dispersed particle. In accordance with statement, this approach treats this phase in a way that is similar to one described for the molecular dynamics in Equation 2.1. Thus, the following expression defines the treatment of the model for the discrete phase:

$$\frac{du_p}{dt} = F_D\left(u - u_p\right) + g\,\frac{\rho_p - \rho}{\rho} + F_x \qquad 2.15$$

  The particle acceleration of is determined by the drag force exerted by the continuous phase on the dispersed phase ($F_D(u-u_p)$), the buoyancy effects and the acceleration terms attributed to additional forces (F_x). Further details about the momentum balance will be discussed in the section 2.1.5. Moreover, this scheme allows considering the particle-particle interactions that are constituted by the collisions of the dispersed phase. Therefore, the main advantage of this model is associated to its capability of resolving every impact force of the particle (Schellander, 2014). For this purpose, it can constitute a stochastic or deterministic technique, which is also known as Discrete Element Methods (DEM). Nonetheless the main disadvantage of the E-L model relies on the computational cost that is required for the calculation process. Schellander (2014) established that the calculation efforts rise by the square of the number of particles.

  The Lagrangian approach that is established according to a Discrete Element Method (DEM) was developed by Cundall & Strack (1979). This approach was envisaged to consider a suspension as a system defined by multi-body collisions. These interactions determine the trajectories and velocities of the dispersed particles. Thereafter, this technique can be coupled to a Computational Fluid Dynamics (CFD) method to describe the eventual interactions with a fluid flow. The most common analysis relied on the description of the phase pneumatic conveying of a dense phase by taking into account the fluid forces exerted on several particle assemblies (Tsuji et al., 1993). Initially, the models were simulated in simple systems such as two-dimensional fluidized beds. The first results obtained with this insight characterized the circulation of macroscopic scaled mixtures.

  The combined continuum and discrete model (CCDM) has been developed by enhancing the previous models to describe mixtures submitted to external forces (e.g. magnetic fields). These

models have also been improved by the augmentation of the computational resources, which make them capable of modelling systems with higher solids concentrations (e.g. four-way coupling). This fact has defined this well-recognized approach as an effective method to study the fundamentals of particle–laden flows under different conditions (Chu & Yu, 2008). This condition is observed because this technique has allowed reproducing various representative behaviors of the particles fluidization (Guo et al., 2014). Moreover, the scope of the simulation analyses has also envisaged the description of other phenomena such as the heat transfer among the phases that compose the multiphase flow.

- ***Eulerian-Eulerian approach (E-E):*** This scheme treats the dispersed phase as a continuous medium. Hence, the properties are replaced by representative quantities of velocity, density and volume fraction of the dispersed phase (Schellander, 2014). These variables are calculated as smooth functions of position and time. Thus, a control volume is fixed to perform the balances described by the Navier-Stokes equations. For this purpose, this model implements the definitions of the granular temperature and the stresses that are obtained from the kinetic theory. These characteristics are complemented with a momentum exchange correlation for the fluid and the dispersed phase.

  The utilization of this approach constitutes a less realistic description of a particle-laden flow. Thereupon, the computational effort is lower than that associated to an Eulerian-Lagrangian approach. This condition is observed because it just demands the solution of a set of conservation equations for the whole dispersed phase (Schellander, 2014). Unfortunately, this envisagement of the dispersed phase as a continuum represents the omission of the Magnus force because this interaction is constituted by the rotational inertia of the dispersed particles. Moreover, another deficiency of this approach is evidenced when there is a polydispersed phase. The E-E approach requires the definition of a continuum for every diameter. Nevertheless, this technique can still be a recommendable option for the characterization of flows that are highly influenced by the inter-particle collisions if the representative parameters are set correctly. The Eulerian-Eulerian can be represented according to the Mixture model and the Eulerian model. These schemes are described as follows:

  - *Mixture Model:* This model defines a set of separate phases that can interact with each other. For this purpose, it assumes a local equilibrium over short spatial length scales. Thereupon, it calculates the continuity, momentum and energy for the mixture and the volume fraction of every secondary phase (Ansys Inc., 2009). This scheme is simpler than the full Eulerian model because it solves fewer variables. For this reason, it is advisable to consider it for the study of bubbly flows, sedimentation, and cyclone separators. The following expressions describe the multiphase Navier-Stokes posed for this model:

Continuity:
$$\frac{\partial}{\partial t}(\rho_m)+\nabla\cdot(\rho_m u_m)=0 \qquad 2.16$$

Momentum:
$$\frac{\partial}{\partial t}\left(\sum_{k=1}^{N_{phases}}\rho_m u_m\right)+\nabla\cdot\left(\sum_{k=1}^{N_{phases}}\rho_m u_m u_m\right)=-\nabla p+\rho_m g+F_B$$
$$+\nabla\cdot\left[\mu_m\left(\nabla u_m+\nabla u_m^T\right)\right]+\nabla\cdot\left(\sum_{k=1}^{N_{phases}}a_k\rho_k(u_k-u_m)(u_k-u_m)\right) \qquad 2.17$$

Energy:
$$\frac{\partial}{\partial t}\left[\sum_{k=1}^{N_{phases}}a_k\rho_k\left(h_k-\frac{p}{\rho_k}+\frac{u_k^2}{2}\right)\right]+\nabla\cdot\left\{\sum_{k=1}^{N_{phases}}a_k u_k\left[\rho_k\left(h_k-\frac{p}{\rho_k}+\frac{u_k^2}{2}\right)+p\right]\right\}$$
$$=\nabla\cdot\left(k_{eff}\nabla T\right)+S_E \qquad 2.18$$

With:
$$\rho_m=\sum_{k=1}^{N_{phases}}a_k\rho_k \qquad 2.19 \qquad u_m=\sum_{k=1}^{N_{phases}}\frac{a_k\rho_k u_k}{\rho_m} \qquad 2.20$$

$$\mu_m = \sum_{k=1}^{N_{phases}} a_k \mu_k \qquad 2.21 \qquad k_{eff} = \sum_{k=1}^{N_{phases}} a_k \left(k_k + k_t\right) \qquad 2.22$$

where a_k, ρ_k, μ_k, u_k and h_k are the volume fraction, density, viscosity, velocity and enthalpy of the phase k respectively. The same variables with the subscript m correspond to the values of the mixture. The effective conductivity (k_{eff}) is defined by the contribution of each phase and the turbulent thermal conductivity (k_t). In addition, T, p and g represent the temperature, pressure and gravitational acceleration of the system. Finally, some additional terms can be included to denote the external body forces (F_B) and the external energy sources (S_E).

- *Eulerian Model:* This model differs from the 'Mixture model' because it handles a set of momentum and continuity equations for each phase. Coupling is achieved through the pressure and interphase exchange coefficients. The manner in which this coupling is handled depends upon the type of phases involved; granular (fluid-solid) flows are handled differently than non-granular (fluid-fluid) flows. For granular flows, the properties are obtained from application of kinetic theory. Momentum exchange between the phases is also dependent upon the type of mixture being modeled. Applications of the Eulerian multiphase model include bubble columns, risers, particle suspension, and fluidized beds (Ansys Inc., 2009). This model is calculated according to the following equations:

Continuity:
$$\frac{\partial}{\partial t}\left(a_k \rho_k\right) + \nabla \cdot \left(a_k \rho_k u_k\right) = \sum_{p=1}^{N_{phases}} \left(m_{pk} - m_{kp}\right) + S_k \qquad 2.23$$

Momentum:
$$\frac{\partial}{\partial t}\left(a_k \rho_k u_k\right) + \nabla \cdot \left(a_k \rho_k u_k u_k\right) = -a_k \nabla p + \nabla \cdot \overline{\overline{\tau}}_k + a_k \rho_k g + \sum_{p=1}^{n}\left(R_{pk} + m_{pk} u_{pk} - m_{kp} u_{kp}\right) + F_B + F_{lift,k} + F_{vm,k} \qquad 2.24$$

Energy:
$$\frac{\partial}{\partial t}\left(a_k \rho_k h_k\right) + \nabla \cdot \left(a_k \rho_k u_k h_k\right) = a_k \frac{\partial p_q}{\partial t} + \overline{\overline{\tau}}_k : \nabla u_k - \nabla q_k + S_k + \sum_{p=1}^{n}\left(Q_{pk} + m_{pk} h_{pk} - m_{kp} h_{kp}\right) \qquad 2.25$$

with:
$$\overline{\overline{\tau}}_k = \sum_{k=1}^{N_{phases}} a_k \mu_k \left(\nabla u_m + \nabla u_m^T\right) + a_k \left(\lambda_k - \frac{2}{3}\mu_k\right) \nabla \cdot u_k \overline{\overline{I}} \qquad 2.26$$

The continuity equation is defined by the mass transfer between the phases p and k (m_{pk}) and the interphase velocity (u_{kp}), which is the velocity of the phase that receives the mass transferred. Moreover, the momentum balance can be defined for the phase k by taking into account the external body forces (F_B), virtual mass forces ($F_{vm,k}$), lift forces ($F_{lift,k}$) and the interaction forces between phases (R_{pk}).

In addition, this model considers the shear (μ_k) and bulk viscosity (λ_k) of the phase. Finally, the energy balance is determined by the heat flux (q_k), the external source terms in the phase k (S_k), the heat exchange between the phases (Q_{pk}) and the interphase enthalpy (h_{pk}).

2.1.2 Selection criteria for the computational approach

The simulation technique that was considered for this study was chosen by taking into account the objectives of the analysis and conditions of the confined system. Previously, this chapter posed the scale and the domain in which a combustible cloud develops within the dispersion chamber of a flammability test. This context was considered to choose the most appropriate simulation technique among the available alternatives. This procedure was carried out with a confrontation of the options in the analysis of three different aspects:

- Size of the flow domain
- Computational cost
- Description of the dispersion phenomena and solids concentration

These aspects are discussed below, but previously it was necessary to define the simulation problem. For this purpose some of the most relevant characteristics of the phases involved in the combustible dust clouds are summarized in Table 2.2:

Table 2.2. General description of the main components of the combustible dust cloud

COMPONENT	GENERAL DESCRIPTION
General system	The time scope for the description of the dispersion process of the combustible dust in the modified Hartmann tube ranges between 60 and 200 ms and between 30 and 150 ms for the 20 L sphere. In addition the dispersion chambers of these apparatuses are constructed in volumes equal to 1.2 and 20 liters respectively.
Dispersion gas	The fluid flow is characterized by different regimes during the dust dispersion because the injection corresponds to a finite amount of pressurized gas. Therefore, the initial stages of the dust dispersion are distinguished due to high turbulence levels and transonic conditions. On the contrary, the final period is submitted to a low turbulence due to the energy dissipation.
Combustible dust	The combustible dust defines a polydispersed discrete phase whose size distribution ranges between 10 and 100 μm. In addition, the combustible dust exhibits different segregation levels that are caused by the turbulent eddies generated in the flow. Moreover, the dust is submitted to various phenomena due to the turbulence variations in the fluid flow. These mechanisms include fragmentation, agglomeration and sedimentation.

A. *Size scale of the flow domain*

The characterization of a combustible dust cloud demands the analysis of the segregation phenomenon as well as the evolution of the turbulence levels in the two-phase flow. For this reason, it is necessary to take into account the geometry of the flow domain. Some design specifications of the equipment such as the size of the dispersion chamber and shape of the internal elements (nozzle, ignitors, etc.) establish the distribution of the injected mixture within the test apparatus. Therefore, it is necessary to consider the whole volume of the vessel rather than a specific region.

The molecular dynamics might be inconvenient for this analysis because of this restriction. Indeed, the free path of the air is 66 nm at sea level. In addition, the collision time between two fluid particles is near 10^{-10} seconds. Hence, this technique would imply a high computational effort that cannot be accomplished with the resources that are currently available. Moreover, a simulation performed with a DPD analysis would pose the same limitation but it would have a lower computational demand. Therefore, the scope of this study must not be established in a microscopic characterization of the two-

phase flow and the gas should be considered as a continuum medium. This conclusion can be also obtained from the examination of Figure 2.3, which recommends the implementation of the Computational Fluid Dynamics and the mesoscopic theory for a length scale situated between several micrometers and millimeters.

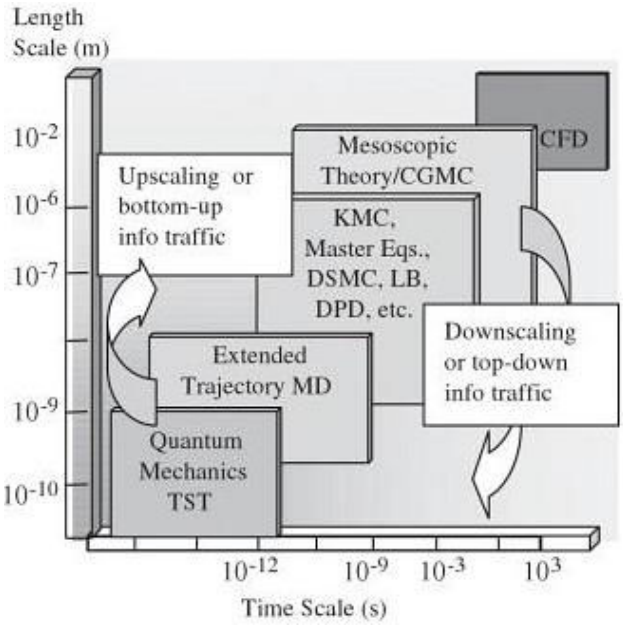

TST: Transition State Theory

MD: Molecular Dynamics

KMC: Kinetic Monte Carlo

DSMC: Direct Simulation Monte Carlo

LB: Lattice-Boltzmann

DPD: Dissipative Particle Dynamics

CGMC: Coarse-grained Monte Carlo

CFD: Computational Fluid Dynamics

Figure 2.3. Schematic representation depicting scales and various simulators (Marin, 2005)

This condition was also discussed by Marin (2005). The multiscale analysis of different phenomena has become a paradigm in the development of the chemical engineering. However, it creates new degrees of freedom when it passes from a fine to a coarse scale. Despite the fact that the turbulent flow can be described more precisely with the approaches discussed above, the omission of the microscopic particle methods also leaves out the characterization of some of the most relevant interaction mechanisms such as the Van der Waals forces. For this reason, this selection must be performed more precisely in the description of clouds composed by nanometric dusts.

B. *Computational cost*

The description of the flow domain must be performed in a multi-scale approach. However, the description of a characteristic of the dust cloud of a given length scale will limit the explanation of a property analyzed in other scale. Indeed, a code based on these techniques can be adapted to take into account any particular force of a particle-laden flow. Hence, the utilization of a particle method as a computational approach can be advantageous for certain types of analysis of a dust cloud. For instance, Wang et al. (2015) have shown how the LBM can implement rigorous methods such as the Particle-resolved simulations (PRS). This fact allows considering a more accurate treatment in the model that identifies phenomena such as the disturbances created by a no-slip condition defined for every dispersed particle. This characteristic becomes a determining factor for the description of the behavior in the smallest length and time scales especially when the particle diameter is comparable to the Kolmogorov length or even larger. The simulations that can be developed with these approaches are clearly defined by the computational resources that are available. Indeed, the accuracy of a particle method is established by the number of particles and their interaction mechanisms. Thereupon, a discretization of this type demands a higher computational effort than other techniques like CFD.

The technique that was adopted for this study is based on a Computational Fluid Dynamics simulation. This alternative was considered because it allows discretizing the irregular flow domain with a simple

methodology and it takes into account the most relevant physics of the dust cloud. This condition is achieved by the inclusion of certain correlations to predict the behavior of both phases. In addition, this approach has been developed and adjusted for the analysis of turbulent flows in a reactor engineering scale whereas the LBM and the BD have a better adaptability for the descriptive analysis of specific micro and mesoscopic scenarios. Nevertheless, LBM and CFD have implemented similar RANS models for the description of turbulent flows (Chen, 2012). Therefore, this particle method could also have been adopted for this study as well.

C. *Description of the dispersion phenomena and solids concentration*

The final solids volume fraction in the dust clouds formed in the standard apparatuses for the experimental tests of this thesis is below 10%. This fact implies that the presence of the dispersed phase is not high enough to define the powder as a continuum medium. Therefore, the Eulerian-Eulerian techniques do not constitute the most appropriate approach for the description of the evolution of the dust cloud. This condition is determined because the interactions of the solid phase are not strong enough to represent the influence on the momentum of the gas flow that would be predicted by the Eulerian model. Moreover, an Eulerian-Eulerian approach is not capable to describe properly the agglomeration and fragmentation phenomena that are associated to the dispersion of a cohesive combustible dust. Actually, this description requires the analysis of every single particle rather than a set of dispersed particles depicted as a continuum.

Finally, the technique considered for this analysis is the CFD based on an Eulerian-Lagrangian approach. A simple scheme that poses the selection process of the computational technique is shown in Table 2.3. This model should consider a two-way coupling method because the volume fraction of the dust is located in the span associated to this analysis. This fact will allow considering the main interaction mechanisms that determine the momentum exchange between the two phases.

The CFD simulations that were considered for this study in this study were developed by utilizing two different commercial alternatives: ANSYS Fluent 13.0 and Star CCM+ 10.04.009 R8. The former was considered to describe the behavior of a combustible dust cloud in the modified Hartmann tube and the latter was taken into account for the analysis of the flow developed within the 20 L sphere. Two CFD codes were implemented in this analysis because the injection of pressurized gas was defined in a different way for each test apparatus. On the one hand, ANSYS Fluent has a constraint for the maximum number of finite volumes that can be considered for the flow domain; hence the velocity field was computed with a variable boundary that was set with a user defined function. On the other hand, STAR CCM+ does not have this restriction. Therefore, it was chosen for the setup that required the discretization of the largest flow domain envisaged for the computational approach. Further details about the simulation of the dispersion process developed with this approach will be discussed in Chapter 4.

Table 2.3. Selection of the computational method for the description of a combustible dust cloud (✓= Accepted – X= Rejected)

COMPUTATIONAL TECHNIQUE		FLOW DOMAIN 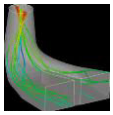	COMPUTATIONAL COST	DISPERSION PHENOMENA
PARTICLE METHODS	MICROSCOPIC SCALES -Molecular Dynamics -Monte Carlo simulations	X -The flow domains considered by these techniques are defined in length and time scales that are limited by the particle size. The system of this study is in other scale. -The system is dynamic.		
	MESOSCOPIC SCALES -Dissipative Particle Dynamics -Brownian Dynamics -Lattice-Boltzmann	✓ The case study envisages scenarios that are in an engineering scale that can be analyzed with these techniques.	X A too large number of particles would be required for an accurate description of the fluid flow phenomena.	
	MACROSCOPIC SCALES -Vortex Methods -Lattice-Boltzmann			
COMPUTATIONAL FLUID DYNAMICS	EULER-EULER -Mixture model -Eulerian model		✓ The computational cost is mainly determined by the number of finite volumes that compose the grid. This number can be quite important too. However, the number of vortex that is required for the description is greater than the number of cells. Therefore, they are usually considered for calculation of the flow conditions at the boundaries in certain LES simulations	X The volume fraction of the solid is below 10%. Thus, the description of the solid phase as a fluid may not describe properly the agglomeration and fragmentation phenomena.
	EULER-LAGRANGE			✓ The Discrete Element Method allows modelling the collisions of the dispersed particles.

2.1.3 Numerical description of the gas flow turbulence

The Computational Fluid Dynamics can predict the behavior of a turbulent flow according to different models. These methods describe the evolution of the turbulence levels of the gas flow according to a specific numerical treatment and the spatiotemporal discretization of the flow domain. These parameters must be established according to the physical models that will be implemented on the CFD simulations. The first model that was included in the numerical treatment corresponded to the prediction of the turbulence of the gas flow. The selection of the turbulence model was performed according to a classification that considered the different formulations that can be associated to the finite-volume method. For this particular case, the formulation that was defined for the continuous phase was established according to the most relevant characteristic of the fluid flow in the gas-solid dispersion, which is the gas injection that causes the variations of turbulence of the flow domain.

A. *Numerical methods to describe the flow turbulence in Computational Fluid Dynamics*

The Computational Fluid Dynamics intends to characterize the flow of eddies and capture the effects of the turbulence (Versteeg & Malalasekera, 2007). For this purpose, it has implemented various numerical methods, which describe the turbulent eddies developed at different length and time scales. The methods have been classified by in the following categories (Versteeg & Malalasekera, 2007):

- ***Reynolds-Averaged Navier–Stokes (RANS) equations:*** The main purpose of these numerical methods relies on the description of the mean flow properties along with the description of the effects of turbulence on the mean flow. This is accomplished by averaging the Navier-Stokes equations in the set of flow properties that can be described by the Reynolds decomposition. This decomposition establishes any flow property (φ) is equal to the sum of the mean component (Φ) and the fluctuating component (φ'). The averaging process can be performed through the time, space or the ensemble of measurements:

  Time averaging:
  $$\Phi(x,t) = \frac{1}{\Delta t}\int_0^{\Delta t} \varphi_i(x,t)\,dt \qquad 2.27$$

  Favre averaging:
  $$\Phi(x,t) = \frac{\overline{\rho\varphi}}{\overline{\rho}} \qquad 2.28$$

  $$\rho = \overline{\rho} + \rho' \qquad 2.29$$

  Space averaging:
  $$\Phi(x,t) = \lim_{V\to\infty}\frac{1}{V}\iiint_V \varphi_i(x,t) \qquad 2.30$$

  Ensemble averaging:
  $$\Phi(x,t) = \lim_{N_{meas}\to\infty}\frac{1}{N_{meas}}\sum_{i=1}^{N_{meas}} \varphi_i(x,t) \qquad 2.31$$

  Most commercial CFD codes are developed according a time averaging model for the turbulence description in engineering analyses. Moreover, the Favre averaging (also known as mass-weighted averaging) is usually considered for compressible flows in order to complement the Reynolds averaging. This fact simplifies the extended RANS equations that are obtained by averaging the variable density. Nevertheless, not all the available codes consider this averaging process because the error arisen from the utilization of the RANS models for incompressible flows is significant only for certain supersonic flows and the enhanced precision does not compensate the augmentation of the computational cost. For this reason, other alternatives pose the combination of the Reynolds and Favre averaging equations. In accordance with this statement, the velocity and thermodynamic variables are Favre-averaged whereas the density and pressure are Reynolds averaged (Masatsuka, 2013).

The averaging process of the RANS equations implies the inclusion of additional terms in the momentum equations. These terms are denominated as Reynolds stresses. They correspond to the product of fluctuating velocities ($\overline{u_i' u_i'}$) and are associated to the convective momentum transfer that is caused by the turbulent eddies (Versteeg & Malalasekera, 2007).

$$\frac{\partial \overline{u_x}}{\partial t} + \mathrm{div}\left(\overline{u_x} u\right) = -\frac{1}{\rho}\frac{\partial P}{\partial x} + \nu \mathrm{div}\left(grad(u_x)\right) + \frac{1}{\rho}\left[\frac{\partial\left(-\rho\overline{u_x'^2}\right)}{\partial x} + \frac{\partial\left(-\rho\overline{u_x' u_y'}\right)}{\partial y} + \frac{\partial\left(-\rho\overline{u_x' u_z'}\right)}{\partial z}\right] \quad 2.32$$

$$\frac{\partial \overline{u_y}}{\partial t} + \mathrm{div}\left(\overline{u_y} u\right) = -\frac{1}{\rho}\frac{\partial P}{\partial y} + \nu \mathrm{div}\left(grad(u_y)\right) + \frac{1}{\rho}\left[\frac{\partial\left(-\rho\overline{u_x' u_y'}\right)}{\partial x} + \frac{\partial\left(-\rho\overline{u_y'^2}\right)}{\partial y} + \frac{\partial\left(-\rho\overline{u_y' u_z'}\right)}{\partial z}\right] \quad 2.33$$

$$\frac{\partial \overline{u_z}}{\partial t} + \mathrm{div}\left(\overline{u_z} u\right) = -\frac{1}{\rho}\frac{\partial P}{\partial z} + \nu \mathrm{div}\left(grad(u_z)\right) + \frac{1}{\rho}\left[\frac{\partial\left(-\rho\overline{u_x' u_z'}\right)}{\partial x} + \frac{\partial\left(-\rho\overline{u_y' u_z'}\right)}{\partial y} + \frac{\partial\left(-\rho\overline{u_z'^2}\right)}{\partial z}\right] \quad 2.34$$

The computation of a turbulent flow with a RANS model requires the prediction of the Reynolds and the scalar transport terms stresses through a turbulence model. These models are based on the solution of some additional transport equations that constitute the closure required for the variables calculation (Versteeg & Malalasekera, 2007). The number of equations solved with the averaged equations determines the computational cost and the accuracy of the description of the turbulent eddies. For this reason, Table 2.4 presents the classification of the turbulence models according to their number of additional equations:

Table 2.4. Classification of the RANS turbulence models according to the number of transport equations
(Ansys Inc., 2009; Versteeg & Malalasekera, 2007)

NUMBER OF TRANSPORT EQUATIONS	TURBULENCE MODEL	DESCRIPTION
Zero	Mixing length	The turbulence is described with a velocity scale and a length scale.
One	Spalart–Allmaras model	A modeled transport equation is included to calculate the kinematic eddy (turbulent) viscosity.
Two	-k-ε model -k-ω model -Algebraic stress model	Determination of a turbulent length and time scale by solving two separate transport equations defined for two additional parameters that are associated to the turbulent kinetic energy of the flow and its dissipation rate.
Three	k-kl-ω transition Model	Transport equations for the turbulent kinetic energy, laminar kinetic energy and the inverse turbulent time scale.
Four (Two methods coupled)	Shear Stress Transport (SST) k-ω Models	The transport equations of the k-ω model are coupled with two other transport equations. The first additional expression establishes the intermittency and the other one determines the transition onset criteria.
Seven	Reynolds Stress Model (RSM)	Development of closure the RANS equations by solving a set transport equations for the Reynolds stresses. These expressions are calculated along with an equation posed for the dissipation rate.

The alternative to the averaging process of the RANS models consists of the modeling of the eddies that compose a turbulent flow. This option is considered by two different techniques: DNS and LES. These simulation methods differ from the RANS models because they are based on the

direct solution of the Navier-Stokes equations instead of a statistical approach (Schiestel, 2008). This formulation can constitute an accurate description of the phenomena occurred even at the minimum length scales (Kolmogorov scales). However, this detailed description might be restricted by the computational resources.

- ***Direct numerical simulation (DNS):*** This approach envisages the numerical solution of the Navier-Stokes equations for all the length and time scales without considering any turbulence model. For this reason, these simulations achieve the highest accuracy in the description of the flow behavior. This condition is accomplished by defining a spatial grid that is sufficiently fine to solve the turbulent eddies developed at the Kolmogorov scale. Besides this characteristic, the time steps considered for this technique are small enough to resolve the period of fastest fluctuations (Versteeg & Malalasekera, 2007). These facts allow computing the mean flow and all the turbulent fluctuations as well.

  This model is not considered for industrial applications due to the high computational cost that it represents. Actually, the cost required for DNS to resolve the entire range of scales is proportional to the third power of the turbulent Reynolds number (Ansys Inc., 2009). Therefore, it has always been considered for theoretical analyses of flows with low Reynolds numbers that are defined for research purposes (e.g. the flow near boundary layers).

- ***Large Eddy Simulations (LES):*** The LES model solves the computational limitations of the DNS model by establishing a hybrid approach that is based on the partial simulation of the large eddies and the partial modeling of the small eddies that compose the fluid flow (Schiestel, 2008). The classification of the turbulent eddies according to their size allows describing the main characteristics of the flow because the large eddies are responsible for the transport phenomena of the bulk of the flow whereas the small ones determine the energy dissipation (Versteeg & Malalasekera, 2007); hence the former are dictated by the geometry and conditions of the domain and the latter tend to be more isotropic (Ansys Inc., 2009). For this reason, this turbulence model is conceived to track the behavior of the larger eddies only. For this purpose a spatial filtering is performed on the unsteady Navier-Stokes equations before the calculations. This classification passes the large eddies and rejects the small ones.

$$\bar{\phi}(x,t) = \iiint_V G(x,x',\Delta_{LES})\phi(x',t)\,dx_i'dx_j'dx_k' \qquad 2.35$$

  in which $\bar{\phi}$ is the filtered function, Δ_{LES} is the filter cutoff width, G is the filtering kernel of the LES model and x_i' is one of the convolution variables for the position of the gas flow. This approach requires an additional expression to take into account the effects attributed to the omitted eddies. This condition is satisfied through the implementation a subgrid-scale (SGS) model for the length scales that are smaller than a characteristic filter cutoff. This filter is determined by the characteristics of the flow domain and the mesh refinement. For this reason, this technique demands a level of refinement that is higher than the mesh grid constructed for an analysis performed with a RANS model. Table 2.5 presents a brief description of some of the most common subgrid-scale models:

Table 2.5. Subgrid-scale models developed for a LES simulation (Ansys Inc., 2009)

SUBGRID-SCALE MODEL	DESCRIPTION
Smagorinsky-Lilly	This model is based on the Boussinesq description, which establishes that the smallest eddies are isotropic. Therefore, the subgrid stresses are proportional to the local rate of strain of the resolved flow. The filter cutoff in a fluid cell is defined as the minimum value observed between the product of the Von Karman constant and the distance to the closest and the product of the local grid scale and the Smagorinsky constant (0.17).
Wall-Adapting Local Eddy-Viscosity	This model poses a similar description with regard to the Smagorinsky-Lilly model. However, this technique is designed to determine the correct wall asymptotic behavior of wall bounded flows. Moreover, this alternative is more appropriate for the description of the laminar zones that are developed in the domain. The filter cutoff is determined with a comparison that is very similar to the other model. However, the value of the constant is 0.325.
Dynamic Kinetic Energy Subgrid-scale	This model is not an algebraic method for the solution of the velocity scales as the methods discussed above. For this reason, it does not assume a local equilibrium between the dissipation of kinetic energy at the subgrid-scales and the energy transferred through the grid-filter scale. On the contrary, it considers the transport of the turbulent kinetic energy through the subgrid-scales. The filter cutoff is defined as the cubic root of every cell volume of the flow domain.

Besides, this technique demands more computational resources than a RANS model because it envisages the solution of the unsteady flow equations. However, Versteeg & Malalasekera (2007) affirmed that this turbulence model is starting to address complex geometries due to the development of new computational resources and parallelized solution schemes.

- ***Detached Eddy Simulations (DES):*** This is another hybrid model that uses the RANS and LES formulations in different regions of the flow domain. In accordance with this statement, DES is a three-dimensional unsteady numerical solution that functions as a subgrid-scale model in regions where the grid density is fine enough for a LES approach, and as a RANS model in regions where it is not (Mockett, 2009).

  Despite the fact that both models add different terms in the momentum equations (Reynold stresses and subgrid-scales), it is possible to combine both formulations in a simulation. The switch from RANS to LES is performed by reducing the eddy viscosity in the LES zone appropriately. This coupling can be established because the turbulence models do not carry any information about their derivation after being introduced into the momentum equations (Ansys Inc., 2009). This fact means that RANS and LES models are identical after calculating the turbulent viscosity of the fluid (μ_t).

  The DES model utilizes a zoning methodology to take advantage of RANS and LES. For this purpose it defines a RANS model for the boundary layer and a LES approach on the flow field containing vortices with disperse scales (away from the region where RANS works) (Sun et al., 2013). This turbulence model is a good alternative for cases in which LES becomes prohibitive due to the high computational cost that is defined by the mesh refinement. Indeed, this hybrid model has a computational cost that is lower than a LES formulation and greater than RANS.

B. *Selection of the numerical method to describe the flow turbulence*

The turbulence model that was chosen for this study was determined with an analysis of the main features of the flow domain. Initially, the geometry of the domain is characterized by the irregular shape of the injection nozzles. These regions are also defined by the transonic conditions of the pressurized gas flow. These facts establish that a high refinement level and a small time step are necessary for an accurate description of the propagation of the transient flow in these zones.

These requirements imply that a LES formulation is not suitable for the description of the gas flow in the near-wall regions. Indeed, the computational resources that were available for this analysis do not allow considering a CFD analysis based on a formulation like this for the whole domain. Therefore, a RANS model was considered in an initial stage as an appropriate alternative for the description of the fluid flow phenomena. Nevertheless, the flow domain also consists of several regions that define the core turbulent region as a zone that generates significant energy dissipation rates. Sun et al. (2013) have posed the LES as a more appropriate alternative for the description of certain flows with high Reynolds numbers that are characterized by a complex vorticity.

The velocity field of the core regions of the flow field can be described with a LES formulation because the effects of the wall friction are lower on them due to the separation distance. This technique is more appropriate because these sectors require a better analysis of the influence of the turbulent scales. In addition, the core of the dust cloud becomes a region of interest after considering that the ignition of the dust cloud is carried out in it. These considerations were determinant to establish that a LES technique should also be considered for the characterization of the evolution of the continuous phase. Hence, the computational description of the dust cloud in the modified Hartmann and the 20 L sphere was performed with the hybrid DES model. This model also represented an advantage for the simulation of the modified Hartmann tube because the definition of a transient boundary condition allows considering an improvement of the basic DES formulation that considers the RANS portion of the model in the inner part of the logarithmic layer and the LES in the outer part of the boundary layer (Versteeg & Malalasekera, 2007). Figure 2.4 presents the turbulence models that compose the hybrid formulation that was implemented on the numerical simulations of the two-phase flows developed in the experimental test apparatuses.

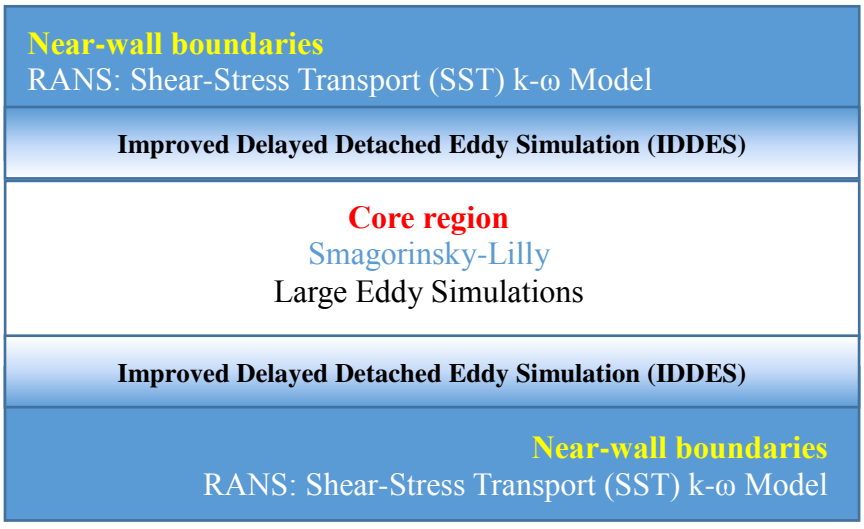

Figure 2.4. Definition of the DES turbulence model in the flow domain

A simple description of this distribution of the turbulence models can be determined by establishing where the turbulent length scale is greater than a comparison factor. Initially, the turbulence variable is defined as 11.11 times the ratio between the turbulent kinetic energy (k) of the flow and the energy dissipation rate (ω). Thereafter, the comparison factor is defined as the product of the largest distance

between the cell center and the centers of the neighboring cells and the blending constant of the RANS models. The comparison of the two values determines the Detached Eddy Simulations correction factor that is shown in Figure 2.5. This parameter identifies the RANS modeled zones with a value equal to 1 and the LES modeled zones with greater values. The LES regions correspond to the cells away from the internal walls, which reach the core of the fluid domain. These zones demand the injection of physically-viable resolved turbulent fluctuations into the solution (Mockett, 2009). This condition is necessary because the transition zones identify how the changeover from the averaging model to the filtering technique is carried out. Further details about the calculation of the turbulent length scales are described in the following section.

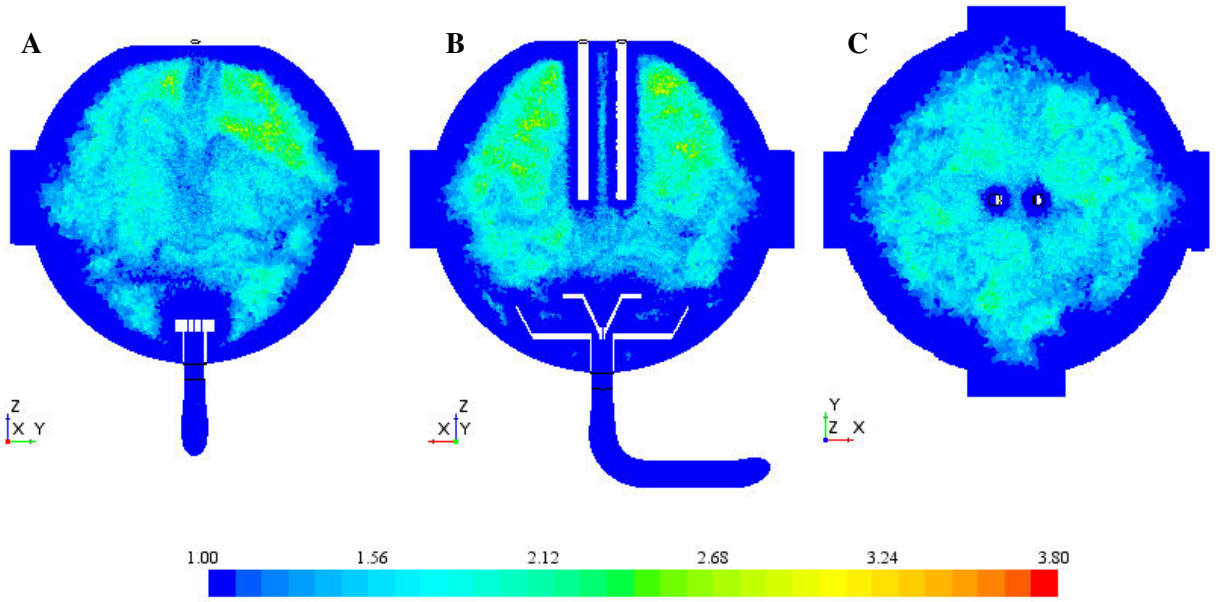

Figure 2.5. DDES correction factor
(RANS Regions = 1 – LES Regions > 1)
A) Lateral view B) Front view C) Upper view

Figure 2.5 provides a good visualization of the distribution of the models. Nevertheless, it constitutes only an estimative value. Shur et al. (2008) affirm that the most widely employed definition of the filter cutoff is the cube root of the cell volume. This is a balanced quantity but the current models determine a comparison according to the wall dimensions as well as the wall distance.

The CFD codes that were considered for this study have included a two-equation RANS model for the description of the boundary layers as well as an algorithm for the definition of the transition to the LES model. The main transport equations of the two approaches that were considered for the computational study of the dust dispersion are presented below in order to explain the calculation of the parameters associated to the turbulence of the gas flow.

2.1.4 Implementation of the DES model in the CFD simulations

A. *Shear Stress Transport (SST) k-ω model*

This RANS model is based on the calculation of the turbulent kinetic energy of the fluid flow (k) and its specific dissipation rate (ω). The transport equations of this model are envisaged to blend the formulation of the k-ω, which provides an accurate description of the near-wall region, with the free-

stream independence of the *k-ε* model (Ansys Inc., 2009). For this purpose, the second RANS model is converted into the *k-ω* formulation.

This method is considered for the description of adverse pressure gradient flows, airfoils and transonic shockwaves. This is achieved with the inclusion of the turbulent shear stress in the definition of the turbulent viscosity (μ_t) (Ansys Inc., 2009). The two parameters of the turbulence model are calculated with the following transport equations:

$$\frac{\partial}{\partial t}(\rho k)+\frac{\partial}{\partial x_i}(\rho k u_i)=\frac{\partial}{\partial x_j}\left(\Gamma_k \frac{\partial k}{\partial x_j}\right)+G_k-Y_k+T_k \qquad 2.36$$

$$\frac{\partial}{\partial t}(\rho \omega)+\frac{\partial}{\partial x_i}(\rho \omega u_i)=\frac{\partial}{\partial x_j}\left(\Gamma_\omega \frac{\partial \omega}{\partial x_j}\right)+G_\omega-Y_\omega+D_\omega+T_\omega \qquad 2.37$$

The previous transport equations comprise various terms for the determination of the effective diffusivity (Γ_k & Γ_ω), production (G_k & G_ω), dissipation (Y_k & Y_ω), cross-diffusion (D_ω) and sources (T_k & T_ω) of each variable. These terms are calculated as follows:

- ***Effective diffusivities:*** The effective diffusivities are calculated from the turbulent viscosity of the fluid flow and the Prandtl turbulent numbers of *k* (σ_k) and *ω* (σ_ω).

$$\Gamma_k=\mu+\frac{\mu_t}{\sigma_k} \qquad 2.38 \qquad\qquad \Gamma_\omega=\mu+\frac{\mu_t}{\sigma_\omega} \qquad 2.39$$

These parameters are determined with equations 2.40 - 2.45 and 2.51:

$$\mu_t=\frac{\rho k}{\omega}\frac{1}{\max\left[\frac{1}{a^*},\frac{SF_2}{0.31\omega}\right]} \qquad 2.40$$

$$\sigma_k=\frac{1}{F_1/1.176+(1-F_1)} \qquad 2.41 \qquad\qquad \sigma_\omega=\frac{1}{F_1/2+1.168(1-F_1)} \qquad 2.42$$

The turbulent Prandtl numbers are defined by the blending function in accordance with the wall normal distance (y_n), the two parameters of the turbulence model and the transport properties of the fluid:

$$F_1=\tanh\left(\left\{\min\left[\max\left(\frac{\sqrt{k}}{0.09\omega y_n},\frac{500\mu}{\rho y_n^2\omega}\right),\frac{4\rho k}{1.168 D_\omega^+ y_n^2}\right]\right\}^4\right) \qquad 2.43$$

$$F_2=\tanh\left(\left[\max\left(\frac{\sqrt{k}}{0.045\omega y_n},\frac{500\mu}{\rho y_n^2\omega}\right)\right]^2\right) \qquad 2.44$$

$$\text{with:}\quad D_\omega^+=\max\left[1.712\frac{\rho}{\omega}\frac{\partial k}{\partial x_j}\frac{\partial \omega}{\partial x_j},10^{-10}\right] \qquad 2.45$$

- ***Production of k and ω:*** The production terms are defined by the turbulent Reynolds number that is defined for the model (Re_t):

$$\mathrm{Re}_t = \frac{\rho k}{\mu \omega} \tag{2.46}$$

The generation of the turbulent kinetic energy is established according to the following equations:

$$G_k = \min\left(-\rho \overline{u_i' u_j'} \frac{\partial u_j}{\partial x_i}, 0.9 \rho k \omega \left(\frac{4/15 + (\mathrm{Re}_t/8)^4}{1 + (\mathrm{Re}_t/8)^4} \right) \left(1 + 1.5 F(M_t)\right) \right) \tag{2.47}$$

With: $$F(M_t) = \begin{cases} 0 & M_t \le 0.25 \\ M_t^2 - 0.0625 & M_t > 0.25 \end{cases} \quad \text{and} \quad M_t = \sqrt{\frac{2k}{\gamma RT}} \tag{2.48}$$

A similar procedure determines the evolution of the generation term of ω:

$$G_\omega = \frac{a}{\mu_t / \rho} G_k \tag{2.49}$$

$$a_\infty = 0.3536 F_1 + 0.3597(1 - F_1) \tag{2.50}$$

$$a^* = a_\infty^* \left(\frac{0.024 + \mathrm{Re}_t/6}{1 + \mathrm{Re}_t/6} \right) \tag{2.51}$$

$$a = \frac{a_\infty}{a^*} \left(\frac{1/9 + \mathrm{Re}_t/2.95}{1 + \mathrm{Re}_t/2.95} \right) \tag{2.52}$$

- ***Dissipation of k and ω:*** The blending function and the turbulent Reynolds number determine the dissipation terms as follows:

$$Y_k = 0.09 \rho k \omega \left(\frac{4/15 + (\mathrm{Re}_t/8)^4}{1 + (\mathrm{Re}_t/8)^4} \right) \left(1 + 1.5 F(M_t)\right) \tag{2.53}$$

$$Y_\omega = \rho \omega^2 \left(0.075 F_1 + 0.0828(1 - F_1)\right) \left[1 - \frac{0.135 F(M_t)}{0.075 F_1 + 0.0828(1 - F_1)} \left(\frac{4/15 + (\mathrm{Re}_t/8)^4}{1 + (\mathrm{Re}_t/8)^4} \right) \right] \tag{2.54}$$

- ***Cross-diffusion modification:*** An additional term is introduced in the transport equation of ω because of the blending process of the two RANS models. This parameter can be established with the following equation:

$$D_\omega = \frac{1.712 \rho (1 - F_1)}{\omega} \frac{\partial k}{\partial x_j} \frac{\partial \omega}{\partial x_j} \tag{2.55}$$

B. *Large Eddy Simulations – Smagorinsky-Lilly*

The LES model develops the filtering process by applying the convolution shown in Equation 2.35 on every flow variable of the Navier-Stokes equations. This process generates their dual definitions in the Fourier space. This calculation associates the spatial cutoff to the cutoff wave number of the Fourier space (Garnier et al., 2009). Thereafter, the Fourier transform of the kernel function is also calculated. This fact allows estimating the value of the flow property in the Fourier space as the product of the kernel transform and the spectrum. Finally, the inverse transform of this product is calculated in order to estimate the flow property in an explicit way (John, 2012). This process generates a resolved and non-resolved part for each flow variable (Garnier et al., 2009). The latter is defined by the subgrid scales, which correspond to the small eddies. The flow information that is omitted by the filtering scheme is modeled according to a subgrid scale model.

For this particular case, the Smagorinsky-Lilly was considered to model the behavior of the small eddies. This turbulence model estimates the behavior of the small eddies according to the filtered values of the velocity field (u_i^*):

$$\tau_{ij} = -2\mu_t S_{ij}^* + \frac{1}{3}\tau_{kk}\delta_{ij} = -\mu_{SGS}\left(\frac{\partial u_i^*}{\partial x_j} + \frac{\partial u_j^*}{\partial x_i}\right) + \frac{1}{3}\tau_{kk}\delta_{ij} \qquad 2.56$$

in which τ_{ij} represents the local subgrid stresses, τ_{kk} is the isotropic part of the subgrid-scale stresses, S_{ij}^* is the rate-of-strain tensor for the resolved scale, δ_{ij} is the Kronecker delta function and μ_{SGS} is the dynamic subgrid viscosity.

The subgrid-scale turbulent flux of a scalar property ($q_{\varphi,j}$) is modeled by using a subgrid-scale turbulent Prandtl number (σ_t):

$$q_{\varphi,j} = -\frac{\mu_t}{\sigma_t}\frac{\partial \varphi}{\partial x_j} \qquad 2.57$$

In the same manner, the compressible subgrid enthalpy flux term is determined by the sensible enthalpy of the fluid (h_s), its heat capacity (C_p) and the filtered temperature (T^*) with the following expression:

$$\overline{\rho}\left[\left(u_i h_s\right)^* - u_i^* h_s^*\right] = -1.176\mu_{SGS} C_p \frac{\partial T^*}{\partial x_j} \qquad 2.58$$

The Smagorinsky-Lilly model calculates the eddy-viscosity as follows:

$$\mu_t = \rho L_s \sqrt{2 S_{ij}^* S_{ij}^*} \qquad 2.59$$

with :

$$L_s = \min\left(\kappa d_{wall}, 0.17\Delta V^{1/3}\right) \qquad \kappa = 0.41 \qquad 2.60$$

in which the mixing length for subgrid-scales (L_s) is determined by the von Kármán constant (κ), d_{wall} is the distance to the closest wall and $\Delta V^{1/3}$ represents the local grid scale.

C. *Improved Delayed Detached Eddy Simulation (IDDES)*

The hybrid RANS-LES formulation that was considered for this study is the Improved Detached Eddy Simulation (IDDES) model. This technique combines two different branches into an integral hybrid model. These parts are the simple DDES model and the Wall-Modeled Large Eddy Simulation model (WMLES). This combination establishes a favorable response of each branch by activating the WMLES modification only when the inflow conditions used in the simulation are unsteady and impose some turbulent content (Ansys Inc., 2009; Shur et al., 2008).

This combination provides a more flexible and convenient scale-resolving simulation (SRS) model for high Reynolds number flows. For this purpose, it covers stable boundary layers in RANS mode. In addition the IDDES function provides shielding similar to the DDES model to avoid affecting the SST model. This fact implies that the boundary layer remains in a steady RANS mode even under grid refinement.

$$F_{IDDES} = \frac{l_{RANS}}{l_{IDDES}} \tag{2.61}$$

A simple RANS model as the Spalart-Allmaras would define the RANS length scale (l_{RANS}) as the wall distance but this model takes into account the solution and defines this variable as follows (Shur et al., 2008):

$$l_{RANS} = 11.11\frac{\sqrt{k}}{\omega}\left(\frac{1+(\mathrm{Re}_t/8)^4}{4/15+(\mathrm{Re}_t/8)^4}\right)\left(\frac{1}{1+1.5F(M_t)}\right) \tag{2.62}$$

The LES length scale (l_{LES}) is defined by the DES model with the following expression for the SST *k-*ω model in accordance with the cell dimensions (Δx_1, Δx_2 and Δx_3) and the wall distance:

$$l_{LES} = 0.61\min\left\{\max\left[C_w d_{wall}, C_w \max\left(\Delta x_1, \Delta x_2, \Delta x_3\right), \Delta_{wn}\right], \max\left(\Delta x_1, \Delta x_2, \Delta x_3\right)\right\} \tag{2.63}$$

in which, C_w is an empirical constant whose value does not depend on the subgrid-scale model and whose value is 0.15. Moreover, Δ_{wn} is the grid step in the wall-normal direction. Thereupon, the IDDES length scale can be calculated with the following equation:

$$l_{IDDES} = f_d^*(1+f_e)l_{RANS} + (1-f_d^*)l_{LES} \tag{2.64}$$

Firstly, the blending function of the IDDES model (f_d^*) is defined by a turbulent marker of the wall region (r_{dt}) and a blending function of the WMLES, which is represented by f_{Blend}. This variable provides rapid switching of the model from RANS mode ($f_{Blend}=1.0$) to LES mode ($f_{Blend}=0$) (Shur et al., 2008):

$$f_d^* = \max\left\{\tanh\left(8r_{dt}^3\right), f_{Blend}\right\} \tag{2.65}$$

These parameters are determined through these equations:

$$r_{dt} = \frac{\nu_t}{\kappa^2 d_{wall}^2 \max\left\{\left[\sum_{ij}\left(\partial u_i / \partial x_j\right)^2\right]^{1/2}, 10^{-10}\right\}} \tag{2.66}$$

$$f_{Blend} = \min\left\{2\exp\left[-9\left(0.25 - \frac{d_{wall}}{\max\left(\Delta x_1, \Delta x_2, \Delta x_3\right)}\right)^2\right], 1.0\right\} \tag{2.67}$$

Secondly, the elevating-function ($f_{Elevate}$) prevents the excessive reduction of the RANS Reynolds stresses that has been observed in the interaction of the RANS and LES regions in the vicinity of their interface. This variable is determined as follows:

$$f_{Elevate} = \max\left\{(f_{Elevate1} - 1), 0\right\} f_{Elevate2} \tag{2.68}$$

with:
$$f_{Elevate1} = \begin{cases} 2\exp\left[-11.09\left(0.25 - \frac{d_{wall}}{\max\left(\Delta x_1, \Delta x_2, \Delta x_3\right)}\right)^2\right] & 0.25 - \frac{d_{wall}}{\max\left(\Delta x_1, \Delta x_2, \Delta x_3\right)} \geq 0 \\ 2\exp\left[-9\left(0.25 - \frac{d_{wall}}{\max\left(\Delta x_1, \Delta x_2, \Delta x_3\right)}\right)^2\right] & 0.25 - \frac{d_{wall}}{\max\left(\Delta x_1, \Delta x_2, \Delta x_3\right)} < 0 \end{cases} \tag{2.69}$$

and:
$$f_{Elevate2} = 1 - \max\left\{f_t, f_l\right\} \tag{2.70}$$

The function $f_{Elevate2}$ depends on the turbulent marker of the wall region (r_{dt}) with its laminar analogue (r_{dl}):

$$f_t = \tanh\left[\left(c_t^2 r_{dt}\right)^3\right] \tag{2.71}$$

$$f_l = \tanh\left[\left(c_l^2 r_{dl}\right)^{10}\right] \tag{2.72}$$

with:
$$r_{dl} = \frac{\nu_{kin}}{\kappa^2 d_{wall}^2 \max\left\{\left[\sum_{ij}\left(\partial u_i / \partial x_j\right)^2\right]^{1/2}, 10^{-10}\right\}} \tag{2.73}$$

Finally, Gritskevich et al. (2012) defined the governing equations of the SST IDDES model as follows:

$$\frac{\partial \rho k}{\partial t} + \nabla \cdot \left(\rho u^* k\right) = \nabla \cdot \left[\left(\mu + \sigma_k \mu_t\right) \nabla k\right] + \min\left(\mu_t S_{ij}^{*2}, 0.9 \rho k \omega\right) - \frac{\rho k^{3/2}}{l_{IDDES}} \tag{2.74}$$

$$\begin{aligned} \frac{\partial \rho \omega}{\partial t} + \nabla \cdot \left(\rho u^* \omega\right) &= \nabla \cdot \left[\left(\mu + \sigma_\omega \mu_t\right) \nabla \omega\right] + 1.712 \rho (1 - F_1) \frac{\nabla k \cdot \nabla \omega}{\omega} \\ &+ \frac{\rho}{\mu_t}\left(0.25 - \frac{d_{wall}}{\max\left(\Delta x_1, \Delta x_2, \Delta x_3\right)}\right) \min\left(\mu_t S_{ij}^{*2}, 0.9 \rho k \omega\right) - \beta^* \rho \omega^2 \end{aligned} \tag{2.75}$$

with: $$\beta^* = 0.09\left(\frac{4/15+(\mathrm{Re}_t/8)^4}{1+(\mathrm{Re}_t/8)^4}\right)\left(1+1.5F(M_t)\right) \quad 2.76$$

2.1.5 Lagrangian approach for the description of the dispersion process of the combustible dust

This section describes the equations considered for the Lagrangian approach of the CFD simulations that was established for the combustible dust. The trajectories of the discrete phase are calculated according to the numerical integration of Eq. 2.15. This section describes the equations considered to define the forces exerted on the dispersed particles:

A. *Drag force*

A multiphase approach is clearly defined by the interphase momentum transfer between the two phases that is constituted by the drag force. Benzarti et al. (2012) performed a set of experimental measurements that characterized the accuracy of the drag models that are available in commercial codes (e.g. Fluent). The results obtained with their analysis gave a satisfying agreement for different operating conditions such as pressure drop, bed expansion, and qualitative gas-solid flow pattern. The drag force of Eq. 2.15 is determined according to the following equation:

$$\text{Drag Force} = m_s F_D\left(u-u_p\right) = m_s \frac{18\mu}{\rho_p d_p^2}\frac{C_D\,\mathrm{Re}}{24}\left(u-u_p\right) \quad 2.77$$

The calculation of the drag coefficient (C_D) has been established by Haider & Levenspiel (1989) for non-spherical particles, which is the case for aluminum and especially for starch (see MEB images in section 3.1). The correlation proposed by these authors depends on the shape factor of the combustible dust. This parameter establishes the ratio between the surface area of a sphere having the same volume as the particle (s_{sphere}) and the actual surface area of the particle (s_p). The shape factors were set equal to 0.77 for the aluminium dust (Novak & Thompson, 1986) and 0.71 for the wheat starch (Wilson et al., 2006). These values agreed with the results of the SEM micrographs obtained for the dust samples of this thesis (Figure 3.1 and 3.4).

$$C_D = \frac{24}{\mathrm{Re}_p}\left(1+b_1\,\mathrm{Re}_p^{b_2}\right)+\frac{b_3\,\mathrm{Re}_p}{b_4+\mathrm{Re}_p} \quad 2.78$$

$$b_1 = \exp\left(2.3288-6.4581S_F+2.4486S_F^2\right) \quad 2.79$$

$$b_2 = 0.0964+0.5565S_F \quad 2.80$$

$$b_3 = \exp\left(4.9050-13.8944S_F+18.4222S_F^2-10.2599S_F^3\right) \quad 2.81$$

$$b_4 = \exp\left(1.4681-12.2584S_F-20.7322S_F^2-15.8855S_F^3\right) \quad 2.82$$

with: $$S_F = \frac{s_{sphere}}{s_p} \quad 2.83$$

and: $$\mathrm{Re}_p = \frac{\rho |u - u_p| d_p}{\mu} \quad 2.84$$

B. ***Contact forces (soft-sphere collision model)***

Deen et al (2007) define a contact force according to the soft-sphere model ($F_{contact,a}$). This force is calculated for the particle *a* as the sum of the contact forces exerted by the particles of the list *b*. This force has a normal ($F_{ab,n}$) and tangential component ($F_{ab,t}$):

$$F_{contact,a} = \sum_{\forall b \in contactlist} \left(F_{ab,n} + F_{ab,t} \right) \quad 2.85$$

The torque (T_a) only depends on the tangential component of the contact force, the radius of the particle *a* (R_a) and the normal unit vector of the position of the colliding particles *a* and *b* (n_{ab}):

$$T_a = \sum_{\forall b \in contactlist} \left(R_a n_{ab} \times F_{ab,t} \right) \quad 2.86$$

with: $$n_{ab} = \frac{x_{p=a} - x_{p=b}}{|x_{p=a} - x_{p=b}|} \quad 2.87$$

The normal and tangential components are determined by a linear-spring and dashpot model that works as a simplified formulation of the forces attributed to the particle interactions.

$$F_{ab,n} = -k_n \delta_n n_{ab} - \eta_n u_{ab,n} \quad 2.88$$

with: $$u_{ab,n} = \left(u_{ab} \cdot n_{ab} \right) n_{ab} \quad 2.89$$

and: $$\eta_n = \begin{cases} \dfrac{-2 \ln e_n \sqrt{m_{ab} k_n}}{\sqrt{\pi^2 + \ln^2 e_n}} & e_n \neq 0 \\ 2\sqrt{m_{ab} k_n} & e_n = 0 \end{cases} \quad 2.90$$

In which k_n is the normal spring stiffness, η_n is the normal damping coefficient, e_n is the coefficient of normal restitution and $u_{ab,n}$ is the normal relative velocity. The normal overlap (δ_n) is defined as follows:

$$\delta_n = R_a + R_b - |x_{p=a} - x_{p=b}| \quad 2.91$$

The reduced mass of the two particles (m_{ab}) is given by:

$$m_{ab} = \left(\frac{1}{m_{p=a}} + \frac{1}{m_{p=b}} \right)^{-1} \quad 2.92$$

The tangential component of the contact force is determined according to a Coulomb-type friction law:

$$F_{ab,t} = \begin{cases} -k_t \delta_t - \eta_t u_{ab,t} & \left|F_{ab,t}\right| \le \mu_f \left|F_{ab,n}\right| \\ -\mu_f \left|F_{ab,n}\right| t_{ab} & \left|F_{ab,t}\right| > \mu_f \left|F_{ab,n}\right| \end{cases} \quad 2.93$$

with:
$$u_{ab,t} = u_{ab} - u_{ab,n} \quad 2.94$$

and:
$$\eta_t = \begin{cases} \dfrac{-2\ln\beta_0 \sqrt{\dfrac{2}{7} m_{ab} k_t}}{\sqrt{\pi^2 + \ln^2 \beta_0}} & \beta_0 \neq 0 \\ 2\sqrt{\dfrac{2}{7} m_{ab} k_n} & \beta_0 = 0 \end{cases} \quad 2.95$$

in which t_{ab} is a tangential unit vector. Moreover, $k_t, \delta_t, u_{ab,t}, \eta_t$ and μ_f are the tangential spring stiffness, tangential overlap, tangential velocity, tangential damping coefficient, and friction coefficient, respectively. Finally, the tangential coefficient of restitution (β_0) is defined in accordance with the relative velocity before the collision ($u_{ab,0}$) in the following equation:

$$n_{ab} \times u_{ab} = -\beta_0 \left(n_{ab} \times u_{ab,0} \right) \quad 2.96$$

C. *Additional forces*

An additional force arises when there are significant pressure gradients in the fluid (Ansys Inc., 2009). This force was considered because the flow develops through an injection of pressurized gas. The following equation describes this force:

$$\text{Pressure Gradient Force} = m_s F_{pg} = m_s \left(\frac{\rho}{\rho_p} \right) u_p \frac{\partial u}{\partial x_i} \quad 2.97$$

Moreover, the shear lift force model calculates the force acting on a particle moving relative to a fluid where there is a velocity gradient in the fluid orthogonal to the relative motion (F_{SL}). This force was determined according to the correlation posed by Sommerfeld (2000):

$$F_{SL} = C_{SL} \frac{\rho \pi}{8} d_p^3 \left[\left(u - u_p \right) \times \omega \right] \quad 2.98$$

$$C_{SL} = \frac{4.1126}{\mathrm{Re}_S^{0.5}} f\left(\mathrm{Re}_p, \mathrm{Re}_S \right) \quad 2.99$$

$$f\left(\mathrm{Re}_p,\mathrm{Re}_S\right)=\begin{cases}\left(1-0.3314\beta_{SL}^{0.5}\right)\exp\left(-0.1\mathrm{Re}_p\right)+0.3314\beta_{SL}^{0.5} & \mathrm{Re}_p\le 40\\ 0.0524\left(\beta_{SL}\,\mathrm{Re}_p\right)^{0.5} & \mathrm{Re}_p>40\end{cases} \qquad 2.100$$

with: $\mathrm{Re}_S=\dfrac{\rho d_p^2|\omega|}{\mu}$ 2.101 and: $\beta_{SL}=\dfrac{\mathrm{Re}_S}{\mathrm{Re}_p}$ 2.102

D. *Fragmentation & agglomeration*

The aggregates are composed by primary spherical particles. Their fragmentation is observed in the CFD-DEM simulation if the tensile or shear stresses among the particles exceed the threshold values. In this moment, the bond that joints the particles breaks and causes their separation. Therefore, the bond fails if the tensile stress exceeds $\delta_{\max}$ or the shear stress exceeds $\tau_{\max}$. These variables are determined for a sphere of radius R_a as follows:

$$\delta_{\max}=-\frac{F_{n-b}}{\pi R_a^2}+\frac{|T_{s-b}|R_a}{\pi/4\,R_a^4}=\frac{-F_{n-b}R_a+4|T_{s-b}|}{\pi R_a^3} \qquad 2.103$$

$$\tau_{\max}=\frac{|F_{s-b}|}{\pi R_a^2}+\frac{|T_{n-b}|R_a}{\pi/2\,R_a^4}=\frac{|F_{s-b}|R_a+2|T_{n-b}|}{\pi R_a^3} \qquad 2.104$$

in which, F_{n-b} and F_{s-b} are the normal and shear components of the force on a particle due to parallel bonds. A similar definition is established for the normal (T_{n-b}) and shear (T_{s-b}) components of the torque.

Furthermore, the agglomeration of particles is considered according to the linear cohesion model. This formulation is usually considered to describe of inter-molecular attraction between particle surfaces. The cohesion force attributed to the linear cohesion ($F_{cohesion}$) is determined by the minimal radius of surfaces in contact ($R_{\min}$)

$$F_{cohesion}=1.5\pi R_{\min}W_{cohesion} \qquad 2.105$$

2.2 APPLICATION OF THE COMPUTATIONAL FLUID DYNAMICS ON THE DESCRIPTION OF GAS-SOLID MIXTURES

The characterization of the dispersion process of a combustible dust cloud must consider various phenomena associated to the gas-solid interactions. These numerical problems have been addressed previously for different industrial and technical applications with studies based on CFD techniques. Some of the most common operations that are considered for the modelling of fluid-solid mixtures are the solids conveying, particles separation in cyclones, particles dispersion in stirred vessels, filters and fluidized beds (Sommerfeld, 2000). The last sections of this chapter present some previous studies that have showed how the computational fluid dynamics can be considered for the description of phenomena occurred in particle-laden flows. The analysis of these cases provided an insight of the

capabilities of the simulation technique that was selected for the description of the behavior of the dust cloud. For this purpose, they were considered prior to the development of the computational approach of this thesis in order to establish the analysis criteria for the description of the velocity field of the gas flow and the solids distribution.

A. *Examples of CFD simulations associated to the solids fluidization*

The solids fluidization is one of the characteristics of a two-phase flow that can be modeled through CFD simulations. The description of this phenomenon is important for the computational approach of this thesis since it determines the formation and evolution of a combustible dust cloud. Moreover, this characteristic of a gas-solid mixture is also an aspect of main interest in different chemical engineering fields. For instance, the fluidized bed technology is widely considered in various processes such as fluid catalytic cracking, solid fuel combustion/gasification, granulation, and coating (Liu et al., 2013). Thereupon, different computational analyses that have envisaged the description of solid-fluid mixtures have been developed with the CFD technique. For instance, Liu et al. (2013) developed a set of CFD-DEM simulations to analyze the behavior of fluidized beds. Figure 2.6 presents the development of the injection of a single bubble in a fixed bed. This case exemplifies how the eulerian-lagrangian approach can describe some of the main characteristics of a typical fluidization problem. For this case study, the turbulent structures of the flow determine the behaviors of the gas and the solid in accordance with the interaction models established for both phases.

The injection of the gas creates a bubble whose size increases as it rises through the fixed bed. Meanwhile, some particles are drawn up and some particles form a compensated flow. This condition is observed because the particles, that are located ahead the bubble, are pushed upward and sideward. Simultaneously, the particles located within the bubble wake are also drawn up and a return flow of particles develops to compensate for the rising bubble (Liu et al., 2013).

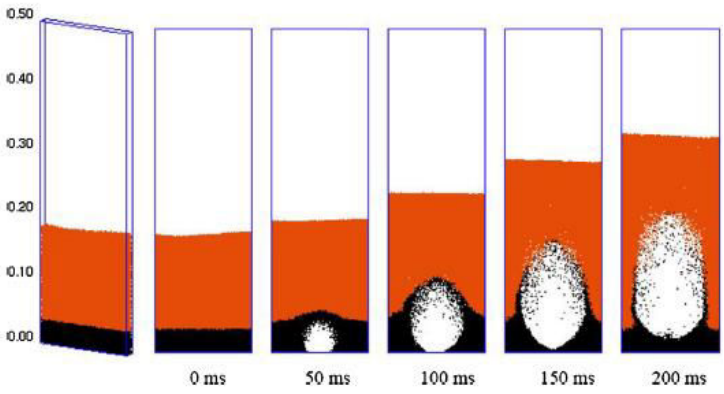

Figure 2.6. A single bubble injection in a fluidized bed (Liu et al., 2013)

Similarly, Fang et al (2013) studied the dynamics of gas-solid flows in internally circulating fluidized beds (ICFB) through a CFD-DEM analysis in order to develop a sensitivity analysis on the technical specifications of the equipment. These apparatuses usually consist of a reaction chamber (RC) as well as a heat exchange chamber (HEC). There is a gas injection located at the bottom of every region; hence their rising velocities can be set to different values to regulate the circulation of the solid phase. The distribution of the two phases in every chamber is shown in Figure 2.7. The CFD became an important design tool to analyze the influence of the technical operating specifications and the baffle that divides both chambers on the flow patterns.

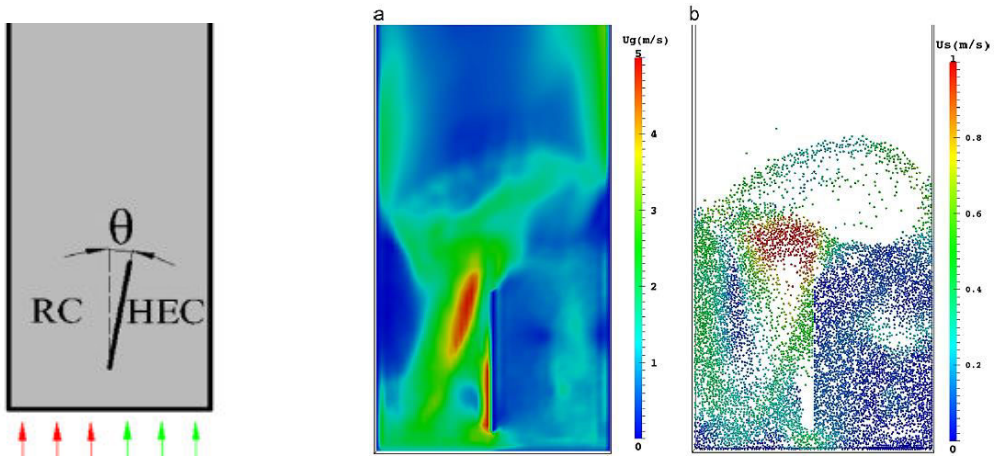

Figure 2.7. Gas–solid distribution at a simulation time of 5.2 s as a representative case a) Gas velocity b) Particle velocity (Fang et al., 2013)

The numerical description of the two-phase flow allowed establishing the influence of the regulation of the rising velocities in the fluidized bed reactor and the inclination angle of the baffle on the performance of the equipment. The results established the velocity of the aeration gas injected in the reaction chamber must be at least the double of the minimum fluidization velocity in order to keep a circulation rate over 65%. Moreover, a slight increase of the angle from 0° to 6° represented an augmentation of 11.8% in the gas bypassing flux and 11.3% of the solid circulating flux. This fact allows enhances the transport of the solids in this region into the reaction zone. These results show how the CFD simulations can provide an important contribution for the definition of the design and operating parameters of an ICFB. This can be accomplished by developing a sensitivity analysis on the most relevant variables of the equipment.

Furthermore, the solids fluidization is an aspect of main interest in the process safety field. For instance, Kosinski & Hoffmann (2007) developed a CFD simulation to analyze the formation of dense dust clouds due to the lift of dust layer that is caused by a propagating shock wave. The scheme of the flow domain is shown in Figure 2.8. This study analyzed the particles spreading and entrainment that is caused by the fluid and the particle collisions. For this purpose, it considered a discrete approach instead of the eulerian description for the solid phase in spite of the high solids concentration. This fact allowed comparing the magnitude of the forces exerted on the particles. The results established that the drag forces are considerably more important than the Magnus forces for the case study because their order of magnitude is 10^5 greater. However, this ratio varies according to the particle size distribution.

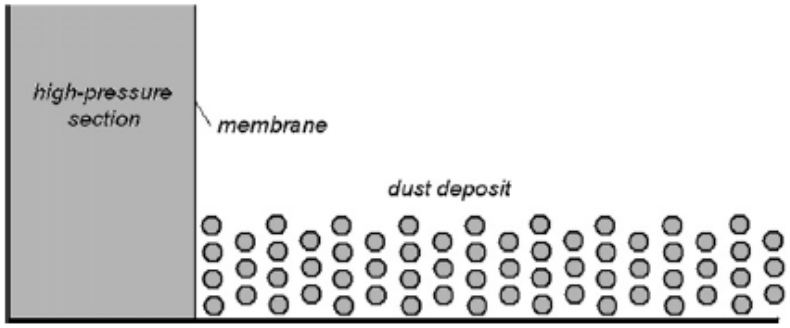

Figure 2.8. The scheme of the computational domain (Kosinski & Hoffmann, 2007)

Moreover, Figure 2.9 showed how this computational analysis compared the elevation reached by particles of different sizes: 50, 100 and 150 µm. These particles were initially settled at layers of different thicknesses: 0.7, 1.1 and 1.5 mm. The results established that the thickness of the dust layer

does not represent a high influence on the particles mean elevation whereas the size distribution constitutes the major variation of the height of the formed dust cloud.

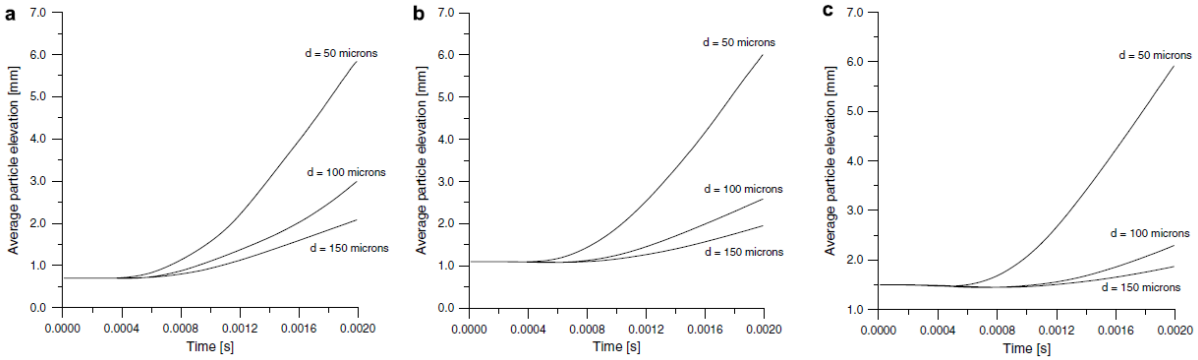

Figure 2.9. Average particle elevation as a function of time for different particle diameters layer thicknesses
A. 0.7 B. 1.1 C. 1.5 mm (Kosinski & Hoffmann, 2007)

Moreover, the computational description of the fluidization of combustible dusts has also been considered in the flammability test apparatuses. For instance, Di Benedetto et al. (2013) developed a CFD simulation that described the dispersion process of a dust cloud within the 20 L sphere before its ignition. For this purpose, their study described a flow domain according to the operating parameters of the experimental setup.

This CFD simulation envisaged a flow domain composed by the explosion chamber, and two elements that represented the pressurized canister: a connection tube and a smaller sphere (Figure 2.10). This domain was divided in 1016951 cells (1.72% canister – 98.28% sphere). The velocity field of the gas flow and the distribution of the combustible dust were computed according to an Eulerian-Lagrangian approach, in which the turbulence of the gas flow was characterized according to the RANS k-ε model. Moreover, the discrete phase corresponded to a powder of 10 µm and a density of 2100 kg/m^3 whose nominal concentration is equal to 250 g/m^3. The simulation was developed in ANSYS Fluent™ with a first order discretization scheme for convection terms and a second order for diffusion terms. The equations of each phase were solved with a time step of 10^{-4} seconds.

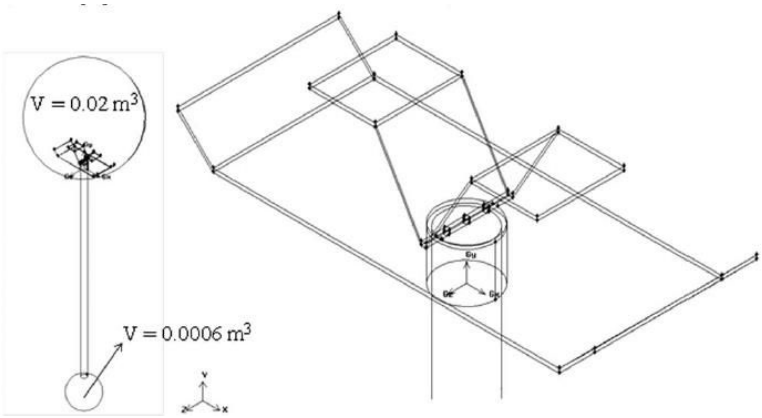

Figure 2.10. Computational domain
(Di Benedetto et al., 2013)
A. Full equipment B) Standard rebound nozzle

Moreover, Figure 2.11 shows that the vortex formed during the dispersion process affect the distribution of the powder in the 20 L sphere. This condition is evidenced because the powder does not accumulate in the vortex centers but in the surrounding areas. Therefore, the dispersed phase is

localized near the walls at the ignition time (typically 60 ms). This is an important aspect since the explosibility tests performed with this apparatus usually assume that the mixture is homogeneous within the sphere. Thus, the experimental determination of the dust cloud ignitability might represent a high uncertainty level due to the variations of the local concentration at the ignition zone (center of the sphere).

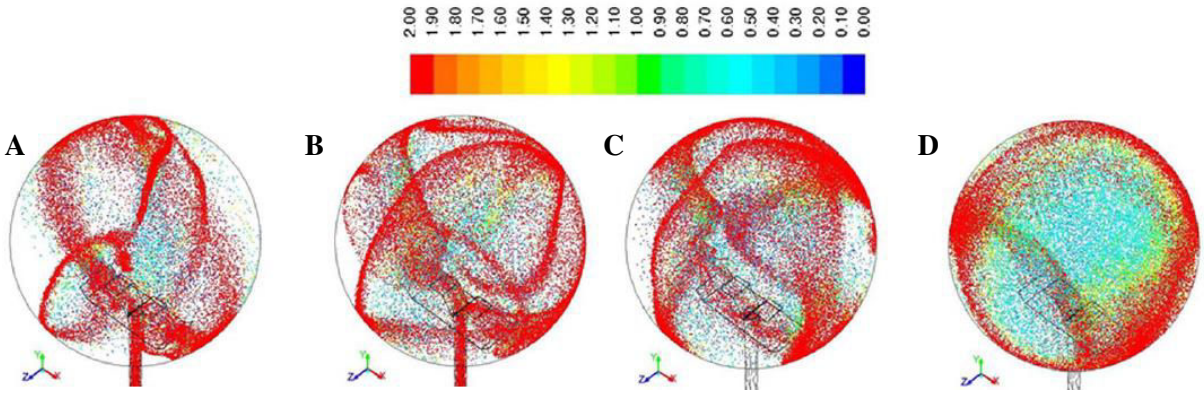

Figure 2.11. Ratio between the local dust concentration and the nominal dust concentration A) 20 ms B) 37ms C) 60 ms D) 150 ms (Di Benedetto et al., 2013)

The computational results established that the injection of the dust-air mixture lasts 60 ms approximately. During this stage, the gas velocity at the entrance is sonic. After this stage, the gas velocity significantly decreases, decaying in time. For this reason, Di Benedetto et al. (2013) characterized the turbulence levels in the equatorial region of the sphere 20 L (Figure 2.12). The results show a significant difference for RMS speeds during the first thirty milliseconds dispersion. Nevertheless, the differences fade as the dispersion develops in the equipment.

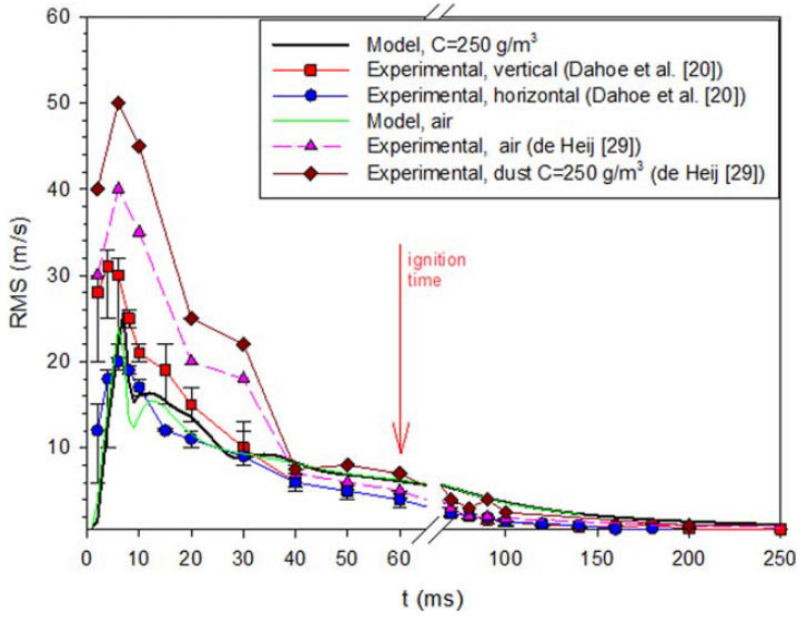

Figure 2.12. Temporal trend of the root mean square velocity Green: Injection of pressurized air – Black: Injection of dust-air mixture (Di Benedetto et al., 2013)

This computational analysis constituted an important reference for the study of this study due to the similarities found in the main objectives and the approaches considered for the description of the dispersion process in the 20 L sphere. Thus, the main results of this study will also be considered in the fourth chapter for the discussion of the computational approach of this thesis.

In summation, this section has presented some case studies that have considered the description of solids fluidization with CFD computational analyses for different purposes. Nowadays, the most of the calculation schemes are based on the approach of soft-spheres in analyses that may reach 100,000 particles per CPU core. Nevertheless, some recent studies have envisaged the inclusion of the hard-sphere collision model in the DEM calculation algorithm (Kosinski & Hoffmann, 2007; Wu et al., 2006). Moreover, some additional efforts have been focused in the development of parallelization schemes to perform the calculation of a greater number of particles (Kafui et al., 2011; Natsui et al., 2012). In addition, more elaborated DEM models are also being developed in order to obtain more realistic descriptions of the dispersion processes (Jasion et al., 2011; Kruggel-Emden et al., 2011). Additionally, some complementary physics are also being included in current research projects. For instance, Zhao & Shan (2013) have considered the heat transfer and chemical reactions in multi-physics problems that couple DEM too.

B. *Examples of CFD simulations associated to the separation of gas-solid mixtures*

Another phenomenon that was characterized for the combustible dust clouds is the solids segregation in the particle-laden flow. The trajectories followed by the dispersed particles are determined by the internal gas flow conditions. This is also the case on the design of cyclone separators. Chu & Yu (2008) considered the Eulerian-Lagrangian approach in a CFD simulation to describe a gas-solid flow developed within a Lapple cyclone to analyze the operating variables that determine the efficiency of the separation process. The technique considered for this study posed the influence of the solid particles on the gas flow because its tangential velocity is significantly diminished when the particles are loaded. Figure 2.13 shows that this condition is more evident in the apex region of the cyclone. In addition, the results show that the inclusion of the particles also causes the displacement high towards the center of the axial velocity region as well as the destruction of the vortex structure that develops within the pure gas flow. These facts clearly evidence the interaction between the two phases when the solids loading is high. The effects of a lower axial velocity on the pressure drop were also discussed by Wasilewski & Duda (2016) who established that the diminution of this velocity represents a reduction of the intermixing of the upward and downward flows by developing another CFD analysis on a multi-stage cyclone.

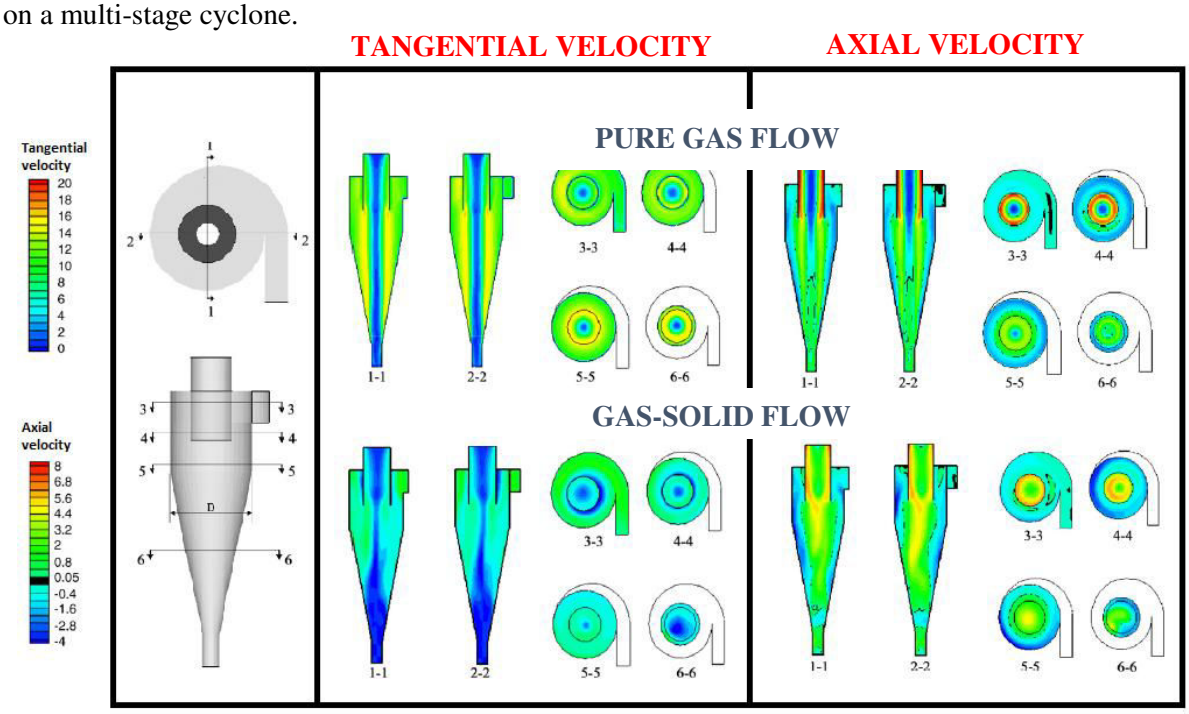

Figure 2.13. Velocity distribution of the simulated cyclone at different sections (Chu & Yu, 2008)

Furthermore, other important characteristics of the performance of the equipment were observed in the computational results. These conditions include the congregation of solid particles on the wall, the stranded flow and particle accumulation in the apex in cyclone separator (Chu & Yu, 2008). Some additional effects of the dispersed solid phase were also observed by Bardin-Monnier et al. (2009) who analyzed the influence of the particle size distribution on the efficiency of the separation of low density solids. A sensitivity analysis performed on a cyclone, designed for laboratory purposes, established that the efficiency is near 58% for particles below 1 µm when the gas flow was 100 L/min. Nevertheless, this variable is reduced to zero when the gas flow was reduced in 90%.

C. *Examples of CFD simulations associated to the solids dispersion & air quality modelling*

The last application of the CFD simulations that will be discussed in this chapter corresponds to the computational characterization of gas-solid flows on cases related to air quality modeling. This option is presented due to capacity of the CFD technique to predict the solids distribution in confined environments. For instance, Beghein et al. (2005) performed a computational study based on an Eulerian-Lagrangian approach that characterized the airflow pattern and the particle dispersion in confined environments (e.g. buildings) to predict the concentration of an indoor pollutant and assess the eventual health risks. The gas flow was defined in the CFD simulation according to the LES-Smagorinsky turbulence model whereas the trajectories particles were described according to a discrete momentum equation. The flow domain consisted of 266418 cells that represented a volume of 15.6 m^3.

This analysis was performed by considering the suspension of solid particles in two different configurations of a ventilated room. The comparison of the stratification profiles shown in Figure 2.14 describes the influence of the position of the gas ventilation. The results present a higher level of particles suspension when the ventilation was injected through the top of a lateral wall and ejected through the bottom of the opposing wall.

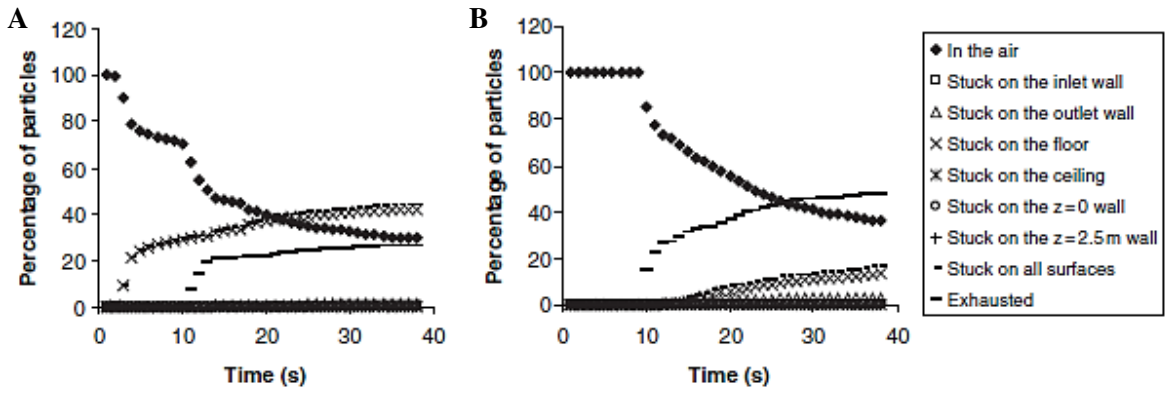

Figure 2.14. Temporal stratification of 20 µm particles in a ventilated room (Beghein et al., 2005)
A) Inlet: Bottom – Outlet: Top B) Inlet: Top – Outlet: Bottom

The CFD model was validated with experimental data obtained from the literature. In accordance with the computational results obtained by Beghein et al. (2005), the airflow posed a similar tendency in the evolution of the turbulence levels with regard to the profile that was determined experimentally with a

high-resolution camera. This result provided some important suggestions for the definition of the operating parameters of a ventilation system in order to obtain a high indoor air quality.

Similarly, Gorlé et al (2009) studied the influence of the turbulent kinetic energy on the dispersion of fine particles by comparing the results of a CFD simulation with the Gaussian models that are usually considered to estimate the concentration of a pollutant in the environment. For this purpose, a simulation of a rectangular wind tunnel was developed according to an Eulerian-Lagrangian approach. The analysis of the dispersion levels of small particles was performed by considering the dispersion of 20,000 particles of 1 µm (ρ_p = 1550 kg/m^3) that are injected from a circular source. The main results of this study are shown in Figure 2.15:

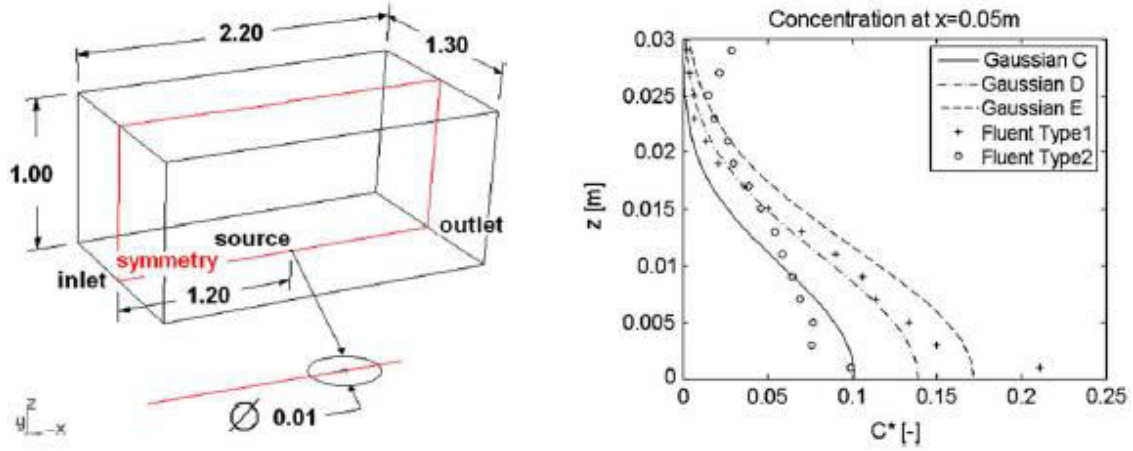

Figure 2.15. Flow domain of the wind tunnel and comparisons of the non-dimensional concentrations predicted by the CFD and the Gaussian models of 3 stability classes. Fluent type 1 = low k Fluent type 2 = High k (Gorlé et al., 2009)

The analysis developed by Gorlé et al. (2009) concluded that the lowest kinetic energy levels represent the highest maximum concentrations near the source location. Moreover, the study also analyzed the validity of the simple Gaussian dispersion models in the prediction of the solids distribution. The results showed that the lowest concentrations are evidenced for the lowest stability classes. Therefore, there is a significant difference between the concentrations predicted by the detailed CFD simulation and the Gaussian model that is explained by the dependence of the constants of the second model on the estimation of the stability class.

2.3 APPLICATION OF THE COMPUTATIONAL FLUID DYNAMICS ON DUST EXPLOSIONS

The following steps of the implementation of computational tools on the characterization of dust explosions are focused on the development of predictive studies that provide a better comprehension of the behavior of explosive dust clouds emerged in industrial environments. This study is submitted to the challenges established by the length and time scales of the dispersion and combustion phenomena that were discussed above. Nevertheless, the computational fluid dynamics has constituted an important alternative for the development of the risk assessment analyses that required for the design of a facility that handles combustible dusts. An example of the utilization of the CFD simulations on the process safety field relies on the developnet of the FLACS-DustEx code.

FLACS-DustEx is one of the commercial codes established to implement the finite-volume methods into the process system engineering scale (Figure 2.1) and assess the probability and severity of a dust explosion. This tool intends to provide a new useful approach that helps predicting the consequences associated to an accidental release and ignition of a combustible dust. This purpose takes the scope of this code into an industrial context whose limitations are associated to the main purposes of the final

user. Actually, a code like this must face several challenges to provide an accurate description of an industrial incident. Thereupon, it is compulsory to establish that an approach developed with this tool might be very handy for the estimation of the severe consequences and the constitution of a risk assessment but it may not provide enough information about the phenomena evolved at micrometric or nanometric scales. However, this gap will reduce as the computational resources increase and the predictive correlations become more accurate.

2.3.1 Characterization of the flame velocity

Skjold (2007) has performed a brief description of the empirical correlations that have been implemented on the FLACS-DustEx code to predict the evolution of an ignited dust-air mixture. This set of equations is envisaged to adapt the current available models of prediction of fluid combustible mixtures to dust clouds. For this purpose the DESC software, which was the previous denomination of the FLACS-DustEx code, incorporated the correlating parameters that determine the turbulent speed of the flame (S_f) from its laminar burning velocity (S_u):

$$S_f = 15.1 S_u^{0.784} u_{rms}^{0.412} l_I^{0.196} \qquad 2.106$$

The determination of the laminar velocity is usually performed from pressure-time histories obtained from experimental data. In addition this parameter is also defined by the root mean square velocity (u_{rms}) and the integral length scale of the turbulent flow (l_I), which is determined by the RANS *k-ε* turbulence model according to the initial and boundary conditions defined by the FLACS-DustEx user. These parameters constitute the link between the input data and the simulation results. Nevertheless, Skjold (2007) also affirmed that there is a grid-dependence of the prediction of the flame thickness because it is usually estimated as three grid cells approximately. This fact implies that a coarse grid might represent an inconvenient for the accurate description of the flame propagation because the order of magnitude of the flame thickness (millimeters) does not always correspond to finite-volume discretization at industrial scale (centimeters or meters).

One of most important characteristics of this model relies on the input data that is demanded for the calculation. In fact, the model does not require parameters such as the volatile content, the exact chemical composition, or the particle size distribution (Skjold, 2007). This condition is established because the scaling of the relative reactivity is performed through the implementation of the deflagration index (K_{St}) defined previously with the 20 L sphere. This fact means that Equation 2.106 is based on the implementation of a flame propagation velocity that was determined in a spherical vessel in other case studies with different geometries and conditions. This fact means that the influence of the flame front stretching and thickening can be neglected in the predictive calculations of the flame propagation process. This assumption might represent an important limitation in the description of the dust explosion due to the omission of the effects of the gas dilatation and the combustion reaction zone (Cuervo, 2015). For this reason, the curvature of a flame front in a non-uniform flow must be characterized according to the confinement geometry and the characteristics of the explosive mixture. This can be achieved by the determining the Markstein length of the flame with high-speed videos that record its development during the combustion process (Cuervo, 2015; Dahoe et al., 2002).

Moreover, the omission of certain characteristics of the solid phase such as its particle size distribution also limits the description of their influence on the heat and mass transfer mechanisms. This fact represents a shortcoming of the model when it has to predict the evolution of combustible clouds composed by agglomerates that can break up. This characteristic of the material represents variations

in the dispersibility of the combustible dust and the transport phenomena that determine the combustion rate.

Moreover, Skjold et al. (2006) have posed the necessity of a good modeler's ability to identify and handle the most significant physical and chemical processes that are involved in dust explosions. This characteristic will determine the reliability and the accuracy of the CFD results. Therefore, the simplified model that was developed for the computational code is not absolutely predictive and it may require some experimental data for the description of the phenomena associated to the flame thickness. Some of these important aspects, which must be taken into account for the characterization of the behavior of a combustible dust cloud, are shown in Table 2.6:

Table 2.6. Summary of some of the physical and chemical processes and properties that may be relevant with regards to dust explosion modeling (Skjold et al., 2006)

Flow related processes	Combustion related processes	Fuel related processes
Agglomeration	Chemical kinetics	Chemical composition
Dust lifting	Devolatilisation	Volatile content
Dust settling	Pyrolysis	Moisture content
Particle-laden flow	Heterogeneous combustion	Particle size distribution
Transient flow	Flame acceleration	Heat of combustion
Turbulent flow	Turbulent combustion	Specific heat of combustion
Single particle movement	Single particle combustion	Thermal conductivity

The simplifications of the description of the particle-laden flow and the flame speed may represent an uncertainty factor, but the prediction of fundamental properties such as the laminar burning velocity is very difficult for gaseous mixtures (Skjold et al., 2006) and even more for dust or hybrid mixtures (Cuervo, 2015). For this reason, this information is considered as the input data that is obtained from experimental tests and the worst-case scenarios are usually considered for the risk assessments.

The description of these phenomena constitutes one of the current challenges on the development of a computational tool that characterizes dusts dispersions and explosions. These aspects will be addressed as the computational resources are developed and the empirical models provide more accuracy in their results. However, the industrial operating conditions usually differ from the worst-case scenarios (coarse particle distributions, high moisture contents and concentrations lower than the minimum explosive value). Hence, it is not always necessary to take into account all the phenomena that modify the dust explosibility. For instance, the combustion model of FLACS-DustEx seems to work reasonably well for some fine organic dusts because they have high volatilization rates. However, this is not always the case for metallic or coarse organic dusts because of the influence of the particle size distribution on the combustion mechanisms. For these reasons, it is plausible to consider this approach for the characterization of certain combustible dust clouds if the context allows it. This fact means that the main purpose of the analysis is the estimation of the consequences in environments that are not highly influenced by the phenomena developed at microscopic scale.

2.3.2 Description of dust explosions with the FLACS-DustEx code

Tascón et al. (2011) described in detail the procedure to simulate a dust explosion with FLACS-DustEx by considering a case study. The scenarios are based on the analysis of the risk associated to the dust clouds that are formed within a storage silo during the filling or empting process of some combustible materials. For this reason, the maximum overpressures were considered to discuss the normative that regulates the sizing of venting areas (EN 14491 & NFPA 68).

One of the main challenges of developing a predictive study through a CFD simulation relies on the definition the initial turbulence levels of the flow domain. This issue was addressed by setting the

mean air velocities, the RMS turbulence and the initial dust concentrations were set to the experimental data that was acquired previously. This input data is an important factor for determining the evolution of the turbulence of the combustible cloud. However, it is not the only aspect that must be taken into account to establish the evolution of the velocity field.

The evolution of turbulence is calculated by FLACS-DustEx according to the RANS k-ε model. This technique considers an isotropic behavior of the turbulent eddies because it is based on the Boussinesq hypothesis. In accordance with this model, the turbulence length scale is computed according to the turbulent kinetic energy of the flow (k) and its dissipation rate (ε) as shown in Equation 2.107:

$$l_1 = 0.09\frac{k^{3/2}}{\varepsilon} \qquad 2.107$$

The RANS k-ε model is usually considered for large-scale systems because it represents lower computational costs for the calculations of the turbulent viscosity and many technical flows are well-described by this technique (Ansys Inc., 2009). In addition, the distributed porosity concept is included to map all the solid elements that compose the flow domain to the simulation grid.

Another relevant characteristic of the description of the velocity field is the spatial discretization that is usually established for the flow domain. The meshes that were tested by Tascón et al. (2011) during the computational analysis ranged between 0.1 and 0.5 meters. The size of the cells represents a limitation on the description of the transport phenomena because it assumes a homogeneity condition in regions that might be too large. This fact clearly evidences the difficulties that must be considered during the characterization of an industrial-scale domain. This aspect was analyzed by Tascón et al. (2011) who analyzed the variations in the prediction of P_{max} and $(dP/dt)_{max}$ that are shown in Table 2.7 when the mesh sizing was changed:

Table 2.7. Overpressure and maximum rate of pressure rise obtained predicted by a CFD simulation for a maize starch explosion in a silo (D=2 m. L=3 m) (Tascón et al., 2011)

Grid size (m)	Maximum overpressure (Pmax) (bar)	Maximum rate of pressure rise ((dP/dt)max) (bar)
0.1	8.80	26.52
0.2	8.80	25.84
0.5	8.82	18.37

The fluctuations are more critical on the kinetic flammability parameter whereas the thermodynamic one does not seem to be highly influenced by the size of the grid. This condition is evidenced because the severity parameters of the combustible dust can become an important source for the turbulence generation. This information is an input data for the calculation scheme as well. Initially, this approach is comprehensible as it considers the same reasoning that is adopted for the sizing of venting areas, which are usually dimensioned according to the experimental data that are obtained with the standard tests. However, the variations of the turbulence levels between the laboratory conditions and the industrial facilities may differ significantly in certain cases (Going et al., 2000). Therefore, some variations on the ignitability and the severity of the combustible dust may occur due to the variations of the turbulence levels and the particle size distribution (Eckhoff, 2003). This condition must be considered when the information of the powder is entered into the predictive CFD code and the size of the mesh grid is determined.

The calculation parameters discussed above are compulsory for a CFD simulation defined on the scale of process engineering. Indeed, the phenomena occurred at smaller scales cannot be accurately described with the current computational resources. Thus, it is necessary to predict the evolution of turbulence with certain simplifications that may influence the general results in some cases.

In summation, the FLACS-DustEx code is an insight into the description of dust explosions in industrial facilities. Therefore, its predictive results must be considered cautiously nowadays due to its uncertainty factors (Skjold, 2007; Tascón et al., 2011). However, it can still provide some useful data for the development of an industrial risk assessment. On the contrary the study proposed for this thesis intends to describe the dispersion of a combustible dust cloud in a different engineering scale, which corresponds to the laboratory conditions. For this reason, some of the most representative limitations of a simulation developed with FLACS-DustEx were not considered for this research project. Hence, the computational results that were obtained are associated to a different context. This fact implies that both predictive approaches can complement each other by constituting a multi-scale analysis of the behavior of the dust cloud.

2.4 SUMMARY

L'étude descriptive de l'évolution d'un nuage des poussières combustibles peut être réalisée à partir de la description numérique de l'évolution d'un écoulement diphasique. Cette analyse peut envisager des caractéristiques différentes du nuage selon la technique numérique qui soit utilisée. Alors la sélection d'une technique computationnelle est devenue un aspect important pour le développement de l'étude de cette thèse. Les critères de la sélection sont déterminés notamment par les objectifs de l'étude et les phénomènes qui seront caractérisés. Donc ces conditions poseront le cadre de l'étude approfondie ainsi que les limitations correspondantes. À cette fin, une classification de techniques a été proposée pour les alternatives les plus utilisées pour la représentation numérique des systèmes homogènes et hétérogènes.

La classification proposée a envisagé deux facteurs pour établir les catégories du classement. La première division détermine si chaque phase composante du mélange est décrite comme un système de particules ou comme un milieu continu. En conséquence, cette analyse a posé une série de méthodes de particules ainsi que les techniques basées sur la mécanique des fluides numérique (CFD, selon son sigle en anglais). La différence entre les modèles consiste à la description du gaz de dispersion. En effet les modèles de particules représentent ce fluide comme un groupe de particules alors que la CFD caractérise cette phase comme un système continu. Cette catégorie est subdivisée comme une simulation eulérienne-eulérienne ou eulérienne-lagrangienne selon le critère de représentation de la poussière combustible. De même, un deuxième classement a été fixé pour les méthodes de particules selon la taille des échelles qui sont normalement considérées. De cette manière, les méthodes de particules ont été subdivisées dans trois catégories : microscopique, mésoscopique et macroscopique.

La première étape de l'analyse comparative a posé la mécanique des fluides numérique comme une alternative appropriée pour la caractérisation des mélanges gaz-solide générés à l'intérieur des chambres de dispersion des dispositifs expérimentaux. Cette conclusion a été établie à partir d'une discussion des aspects les plus importants de la simulation tels que la taille du domaine de l'écoulement et le cout computationnel. Ensuite une sélection ultérieure a établi que les interactions de particules seraient décrites plus précisément avec une approche eulérienne-lagrangienne qui prend en compte les trajectoires de chaque particule solide et ses collisions.

Ensuite, la deuxième étape a posé les modèles numériques de caractérisation de la turbulence de l'écoulement du gaz. Cette partie de l'étude a énuméré les modèles RANS et les modèles de la simulation aux grandes échelles (LES, selon son sigle en anglais). Les premières techniques font un traitement statistique afin de réaliser un moyennage des équations de Navier-Stokes tandis que les autres prennent en compte les perturbations turbulentes de grande taille et modélisent les effets des petites. De la même manière il y a modèles hybrides qui considèrent une pondération des approches RANS et LES. Ces techniques dépendent de la discrétisation spatiale du domaine et de la distance de l'écoulement aux parois. Une analyse descriptive réalisée a établi que l'alternative choisie pour cette étude devrait profiter des avantages d'une simulation LES dans la description des cascades d'énergie

cinétique turbulente pour les écoulements séparés et des paramètres de modélisation d'une simulation RANS dans les régions qui sont près des parois. Donc, une méthode hybride qui est nommée *Detached Eddy Simulation (DES)* a été sélectionnée pour le développement des simulations numériques du mélange gaz-solide. Cette méthode fait une pondération des échelles de longueur de chaque modèle de turbulence pour calculer les propriétés turbulentes de l'écoulement (ex. viscosité turbulente). L'approche hybride DES est basée sur le modèle *Shear Stress Transport k-ω* (RANS) couplé avec le modèle LES. Le dernier est défini avec la méthode Smagorinsky-Lilly pour la modélisation des petites échelles.

En outre la modélisation des particules est réalisée à partir de l'intégration numérique d'un bilan de quantité de mouvement qui est défini pour chaque particule. Ce bilan prend en compte les forces principales qui sont exercées sur la surface des particules. En plus le bilan ajoute une force de contact qui est déterminée par les collisions des particules en suspension. Ces phénomènes sont modélisés avec la méthode des sphères molles, laquelle est disponible sur plusieurs codes CFD qui prédisent le comportement de mélanges composés par des éléments discrets.

Finalement, l'approche lagrangienne est complémentée avec l'inclusion d'un modèle de fragmentation et d'agglomération. L'équation du modèle de cohésion linéaire détermine une valeur critique pour laquelle les contraintes du fluide peuvent modifier la distribution des tailles de particules des agrégats dispersés. Cette valeur est calculée à partir de la force cohésive associée au matériau solide.

La mécanique des fluides numérique a permis de caractériser l'évolution des nuages de poussières combustibles à l'intérieur des chambres de dispersion des appareils standardisés. Néanmoins, le domaine de recherche associé à l'utilisation de cet outil numérique englobe aussi autres sujets qui considèrent des dispersions de particules. Brièvement certains cas d'étude qui ont envisagé des approches numériques pour la caractérisation des écoulements diphasiques ont été décrits. Cette révision a montré la possibilité d'utiliser la CFD pour des analyses liées à la caractérisation du comportement des lits fixes et des lits fluidisés, la modélisation de la qualité de l'air, le transport pneumatique et hydraulique de solides, la dispersion de particules et la séparation à travers de cyclones et des systèmes de filtration.

Finalement, la sécurité des procédés a posé un autre objectif de recherche pour la mécanique des fluides numérique. Par exemple, cet outil peut contribuer à la description de dispersions accidentelles des substances toxiques ou explosives. En outre, l'évolution d'une onde de surpression établie par une explosion de poussières pourrait être prédite à partir d'une analyse numérique réalisée avec cette approche. À cette fin un code CFD, nommé FLACS-DustEx, a été développé pour faire une estimation des variables associées à la génération d'un nuage de poussières combustibles (ex. concentration) ainsi que les variables associées à la sévérité de l'explosion (ex. température et surpression). En effet une technique numérique de ce type peut constituer un bon outil pour le développement des analyses de risques et la définition des mesures de protection. Nonobstant il faut prendre en compte les limitations concernées à l'application de cette approche à un écoulement diphasique dispersé dans un domaine de la taille d'une usine industrielle.

La description des phénomènes associés à un écoulement diphasique avec une technique CFD dépend notamment des paramètres de discrétisation spatiale et temporelle. Évidemment l'utilisation d'un maillage fin ou d'un modèle de discrétisation de grand ordre est restreinte à cause du cout computationnel de la simulation. L'utilisation d'un maillage gros et d'un grand pas de temps peut représenter une limitation dans la description des phénomènes d'interaction des phases composantes du nuage. Également, la description de certaines caractéristiques de l'explosion telles que la vitesse de propagation de la flamme et les mécanismes de combustion (pyrolyse ou oxydation de surface) est limitée par l'approche numérique du code CFD. Néanmoins l'outil a montré des résultats satisfaisants pour les poussières organiques qui volatilisent facilement leurs composants inflammables. En effet cette condition établit que l'exactitude de la prédiction du processus de combustion sera plus importante à mesure que les ressources computationnelles augmentent significativement et les modèles empiriques deviennent plus détaillés.

2.5 LIST OF VARIABLES

a_k	Volume fraction of the phase *k*	[-]
C_D	Drag coefficient between the solid particle and the fluid	[-]
C_p	Heat capacity of the fluid at constant pressure	[J· kmol^{-1}·K $^{-1}$]
C_{SL}	Coefficient of the shear lift force	[-]
C_w	Empirical constant for calculation of the LES length scale	[-]
D_ω	Cross-diffusion of the turbulent kinetic energy and the specific dissipation rate (*k*-*ω* model)	[J·m^{-5}]
d_p	Particle diameter	[m]
d_{wall}	Distance of a cell to the closest wall (CFD)	[m]
E	Potential energy of the system	[kJ·kmol^{-1}]
e_n	Coefficient of normal restitution	[-]
$F\left(x_p\right)$	Vorticity sources located at the solid boundaries (vortex method)	[s^{-2}]
$F_{ab,n}$	Normal component of the contact force of the particles *a* and *b*	[N]
$F_{ab,t}$	Tangential component of the contact force of the particles *a* and *b*	[N]
F_B	External body forces (Eulerian approach)	[N]
f_B	Random force (Brownian Dynamics)	[N]
f_{Blend}	Blending function of the Wall-Modeled Large Eddy Simulation model (WMLES)	[-]
$F_{cohesion}$	Cohesion force attributed to the linear cohesion	[N]
$F_{contact,a}$	Contact force of the particle *a* (soft-sphere model)	[N]
F_D	Drag coefficient determined by the slip velocity of the particle and the fluid (Lagrangian approach)	[s^{-1}]
f_d^*	Blending function of the IDDES model	[-]
f_{EF}	Force exerted by an external field in the Brownian Dynamics method	[N]
$f_{Elevate}$	Elevating function (IDDES model)	[-]
$f_{i,LBM}\left(x,t\right)$	Distribution function of the Lattice Boltzmann method for the position *x* at the time *t*	[-]
F_{IDDES}	Ration between the RANS and IDDES length scales	[-]

$F_{lift,k}$	Lift force	[N]
f_n	Total force exerted on the representative molecule or particle *n* (MD)	[N]
F_{n-b}	Normal component of the force on a particle due to parallel bonds	[N]
F_{nj}^{C}	Conservative forces between the particles *n* and *j*	[N]
F_{nj}^{D}	Dissipative forces between the particles *n* and *j*	[N]
F_{nj}^{R}	Random forces between the particles *n* and *j*	[N]
F_{pg}	Coefficient of the pressure gradient force (Lagrangian approach)	[m·s^{-2}]
F_{s-b}	Shear component of the force on a particle due to parallel bonds	[N]
F_{SL}	Shear lift force	[N]
F_{SPH}	External force fields experienced by a particle (SPH)	[N]
$F_{vm,k}$	Virtual mass force	[N]
F_x	Additional forces exerted on a dispersed particle (Lagrangian approach)	[m·s^{-2}]
g	Gravitational acceleration	[m·s^{-2}]
G_k	Production of the turbulent kinetic energy (*k*-ω model)	[W·m^{-3}]
G_ω	Production of the specific dissipation rate (*k*-ω model)	[J·m^{-5}]
H_H	Helmholtz free energy of a determined number of particles	[kJ·kmol^{-1}]
h_k	Enthalpy of the phase *k*	[J·kg^{-1}]
h_{pk}	Interphase enthalpy (Eulerian approach)	[J·kg^{-1}]
h_s	Sensible enthalpy of the fluid enthalpy	[J·kmol^{-1}]
k	Turbulent kinetic energy	[m^2·s^{-2}]
k_{eff}	Effective thermal conductivity of the mixture (Mixture model)	[W·m·K^{-1}]
k_n	Normal spring stiffness	[N·m^{-1}]
k_t	Tangential spring stiffness	[N·m^{-1}]
K_ε	Biot-Savart kernel	[m^{-2}]
l_{IDDES}	IDDES length scale	[m]
l_{LES}	LES length scale	[m]

l_{RANS}	RANS length scale	[m]
L_s	Mixing length for subgrid-scales	[m]
m_{ab}	Reduced mass of the two particles	[kg]
m_n	Mass of molecule or particle *n*	[kg]
m_s	Mass of a solid particle	[kg]
m_{pk}	Mass transfer between the phases *p* and *k*	[kg·s^{-1}]
n_{ab}	Normal unit vector of the positions of the particles *a* and *b*	[-]
N_{meas}	Number of measurements for the ensemble averaging (CFD)	[-]
N_p	Number of particles considered for a particle method	[-]
p	Pressure of the system	[Pa]
q	Heat flux	[W·m^{-2}]
$q_{\varphi,j}$	Subgrid-scale turbulent flux of a scalar property	Defined by φ
Q_{pk}	Heat exchange between the phases *p* and *k*	[W·m^{-3}]
q_k	Heat flux of the phase *k* (Eulerian approach)	[W·m^{-2}]
R	Ideal gas constant	[kJ·kmol^{-1}·K^{-1}]
R_a	Radius of the particle *a*	[m]
R_b	Radius of the particle *b*	[m]
r_{dl}	Laminar marker of the wall region	[-]
r_{dt}	Turbulent marker of the wall region	[-]
$R_{\min}$	Minimal radius of surfaces in contact	[m]
Re_p	Reynolds numbers based on the particle diameter	[-]
Re_S	Reynolds numbers based on the shear flow	[-]
Re_t	Turbulent Reynolds number (*k*-ω model)	[-]
R_{pk}	Interaction force between the continuous phases *p* and *k*	[N]
S	Entropy of the system	[kJ·kmol^{-1}·K^{-1}]
S_E	External energy source terms in the flow domain (Mixture model)	[W·m^{-3}]

S_F	Shape factor of the combustible dust	[-]
S_{ij}^*	Rate-of-strain tensor for the resolved scale	[s^{-1}]
S_k	External energy source terms in the phase *k* (Eulerian approach)	[$W \cdot m^{-3}$]
s_p	Surface area of the solid particle	[m^2]
s_{sphere}	Surface area of a sphere having the same volume as the solid particle	[m^2]
T	Temperature of the system	[K]
T^*	Filtered temperature of the system (LES model)	[K]
T_a	Torque of the particle *a*	[N·m]
t_{ab}	Tangential unit vector	[-]
T_k	Source of turbulent kinetic energy (*k*-ω model)	[$W \cdot m^{-3}$]
T_{n-b}	Normal component of the torque on a particle due to parallel bonds	[N·m]
T_{s-b}	Shear component of the torque on a particle due to parallel bonds	[N·m]
T_ω	Source of specific dissipation rate (*k*-ω model)	[$J \cdot m^{-5}$]
u	Velocity of the fluid flow	[$m \cdot s^{-1}$]
U_0	Solution of the homogeneous Poisson equation	[$m \cdot s^{-1}$]
u_{ab}	Relative velocity of the particles *a* and *b*	[$m \cdot s^{-1}$]
$u_{ab,n}$	Normal component of the relative velocity of the particles *a* and *b*	[$m \cdot s^{-1}$]
$u_{ab,t}$	Tangential component of the relative velocity of the particles *a* and *b*	[$m \cdot s^{-1}$]
$u_{ab,0}$	Relative velocity of the particles *a* and *b* before collision	[$m \cdot s^{-1}$]
u_i	Component *i* of the velocity of the fluid flow	[$m \cdot s^{-1}$]
u_i'	Component *i* of the velocity fluctuations of the fluid flow	[$m \cdot s^{-1}$]
u_i^*	Component *i* of the filtered velocity	[$m \cdot s^{-1}$]
u_k	Velocity of the phase *k*	[$m \cdot s^{-1}$]
u_p	Particle velocity	[$m \cdot s^{-1}$]
u_{kp}	Interphase velocity of the phases *k* and *q*	[$m \cdot s^{-1}$]
u_q	Velocity of the discrete particle (Vortex method and SPH)	[$m \cdot s^{-1}$]

V	Volume of the flow domain	[m^3]
v_q	Volume of the discrete particle (Vortex method and SPH)	[m^3]
$W\left(u_p - u_q, h\right)$	Mollifier kernel (SPH)	[m^{-2}]
$W_{cohesion}$	Work of cohesion	[$J \cdot m^{-2}$]
x_i	Component *i* of the position vector of the velocity of the fluid flow	[m]
x_n	Position of molecule or particle *n*	[m]
x_p	Position of the fluid element (Vortex method)	[m]
x_q	Position of the vortex blob *q*	[m]
y_n	Wall normal distance	[m]
Y_k	Dissipation of the turbulent kinetic energy (*k-ω* model)	[$W \cdot m^{-3}$]
Y_ω	Dissipation of the specific dissipation rate (*k-ω* model)	[$J \cdot m^{-5}$]

Greek symbols

β_{SL}	Ratio between the Reynolds numbers based on the shear flow and the particle diameter	[-]
γ	Heat capacity ratio of the gas	[-]
Γ_k	Effective diffusivity of the turbulent kinetic energy (*k-ω* model)	[$J \cdot s \cdot m^{-3}$]
Γ_ω	Effective diffusivity of the specific dissipation rate (*k-ω* model)	[$J \cdot s \cdot m^{-3}$]
δ_{ij}	Kronecker delta function	[-]
$\delta_{\max}$	Maximum tensile stress before the agglomerates fragmentation	[Pa]
δ_n	Normal overlap of the particles *a* and *b*	[m]
δ_t	Tangential overlap of the particles *a* and *b*	[m]
Δt	Temporal discretization of the flow simulation	[s]
Δx	Spatial discretization of the flow domain	[m]
ΔV	Volume of fluid cell of the flow domain (CFD)	[m^3]
Δ_{wn}	Grid step in the wall-normal direction	[m]
ε	Specific dissipation rate of the fluid flow (k-epsilon model)	[$m^2 \cdot s^{-3}$]

ε_q	Size of the vortex blob *q*	[m]
η_n	Normal damping coefficient	[kg·s^{-1}]
η_t	Tangential damping coefficient	[kg·s^{-1}]
η_ε	Even function for the discretization of the Biot-Savart equation	[-]
κ	Von Kármán constant	[-]
λ_k	Bulk viscosity of the fluid	[Pa·s]
μ	Dynamic viscosity of the fluid	[Pa·s]
μ_f	Friction coefficient	[-]
μ_k	Dynamic viscosity of the phase *k* (Eulerian approach)	[Pa·s]
μ_{SGS}	Dynamic subgrid viscosity	[Pa·s]
μ_t	Turbulent viscosity of the fluid flow	[Pa·s]
ν_{kin}	Kinematic viscosity of the gas	[m^2·s^{-1}]
ν_t	Turbulent kinematic viscosity of the gas	[m^2·s^{-1}]
ρ	Fluid density	[kg·m^{-3}]
ρ_k	Density of the phase *k*	[kg·m^{-3}]
ρ_p	Particle density	[kg·m^{-3}]
σ_k	Turbulent Prandtl number of *k* (*k*-ω model)	[-]
σ_ω	Turbulent Prandtl number of ω (*k*-ω model)	[-]
τ	Shear and normal stresses of the continuous phase	[Pa]
$\underline{\underline{\tau}}$	Stress tensor of the flow (SPH method)	[Pa]
τ_{ij}	Subgrid-scale stress	[Pa]
τ_{kk}	Isotropic part of the subgrid-scale stress	[Pa]
$\tau_{\max}$	Maximum shear stress before the agglomerates fragmentation	[Pa]
Φ	Mean component of the gas flow property (CFD)	[-]
φ	Gas flow property (CFD)	[-]
φ'	Fluctuating component of the gas flow property (CFD)	[-]

ω	Specific dissipation rate of the fluid flow (k-omega model)	[s^{-1}]
ω_p	Vorticity of the vortex fluid element (Vortex method and SPH)	[s^{-1}]
ω_q	Vorticity of the discrete particle (Vortex method and SPH)	[s^{-1}]

2.6 REFERENCES

Abu-Nada, E. (2015). Dissipative particle dynamics simulation of natural convection using variable thermal properties. *International Communications in Heat and Mass Transfer*, *69*, 84–93.

Alletto, M., & Breuer, M. (2012). One-way, two-way and four-way coupled LES predictions of a particle-laden turbulent flow at high mass loading downstream of a confined bluff body. *International Journal of Multiphase Flow*, *45*, 70–90.

Ansys Inc. (2009). ANSYS FLUENT 12.0 Theory Guide.

Bardin-Monnier, N., Altmeyer, S., Schreiber, V., & Marecat, A. (2009). Comparison of two methods of cyclones simulation: semi-empirical model and CFD. Example of a specific cyclone design.

Beghein, C., Jiang, Y., & Chen, Q. Y. (2005). Using large eddy simulation to study particle motions in a room. *Indoor Air*, *15*(4), 281–290.

Benzarti, S., Mhiri, H., & Bournot, H. (2012). Drag models for Simulation Gas-Solid Flow in the Bubbling Fluidized Bed of FCC Particles. *World Academy of Science, Engineering and Technology*, *61*, 1138–1143.

Chen, X.-P. (2012). Applications of Lattice Boltzmann Method to Turbulent Flow Around Two-Dimensional Airfoil. *Engineering Applications of Computational Fluid Mechanics*, *6*(4), 572–580.

Chu, K. W., & Yu, A. B. (2008). Numerical simulation of complex particle–fluid flows. *Powder Technology*, *179*(3), 104–114.

Cuervo, N. (2015). *Influences of turbulence and combustion regimes on explosions of gas-dust hydrid mixtures*. Université de Lorraine.

Dahoe, A. E., Hanjalic, K., & Scarlett, B. (2002). Determination of the laminar burning velocity and the Markstein length of powder–air flames. *Powder Technology*, *122*(2–3), 222–238.

Deen, N. G., Van Sint Annaland, M., Van der Hoef, M. A., & Kuipers, J. A. M. (2007). Review of discrete particle modeling of fluidized beds. *Chemical Engineering Science*, *62*(1–2), 28–44.

Di Benedetto, A., Russo, P., Sanchirico, R., & Di Sarli, V. (2013). CFD simulations of turbulent fluid flow and dust dispersion in the 20 liter explosion vessel. *AIChE Journal*, *59*(7), 2485–2496.

Eckhoff, R. (2003). *Dust Explosions in the Process Industries, Third Edition: Identification, Assessment and Control of Dust Hazards* (3 edition). Amsterdam ; Boston: Gulf Professional Publishing.

Elghobashi, S. (1991). Particle-laden turbulent flows: direct simulation and closure models. *Applied Scientific Research*, *48*(3-4), 301–314.

Eymard, R., Gallouët, T., Herbin, R., & Latché, J. C. (2007). Analysis tools for finite volume schemes. *Acta Math. Univ. Comenianae*, *76*(1), 111–136.

Fang, M., Luo, K., Yang, S., Zhang, K., & Fan, J. (2013). LES-DEM investigation of gas–solid flow dynamics in an internally circulating fluidized bed. *Chemical Engineering Science*, *101*, 213–227.

Garnier, E., Adams, N., & Sagaut, P. (2009). *Large Eddy Simulation for Compressible Flows*. Dordrecht: Springer Netherlands. Retrieved from http://link.springer.com/10.1007/978-90-481-2819-8

Going, J. E., Chatrathi, K., & Cashdollar, K. L. (2000). Flammability limit measurements for dusts in 20-L and 1-m3 vessels. *Journal of Loss Prevention in the Process Industries*, *13*(3–5), 209–219.

Gorlé, C., van Beeck, J., Rambaud, P., & Van Tendeloo, G. (2009). CFD modelling of small particle dispersion: The influence of the turbulence kinetic energy in the atmospheric boundary layer. *Atmospheric Environment*, *43*(3), 673–681.

Gritskevich, M. S., Garbaruk, A. V., Schütze, J., & Menter, F. R. (2012). Development of DDES and IDDES Formulations for the k-ω Shear Stress Transport Model. *Flow, Turbulence and Combustion*, *88*(3), 431–449.

Guo, L., Morita, K., & Tobita, Y. (2014). Numerical simulation of gas–solid fluidized beds by coupling a fluid-dynamics model with the discrete element method. *Annals of Nuclear Energy*, *72*, 31–38.

Haider, A., & Levenspiel, O. (1989). Drag coefficient and terminal velocity of spherical and nonspherical particles. *Powder Technology*, *58*(1), 63–70.

Jasion, G., Shrimpton, J., Danby, M., & Takeda, K. (2011). Performance of numerical integrators on tangential motion of DEM within implicit flow solvers. *Computers & Chemical Engineering*, *35*(11), 2218–2226.

John, V. (2012). *Large Eddy Simulation of Turbulent Incompressible Flows: Analytical and Numerical Results for a Class of LES Models*. Springer Science & Business Media.

Kafui, D. K., Johnson, S., Thornton, C., & Seville, J. P. K. (2011). Parallelization of a Lagrangian–Eulerian DEM/CFD code for application to fluidized beds. *Powder Technology*, *207*(1-3), 270–278.

Kosinski, P., & Hoffmann, A. C. (2007). An Eulerian–Lagrangian model for dense particle clouds. *Computers & Fluids*, *36*(4), 714–723.

Koumoutsakos, P. (2005). Multiscale Flow Simulations Using Particles. *Annual Review of Fluid Mechanics*, *37*(1), 457–487.

Kruggel-Emden, H., Stepanek, F., & Munjiza, A. (2011). Performance of integration schemes in discrete element simulations of particle systems involving consecutive contacts. *Computers & Chemical Engineering*, *35*(10), 2152–2157.

Li, J., Ge, W., & Kwauk, M. (2009). Meso-scale phenomena from compromise–a common challenge, not only for chemical engineering. *arXiv Preprint arXiv:0912.5407*. Retrieved from http://arxiv.org/abs/0912.5407

Liu, D., Bu, C., & Chen, X. (2013). Development and test of CFD–DEM model for complex geometry: A coupling algorithm for Fluent and DEM. *Computers & Chemical Engineering*, *58*, 260–268.

Marin, G. B. (2005). *Advances in Chemical Engineering: Multiscale Analysis*. Academic Press.

Masatsuka, K. (2013). *I do like CFD. Governing Equations and Exact Solutions* (Second Edition). Lulu.

Mockett, C. (2009). *A Comprehensive Study of Detached Eddy Simulation*. Univerlagtuberlin.

Mooney, C. Z. (1997). *Monte Carlo Simulation*. SAGE Publications.

Natsui, S., Ueda, S., Nogami, H., Kano, J., Inoue, R., & Ariyama, T. (2012). Gas–solid flow simulation of fines clogging a packed bed using DEM–CFD. *Chemical Engineering Science*, *71*, 274–282.

Novak, J. W., & Thompson, J. R. (1986). Extending the use of particle sizing instrumentation to calculate particle shape factors. *Powder Technology*, *45*(2), 159–167.

Pandey, A., Hardt, S., Klar, A., & Tiwari, S. (2016). Brownian dynamics of rigid particles in an incompressible fluctuating fluid by a meshfree method. *Computers & Fluids*, *127*, 174–181.

Phan-Thien, N., Mai-Duy, N., Khoo, B. C., & Duong-Hong, D. (2016). Strongly overdamped Dissipative Particle Dynamics for fluid-solid systems. *Applied Mathematical Modelling*. Retrieved from http://linkinghub.elsevier.com/retrieve/pii/S0307904X16300476

Satoh, A. (2011). 1 - Outline of Molecular Simulation and Microsimulation Methods. In A. Satoh (Ed.), *Introduction to Practice of Molecular Simulation* (pp. 1–27). London: Elsevier.

Schellander, D. (2014). *CFD simulations of particle laden flows: Particle transport and separation*. Anchor Academic Publishing.

Schiestel, R. (2008). *Modeling and simulation of turbulent flows*. London : Hoboken, NJ: ISTE; Wiley.

Shur, M. L., Spalart, P. R., Strelets, M. K., & Travin, A. K. (2008). A hybrid RANS-LES approach with delayed-DES and wall-modelled LES capabilities. *International Journal of Heat and Fluid Flow*, *29*(6), 1638–1649.

Skjold, T. (2003). *Selected Aspects of Turbulence and Combustion in 20-litre Explosion Vessels. Development of Experimental Apparatus and Experimental Investigation*. University of Bergen, Bergen.

Skjold, T. (2007). Review of the DESC project. *Journal of Loss Prevention in the Process Industries*, *20*(4-6), 291–302.

Skjold, T., Larsen, Ø., & Hansen, O. R. (2006). Possibilities, limitations, and the way ahead for dust explosion modelling. *Flame Propagation in Dust Clouds. Numerical Simulation and Experimental Investigation*. Retrieved from https://bora.uib.no/handle/1956/8948

Sommerfeld, M. (2000). Theoretical and Experimental Modelling of Particulate Flows. *Technical Report Lecture Series 2000-06, von Karman Institute for Fluid Dynamics*, pp. 20–23.

Sun, D., Li, Q., & Zhang, H. (2013). Detached-eddy simulations on massively separated flows over a 76/40° double-delta wing. *Aerospace Science and Technology*, *30*(1), 33–45.

Tascón, A., Ruiz, Á., & Aguado, P. J. (2011). Dust explosions in vented silos: Simulations and comparisons with current standards. *Powder Technology*, *208*(3), 717–724.

Toro, J. R. (2006). *Dinámica de fluidos con introducción a la teoría de la turbulencia*. Uniandes.

Versteeg, H., & Malalasekera, W. (2007). *An Introduction to Computational Fluid Dynamics: The Finite Volume Method* (2 edition). Harlow, England ; New York: Prentice Hall.

Walther, J. H., Jaffe, R. L., Kotsalis, E. M., Werder, T., Halicioglu, T., & Koumoutsakos, P. (2004). Hydrophobic hydration of C60 and carbon nanotubes in water. *Carbon*, *42*(5-6), 1185–1194.

Wang, L.-P., Peng, C., Guo, Z., & Yu, Z. (2015). Lattice Boltzmann Simulation of Particle-Laden Turbulent Channel Flow. *Computers & Fluids*.

Wasilewski, M., & Duda, J. (2016). Multicriteria optimisation of first-stage cyclones in the clinker burning system by means of numerical modelling and experimental research. *Powder Technology*, *289*, 143–158.

Wendt, J. F. (1992). *Computational Fluid Dynamics an Introduction*. Berlin, Heidelberg: Springer Berlin Heidelberg.

Wilson, J. D., Bechtel, D. B., Todd, T. C., & Seib, P. A. (2006). Measurement of Wheat Starch Granule Size Distribution Using Image Analysis and Laser Diffraction Technology. *Cereal Chemistry Journal*, *83*(3), 259–268. http://doi.org/10.1094/CC-83-0259

Wu, C. L., Zhan, J. M., Li, Y. S., & Lam, K. S. (2006). Dense particulate flow model on unstructured mesh. *Chemical Engineering Science*, *61*(17), 5726–5741.

Zhao, J., & Shan, T. (2013). Coupled CFD–DEM simulation of fluid–particle interaction in geomechanics. *Powder Technology*, *239*, 248–258.

CHAPTER III

EXPERIMENTAL STUDY OF THE DUST DISPERSION AND ITS EFFECTS ON THE EXPLOSIBILITY PARAMETERS

The experimental analyses of the flammability tests provide an insight to the detailed description of the dispersion process inside the combustion chambers. For this reason, this study has considered several tools to characterize the phenomena linked to the interaction of the two phases that constitute a combustible dust cloud. This chapter will describe in detail the different tools used to evaluate experimentally the main characteristics of the dust cloud. The results established an important basis for the development of the computational analysis by identifying the variations in the conditions of the gas-solid mixture throughout a set of experiments that have guided the subsequent steps of this research project.

This experimental approach has been directed towards the description of the factors that characterize the dust cloud dynamics before its ignition. In accordance with this statement, this study envisages the analysis of the dispersion process that is defined by the initial turbulence of the two-phase flow. For this purpose, this part of the project has been focused on the study of the influence of some physical properties of the solid and the operating parameters on the results obtained with a flammability test.

Initially, this chapter presents the main properties of the combustible dusts that were considered for the experimental analyses. The description of the physical and chemical characteristics of these powders allowed determining their fluidization characteristics. This study considered aluminum (metallic dust) and wheat starch (organic dust) in order to consider the dispersion of two micrometric dusts that will differ significantly not only on their fluidization behavior but also on their combustion mechanisms.

Afterwards, the experiments that were proposed as complementary tools for the analysis of the evolution of the dust cloud are defined according to their specific principles. The second part of this chapter poses the main principles of the test that evaluated of the continuous variations of the particle size distributions of the combustible dust through the dispersion process. The evolution of this variable must be considered as an aspect of main interest due to the evidences discussed previously by Dufaud et al. (2010), Gerhold & Stahmer (2014) and Castellanos et al. (2014) who posed the particle size distribution as a determining factor in the kinetics and transport phenomena of the combustion process. The description of this variable was achieved by performing a set of granulometric analyses that contributed to identify the different stages of dispersion of a powder during a flammability test.

The variations of the particle size distribution determined the importance of considering its segregation levels inside the dispersion chambers. For this reason, the next step of this approach was directed towards the acquisition of qualitative and quantitative data in order to evaluate the influence of the test parameters on the homogeneity of the mixture during the dispersion process. For this purpose, several dispersion tests were performed in order to record high-speed videos that showed how the injection nozzle distributes the injected flow inside the explosion chambers. These analyses were supported by a numerical analysis that was performed with a Particle Image Velocimetry (PIV) study which assessed the turbulence levels in the gas flow by implementing a particle tracking methodology whose general principles are briefly described on the third section of this chapter.

Thereafter, the characterization tests began with the description of the injection process in the modified Hartmann tube through a preliminary analysis that was posed for this study. This analysis was performed to establish the injection conditions of the pressurized gas on the dispersion tube. For this purpose, the injection system was coupled to an expandable body in order to determine the duration of the injection through the visualization of the volume variations. The fourth part of this chapter shows how the experimental results of this study were complemented by a numerical scheme that allowed determining the mass flow and the injection pressure of the injected gas. This preliminary analysis was only performed with the modified Hartmann tube because the conditions of the gas

injection in the 20 L require the description of the whole flow domain and not only the dispersion chamber.

Finally, the last two parts of this chapter present the experimental results that were obtained for the modified Hartmann tube and the 20 L sphere respectively. The dispersion processes that are defined by the standard test methods were described with the tests that were discussed above. Thereafter, some of the operating parameters were modified in order to establish their influence on the dust cloud dynamics by performing a sensitivity analysis. The results of these tests allowed identifying several characteristics of the combustible dust clouds such as their segregation, variations of particle size distribution and turbulence regimes, influence of the injection pressure and the ignition delay on the dust explosibility, among others. These results were complemented by the information acquired from the CFD simulations, which will be described in the next chapter.

3.1 COMBUSTIBLE DUSTS ANALYZED

The dispersion analyses considered two different types of dusts. These characterizations were performed with micrometric aluminum (metallic dust) and micrometric wheat starch (organic dust). The explosibility of these powders has been widely analyzed by different authors who have studied their combustion mechanisms (Proust, 2006; Rzal & Veyssiere, 1994; Skjold, Castellanos, Olsen, & Eckhoff, 2014) as well as their different physical properties, which are considerably affected by some conditions of the environment (e.g. relative humidity) (Dufaud et al., 2010; Traoré et al., 2009).

Some of these physical properties also determine their fluidization characteristics due to the different interaction mechanisms developed by the dispersion gas and the combustible dust. This section will describe the main explosibility characteristics of these combustible dusts along with determination of the particle size distributions and densities, which are the properties considered to characterize the dispersibility of these powders.

3.1.1 Aluminum

Aluminum is a metallic powder that is widely used as an important industrial raw material in the manufacturing of different products such as pigments, paints, fireworks, metallurgy and aircrafts. The annual sales of aluminum powders and granules (< 1 mm) worldwide are estimated at approximately 200 thousand tons per annum (tpa). Due to the ignition sensitivity of this metal powder, the aluminum dust explosions have constituted several major and minor incidents in unit areas associated to the storage, transport and manipulation of the pulverized material (Abbasi & Abbasi, 2007; Eckhoff, 2003; Marmo et al., 2004). These events pose the necessity of determining the negative consequences associated to the combustion phenomena of this metallic dust.

The combustion process of aluminum dust undergoes an exothermic reaction in the presence of air on the surface of every suspending particle. Because of this condition, aluminum is one of the most flammable materials when ignited but it is also known as one of the most ignition-resistant materials. Aluminum high level of ignition resistance is caused by a refractory oxide that forms rapidly at ambient conditions on the particle surface. Such oxide layer is very protective, expands in volume upon formation and melts at 2320 K whereas aluminum melts at 932 K (Chiffoleau et al., 2006).

This layer defines a Pilling-Bedworth ratio equal to 1.29 (Xu & Gao, 2000). This proportion is determined by the particle size. For instance, the total presence of aluminum oxide in an Alu 5456 aluminum sample whose mean diameter is 4.8 µm was determined by Escot Bocanegra (2007) with an

EDS analysis. The results established that the analyzed sample consisted of Aluminum (87.2%), Oxygen (5.0%) and Carbon (7.8%), which showed a very little oxidized nature of the powder and a low level of contamination.

Moreover, the combustion of this powder can be considered as a set of consecutive reactions. At the beginning of this oxidation process, part of the suspended aluminum dust is heated. Then, the heat is transferred to the nearby powder and the process continues. Actually, the combustible dust-air mixture explosion is a kind of gas-solid burning phenomenon. This condition is caused by the fact that the gas stored in the dust takes part in the explosive reaction after being heated inside the dust pores (Maoling, 2012). For this reason, an aluminum dust explosion is usually classified as a major incident because of the negative consequences of its very powerful expansion wave. Additionally, Maoling (2012) established that the air of the dust cloud can be heated up to 200-3000°C during the explosion due to the heat of combustion of the metallic dust and the kinetics of the chemical reaction. These characteristics explain why an entire facility can be affected because of this type of incidents.

Furthermore, the chemical reaction that corresponds to the oxidation process of the aluminum is shown in Equation 3.1. However, this metallic dust can promote the explosion violence by reacting with the water present in the cloud to produce hydrogen as shown in Equation 3.2. The second reaction does not occur if the alumina layer is intact and if water is not chemisorbed or physisorbed onto the oxide layer (O. Dufaud et al., 2010). Both chemical reactions are denoted as follows:

$$4Al + 3\left(O_2 + (79/21)\,N_2\right) \rightarrow 2Al_2O_3 + (79/7)\,N_2 \qquad 3.1$$

$$2Al + 3\,H_2O \rightarrow Al_2O_3 + 3\,H_2 \qquad 3.2$$

This combustion process of this metallic dust has been widely studied (Chiffoleau et al., 2006; Dreizin, 1996; Washburn et al., 2010). Nevertheless, the combustion parameters that are found in the literature for aluminum are usually incomplete because they are not reported with the respective information about the particle size distribution (Castellanos et al., 2014). The description of this variable is important because the reaction rate is clearly defined by the specific area of the dust (O. Dufaud et al., 2010; Eckhoff, 2003). For this reason, the explosibility studies of this powder are usually carried out with samples with a low size polydispersity in order to determine its burning velocity, ignition temperature, combustion and ignition time (Castellanos et al., 2014). Nevertheless, the particle size distribution of the combustible dust is submitted to significant variations that are attributed to the dust cloud dynamics, dust concentration and the initial size distribution (Wengeler & Nirschl, 2007). Additionally, the activity of this powder can be affected by the presence of impurities in the raw materials during the metal vaporization process that is performed during the manufacturing process of this solid material (Jiang et al., 2011).

Jiang et al. (2011) described the morphologies of different types of aluminum powders by performing a Scanning Electron Microscopy analysis (SEM). Their results showed the significant differences between the structures of the agglomerates of micrometric aluminum powders (75µm) and those of nanometric aluminum dusts (100 nm). Thus, the nanometric powders are spherical and their shapes are like heaped beans while the micrometric dusts are developed in several layers (Jiang et al., 2011). The structure of micrometric aluminum is shown in Figure 3.1. This difference is caused by some agglomerations formed among the aluminum powder which make it difficult to determine their average particle sizes. The scanning electron microscopy that was performed on the micrometric aluminum samples also showed the shapes of the largest particles are rather ellipsoidal than spherical. Another important characteristic of this metallic powder is its density which is equal to 2700 kg/m^3 according to several manufacturers such as Sigma-Aldrich and Goodfellow.

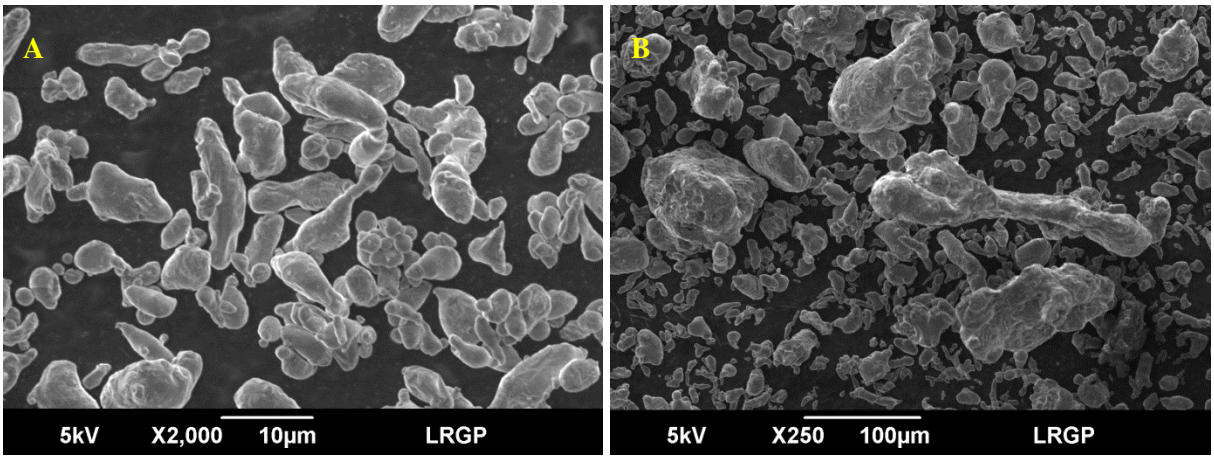

Figure 3.1. Scanning electron microscopy of micrometric aluminum
A. Aluminum micro-Al 7 B. Aluminum micro-Al 42

The water activity for aluminum was determined by Traoré et al. (2009) by evaluatng its adsorption isotherm (Figure 3.2). The results establish that the water uptake of this powder is considerably low with regard to the organic dust utilized in this study. For this reason, it can be considered that the fluidization properties are not significantly affected by the humidity of the environment.

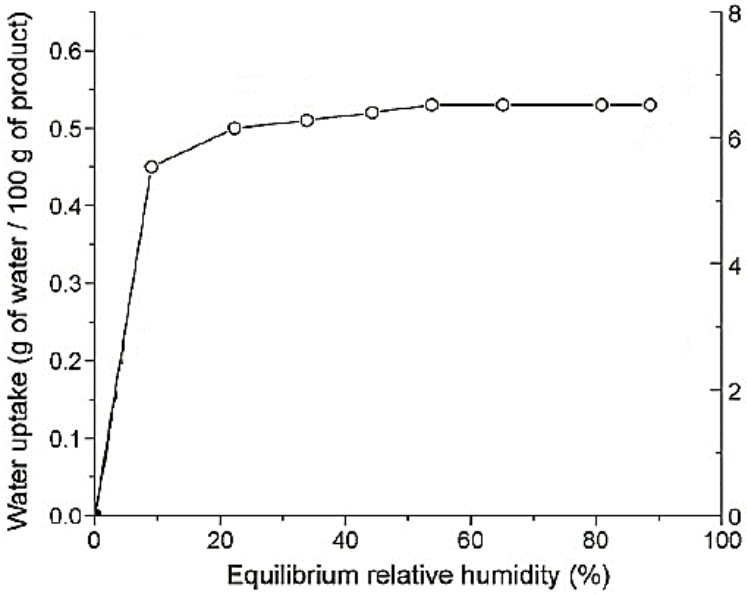

Figure 3.2. Adsorption isotherm of aluminum at 25°C
(Traoré et al., 2009)

- **Initial particle size distribution determination by sedimentation analyses**

The determination of the initial Particle Size Distribution (PSD) was envisaged for the identification of the fragmentation and agglomeration phenomena in the dispersion chambers and for the description of the disperse phase in the computational fluid dynamics simulations. This analysis was developed by taking into account the influence of the dispersion medium on the size distribution of the powders.

Some environmental aspects such as the humidity level, the presence of electrostatic forces and the regime of the fluid flow might affect the aggregation level of the disperse phase (Azema, 2006). In accordance with this statement, the solid samples were analyzed by the development of sedimentation

tests under quiescent conditions. Thus, the experimental results could be obtained with a high reliability due to the lack of high stresses on the surface of the solid agglomerates. These stresses might affect the measurement if they overcome the interaction forces that favor the solids aggregation. Moreover, the sedimentation tests were performed under low and stable humidity conditions in order to reduce the effect of this variable on the size determinations. Thereupon, the particle size distribution shown in Figure 3.3 was obtained for aluminum by performing a granulometric analysis in a sedimentation test. For this test, two aluminum samples provided by Goodfellow were dispersed in a vertical tube filled with quiescent air:

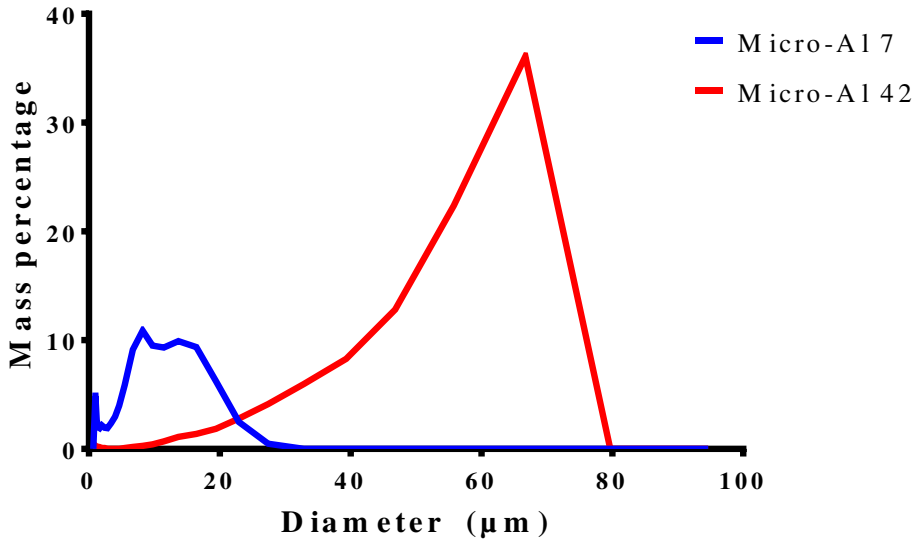

Figure 3.3 Initial particle size distribution of the micrometric aluminum samples

It should be noted that PSD measurements could have been carried out in ethanol or water for instance, but the results would not have been transposable to this study due to the effects attributed to the dispersion medium. This condition was verified by determining the particle size distributions of wet samples with a laser diffraction analyzer (Mastersizer, Malvern Instrument) and on dried samples by using a laser diffraction sensor HELOS-VARIO/KR (SYMPATEC GmbH). The main characteristics of the particle size distributions are given in Table 3.1:

Table 3.1. Main characteristics of the size distributions of the micrometric aluminum

Powder	Dispersion medium	d_{10} (µm)	d_{50} (µm)	d_{90} (µm)	$d_{3,2}$ (µm)
Micro-Al 7	Ethanol	3	7	13	3
	Dry	1	7	15	3
Micro-Al 42	Ethanol	13	42	109	27
	Dry	7	34	77	17

The size distribution that was determined for the micro-Al 42 samples on a liquid medium (ethanol) differs from the characterizations performed on quiescent air for the large micrometric agglomerates. On the contrary, the micro-Al 7 particles do not pose a significant difference between the two methods. These conditions can be explained after considering that the fragmentation levels that can be achieved by both samples in the dispersion media. The small agglomerates have been previously sieved to a particle size that is close to their fragmentation levels in the liquid suspension; hence they will not be significantly affected by the stresses exerted by the fluid.

3.1.2 Wheat starch

Starch is a combustible dust which is well-known as a raw material for several industrial applications. For instance, the sweeteners industry considers the acid hydrolysis of starch as one of the main steps of the industrial production of glucose syrups. Moreover, the utility of this material has been enhanced by the development of significant advances in the enzyme technology which provided higher purities and more applications for the industrial syrups (BeMiller and Whistler, 2009). This chemical compound is also characterized for its versatility in some areas related to the synthesis of polyols, amino acids and organic acids as well. The availability of this organic compound comes from different sources. The production of the different varieties of this substance can be established from flours that are obtained from wheat, corn, potato and other plantations developed recently such as the cull banana and the amaranth (BeMiller & Whistler, 2009).

One of the main hazards that concern the design and operation of starch facilities relies on the coating of starch dust on the floor and the equipment located in the packaging and grinding units. This fact represents an important aspect for the staff in charge of the risk management of these plants because the haze areas that are generated by the confined dust clouds represent an explosion hazard. This issue is more significant if the dust is dispersed in units such as cyclones or hoppers. For these reasons, the ATEX classification standard and the normativity established by the NFPA are the main instructions for procedures related to the facility housekeeping and the material storage. The chemical reaction that corresponds to the combustion process of this organic powder in lean mixtures is shown in Equation 3.3:

$$\left(C_6H_{10}O_5\right)_n + 6O_2 \rightarrow n\left(6CO_2 + 5H_2O\right) \qquad 3.3$$

Wheat starch has been considered to be one of the combustible dusts used for the case study of this thesis because its explosibility parameters are well-known and has some important dispersibility characteristics that have been widely discussed. These conditions promoted the analysis of reproducibility and accuracy of the tests performed. According to this procedure proposed for the characterization tests, the dust samples that were used in the descriptive tests performed during this research project were provided by Sigma-Aldrich. Figure 3.4 shows the agglomeration degrees of the oval primary particles of this organic powder. The aggregation phenomenon is evidenced due to the strong adhesion forces of this combustible dust.

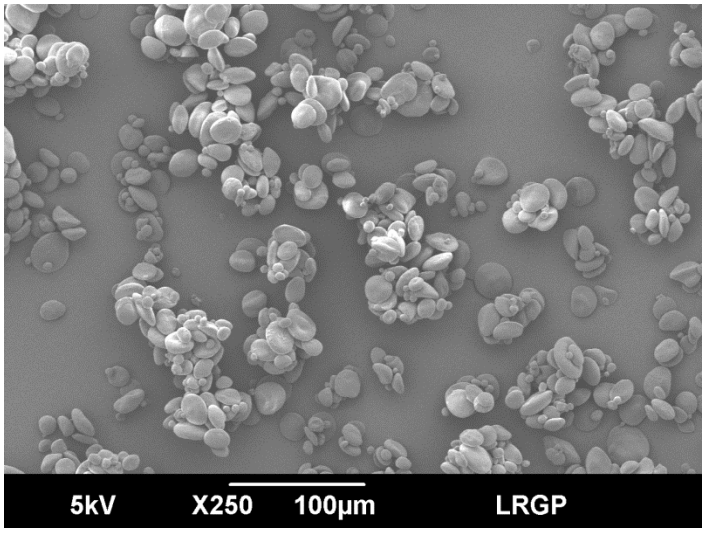

Figure 3.4. Scanning electron microscopy of micrometric wheat starch

The particle size distribution was determined experimentally with the same methodology that was proposed for the aluminium dust after taking into account the moisture content reported by the

manufacturer (Sigma-Aldrich): 8.8 - 11.5 %. The results that were obtained with a granulometric analysis performed with a sedimentation test are shown in Table 3.2 and Figure 3.5:

Table 3.2. Technical data sheet of wheat starch

Powder	Dispersion medium	d_{10} (µm)	d_{50} (µm)	d_{90} (µm)	$d_{3,2}$ (µm)
Micrometric wheat starch	Dry	28.16	65.20	83.05	24.51

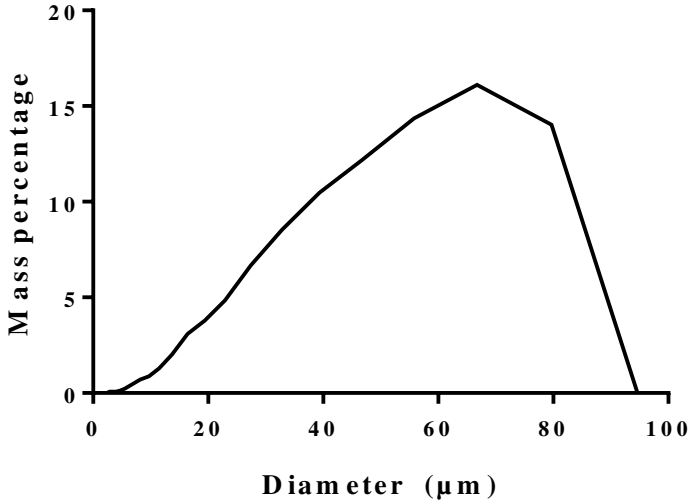

Figure 3.5. Initial particle size distribution of the micrometric wheat starch samples

The dust samples were not dried due to their high higroscopicity. It was clearly evidenced that the weight gain of the powders was established at times inferior to the development of a flammability test. Therefore, the dust samples were utilized without performing a preliminary sampling procedure. The characterization of the hygroscopic behavior of this different types of wheat starch has been determined experimentally by Olayemi et al. (2008). The experimental results obtained in this comparative study are summarized in Table 3.3. The remarkable difference of the varieties of powder was observed through the photomicrographic analyses, which evidenced that the wheat starch has the largest size distribution and its grains are ovoid. These characteristics favor the acquisition of high moisture contents because a larger average grain size of a sample implies there are larger pore sizes in it and an irregular shape promotes a separate packing. For these reasons, the humidity level in the starch samples and their particle size distribution were considered as some of the most important aspects of the subsequent descriptive tests. The hygroscopic behavior of this organic powder represents a significant variation of the particle density. For this reason, the density of the dust samples used in this study was determined prior to the development of the fluidization tests.

Table 3.3. Physicochemical properties of wheat starch (Olayemi et al., 2008)

PARAMETER	MAIZE STARCH	RICE STARCH	WHEAT STARCH	METHOD
Shape	Round	Polygonal	Oval	Photomicrographic analyses at X40 magnification
Moisture content (%)	4	6	12	Gravimetric analysis by water evaporation
Moisture sorption capacity (%)	4.87	1.86	2.55	Weight gained by 2g of starch located in a desiccator containing distilled water at room temperature

The true density of the solid's particle was determined by using a gas displacement pycnometry system. An AccuPyc II 1330 Pycnometer was used to measure this parameter and the inert gas used to perform the purge and filling processes was helium due to its very low reactivity and the small size of He atoms, which makes them capable of filling the internal pores of the solid particles. The sample was placed inside a chamber that was filled with gas injected at 22 psi and then it was emptied in order to purge it and calculate the true density of the powder. Finally, the particle true density was calculated after 12 tests with a mean value of 1401.0 kg/m^3 and a standard deviation of 1.8 kg/m^3. Moreover, Sujka & Jamroz (2010) performed a set of mercury porosity measurements to determine the volume of the pores in several wheat starch samples that were obtained from different sources. Then, the results of their experiments reported the porosity of the wheat starch granules as 56.16%. This value was considered to establish the value of the density of the porous particles which is 614.88 kg/m^3.

The influence of the humidity level on the particle density was also discussed by Stasiak et al., (2013). These authors analyzed the variations of this variable which can be linked directly to the compressibility of the powder. The results of their experimental work showed how an increase in the solid's moisture content represents a decrease of the particle density and an augmentation of the material's compressibility (Stasiak et al., 2013). For this reason, the authors also affirmed that some variations in the rigidity of these materials might be considered when the solid's humidity changes in a significant way. Table 3.4 presents the values a comparison between the experimental determination of the solid's density and the values reported by Stasiak et al. (2013). The dissimilarity corresponds to the differences found in the particle size distributions of the samples. This author characterized powder samples whose diameters d_{50} were 12.3 µm for a humidity level of 20% and 13.3 µm for a humidity level of 6%. On the contrary, the samples characterized for this thesis had a diameter d_{50} equal to 65.2 µm because they were not sieved previously. This fact implies a better organization of the small solid particles; hence their density is greater than the samples analyzed in this study.

Table 3.4. Comparison of the density values determined experimentally with the values reported in the literature for micrometric wheat starch

BULK SOLID	PARTICLE TRUE DENSITY (kg/m^3)
Wheat starch sample (11.5%)	615
Wheat starch (6%) (Stasiak et al., 2013)	849
Wheat starch (20%) (Stasiak et al., 2013)	621

The conclusions obtained during the previous studies and analyses of the physical properties of the combustible dust confirmed the importance of performing the subsequent experiments in an environment with low humidity fluctuations. Additionally, the experimental protocols were defined to reduce this uncertainty factor, which is inherent to the characteristics of the material, by providing enough contact time between the dust samples and the environment in order to reach similar levels in the moisture content of combustible solid.

3.1.3 Adjustment of the particle size distribution to the Rosin-Rammler equation

These particle size distributions that were determined experimentally for the combustible dusts of this study were adjusted to the Rosin-Rammler distribution. This equation represents this physical property of the powder as a continuous function thanks to two adjusted parameters:

$$Y_d = \exp\left[(-d_p / \bar{d})^{n_{sd}} \right] \quad 3.4$$

where Y_d is the mass fraction of solids larger than the diameter d_p, $\bar{d}$ is the size constant and n_{sd} is the size distribution parameter. This size distribution, also known as Weibull's distribution, has been a useful model for particle size characterization (Peleg, 1996). Moreover, this expression poses an important advantage that establishes that their parameters can be adjusted by graphical methods and from some basic information about the size distribution of the solid sample such as the mode and variance. The parameters of this expression obtained for the particles tested are shown in Table 3.5:

Table 3.5. Parameters of the Rosin-Rammler size distribution for the analyzed combustible dusts.

COMBUSTIBLE DUST	SIZE CONSTANT (µm)	SIZE DISTRIBUTION PARAMETER	MEAN ERROR (%)
Wheat starch	71.80	4.734	10.2
Aluminum micro-Al 42	64.91	3.489	8.3

Additionally, the Geldart classification of the samples of the combustible dusts was determined to establish their fluidization behavior in the modified Hartmann tube, which is the apparatus that considers the lowest injection pressures. This characteristic is defined by the density of the two phases and the PSD of the fluidized solid material. Yang (2007) proposed a classification scheme based on the Archimedes number (*Ar*). This number is shown in Equation 3.5 where d_p is the particle diameter, g is the gravity acceleration term, μ is the molecular gas viscosity and ρ_p and ρ are the density of the powder and the density of the gas respectively. The densities of the combustible dusts that were reported in Section 3.1 were considered for this classification.

$$Ar = \frac{d_p^3 \rho \left(\rho_p - \rho \right) g}{\mu^2} \quad 3.5$$

$$DD = \frac{\rho_p - \rho}{\rho} \quad 3.6$$

On the one hand, the micrometric wheat starch can be analyzed with a dimensionless density (*DD*) that varies between 72 at the beginning of injection and 506 (atmospheric pressure). On the other hand, this variable ranges from 322 to 2241 for the aluminum. Nevertheless, both combustible dusts can be classified under the same category. Table 3.6 shows an Archimedes number with values under 100 for the combustible dusts. These results show that the largest aggregates have a fluidization behavior similar to a powder of type A in a Geldart classification (easy fluidization). Nevertheless, the smallest particles might be in a transition zone to the C type which is susceptible to cohesive interaction mechanisms.

This condition will be become a determining factor of the dispersibility of combustible dusts that are submitted to a fragmentation phenomenon in the particle-laden flow generated by the pressurized gas in the explosion chambers. For this reason, it is possible that the regions marked in Figure 3.6 will be displaced to the left due to the size reduction of the dispersed agglomerates.

Table 3.6. Archimedes number of the combustible dusts

Cumulative mass fraction	Aluminum		Wheat starch	
	Diameter (µm)	Archimedes number	Diameter (µm)	Archimedes number
0.10	26.63	2.8	28.16	3.3
0.16	33.18	5.4	36.95	7.5
0.50	57.41	28.1	65.20	41.2
0.84	76.75	67.2	80.69	78.1
0.90	80.60	77.8	83.05	85.2
0.99	86.36	95.8	86.61	96.6

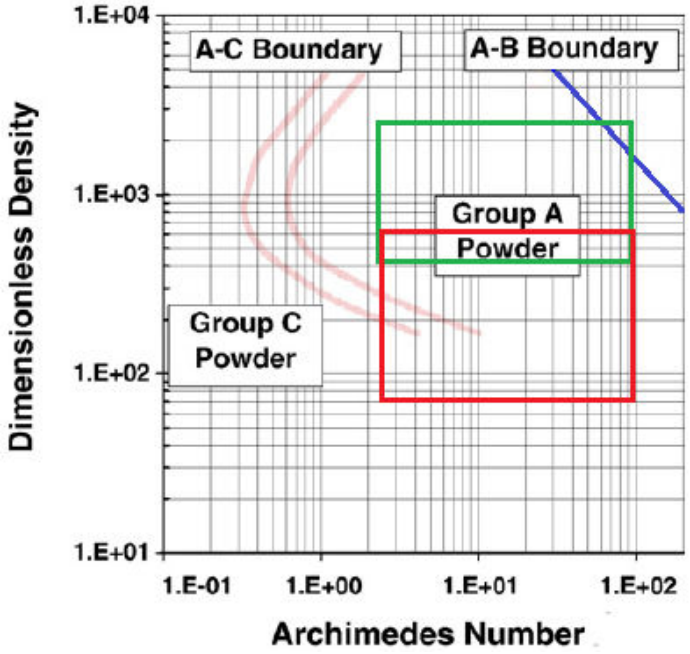

Figure 3.6. Geldart classification of the aluminum and the micrometric wheat starch according to their initial PSD
(Yang, 2007)
Green region: Aluminum micro-Al 42 – Red region: Wheat starch

3.2 GRANULOMETRIC ANALYSES

The particle size distributions of different particulate matter have been increasingly determined by diffraction pattern analyses (Heuer & Leschonski, 1985). This technique is commonly used to measure the size of an individual particle, an average size, or the size distribution by establishing the scatter of an incident beam into a certain angle of space. Hence, this technique is characterized by providing reproducible results very quickly.

Optical particle counters have been widely used for particle classification due to their advantageous characteristics such as the high size resolution and speed in counting and measuring distributions of particles in suspensions (Sommer et al., 1992). The light scattering techniques can be defined according to the Mie scattering theory or the Fraunhofer diffraction theory. The first method demands a correspondence relationship between particle size and light intensity distribution pattern to determine

the particle size distribution. On the contrary, the second method is an approximate approach since it does not require calibration data. Thus, its validity is submitted to the size of the dispersed dust.

Nai-Ning et al., (1992) discussed how broad the size range covered by the Fraunhofer diffraction theory is. This analysis is suitable for tests with particles ranging from sub-microns to thousands of microns. This range covers most of the practical needs in different applications. Nevertheless, the Fraunhofer theory is applicable only when the particle size is much larger than the wavelength of the incident beam (Nai-Ning et al., 1992). For this reason, this variable was checked in order to verify the validity of the model. The value set for this technical specification corresponds to 632 nm whereas the size of the finest dispersed particles is considerably larger (Al: 4.2 µm – Wheat starch: 9.0 µm approx.). Therefore, this model is suitable for the analysis of dust clouds formed with these particles but an analysis of nanometric dusts should consider the Mie scattering theory.

The Fraunhofer diffraction theory assumes that the particles dispersed in the dust cloud possess a random and ideal movement. These facts allow establishing that the laser scattering is proportional to the particle size. This model is well-known for its capability to describe forward light scattering by opaque particles at a large distance compared to the size of the particle. Thus, a direct relation between the projection images and the corresponding diffraction patterns can be found without additional information about the physical properties of the particle and the dispersion medium is needed for the data interpretation (Ulrich et al., 2010).

Experimental apparatus

The experimental apparatus used for the laser diffraction analyses is the Granulometer HELOS/KR (Sympatec^{TM}). This instrument has been standardized for particle size analysis of dry and wet samples (powders, suspensions, emulsions or sprays) according to the specifications of ISO 13320 "*Particle size analysis - laser diffraction methods*". This equipment possesses an optic system which is composed by a laser emission and detection device. The characterization of particle size distributions can be performed by laser scattering with 32 different detectors located in a circular arrangement. The incident beam is generated by a 5mW Helium-Neon source that can be adapted with different sizes (2mm – 13 mm). The system has several Fourier lenses that provide a high precision and accuracy in measurements for a specific size range. Some additional technical specifications of the granulometer HELOS/KR of the equipment are shown in Table 3.7:

Table 3.7. Technical specifications of the Granulometer HELOS/KR

CHARACTERISTIC	SPECIFICATION	ADDITIONAL INFORMATION
Sensor	HELOS/KR	Range: 0.1 µm - 8750 µm
Principle	Laser diffraction	λ = 632.8 nm
Dispersion	Adaptable modules	Aerodispersion, sprays, suspensions, emulsions
Measurement	Multi-element detector frequency	31 semi-circular elements 2000/s, permanent autofocus
Evaluation	Fraunhofer Enhanced Evaluation (FREE)	Mie Extended Evaluation MIEE as an option
Ranges	Optical modules	R1: 100 nm – 35.0 µm R3 : 500 nm – 175.0 µm
Performance	Accuracy Repeatability Comparability x10, x50, x90	σ < 2% mean rel. SD to absolute value σ < 0.04% typical (repeated sample) σ < 0.3% typical (riffled sample) s < 1%mean rel. SD |Δx| < 2.5% rel max. deviation
Applications	Laser power Beam diameter	5 mW R1: 2.2 mm - R3: 13 mm

Figure 3.7 describes the experimental arrangement that was considered for the granulometric analyses. The dispersion chambers of the apparatuses are located between the sensor and the detection unit. Then, the two-phase flow is induced according to the operating parameters of the tests and passes through the optical measurement volume. Afterwards, the particles dispersed in the dust cloud will scatter the light in various directions. The scattered light is captured by the extinction photodetector and recorded as an intensity defect on the beam. This fact occurs because the fraction of the light that is scattered in the direction of the collection optics is focused on the scattering photo detector. (Sommer et al., 1992).

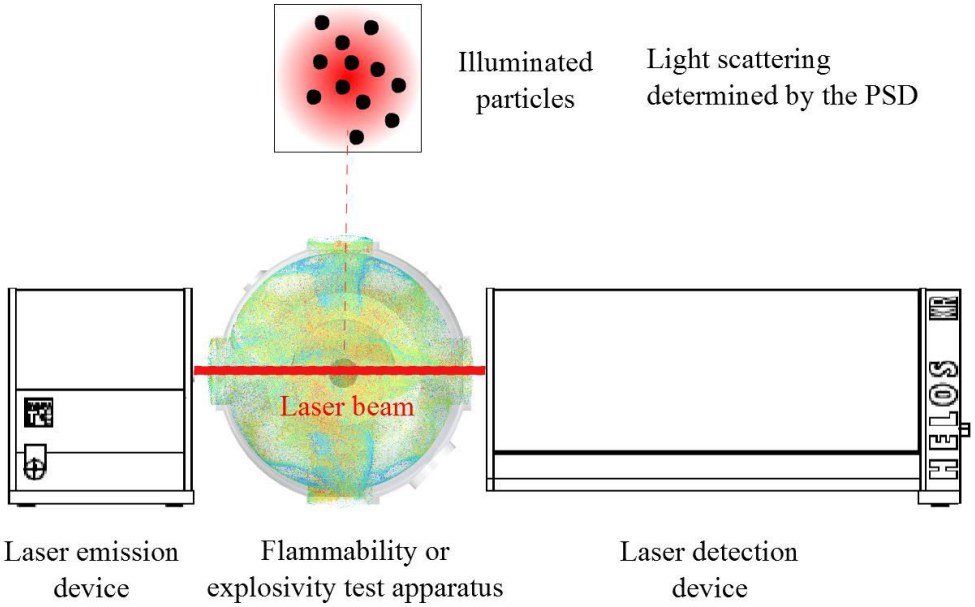

Figure 3.7. Experimental arrangement of the granulometric analyses

The laser has been located at the same height than the ignition sources in order to establish the variations of the size distribution of a dust during the dispersion process. The methodology used to develop a randomized two-phase flow characterization includes different steps associated with setting up the equipment and the placement of material:

A. Equipment cleaning: Cleaning is performed in the glassy walls of the equipment to remove particles located by the previous tests or the environmental conditions. This procedure involves a rinse with a concentrated solution of ethanol and the placement of a film by spraying a liquid. This procedure prevents the particles adhesion on the walls due to static charges.

B. Material preparation: Placement of a sample of the combustible dust at the bottom of the modified Hartmann tube or the canister of the 20 L sphere. Subsequently, the equipment's software is adjusted to specify the parameters required by the granulometer such as the particle true density and its shape factor.

C. Parameter settings of granulometric system: The data collection can be manipulated with the software WINDOX 5^{TM} (Sympatec). It is possible, for instance, to adjust the equipment to record data between a period that begins 50 ms before the detection of an optical concentration of 2% and 50 ms later. The results presented correspond to time averaged values of measurements performed every millisecond. These averages are calculated for time intervals that are determined according to the characteristics of the dust cloud. For the tests developed in this study, the averaging interval is 5 ms.

Additionally, it is necessary to adjust the lens before the test to ensure its proper targeting. If there is no contingency that hinders the collection of samples, a reference measurement can be taken.

D. Reference measurement: Determination of the background signal that will be subtracted from the measured signal. This step is developed to determine accurately the optical concentration of the dilute dispersions by neglecting the particles that are stuck onto the glass walls.

E. Adjustment of the injection system: A check is performed on the system that generates the gas pulse in order to verify the pressure in the line and the deactivation of the ignition sources.

F. Gas Injection and data analysis: After activating the granulometer and the injection system simultaneously, a data analysis is developed to identify the evolution of particle size distribution.

3.3 DIGITAL PARTICLE IMAGE VELOCIMETRY (DPIV)

Particle image velocimetry (PIV) is an experimental technique that was conceived for non-intrusive qualitative and quantitative flow visualizations (Thielicke, 2014). This analysis is one of the most common optical techniques that have been developed in the last three decades for flow visualization. Thus, the scope of PIV is similar to the scope of other techniques such as Laser Doppler Velocimetry (LDV), which was considered by Dahoe et al. (2001) to characterize the initial turbulence in the 20 L sphere. Moreover, several derivatives have also been developed for the Particle Image Velocimetry (PIV). The list of derivatives includes Laser Speckle Velocimetry (LSV), Holographic Particle Image Velocimetry (HPIV), Digital Particle Image Velocimetry (DPIV) and Particle Image Velocimetry 3D (PIV3D), among others (Soares et al., 2013).

This method is based on the principle of particle tracking performed by laser scattering. Moreover it has been applied for velocity measurement in both single and multi-phase flows. In such analysis, a fluid flow is described by illuminating a plane within the flow domain that contains a group of reflective and neutrally buoyant tracer particles. In general, DPIV is widely adopted for flow characterizations because its scope achieves a similar purpose that is usually considered for other techniques such as phase Doppler anemometry and laser Doppler velocimetry (Giuliani et al., 2008). For this reason, these alternatives have shown a satisfactory agreement in determinations of velocity fields (Pedersen et al., 2003). Furthermore, Brossard et al. (2009) pose that the major asset of the PIV technique is its capacity to deliver a quantitative and instantaneous measurement of the velocity not only at one point, like Laser Doppler Velocimetry, but over a whole plane simultaneously.

One of the most important requirements of the DPIV analyses relies on the illumination of the flow field. Indeed, the particles have to be illuminated at least with two light pulses within a short time interval in order to determine the fluid velocity field from the positions of the particles. Evidently, the time delay between the pulses must be adjusted according to the magnification of the imaging process and the mean flow velocity. Figure 3.8 shows a descriptive scheme of the experimental setup that was considered for the DPIV analyses of the flammability tests:

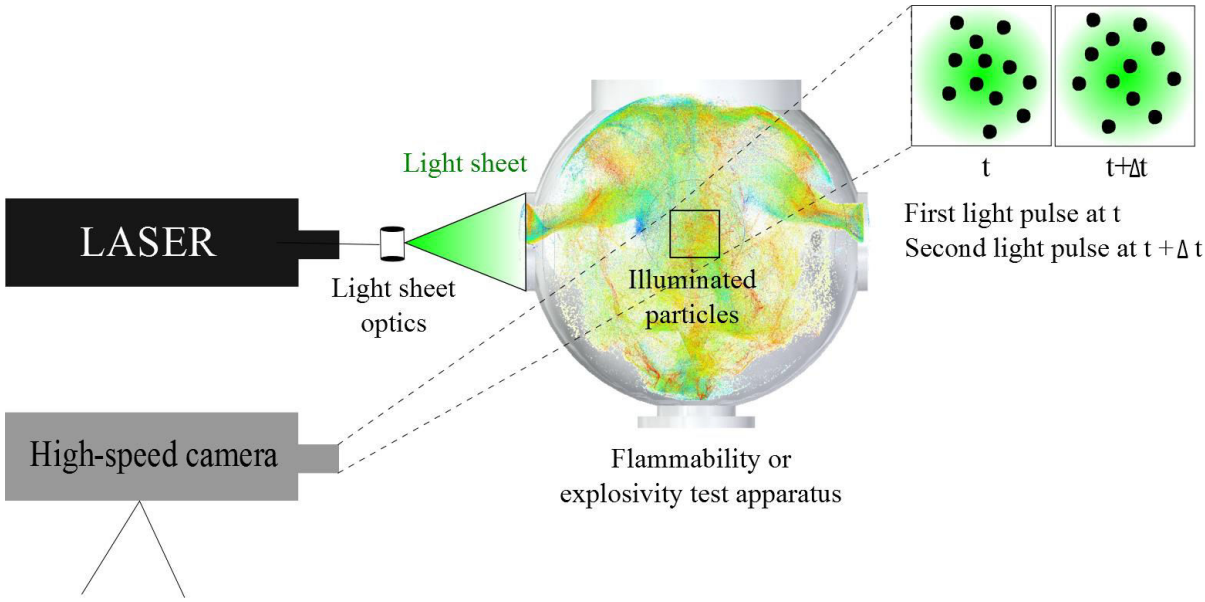

Figure 3.8. Experimental arrangement for a digital particle image velocimetry analysis

The DPIV analysis can be divided in two steps. Initially, the flow is seeded with the tracer particles and the region of interest is illuminated by a laser light whose intensity is adapted according to the conditions for the flow environment. Then, a set of images is captured by video or photographic means. Subsequently, a second step is developed by performing the corresponding numerical study of the image record. For this step it is necessary to include an analysis system, which consists of a reading optics, a computer and the analysis software (Stanislas et al., 2000). The two steps can be decoupled during the experimental procedure in order to determine the most suitable combination of test parameters and analytical methods for every step.

3.3.1 Continuous wave laser

The illumination of the region of interest of the DPIV analyses was performed with a high power laser. The brilliance of the recorded images is adjusted by transforming a parallel light into a thin sheet in a specific position of the flow domain. For the experimental tests of this study, a diode pumped solid state laser (DPSS) has been chose due to its very compact size and its high efficiency (Thielicke, 2014). This laser is a Neodym-Yttrium-Aluminum-Garnet (Nd:YAG) whose laser beam has a wavelength of 532 nm.

The classification of DPSS lasers poses two different types according to their operating mode. At first, the pulsed lasers achieve very high peaks during short pulses and make it possible to reduce the exposure time of the camera. On the other hand, the continuous wave lasers (CW) require a longer exposure to meet light intensity requirements. This characteristic of the second type can lead to excessive motion and blur (Thielicke, 2014). Nevertheless, the CW lasers need a less complicated set-up because there is no need to synchronize the high-speed camera with the laser pulses. Thus, fewer repetitions would be required for the flow characterization. For these reasons, a CW laser has been considered for the DPIV analyses instead of a pulsed laser.

The CW laser that was used for the experimental tests considered for the flow visualization is a RayPower 2000 (DANTEC DYNAMICS). The technical specifications of this equipment are listed in Table 3.8:

Table 3.8. Technical specifications of the continuous wave laser

PARAMETER	SPECIFICATION
Wavelength	532 nm ± 1 nm
Output power	>2000 mW
Operating mode	CW
Beam diameter at the aperture	~3.0 mm
Mains supply	100-240VAC 3A max, 50-60 Hz

3.3.2 Tracer particles

A. Tracer particles & dispersion fluid

One of the most representative characteristics of the DPIV relies on the nonintrusive character of the measurements. For this reason, it is necessary to take into account the accuracy of the representation of the fluid motion that is obtained by tracking the disperse particles and the drawbacks that come from the inclusion of an additional powder. Hence, the tracer particles used for the DPIV analyses were the wheat starch particles. This combustible dust represented several advantages for the acquisition and analysis of the recorded images due to its color and size distribution, which enhanced the contrast of the analyzed images.

Previously, the influence of the particle size was discussed by (Thielicke, 2014) who performed a set of DPIV measurements in water at 20°C by using polyamide particles whose density and diameter are 1140 kg/m^3 and 57 µm respectively. This author recommended the development of the measurement tests with solids with a density similar to the fluid's density. A similar conclusion was posed by (Giuliani et al., 2008) who characterized a laser deposition system in a gas flow by using iron particles of 44 µm (mesh 325). Additionally, Diez et al. (2011) evidenced a significant variation in the profiles developed by fresh water jets after injecting a mass particle load of 2.0%. The centerlines of the liquid jets were modified due to the interaction between the fluid flow and the solid particles. Their results agreed with the conclusions posed by Crowe (2000) who affirmed that the small particles tend to attenuate the turbulence of the fluid whereas the large particles increase it. However, this influence is determined by the ratio of the turbulence length scale and the particle diameter; hence nanometric dusts do not represent significant variations in macroscopic turbulent flows.

The influence of the fluid-particle interactions on the determination of the velocity fluctuations of the gas flow was considered according to the approach proposed by Raffel (2007). The slip velocity (u_s) caused by the different velocities of the two phases that constitute the dust cloud can be derived from the Stoke's drag law:

$$u_s = u_p - u = d_p^2 \frac{\left(\rho_p - \rho\right)}{18\mu} a = \tau_s a \qquad 3.7$$

where d_p is the particle diameter, μ is the fluid dynamic viscosity (1.82.10^{-5} Pa·s at 20°C and 1 atm), ρ_p is the particle density (615 kg/m^3), ρ is the fluid density (1.204 kg/m^3 at 20°C and 1 atm), u is the fluid's velocity, u_p is the solid's velocity and a is the acceleration term. The step response of u_p should follow an exponential law for the combustible dust cloud because the density of the tracer particles is much greater than the density of the gas:

$$u_p = u\left[1-\exp\left(-t\frac{18\mu}{\rho_p d_p^2}\right)\right] = u\left[1-\exp\left(-\frac{t}{\tau_s}\right)\right] \qquad 3.8$$

Then, the velocity can be established from the physical properties of the combustible dust and the air at 20°C and 1 atm. The relaxation time (τ_s), which multiplies the acceleration term in Equation 3.7, was calculated for micrometric wheat starch with the diameter d_{50} (65.2 µm) in order to estimate the lag between the velocities of the two phases. The value obtained for this factor with the Stoke's drag law was $7.98.10^{-3}$ s. In the same way, this parameter was also determined for the aluminum dust with a value of $9.53.10^{-3}$ s. The acceleration is not constant during the dispersion process. Nevertheless, the relaxation time remains a convenient measure of the particles to attain velocity equilibrium with the fluid (Raffel, 2007). Therefore, a greater lag can be expected with the utilization of the metallic dust.

This fact becomes an important aspect for the analysis of the explosibility tests. During the first 5 ms, the particles acceleration constitutes an important lag due to the high pressure gradients that are generated between the pressurized canisters and the explosion chambers. However, the injection of a finite amount of gas in the apparatuses and the energy dissipation establish a low velocity lag after the first 10 ms of dispersion.

B. Light scattering in tracer particles

Raffel (2007) discussed how the contrast of the DPIV recordings is directly proportional to the scattered light power. For this reason, the laser power and the exposure of the video camera were set to achieve a sufficient contrast level in the interrogation area. Nevertheless, the light scattering of the laser beam is affected by several properties of the combustible dust such as their sizes, shapes and orientation.

The analysis of the particle size distribution was taken into account for the image analysis after considering the variations in the light scattering intensity. These changes constituted an important aspect during the experimental characterization of the dispersion process of the combustible dust. This fact is due to the significant differences in the inertial effects and the drag force exerted on every particle surface. Hence, the particle size distribution plays an important role on the intensity of the image quality. Figure 3.9 shows two different images that were analyzed for the description of the wheat starch dispersion inside the 20 L sphere. These two images correspond to two different flow regimes that were observed for the dust cloud during the image recording. At first, Figure 3.9A shows the tracked particles with dissimilar intensities during the rising of the bulk of the dust cloud. This image evidences the how large particles have a higher velocity by posing a significant separation among them. Moreover, these tracers could be identified more easily during the initial stage of dust dispersion while the smallest ones are hazy or blurry. This issue was resolved by implementing certain basic algorithms that improved considerably the quality of the first images.

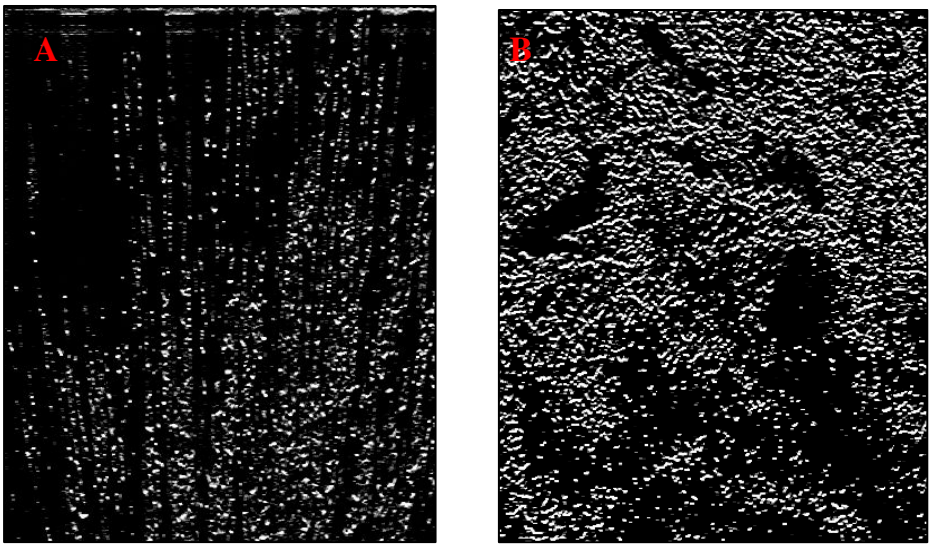

Figure 3.9. Wheat starch dispersion in the 20 L sphere
A) 1 ms B) 250 ms

On the other hand, the images of the latest stages (Figure 3.9B) of dust dispersion have better contrasts between the particles and the fluid. This feature is caused by the lower velocities and the agglomeration phenomena of the disperse phase. Furthermore, an advantageous characteristic of the system relies on the dispersion fluid. Since the refractive index of the air is approximately one, the light scattering is only attributed to the light scattering generated by the dispersed combustible dust.

3.3.3 Image analysis

The issues that were observed in the images recorded during the first stages of the dust dispersion were resolved by applying a set of pre-processing techniques. These procedures were implemented in order to enhance the contrast between the particles and the image background and the measurement quality. The numerical algorithms associated to these techniques are implemented as an open source code which is supported on a Matlab toolbox.

PIVLAB 1.35 was developed by Thielicke (2014) as a tool conceived for the DPIV analyses. For this purpose, the tool is set to perform the image pre-conditioning, interpolation algorithms, smoothing methods and data validation. Previous studies have shown a good agreement between the results of DPIV analyses performed on gas-fluidized beds with PIVLAB and the results of other reliable measurement techniques such as Positron emission particle tracking (PEPT) or radioactive particle tracking (RPT) (Tebianian et al., 2015). Thus, some improvement techniques were considered to improve the quality of the images recorded for the dust cloud. These algorithms are briefly described in Appendix A:

- Contrast limited adaptive histogram equalization (CLAHE).
- Intensity capping
- Noise filter

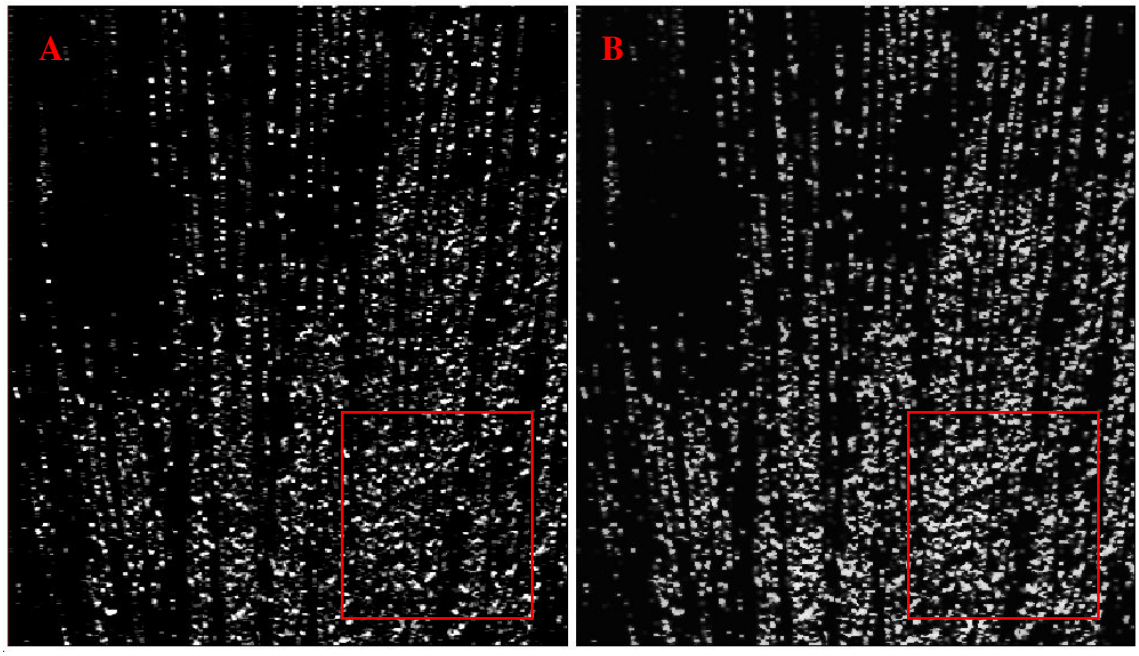

Figure 3.10. Comparison of between an original and a modified image of starch dispersion
A) Original image of wheat starch B) Image with filters (CLAHE, capping and noise filter)

Figure 3.10 presents a direct comparison of an image recorded for the dispersion of wheat starch inside the 20 L sphere with an image modified with the filters developed by Thielicke (2014). The improvement of the image quality has provided a better contrast for the small particles. These modifications have increased significantly the density of detectable particles, which are necessary to obtain a more accurate description of the velocity field. These modifications enhanced the image analysis, which is also limited by the weight of the starch sample. In accordance with this statement, the experimental results were determined with a nominal concentration of 30 g/m^3 (50% of the minimum explosive concentration).

A. Image acquisition and time span

During a DPIV analysis, each image is divided into a grid of overlapping interrogation spots. Every spot inside a specific cell of the grid is interrogated to determine the mean displacement of the particles located within the interrogation cell. This cell corresponds to the intersection of the interrogation spot area and the thickness of the laser sheet (Adrian, 2005). The size of each interrogation area must be determined according to the restrictions posed by the particle image density. (Tebianian et al., 2015) recommended a minimum value for this parameter, which establishes that there should be at least 4 particles in each interrogation area in order to obtain a reliable displacement rate. On the contrary, a huge size of the grid can be associated to an increase of the unsuccessful correlations because all the DPIV algorithms cannot accept more than 20 particles per interrogation area (Huang et al, 1997; Thielicke, 2014). Further details about the setting parameters of the PIV analyses will be specified in Sections 3.5.2B and 3.6.4B.

Another important aspect for the characterization of the dust cloud through a DPIV technique lies on the number of images that were recorded to describe the dust dispersion process. The resolution of the images is adapted according to the framerate of the video. Moreover, the two-phase flows developed in the dispersion chambers of the flammability tests considered in this thesis can reach sonic velocities during the injection of the gas. This fact is attributed to the high pressure difference between the compressed fluid contained in the storage vessels and the dispersion chambers.

B. Image evaluation

The statistical methods considered for a typical determination of the velocity field of a fluid flow are based on the numerical estimation of a correlation matrix, which determines the most probable displacement of a group of particles. The comparative analysis of every numerical approach is performed by solving Equation 3.9 (H. Huang et al., 1997):

$$C(m,n) = \sum_{i}\sum_{j} A(i,j)B(i-m,j-n) \qquad 3.9$$

The position of the intensity peak of the correlation matrix (C) determines the most probable displacement of the particles located within the interrogation areas of the images A and B. For this purpose, all the pixels are assessed in these images divided in regions of size $m \times n$.The two approaches that determine the flow patterns of the dust particles are described below:

- **Direct cross-correlation (DCC):** This method computes the correlation matrix in the spatial domain by comparing two interrogation areas obtained from two consecutive frames. Indeed, the cross-correlation of the pair of exposed recordings determines the displacement correlation from a set of random variables associated to the position of the particles. For this purpose, the intensity fields are correlated for the two images in order to identify their peaks, whose coordinates establish the mean displacement of the flow pattern (Raffel, 2007).

  The size of the interrogation area of the second image must be adapted according the size of the first one and the expected displacement. This fact will provide a reliable correlation based on a low presence of background noise (Thielicke, 2014). The main drawback of this approach relies on its computational cost, which usually limits the application of this method in case studies that require a great detail for the image evaluation.

- **Discrete Fourier Transform (DFT):** This method is based on the capability of a far field diffraction pattern of an aperture transmissivity distribution to be represented by its Fourier transform (Buchhave, 1992). This approach can be implemented through a single or multiple pass analysis.

  The single pass DFT considers interrogation areas with the same size to identify the variations in the intensity of the compared frames. Additionally, this simple approach considers a uniform motion of the particles in the region interrogated (Raffel, 2007). This fact widens the peak estimated during the calculation. Therefore, a lower computational cost is accomplished at expense of a loss of information.

  On the other hand, a multiple pass DFT solves these issues by performing a spline interpolation among several interrogation areas of different sizes. Moreover, the first pass determines the displacement of the particles at the center of every interrogation area. This condition provides more information about the displacement in the borders and the corners of the analyzed area. Afterwards, the interrogation area of the image B is deformed according to the first displacement estimation. Then, a subsequent pass repeats this procedure in order to achieve a higher precision for the velocity field (Thielicke, 2014).

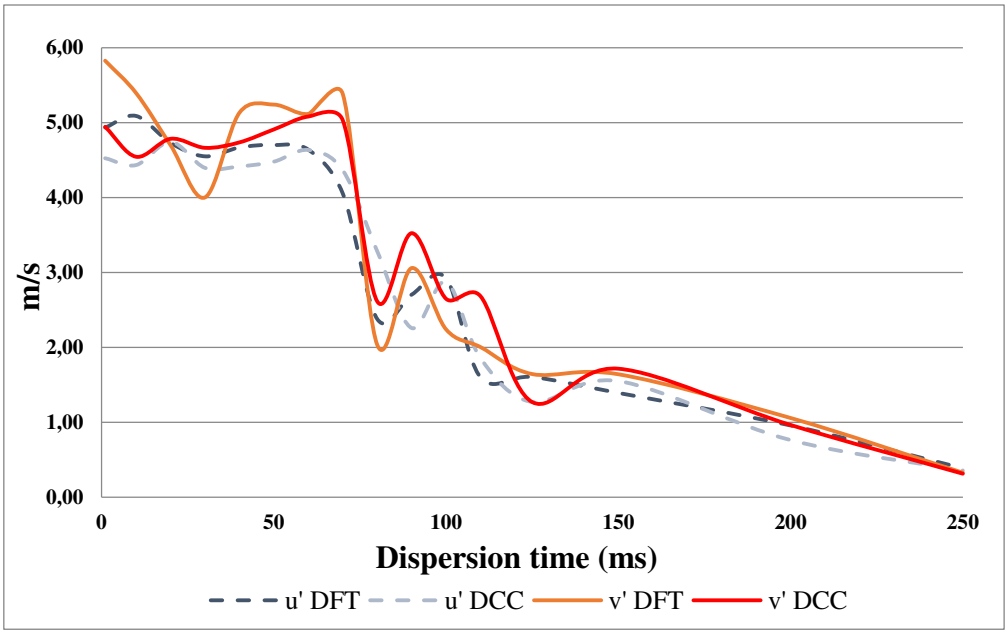

Figure 3.11. Comparison of the velocity fluctuations estimated with the DCC method and the multi-pass DFT

The selection of the statistical method was accomplished after comparing the numerical results obtained for a test of wheat starch dispersion in the 20 L sphere that was induced by an air injection at 20 bars. Figure 3.11 presents a comparison of the gas flow fluctuations determined by a DCC and a multiple pass DFT method. The results pose a similar tendency for the two numerical methods. Nevertheless, the second approach represents a technical advantage because it allows considering different sizes for the interrogation areas. This characteristic represents a better adaptability for the initial stages of dust dispersion. For these reasons, the Discrete Fourier transform was chosen for the latter DPIV tests.

The characterization of turbulence of the gas flow was performed by establishing the mean velocity and the mean fluctuations on the regions of the test apparatuses. These analyses envisaged the regions where dust clouds are ignited. These obtained data were associated to the flow turbulence through the determination of the turbulent intensity or the root-mean-square velocity (v_{rms}). Further details about the analysis of the flow turbulence are provided in Sections 3.5.2C and 3.6.4B.

3.4 DETERMINATION OF THE CHARACTERISTICS OF THE PRESSURIZED GAS INJECTION

The computational approach defined for the two flammability tests analyzed in this thesis is based on two different descriptions of the flow domain. Indeed, the flow domain considered for the 20 L sphere considers the canister and the dispersion sphere whereas the geometry of the Hartmann tube is depicted as the dispersion tube and an injection surface. For this reason, the approach of the experimental analyses is focused on the description of the dynamics of a gas injection at dynamic conditions. This analysis will provide information that is required for the characterization of the conditions of gas dispersion in the modified Hartmann tube (MIKE 3). On the contrary, this analysis is not necessary for the 20 L because the computational model that was envisaged for this apparatus envisaged the whole geometry of test apparatus. Further details about this difference are discussed in Section 4.2.

A simple descriptive test was performed in order to characterize the evolution of a pressurized gas injection. This fact can be accomplished by implementing a source model equation for the estimation of the mass flow in order to establish the variations of the internal conditions of the gas at the inlet surface. A more theoretical approach could have been carried out by considering an isentropic expansion of the gases through the injection valve. Nevertheless, in order to more efficiently represent the injection system and to take into account the pressure drop caused by the friction and the minor losses, a set of descriptive tests has been carried out with a visualization system.

For the development of the model, a basic set-up was constructed to represent the injection system. This experimental setup was developed by coupling the canister of the pressurized gas to a balloon. Indeed, the volume increase of the balloon can be recorded with a high-speed camera in order to determine its variations by performing an image analysis. Then, the numerical results of this study might also be included in mass and energy balances that determine the conditions of the fluid flow at the inlet of the tube. According to the scheme considered for this study, Figure 3.12 describes a system that couples a vessel that stores high pressure air and a balloon that will be filled with the gas by opening a solenoid valve:

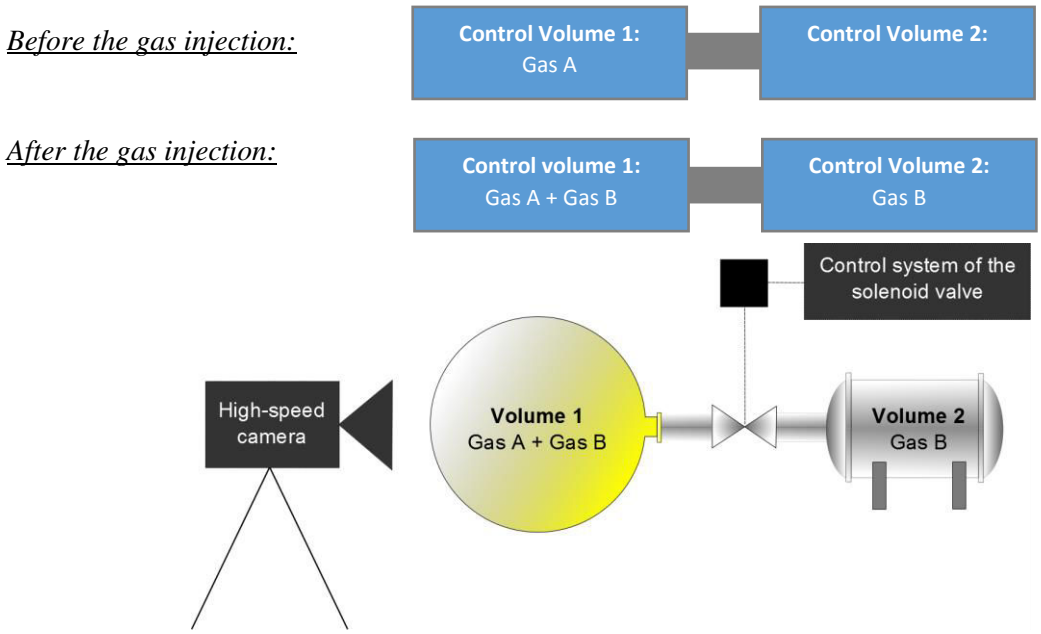

Figure 3.12. Experimental setup for the characterization of the gas flow in the modified Hartmann tube

For the description of this method, the system can be considered with two different gases. Therefore, the gas A will be air that is in the balloon before the valve opening and the gas B is pressurized air that is stored inside the vessel before the injection. In addition, two control volumes were considered with different transient conditions. The first volume is the inflation balloon while the second volume is the metallic vessel. Hence, the first volume will have a pressure increase whereas the pressure of the other one will be reduced due to the gas injection. Thus, the pressures of both volumes will equalize at the end of the injection process.

The recorded videos will be linked to the model that has been proposed for the definition of the velocity of the gas injected for the dispersion of the combustible dust. Then, a transient analysis of the evolution of the size of the balloon is necessary to characterize and determine the time required for the gas injection and the characterization of the variables that describe this process such as the pressure and the speed of the fluid flow.

The proposed model consists of a mass and energy balance performed for the two control volumes that compose the system. Hence, the simultaneous solution of the set of equations by an iterative method

explains in simple terms the evolution of the system. The numerical scheme of this analysis is described below.

3.4.1 Mass balance

The following expressions give the number of moles in the balloon (Volume 1) during the gas injection:

$$n_{A,1} = n_{A0,1} \tag{3.10}$$

$$n_{B,1} = \sum \frac{\dot{m}\Delta t}{M} \tag{3.11}$$

The number of moles of gas A within the balloon ($n_{A,1}$) is equal to the initial value ($n_{A0,1}$) during all the injection. On the other hand, the number of moles of gas B ($n_{B,1}$) depends on the mass flow at the inlet ($\dot{m}$) and the molecular weight of the gas (M). A similar analysis determines the values of the numbers of moles in the storage vessel (Volume 2):

$$n_{A,2}(t) = 0 \tag{3.12}$$

$$n_{B,2} = n_{B0,2} - \sum \frac{\dot{m}\Delta t}{M} \tag{3.13}$$

The mass flow rate has two different conditions that depend on the pressures of the two control volumes. Crowl & Louvar (2011) present a comparison of these variables to determine if the flow has achieved a maximum value or not. The maximum mass flow is evidenced during a critical condition, which corresponds to a choked flow of the gas that comes out from the vessel. For this reason, two different equations for a choked and non-choked mass flow must be distinguished as a function of the Mach number of the flow:

Choked flow:

$$\dot{m}_{choked}(t) = C_0 A P_2 \sqrt{\frac{\gamma g_c M}{R T_2}\left(\frac{2}{\gamma+1}\right)^{(\gamma+1)/(\gamma-1)}} \tag{3.14}$$

Non-choked flow:

$$\dot{m}(t)_{non-choked} = C_0 A P_2 \sqrt{\frac{2 g_c M}{R T_2}\frac{\gamma}{\gamma-1}\left[\left(\frac{P_1}{P_2}\right)^{2/\gamma} - \left(\frac{P_1}{P_2}\right)^{(\gamma+1)/\gamma}\right]} \tag{3.15}$$

Equation 3.14 evidences how a choked flow depends only on the conditions of the gas inside the vessel. Therefore, the pressure (P_2) and the temperature (T_2) of the gas B determine the mass flow that passes through the pipe that joins the two volumes (A), the discharge coefficient of the vessel outlet (C_0) and the heat capacity ratio of the fluid (γ), which is equal to 1.401. On the other hand, a non-choked flow depends not only of these variables but on the pressure of the balloon (P_1) as well.

This comparison is strictly necessary because the gas flow can achieve some characteristic conditions during the early stages of the injection. For instance, a descriptive analysis of the flow channel shows that, in the previous case, the velocity of the flow throat is equal to the speed of sound and its local pressure corresponds to the choked pressure of the fluid flow (P_{choked}) (Perry et al., 1997). Therefore,

the determination of the latter variable will define the equation that will be used. This comparison is performed according to the criteria shown below:

$$\dot{m}(t) = \begin{cases} \dot{m}_{choked}(t) & \text{if } P_2 \geq P_{choked} \\ \dot{m}_{non-choked}(t) & \text{if } P_2 < P_{choked} \end{cases} \quad 3.16$$

The choked pressure is defined by the physical properties of the gas and the pressure of the volume control N°1 (H. Z. Li et al., 2009):

$$P_{choked} = P_2 \left(\frac{2}{\gamma + 1} \right)^{\gamma/(\gamma-1)} \quad 3.17$$

Hence, it is possible to calculate the mass flow by defining the parameters associated to the specific empirical equation. Then, the discharge coefficient (C_0) is determined from a correlation obtained from the Reynolds number (Re) of the gas flow and the internal diameters of the vessel (D_V) and the pipe (D_o) that joins the two control volumes (Biswas, 2003):

$$C_0 = \frac{C_d}{\sqrt{1 - \left(\frac{D_o}{D_V} \right)^4}} \quad 3.18$$

$$C_d = \begin{cases} 0.984 & \text{if } \mathrm{Re} \geq 2 \times 10^5 \\ 0.610 & \text{if } \mathrm{Re} = 3 \times 10^4 \end{cases} \quad 3.19$$

The values of Equation 3.19 were adjusted to a simple expression for the calculation of C_d:

$$C_d = 0.5606 \exp(2.813 \times 10^{-6}\, \mathrm{Re}) \quad 3.20$$

For every time step, the gas flow is considered as turbulent. This initial assumption is adopted due to the low viscosity of the fluid which allows considering a high Reynolds numbers even for low air velocities. However, this assumption is validated by calculating the Reynolds number after determining the fluid flow velocity.

Due to the pressure changes that are evidenced in the control volumes 1 and 2, a numerical scheme that allows determining the expression to use for Equations 3.11 and 3.13 must be considered for every time step. Therefore, it is also necessary to define an energy balance for the two control volumes.

3.4.2 Analysis of the high-speed videos

The variations of the gas pressure inside the balloon and the vessel are determined from two different types of data:

- **Characterization of the initial conditions of the two control volumes:** The method considered for the numerical integration of the mass and energy conservation equations requires the determination of the geometric design parameters of the vessel and the initial volume of the balloon. Besides these variables, the initial pressures and temperatures of the volumes were also necessary to establish the initial mass of the gases A and B and the mass flow at the beginning of

the dispersion process. These data were obtained from the design specifications of the equipment and an image analysis that was performed with the first frame of the recorded video.

- **Experimental determination of the volume of the balloon with high-speed videos:** Several snapshots of the balloon were taken with a high-speed video camera to perform an image analysis. This process began with the binarization of the recorded video (Figure 3.14). This step allowed establishing the variation of the projected surface of the balloon during its expansion. Then, these data were collected to constitute the main source of information about the evolution of the size of the balloon that is caused by the entrance of the pressurized gas.

The software Simulink™ was used for the analysis of the recorded images. For this purpose, a functional environment diagram was set up for the dynamic simulation. This diagram was defined to describes the steps followed during this procedure. Then, a simple algorithm was implemented according to the scheme shown in Figure 3.13:

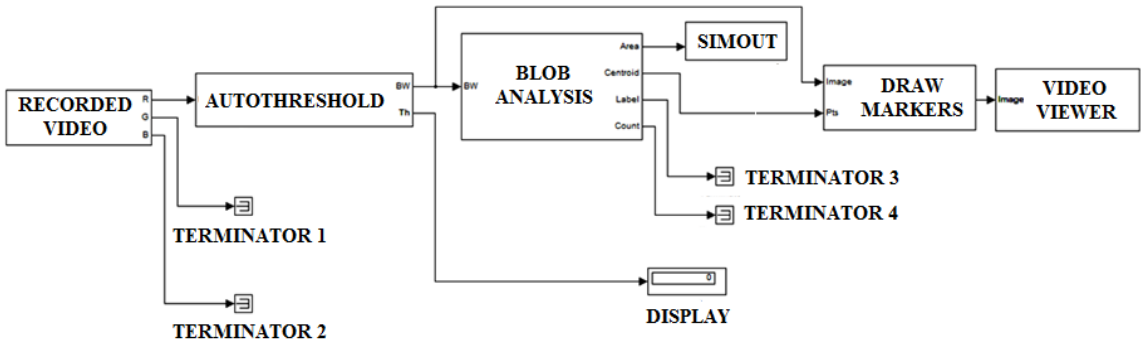

Figure 3.13. Block diagram of the dynamic analysis of the high-speed videos

Initially, every frame of the video was turned into a black and white image with the "Autothreshold" function in order to differ the image of the balloon from the background of each frame. This step of the procedure identified a white region (blob) that corresponds to the projected surface of the balloon. Afterwards, the total area of this surface was measured through a blob Analysis. This step compared the color of the pixels in the image to determine the size of the white blob. Then, this information was transferred to MATLAB™ software through the block "Simout". Thereafter, the area of the balloon and its centroid could be observed by adding the blocks "Draw Markers" and "Video viewer". Finally, the results displayed in Figure 3.14 were obtained.

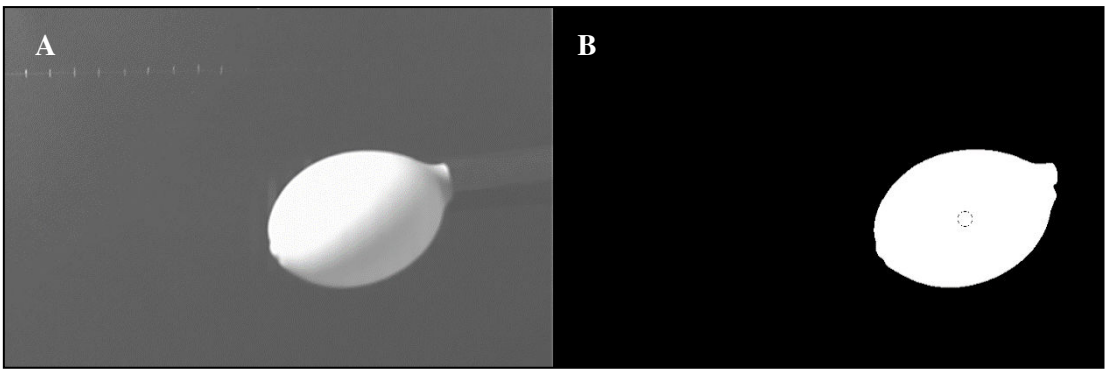

Figure 3.14. Image analysis of the expansion of the balloon
A. Recorded image B. Binarisation and identification of the center of mass

This figure shows the direct comparison of the images recorded at the beginning of the expansion of the balloon. The initial diameter of the balloon was determined from a measurement performed on the pixels of the image shown in Figure 3.14B, which established that this variable was equal to

0.047 m. Another important aspect that had to be considered during the analysis of the video relies on the brightness variations that were observed due to growth and the movement of the balloon. This factor constituted the main reason for the disturbances shown in Figure 3.15.

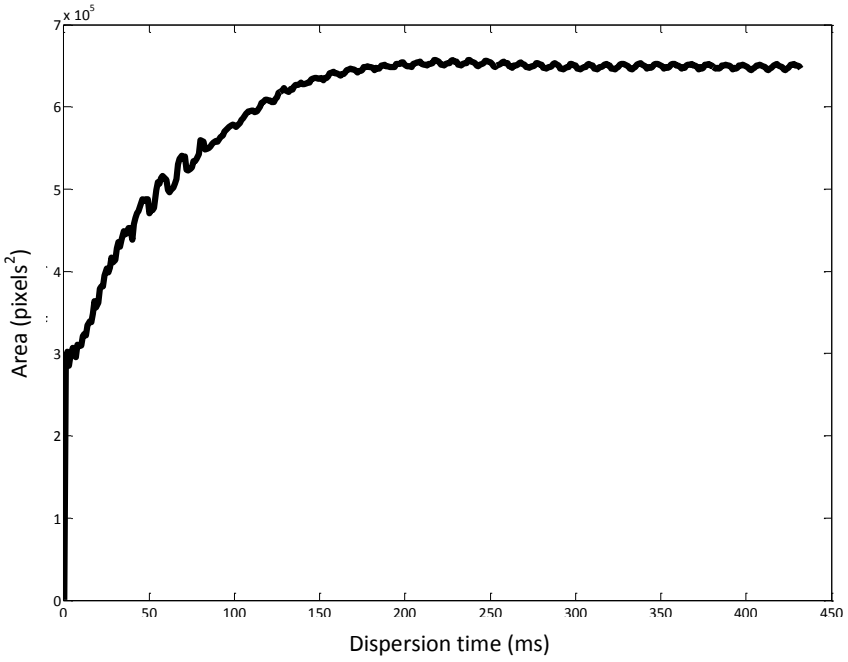

Figure 3.15. Projected surface of the balloon during the gas expansion

The calibration of the video showed that 68 pixels correspond to one centimeter in each image. Afterwards, the volume of the balloon during the expansion was determined with an approximation of an ellipsoidal shape that was adjusted to a trend line for the data of the previous figure. Therefore, the ratio of the cross section and the total volume of an ellipsoid provided an estimate of the volume of the balloon that is displayed in Figure 3.16:

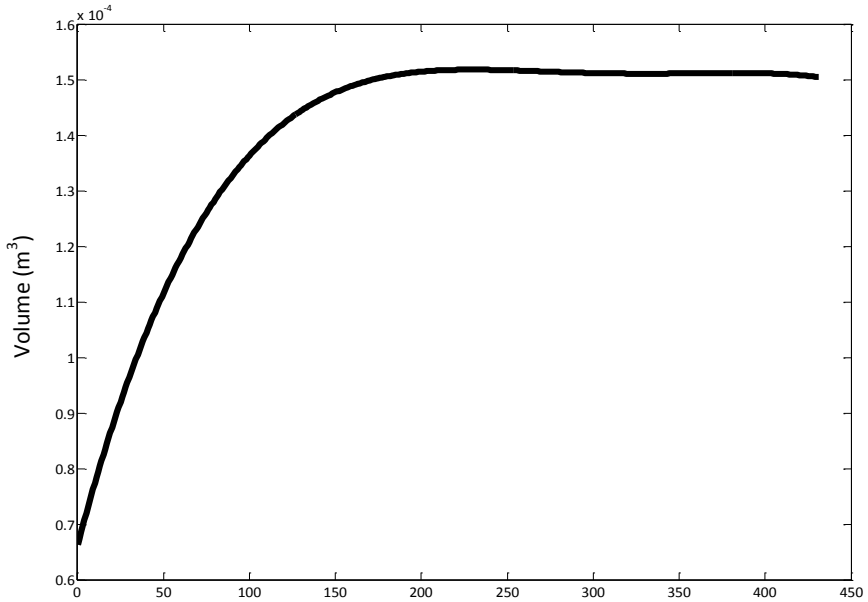

Figure 3.16. Experimental determination of the variation of the volume of the balloon due to the injection of gas.

Thereupon, a new variable will be defined to represent the number of moles of gas B that gets into the balloon in the time between $t-\Delta t$ and t (n_v). This variable corresponds to the change of the number

of moles of the gas B in each volume. This definition facilitates the comprehension of the equations proposed to calculate the pressures of each room:

$$n_v = n_{B,1,t} - n_{B,1,t-\Delta t} = n_{B,2,t-\Delta t} - n_{B,2,t} \quad 3.21$$

3.4.3 Transient pressure of the vessel

The iterative scheme of the model considered in this study to determine the transient conditions of the gas in the two volume controls is based on the numerical integration of the equations associated to the mass balance. Moreover, the knowledge of the thermodynamic variables of the gas at the previous time step is necessary to complete the energy balance that determines the temperature and the pressure of the gas in the vessel in the following time step:

$$\text{Energy Flux} = \text{Accumulation} \quad 3.22$$

For Equation 3.22, the energy flow is associated to the outflow of the gas B. Hence, the enthalpy of this flow determines the decrease of the internal energy of this gas inside the vessel. Afterwards, Equation 3.23 describes more precisely the energy balance:

$$-n_v h_v = n_{B,2,t} e_{2,t} - n_{B,2,t-\Delta t} e_{2,t-\Delta t} \quad 3.23$$

Then, certain system conditions must be taken into account to establish the numerical simplifications that are needed to facilitate the implementation of the model. For instance, air is considered to be an ideal gas for the determination of its thermodynamic properties. This condition can be assumed due to the low pressures of the two control volumes. Therefore, the enthalpy (h_v) and the internal energy of the fluid (e_2) can be defined as thermodynamic properties that depend only on the fluid temperature. For this reason, the previous equation can be written as follows for a time step (Δt) equal to 10^{-3} s:

$$-n_v \int_{T_{ref}}^{T_{2,t-\Delta t}} C_p dT = n_{B,2,t} \int_{T_{ref}}^{T_{2,t}} C_v dT - n_{B,2,t-\Delta t} \int_{T_{ref}}^{T_{2,t-\Delta t}} C_v dT \quad 3.24$$

For the previous expression it is necessary to perform an iterative calculation sequence that assumes a value for $T_{2,t}$ which will be validated afterwards. Moreover, the enthalpy and the internal energy are calculated by the integration of the heat capacity of the fluid between a reference temperature (T_{ref}) and the gas temperature in the volume controls. This reference value is established from a condition near the temperature of the fluid at the test conditions. Thus, it would be possible to use an average value of the heat capacities for the numerical integration of the equation above. Therefore, the reference temperature is 298.15 K. Subsequently, a simple expression is obtained for the temperature of the gas in the vessel from the energy balance:

$$-n_v C_p \left(T_{2,t-\Delta t} - T_{ref}\right) = n_{B,2,t} C_V \left(T_{2,t} - T_{ref}\right) - n_{B,2,t-\Delta t} C_V \left(T_{2,t-\Delta t} - T_{ref}\right) \quad 3.25$$

$$T_{2,t} = T_{ref} + \left(T_{2,t-\Delta t} - T_{ref}\right)\left(\frac{n_{B,2,t-\Delta t} - n_v \gamma}{n_{B,2,t}}\right) = T_{ref} + \left(T_{2,t-\Delta t} - T_{ref}\right)\left(\frac{n_{B,2,t-\Delta t} - n_v \gamma}{n_{B,2,t-\Delta t} - n_v}\right) \quad 3.26$$

Thus, the previously assumed temperature can be determined with Equation 3.26. Then, the pressure of gas B within the volume 2 is determined from the ideal gas equation. This value is used to calculate the mass flow of the following time step.

$$P_{2,t} = \frac{n_{B,2,t} R T_{2,t}}{V_2} \tag{3.27}$$

3.4.4 Transient pressure of the vessel

A procedure similar to the method considered for the energy balance in the vessel was posed for the determination of the pressure of the balloon. Given the conditions and simplifications discussed above, a simple equation can be established from the first law of thermodynamics defined for control of volume 1:

$$\text{Energy Flow} = \text{Work} + \text{Accumulation} \tag{3.28}$$

The gas B that gets into the balloon increases its volume. During this process, a boundary work is done by the expanding gas. This condition corresponds to a polytropic process that poses a direct relationship between the pressure and the volume of the fluid. Hence, by definition, the multiplication of the pressure and the specific volume of fluid to the power of the heat capacity ratio (γ) has a constant value (isentropic process). This feature identifies an expression for the boundary work associated to the experimental tests.

$$W = \int_{V_{1,t_0}}^{V_{1,t_f}} P dV_1 = \int_{V_{1,t_0}}^{V_{1,t_f}} C V_1^{-\gamma} dV_1 = C \frac{P_1 V_1^{-\gamma+1}\Big|_{t_f} - P_1 V_1^{-\gamma+1}\Big|_{t_0}}{-\gamma+1} = \frac{nR\left(T_{1,t_f} - T_{1,t_0}\right)}{1-\gamma} \tag{3.29}$$

$$C = P_1 V_1^{-\gamma+1}\Big|_{t_f} = P_1 V_1^{-\gamma+1}\Big|_{t_0} \tag{3.30}$$

The boundary work will be divided into 2 sections because the gas that comes from the vessel B (n_v) has a different temperature from the gas that is already inside the balloon ($n_{A,1} + n_{B,1,t-\Delta t}$). Therefore, Equation 3.28 can be written as follows:

$$n_v h_v = \frac{R}{1-\gamma}\left\{W_{n_v} + W_{n_{A,1}+n_{B,1,t-\Delta t}}\right\} + \left(n_{A,1} + n_{B,1,t}\right) e_{1,t} - \left(n_{A,1} + n_{B,1,t-\Delta t}\right) e_{1,t-\Delta t} \tag{3.31}$$

The calculations of the air enthalpy (h_v) and its internal energy (e_1) consider the same simplifications discussed above. In order to have an expression determined by the fluid temperatures. Additionally, Equation 3.29 is substituted in Equation 3.31:

$$\begin{aligned} n_v C_p \left(T_{2,t-\Delta t} - T_{ref}\right) = \frac{R}{1-\gamma}\left\{\left[n_v\left(T_{1,t} - T_{2,t-\Delta t}\right)\right] + \left[\left(n_{A,1} + n_{B,1,t-\Delta t}\right)\left(T_{1,t} - T_{1,t-\Delta t}\right)\right]\right\} \\ + \left(n_{A,1} + n_{B,1,t}\right) C_V \left(T_{1,t} - T_{ref}\right) - \left(n_{A,1} + n_{B,1,t-\Delta t}\right) C_V \left(T_{1,t-\Delta t} - T_{ref}\right) \end{aligned} \tag{3.32}$$

Afterwards, the ratio between the number of moles that get into the balloon and the total number of moles inside it is also established:

$$Y^* = \frac{n_v}{n_v + n_{A,1} + n_{B,1,t-\Delta t}} \tag{3.33}$$

If Equation 3.32 is divided by $n_v + n_{A,1} + n_{B,1,t-\Delta t}$, a simple expression can determine the current temperature inside the balloon from the variables that are already known:

$$Y^{*}C_{p}\left(T_{2,t-\Delta t}-T_{ref}\right)=\frac{R}{1-\gamma}\left\{\left[Y^{*}\left(T_{1,t}-T_{2,t-\Delta t}\right)\right]+\left[\left(1-Y^{*}\right)\left(T_{1,t}-T_{1,t-\Delta t}\right)\right]\right\} + \frac{\left(n_{A,1}+n_{B,1,t}\right)}{\left(n_{A,1}+n_{B,1,t-\Delta t}\right)}C_{V}\left(T_{1,t}-T_{ref}\right)-\left(1-Y^{*}\right)C_{V}\left(T_{1,t-\Delta t}-T_{ref}\right) \quad 3.34$$

$$T_{1,t}=\left[\frac{n_{A,1}+n_{B,1,t-\Delta t}}{n_{A,1}+n_{B,1,t}}\right]\left[\frac{Y^{*}C_{p}T_{2,t-\Delta t}-\frac{R}{1-\gamma}\left\{\left[Y^{*}\left(T_{1,t}-T_{2,t}\right)\right]+\left[\left(1-Y^{*}\right)\left(T_{1,t}-T_{1,t-\Delta t}\right)\right]\right\}+\left(1-Y^{*}\right)C_{V}T_{1,t-\Delta t}}{C_{V}}\right] \quad 3.35$$

The temperature that was previously assumed ($T_{1,t}$) can be determined with Equation 3.35. Then, the total gas pressure inside the volume 1 is determined from the ideal gas equation. In addition, this variable can be viewed as the sum of the partial pressures of gases A and B. This value is used to calculate the mass flow rate of the following time step.

$$P_{2,t}=\frac{\left(n_{A,2,t}+n_{B,2,t}\right)RT_{2,t}}{V_{2}} \quad 3.36$$

3.4.5 Gas velocity and Reynolds number

Now it is possible to establish the values of the mean volumetric flow (Q) and the mean speed (v_B) of the gas flow in order to validate the assumption of the Reynolds number that has been discussed above:

$$Q=\frac{\dot{m}}{\rho_{2}}=\frac{\dot{m}RT_{2}}{P_{2}M} \quad 3.37$$

The ratio between the volumetric flow rate and the cross-section of the connecting pipe provides the mean gas velocity at the pipe that connects the vessel and the volume:

$$v_{B}=\frac{Q}{A} \quad 3.38$$

Now, the Reynolds number (Re) of the gas flow B can be calculated from the gas density (ρ_2), its dynamic viscosity (μ) and the diameter of the connection pipe (D_o) in order to validate the assumption made on the previous section:

$$\mathrm{Re}=\frac{\rho_{2}v_{B}D_{o}}{\mu} \quad 3.39$$

3.4.6 Pressure drop of the gas flow

The pressure drop of the gas flow between the vessel and the balloon is determined from a simple model that is defined according to the set of accessories that is installed in the pipe. Hence, the pressure drop of this fluid mainly due to the friction against the walls and the minor losses that can be

attributed to the pipe accessories. Furthermore, Equations 3.14 and 3.15 show that the maximum flow of gas is achieved at the beginning of the injection because the higher pressure gradients are established during this stage. According to these considerations, Equation 3.40 calculates the pressure drop for every moment of the air injection:

$$\Delta P = K_{contraction}\left(\frac{v_B^2}{2}\right)\rho_2 + \left(f\frac{L_o}{D_o} + K_{valve} + K_{expansion}\right)\left(\frac{v_{B*}^2}{2}\right)\left(\frac{\rho_1+\rho_2}{2}\right) \quad 3.40$$

The continuity condition of the flow establishes that the density and the velocity of the gas are inversely proportional. Therefore, the main effect of friction relies on the reduction of the density of a compressible gas that flows under subsonic conditions. This phenomenon is related to the increase in velocity of the fluid flow and its Mach number as well. On the other hand, a supersonic flow shows the opposite behavior by decelerating during a flow inside a duct.

These density variations require a modification of the calculation scheme in order to consider the gas pressure drop. For this reason, the first term of the right side of Equation 3.40 was calculated with the density of the gas in the vessel (ρ_2) and the speed at the outlet of this control volume. Then, the other terms were determined with the average density of the gas defined on the two extremes of the pipeline. The parameter v_{B*} is the average speed calculated from the continuity equation of the mean flow.

$$\rho_2 v_B = \left(\frac{\rho_1+\rho_2}{2}\right)v_{B*} \quad 3.41$$

The gas that comes out of the vessel B has a contraction caused by the difference between the diameter of the vessel and the diameter of the pipeline. This condition is represented by the constant $K_{contraction}$. Moreover, a similar condition is observed during the inflation of the first volume control, because the gas is subjected to a sudden expansion when it gets into the balloon. Therefore, Equation 3.40 considers this minor loss by including the parameter $K_{expansion}$. These constants are defined with values that have been proposed by Çengel & Cimbala (2013):

Rounded contraction: $K_{contraction} = 0.03$ 3.42

Expansion at 45 degrees: $K_{expansion} = 0.04$ 3.43

Then, the pressure drop associated with the solenoid valve was determined with the information provided by the manufacturer Bürkert™ for the reference of the valve that was used in the assembly:

Table 3.9. Technical specifications of the 2/2-way Solenoid Valve

	Orifice [mm]	DN 1.0-6.0
	Body material	Brass with stainless steel seat 1.4305
	Coil material	Epoxy
	Media temperature [°C]	-40 to +180
	K_v value water [m^3/h]	0.8 measured at +20°C, 1 bar pressure at valve inlet and free outlet
	Weight [kg]	0.6 (brass version)

The value of K_{valve} is established from the internal diameter of the valve (3.5 mm) along with the pressure and temperature defined in the technical data sheet of the solenoid valve. Hence, Equation 3.45 can determine the value associated to the constant:

$$K_{valve}\frac{\left(\text{Calibration velocity}\right)^2}{2}=\frac{\text{Standardised Pressure drop}}{\text{Water density at 20°C}} \qquad 3.44$$

$$K_{valve}\left(\frac{0.8m^3/h}{2}\right)\left(\frac{h}{3600s}\right)\left(\frac{1}{\pi/4\left(0.0035m\right)^2}\right)=\frac{100000Pa}{998kg/m^3}=0.376 \qquad 3.45$$

Afterwards, the major losses are calculated for a stainless steel pipe whose relative rugosity is (r) 0.002 mm (Çengel & Cimbala, 2013). For the turbulent gas flow, the pressure drop is calculated for a pipeline whose length is 0.035m. Then, the Moody's friction factor (f) is determined from the Colebrook's equation because the gas flow is turbulent:

$$\frac{1}{\sqrt{f}}=-2\log\left(\frac{r/D_o}{3.7}+\frac{2.51}{\text{Re}\sqrt{f}}\right) \qquad 3.46$$

A better description of this calculation scheme can be obtained from the analysis of an air injection at 7 barg. For this test, the gas velocity is 201 m· s^{-1} and the Reynolds number is equal to $1.65\cdot10^6$. Thus, a numerical iteration procedure establishes that the value of the friction factor is 0.0172. Finally, Equation 3.47 determines the pressure drop for the start of injection:

$$\Delta P=0.03\left(\frac{201^2}{2}\right)9.071+\left(0.0172\frac{0.035}{0.0035}+0.376+0.04\right)\left(\frac{343^2}{2}\right)\left(\frac{1.164+9.071}{2}\right)=183304Pa \qquad 3.47$$

Initially, the standard value of the modified Hartmann tube (8.03 bars) was analyzed. The pressure drop estimated for this case represented the 22.8% of the vessel pressure. Therefore, the numerical results established that this variable cannot be neglected for the remainder of this analysis. For this reason, a comparison between the vessel pressure and the injection pressure was performed for the time elapsed during the gas injection. This extended analysis is shown in Figure 3.17. The conclusions of this study showed that the pressure drop is an important factor during the first 40 ms of the gas injection (green line).

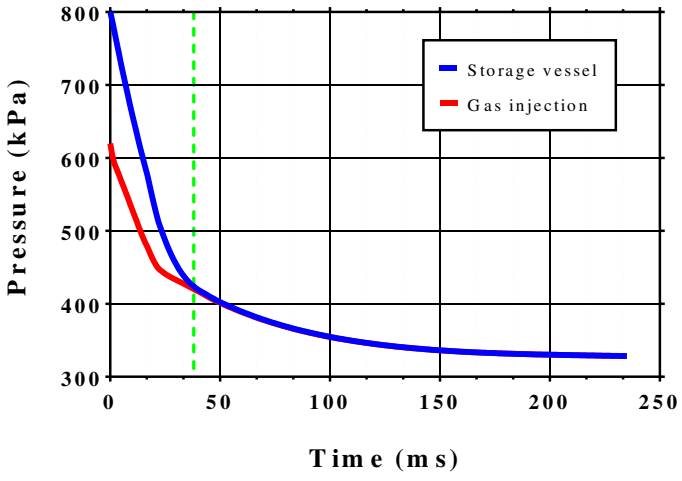

Figure 3.17. Comparison between the pressure of the vessel and the injection point

In addition, the evolution of the pressure in the balloon and the vessel is shown in Figure 3.18. The two profiles that are shown in the chart establish that the equality of these two variables is achieved 196 ms after the beginning of the injection. This result agrees with the experimental results obtained from the video recorded during the inflation of the balloon. Thus, the profile of the gas pressure at the injection surface can be considered to represent this variable as a boundary condition in the computational fluid dynamics simulation that was developed subsequently.

Afterwards, the variation of the gas velocity at the outlet of the vessel was analyzed in Figure 3.19. The characteristic profile that describes the behavior of this variable clearly evidences the two regimes that were considered for the mean flow. The choked flow is evidenced during the first 14 ms where the gas speed achieves its maximum value. Then, the decline of this variable is drastic during the next 26 ms. Additionally, the numerical results establish that the 44.4% of the gas to be injected has gotten into the balloon during this period. Then, the rest of the gas is injected during a stabilization that lasts 150 ms approximately. This final stage is characterized by a small pressure difference between the control volumes.

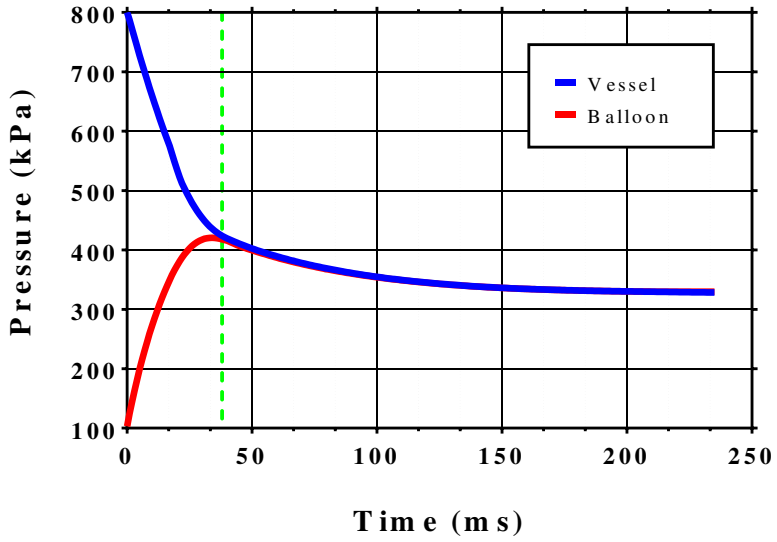

Figure 3.18. Comparison of the gas pressure inside the two control volumes during the air injection

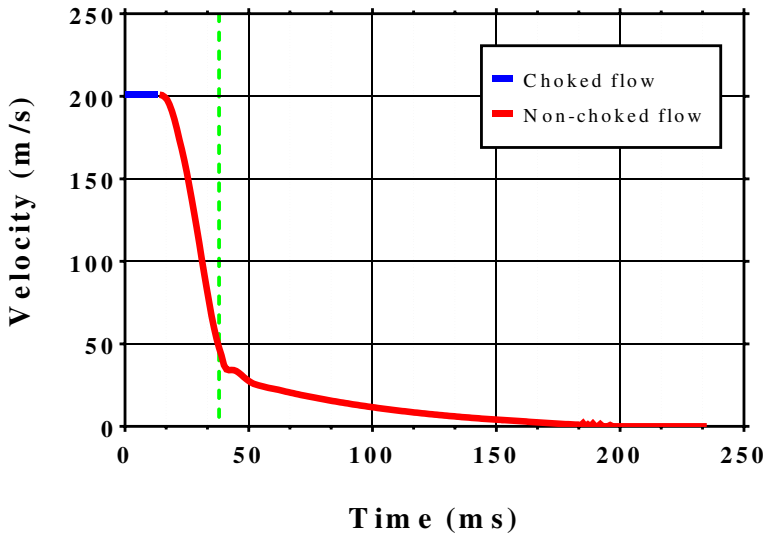

Figure 3.19. Gas velocity at the vessel outlet during the air injection

3.4.7 Description of the gas injection into the modified Hartmann tube

The validation of the model that is presented in this chapter showed that it can be adapted for the prediction of the main conditions of the air injection. This fact has been considered to define the pressure of the gas injected Hartmann dispersion tube ($P_2 - \Delta P$) at the inlet surface. Then, the numerical study of the influence of the conditions of the pressurized gas was achieved through the implementation of certain changes to the model discussed above. The results have established a profile which determines the conditions of the dispersion gas at the inlet of the tube. The modified settings are listed below for a better comprehension of the adjustments that were proposed for the predictive model.

- The initial pressure of the vessel is adjusted according to the sensitivity analysis that is proposed in this thesis. Hence, this parameter varies between 3 and 7 barg.
- The volume of the dispersion chamber that replaces the balloon in the predictive model is defined by the design specifications of the test apparatus. Therefore, the number of moles of the gas A has increased.
- The gas velocity at the entrance of the tube (v_{inj}) is determined from a mass balance that is defined for the two extremes of the tube. This balance is established from the cross section of the injection point of the gas tube (A_T):

$$\rho_2 v_B A = \frac{(P_2 - \Delta P) M}{R\left(\frac{T_1 + T_2}{2}\right)} A_T v_{inj} \qquad 3.48$$

Thus, Figure 3.20 shows the pressure profiles that were estimated for the dispersion gas and its velocity at the entrance of the tube that were defined for five different levels of compression of the gas pressurized inside the vessel.

The results pose a decrease of 4 bars of the pressurized gas inside the vessel, which constitutes a delay of 16 ms for the beginning of the non-choked injection. Hence, the gas flow changes its regime after 32 and 48 ms with an injection of 3 and 7 barg respectively. In addition, this pressure change also represents a time delay of 26 ms for the end of the injection of the fluid.

Finally, these profiles were considered as a basic parameter of a descriptive study of two-phase flow developed inside the modified Hartmann tube. The curves displayed below have been considered as a boundary condition in the computational approach that was conducted for the sensitivity analysis associated to this thesis. Further details about the utilization of curve fittings for the computational analyses are provided in Chapter 4.

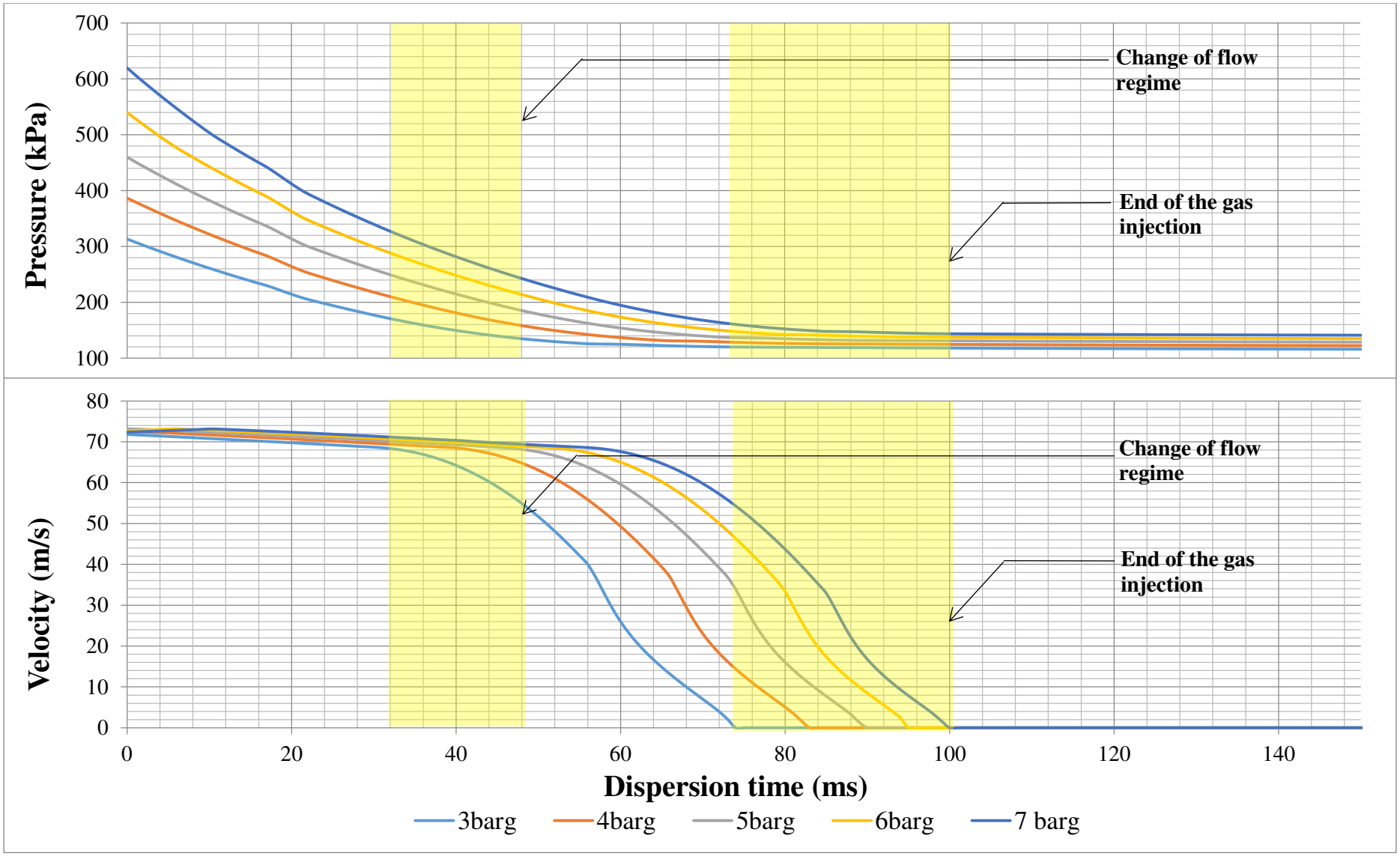

Figure 3.20. Pressure and velocity profiles of the air injection at the entrance of the modified Hartmann tube

3.5 DETERMINATION OF THE DUST DISPERSION CHARACTERISTICS INSIDE THE MODIFIED HARTMANN TUBE

The dispersion of the combustible dusts inside the modified Hartmann tube was analyzed with an experimental methodology that focused on the description of the behavior of the dust cloud in the time lapse before the dust ignition that is caused by the electrodes activation. Several tests were performed for the acquisition of qualitative and quantitative data about the two-phase flows that develop within the dispersion tube of this standardized apparatus. These analyses were proposed to establish the segregation levels of the disperse phase inside the dispersion tube along with the variations in its particle size distribution.

3.5.1 Experimental setup

A. Dispersion tubes

Two new vertical tubes were constructed for the experimental tests (Figure 3.21). They are characterized by some important features that facilitate the development of the light scattering analyses. One of these characteristics relies on their cross sections, which are squared in order to reduce the effects associated to the laser diffraction of the tube walls during the granulometric analyses. This feature makes them different from the modified Hartmann tube, which is cylindrical. Additionally, the height of one of the tubes was increased to 1 m in order to acquire clear evidences about the evolution of the dust dispersion and to avoid the reflection phenomenon due to the proximity of the top of the tube in shorter configurations. On the contrary, the second tube is as high as the modified Hartmann tube (0.3 m). In addition, both tubes are 0.07 m wide in accordance with the diameter of the standard apparatus.

Moreover, the tubes were constructed with 4 glass windows (thermally treated borosilicate) for the visualization of the two-phase flow. Additionally, each dispersion tube also consists of an injection nozzle that is located at the bottom of each tube. This item is installed in order to distribute the gas injected and form the dust cloud by collecting the solid sample that is located around the nozzle.

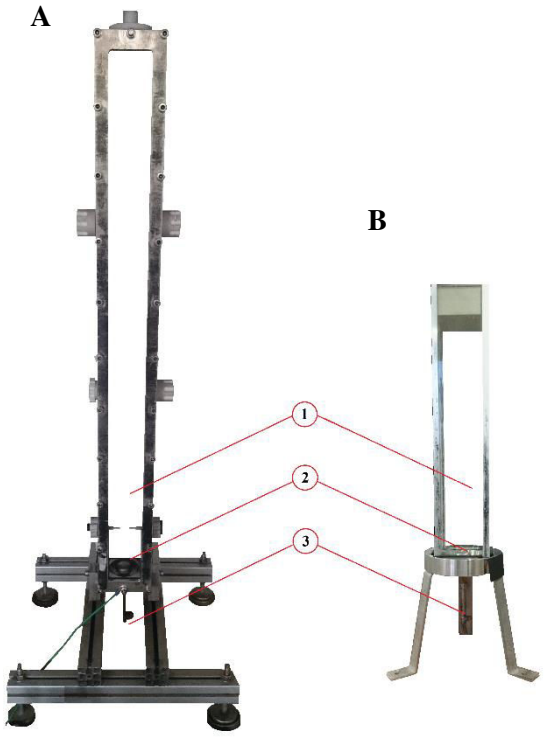

Figure 3.21. Dispersion tubes
A. 1 m tube B. 30 cm tube
A. Dispersion tube B. Nozzle C. Injection point

On the one hand, the high tube was considered for the dispersion analyses performed with micro-Al 42 samples and the PIV characterization tests that were developed by Cuervo et al. (2014) with micrometric wheat starch. On the other hand, the short tube was considered for the other tests performed with the organic dust (granulometric tests and high-speed videos) and to define the geometry of the flow domain that was envisaged for the computational approach.

B. Injection system

The injection system was conceived according to the sensitivity analysis that was proposed to determine the influence of the injection pressure on the development of the dust cloud. In accordance with this definition, the system consists of a storage vessel whose volume is equal to the volume of the vessel of the modified Hartmann tube (50 mL). Additionally, the injection system also consists of a manometer and two valves that are installed at its two extremes. The valve D, which is connected to the pressurized line, must be open in order to fill the vessel C until the specified pressure. Then, this valve is closed and the solenoid valve A is opened with an electronic device that represents the control software of the Hartmann tube. The modeling of this system has been described in detail in Section 3.4.

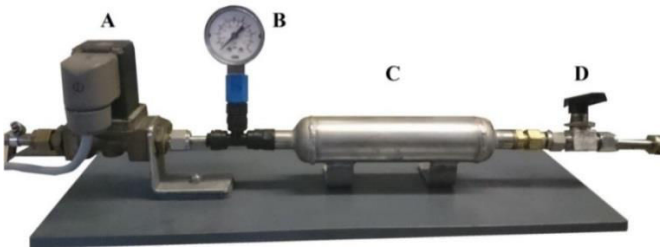

Figure 3.22. Injection system used for dust dispersion in the 1 m tube
A. Solenoid valve B. Manometer C. Vessel D. Valve

3.5.2 Set of experiments

The development of the particle-laden flows of the combustible dusts studied in this thesis was described according to two different frameworks in order to analyze the dispersion process of these materials during a flammability test. Thus, a description of the evolution of the confined dust cloud was achieved in a qualitative and semi-quantitative approach in order to establish the variation of some specific characteristics of the dispersed powder during time elapsed before the dust ignition. This aspect was considered in this thesis because these characteristics determine the main properties of the ignition, flame propagation and the safety parameters obtained with a modified Hartmann tube.

This procedure consisted of two steps that contemplated the characterization of the combustible dusts in two different environments. Initially, the particle size distributions of the combustible dusts were determined by performing a set of sedimentation tests that ascertained the agglomeration level of the analyzed powders at the normal conditions of the laboratory. This step defined the reference data for the comparison of the subsequent experimental tests. Afterwards, the description process was fulfilled with high-speed videos that determined the segregation levels of the combustible dust and the mean rising velocity of the dust cloud. Additionally, some analyses were carried out with the granulometer HELOS/KR to determine the variations of the particle size distribution of the powder located at the height of the ignition sources (10 cm). The experimental results posed some differences in the evolution of the dust clouds of the tested materials. For this reason, the influence of the injection pressure and the height of the ignition sources have also been assessed. The set of experiments developed for the characterization of the dispersion process in the modified Hartmann tube is briefly described in Figure 3.23:

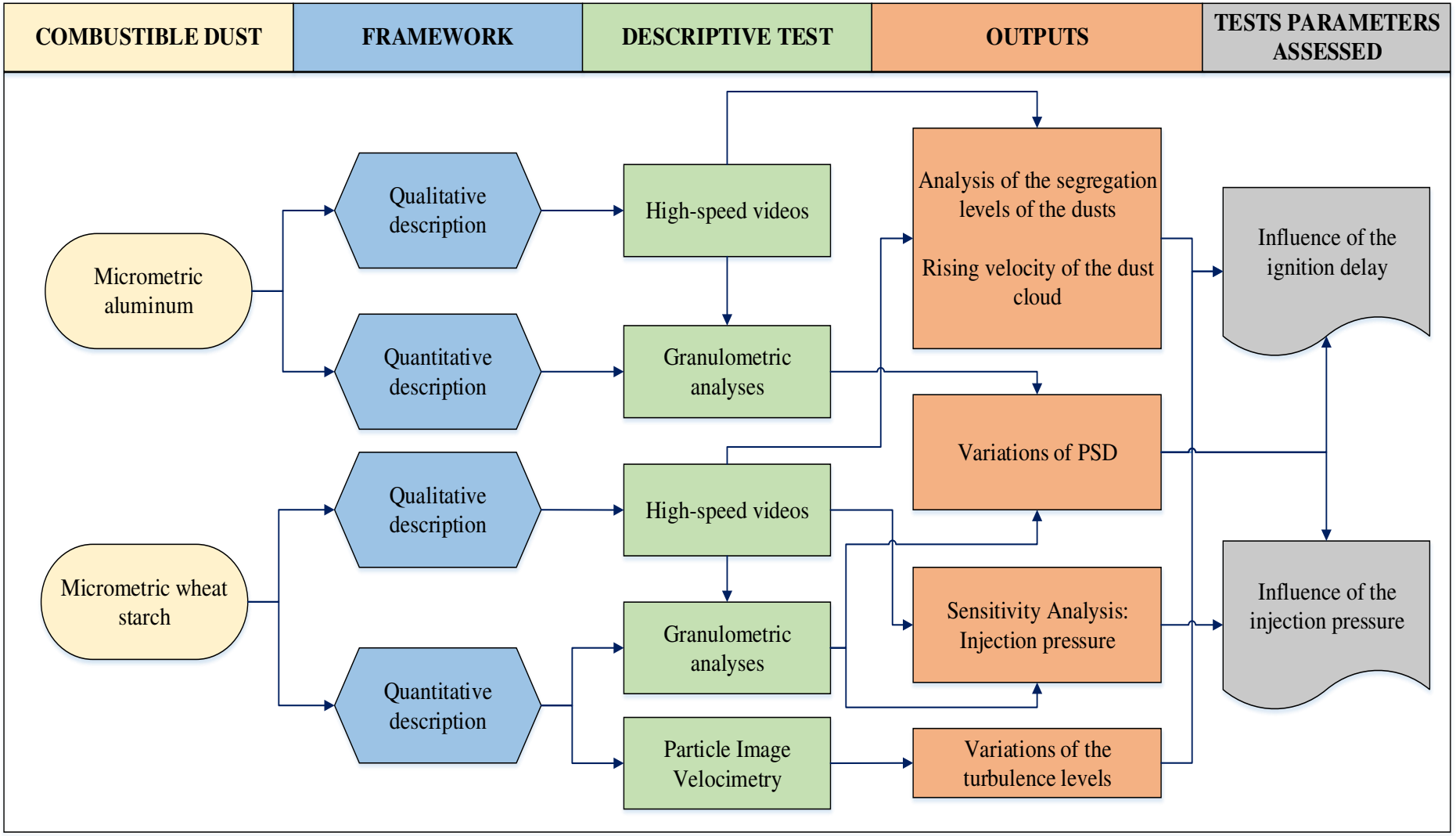

Figure 3.23. Set of experiments with the modified Hartmann tube

A. *Dispersion of micrometric aluminum*

Initially, the experimental approach was defined as a qualitative analysis in order to describe the behavior of the dust cloud inside the tube. This analysis was performed by recording the dispersion process with high-speed videos. For this reason, a high-speed camera was placed in front of the experimental apparatus in order to obtain a visual evidence of the evolution of the dust cloud at the low region of the dispersion tube. Thus, the influence of some important test parameters on the homogeneity of the mixture was clearly evidenced. Afterwards, the analysis of the internal conditions of the solids dispersion posed the importance of considering the variations of the particle size distribution with a granulometric analysis as well.

The tests were developed by placing a weighted sample of the combustible dust at the bottom of the dispersion tube and injecting the pressurized gas as it is done under standardized conditions. Then, the evolution of the dust cloud was analyzed during the first 120 ms in the low region of the tube in order to evaluate the influence of the standardized values for the flammability test on the experimental apparatus. This qualitative analysis allowed assessing the validity of some common assumptions that are considered for the experimental characterization of a combustible dust.

Firstly, the initial stages of a dispersion of micrometric aluminum, which was produced by the injection of air at 7 barg, were described through a visual analysis. The registration of this process has been developed with a Phantom V91 high speed video-camera that was focused on the lowest 10 centimeters of the dispersion tube. For this adjustment, the recording device was set to a resolution of 1632x1200 pixels and an exposure of 980 µs. These settings allowed registering the development of the two-phase flow at a rate of 1016 frames per second. Then, the images shown in Figure 3.24 were obtained for the first 120 ms of dust dispersion of a sample composed by 0.6 grams of the metallic combustible dust.

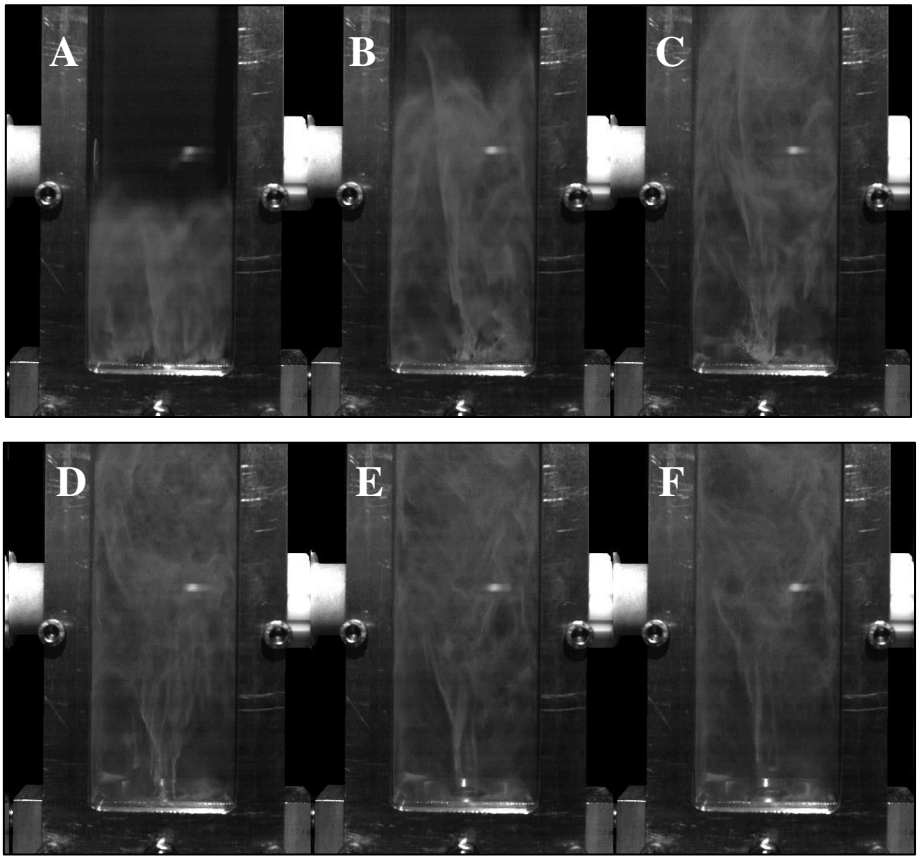

Figure 3.24. Dispersion of Micro-Al 42 dust within the modified Hartmann tube. A. 20 ms B. 40 ms C. 60 ms D. 80 ms E. 100 ms F. 120 ms.

The internal conditions allow classifying the rising process of the dust cloud into three different stages. The first stage evidences a homogeneous distribution, in which, the aggregates dispersed in the dust cloud rise with a characteristic profile that constitutes a flat front. This behavior can be seen in the first two images of Figure 3.24 which pose a high concentration of the dust cloud. Afterwards, these characteristics were significantly affected by the gas flow distribution in a time lapse that began after 40 ms of dispersion and finished 40 ms later. During this stage, the vorticity structures were clearly identified and the decrease of the local concentrations at the low regions of the tube was also evidenced. Finally, the time period that began after 60 ms of dust dispersion established a different behavior of the dust cloud. During this period, the mixture is characterized by a smaller size of the vorticity structures and the sedimentation of some aluminum particles that are located near the tube walls.

As previously noted, some characteristics of the combustion process of the aluminum can vary significantly because of a change in the particle size distribution of the disperse phase in a particle-laden flow. For instance, the flame speed increases with decreasing aluminum size according to a specific $d_p^{-0.92}$ law (Huang et al., 2009). This fact is attributed to the enhancement of the oxygen diffusion that comes from a decrease in the particle size (Bouillard et al., 2010). For this reason, the evolution of the PSD was also determined for the 100 ms elapsed since the beginning of the gas injection. For this purpose, the granulometric analyses were developed in measurement cycles of 1 ms and reported for intervals of 5 ms.

The particle size distribution is associated to the ratio between the dispersion forces exerted by the fluid and the adhesion forces of the solid particles. Evidently, in the early stages of dust dispersion, the dispersion forces are equal to or stronger than the maximum adhesion force of the aluminum aggregates. Then, the decrease of these forces, which is caused by the expansion of the gas and the friction of the flow, reduces the efficiency of the dispersion and favors other phenomena such as the agglomeration or sedimentation of the dispersed particles (Masuda, 2009). Therefore, the stages of the dust dispersion process can be defined according to the variations of the size distribution as well. This division is described as follows:

- ***Instability stage (0 ms - 40 ms):*** A detailed analysis of the first frames posed that during the first 40 ms of the dispersion process, the mean velocity of the dust cloud front was approximately constant. This fact can be attributed to the fragmentation process because the initial particle size distribution (Figure 3.3) exhibited a high standard deviation. This condition shows that the size disparity of the aluminum sample can be reduced by the aerodynamic stresses exerted by the fluid flow. Indeed, Weiler et al. (2010) established that the PSD varies significantly during this process due to the velocity field of the gas flow and the impaction of two or more colliding agglomerates. These conditions are established by the high relative velocities between the two phases, which cause not only the aggregates lift but also their fragmentation. For this reason, it is necessary to take into account the influence of some properties of the sample of combustible dust such as its weight and the particle density in order to establish their influence on the energy dissipation produced throughout the dispersion tube.

  Figure 3.25 describes the rise of the dust cloud inside the tube through the evolution of the size distribution at the height of the electrodes in the dispersion tube (10 cm). The fragmentation levels have been established for two different samples of micrometric aluminum. The comparison of the PSD profiles shown in Figure 3.25A and Figure 3.25B pose that both samples undergo an important reduction on their mean sizes during their dispersions. However, the displacement of the distributions is more evident for the largest particles (micro-Al 42). Indeed, the mode of the distribution of these particles is reduced until 11 µm approximately (13% of the initial value) whereas it is diminished until 2 µm approximately (20% of the initial value) for the micro-Al 7 particles. This aspect becomes a determinant for the eventual combustion of the dust cloud after considering that the particle burning-time model switches from the $d_p^{1.8}$ law to either the $d_p^{0.3}$ or the $d_p^{1.0}$ law at a particle size of around 12 µm (Y. Huang et al., 2009). Additionally, some inertial effects were evidenced for the micro-Al 42 particles during the first stage of dispersion. In fact,

these effects ease the fluidization of the largest aggregates and contribute to their early detection at the height of the ignition sources.

- ***Transition stage (40 ms - 80 ms):*** This period can be noticed when the two-phase flow is redistributed through the ignition zone (10 cm over the nozzle) due to the vorticity induced by the walls and the high turbulence of the fluid. During this stage, the injected air flows at slower velocities as well as the solid particles. Moreover, the large vorticity structures rose along the tube whereas the low regions evidence a low solids concentration, which can be attributed to the rising of the bulk flow. This fact implies a decrease in the drag forces that reduce the mean size of the powder. Nevertheless, it is necessary to take into account that the collision probability at the ignition zone of the tube is still high (Masuda, 2009). These facts constitute small variations of the PSD distribution because the turbulence of the flow is still high in spite of the energy dissipation.

- ***Stability stage (80 ms - 120 ms):*** The final period is clearly evidenced by the similarity of the last two images of Figure 3.24. These pictures show that the rising currents of the dispersed solid have almost disappeared. This fact implies that the sedimentation process of the dispersed particles is favored as well as the agglomeration because the dispersion forces are weaker than the adhesion forces (A. Li & Ahmadi, 1992; Weiler et al., 2010). Moreover, the stabilization that is evidenced at 120 ms indicates the absence of large vorticity structures and the reduction of the turbulence levels of the two-phase flow. This fact represents a technical advantage for the development of a flammability test because a high turbulence might interfere with the development of the flame front and favor the energy dissipation. For this reason, this stage is recommended for the dust ignition. Nevertheless, the dissipation of the rising currents and the turbulence reduction promote the solids aggregation and sedimentation; hence it can be advisable to ignite the combustible cloud before the standardized ignition delay (120 ms).

  According to the results obtained by the experimental tests, a minimum ignition delay of 60 to 80 ms is recommended for the ignition of the Micro-Al 42 dust cloud whereas a Micro-Al 7 dust cloud can be ignited in a period elapsed between 80 and 100 ms. The different ignition delays are defined because the PSD of the fine dust is not affected as the coarse one by the turbulence of the gas flow.

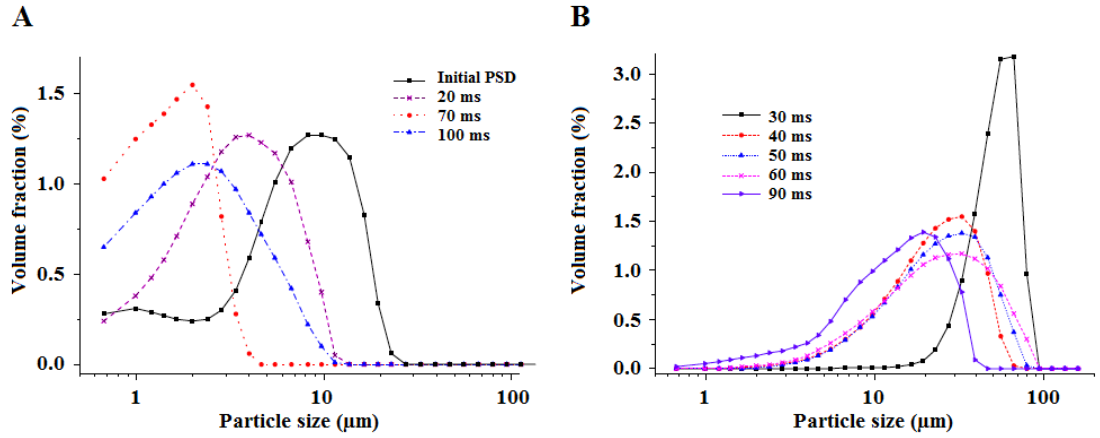

Figure 3.25. Evolution of the PSD of aluminum micrometric particles during their dispersion. A. Micro-Al 7 aggregates (PSD below 15 µm) B. Micro-Al 42 aggregates (PSD below 125 µm)

The adjustments of the ignition delays can be considered to achieve the most conservative conditions for the analysis of the combustion process of this metallic powder. These results will be compared to the numerical results that were obtained with the computational approach. However, similar phenomena can occur with other powders, but not necessarily with the same behavior. Hence, it should be remarked that these results are only valid for a specific powder because an important change of the physical properties of the material will lead to different dispersion characteristics.

B. *Dispersion of micrometric wheat starch*

The conditions that were evidenced for the dispersion of micrometric wheat starch were compared with the results that were analyzed in the previous section for the aluminum dust. Initially, Figure 3.24A and Figure 3.26A show that the starch dust has achieved a height equal to 5 cm approximately after the first 20 ms of dispersion whereas the aluminum has risen to 7 cm. This condition was observed for the subsequent time steps as well. For this reason, it is possible to establish that the rising velocities of the bulk of the dust cloud of the organic dust were slower than the velocities of the metallic one. Hence, there is a significant difference between the transient conditions of the former dust cloud and the latter. This condition was observed in all the tests in spite of the higher density of the metallic dust.

The SEM images (Figure 3.1 and Figure 3.4) showed that the shapes of the solid particles do not differ significantly. Therefore, the drag coefficients do not represent significant variations for the rising velocities of the combustible dusts. These characteristics establish that the differences found in the rising velocities of the dust clouds can be explained by a higher fragmentation level of the aluminum. Indeed, the aluminum powder is submitted to an increase of the total surface of the solid sample that is caused by the augmentation of the amount of small aggregates of aluminum. This condition enhances the drag force that is exerted by the gas on the solid phase. Moreover, the dust with the smallest average size constitutes a fully developed dust cloud more quickly and more easily (Yuan et al., 2012). For these reasons, the instantaneous position of the bulk of the dust cloud is not the same for the two combustible dusts at the moment when the mixture is ignited.

Another remarkable aspect of the characteristics of the dispersion process of the wheat starch relies on the development of some internal eddies that are clearly evidenced near the walls at the bottom of the tube (Figure 3.26C to Figure 3.26E). They can be explained from the influence of the injection nozzle on the distribution of the two-phase flow. The images show that the geometry of the injection system directs the flow towards the internal walls of the tube. As a consequence, the vortex structures that are observed in this region are larger than the structures that are developed elsewhere. This condition was more easily evidenced with the organic powder because of its low particle density, which determined a greater number of particles.

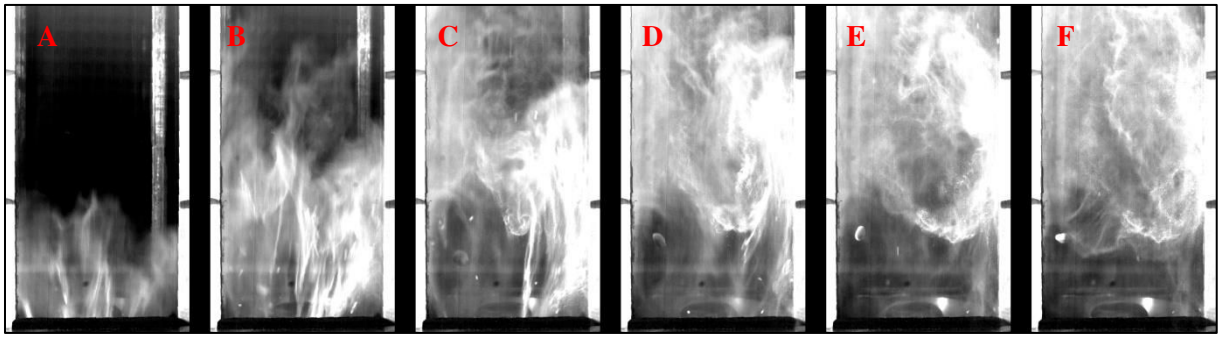

Figure 3.26. Dispersion of the starch micrometric dust with an injection at 7 barg
A. 20 ms B. 40 ms C. 60 ms D. 80 ms E. 100 ms F. 120 ms.

Furthermore, Cuervo et al. (2014) analyzed the unsteady behavior of the combustible dust cloud of wheat starch inside the modified Hartmann tube with a PIV analysis. This study was performed with a discontinuous laser (Dantec Dynamics) that set a double pulsed light sheet. The dispersion process was recorded with a CCD camera that was set to a resolution of 1.008×1.016 pixels. This setup described the variations of the flow turbulence in the region located between 6.5 cm and 14 cm over the dispersion nozzle, which is the region of interest of this work because it is the zone where the ignition sources are located (10 cm). Their experimental results established that the mean value of the horizontal velocity remains stable and almost null in the region of interest (Figure 3.27B). On the other hand, Figure 3.27A shows that the vertical velocity and its fluctuations posed a big difference between the turbulence levels that were determined at the two limit heights of the interrogation window. This

fact was attributed to the energy dissipation of the dust cloud during the dispersion and the different rising velocities of the solid particles. However, the experimental tests made it possible to determine the tendency of the vertical velocity of the two-phase flow. When the dust cloud rises up to the electrodes height, the vertical velocity and its fluctuations increase due to the gas injection during 25 ms approximately. Then, a stable decrease is observed in these variables until 100 ms of dust dispersion have elapsed. Afterwards, a transition stage is evidenced when the slope of the curve increases until a limit value during a temporary phase that lasts 40 milliseconds approximately. Finally, the mean vertical velocity is approximately zero in a stage that is characterized by the sedimentation of the solid phase.

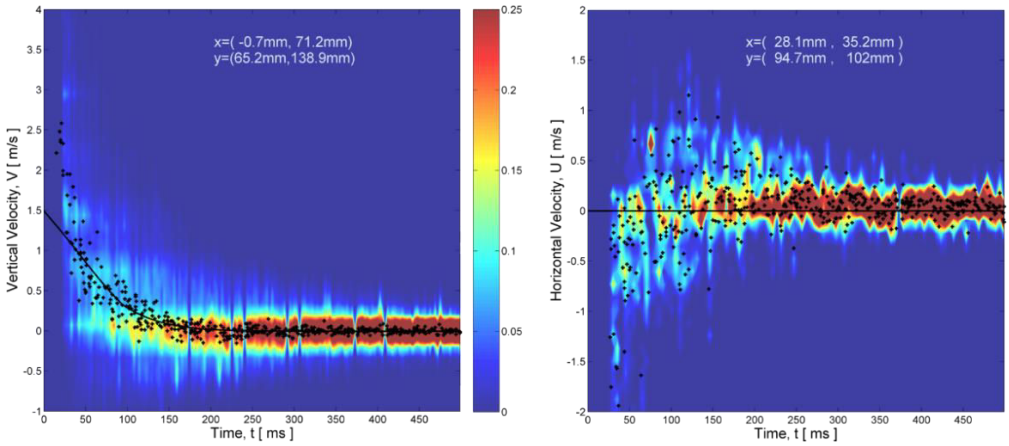

Figure 3.27. Vertical (left) and horizontal (right) velocities versus time in a square tube for 70 dispersions of 78 mg of wheat starch.
(Cuervo et al., 2014)
Black dots: Mean velocity of the vector field

Finally, Cuervo et al. (2014) also discussed the significant differences that were found on the rising and sedimentation of different powders. For this purpose, their PIV analysis considered the dispersion of glass beads as well. The particle density of this material (1600 kg/m^3) limited the maximum analysis time. This restriction was originated by the drastic decrease in the particle density in the interrogation window. Even if, the latter experiment has been carried out with a non-combustible dust, this fact also confirms the need to adapt the ignition delay of a powder according to its physical properties.

C. *Influence of the injection pressure on the flammability parameters of the modified Hartmann tube*

The high-speed videos were also considered for the analysis of the influence of one of the main parameters of the flammability test performed with the modified Hartmann tube. For this purpose, a sensitivity analysis was established for the injection pressure in the description of the dispersion of micrometric wheat starch. Thus, the effects of this variable are discussed in this section given the relevance of the ignition delay and the internal conditions of the combustible dust cloud on the experimental determination of the flammability parameters.

Initially, the pressure of the injected gas was varied between 3 and 6 barg in order to compare the characteristics of the dust clouds that are developed under these conditions with the characteristics of a dust cloud that is established under the standardized value (7 barg). The description of the influence of this test parameter on the segregation level of the solid phase was performed with the analysis of Figure 3.28. The results pose a similar rising velocity of the bulk of the dust cloud for the injections between 4 and 6 barg. Hence, the main differences can be associated to the temporal turbulence of the gas-solid mixture. The comparative study of the dispersion process of the two-phase flows that were developed during this sensitivity analysis showed that the fragmentation levels are increased when the

pressure is augmented. Moreover, the injections performed at 3 and 4 barg pose a very low capability to break up the largest agglomerates. On the other hand, the conditions of the other two injections are very similar to the conditions of the standard value and present a very low number of large aggregates.

Furthermore, the increase of the injection pressure causes a continuous deformation of the rising profile of the bulk of the dust cloud. This condition is due to the inertial effects exerted on the largest aggregates which tend to have higher velocities during the initial stage and during sedimentation. Therefore and once again, it is necessary to consider the main characteristics of the particle size distribution in the samples that are commonly used in a typical flammability test in order to set the appropriate value for the injection pressure.

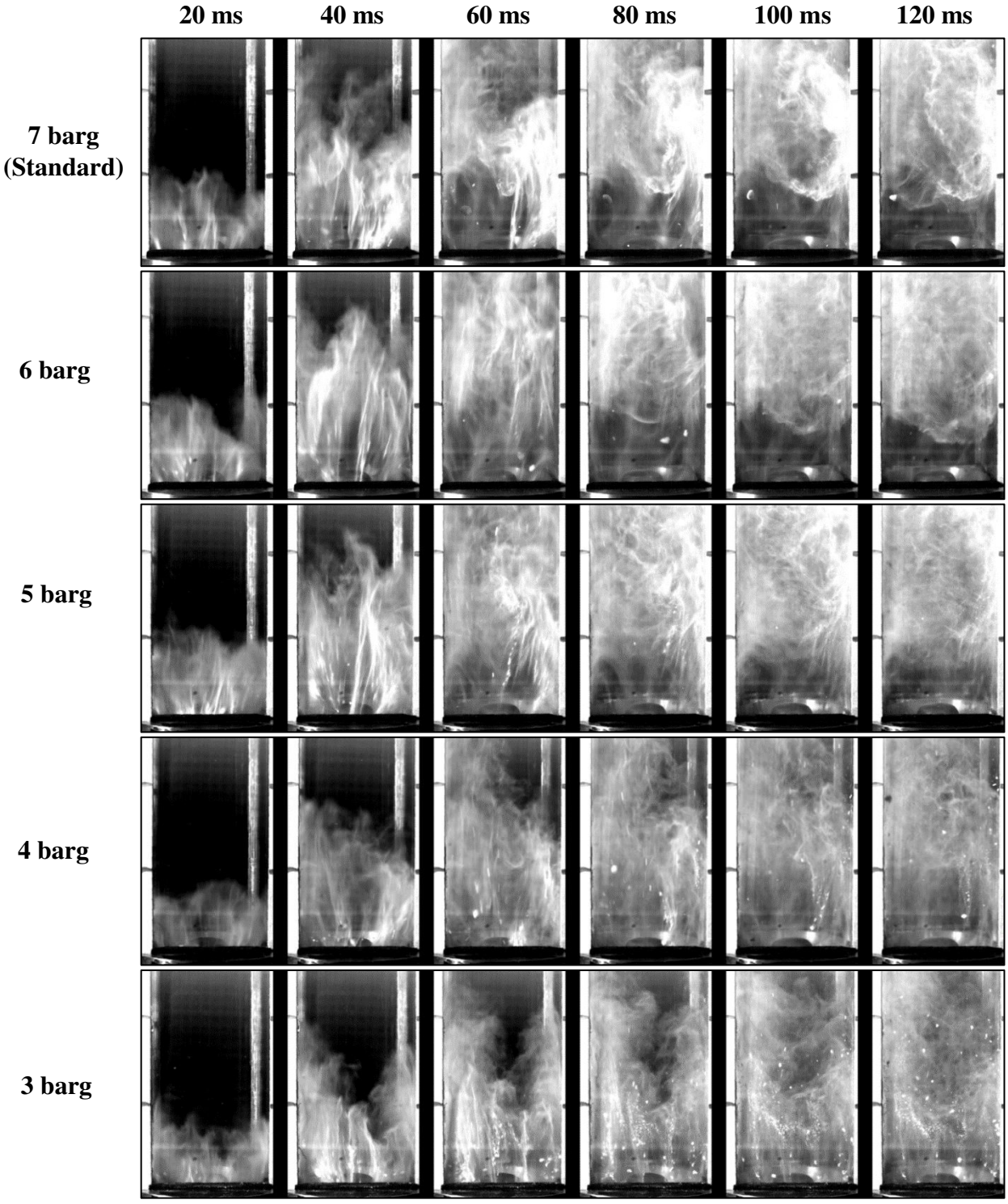

Figure 3.28. Sensitivity analysis of the injection pressure

The analyses performed on the videos show that the rising velocities of the dust cloud are very similar for the pressure injections that range between 4 and 6 barg. Nevertheless, the segregation levels have significant variations for the analyzed starch samples. These characteristics of the two-phase flow have been considered through a comparative analysis of the turbulence of the gas flow and the distribution of the combustible dust inside the dispersion tube.

Moreover, it is also necessary to discuss the influence of the nozzle on the spatial distribution of the dust cloud. The experimental results shown in Figure 3.29 present the upper view of the dispersion process that develops inside the modified Hartmann tube throughout the sensitivity analysis that is proposed for the injection pressure. The examination of the radial distribution of the two-phase flow allows establishing the evolution of the bulk of the flow. The frames obtained during the first 40 milliseconds show how the gas flow is directed towards the walls at the bottom of the tube and they also indicate the fast lift of the largest aggregates. Additionally, all the profiles have very similar tendencies for the segregation of the solid material. Indeed, the main difference among the injection pressures relies on the depth of the front of the rising bulk of the dust cloud. As a matter of fact, the maximum level of homogeneity of the cloud is achieved after 60 ms of dust dispersion for all the injections, but it is evidenced at different heights nonetheless. Finally, these conditions allow concluding that the radial distribution of the powder is mainly defined by the nozzle whereas the axial distribution and the turbulence levels are defined by the pressure of the dispersion gas.

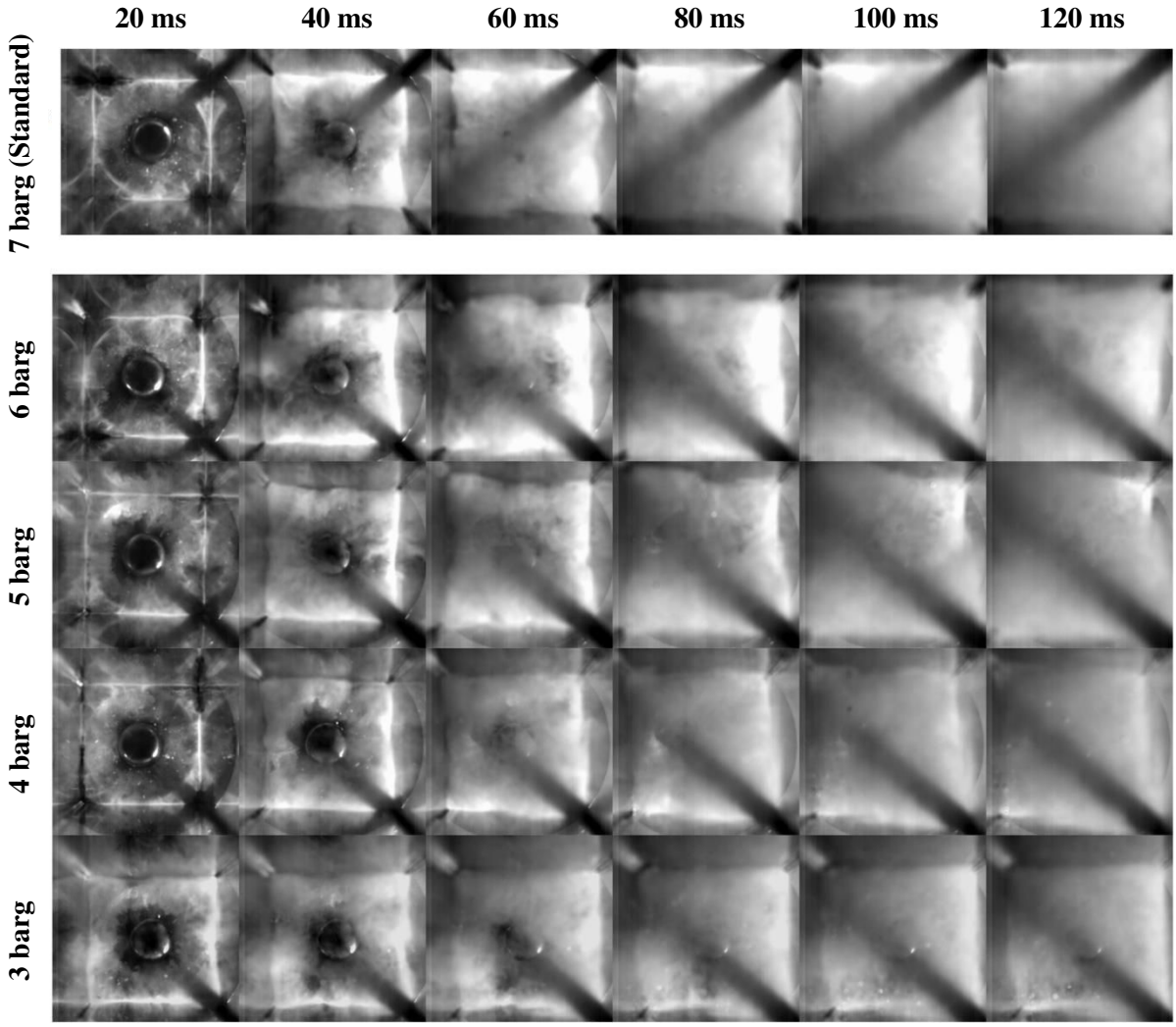

Figure 3.29. Radial distribution of micrometric wheat starch with different injection pressures.

The different distribution of the flow explains the generation of the vortex structures that were shown in Figure 3.24 and Figure 3.26. The gas flow will rise more slowly near the walls and will induce a high vorticity in the flow and the accumulation of the dust. It also poses that the zones with high

turbulence are located in the middle of the lowest regions of the flow domain of the vessel and away from the walls at the middle of the dispersion column. These results present the geometry of the dispersion nozzle and the location of the injection as interesting variables for future descriptive analyses of the flammability characterization tests. It will also be interesting to relate the flame velocity with the turbulence of the dust cloud during ignition (Di Benedetto et al., 2011).

Furthermore, the variations that modify the turbulence levels of the gas flow also affect the particle size distribution of the combustible dust which is susceptible to fragmentation (Weiler et al., 2010). These variations are an aspect of main interest due to the segregation levels and the flow distribution that were observed experimentally. The characterization of the fragmentation phenomenon was performed by establishing the variations of the mean diameter with granulometric analyses. This description was determined by placing 0.6 grams of the organic powder at the bottom of the standard apparatus in order to obtain a nominal dust concentration equal to 500 $g \cdot m^{-3}$. Then, the evolution of the PSD was determined for the 140 ms elapsed since the beginning of the gas injection. For this purpose, the granulometric analyses were developed in measurement cycles of 1 ms and reported for intervals of 5 ms. The experimental results that are shown in Figure 3.30 describe how the highest pressures enhance the fragmentation of the starch agglomerates dispersed in the gas:

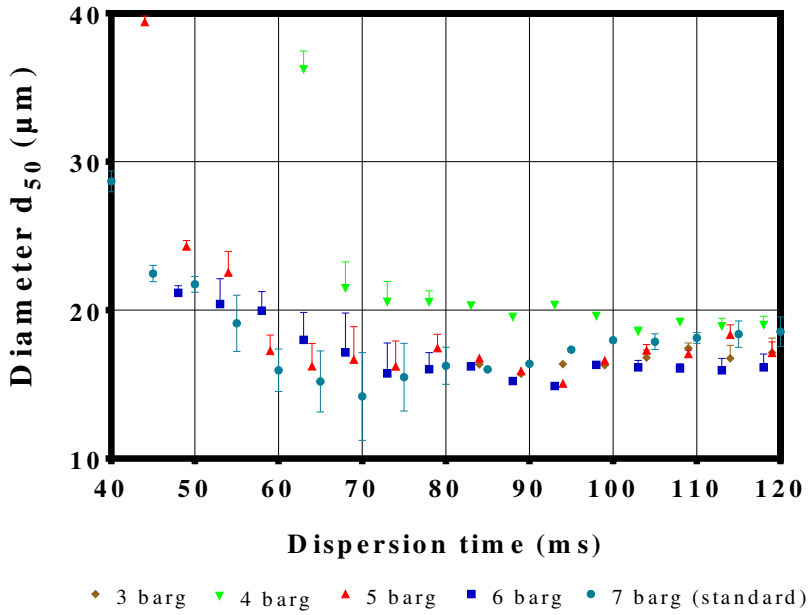

Figure 3.30. Particles size distributions at 10 cm over the nozzle for the different pressure injections.

The diameter d_{50} shows a similar behavior with regard to the variables previously discussed due to its significant variations during the first 80 ms and its subsequent stabilization. However, this parameter also provides useful information for the adjustment of the injection pressure. Indeed, the injections at 5 and 6 barg cause a substantial decrease of the mean diameter which is 18.85% lower than the minimum value obtained with the lowest pressure. This fact becomes more important if the influence of the size distribution on the dust ignitability is considered (Eckhoff, 2003). Nevertheless, it is necessary to take into account how the agglomeration phenomenon, which is attributable to the cohesion of the solid material, reduces the differences in the mean diameter of the dust cloud at the height of the ignition electrodes. For this reason, it is possible to consider the brief time elapsed between 80 and 120 ms as the period with the lowest values for the diameter d_{50} which imply very small size distributions. Therefore, the results of this study suggest that the ignition of the micrometric wheat starch for determination of the dust flammability parameters in a modified Hartmann tube should be performed with a time delay adjusted for this specific period of time.

Moreover, the differences that are observed in the mean diameter profiles can also be explained by a comparison of the turbulence levels achieved by the analyzed injection pressures with regard to the standardized value. In accordance with these results, the modification of the injection pressure is also

suggested for this combustible dust in order to achieve a significant reduction of the size of the disperse aggregates with low turbulence levels respect to the standard parameter value. For this purpose, the flammability test of the modified Hartmann tube can be performed with an injection at 5 or 6 barg. Nevertheless, it is necessary to take into account the limitations posed by the powder because a reduction of the turbulence also limits the ignition delay due to the sedimentation and agglomeration of the dispersed particles.

Furthermore, the granulometric analyses also considered the variations of the particle size distribution at different positions within the dispersion tube. Figure 3.31 shows the evolution of the diameter d_{50} at three heights over the dispersion nozzle: 5 cm, 10 cm and 15 cm. The high-speed videos showed that the variations of the rising velocity caused different concentrations along the tube. This condition was attributed to the development of the two-phase flow at the low regions of the tube and the energy dissipated as the flow rises. This condition also affects the particle size distribution since the fluidization and fragmentation levels of the solid sample.

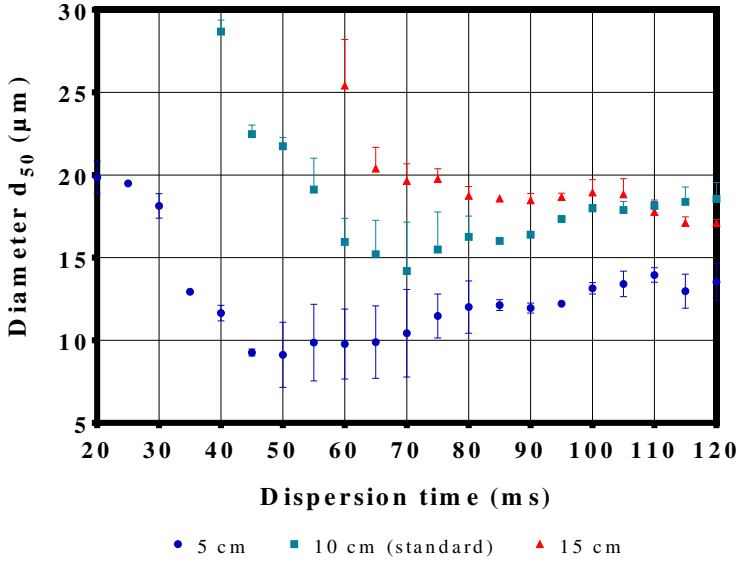

Figure 3.31. Particles size distributions at different heights for an injection at 7 barg.

Figure 3.31 shows that an ignition at 5 cm represents a smaller mean particle diameter (d_{50}). This condition is caused by the high turbulence levels achieved by the two-phase flow at this point. This condition might represent a higher dust ignitability due to the reduction of the particle size. However, it is necessary to take into account that this variation is caused by the high turbulence and stresses exerted by the gas flow at this point. Therefore, it is not advisable to install the ignition sources at this point. Moreover, a high ignition point is not advisable either in spite of reaching the same mean particle size. The dust stratification observed in Figure 3.26 posed that the bulk of the cloud reached the middle of the tube (15 cm) 60 ms after the beginning of the dispersion process with a visual concentration that may be too low to determine the dust ignitability. The facts allow concluding that the height proposed by the international standards is appropriate for the flammability tests. Nevertheless, it also poses an important interrogation about the evolution of the turbulent kinetic energy inside the tube. For this reason, this variable was analyzed in the computational approach developed subsequently.

The experimental results of this study suggest that the determination of the ignitability of a combustible dust in a modified Hartmann tube should be performed with an adaptation of the conditions to form a dust cloud and the ignition delay. These adjustments will form a well-dispersed dust cloud and establish a turbulence level that represents a sufficient reduction of the particle size distribution without reducing significantly the ignitability of the cloud by energy dissipation.

The descriptive results obtained with the experimental tests will be complemented with the computational characterization of the two-phase flow that will be discussed in the next chapter. This complementary analysis will allow determining the operating parameters of the modified Hartmann tube that can provide the most conservative information about the ignitability of the two combustible dusts. Likewise, the next part of this chapter will describe the experimental tests that were proposed for the description of the dispersion process in the 20 L sphere in order to characterize the dispersion process inside this test apparatus in the same way that was proposed for the dispersion tube.

3.6 DETERMINATION OF THE CHARACTERISTICS OF THE DUST DISPERSION INSIDE THE 20 L SPHERE

The dispersion process of a combustible dust inside the 20 L sphere was described by different methods that determined the internal conditions of the two phases of the particle-laden flow. In accordance with this objective of the research project, the experimental approach that was proposed for the descriptive analysis is discussed in this section. The first two subsections discuss briefly the apparatus and the nozzle that were built for the development of the characterization tests. Afterwards, the set of experiments that was considered for this stage of the research project is explained in section 3.6.3. For this purpose, the influence of certain variables of the test on the evolution of the dust cloud was determined by the methods that were detailed in sections 3.2 and 3.3.

Finally, the results of the experimental tests that were carried out for the experimental description of this study are analyzed in Section 3.6.4 in order to discuss the variations of the behavior of the dust cloud during the dispersion process and the influence of the operating variables that were considered.

3.6.1 Experimental setup

The descriptive study of the behavior of a combustible dust cloud in the 20 L sphere is hard to accomplish because of the design specifications of the dispersion vessel. The standard apparatus is conceived to remain rigid as a flammability test is carried out. For this reason, it is not composed of a visualization window big enough to provide some useful information about the dispersion of the dust. For this reason, a whole new dispersion vessel was constructed in order to obtain a visualization field from different views. The apparatus that is shown in Figure 3.32 was built with stainless steel and was installed on the outlet valve of the experimental setup in order to replace the original chamber.

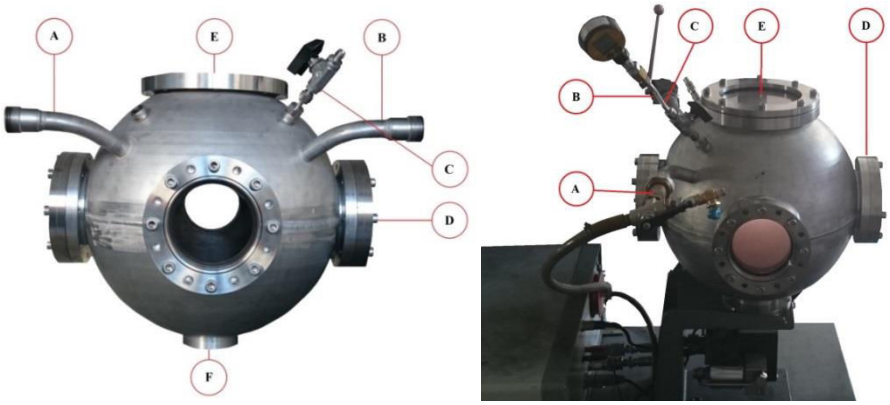

Figure 3.32. Dispersion sphere
A) Vacuum system B) Venting C) Valve for manometer D) Lateral window
E) Upper window F) Tube for the outlet valve

Some modifications were included in the design of this vessel to make it suitable for a dispersion analysis. For this purpose, five windows have been placed in the structure of the chamber to provide several points for the visualization of the dust cloud. There are four circular windows located at the lateral extremes of the apparatus and another one on the top of it. On the one hand, the lateral windows are made of borosilicate with a diameter of 9.7 cm and are sustained by flanges. They were utilized for the data acquisition through the recording of high-speed videos and for the temporary pass of the laser beams as shown in Figure 3.7 and Figure 3.8. On the other hand, the window that is located at the top of the vessel is made of polymethyl methacrylate and has a diameter of 14 cm. This window was used for the recording of the dispersion process from an upper view and for cleaning purposes.

However, the modifications pose several restrictions that forbid the implementation of this chamber on a typical flammability test. The use of supported glass windows limits the maximum pressure that can be handled on the sphere without causing its failure and the release of the contained materials. For this reason, the new sphere was only conceived for the analysis of the dispersion process. This fact determined that it was not necessary to include the cooling system on the apparatus.

3.6.2 Dispersion nozzles

Currently, the explosibility of dust clouds can be determined by following the procedures described in the international standards that were discussed in Section 1.5.3. These standards report the perforated annular ring and the dispersion rebound nozzle as the two alternatives for the injection system that must be placed inside the explosibility test chamber (Figure 1.15). These nozzles have been developed for the assessment of the explosion hazards with the 20 L sphere in technical configurations that are intended to provide the optimal dispersal arrangement.

The standard rebound nozzle was developed by Siwek (1988) after considering the flammability parameters that were determined with the perforated ring in the 20 L apparatus for certain powders that are usually utilized in the food industry. The results obtained for these combustible dusts were within the limits of the experimental error of the 20 L apparatus (5-10%) and were considerably lower than the results obtained with the 1 m^3 container as well. Thus, these conditions were attributed to a high difficulty of the discharge process performed with the perforated ring (Siwek, 1988). Hence, the rebound nozzle was developed as a new dispersal arrangement that might replace the customary ring. Then, the results obtained by Siwek determined that the nature of the nozzle did not have a significant effect on dusts with a good flow behavior. On the other hand, this is not always the case for the products with a poor flow behavior (e.g. cellulose & cornstarch). Finally, this study concluded that the rebound nozzle could be a replacement for the perforated ring because it could eliminate the common problems that are found with the other injection system.

These variations in the dust concentration inside the test apparatus pose an interesting question about the homogeneity of the dust cloud due to the unequal distribution of certain powders during the injection. Moreover, the experimental evidences establish that an injection system may represent a more convenient alternative for the distribution of some combustible dusts. For this reason, some similar studies (Dahoe et al., 2001; Zhang & Zhang, 2015) developed some new injection nozzles that were designed to favor the homogeneous distribution of the two-phase flow. They are shown in Figure 3.33.

On the one hand, the Dahoe nozzle produces high jets which sustain their velocity and their preferential direction for long periods of time (Dahoe et al., 2001). For this purpose, the flow is injected through a unique front that rises near the internal walls of the vessel. This system has posed some similar characteristics to the ones observed with the standard rebound nozzle (Mercer et al., 2001). On the other hand, the half spherical nozzle developed by Zhang & Zhang (2015) consists of several holes at the surfaces of the nozzle that create a group of jets that are directed towards many regions of the vessel. This nozzle constitutes a more homogeneous distribution of the combustible dust but represents a reduction of the mean velocity due to the generation of many thin jets (Dahoe et al.,

2001). This device was used for the characterization of the influence of the ignition delay on the experimental characterization of the explosibility parameters of the corn starch.

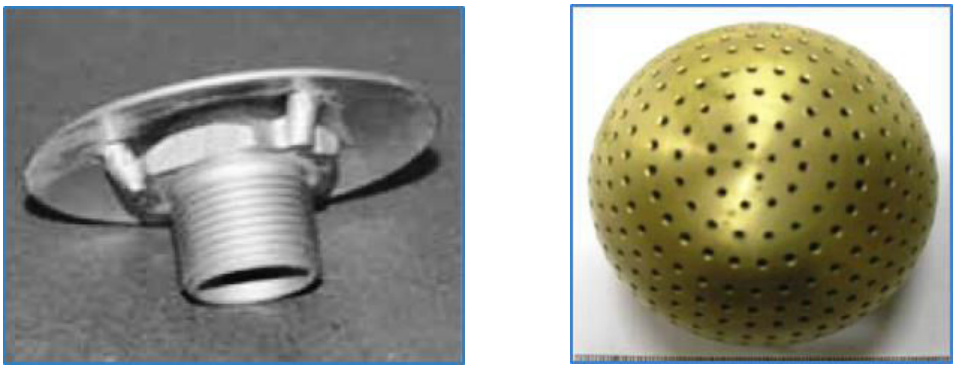

Figure 3.33. Dahoe nozzle & half spherical nozzle (Dahoe et al., 2001; Zhang & Zhang, 2015)

In accordance with the studies discussed above, the description of the dust dispersion was also performed with a new nozzle that was constructed for the experimental analyses. The injection process developed by this device was compared with the injection generated by the standard rebound nozzle. The design of this injection is specified in Section 3.6.4A.

3.6.3 Set of experiments

The experimental tests that were developed with the 20 L sphere were performed with micrometric wheat starch. These tests were intended to analyze the influence of certain operating parameters that define the main characteristics of the combustible dust cloud before its ignition. Indeed, the experimental tests that were considered for the description of a particle-laden flow in the modified Hartmann tube were utilized for this case too. For this purpose, four variables were studied in order to establish their influence on the experimental results of a flammability test. An explanatory scheme of the descriptive tests that were performed with this apparatus is shown in Figure 3.34:

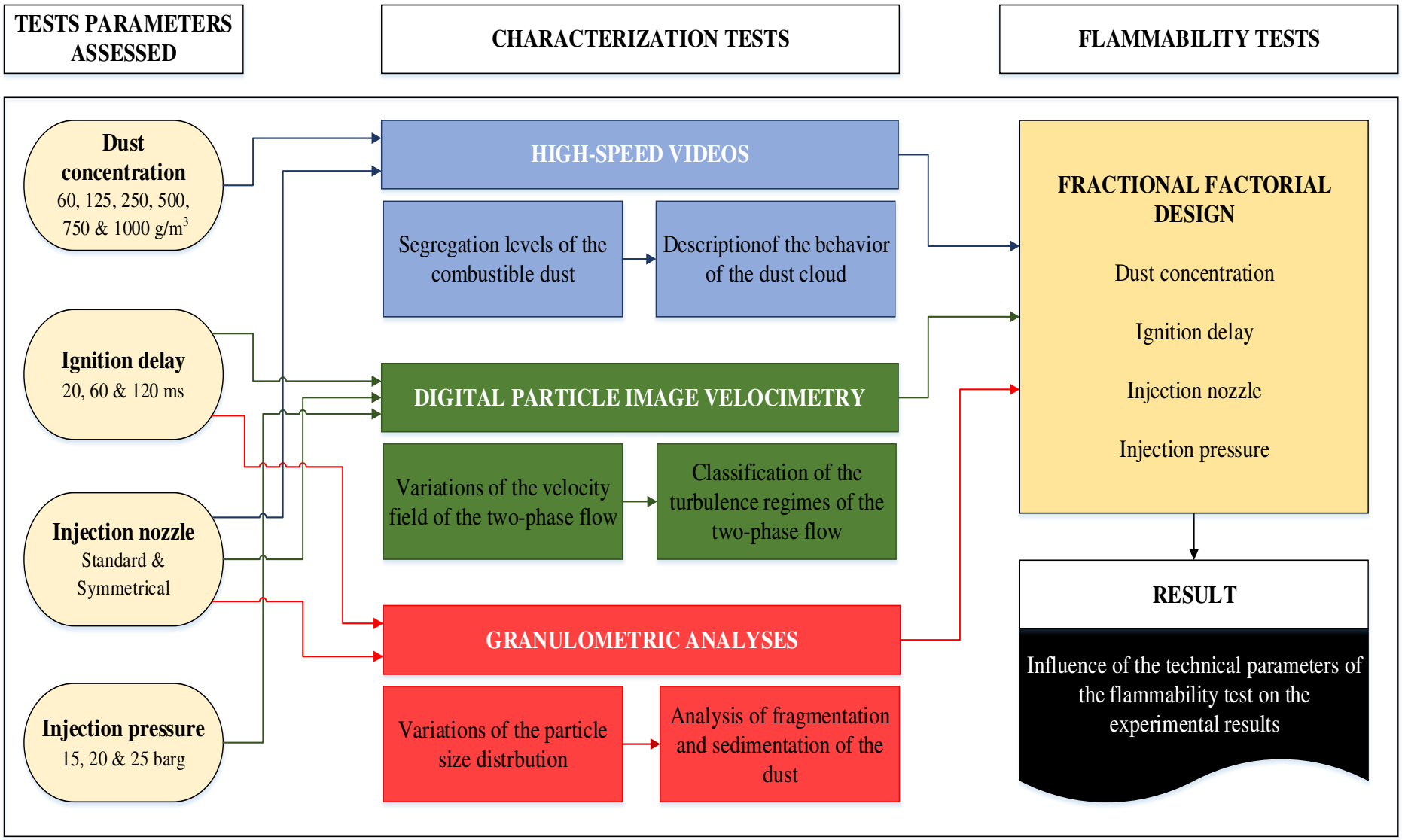

Figure 3.34. Set of experiments with the 20 L sphere

Initially, the evolution of the dust cloud was filmed with a high-speed camera in order to constitute a qualitative analysis of the behavior of the dust cloud by identifying the segregation levels of the dust within the sphere. These results provided an insight about the concentration of the dust in the biphasic mixture and the time lapse that should be analyzed in the subsequent descriptive tests of the experimental approach. Afterwards, the macroscopic behavior of the cloud was associated to the phenomena that characterize the two-phase flow by two complementary means. For instance, the variations of the turbulence of the flow were studied through a DPIV analysis, which established the different regimes that are constituted by the turbulent kinetic energy dissipation of the flow. Afterwards, the experimental results that were obtained with this test were considered to describe the variations of the particle size distribution of the combustible dust that is caused by the aggregates fragmentation and sedimentation.

Furthermore, some operating parameters were modified during the development of the description tests in order to establish their influence on the evolution of the dust/air mixture. Therefore, the injection pressure of the dispersion gas was set to a value greater than the standard and to a lower one as well. Likewise the new injection nozzle was also considered to study the influence of the geometry of the injection device on the distribution of the powder in the vessel. The comparative analysis of the standard rebound nozzle and the new prototype was accomplished by filming the injection of the flow and identifying the variations in the velocity field of the gas flow and the fragmentation levels of the solid material.

Finally, the flammability characterization test of the micrometric wheat starch was submitted to a fractional factorial design analysis that considered certain values of the four analyzed variables and determined their actual influence on the experimental results obtained with the 20 L sphere.

3.6.4 Experimental analyses

A. *Dispersion videos*

The first analysis of this phase was associated to the comparison of the segregation of the combustible dust that is caused by the flow injection. The influence of the injection system was established by analyzing the variations in the intensity in a high-speed video that was recorded for the surroundings of the rebound nozzle. For this purpose, the experimental setup that is shown in Figure 3.35 was set for the dispersion sphere that was constructed for the research work of this thesis. The set-up consists of a high-speed video camera (B) that was installed to provide a clear description of the dispersion process from a top view. This device is supported by an illumination lamp (A) that is installed to improve the images recorded by the camera. Besides these two elements, this set-up is also composed by the granulometer HELOS/KR (B) and a computer (D), which will be discussed below.

The high-speed video camera was set to a resolution of 1632 x 1200 pixels and an exposure of 990 µs in order to obtain a sample rate of 1000 fps. These settings were defined to focus the recordings on the regions that surround the rebound nozzle. These videos can be analyzed in two different stages to analyze the influence of the nozzle on the flow distribution and the subsequent evolution of the dust cloud. The former corresponds to the first 10 ms of dust dispersion and the latter to the following 110 ms.

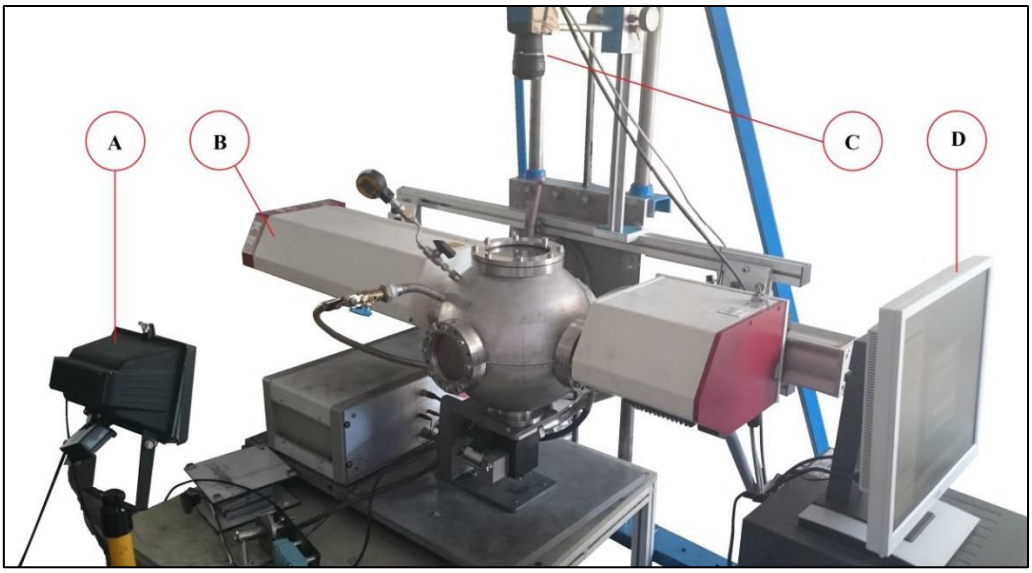

Figure 3.35. Experimental setup established for the granulometric analyses and the recording of high-speed videos in the 20 L sphere
A) Lamp B) Granulometer HELOS/KR C) High-speed video camera D) Analysis PC

Figure 3.36 presents the first stage of the flow injection seen from the top of the dispersion chamber. The results clearly identify three jets that constitute the two-phase flow in the dispersion chamber. The images evidence an unequal distribution between the two jets that are directed towards the extremes of the nozzle and the one that develops at the middle of it. This fact represents an important characteristic of this standardized configuration of the 20 L sphere. In fact the two fronts developed at the extremes of the nozzle expand quickly due to their high pressure respect to the sphere that is initially at 0.4 bars. On the other hand, the middle front, which is injected through the 3 central holes of the nozzle, is directed towards the geometric center.

Furthermore, Figure 3.36B shows two important regions that are located at the top and the bottom of the picture. These zones can be clearly identified because of the absence of combustible dust. This asymmetrical distribution of the solid phase within the sphere can be attributed to the characteristic shape of the rebound nozzle. Moreover, Figure 3.36C shows a high concentration zone that was observed in the middle of the sphere. This variation of the dust cloud was produced when the two fronts of the lateral flows collided. This collision was evidenced for micrometric wheat starch after 7 ms of dust dispersion. This behavior was also observed by Du et al. (2015), who recorded the dispersion process inside a transparent polymethyl methacrylate sphere and evidenced the same characteristics in the injected flow.

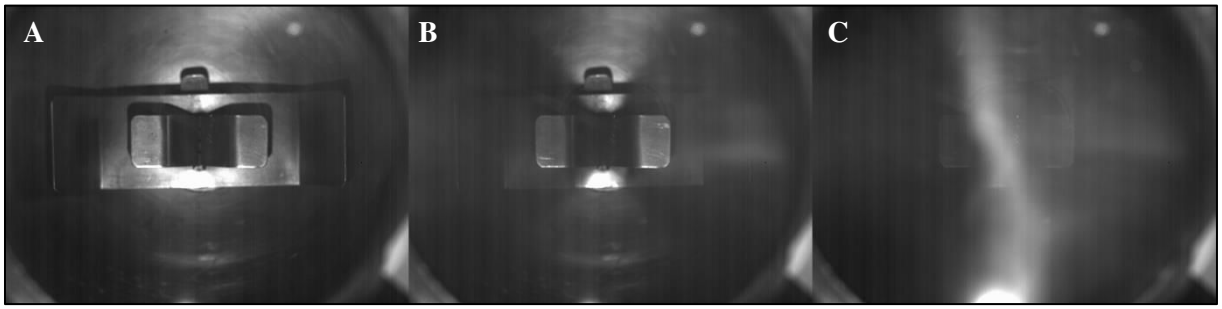

Figure 3.36. Injection of a combustible dust developed with the standard rebound nozzle
A) Empty sphere B) Injection jets C) Collision of the lateral fronts

The figure shown above also provides some basic information about the time that is required for the combustible dust to achieve a stable concentration inside the vessel. The frames allow establishing that the two fronts associated to the extremes of the nozzle will try to distribute the solid sample when their

trajectories coincide at the top of the dispersion vessel. This experimental result agrees with the results obtained by Kalejaiye et al. (2010). and Du et al., (2015). They have opted for the light transmission analysis to estimate the concentrations levels within the dispersion chamber of the apparatus in order to link the light transmission to the concentration of the dispersed phase.

The results obtained by Du et al. (2015) and Dahoe et al. (2001) also show that the concentration at the geometric center of the sphere increases during the first 8 ms and then remains stable until 50 ms. Afterwards, the sedimentation of the dispersed particles will reduce the concentration of the dust in the cloud. Indeed, these characteristics of the concentration profile of the combustible dust can be attributed to the pass of the solids that are injected through the middle of the dispersion nozzle and the subsequent pass of the bulk of the cloud. Initially, the powder that drops by this zone causes an instantaneous decrease of the light transmission in the detection device used by Du et al. (2015). However, these lumps of the combustible dust represent a minimum fraction of the solid sample and also go through this zone with a very high velocity. Then, the solids concentration will increase when the two fronts injected from the nozzle extremes arrive to the considered region. This condition was evidenced with the frames that were recorded for the DPIV analyses of the test apparatus as well.

Figure 3.37 shows the evolution of the dust cloud in the first 120 ms of the dispersion process. The color of the frames was modified to improve the contrast between the dispersed solid and the background of the images. The frames show the characteristic behavior of the two segregated flows after their collision. Previous studies developed by Mercer et al. (2001) have posed that these flows interact and combine to create a predominant downward flow in the region of the geometric center. This condition can be confirmed with the analysis of the first four frames (A-D) which show a significant accumulation of the dust at the middle of the vessel that comes from the two merging fronts. Afterwards, there is a displacement of this zone of high concentration because the right front was more intense than the left one. Nevertheless, this asymmetrical condition can be considered as temporal due to the injection of more gas from the nozzle. This asymmetrical stage can be attributed to the construction of the outlet valve assembly. Mercer et al. (2001) posed that the bulk of the injected air is channeled to one of the sides of the assembly because that path represents the least resistance for the flow. In fact, this side corresponds to the position where the pressurized canister is mounted. This characteristic influences the initial distribution of the dust in the vessel. From such observations, it is possible to affirm that a new injection system is necessary to constitute a symmetric distribution of the combustible dust.

The following four frames (E-H) show the dissipation of the regions with a high concentration in the two-phase flow (red zones). This condition is mainly caused by the turbulence of the flow and the internal eddies. These factors favor the homogenization of the mixture by distributing the powder within the vessel. Finally, most of the regions have a high concentration because the large lumps have been dissipated and the sedimentation process has begun for certain aggregates.

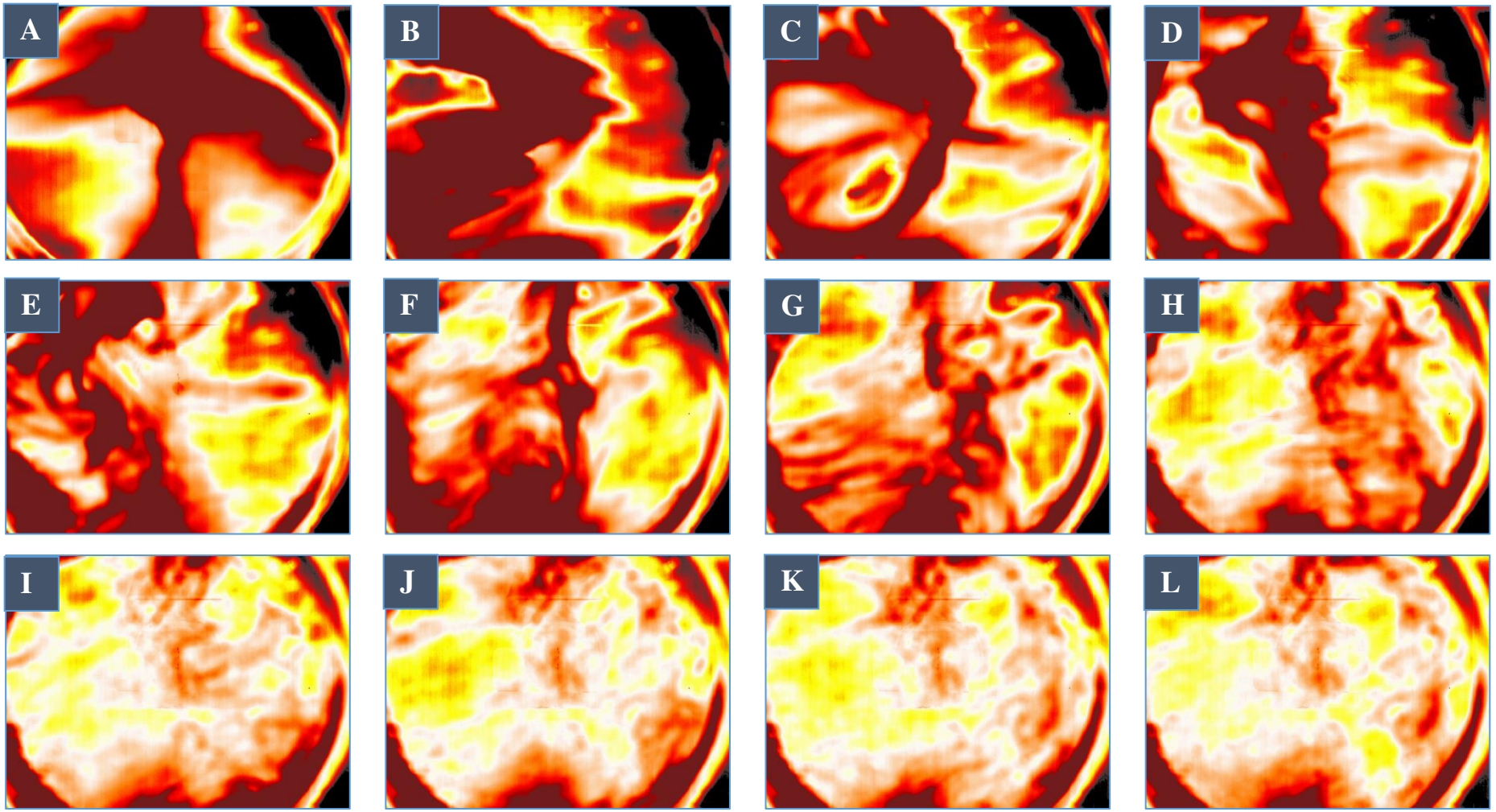

Figure 3.37. Evolution of the combustible dust cloud within the 20 L sphere
A) 10 ms B) 20 ms C) 30 ms D) 40 ms E) 50 ms F) 60 ms G)70 ms H) 80 ms I) 90 ms J) 100 ms K) 110 ms L) 120 ms

However, these researchers also affirmed that the dissipation of the largest lumps does not constitute the most representative scenario of a homogeneous cloud in spite of the stabilization of the dust concentration. For this reason, the injection of the particle-laden flow was also recorded with a new rebound nozzle that was designed for this study. This injection system was designed according to a similar conception of the standard rebound nozzle. Nevertheless, the new nozzle is distinguished from the standard system by its symmetrical shape which is intended to spread out the combustible dust inside the dispersion vessel under a more homogenous distribution.

The modification of the standard rebound nozzle was accomplished with a reduction of the diameter of the base-plate of the nozzle and an increase of the angle of the bends of its extremes. Figure 3.38 shows the symmetrical rebound nozzle that was designed for the descriptive analyses of the two-phase flow.

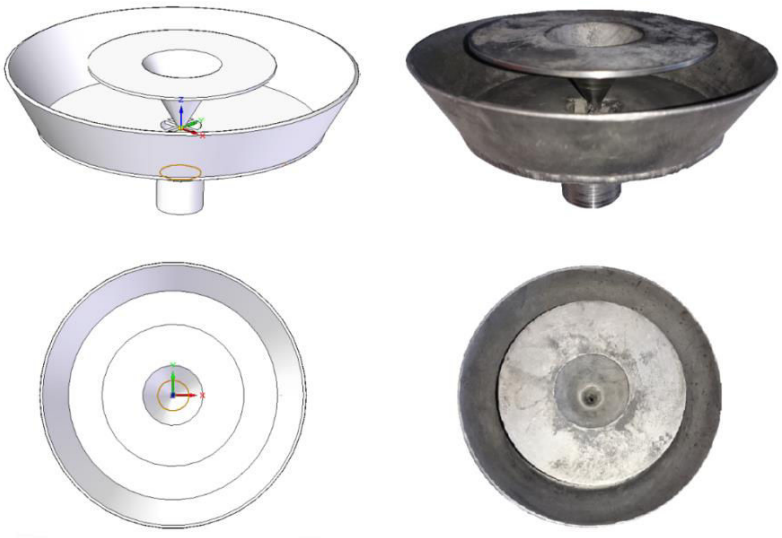

Figure 3.38. Symmetrical rebound nozzle of the 20 L sphere

The two dispersion systems were characterized by the development of granulometric analyses and a detailed description of the variations of the turbulence levels. Thus, some special characteristics of the two nozzles could be established by the description of the transient behavior of the dust clouds of micrometric wheat starch that are developed for both cases.

This system posed a significant difference in the distribution mechanism of the dispersed phase within the vessel. Indeed, the images shown in Figure 3.39 evidence two important characteristics of the rising fronts of the dust cloud.

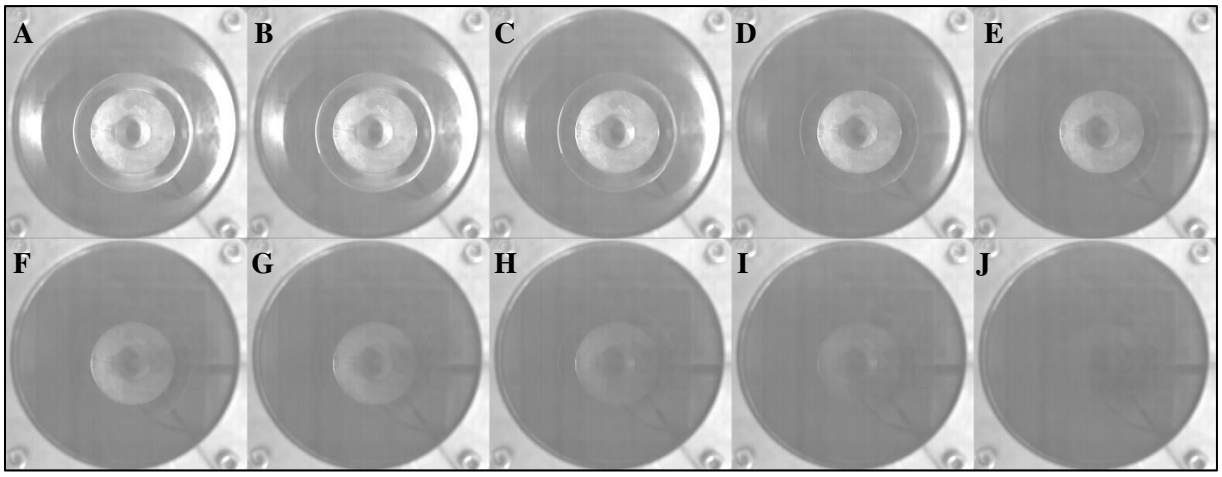

Figure 3.39. Injection of a combustible dust developed with the symmetrical rebound nozzle
A) 0 ms B) 1 ms C) 2 ms D) 3 ms E) 4 ms F) 5 ms G) 6 ms H) 7 ms I) 8 ms J) 9 ms

At first, only two fronts can be identified in the injection. The first rising front, which develops in the middle of the frame, is attributed to the hole that is located in the center of the nozzle. Additionally, a circular front that is directed towards the internal walls of the sphere is evidenced from the base of the nozzle. The most remarkable characteristic in the distribution of the combustible dust relies on the uniform spreading of the sample that comes from the bottom of the vessel. This condition reduces the initial segregation level of the bulk of the cloud by creating only one front. Nevertheless, the behavior of the injected fronts is similar to the ones that are obtained with the standard rebound nozzle. Despite the fact that the solid sample is distributed more homogenously inside the vessel, a downward flow will still be produced in the middle of the dispersion chamber.

Moreover, other important feature of the new nozzle is associated to the plate that constitutes the base of the device. The diameter of this part of the nozzle was reduced and the angle of the bends of its extremes was increased from 45° to 60° so it could fit it into the vessel. For this reason, the two-phase flow is more prone to be guided to the top of the vessel. This fact constitutes a significant change on the paths followed by the gas and the dispersed particles that alters the internal conditions of the dust cloud.

B. *Digital Particle Image Velocimetry (DPIV)*

After the injection of the pressurized flow, a confined dust cloud of transient conditions will form within the explosion chamber. During this period, the initial or cold turbulence will vary due to the energy dissipation. This fact poses the need to analyze the evolution of the evolution of the velocity field of the dust cloud. For this purpose, a set of DPIV analyses has been carried out with the standard rebound nozzle in the dispersion sphere. The velocity field was determined in the geometric center of the 20 L sphere by developing the experimental setup that is shown in Figure 3.40 in accordance with the scheme shown in Figure 3.8:

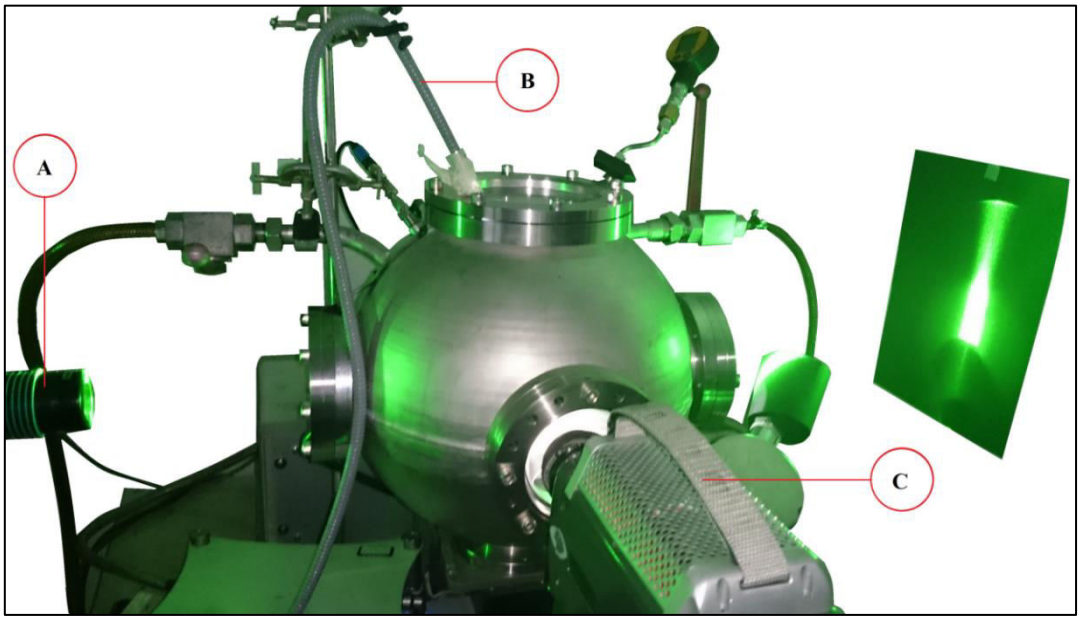

Figure 3.40. Experimental set-up established for the DPIV analyses of the 20 L sphere
A) Continuous wave laser B) Lamp C) High-speed video camera

This arrangement coupled the continuous wave laser (A) to the high-speed video camera of the Phantom V91 series by using the lateral windows of the dispersion vessel. The contrast of the recorded images was enhanced by placing an additional light source (B) over the superior window and implementing the image treatment that was discussed on Section 3.3. The settings of the camera (C) were adjusted to visualize a region of 2.95 cm x 2.80 cm with an image resolution of 480 x 480 pixels.

These parameters allowed recording the dispersion process of micrometric wheat starch at a framerate of 6410 fps (a picture every 0.156 ms). Then, the recorded images were divided in interrogation areas of different sizes in order to apply a numerical method for the statistical analysis.

The characteristics of the flow distribution observed with the standard rebound nozzle pose an interrogation about the velocity of the two phases of the mixture. For this reason, a set of experiments determined the variations of the flow field that are developed on the two sides of the nozzle. The analysis of the variations of the mean fluctuations of the two components of the velocity field in the interrogation window was performed in order to determine the difference between the two common positions of the rebound nozzle. As a reference, the positions will be named according to their position respect to the light sheet (parallel & perpendicular).

The first frames showed some rising lumps in the interrogation window (Figure 3.9A). The mass of the dust was similar in both cases because of the short duration of the pass of the dust and the small size of the region of interest. Nevertheless, this condition was associated to one of the two rising fronts on the parallel position whereas it corresponded to the dust that was injected through the middle holes in the perpendicular position. Then, a downward flow was observed because of the collision of the rising fronts at the top of the vessel. This fact showed that the particle density in the frames increased as the chaotic behavior of the flow diminished.

The same division that was proposed for the flow regimes in the study of the modified Hartmann tube can be considered for this case because both apparatuses consider the dose of a finite amount of pressurized gas. In accordance with this classification, the dispersion process consists of three regimes, which are described in Figure 3.41. Moreover, an additional frame has been included to show the increase of the particles density in the recorded images that is caused by the dust sedimentation occurred during the final stage. This description of the evolution of the dust cloud agrees with the results obtained by Du et al (2015) who also proposed the division of the dispersion process into three different stages according to their mean turbulence levels.

The results establish that the particles density in the interrogation window increases as the flow develops within the explosion chamber. This fact corresponds to the decrease of the number and size of the vortex structures of the gas flow that is caused by the turbulent kinetic energy dissipation. These results evidence the main difficulties that are associated to short ignition delays, which constitute a low concentration of the combustible dust in the region where ignition occurs and the high velocity fluctuations, which represent a reduction of the ignition energy due to the high number or turbulent eddies. On the contrary, long ignition delays will be characterized by the presence of a high number of particles, but they will be influenced by the interactions among the solid particles. This consideration posed the relevance of characterizing the velocity field of the flow during the dispersion process.

Figure 3.42 presents the evolution of the two velocity components in the interrogation window. This chart shows that the horizontal component has a very low mean value. This result can be explained by the development of the downward flow in the middle of the vessel. In fact, the erratic behavior of this velocity component is developed by the jets that constitute the internal pressure gradients and the turbulent eddies caused by the vorticity of the flow. On the contrary, the vertical component presents some significant variations. Figure 3.42 shows that the downward flow lasts 20 ms approximately and is followed by an upward flow that reaches its peak at 80 ms and finishes 20 ms after it. Then, a sedimentation stage begins when a vertical velocity is approximately zero.

The fluctuations of the horizontal velocity component are a little lower than the fluctuations of the vertical one. The tendencies observed for both components agree with the behavior that was expected before the development of the DPIV analyses. The turbulence levels remain high during the first 50 ms (flow injection) and then decrease during the following 60 ms. Finally, the fluctuations achieve a stabilization process, which is mainly characterized by the behavior that was determined by Dahoe et al (2001).

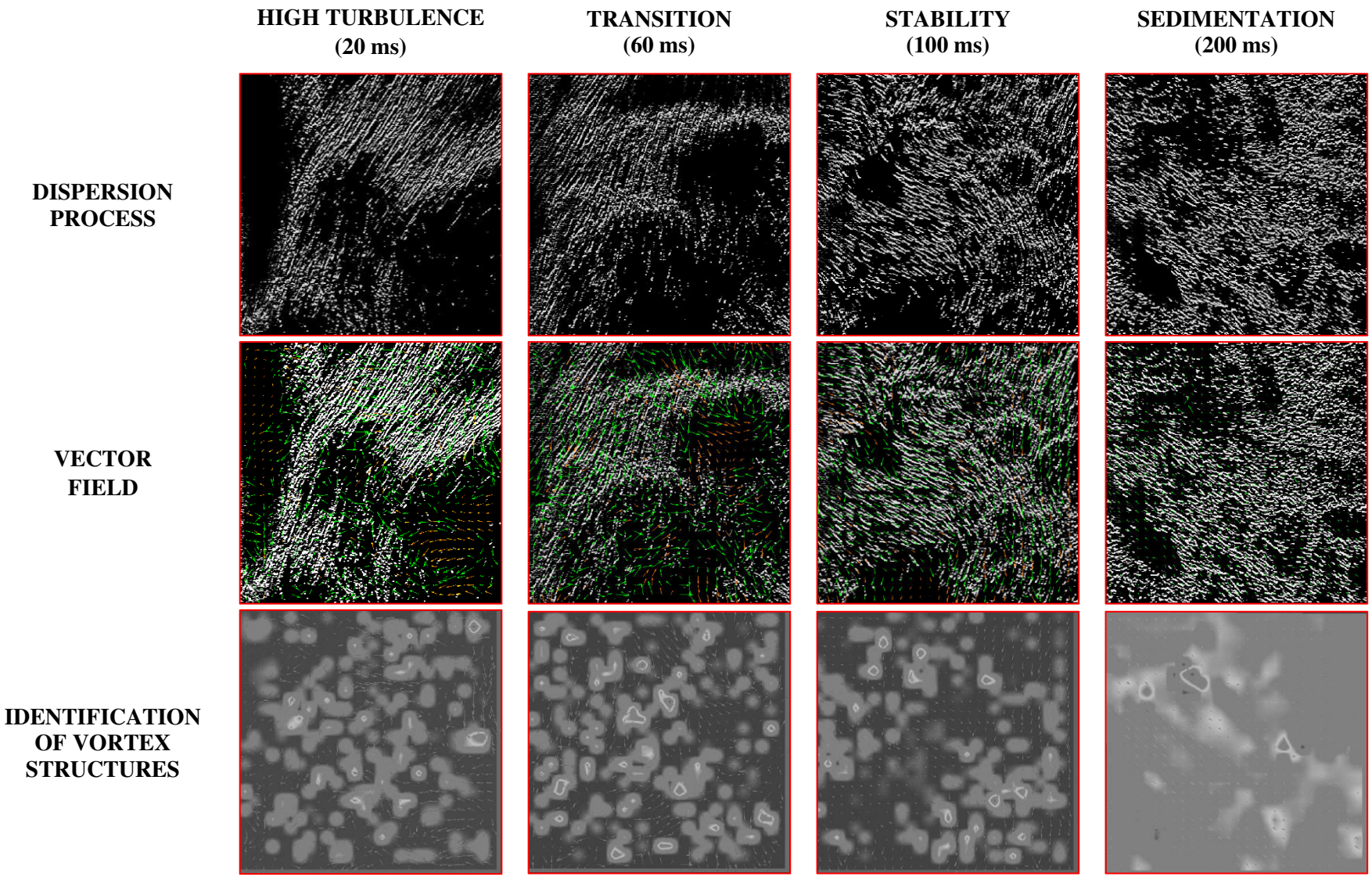

Figure 3.41. Evolution of the dust cloud in the geometric center of the 20 L sphere

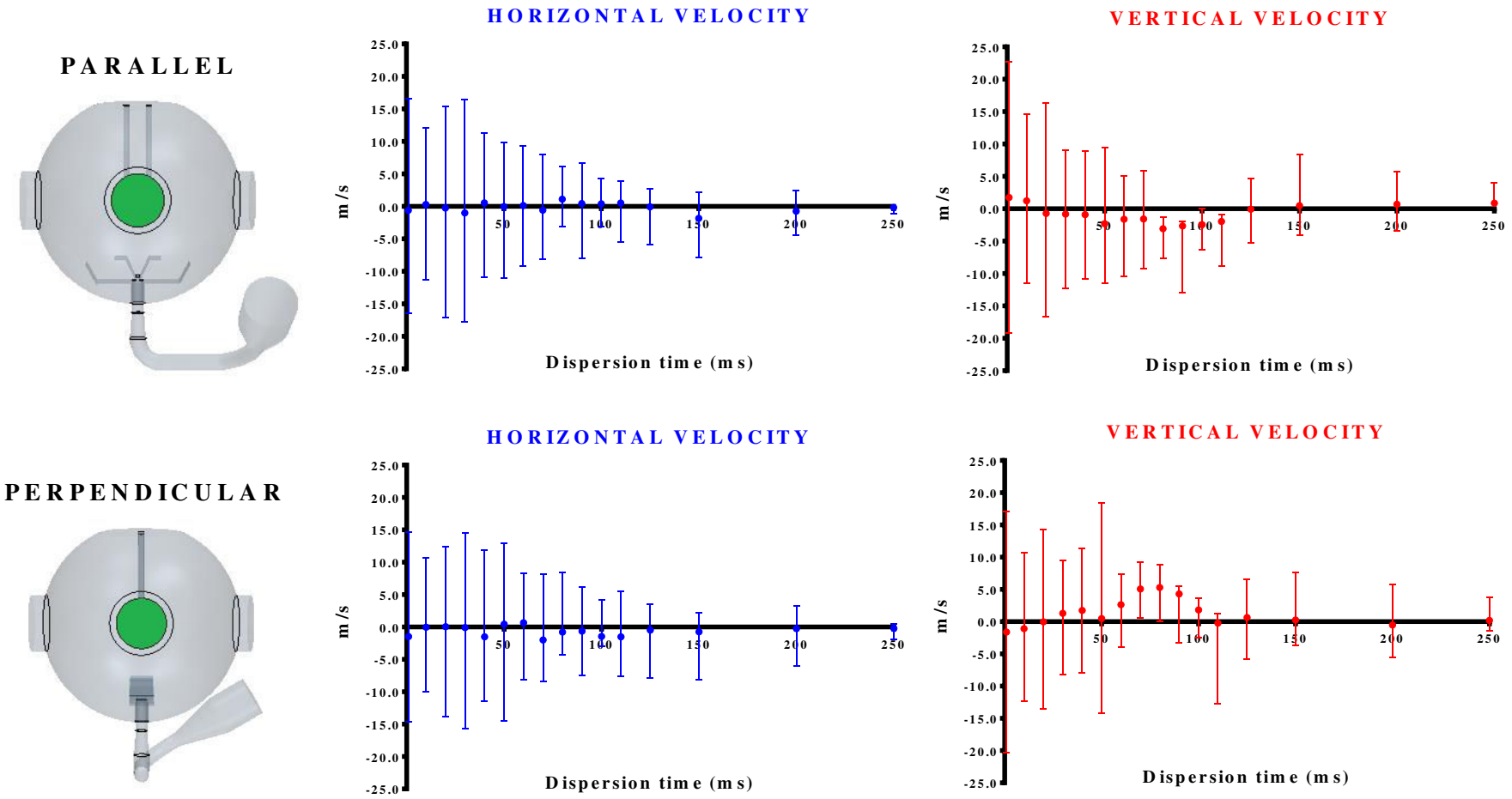

Figure 3.42. Velocity components of the gas flow developed within the 20 L sphere an injection of pressurized air at 20 barg

The main characteristics of the flow turbulence during these stages will now be discussed according to the variations of the magnitude of the mean fluctuations (Figure 3.43 and Figure 3.44):

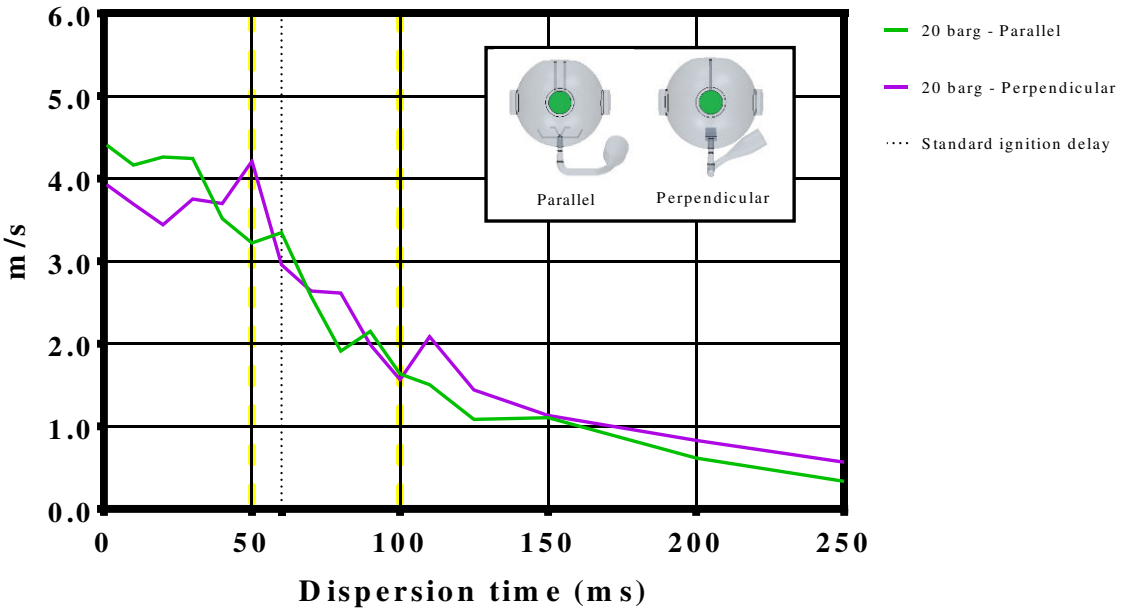

Figure 3.43. Mean fluctuations of the horizontal component of the gas velocity

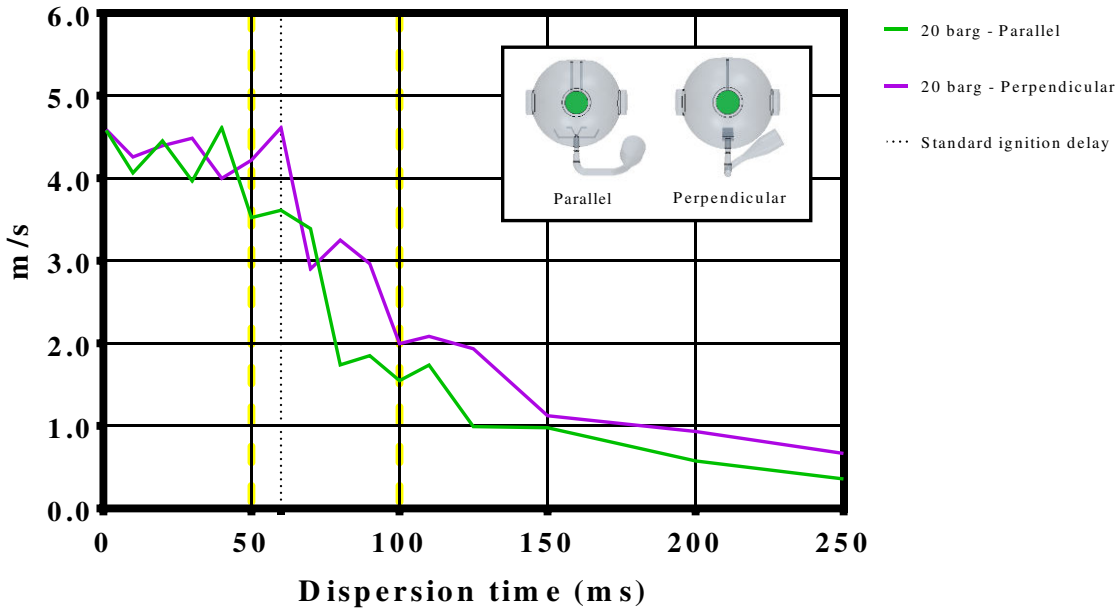

Figure 3.44. Mean fluctuations of the vertical component of the gas velocity

- **Instability stage (0 ms - 50 ms):** During the initial stage of the dispersion process, the bulk of the dust cloud was characterized by a high turbulence. This can be evidenced because the fluctuations reach values of approximately 20 m/s (mean values of 4.5 m/s approximately). For this period, the vertical fluctuations were slightly greater than the horizontal ones due to the unsteady injection of the pressurized gas.

- **Transition stage (50 ms – 100 ms):** Most of the sample has been discharged into the vessel and the mean values of the fluctuations start to decrease. From this moment, the difference between the two positions becomes more important. Indeed, the perpendicular position poses the remaining

of the flow injection and the downward flow whereas the parallel arrangement only considers the latter. This fact also explains why the vertical component of the particles is more affected by the position of the nozzle. However, this result does not represent a drastic difference between the turbulence levels of both cases as discussed by Mercer et al (2001).

- **Stability stage (100 ms – End of dispersion):** The mean velocity fluctuations have decreased to values inferior to 1 m/s. Therefore, the turbulence level is not high enough to keep the chaotic behavior of the dispersed particles.

In conclusion, the experimental results of the DPIV analyses recommend setting the ignition delay of the micrometric wheat starch to 80 milliseconds. This time lapse guarantees that most of the solid sample has been charged into the vessel and that the uncertainty level that is associated to the high turbulence of the two-phase flow and the variable behavior of the cloud can be reduced. Moreover, the upper limit of the ignition delay might be established from an additional source. For this case study, it was determined from the experimental results obtained with the granulometric analyses that are discussed in the following section.

Influence of the injection pressure on the turbulence levels

Dahoe et al (2001) have put forward three different mechanisms that can be considered as the main sources of turbulence of the fluid. Initially, the wall friction can be considered. Indeed, the pass of the flow through the duct and the nozzle generates turbulence in the fluid flow. Moreover, shear turbulence is established in the flow as it is injected into the vessel when the mixture is charged at high velocities with preferential directions. This fact constitutes the sliding and shearing effects on the fluid layers. Nevertheless, Dahoe et al (2001) and Skjold (2003) posed the baroclinic effect as the main source of turbulence. Indeed, the high pressure difference that is defined between the pressure of the air that is compressed in the canister and the air located within the sphere that was evacuated establishes that the surfaces of constant pressure and constant density are not aligned in the injection duct. This baroclinic effect represents not only a source of turbulence but also a source of vorticity that depends on the magnitudes of the pressure and density gradients. This condition explains why Kalejaiye et al (2010) defined the connection duct as the region where most of the fragmentation mechanisms are developed.

Furthermore, the DPIV analyses were also considered to determine the influence of the injection pressure on the evolution of the turbulence of the flow. Given the relevance of the this variable on several mechanisms that determine the variations of the PSD and the eventual characteristics of a combustion flame, it would be interesting to determine how the pressurization of the gas stored in the canister influences the evolution of the velocity field of the gas. For this purpose, three different injection pressures were tested in this DPIV analysis: 15, 20 and 25 barg. The mean velocities and the mean fluctuations of the gas flow that were produced by the considered pressures are shown in Figure 3.45:

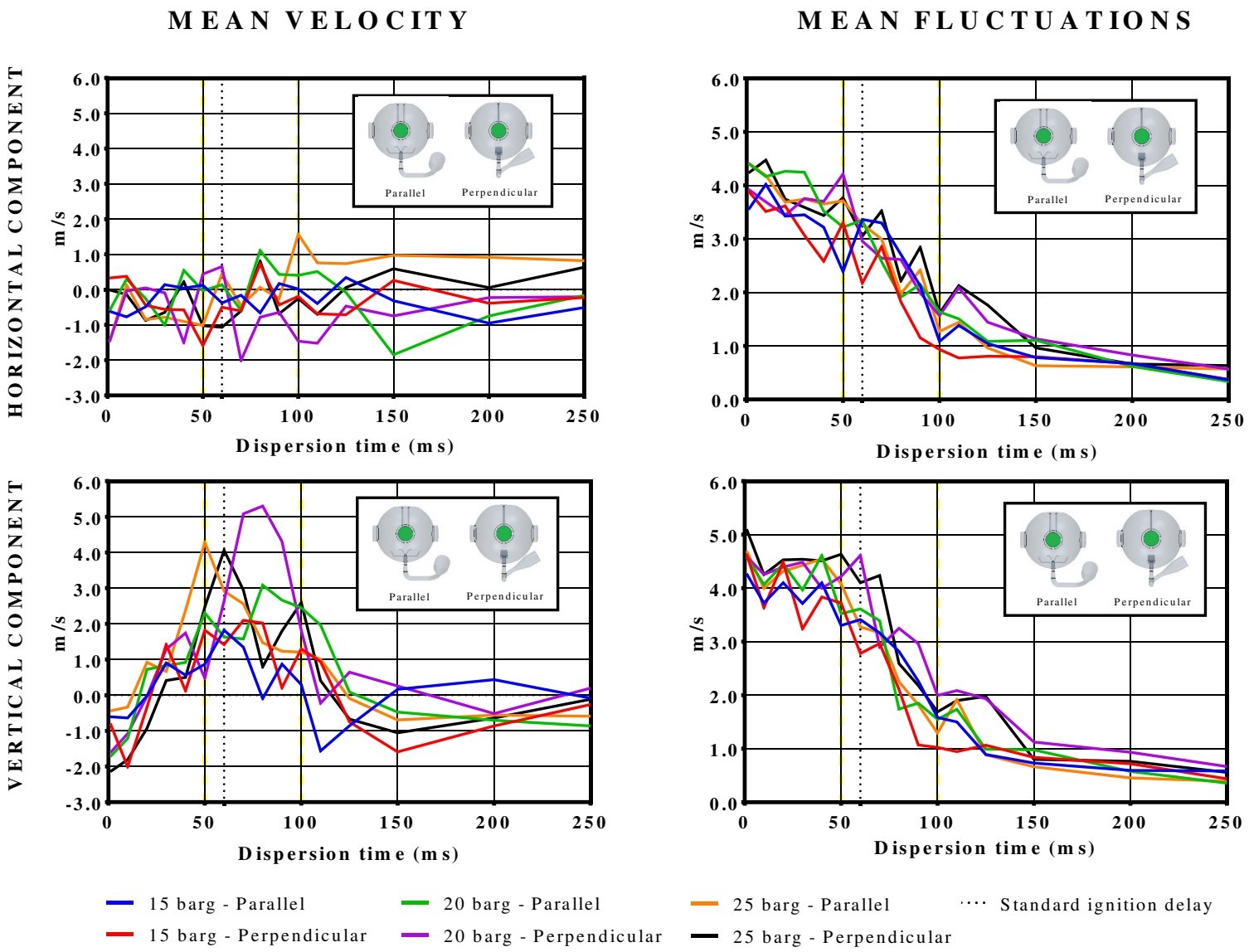

Figure 3.45. Influence of the injection pressure on the gas velocity at the geometric center of the 20 L sphere

The tendencies analyzed for the 3 cases assessed in this sensitivity analysis corroborate the influence of the nozzle position on the evolution of the dust cloud. The mean horizontal velocity was not affected by the modification of the injection conditions because an important fraction of the turbulent kinetic energy of the flow is dissipated in the collision of the two rising fronts. In fact, this variable only constitutes a difference in the behavior of the horizontal of the cloud when the chaotic behavior of the cloud has ceased. Nevertheless, the vertical velocity presented several variations during this sensitivity analysis. The results of the parallel position show that a pressure of 15 barg might submit the combustible dust to the sedimentation process about 30 ms before the other injections. Moreover, the highest pressure constitutes a higher mean vertical velocity during the first 70 ms of dust dispersion and then reaches values very similar to the velocities of the other injections. The experimental data of the perpendicular position is characterized by the presence of several peaks that are associated to the flow streamlines, which are defined by the high vorticity of the flow. This position submits the DPIV results to a higher probability of pass of particles that are located outside the light sheet. This fact explains the unexpected behavior that was observed in the perpendicular position when the lowest mean vertical velocity was achieved by the standard value. However, the results allow concluding that the downward flow developed at the top of the sphere is clearly defined by the injection.

Furthermore, the fluctuations of the velocity do not seem to be highly influenced by the increase of the injection pressure because its tendency is very similar to the standard. However, the lowest pressure does not accomplish fluctuations as high as the other two pressures in the perpendicular position. The variations of the pressurization of the stored gas did not constitute a gap for the beginning of the three stages of the dust dispersion that were proposed according to the turbulence levels. The fluctuations remained in quite similar time intervals in spite of the variation of the injection conditions. Moreover, the pressure increase represented a greater number and amplitude of the peaks of the mean velocity (Figure 3.45). This fact poses that the turbulence in the geometric center of the sphere will not be affected in a significant way by the variation of the gas pressure after a critical value. For this reason, it is possible to consider this variable as a possible adjustable setting of the experimental test. This condition might contribute to determine the beginning of the sedimentation process of a combustible dust that is going to be characterized as well as the appropriate ignition delay for the flammability test.

Finally, the root-mean-square velocities (v_{rms}) of the gas flow were calculated according to the following expression for all the configurations analyzed (Figure 3.46):

$$v_{rms} = \sqrt{\frac{1}{N}\sum_{i=1}^{N} u_i'^2} \qquad 3.49$$

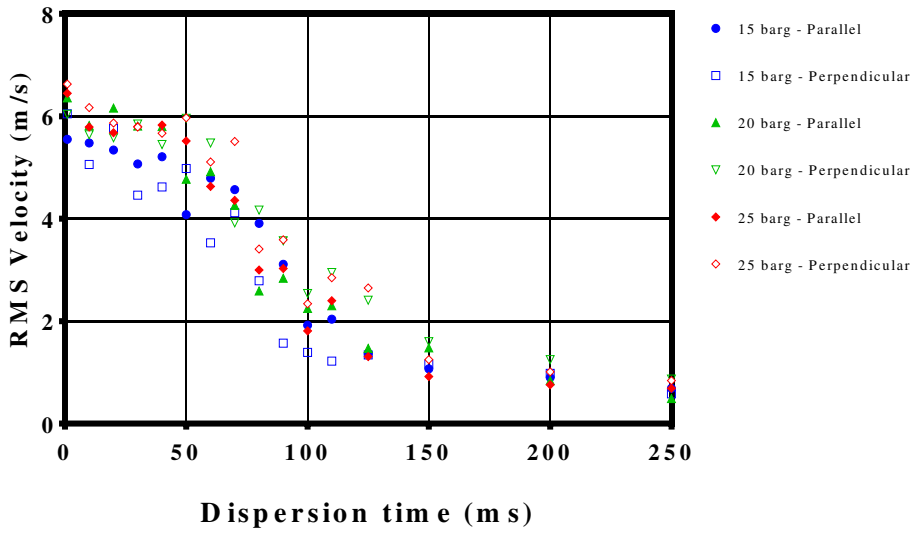

Figure 3.46. Root-mean-square velocity of the gas flow

Thereafter, the analyzed injection pressures were correlated to Equation 3.50 to establish their rate decay of turbulence. This calculation was performed according to the model proposed by Dahoe et al (2001). For this purpose, the initial time ($t_{rms,o}$) was defined as 60 ms and the average values were considered.

$$\left(\frac{v_{rms}}{v^{o}_{rms}}\right)=\left(\frac{t}{t_{rms,o}}\right)^{n} \qquad 3.50$$

Table 3.10 lists the values obtained for the root-mean-square velocities at 60 ms along with the decay exponent (*n*), which corresponds to the slope of a regression line of both sides of Equation 3.50 drawn in a logarithmic scale (Figure 3.47).

Table 3.10. Curve fitting of the root-mean-square velocities from 60 to 200 ms in the 20 L sphere

PRESSURE (barg)	POSITION OF THE NOZZLE			
	Parallel		Perpendicular	
	Vrms° (m·s-1)	Decay exponent (n)	Vrms° (m·s-1)	Decay exponent (n)
15	4.80	-1.52 ± 0.41	3.58	-1.24 ± 0.06
20	4.93	-1.47 ± 0.23	5.53	-1.26 ± 0.23
25	4.64	-1.50 ± 0.23	5.11	-1.36 ± 0.11

The values of the curve fitting exponent and $V_{rms}°$ that were obtained for the parallel position at 20 barg with the rebound nozzle are -1.47 and 4.93 m/s respectively. These values had a good agreement with the values of -1.61 and 3.75 m/s that were determined with an anemometry study (Dahoe et al., 2001). Furthermore, Skjold (2003) developed a set of experiments in a cubical vessel by adopting the same smoothing procedure that was followed by Dahoe. This study determined that an exponent equal to - 1.70 and a $V_{rms}°$ equal to 1.93 m/s represented the decay of turbulence. The discrepancy of the results was attributed to a higher surface-to-volume ratio of the cube and the development of secondary flows in the corners. It is thus possible to conclude that the parameters that were determined by a DPIV analysis also predict the evolution of the turbulence levels after 60 ms of dust dispersion. Nevertheless, it is recommended to perform a greater number of repetitions in order to increase the precision of the experimental data.

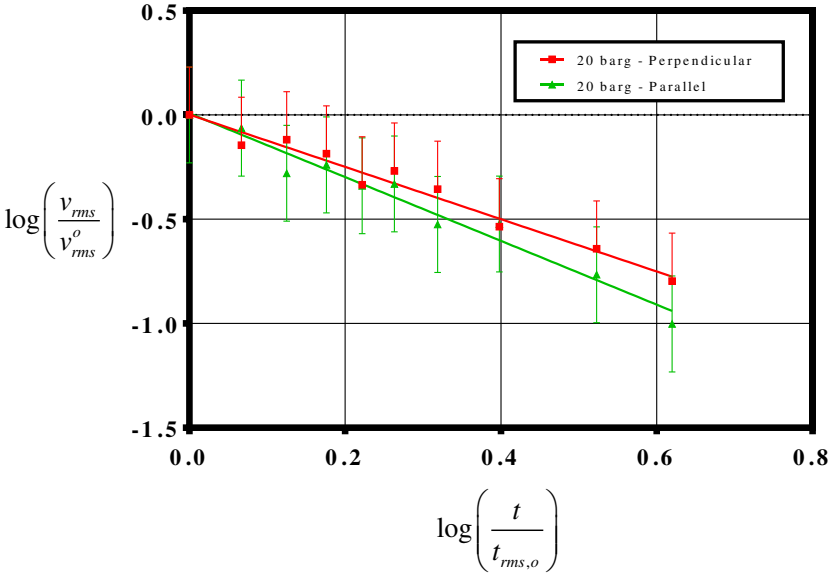

Figure 3.47. Determination of the decay exponent (n) for the injections performed at 20 barg

The main differences that were found on the rates of decay of turbulence are associated to the position of the standard rebound nozzle. Indeed, the turbulence decreases more slowly on the sides of the sphere where the two injected fronts rise. This fact corroborates the results obtained by Du et al. (2015) and Yuan et al (2012) who have questioned the validity of the common assumption of the homogeneity of the dust/air mixture.

C. *Granulometric Analyses*

The variations of the particle size distribution (PSD) of the micrometric wheat starch within the 20 L sphere were also considered for the classification of the dispersion stages of the flammability test performed with this apparatus. This condition can be considered by taking into account the relation between the turbulence levels of the two-phase flow and the fragmentation and agglomeration phenomena of the dust. In fact, the manufacturer of the 20 L test apparatus (Kühner AG) affirmed that the combination of the outlet valve and the dispersion nozzle might lead to particle size reduction in the course of dispersion due to their grinding effect on the dust particles (Kalejaiye et al., 2010; Kühner, 1994). In accordance with this statement, the manufacturer usually recommends to perform a complementary dispersion test in order to collect and analyze the solid sample. Thus, the fragmentation of the dust can be established from a comparative analysis between the PSD determined prior to the dispersion test and the one that is obtained after it. Nevertheless, this procedure poses as its main drawback the significant difference between the conditions of the dispersion test and the test used to establish the PSD of the collected sample. For this reason, some granulometric analyses were carried out in situ to establish the fragmentation levels of the solid agglomerates during the dispersion process. These analyses are important because the broad PSD can be thought as a series of narrow size distributions that make a contribution to the explosibility of the solid material (Amyotte et al., 1991). These tests were performed with the experimental set-up that is shown in Figure 3.35 (elements B and D).

At first, the height of the incident laser beam was adjusted to pass through the middle of the dispersion sphere. This zone was considered as the region of main interest because it constitutes the location of the ignition spark inside the sphere. Despite the fact that the homogeneity of the dust cloud has been controverted by the results obtained from different experimental approaches (Dahoe et al., 2001; Du et al., 2015; Kalejaiye et al., 2010), the geometric center of the dispersion vessel can be considered for this analysis because it will establish the condition of the solid aggregates in the region where the combustion of the first fraction of the dust cloud is developed. Afterwards, 0.6 grams of micrometric wheat starch were charged to the storage canister of the standard apparatus in order to obtain a nominal dust concentration equal to 30 g/m^3. Then, a set of five replicate tests was performed for the granulometric analysis in order to verify the repeatability of the tendencies evidenced in the experimental results. Finally, the evolution of the PSD was determined for the 120 ms elapsed after the arrival of the bulk of the dust cloud to the position of the laser beam. For this purpose, the granulometric analyses were developed in measurement cycles of 1 ms and reported for intervals of 5 ms.

Figure 3.48A shows the evolution of the PSD of the combustible dust during the dispersion process that developed from an injection performed with the standard rebound nozzle. The results pose an important shift of the size distributions respect to the initial PSD (determined by sedimentation analyses). Indeed, the diameter d_{50} decreased from 65.20 µm to 15.95 µm during the first 15 ms. Furthermore, the experimental results obtained for this analysis established that the size distributions of the wheat starch had a low variation in the region of interest during the dispersion process. This condition can be associated to the continuous displacement of the solid particles in the turbulent eddies that are developed by the two-phase flow. Nevertheless, the three dispersion stages that were proposed by Du et al. (2015) could be identified.

This condition can be observed with other combustible dusts that are submitted to fragmentation in a

dispersion process. The main differences will be associated to the maximum reduction levels of the PSD that are defined by the particles cohesion and the fraction of fine particles in the initial PSD. This condition was established for the aluminum samples, which showed that the variations of the PSD of the micro-Al 7 samples had smaller variations than the micro-Al 42 particles (Section 3.5.2A).

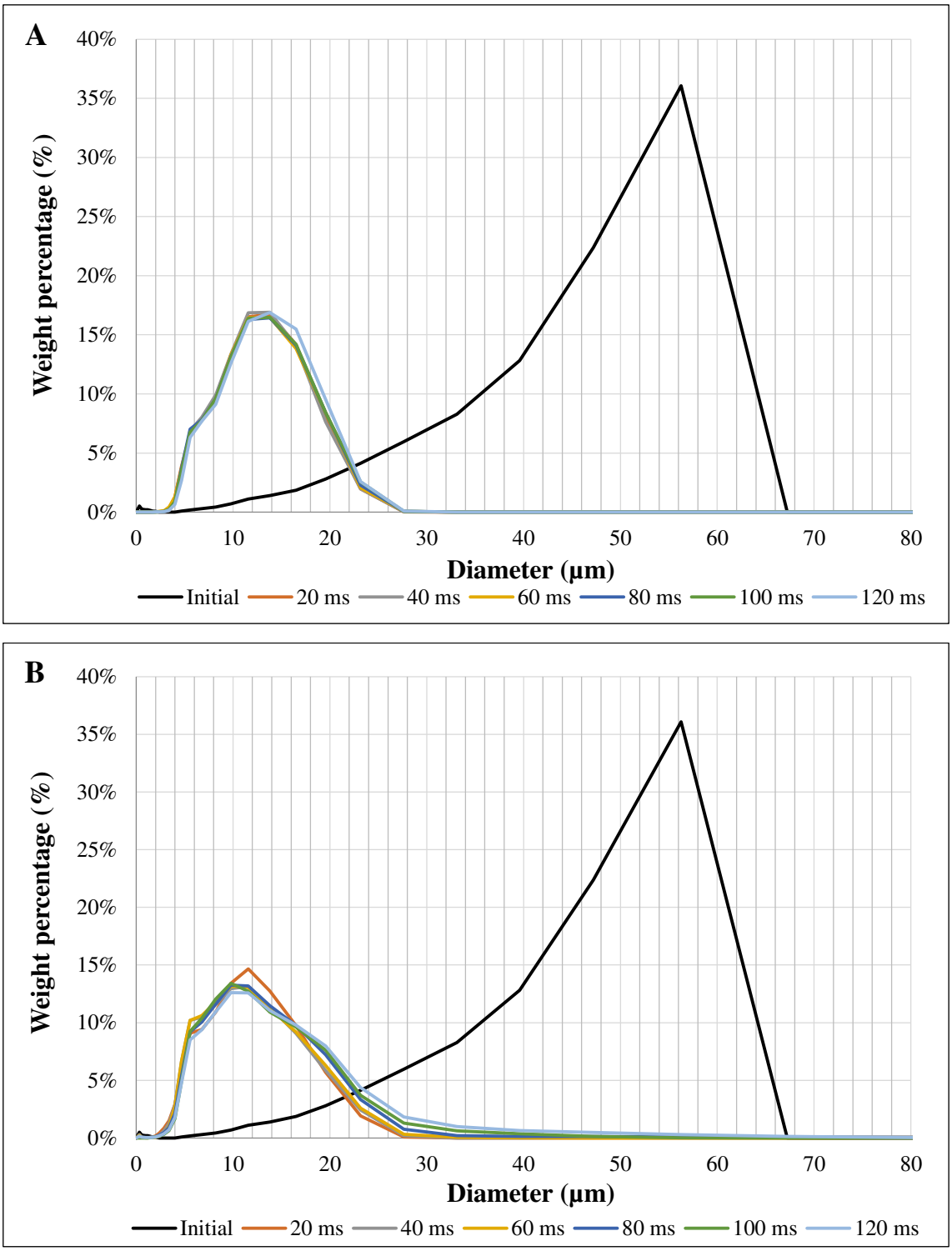

Figure 3.48. Particle Size Distributions in the 20 L sphere after the injection with different nozzles
A) Standard rebound nozzle B) Symmetric nozzle

The first stage was observed during the first 50 ms of dust dispersion. This time lapse is characterized by the largest standard deviations if the diameter d_{50}. This interval corresponds to the temporary pass

of the lump injected through the three holes of the middle of the dispersion nozzle (0-10 ms) as well as the fragmentation of most of the injected particles. The peaks that are observed in the curve of the standard rebound nozzle in Figure 3.49 at 25 and 40 ms correspond to the time interval that was associated to a high instability in the DPIV analyses. During the intermediary stage of the dispersion, the turbulence of the fluid flow is high enough to keep a reduced agglomeration level in the solid aggregates in spite of its continuous decrease. Moreover, the highest deviations of the diameters analyzed with these tests are evidenced in the third stage, which is attributed to the agglomeration and sedimentation phenomena in the middle of the dispersion chamber. This final stage is considered to begin for micrometric wheat starch after 90 ms of dust dispersion approximately.

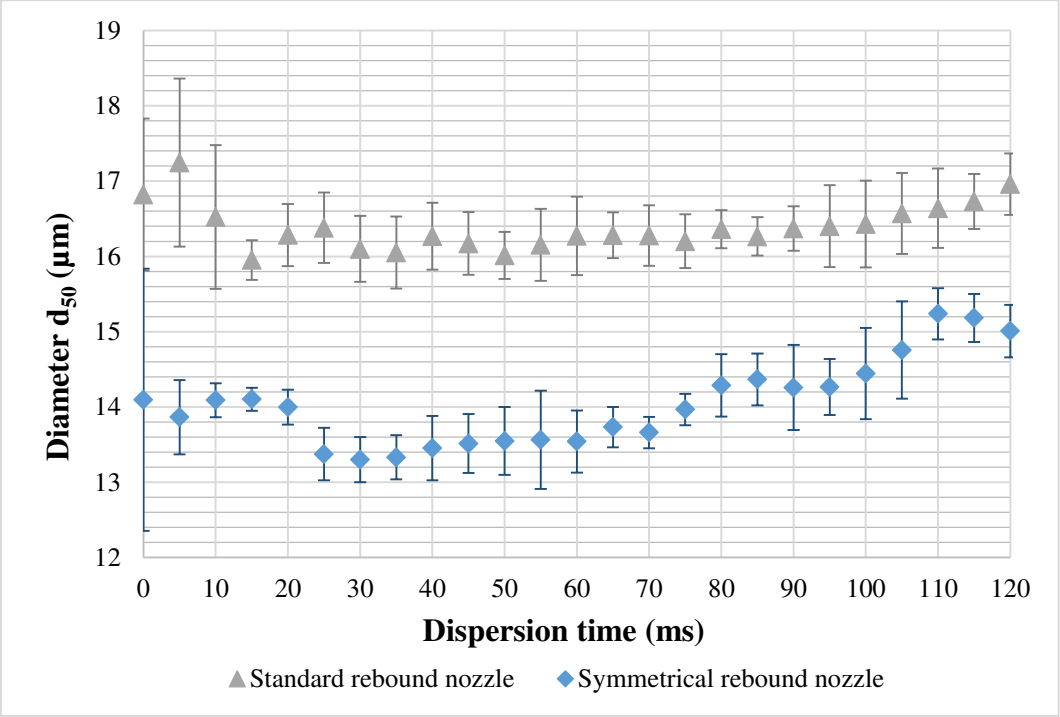

Figure 3.49. Diameter d_{50} at the geometric center of the sphere

The analysis of the fragmentation phenomenon also describes some important characteristics of the dust dispersion and its ignitability. Previously, Calvert et al. (2013) posed that the small aggregates of the cohesive dust disperse by disintegration, whereas large aggregates disperse by particles gradually peeling from the cluster surface. This condition is associated to the force propagation across the aggregate. For this reason, the drag force may constitute a partial dispersion of the combustible dust. Despite the fact that the turbulent conditions were capable of breaking up even the smallest aggregates, the diameter d_{50} of the PSD remained at value of 16 µm. This fact implies that the largest aggregates could only be fragmented until this size. This condition is determined by the shear rate generated by the dispersion medium and the cohesion forces. For this reason, this characteristic is more determinant for the dispersion process of nanometric dusts. This fact is evidenced because their agglomeration degrees are considerably determined by the particle interactions, which mainly correspond Van der Waals forces (Henry, 2013). Moreover, this condition also establishes the level of homogeneity that might be expected during a typical flammability test respect to other cohesive powders. For this reason, the cohesive behavior of the dust represents an important aspect for the determination of the ignition delay of the powder.

Furthermore, the symmetrical rebound nozzle was also tested with the experimental protocol that was followed for the standard injection system. Figure 3.48B presents the evolution of the PSD of the wheat starch that was determined for the device that was constructed for this study. The results pose a similar fragmentation level for the dust and a modest variation of the particle size distribution as well. Previously, Kalejaiye et al. (2010) established that the reduction in particle size is mainly attributed to the shear stresses exerted on the aggregates during their pass through the outlet valve rather than the

impaction against the injection nozzle. In other words, the high velocity of the particle-laden flow through the valve is the main responsible of the reduction in the particle size and not the action of the dispersion nozzle. In accordance with this statement, the contribution of the nozzle on the fragmentation of the dust can be considered as a minimal. This condition explains the high similarity between the profiles obtained with both injection systems.

Nevertheless, the granulometric analyses also show that the flammability parameters that are determined with this injection nozzle can be more susceptible to the variations of the ignition delay defined for the test. This condition can be evidenced after observing how the presence of the large aggregates is favored as the dispersion process develops. This condition poses that the influence of the nozzle relies on the trajectories and the segregation of the two-phase flow. Indeed, the presence of a unique front directs the most of the aggregates to the geometric center of the dispersion chamber. This condition enhances the sedimentation process of the solid phase when the turbulence levels are low enough. This characteristic is clearly evidenced in Figure 3.49, which describes the evolution of the diameter d_{50}. Despite the fact that the symmetrical rebound nozzle provides a greater reduction of the diameter d_{50}, this injection system has an important increase in the value of this variable and its fluctuations after the first 70 ms dispersion. This condition shows that the dispersion developed with the new injection system can be divided in the same stages that were proposed by Du et al. (2015) for the standard device. These results determine that the ignition delay that should be defined for the wheat starch in the 20 L sphere should not be greater than 80 ms for the symmetrical rebound nozzle and 90 ms for the standard device.

Finally, the results pose that the granulometric analyses constitute a useful tool for the implementation of a specific nozzle in a flammability characterization test. For this reason, it is recommended to analyze the variations of the particle size distribution of a combustible dust in order to determine the ignition delay that establishes the most conservative conditions for the flammability test by taking into account the physical properties of the solid material.

D. *Influence of the dispersion characteristics on the explosivity results of the 20 L sphere*

The final test that was proposed for the experimental approach of the descriptive study of the dispersion process of micrometric wheat starch in the 20 L sphere was focused on the development of confined explosions on the standard setup. This analysis was carried out to determine the real influence of the parameters that were assessed on the flammability parameters of the combustible dust. For this purpose, a fractional factorial design was developed with the four operating parameters that are shown in Table 3.11 (Antony, 2014).

In accordance with this analysis, two different nozzles, six dust concentrations, four injection pressures and three ignition delays were assessed. For this purpose, the flammability tests determined the maximum pressure of the dust explosion and the maximum rate of pressure increase associated to the expansion wave. Moreover, 26 combinations were considered from the 144 arrangements that could be performed on a complete factorial design. The central value was tested with four repetitions and the analyses of the other points were performed with two repetitions.

Table 3.11. Normalization of the factors analyzed in the fractional factorial design

VARIABLE	PARAMETERS	CENTRAL REDUCED VARIABLE	NORMALIZATION EQUATION
Nozzle	Symmetric Standard	-1 1	-
Ignition delay (ms)	20 60 110	-1.00 -0.11 1.00	$Y = \frac{t_v - 65}{45}$
Concentration (g/m3)	60 125 250 500 750 1000	-1.000 -0.862 -0.596 -0.064 0.468 1.000	$Y = 0,0021C - 1,1276$
Pressure (barg)	15.0 16.3 20.0 25.0	-1.00 -0.74 0.00 1.00	$Y = \frac{P - 20}{5}$

- **Influence of the ignition delay:** The ignition delay constitutes an important factor if the weight of the dust sample is high enough to define a significant change of the solid concentration. Indeed, the characterizations of a combustible dust that are performed at high concentrations are defined by the ignition delay. If this parameter is too short, the cloud may still be in a developing stage in which the dust is not fully dispersed within the sphere. On the other hand, the dust explosions can be weakened if the mixture is ignited too late because the disperse particles have agglomerated and settled down. These conditions define the main characteristics of the propagation of the flame (Yuan et al., 2012).

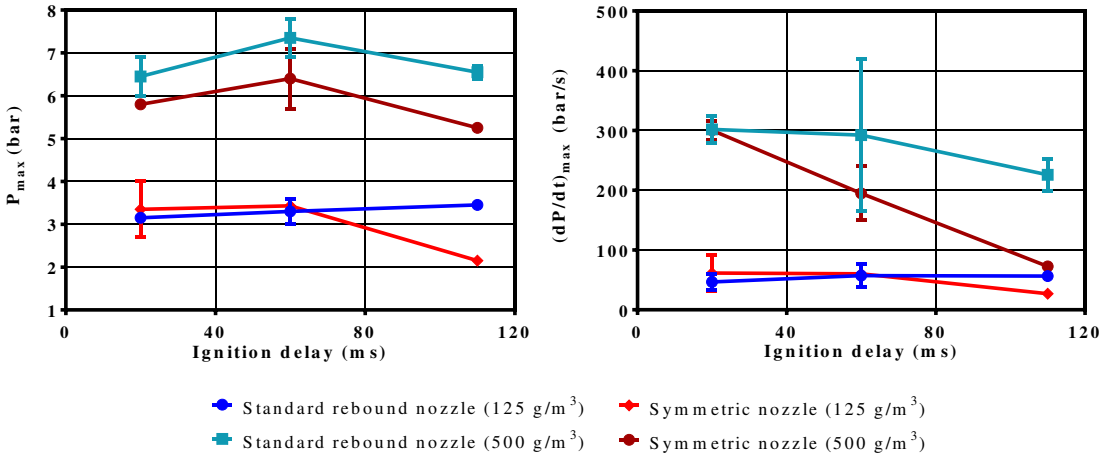

Figure 3.50. Influence of the injection pressure on the flammability parameters of wheat starch determined in the 20 L sphere

Figure 3.50 shows that an explosion carried out with a concentration of 125 g/m^3, which is very close to the MEC, is not affected by a variation of the ignition delay when the standard rebound nozzle is utilized. This fact is evidenced because the concentration is too low. Indeed, there is not too much energy for the combustion process. Nevertheless, some important characteristics can still be analyzed from the results obtained. The explosions that were carried out at 20 ms of dust dispersion are exposed to an important uncertainty level that is attributed to the high turbulence level of the two-phase flow that is developed during the charge of the mixture into the vessel. These fluctuations decrease as the ignition delay time increases due to the reduction of the

turbulence of the flow. In fact, this condition is evidenced because the high turbulence constitutes a quenching effect on the flame kernel growth (Glarner, 1984). Furthermore, there is a decrease of the two flammability parameters determined with symmetrical nozzle when the cloud is ignited at 110 ms. This condition can be explained with the changes of particle size distribution that were observed in the granulometric analyses. In fact, the trajectories followed by the solid particles within the sphere pose a wider distribution of the dust. Despite the fact that the symmetrical nozzle accomplishes a higher fragmentation level during the dispersion process, it is submitted to more significant fluctuations of the particle size for ignitions occurred after the first 80 ms.

These characteristics were evidenced with the explosions performed with a concentration of 500 g/m^3 as well. This concentration poses these characteristics more clearly because the variations of the internal conditions of the cloud have an effect on a greater amount of mass that represents more available energy for the combustion process. These results corroborate the conclusion obtained with the lower concentration that poses how a long ignition delay constitutes an operating drawback for the symmetrical nozzle. The assessment of several ignition delays can establish the most appropriate ignition delay for the wheat starch which must be inferior to 100 ms for both nozzles.

- **Influence of the concentration of the combustible dust:** The increase of the weight of the sample escalated the flammability parameters to define a critical peak for each one. These results are attributed to an augmentation of the amount of energy that can be released during the dust explosion. The worst-case concentration was determined to be 750 g/m^3, which is considerably higher than the stoichiometric value (246.6 g/m^3). Moreover, the highest concentration defined a slight reduction on the severity of the combustion process of the dust because an excess of combustible dust also represents a quenching effect. Indeed, a higher number of disperse particles represents a major interaction between the two phases, which favors the subsequent solids agglomeration. Additionally, this increase defines a factor of energy absorption because of the dust that does not participate in the chemical reaction. This phenomenon was termed by Skjold (2003) as a heat sink effect.

Moreover, Figure 3.51 shows that the symmetrical nozzle exhibits lower values for the explosion severity parameters of the wheat starch. The difference decreases as the concentration of the dust increases.

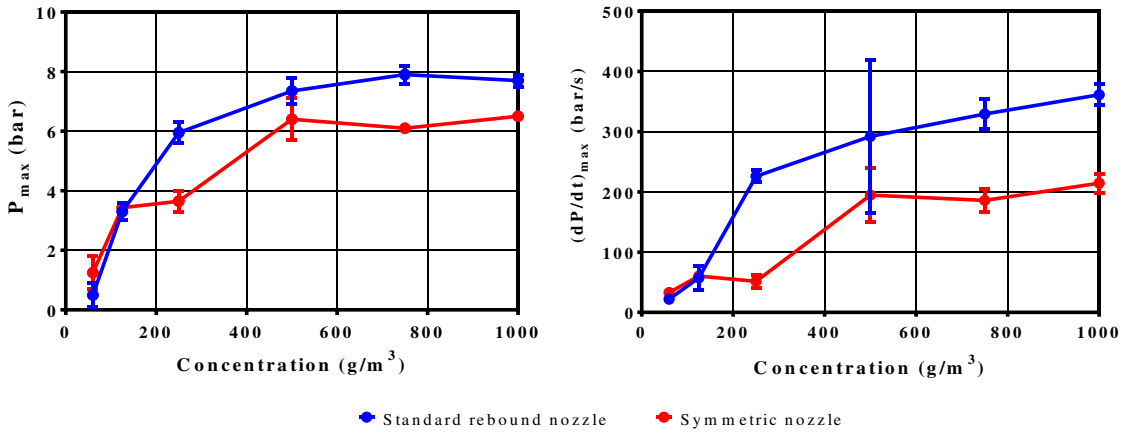

Figure 3.51. Influence of the injection pressure on the flammability parameters of wheat starch determined in the 20 L sphere

The symmetrical nozzle exhibits lower values for the explosibility parameters of the wheat starch. However, the difference between the two nozzles decreases as the concentration of the dust increases. This fact poses that the spatial distribution of the solid within the sphere becomes less important for the tests carried out from a specific concentration. This characteristic mainly

depends on the physical properties of the combustible dust. For the micrometric wheat starch, the utilization of the new injection increased the cohesion of the dust to the internal walls, which represented a lower value of the flammability parameters. Nevertheless, this nozzle defined a lower deviation of the experimental data for the variations of the solid concentration as well. For this reason, the development of flammability tests with non-cohesive powders is recommended for future analyses with this injection system.

- **Influence of the injection pressure:** The injection pressure must guarantee the achievement of the appropriate levels of fragmentation and turbulence of the dust cloud. The range of P_d (pressure increase caused by the gas injection), that is defined as the international standard, establishes that the pressurization of the compressed air must be between 16.4 and 20 barg. In accordance with this statement, this value was also considered for the assessment of the injection parameter. The results presented in Figure 3.52 pose that the range is suitable for the performance of flammability tests because a significant variation of the flammability parameters is not evidenced in this interval. Moreover, an increase of the injection pressure did not constitute any dissimilarity with the experimental results of the standard either. However, the implementation of the lowest pressure represented a drastic decrease of the maximum pressure and the maximum rate of pressure increase.

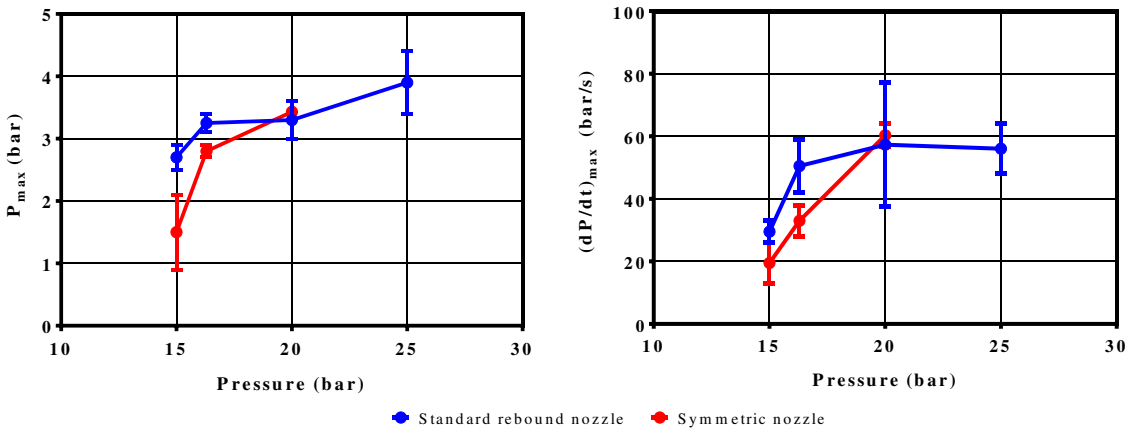

Figure 3.52. Influence of the injection pressure on the flammability parameters of wheat starch determined in the 20 L sphere

Indeed, these results agree with the experimental data that was obtained in the DPIV analyses. These results established that the turbulence levels obtained with a pressurization of the air performed at 15 barg may not be high enough for the development of a flammability test. Moreover, these results also established that the compression of the gas until 25 barg did not represent a significant increase of the turbulence levels respect to the standard. These characteristics allow establishing that the fragmentation of the micrometric wheat starch is not sufficient if the injection is performed at pressures below the standard values. In this particular case, the injection requires at least a pressurization of 20 barg.

- **Linear model equation**

The first three parameters that were studied in this analysis were adapted to a linear model according to the basic principles of a fractional factorial design. The injection pressure did not pose a significant variation for the values considered. Therefore, this analysis focused on the influence of the injection nozzle, the ignition delay and the dust concentration on the experimental results. The model proposed for this analysis considered Equation 3.51 to establish the influence of every variable as well as their interactions.

$$\text{Explosivity Parameter} = a_0 + a_1X_1 + a_2X_2 + a_3X_3 + a_{12}X_1X_2 + a_{13}X_1X_3 + a_{23}X_2X_3 + a_{123}X_1X_2.Y \quad 3.51$$

X_1: Nozzle type
X_2: Ignition delay (ms)
X_3: Dust concentration (g/m^3)

The coefficients of the correlation were established by performing a multilinear regression on the explosivity parameters that were determined previously. This model was chosen due to its capability to interpolate with the experimental data. Moreover, the 8 coefficients were determined with the results obtained from 43 flammability tests in order to determine their confidence intervals with 95% significance level. These results are shown in Table 3.12:

Table 3.12. Factorial design coefficients determined for the injection nozzle, ignition delay and dust concentration on the wheat starch explosivity parameters

Coefficient	Pmax			(dP/dt)max		
	Value	Confidence interval (95%)	Result	Value	Confidence interval (95%)	Result
a_0	6.38	(4.43 – 8.34)	Accepted	223.0	(126.0 – 320.0)	Accepted
a_1	0.58	(-1.37 – 2.53)	Neglected	51.0	(-46.0 – 147.9)	Neglected
a_2	-0.12	(-3.68 – 3.45)	Neglected	-79.8	(-257.1 – 97.6)	Neglected
a_3	3.95	(0.89 – 7.01)	Accepted	186.4	(34.1 – 338.7)	Accepted
a_{12}	0.14	(-3.43 – 3.71)	Neglected	39.1	(-138.3 – 216.5)	Neglected
a_{13}	0.45	(-2.61 – 3.51)	Neglected	45.8	(-106.5 – 198.0)	Neglected
a_{23}	0.12	(-5.72 – 5.96)	Neglected	-83.6	(-373.9 – 206.7)	Neglected
a_{123}	-0.29	(-6.12 – 5.55)	Neglected	33.5	(-256.8 – 323.8)	Neglected

The results establish that the conditions of the combustible dust constitute the most determining factors in the determination of the explosivity parameters. This fact implies that the major influence of the dispersion systems and the ignition delay is not directly associated to the value of the flammability parameter. In fact, the data analysis established that the uncertainty levels of the experimental results are the variables that are most significantly affected by the variation of the dispersion conditions. This condition can be observed in Figure 3.53, which shows the ratio of the standard deviation and the mean value of the maximum pressure and maximum rate of pressure increase for two fixed dust concentrations:

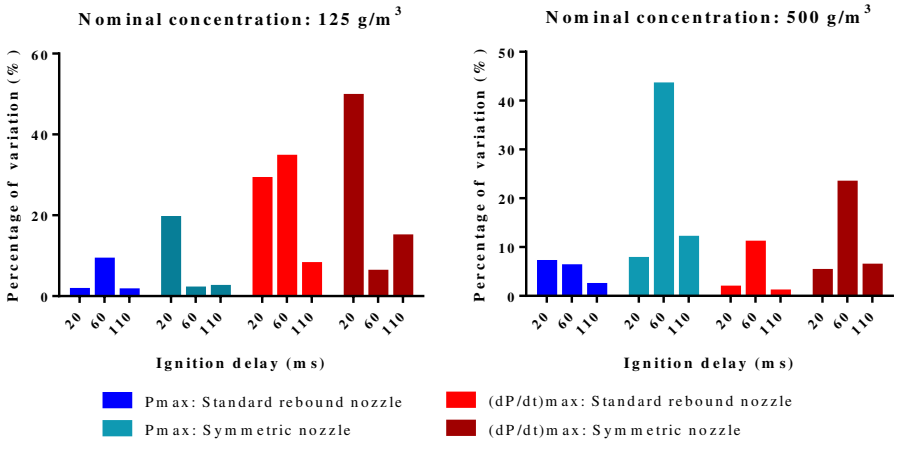

Figure 3.53. Variations of the explosivity parameters

Thereafter, a subsequent fractional factorial design considered the influence of the injection nozzle and the ignition delay for two fixed dust concentrations: 125 and 500 g·m^{-3}. The model equation that corresponds to each particular case is defined as follows:

$$\begin{matrix}\text{Explosivity}\\ \text{Parameter}\end{matrix} = a_0 + a_1 X_1 + a_2 X_2 + a_{12} X_1 X_2 \qquad 3.52$$

A coefficient is neglected when the value of zero is within its confidence interval. Thus, the results shown in Table 3.13 and Table 3.14 show that these factors must be considered mainly when the dust concentration is augmented. For dense dust clouds, the momentum transfer and the particle interactions occur more frequently than in dilute mixtures; hence the agglomeration and sedimentation phenomena have a higher probability of occurrence as well.

Furthermore, this analysis also established two important characteristics of the flammability parameters. Initially, it is possible to evidence that the maximum rate of pressure rise is the parameter that is more affected by these two variables. On the contrary, the maximum pressure is just slightly affected by the dispersion nozzle. This condition is evidenced because P_{max} is mainly defined by the thermodynamic properties of the dust whereas the $(dP/dt)_{max}$ is affected by the transport phenomena of the dust cloud (Dufaud et al., 2012).

Table 3.13. Factorial design coefficients determined for the injection nozzle and ignition delay on the wheat starch explosivity parameters (Fixed nominal concentration: 125 g/m^3)

Coefficient	P_{max}			$(dP/dt)_{max}$		
	Value	Confidence interval (95%)	Result	Value	Confidence interval (95%)	Result
a_0	3.02	(2.39 – 3.66)	Accepted	47.9	(15.0 – 80.8)	Accepted
a_1	0.28	(-0.36 – 0.91)	Neglected	3.6	(-29.3 – 36.5)	Neglected
a_2	-0.22	(-0.86 – 0.41)	Neglected	-6.2	(-39.0 – 26.8)	Neglected
a_{12}	0.38	(-0.26 – 1.01)	Neglected	11.1	(-21.8 – 44.0)	Neglected

Table 3.14. Factorial design coefficients determined for the injection nozzle and ignition delay on the wheat starch explosivity parameters (Fixed nominal concentration: 500 g/m^3)

Coefficient	P_{max}			$(dP/dt)_{max}$		
	Value	Confidence interval (95%)	Result	Value	Confidence interval (95%)	Result
a_0	6.01	(5.54 – 6.49)	Accepted	225.2	(187.4 – 263.1)	Accepted
a_1	0.49	(0.01 – 0.96)	Accepted	38.8	(0.9 – 76.6)	Accepted
a_2	-0.11	(-0.59 – 0.36)	Neglected	-76.0	(-113.8 – -38.2)	Accepted
a_{12}	0.16	(-0.31 – 0.64)	Neglected	38.0	(0.1 – 75.9)	Accepted

Finally, the following linear regressions denote the multilinear regression posed for the explosivity of a dust cloud of micrometric wheat starch with a nominal concentration of 500 g/m^3.

$$P_{max} = 6.09 + 0.49 X_1 \qquad 3.53$$

$$\left(dP/dt\right)_{max} = 225.2 + 38.8 X_1 - 76 X_2 + 38 X_1 X_2 \qquad 3.54$$

3.6.5 Determination of the ignition delay

The results of the experimental tests that were performed with the 20 L dispersion sphere allowed identifying different dispersion regimes. The behaviors that were observed correspond to the evolution of the velocity field during the gas injection and the subsequent time periods. For this reason, Figure 3.54 presents a comparison of the velocity distribution of the gas that was determined with the DPIV analyses and the diameter d_{50} that was established with the granulometric tests.

The results obtained from the different the different analyses allow establishing an appropriate ignition delay for the dust cloud formed with the organic dust that was considered for this thesis. Evidently, an ignition of the dust cloud in the instability stage (0-50 ms) will be submitted to high gas velocities. The main issue associated to the condition represented in Figure 3.54A relies on the low dust concentration that is observed in the region where the cloud is ignited. This fact represents a high uncertainty level not only because of the instantaneous variations of the solids concentration but also due to the important variations of the particle size distribution and the high energy dissipation. On the contrary, an ignition in the late stage of dust dispersion (after 100 ms) represents a higher ignitability of the cloud due to the increase of the local concentration of the dust at the geometric center of the 20 L sphere (Figure 3.54C). Nevertheless, this time period is recommended only if the soli material is not considered as a cohesive powder. In accordance with this statement, it is possible to establish that the intermediate region that is developed at the end of the instability region (50-90 ms) is appropriate to achieve an important reduction of the particle size distribution without considering a high uncertainty level in the results of the explosibility test (Figure 3.54B).

This analysis becomes more relevant on the characterization of the flammability parameters of high concentration dust clouds formed in conditions that promote the solids agglomeration (e.g. high humidity). For these particular cases, it is recommended to reduce slightly the ignition delay to develop the combustion process in conditions that do not constitute a rapid augmentation of the mean diameter.

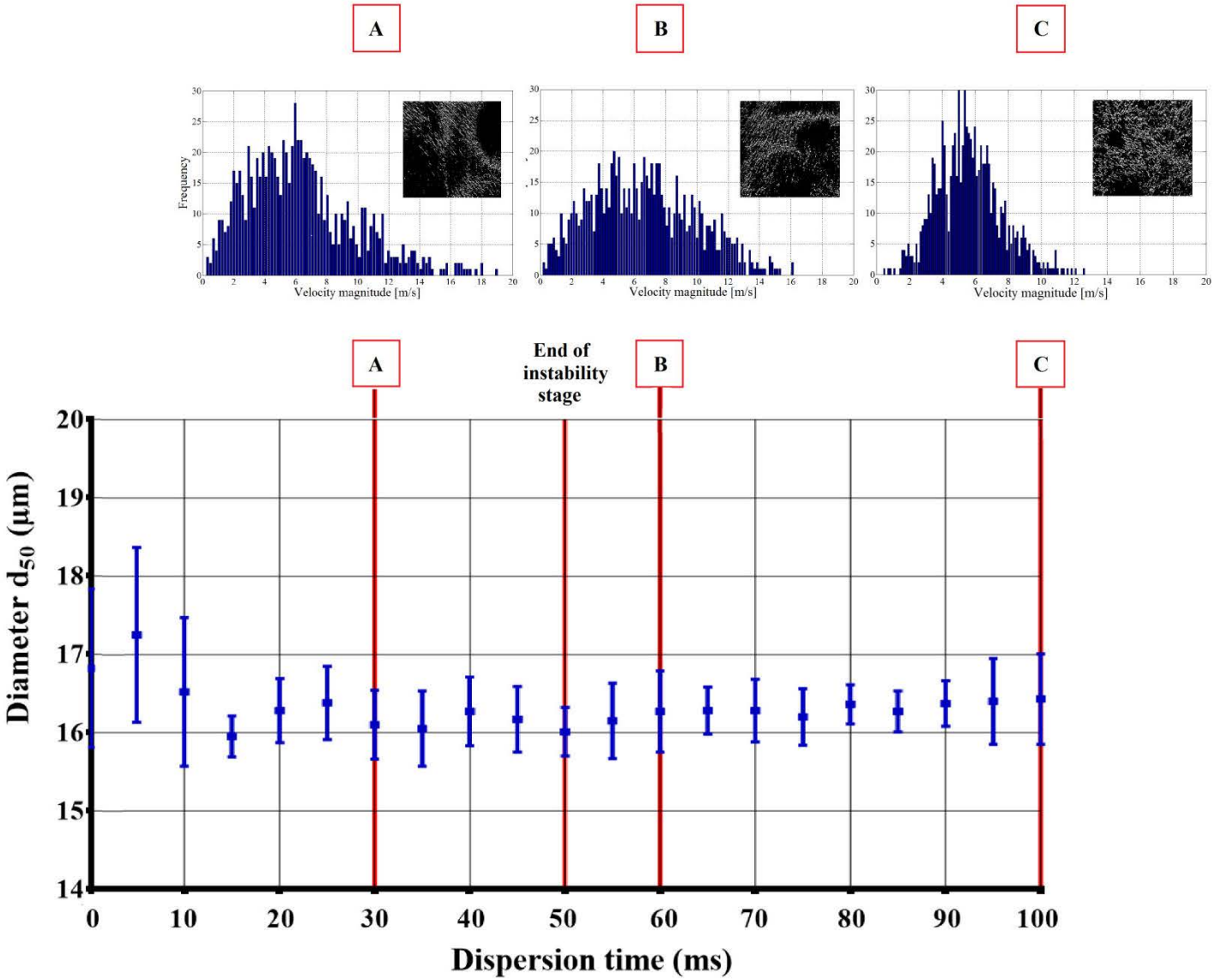

Figure 3.54. Influence of the velocity field on the variations of the Particle Size Distribution of a dust cloud formed with an injection at 20 barg
A. Instability stage (30 ms) B. Ignition delay (60 ms) C. Stability stage (100 ms)

3.7 CONCLUSIONS

L'approche expérimentale de l'étude descriptive qui a été proposée pour cette thèse a caractérisé deux tests d'inflammabilité. À cette fin, l'implémentation des outils différents a été envisagée pour établir l'influence des paramètres d'opération sur la détermination de l'explosivité des poussières combustibles. Dans le cadre de cette étude, l'aérodynamique associée à la dispersion de poudres a été décrite à partir de l'analyse de certains aspects associés aux phénomènes caractéristiques du nuage combustible. Alors, les tests expérimentaux ont été focalisés sur l'évolution des niveaux de turbulence et ses effets sur les conditions du mélange. Ensuite, les conclusions obtenues à partir des tests réalisés avec les deux appareillages seront discutés ci-dessous.

Tube Hartmann modifié

Les tests descriptifs se sont déroulés avec des échantillons de l'aluminium et de l'amidon de blé. Au départ, la dispersion de ces poussières micrométriques a montré que la distribution de tailles de particule et la densité de particule établissent une vitesse de montée différente pour chaque matériau. Cette condition est attribuée aux niveaux de fragmentation caractéristiques des poudres analysées. En effet, l'aluminium accomplit une distribution de tailles plus réduite qui favorise les contraintes de trainée à cause d'une augmentation de la surface totale de l'échantillon. Pour cette raison, la majeure partie du nuage peut être localisée à hauteurs différentes lors du moment de l'ignition.

En outre, les résultats ont permis de classifier la dispersion des poudres combustibles en trois étapes à partir des variations observées dans les distributions de tailles de particules des deux matériaux testés ainsi que la turbulence de l'écoulement de gaz. Donc, il y a une étape caractérisée pour une haute turbulence dans l'écoulement. Cette période favorise la réduction de taille des particules ainsi que la dispersion de la poudre. Cette phase est suivie par une courte étape de transition et une phase de stabilisation qui favorise l'agglomération et la sédimentation des agrégats.

En outre, les résultats ont posé une base de fondement sur les limitations de l'hypothèse d'homogénéité du nuage à l'intérieur du tube de dispersion qui est normalement considérée pour la caractérisation des poussières combustibles.

Ensuite, une analyse de sensibilité a été réalisée pour l'étude de l'influence de la pression d'injection certains paramètres sur la dispersion de l'amidon de blé tels que la ségrégation et la fragmentation. L'évaluation de la influence de la pressurisation du gaz injecté au tube de dispersion a établi que la valeur qui est définie aux standards (7 barg) peut être modifiée afin d'obtenir les niveaux de turbulence appropriés sans compromettre les niveaux de fragmentation qui caractérisent l'explosivité de la poudre. Pour le cas spécifique de l'amidon de blé, les injections de gaz réalisées à 5 et 6 barg ont montré des résultats satisfaisants parce qu'ils gardent un bon accord avec la valeur standard.

Sphère de 20 litres

L'approche expérimentale de la sphère de 20 litres a envisagé plutôt l'évaluation de ses paramètres d'opération. Pour cette phase du projet, la dispersion de l'amidon de blé a été prise comme le cas d'étude. Cette analyse a été focalisée sur les paramètres suivants afin d'établir leur influence sur les résultats expérimentaux de l'appareil :

- Concentration de la poudre
- Temps d'ignition

- Pression d'injection

Pour le développement des tests descriptifs, une nouvelle sphère a été construite en acier inoxydable. L'appareillage est composé de cinq fenêtres qui ont permis de coupler de systèmes d'analyse de champs de vitesse et des distributions de tailles de particule ainsi que filmer l'évolution du nuage avec une caméra de haute vitesse. De la même manière, un nouveau disperseur a été construit pour constituer un point de référence pour la caractérisation du disperseur qui est défini dans les normes standardisées. Alors, le design de ce système d'injection a été conçu pour faire une distribution symétrique de la poudre à l'intérieur de la chambre de dispersion de la sphère.

Les vidéos de haute vitesse ont montré que la distribution de la poudre à l'intérieur de la chambre de dispersion est plus homogène avec le nouveau disperseur. Néanmoins, une analyse de sensibilité réalisée pour l'influence de la concentration sur la sévérité des explosions a établi que ce disperseur détermine une valeur inférieure pour chaque paramètre d'inflammabilité. Évidemment, la concentration de la poudre est inférieure lorsque la poudre est plus distribuée dans la sphère. Néanmoins, l'écart entre les deux systèmes d'injection réduit lorsque la masse de l'échantillon est augmentée et il y a une majeure disponibilité d'énergie.

En plus, les données expérimentales ont également montré que ces dispositifs représentent une faible influence sur la fragmentation de la poudre. En effet, les variations de la distribution de taille sont associées plutôt aux contraintes exercées par le fluide de dispersion sur la surface des agrégats. Pour cette raison, une analyse a été proposée pour décrire l'évolution du nuage à l'intérieur de la sphère et déterminer la pertinence des valeurs qui sont fixés pour la pressurisation du gaz et l'allumage des sources d'ignition.

En outre, la caractérisation réalisée avec les analyses DPIV a établi que le nuage a un comportement qui permet de faire une classification similaire à la classification proposée pour les étapes de dispersion de la poudre dans le tube Hartmann modifié. Donc, les résultats ont montré que le temps d'allumage qui est standardisé pourrait être augmenté pour l'amidon de blé. Cette modification est proposée parce que le mélange est dans la période de transition 60 ms après le début de l'injection et il n'y a pas une grande variation des tailles de particule pendant les 30 ms suivantes.

Finalement, les résultats ont montré que la duration des étapes n'est pas affectée par les variations de la pression d'injection. Néanmoins, l'analyse a posé que l'intensité de la turbulence est définie par cette variable. Par conséquent, il est possible d'établir qu'il y a une pression minimale pour le développement d'un test d'inflammabilité. Alors, la valeur de cette pression dépend des propriétés du matériau combustible. Pour le cas d'étude qui a été considéré ci-dessus, la pression minimale est environ 20 barg.

Les résultats de ce chapitre constituent les données de support et de validation des simulations prédictives qui ont été proposées pour l'approche numérique. Donc, elles seront reprises ultérieurement afin de réaliser une description plus détaillée du comportement du nuage et des phénomènes associés.

3.8 LIST OF VARIABLES

A	Cross-section of the inlet of the vessel orifice	[m^2]
Ar	Archimedes number	[-]
A_T	Cross-section of the inlet of the modified Hartmann tube	[m^2]
a	Particle acceleration	[$m \cdot s^{-2}$]
C	Constant of the polytropic expansion of the gas	[$kPa \cdot m^3$]
C_{AB}	Intensity correlation matrix	[-]
C_d	Adjustment parameter of the discharge coefficient	[-]
C_0	Discharge coefficient	[-]
C_p	Heat capacity of the gas B at constant pressure	[$kJ \cdot kmol^{-1} \cdot K^{-1}$]
C_v	Heat capacity of the gas B at constant volume	[$kJ \cdot kmol^{-1} \cdot K^{-1}$]
D_o	Internal diameter of the connection pipe	[m]
D_V	Internal diameter of the vessel	[m]
$\overline{d}$	Size constant of the Rosin-Rammler equation	[m]
d_p	Particle diameter	[m]
e_1	Internal energy of the gases A and B inside the balloon	[$kJ \cdot kmol^{-1}$]
e_2	Internal energy of the gases A and B inside the vessel	[$kJ \cdot kmol^{-1}$]
f	Moody's friction factor	[-]
g	Gravitational acceleration	[$m \cdot s^{-2}$]
g_c	Conversion factor	[$kg \cdot m \cdot kN^{-1} \cdot s^{-2}$]
h_v	Enthalpy of the gas B that passes from the vessel to the balloon between the times t-Δt and t	[$kJ \cdot kmol^{-1}$]
$K_{contraction}$	Pressure drop constant for the gas contraction at the vessel outlet	[-]
$K_{expansion}$	Pressure drop constant for the gas expansion at the balloon inlet	[-]
K_{valve}	Pressure drop constant of the electro-valve	[-]

L_o	Length of the connection pipe	[m]
M	Molecular weight of the gas	[kg·kmol $^{-1}$]
$\dot{m}$	Mass flow of the gas B	[kg· s^{-1}]
$\dot{m}_{choked}$	Choked mass flow of the gas B	[kg· s^{-1}]
$\dot{m}_{non-choked}$	Non-choked mass flow of the gas B	[kg· s^{-1}]
n_{sd}	Distribution parameter of the Rosin-Rammler equation	[-]
η	Exponent of decay of turbulence in the gas flow	[-]
$n_{A,1}$	Moles of the gas B inside the balloon	[kmol]
$n_{A,2}$	Moles of the gas B inside the vessel	[kmol]
$n_{A0,1}$	Moles of the gas A inside the balloon before the injection	[kmol]
$n_{B,1}$	Moles of the gas B inside the vessel	[kmol]
$n_{B,2}$	Moles of the gas B inside the vessel	[kmol]
$n_{B0,2}$	Moles of the gas B inside the balloon before the injection	[kmol]
n_v	Moles of the gas B that pass from the vessel to the balloon between the times t-Δt and t	[kmol]
P	Pressure of the fluid in the flow domain	[Pa]
P_{choked}	Choked pressure of the flow of the gas B	[kPa]
P_1	Pressure of the gas inside the balloon	[kPa]
P_2	Pressure of the gas inside the vessel	[kPa]
Q	Volumetric flow of the gas B	[m^3·s^{-1}]
q	Normalized diameter of the Mie's theory	[m]
R	Ideal gas constant	[kJ·kmol^{-1}·K $^{-1}$]
r	Relative rugosity of the pipe	[mm]
Re	Reynolds number of the gas flow	[-]
T_1	Temperature of the gas inside the balloon	[K]
T_2	Temperature of the gas inside the vessel	[K]

T_{ref}	Reference temperature for the determination of the thermodynamic properties of the fluid	[K]
t	Time elapsed during the gas injection	[s]
$t_{rms,o}$	Initial time for the curve fitting of the decay of turbulence	[ms]
t_0	Initial time of the gas injection	[s]
t_f	Final time of the gas injection	[s]
u	Velocity of the fluid	[m·s^{-1}]
u_s	Slip velocity between the gas and the solid particle	[m·s^{-1}]
u_p	Particle velocity	[m·s^{-1}]
V_1	Balloon volume	[m^3]
V_2	Vessel volume	[m^3]
v_{inj}	Velocity of the gas B at the modified tube's inlet	[m·s^{-1}]
v_B	Velocity of the gas B at the canister's outlet	[m·s^{-1}]
v_{rms}	Root-mean-square velocity of the gas flow	[m·s^{-1}]
$v_{rms,o}$	Root-mean-square velocity of the gas flow at the initial time of the decay of turbulence	[m·s^{-1}]
W_{n_v}	Boundary work of the gas that that comes from the canister	[kJ·s^{-1}]
$W_{n_{A,1}+n_{B,1,t-\Delta t}}$	Boundary work of the gas that is inside the balloon at the time t-Δt	[kJ·s^{-1}]
Y^*	Ratio between the number of moles of gas that get into the balloon and the gas inside this control volume	[-]
Y_d	Mass fraction of solids having a diameter larger than a given particle	[-]

Greek symbols

γ	Heat capacity ratio of the gas	[-]
ΔP	Pressure drop of the gas flow between the two volume controls	[Pa]
Δt	Temporal discretization of the flow simulation	[s]
μ	Dynamic viscosity of the fluid	[Pa·s]
ρ	Fluid density	[kg·m^{-3}]

ρ_p	Particle density	[kg·m^{-3}]
ρ_1	Gas density at the conditions of the control volume N°1	[kg·m^{-3}]
ρ_2	Gas density at the conditions of the control volume N°2	[kg·m^{-3}]
τ_s	Relaxation time of a solid dispersed particle according to the Stoke's law	[s]

3.9 REFERENCES

Abbasi, T., & Abbasi, S. A. (2007). Dust explosions–Cases, causes, consequences, and control. *Journal of Hazardous Materials*, *140*(1-2), 7–44.

Adrian, R. J. (2005). Twenty years of particle image velocimetry. *Experiments in Fluids*, *39*(2), 159–169.

Amyotte, P. R., Mintz, K. J., Pegg, M. J., Sun, Y.-H., & Wilkie, K. I. (1991). Laboratory investigation of the dust explosibility characteristics of three Nova Scotia coals. *Journal of Loss Prevention in the Process Industries*, *4*(2), 102–109.

Antony, J. (2014). *Design of Experiments for Engineers and Scientists*. Elsevier.

Azema, N. (2006). Sedimentation behaviour study by three optical methods — granulometric and electrophoresis measurements, dispersion optical analyser. *Powder Technology*, *165*(3), 133–139.

BeMiller, J. N., & Whistler, R. L. (2009). *Starch: Chemistry and Technology*. Academic Press.

Biswas, G. (2003). *Introduction to Fluid Mechanics and Fluid Machines,2e*. Tata McGraw-Hill Education.

Bouillard, J., Vignes, A., Dufaud, O., Perrin, L., & Thomas, D. (2010). Ignition and explosion risks of nanopowders. *Journal of Hazardous Materials*, *181*(1-3), 873–880.

Brossard, C., Monnier, J. C., Barricau, P., & Vandernoot, F. X. (2009). Principles of Particle Image Velocimetry. *Aerospace Lab*, (1). Retrieved from http://aerospacelab.onecert.fr/sites/www.aerospacelab-journal.org/files/Al1-03.pdf

Buchhave, P. (1992). Particle image velocimetry—status and trends. *Experimental Thermal and Fluid Science*, *5*(5), 586–604.

Calvert, G., Hassanpour, A., & Ghadiri, M. (2013). Analysis of aerodynamic dispersion of cohesive clusters. *Chemical Engineering Science*, *86*, 146–150.

Castellanos, D., Carreto-Vazquez, V. H., Mashuga, C. V., Trottier, R., Mejia, A. F., & Mannan, M. S. (2014). The effect of particle size polydispersity on the explosibility characteristics of aluminum dust. *Powder Technology*, *254*, 331–337.

Çengel, Y. A., & Cimbala, J. M. (2013). *Fluid mechanics: fundamentals and applications*. New York: McGraw-Hill.

Chiffoleau, G., Newton, B., Holroyd, N., & Havercroft, S. (2006). Surface Ignition of Aluminum in Oxygen. *Journal of ASTM International*, *3*(5), 13536.

Crowe, C. T. (2000). On models for turbulence modulation in fluid–particle flows. *International Journal of Multiphase Flow*, *26*(5), 719–727.

Crowl, D. A., & Louvar, J. F. (2011). *Chemical process safety: fundamentals with applications*. Upper Saddle River, NJ: Prentice Hall.

Cuervo, N., Murillo, C., Dufaud, O., Bardin-Monnier, N., Skali-Lami, S., Remy, J.-F., … Perrin, L. (2014). Combining CFD simulations and PIV measurements to optimize the conditions for dust explosion tests. *Chemical Engineering Transactions*, *36*, 259–264.

Dahoe, A. E., Cant, R. S., Pegg, M. J., & Scarlett, B. (2001). On the transient flow in the 20-liter explosion sphere. *Journal of Loss Prevention in the Process Industries*, *14*(6), 475–487.

Dahoe, A. E., Cant, R. S., & Scarlett, B. (2001). On the decay of turbulence in the 20-liter explosion sphere. *Flow, Turbulence and Combustion*, *67*(3), 159–184.

Di Benedetto, A., Garcia-Agreda, A., Dufaud, O., Khalili, I., Sanchirico, R., Cuervo, N., … Russo, P. (2011). Flame propagation of dust and gas-air mixtures in a tube. In *Proceedings of the 7th Mediterranean Combustion Symposium*. Chia Laguna Cagliari, Sardinia, Italy.

Diez, F. J., Torregrosa, M. M., & Pothos, S. (2011). A comparison between round turbulent jets and particle-laden jets in crossflow by using time-resolved stereoscopic particle image velocimetry. *Journal of Fluids Engineering*, *133*(9), 091301.

Dreizin, E. L. (1996). Experimental study of stages in aluminium particle combustion in air. *Combustion and Flame*, *105*(4), 541–556.

Du, B., Huang, W., Liu, L., Zhang, T., Li, H., Ren, Y., & Wang, H. (2015). Visualization and analysis of dispersion process of combustible dust in a transparent Siwek 20-L chamber. *Journal of Loss Prevention in the Process Industries*, *33*, 213–221.

Dufaud, O., Perrin, L., Bideau, D., & Laurent, A. (2012). When solids meet solids: A glimpse into dust mixture explosions. *Journal of Loss Prevention in the Process Industries*, *25*(5), 853–861.

Dufaud, O., Traoré, M., Perrin, L., Chazelet, S., & Thomas, D. (2010). Experimental investigation and modelling of aluminum dusts explosions in the 20 L sphere. *Journal of Loss Prevention in the Process Industries*, *23*(2), 226–236.

Eckhoff, R. (2003). *Dust Explosions in the Process Industries, Third Edition: Identification, Assessment and Control of Dust Hazards* (3 edition). Amsterdam ; Boston: Gulf Professional Publishing.

Escot Bocanegra, P. (2007). *Études expérimentales et modélisation de la combustion des nuages de particules micrométriques et nanométriques d'aluminium*. Université d'Orléans.

Gerhold, M., & Stahmer, K.-W. (2014). Correlation of Pmax and KSt to specific surface area and calorific value of a dust. *Journal of Loss Prevention in the Process Industries*. Retrieved from http://linkinghub.elsevier.com/retrieve/pii/S0950423014002319

Giuliani, V., de Witt, B., Salluzzi, M., Hugo, R. J., & Gu, P. (2008). Particle velocity detection in laser deposition processing. *Rapid Prototyping Journal*, *14*(3), 141–148.

Glarner, T. (1984). Mindestzündernergie-Einfluss der Temperatur. *VDI-Berichte*, *494*, 109–118.

Henry, F. (2013). *Dynamique des systèmes nanodispersés : application au cas de l'agglomération des nanoparticules*. Université de Lorraine.

Heuer, M., & Leschonski, K. (1985). Results obtained with a new instrument for the measurement of particle size distributions from diffraction patterns. *Particle & Particle Systems Characterization*, *2*(1-4), 7–13.

Huang, H., Dabiri, D., & Gharib, M. (1997). On errors of digital particle image velocimetry. *Measurement Science and Technology*, *8*(12), 1427.

Huang, Y., Risha, G. A., Yang, V., & Yetter, R. A. (2009). Effect of particle size on combustion of aluminum particle dust in air. *Combustion and Flame*, *156*(1), 5–13.

Jiang, B., Lin, B., Shi, S., Zhu, C., & Li, W. (2011). Explosive characteristics of nanometer and micrometer aluminum-powder. *Mining Science and Technology (China)*, *21*(5), 661–666.

Kalejaiye, O., Amyotte, P. R., Pegg, M. J., & Cashdollar, K. L. (2010). Effectiveness of dust dispersion in the 20-L Siwek chamber. *Journal of Loss Prevention in the Process Industries*, *23*(1), 46–59.

Kühner, A. (1994). *Operating instructions for the 20 litre apparatus 5.0*. Basel, Switzerland.

Li, A., & Ahmadi, G. (1992). Dispersion and Deposition of Spherical Particles from Point Sources in a Turbulent Channel Flow. *Aerosol Science and Technology*, *16*(4), 209–226.

Li, H. Z., Wang, J., & Fan, J. M. (2009). Analysis and modelling of particle velocities in micro-abrasive air jet. *International Journal of Machine Tools and Manufacture*, *49*(11), 850–858.

Maoling, L. (2012). Research on Protection Measures and Explosion about Aluminum Dust. *Procedia Engineering*, *43*, 516–518.

Marmo, L., Cavallero, D., & Debernardi, M. L. (2004). Aluminium dust explosion risk analysis in metal workings. *Journal of Loss Prevention in the Process Industries*, *17*(6), 449–465.

Masuda, H. (2009). Dry dispersion of fine particles in gaseous phase. *Advanced Powder Technology*, *20*(2), 113–122.

Mercer, D. B., Amyotte, P. R., Dupuis, D. J., Pegg, M. J., Dahoe, A., de Heij, W. B. C., … Scarlett, B. (2001). The influence of injector design on the decay of pre-ignition turbulence in a spherical explosion chamber. *Journal of Loss Prevention in the Process Industries*, *14*(4), 269–282.

Nai-Ning, W., Hong-Jian, Z., & Xian-Huang, Y. (1992). A versatile Fraunhofer diffraction and Mie scattering based laser particle sizer. *Advanced Powder Technology*, *3*(1), 7–14.

Olayemi, O. J., Oyi, A. R., & Allagh, T. . S. (2008). Comparative evaluation of maize, rice and wheat starch powders as pharmaceutical excipients. *Nigerian Journal of Pharmaceutical Sciences*, *7*(1), 131–138.

Pedersen, N., Larsen, P. S., & Jacobsen, C. B. (2003). Flow in a Centrifugal Pump Impeller at Design and Off-Design Conditions—Part I: Particle Image Velocimetry (PIV) and Laser Doppler Velocimetry (LDV) Measurements. *Journal of Fluids Engineering*, *125*(1), 61.

Peleg, M. (1996). Determination of the parameters of the Rosin-Rammler and beta distributions from their mode and variance using equation-solving software. *Powder Technology*, *87*(2), 181–184.

Perry, Robert, H., & Green, D. W. (1997). *Perry's Chemical Engineers' Handbook* (7th Edition). McGraw-Hill Professional.

Proust, C. (2006). Flame propagation and combustion in some dust-air mixtures. *Journal of Loss Prevention in the Process Industries*, *19*(1), 89–100.

Raffel, M. (2007). *Particle Image Velocimetry*. Berlin, Heidelberg: Springer Berlin Heidelberg. Retrieved from http://link.springer.com/10.1007/978-3-540-72308-0

Rzal, F., & Veyssiere, B. (1994). Propagation mechanisms of starch particles-air flames. *Proceedings of the Sixth International Colloquium on Dust Explosions*, 186–200.

Siwek, R. (1988). Reliable determination of the safety characteristics in 20-l apparatus. In *Proceedings of the Flammable Dust Explosion Conference* (pp. 529–573). St. Louis: Missouri.

Skjold, T. (2003). *Selected Aspects of Turbulence and Combustion in 20-litre Explosion Vessels. Development of Experimental Apparatus and Experimental Investigation*. University of Bergen, Bergen.

Skjold, T., Castellanos, D., Olsen, K. L., & Eckhoff, R. K. (2014). Experimental and numerical investigation of constant volume dust and gas explosions in a 3.6-m flame acceleration tube. *Journal of Loss Prevention in the Process Industries*, *30*, 164–176.

Soares, R. R., Barbosa, H. C., Braga, R. A., Botega, J. V. L., & Horgan, G. W. (2013). Biospeckle PIV (Particle Image Velocimetry) for analyzing fluid flow. *Flow Measurement and Instrumentation*, *30*, 90–98.

Sommer, H. T., Harrison, C. F., & Montague, C. E. (1992). Particle Size Distribution From Light Scattering. In *Particle Size Analysis*. Retrieved from http://pubs.rsc.org/en/content/chapter/bk9780851864877-00163/978-0-85186-487-7

Stanislas, M., Kompenhans, J., & Westerweel, J. (Eds.). (2000). *Particle Image Velocimetry. Progress towards Industrial Application* (Vol. 56). Dordrecht: Springer Netherlands. Retrieved from http://link.springer.com/10.1007/978-94-017-2543-9

Stasiak, M., Molenda, M., Opaliński, I., & Błaszczak, W. (2013). Mechanical Properties of Native Maize, Wheat and Potato Starches. *Czech Journal of Food Science*, *31*(4), 347–354.

Sujka, M., & Jamroz, J. (2010). Characteristics of pores in native and hydrolyzed starch granules. *Starch - Stärke*, *62*(5), 229–235.

Tebianian, S., Dubrawski, K., Ellis, N., Cocco, R. A., Hays, R., Reddy Karri, S. B., … Grace, J. R. (2015). Investigation of particle velocity in FCC gas-fluidized beds based on different measurement techniques. *Chemical Engineering Science*, *127*, 310–322.

Thielicke, W. (2014). *The Flapping Flight of Birds – Analysis and Application*. Rijksuniversiteit Groningen.

Traoré, M., Dufaud, O., Perrin, L., Chazelet, S., & Thomas, D. (2009). Dust explosions: How should the influence of humidity be taken into account? *Process Safety and Environmental Protection*, *87*(1), 14–20.

Ulrich, K., Stübinger, T., & Witt, W. (2010). Laser Diffraction Results from Image Analysis Data. *WCPT6 2010 – The World Congress on Particle Technology*.

Washburn, E. B., Webb, J. A., & Beckstead, M. W. (2010). The simulation of the combustion of micrometer-sized aluminum particles with oxygen and carbon dioxide. *Combustion and Flame*, *157*(3), 540–545.

Weiler, C., Wolkenhauer, M., Trunk, M., & Langguth, P. (2010). New model describing the total dispersion of dry powder agglomerates. *Powder Technology*, *203*(2), 248–253.

Wengeler, R., & Nirschl, H. (2007). Turbulent hydrodynamic stress induced dispersion and fragmentation of nanoscale agglomerates. *Journal of Colloid and Interface Science*, *306*(2), 262–273.

Xu, C., & Gao, W. (2000). Pilling-Bedworth ratio for oxidation of alloys. *Material Research Innovations*, *3*(4), 231–235.

Yang, W.-C. (2007). Modification and re-interpretation of Geldart's classification of powders. *Powder Technology*, *171*(2), 69–74.

Yuan, J., Huang, W., Ji, H., Kuai, N., & Wu, Y. (2012). Experimental investigation of dust MEC measurement. *Powder Technology*, *217*, 245–251.

Zhang, Q., & Zhang, B. (2015). Effect of ignition delay on explosion parameters of corn dust/air in confined chamber. *Journal of Loss Prevention in the Process Industries*, *33*, 23–28.

CHAPTER IV

CONFRONTATION OF THE COMPUTATIONAL AND EXPERIMENTAL DESCRIPTION OF THE DUST DISPERSION PROCESS

The experimental approach that was discussed in the previous chapter was complemented with the computational characterization of the dust cloud. This descriptive analysis was performed with a set of CFD simulations. This section presents the calculation scheme of the simulations as well as the main results obtained for the gas flow and the dispersed solid phase. The final stage of this study was developed with two different commercial CFD codes for the description of the dispersion process in the modified Hartmann tube and the 20 L sphere: ANSYS Fluent 14.5 and STAR CCM+ 10.04. This condition was established after considering the suitability of the CFD codes for each particular case. For this reason, the discussion of this computational analysis is divided in two segments, which describe in detail the numerical parameters established for the simulations developed with each code. In accordance with this statement, every subdivision of this chapter explains the methodology followed for the numerical description of the dust-air mixture in each standardized test.

Firstly, the computational approach that was posed in ANSYS Fluent 14.5 for the modified Hartmann tube is presented. The explanation of the simulation of the two-phase flow developed inside the dispersion tube of this apparatus began with the definition of the geometry to represent the internal dimensions of the tube and the discretization of the flow domain through a mesh grid. Afterwards, the numerical schemes that were considered for the solution of the conservation equations are discussed in order to establish the calculation mode. Finally, the main results that depict the evolution of the flow field within the dispersion are presented in order to complement the explanation that was carried out previously with the experimental approach. Thus, a comparison of the numerical results with the experimental data is also comprised in the discussion in order to validate the numerical prediction of the flow variables. In addition, the computational cost of the simulations is also briefly discussed in order to evaluate the applicability of the study in the current analysis and further characterization tests of combustible dusts.

Secondly, a similar procedure is proposed for the description of the evolution of the dust cloud in the 20 L sphere. The results obtained with a set of CFD simulations developed with STAR CCM+ 10.04 describe the dispersion process of the combustible dust that was observed with the standard rebound nozzle and the symmetrical device that was designed. Finally, the results obtained with the computational and experimental description of the dispersion process within the two modified apparatuses were considered to establish the most appropriate operating parameters of the flammability tests. This fact determined the conditions that provide the most conservative information about the ignitability and explosibility of the micrometric wheat starch and the micrometric aluminum powder. Moreover, it posed the relevance of considering the physical properties of the dust on the dispersion process that develops before the ignition of a dust cloud. These results showed how the CFD simulations can be considered as a tool that can be utilized in the determination of the flammability parameters of any solid material.

4.1 DESCRIPTION OF THE DUST DISPERSION IN THE MODIFIED HARTMANN TUBE

The dispersion process of a combustible dust in the modified Hartmann tube was modeled according to the design specifications of the prototype utilized in the experimental analysis. These parameters are established in the international standard ASTM E789 - 95 (2001). In accordance with this statement,

the flow domain that was defined for the simulations of the dispersion of micrometric wheat starch is defined as the assembly of several bodies. The structure of the simulation domain is described in Figure 4.1, which shows an isometric view of the domain as well as some internal depictions that present the injection system:

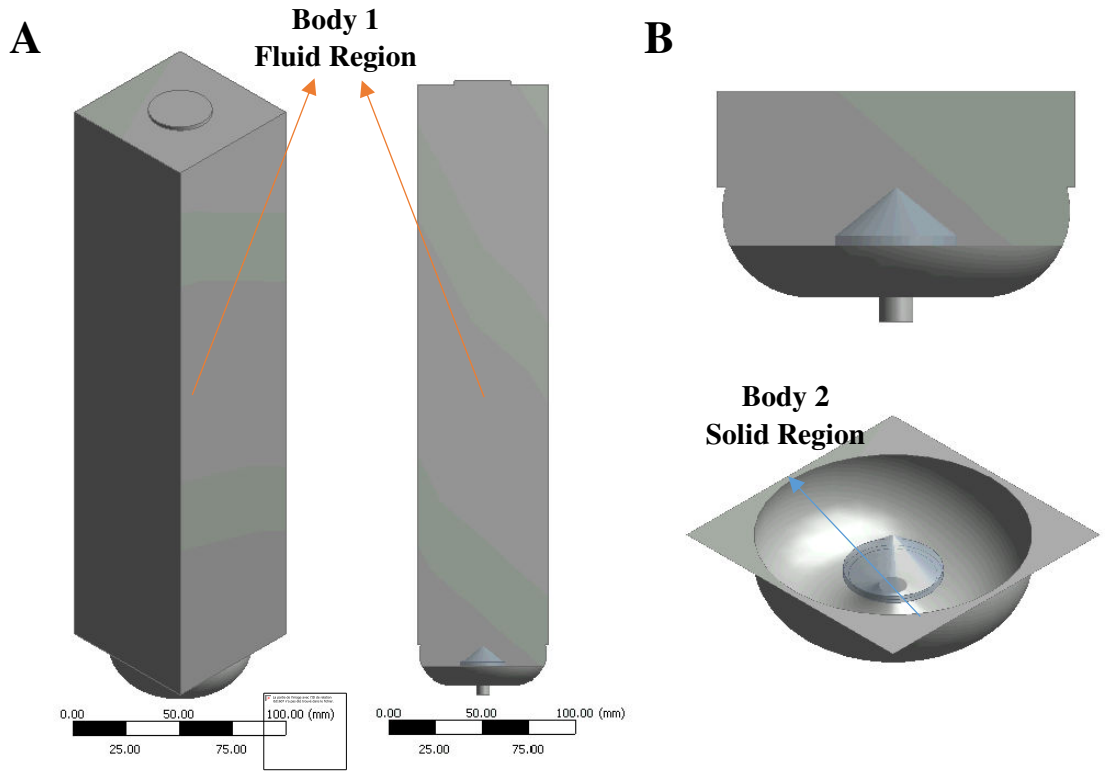

Figure 4.1 Flow domain defined for the modified Hartmann tube
a) Dispersion tube b) Injection nozzle

The structure consists of two bodies that will define the flow domain as well as the internal obstruction associated to the injection device. The first body corresponds to the dispersion tube, which is defined as a fluid region. In addition a second body that represents the injection nozzle is located at the bottom of the tube and consists in a solid region. The definition of an internal solid entity determined the distribution of the injected gas flow at the bottom of the apparatus. The flow domain differs from the geometry of the standardized dispersion tube because it has a squared cross section rather than the circular section of the standard setup. This fact allowed performing the visual tests on flat surfaces (i.e. without optical deformation) as discussed in the previous chapter.

The base of the tube can be observed in Figure 4.1B. This part has a hemispherical shape to locate uniformly the combustible dust before the injection. The pressurized gas that is injected from the bottom of the tube collides against the nozzle and is distributed through the base to disperse the solid sample. Afterwards, the cloud formed by the solids lifting can be described through the particle tracking and the evolution of the flow field.

Finally, there is an additional feature that characterizes the development of the internal flow in the dispersion tube. Figure 4.1A shows a circular vent at the top of the tube that represents the gas outlet placed to release the gas overpressure occurred by an eventual explosion. This part of the structure has an important role on the description of the two-phase flow because it defines a boundary condition for the CFD simulation.

4.1.1 Description of the mesh

The total volume of the flow domain is 1.536 liters. This field is divided in 483,188 tetrahedral cells whose volume ranges between $1.60.10^{-11}$ and $1.17.10^{-8}$ cubic meters. The cells correspond to the discretization of the two bodies presented above. Therefore, the main fraction of the elements of the grid is associated to the fluid body and the dispersion nozzle is represented by a minimum number of solid cells. The meshing grid was constructed in order to achieve the highest element quality possible for the irregular flow domain. In accordance with this statement, Table 4.1 summarizes some of the most important characteristics of the grid that was considered for the discretization of the flow domain:

Table 4.1. Main features of the mesh of the modified Hartmann tube

PARAMETER	VALUE
Meshing method	Tetrahedrons
Number of elements	Fluid: 468,505 Solid: 14,683 Total: 483,180
Number of faces	Interior faces of fluid: 922,735 Interior faces of solid: 28,073 Wall faces: 31,136 Total: 981,944
Average element quality	83.84%

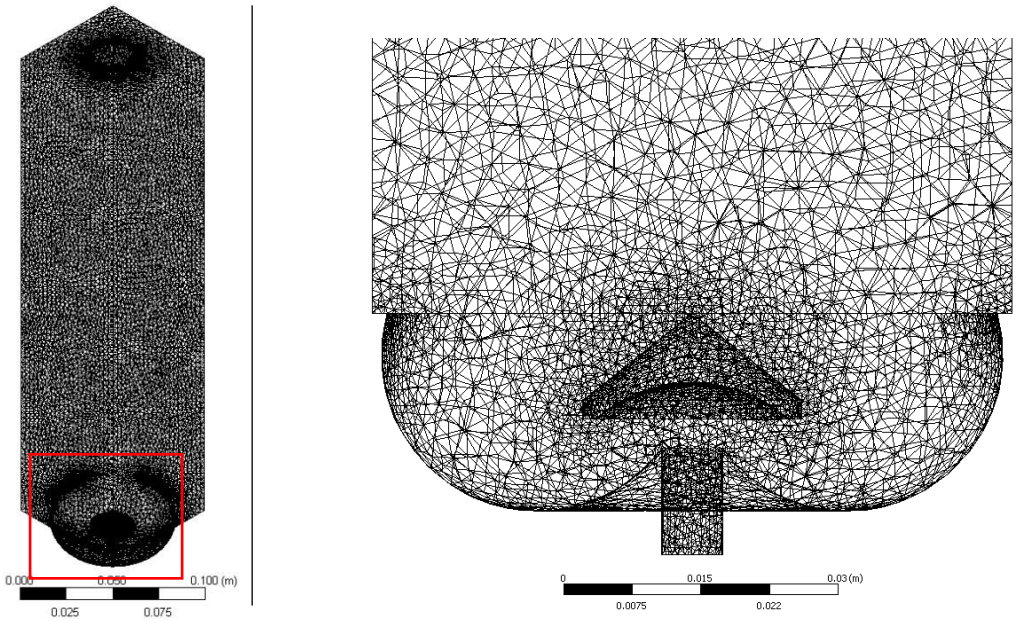

Figure 4.2. Mesh of the flow domain of the modified Hartmann tube

The presence of two different types of regions (fluid and solid) creates certain wall zones that are submitted to two different formulations. For this reason, a shadow or duplicate face is created by the solid body in each side of the interacting faces. This definition allows establishing a distinct wall zone for the fluid and solid regions. In this manner, the solid surfaces determine the direction of the main streamlines of the gas flow according to its distribution at the bottom of the dispersion tube. Figure 4.2 presents the mesh that was considered for the simulation of the two-phase flow in the modified Hartmann tube. This picture also describes the boundaries of the domain that were refined during the generation of the grid.

The geometry of the dispersion tube is irregular, especially in the zones near the injection nozzle. For this reason, the mesh constructed for this study is non-uniform. This fact implies that some

refinements were defined for the regions in which the gas flow reaches the highest expansion velocities. These modifications have been addressed in the regions near the walls and the nozzle in order to characterize properly the zones in which the gas expansion and the no-slip condition generate the greatest velocity gradients in the flow field. Moreover, the size of the finite volumes of the mesh also characterizes the energy dissipation associated to the subgrid scales of the DES turbulence model. Therefore, the specification of a non-uniform mesh has provided an accurate description of the transient conditions of the dust cloud in these zones as well as the enhancement of the convergence of the calculation.

The mesh refinement was performed with the inclusion of a size adaptation constraint that established the size span of the cell volumes. This parameter was set between $8.5.10^{-4}$ and $3.4.10^{-3}$ m. For this purpose, the mesh was constructed with an inflation process defined with a growth rate of 1.2. This factor defines an increase of 20% of the cell thickness with regard to the previous layer as it moves away from the walls. This fact represented a mean aspect ratio of 1.84 for the cells in both bodies. This value is below 1000; hence the stretching of the tetrahedral cells will not compromise the quality of the numerical results (Ansys Inc., 2009).

4.1.2 Boundary and initial conditions

The next step in the definition of the transient simulation consists in the specification of the initial and boundary conditions of the flow domain. These values were established according to the operating protocol of the standard test, which envisages the injection of pressurized gas into a chamber filled with the gas of the environment (see section 3.4). These parameters are very important because they dictate the particular solutions to be obtained with the governing equations (Wendt, 1992). This section briefly describes the conditions established for both phases in the simulation of the modified Hartmann tube.

A. ***Boundary conditions***

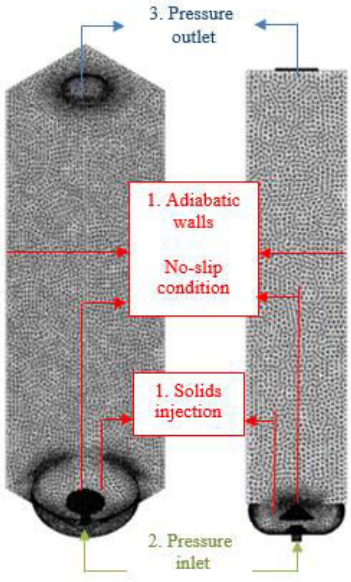

Figure 4.3. Boundary conditions of the CFD simulation of the modified Hartmann tube

The flow domain envisages three different types of boundary conditions that are shown in Figure 4.3. The first condition corresponds to the internal walls and the nozzle (red zones), which were defined as adiabatic surfaces characterized by the no-slip condition. This fact implies that the velocity of the fluid in contact with these regions is equal to their velocity (i.e. null velocity). Moreover, the boundary condition for the solid particles in the walls is defined as a *reflect* condition. This fact implies that the walls cause a change of momentum that is dictated by the coefficient of restitution of the solid phase (see section 4.1.4B).

The second boundary condition corresponds to the gas injection (green zone). This characteristic of the test was modeled with a pressure profile defined for a surface located at the bottom of the flow domain. This specification was accomplished by defining this boundary as a *pressure inlet*. This boundary was defined on the CFD simulation through the implementation of the transient pressure profile that is shown in Equation 4.1. This profile corresponds to the mass and energy balances that were considered in section 3.4 to define the conditions of the gas injection:

$$P_{inlet} = 7.226\times10^{-7}t^4 - 4.699\times10^{-4}t^3 + 0.11108t^2 - 11.21t + 544.5 \quad 4.1$$

Finally, the vent is defined as a *pressure outlet* boundary (blue zone), which is established according to a pressure constant value that corresponds to the environmental conditions (atmospheric pressure). Both inlet and outlet boundaries are defined according to the *escape* condition for the solid particles. This fact means that the trajectory calculations of the parcels that arrive to these surfaces are terminated.

B. ***Initial conditions of the mixture***

- **Fluid phase:** The initial conditions of the flow domain are determined by the environment characteristics. Thus, the pressure of the flow domain is initially set equal to the barometric pressure of the laboratory (101,325 Pa) and the initial temperature was set to 300 K. In addition a null velocity field is defined for the flow domain in order to represent the quiescent state of the fluid within the tube. This condition also implies that the initial value of the turbulent kinetic energy is also equal to zero in the whole domain.

- **Solid phase:** The solid phase is described by a group of parcels that represent a fraction of the total mass according to their particle size distribution. They describe the trajectories of the dispersed phase are placed at the bottom of the dispersion tube, as it is the case for the experimental determination of the MIE. This is accomplished with a surface injection that locates a mass amount equivalent to 0.6 grams in the hemispherical base of the tube. The initial velocity of the parcels is equal to zero in accordance with the experimental protocol of the test, which establishes that particles are placed prior to the beginning of the test.

4.1.3 Numerical parameters associated to the physics of the gas flow

The characteristics of the fluid flow and the mesh determine the numerical parameters of the CFD solver. Thus, the next stage of the problem definition was associated to the selection of the methods that were used by the solver for the evaluation of the physical properties of the flow. This section briefly describes the three numerical aspects that were considered for the setting of the solver parameters. Initially, the main solution algorithm that was posed for the simulation of the gas flow is discussed. Then, the discretization formulations that were adjusted according to the solution scheme to compute the physical properties of the flow field are established. Finally, a brief summary of the numerical models that computed the convective and diffusive terms of the flow properties that arise among the neighboring cells is presented.

A. ***Density-based solver***

The simulations described the evolution with the density-based solver, which is designed for high-speed compressible flows. For this reason, the governing equations of continuity, momentum and energy were solved with an approach that differs from other approaches (pressure-based solver) because initially it establishes the density field from the continuity. Thereafter, it determines the pressure field with an equation of state. The correspondence between these two variables was determined with the Peng-Robinson's cubic equation.

The solution of the governing equations is accomplished when the method creates a system of equations by linearizing the conservation equations in order to obtain a scheme based on an implicit

formulation. This fact implies that the computation of the unknown value of a variable is performed by using a relation that also considers the unknown values of the neighboring cells. Hence the linear equations are coupled and must be solved simultaneously as a "block" system (Ansys Inc., 2009).

The density-based solver develops a sequential computation of the flow variables. Initially, it computes the values associated to the conservation equations and later, it calculates the variables associated to the turbulence of the fluid flow. Finally, the method will solve the equations associated to the interactions with the discrete phase (combustible dust).

A. *Solver parameters*

The algorithm developed for the density-based solver must be set according to the parameters associated to the discretization of the flow domain. These settings determined the way the governing equations were solved for the finite volumes during the transient simulation. For this purpose, a set of discretization schemes was established in a multigrid formulation. This approach allowed calculating the flow variables and the convective and diffusive terms that are transmitted through the cells of the computational grid.

This section provides some basic details about these calculation schemes in order to present the main parameters of the multigrid formulation. Initially, the numerical integration of the equations considered a time step of 10^{-3} seconds for the description of 120 ms of the dust dispersion process. The numerical solution was performed with 40 iterations per time step and the solution was obtained with a Courant number equal to 0.5 to obtain the necessary calculation stability.

- *Spatial discretization:* The gas flow in the modified Hartmann tube is strongly convective. This condition is observed because the velocity field is clearly directed towards a specific direction of the flow domain. For this particular case, the pressure difference between the gas injected at the bottom of the tube and the dispersion tube favors the upward flow. For this reason the second order upwind differencing scheme was selected for the CFD simulation since it is one-sided differencing technique that takes into account the flow of information (Wendt, 1992). Therefore, the calculation of a flow variable in a given node is more influenced by the nodes located upstream (Versteeg & Malalasekera, 2007).

  The second order of the upwind scheme was chosen to address the accuracy limitations that arise when a first-order backward difference formula is used for the spatial discretization (Wendt, 1992). This order of the upwind scheme was established to consider the multidimensional linear reconstruction approach that achieves a higher-order accuracy at cell faces through a Taylor series expansion of the cell-centered solution about the cell centroid (Ansys Inc., 2009). Moreover, Versteeg and Malalasekera (2007) stated that lower discretization schemes like the first-order upwind differencing, which is commonly used in CFD computations with RANS turbulence modeling, might be too diffusive and generate large truncation errors in LES modeling. Therefore, the second-order or higher-order discretization techniques were more suitable for these analyses.

  The discretization model was implemented according to the Monotone Upstream-Centered Schemes for Conservation Laws (MUSCL) method. This is a third-order convection scheme that blends the second-order upwind scheme with the central difference method. This formulation was chosen because it improves the spatial accuracy for all types of meshes by reducing numerical diffusion (Ansys Inc., 2009). This method was explained by Buffard & Clain, (2010) who posed that this technique is widely used in the industrial context due to its simplicity and adaptation capacity to respond to modeling evolutions and complexities.

- *Temporal discretization:* The transient simulation of the fluid flow demanded a temporal discretization of the governing equations, which was defined according to a second-order scheme

as well. Therefore, the value of a physical scalar variable of the gas flow at any given time depended on the previous and the following time steps. For this reason, the numerical integration of the Navier-Stokes equations was carried out by following an implicit formulation. This option was chosen because it is unconditionally stable with respect to time step size ant it could represent an enhanced accuracy of the numerical solution (Ansys Inc., 2009; Wendt, 1992).

B. *Convective and diffusive terms associated to neighboring cells*

- *Calculation of gradients and derivatives:* The values of a scalar property at the faces of every cell are evaluated according to the specific gradients. Moreover, these parameters are also considered for the computation of the diffusion terms and the velocity gradients (Ansys Inc., 2009). The estimation of these variables could be done with a scheme based on a Green-Gauss theorem or the Least Squares Cell-Based (LSCB) method. The formulation that was implemented in the CFD simulations corresponds to the second alternative.

  The accuracy of LSCB method on irregular unstructured meshes is comparable to the most accurate method based on the Green-Gauss theorem (node-based gradient) and is considerably superior to the basic one (cell-based gradient). In addition, this formulation poses a lower computational cost because it assumes a linear variation of the scalar property from a cell to its neighboring elements (Ansys Inc., 2009). Thus, the coefficient matrix that calculates the gradients depends only on the geometry of the mesh. For these reasons, the LSCB method was considered as the most appropriate alternative.

- *Convective fluxes:* The convective terms of the flux vector (ρu , $\rho u u_i + p$, $\rho u u_j + p$, $\rho u u_k + p$, $\rho u E$) are determined by the density (ρ), pressure (p), total energy (E) and the velocity (u) and its components. These variables constitute the system of governing equations along with the cell values and the viscous stress tensor. The formulation that was considered for the determination of the convective terms is the Advection Upstream Splitting (AUSM) method.

  This scheme determines the upwind extrapolation for the convection part of the inviscid fluxes by calculating a cell interface Mach number, which is based on the characteristic speeds from the neighboring cells. This model was enhanced by Liou (2006) to provide an exact resolution of contact and shock discontinuities and keep the flow field free of oscillations at stationary and moving shocks.

These alternatives increase the computational cost of a simulation performed with the DES model significantly with regard to other simple models. Nevertheless, the convergence levels required for the accurate description process demanded high computational resources. For this reason, the description of the dispersion process was performed by including the corresponding formulations along with an algebraic multigrid (AMG) model. This scheme accelerated the convergence of the solver by computing corrections on a series of coarse grid levels. Hence the computational cost required to obtain a converged solution was considerably diminished by reducing the number of iterations.

Previously, Rao & Medina (2003) discussed the main characteristics of multigrid formulations in solutions of hyperbolic equations at a constant time step over a series of spatial domains. Analyses have been focused on the description of numerical results of computational studies that consider variations in grid spacing. This fact implies that the domain with the least grid spacing is addressed as fine domain and the coarse domains correspond to larger spacing values. The conclusions of this study establish that the computational effort required to solve the equations is reduced due to a lower number of grid nodes. This model was implemented in the calculation of three different groups of the flow variables:

- ✓ *Flow variables:* W-cycle.

- ✓ *Turbulent kinetic energy:* Flexible.
- ✓ *Specific dissipation rate:* Flexible.

The solution of the governing equations of the gas flow in the constructed mesh must face various errors whose sources are established by the size of the mesh. Thus, a classification of the CFD errors is usually considered for the computation of the flow variables. This categorization denotes the high-frequency errors as the divergence elements associated to the coarse meshes and the low-frequency errors as those that are linked to fine grids. The high-frequency errors are removed rapidly by the numerical solvers whereas the low-frequency errors are addressed with a residual reduction rate that might become too low sometimes. This diminution rate is determined by the number of nodes that compose the mesh according to an inversely proportional relation.

The AMG solver establishes that it is possible to reduce the required number of iterations by considering coarser meshes for the intermediate calculations of certain flow properties. Indeed the error associated to a fine mesh can be represented temporarily on a coarse mesh where it can become accessible as a local (high-frequency) error (Ansys Inc., 2009). The Coupled and Scalar AMG Solvers were tuned for efficient reduction of local error and were complemented by the fine-grid relaxation schemes or "smoothers", which are point-implicit linear solvers.

The cycle types were established for the flow variables and the turbulence parameters after considering the calculation sequence of the density-based solver, which computes the flow properties prior to the turbulence parameters. On the one hand, the W-cycle is defined by the number of iterations set by the user for the current grid level (pre-relaxation sweeps) and the fine grid to remove the high-frequency error introduced by the multigrid cycles (post-relaxation sweeps). On the other hand, the flexible cycle is based on an algorithm that invokes coarser grid calculations only when the rate of residual reduction on the current grid level is too slow (Ansys Inc., 2009). Table 4.2 lists the setting parameters that controlled the performance of the multigrid models:

Table 4.2. Control parameters of AMG solver for the CFD simulation

MULTIGRID MODEL	FACTOR	PARAMETER
W-Cycle Scalar	Fixed cycle	-Pre-sweeps: 3 -Post-sweeps: 3 -Max cycles: 30
	Coarsening	-Maximum coarse levels: 40 -Coarsening factor: 2
	Smoother type	-ILU
W-Cycle Coupled	Fixed cycle	-Pre-sweeps: 3 -Post-sweeps: 3 -Max cycles: 30
	Coarsening	-Maximum coarse levels: 40 -Coarsening factor: 8
	Smoother type	-ILU
Flexible cycle	Sweeps and relaxation	-Sweeps: 2 -Maximum fine relaxations: 30 -Maximum coarse relaxations: 50

4.1.4 Numerical parameters associated to the physics of the micrometric wheat starch

This section briefly describes the most relevant considerations that were taken into account for the discrete phase in the simulation of the two-phase flow. The numerical parameters that were established for the discrete phase were adjusted in order to represent the cohesive behavior of the combustible dust. An estimation based on the nominal concentration of the dispersed phase established that the volume fraction of the combustible dust is for a dust sample of 0.6 grams in the dispersion sphere is $4.9.10^{-5}$ approximately. Thus, this description was performed in accordance with a two-way coupling

approach since the global volume fractions of the solid are between 10^{-6} and 10^{-3}. The settings of the CFD simulations correspond to the Discrete Elements Method (DEM) that was discussed in chapter 2.

Despite the fact that a complete description of a two-phase flow would always require the description of all interaction forces of the solid particles, the low solids volume fraction establishes that the influence of the combustible dust on the momentum exchange does not demand a four-way coupling formulation. Nonetheless, the description of low-density powders or large dust samples might imply a higher computational cost due to the utilization of computational techniques based on this formulation.

A. *Calculation parameters*

The equations of motion of every solid parcel in the flow domain were integrated by following an Euler implicit tracking scheme. Liu et al. (2013) recommended a smaller time step for the dispersed phase in order to have a good calculation stability. In accordance with this statement, the time step defined for the integration scheme established for the discrete phase model is 10^{-4} seconds and the particles were advanced at the beginning of the time step.

B. *Coefficient of restitution*

The coefficient of restitution of the micrometric wheat starch was estimated according the strain ratio of the powder. The Poisson's ratio (ϑ) of the material was implemented in Equation 4.2 to calculate the parameter that was considered for the momentum balance of the dispersed phase. Despite the fact that there is not an absolute value for this physical property of the combustible dust in the literature, the Poisson's ratio could be fixed from the data found in it since the span associated to the references considered is quite small. For instance, Mangwandi et al. (2007) determined a value of 0.23 for the Poisson's ratio of a porous powder while Jia et al. (2012) considered a value of 0.3 for cohesive fine particles.

The latter value was used to compute the value of the tangential coefficient of restitution (e_t), which was considered to estimate the normal coefficient of restitution (e_n) with the equations proposed by Freireich et al. (2009) who established that the coefficient can be calculated from the stiffness ratio of the material (k_t / k_n). This ratio is determined by an elastic solid mechanics analysis posed by the following equations:

$$\frac{k_t}{k_n} = \frac{1-\vartheta}{1-\vartheta/2} = \frac{0.70}{0.85} = 0.8235 \tag{4.2}$$

$$e_t = -\cos\left(\pi\sqrt{2.5\frac{k_t}{k_n}}\right) = 0.203 \tag{4.3}$$

$$e_n = e_t\frac{k_n}{k_t} = 0.247 \tag{4.4}$$

The coefficient of restitution is usually given as an input parameter for a CFD simulation. For instance, Thakur et al. (2014) set at a value of 0.4 to predict the flow behavior of cohesive powders. Nevertheless, Mangwandi et al. (2007) have discussed the influence of the velocity of a granule on its coefficient of restitution. These authors have identified a significant decrease of this characteristic in several types of granules when the collision velocity increases. For this reason, the coefficient value

was lowered for the collisions against the walls in order to characterize the impaction of the dust aggregates according to their cohesive behavior. Additionally, a similar analysis defined a high value for the friction coefficient which was set at a value of 0.8 in order to achieve a similar behavior between the computational characterization of the dust cloud and the experimental results.

C. *Spring-dashpot constants of the collision law*

The contact forces of the discrete phase were represented by a spring-dashpot collision law. This formulation was associated to a soft-sphere collision model in Section 2.1.5B. The commercial CFD codes usually implement this model instead of the hard-sphere formulation due to its greater adaptability to different user's settings. In fact, the soft-sphere model is capable of accounting for occurrence of multiple collisions at the same instant whereas the other formulation processes the collisions one by one according to the order in which the events occur. Besides, the soft-sphere model was adopted not only by because of its availability but also because a low coefficient of restitution will lead to a drastic decrease in kinetic energy with the hard-sphere model (Deen et al, 2007). Nonetheless, the hard-sphere model has also been considered for analyses of not too dense systems (Helland et al., 2002; Ibsen, 2002).

Initially, the normal and tangential spring constants of the DEM method were defined. These parameters are treated indifferently by the CFD commercial codes utilized in this study. Hence, the adjustment of these parameters of the model did not differ between the normal and tangential components of the spring constants. In accordance with this statement, the corresponding values of both parameters were established in the same way by considering the diameter d_{50} of the particle size distribution (62.5 µm) and the density (ρ_p = 610 kg·m^{-3}) of the combustible dust, the relative velocity between two colliding particles (u_{pr}) and assuming a maximum overlapping (δ = 0.10). The final value was set equal to 32 N·m^{-1}.

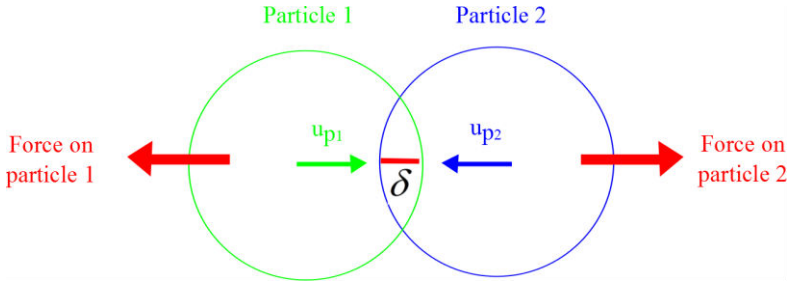

Figure 4.4. Representation of solid particles for the soft-sphere collision model (Ansys Inc., 2009)

$$k = \frac{\pi u_{pr}^2}{3\delta^2} d_{50} \rho_p \qquad 4.5$$

4.1.5 Results and comparison with the experimental approach

The computation of the governing equations of the finite-volume method was performed in a parallelized calculation scheme. The computational resources available consisted of a server Intel Xeon X5650 with 4 processors of 2.66 GHz installed with a set of 48 GB of RAM. The calculation

process was performed in 8 hours approximately with the available computational resources. The computational results obtained with the Eulerian-Lagrangian approach of the CFD simulation are discussed in this section in order to describe the development of the dust cloud within the tube before its ignition.

Initially, the descriptive analysis focused on the description of the dust cloud developed with an injection at 7 barg in order to evaluate the behavior of a dust-air mixture generated within the tube according to the conditions fixed by the international standards (ASTM E789 - 95, 2001; CEI IEC 1241-2-3 Ed. 1.0 b., 1994). Then, the analysis was extended to describe the behavior of the dust cloud when the injection pressure is reduced (variations of the inlet boundary conditions).

A. *Dispersion of micrometric wheat starch in the modified Hartmann tube according to the parameters of the international standards*

The results of the computational approach established that the dispersion process is developed with a gradual injection of the pressurized gas. This fact generates various regimes of dust dispersion within the tube. Hence, the fluid flow is submitted to significant fluctuations that cause non-uniformities of the flow variables in the whole domain. These variations of the flow field have a direct influence on the dispersion of the combustible dust. For the analysis of the relation between these two variables, the main physical conditions of the flow are discussed below. Initially, the velocity magnitude of the gas injection was considered in order to visualize the gradual gas injection. Figure 4.5 shows that the gas is injected into the tube during the first 100 ms of the dispersion process and that the pressurized gas presents a behavior that is characterized by a bulk preceded and followed by lower amounts of air.

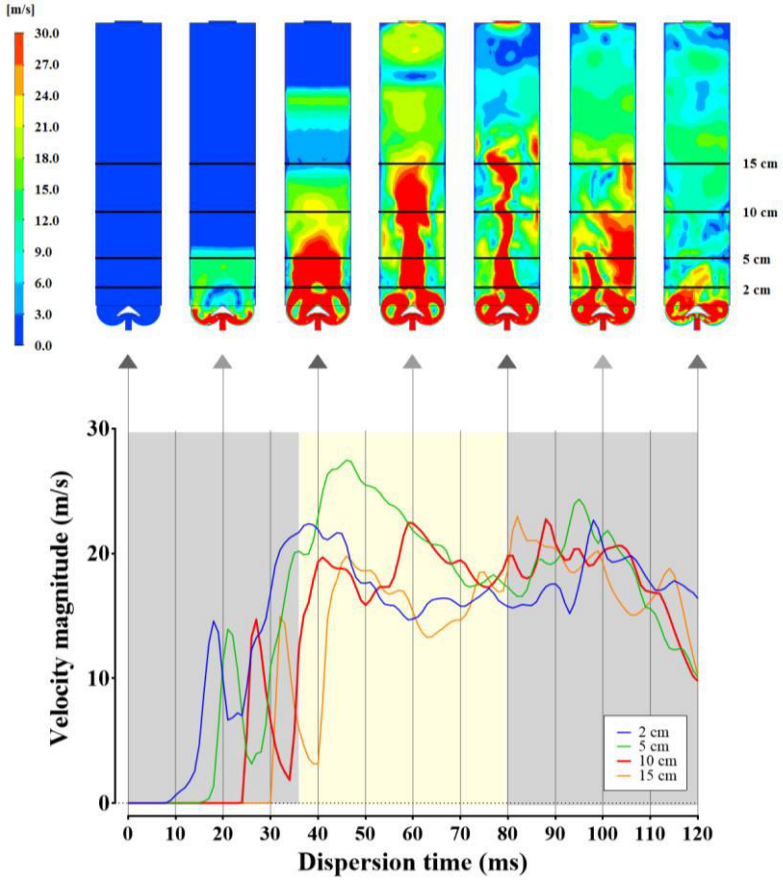

Figure 4.5 .Velocity magnitude of the dispersion gas at different heights of the dispersion tube

This condition confirms that the height of the ignition sources and the ignition delay are relevant parameters for the determination of the most conservative ignition conditions of the combustible dust. Indeed, the velocity profiles shown present several peaks whose amplitudes correspond to the position of the analysis planes and the dispersion time. The highest peaks are generated by the transitory pass of the bulk of the injected gas. Therefore, four different positions were proposed for this analysis. The first two heights are below the actual position of the ignition electrodes (10 cm) whereas the last one is above it.

Some important characteristics of the fluid flow can be observed from the velocity field shown in Figure 4.5. For instance, the gas flow reaches velocities near 20 m/s at the height of the electrodes and 30 m/s in the planes located at 2 and 5 cm over the injection nozzle. These maximum values are reached at different instants and are maintained for larger periods when the height of the analysis plane is lower. However, there is not a remarkable difference between the planes located at 10 and 15 cm. This condition can be explained with the observation of the contours of the velocity field. The results indicate that the flow develops in the lowest region of the tube (0-12 cm). Hence, the dissimilarities among the profiles attributed to the pass of the bulk of the flow are less representative for the highest positions of the dispersion tube.

Moreover, this analysis can be extended to determine the evolution of the three components of the fluid velocity during the dispersion. Figure 4.6 presents the behavior of the transversal components as well as the evolution of the axial component in the analysis planes that were discussed above:

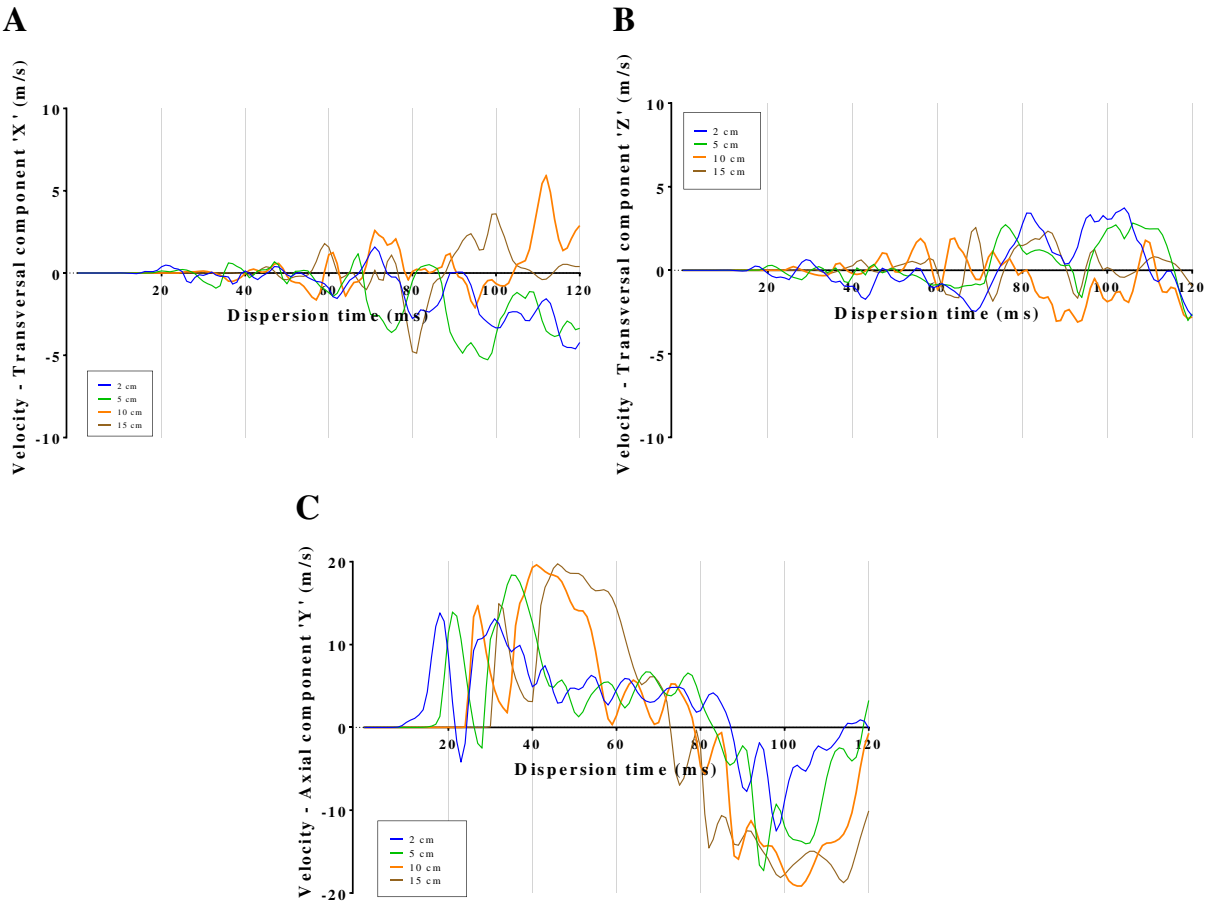

Figure 4.6. Mean values of the three components of the velocity field with an injection at 7 barg A. Transversal (X-axis) B. Transversal (Z-axis) C. Axial (Y-axis).

On the one hand, it can be observed that the fluctuations of the transversal components (X and Z) are located in a span that does not have significant variations during the time elapsed between 20 and 120

ms for all the heights considered except for the lowest plane (2 cm). On the other hand, the profile of the axial component (Y) poses a behavior that differs notably from the other scalar values. The four planes pose a profile that is characterized by three different tendencies. Initially, the axial velocity increases until a maximum value, that is achieved when the bulk drops by the considered height, and then the velocity decreases continuously. Finally, this component stabilizes in a steady negative value. The negative velocities are reached previously and with greater magnitudes for the highest analysis positions. This condition explains why the sedimentation phenomenon that was observed with the high-speed videos (Figure 3.26) occurred at early stages at the highest positions of the dispersion tube.

The presence of greater variations in the axial components allows concluding that this is the variable most affected by the blast conditions. On the contrary, the momentum transfer in the other components corresponds to the instantaneous velocity gradients occurred during the gas expansion and the final sedimentation of the solid particles. Moreover, these results also divide the dispersion process in three different stages that were observed experimentally due to the internal expansion of the injected gas (Section 3.5.2):

- Instability stage: 0 - 40 ms
- Transition stage: 40 – 80 ms
- Stability stage: 0 - 120 ms

The duration of these stages clearly depends on the position of the tube that is being considered. Thus, the time intervals listed above correspond to the position of the ignition electrodes (10 cm). Figure 4.5 and Figure 4.6C show the three different regimes established during the transient process. For the air blast evaluated in this study, the first 40 ms of dispersion show small fluctuations that correspond to the location of the bulk of the dust cloud in the lowest regions of the dispersion tube. Thereafter, the results show a time period that is appropriate for the achievement of the most stable and conservative conditions for the evaluation of the flammability of the dust. This final stage is reached after 80 ms of dust dispersion. Nevertheless, it is compulsory to say that the previous stages might also provide useful information if the ignition of the dust is not performed at the time associated to the high turbulence peaks. Evidently, this assertion depends on the height of the ignition electrodes (Cuervo et al., 2014; Murillo et al., 2015).

Furthermore, the absolute pressure of the gas presents several peaks at the assessed heights during the first 120 ms of the dispersion process. Despite the fact that these variations have low amplitudes during the dispersion process, they indicate how the internal flow develops in the modified Hartmann tube all along the injection. The evolution of this variable is shown in Figure 4.7:

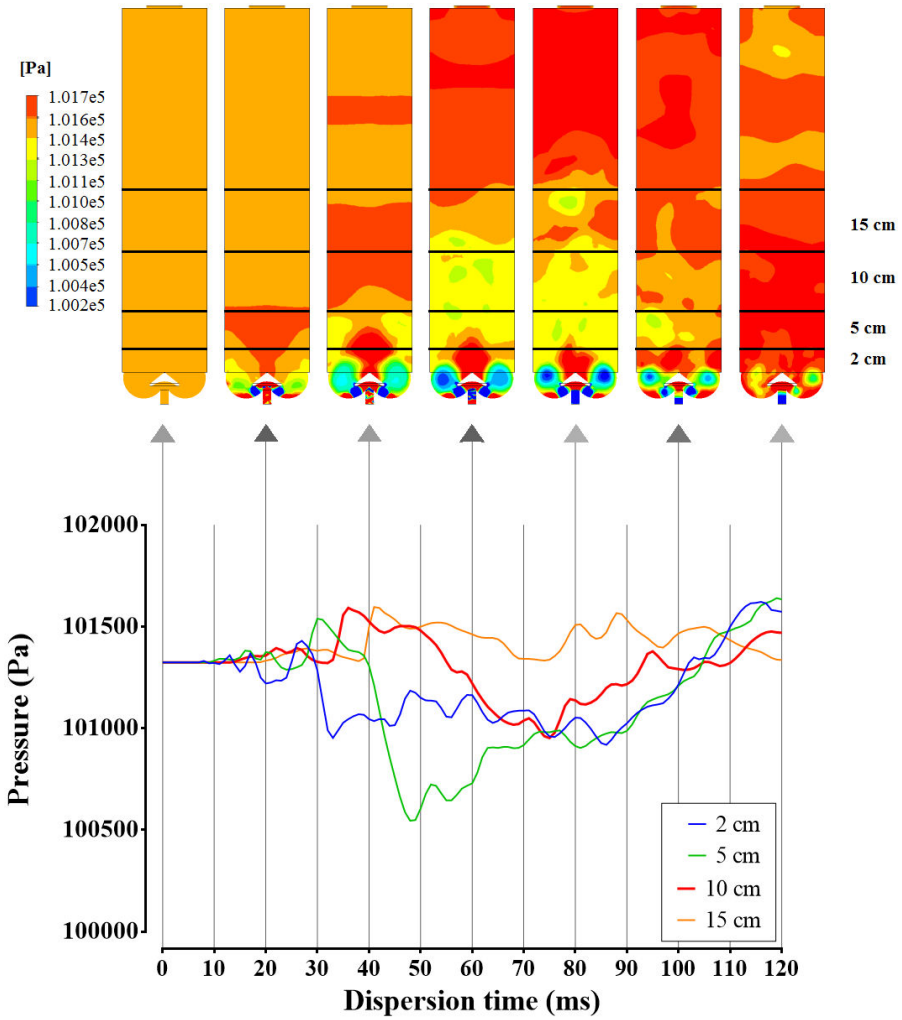

Figure 4.7. Absolute pressure of the dispersion gas at different heights of the dispersion tube

The injection of the pressurized gas causes temporarily an abrupt pressure increase that is immediately followed by a pressure decrease. This reduction of the gas pressure is compensated by the gas fraction that is injected subsequently and the flow induced by the internal pressure gradients. This phenomenon constitutes a heterogeneous distribution of the pressure of the whole system. For instance, a toroidal region located around the nozzle defines a low-pressure zone whereas the high pressure zones are located over the nozzle. Additionally, a reflection wave is evidenced after 40 ms in the surroundings of the outlet vent because of the collision of the two-phase flow with the top of the tube. This condition evidenced how the turbulent flow developed the internal pressure gradients that constituted the fluctuations of the transversal components of the fluid velocity during the transient process. This distribution of the gas pressure inevitably alters the streamlines of the fluid flow; hence some vortex structures are formed at the bottom of the tube. This characteristic of the mean flow will be discussed below.

Furthermore, the turbulence of the gas flow is another important characteristic of the dust cloud that is determined not only by the operating conditions, but also by the presence of the combustible dust in dense clouds (Alletto & Breuer, 2012). This factor becomes determinant after considering that the turbulent kinetic energy of the blast is dispersed continuously due to the fluid expansion and the friction of the two-phase flow. This condition dictates the variations of the transport phenomena associated to the eventual combustion of the cloud as well as the particle size distribution of the dust due to variations of the mixture homogeneity and the flow stresses. Thus, the variations of the turbulence levels of the flow that are caused by these phenomena have a direct influence on the determination of the flammability parameters of the combustible dust. For this reason, the evolution of the turbulent kinetic energy in the tube was also analyzed in this study. Figure 4.8 presents the

evolution of the turbulent kinetic energy of the gas flow that occurs when the fluid is injected at 7 barg:

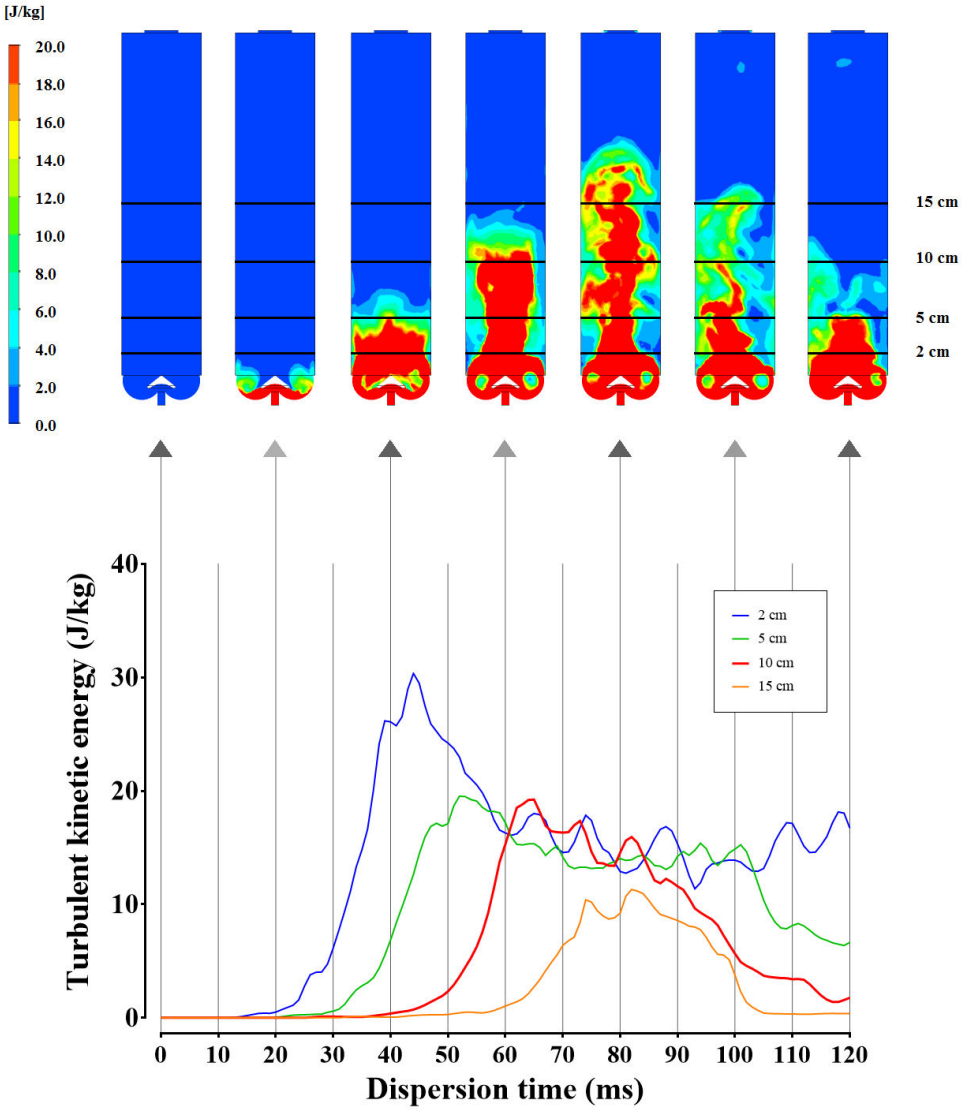

Figure 4.8. Turbulent kinetic energy of the dispersion gas at different heights of the dispersion tube

The variation of the turbulent kinetic energy during the injection process is an important aspect for the determination of the most appropriate position of the ignition electrodes. Indeed, the ignition of a dust air-mixture at the lowest heights is submitted to high fluctuations of the velocity field that imply some notable variations of the transient conditions of both phases. For instance, the energy dissipation at 2 or 5 cm is sustained during longer periods of time; hence the combustion process might be affected by perturbations on the flame propagation and quenching effects on its kernel. Thus, it is not advisable to perform a flammability test at these positions since the reproducibility of the experimental data might be compromised.

In accordance with this statement, the height of the electrodes should be as high as possible. However, a minimum level of turbulence must be achieved at the ignition height in order to avoid the dust segregation and promote the transport of the energy of the chemical reaction to the unreacted gases. In addition, a minimum turbulence level is required to assure a sufficient reduction of the particle size distribution. This condition allows assessing the minimum ignition energy of the combustible dust by taking into account the enhancement of the ignitability of the powder that arises when the dispersed particles are finer. Therefore, the spark generation should not be carried out at 15 cm because the turbulence peak is developed with a low intensity that will represent a low variation of the initial particle size distribution.

The results of the CFD simulation agree with the granulometric analyses performed at different heights (Figure 3.31), which sowed that the reduction of the diameter d_{50} was greater for the dispersion at 5 cm than the one obtained at 10 or 15 cm. In conclusion, the height should be adapted according to the distribution of the gas flow and the segregation of the combustible dust. This parameter must be fixed for wheat starch clouds in a span that ranges between 10 and 15 cm in order to achieve not only an appropriate turbulence level but also a sufficient local concentration of the dispersed dust. For this reason, the computational results were considered to evaluate the segregation of the dust as well.

The influence of the distribution of the gas flow can be evidenced through the analysis of the velocity field focused on the variations that are attributed to the internal geometry of the dispersion tube.

Figure 4.9 shows the local values of the dynamic pressure of the gas flow at the four heights discussed in this analysis. The profiles shown in this figure correspond to the dispersion developed at 60 ms, which is the instant in which the velocity reaches its maximum values. The computational results pose a different behavior for the gas flow in the analyzed positions.

Firstly, it is observed that the lowest position is characterized by the presence of the highest dynamic pressures in the regions near the walls whereas the upper locations are defined only by a jet located in the middle of the tube. The first condition is attributed to the injection nozzle whose geometry is designed to lift uniformly the dust sample that was placed at the bottom of the dispersion tube before the gas injection. This result explains the distribution of the dust cloud towards the walls that was observed in the first milliseconds of the dispersion process (Figure 3.28). Moreover, this characteristic of the gas flow also determines the development of the pressure drop that was evidenced at the bottom of the tube in Figure 4.7.

Afterwards, the gas flow is directed towards the middle of the tube. Evidently, this variation of the fluid flow occurs due to the development of two large eddies in the lower regions. The development of these turbulent eddies can be evidenced in Figure 4.10A which presents the streamlines of the gas flow. It can be established that the large vortex are formed after the pass of the bulk of the dust cloud and disappear when the energy dissipation of the turbulent flow is not compensated by the injected pressurized gas. The comparison of Figure 3.30 and Figure 4.10A shows that the agglomerates fragmentation and the presence of the large vortex structures occur in the same time interval (20-80 ms). This fact defines the relevance of the injection on the development of the mean gas flow and the variations of the particle size distribution of the dispersed phase during the dispersion process.

The end of the gas injection can be evidenced more clearly 20 ms later. The streamlines of the fluid flow at 80 ms pose a more chaotic behavior that is defined by the dissipative tendency of the mean flow. Previously, Figure 4.6C had shown that the negative values of the axial values begin at this instant of the dust dispersion and Figure 4.10A shows that this moment also coincides with the disappearance of the two large turbulent eddies. At this moment, it is possible to draw an important conclusion about the evolution of the dust cloud and its influence on the flammability parameters. The international standards suggest activating the ignition electrodes 120 ms after the beginning of the gas injection. However, this study establishes that the ignition delay can be reduced since the flow turbulence has diminished significantly.

Moreover, it is compulsory to remark that the ignition delay must not be inferior to 80 ms for starch-like samples because it might represent inacceptable uncertainty levels for the experimental results. Nonetheless, it should be stressed that different time delays may be more appropriate for powders with different fluidization properties.

Furthermore, the segregation of the solid phase within the sphere determines the ignitability of the dust cloud as well. Thus, the influence of the physical properties of the combustible dust must be also considered to establish the most appropriate ignition delay in the modified Hartmann tube. For this reason, the dispersibility of the powder should be established from a comparative analysis between the trajectories followed by the gas flow and the dispersed phase.

Figure 4.10B and C present the variations of the local concentration of micrometric wheat starch in the modified Hartmann tube. The micrometric size distribution of this powder causes that the particles dispersed in the cloud follow the same trajectories of the fluid flow during the initial stages of the dust dispersion due to the inertial effects and the drag force exerted by the fluid. However, the behavior is completely different after the first 80 ms of dispersion because the flow exhibits low velocities of the continuous phase that causes the sedimentation of the dispersed particles. For this reason, the results pose that a higher concentration can be obtained at the position of the electrodes (10 cm) if the ignition delay is 100 ms instead of 120 ms.

This modification might constitute the determination of the flammability parameters of the combustible under the most conservative conditions. However, this parameter should be adapted for every powder since their sedimentation velocities can be very different if their size distributions or the particle densities and shapes differ significantly one from each other. This difference was discussed in Section 3.5.2A, which established that the micro-Al 42 powder has a higher rising velocity during the initial stages of dust dispersion and also stabilizes the bulk of the cloud at a higher position in the tube.

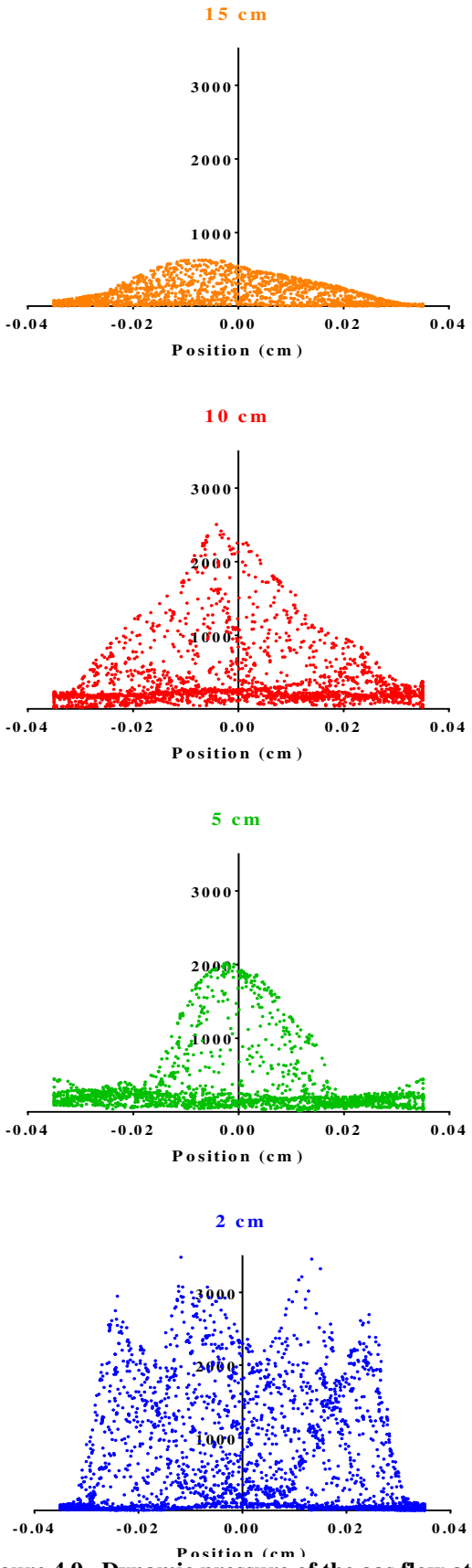

Figure 4.9. Dynamic pressure of the gas flow at 60 ms of dust dispersion

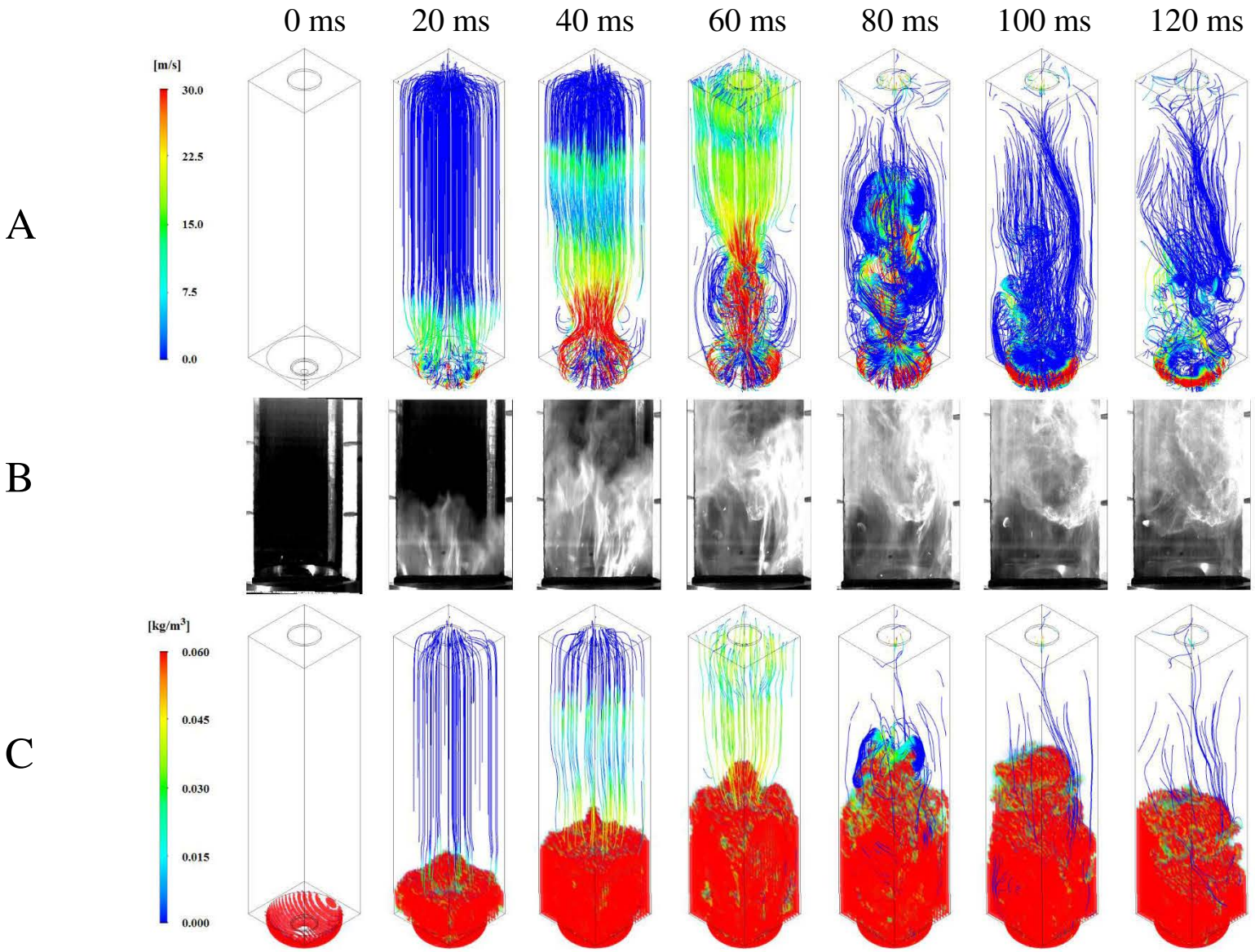

Figure 4.10 Distribution of the wheat starch dust cloud in the modified Hartmann tube
A. Streamlines and velocity of the gas flow (m/s) B. High-speed video C. Dust concentration (kg/m^3)

B. *Sensitivity analysis of the dispersion of micrometric wheat starch in the modified Hartmann tube*

An experimental approach that intended to determine an appropriate ignition delay for the combustible dust through the variation of the injection pressure of the dispersion gas was posed in Section 3.5.2C. This analysis established the variations of the particle size distribution when the pressurization of the fluid varied between 3 and 6 barg. In this way, it was possible to determine the time period in which the d_{50} of the dust indicated an increasing tendency due to the agglomeration and sedimentation phenomena due to the cohesive behavior of the dust (Calvert et al., 2013; Huilin et al., 2010). The solid-solid interactions must be overcome by the turbulent stresses of the fluid flow. For this reason, the computational approach was considered as an interesting alternative to evaluate the evolution of the turbulence levels of the cloud. This analysis will provide a better comprehension of the characteristics of the combustible dust cloud that vary when the injection pressure is reduced. Therefore, the sensitivity analysis that was carried out experimentally was also considered from a computational perspective. For this purpose, the profile of the inlet boundary was adjusted according to the gauge pressures that were considered for the mass and energy balance that was posed in section 3.4. These transient profiles were implemented in the same way that the standard value that was discussed above. The corresponding equations are shown in Table 4.3:

Table 4.3. Pressure profiles established for the inlet boundary in the sensitivity analysis

Injection pressure (barg)	Pressure profile	
6	$P_{inlet} = 7.226\times10^{-7}t^4 - 4.699\times10^{-4}t^3 + 0.11108t^2 - 11.21t + 544.5$	4.6
5	$P_{inlet} = 6.893\times10^{-7}t^4 - 4.358\times10^{-4}t^3 + 0.0995t^2 - 9.69t + 468.3$	4.7
4	$P_{inlet} = 6.578\times10^{-7}t^4 - 4.018\times10^{-4}t^3 + 0.0880t^2 - 8.164t + 392.8$	4.8
3	$P_{inlet} = 5.936\times10^{-7}t^4 - 3.500\times10^{-4}t^3 + 0.0733t^2 - 6.434t + 315.4$	4.9

The influence of the injection pressure was determined with the description of the evolution of the turbulence levels and the dust concentration. These variables were considered to achieve a better comprehension of the most relevant variations of the flow field. Therefore, this computational study complemented the granulometric analyses that were performed on the modified Hartmann tube (See Section 3.5.2C).

Firstly, the computational results shown in Figure 4.11 describe how the turbulent kinetic energy evolves when the injection pressure is reduced. The four injection pressures pose different behaviors that identify the three stages of the dust cloud that were discussed above. On the one hand, the two-phase flows generated at the two lowest pressures are governed by rise of the major fraction of the pressurized gas until 60 ms rather than 80 ms. This fact agrees with the small reductions that were observed experimentally for the diameter d_{50} when the combustible dust was dispersed at 3 and 4 barg. On the other hand, the injections at 5 and 6 barg have a similar tendency to the one performed at the standard conditions since their highest turbulence instant is approximately 80 ms as well (Murillo et al., 2015). This characteristic poses these values as applicable modifications for the flammability tests carried out with micrometric starch.

Moreover, the definition of the injection pressure of the dispersion gas should be determined by the time span that will be considered for a given flammability test. This conclusion arises after evidencing that the achievement of the highest turbulence also means the beginning of the greatest decay of the turbulence levels of the gas flow. Therefore, the only two-phase flow that would represent a similar condition to the one observed with a dust cloud generated at 7 barg at the standard ignition delay (120 ms) is 6 barg (Murillo et al., 2015). On the contrary, the ignition of a dust cloud formed with lower injection pressures is more affected by the phenomena associated to low turbulence (dust agglomeration and segregation).

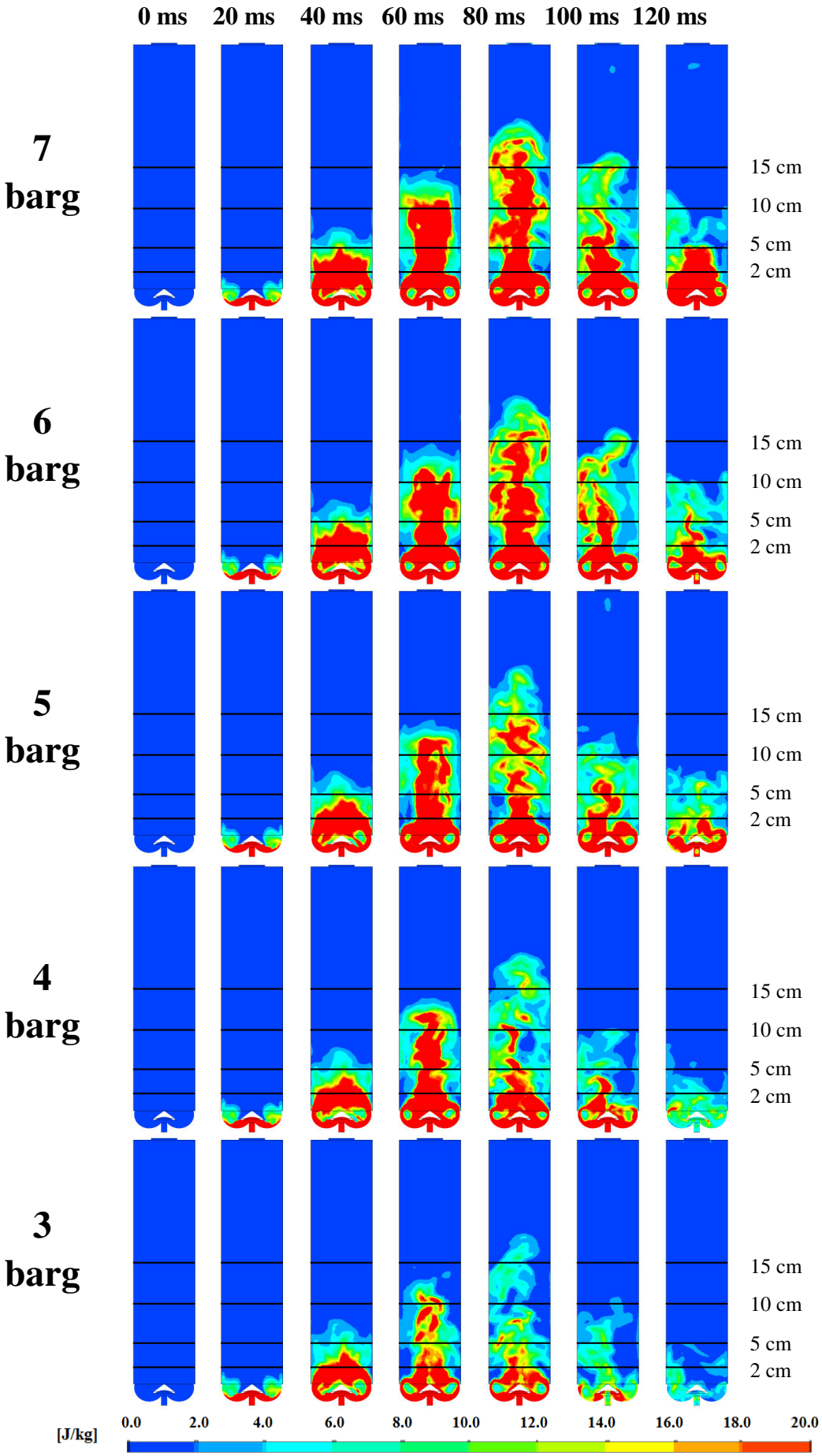

Figure 4.11. Evolution of the turbulent kinetic energy in the modified Hartmann tube at different injection pressures

Furthermore, the experimental results that were discussed in Section 3.5.2C established that the rising velocities of the dust clouds generated at injection pressures between 4 and 6 barg are very similar despite of the different amounts of gas injected. For this reason, the segregation of the combustible dust was also assessed through the computational sensitivity analysis. These variations are presented in Figure 4.12. The concentration profiles shown in this figure complement the analysis of the flow turbulence by establishing the time period the minimum explosible concentration (0.06 kg/m^3) is reached within the dispersion tube. This information is essential to determine the ignition delay of the combustible dust cloud.

A direct comparison of the dispersions generated at 3 and 4 barg with the other injection pressures poses that the initial rising velocities do not differ significantly in the combustible dust. Indeed, the initial pressurization of the gas generates velocities are responsible for drag forces that overcome the particles weight in the first stages of all the analyzed cases (Murillo et al., 2015). This condition can be explained after considering that the pressure of the dispersion tube is considerably lower than the choked pressures of the storage vessel (e.g. the choked pressure of an injection at 3 barg is 2.12 bar). Thus, the most remarkable dissimilarities are associated to two different aspects, which are the position of the bulk of the dust cloud and the deformation of the rising front of the two-phase flow.

The analysis of the dispersions generated between 5 and 7 barg shows that the large turbulent eddies that are formed by a high-pressure injection are capable of retaining the bulk of the cloud at high positions during longer periods of time. This is an important factor for the characterization of dust samples that reach too high velocities due to the inertial effects and the agglomerates fragmentation. The tests of these materials might be associated to the determination of the flammability parameters at too low concentrations. Moreover, the distribution of the dust-air mixture along the tube is also increased when the injection pressure is augmented. This fact reduces the dust segregation and enhances the homogeneity of the dust-air mixture. For this reason, the presence of high concentrations near the walls is promoted by the injections performed at low pressures. This condition was observed because the dispersibility of the solid phase is enhanced by the agglomerates breakup (Eckhoff, 2013). This condition was also evidenced in Figure 3.28 and was attributed to the superiority of the turbulence levels reached by the high-pressure injections. These results allow concluding that the reduction limit for the injection pressure is 5 barg and that an injection over 7 barg would require the placement of the ignition electrodes over 10 cm.

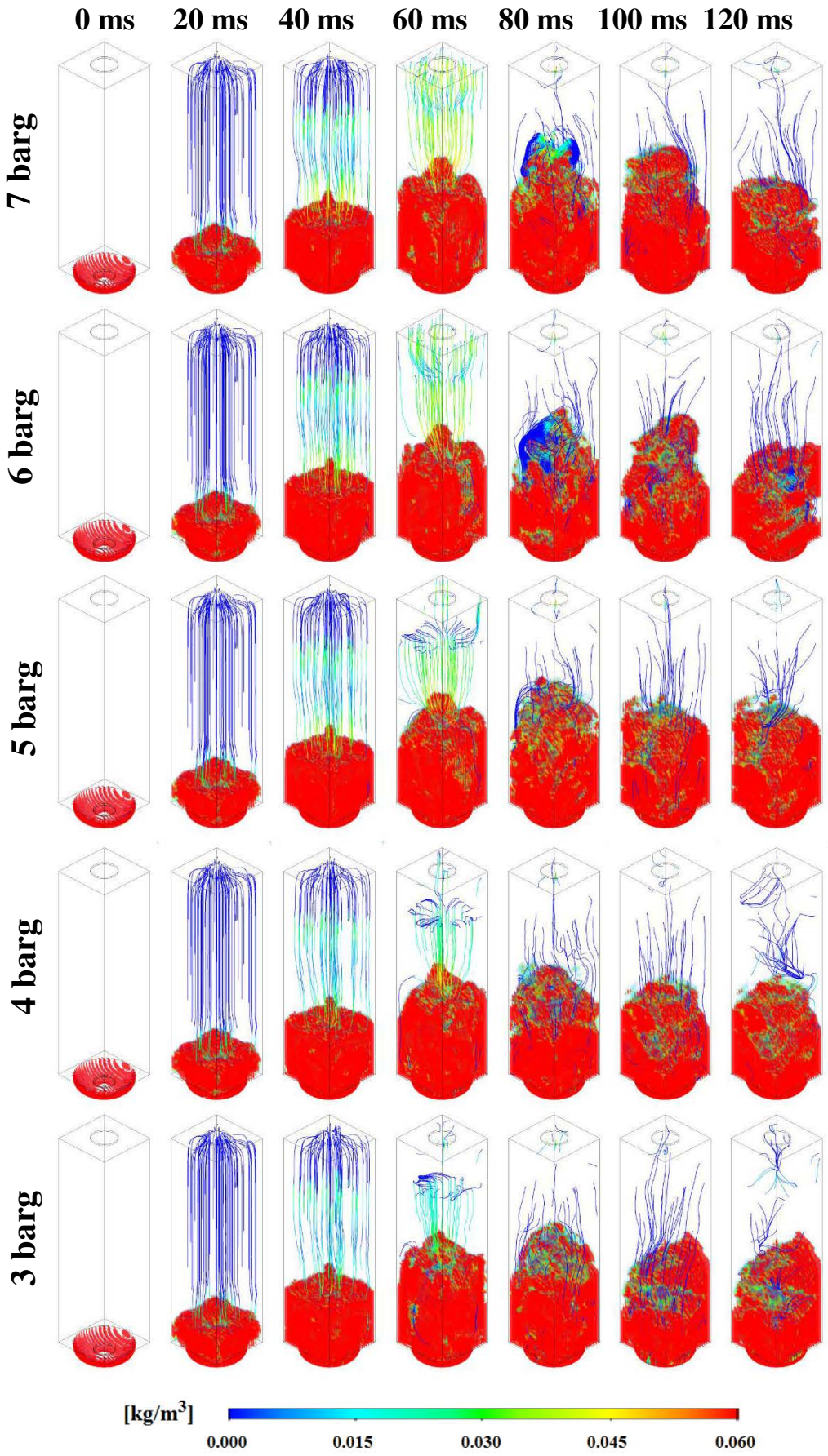

Figure 4.12. Dust concentration in the modified Hartmann tube at different injection pressures

C. *Description of the dispersion process of micrometric aluminum (Micro-Al 42)*

The computational approach that described the dispersion process of the micrometric wheat starch were also considered for the characterization of the dust cloud formed with the Micro-Al 42. For this purpose, the CFD simulations implemented the particle size distribution that was determined by sedimentation analyses for this metallic powder (Figure 3.3). Moreover, the flow domain was defined according to the approach that was proposed for the simulation of the starch-air mixture. This fact implies that the boundaries were specified with the same conditions that were established in Section **Erreur ! Source du renvoi introuvable.**. However, a symmetry condition was included in this simulation in order to compute the velocity field in the half of the flow domain. Further details about the specification of the CFD simulation are described by Murillo et al. (2013).

Figure 4.13 shows the evolution of the aluminum concentration in the modified Hartmann tube. The simulation of the dust cloud formed with this metallic powder posed the same characteristics that were observed with the high-speed videos. The bulk of the cloud has a higher rising velocity than the organic dust due to the presence of finer particles (fragmentation) and different shape factors that modify the drag forces. Thus, the cloud stabilizes at higher positions within the tube (12-15 cm). Therefore, the ignitability of the cloud might be enhanced if the height of the ignition sources was slightly increased or the ignition delay was reduced due to a higher dust concentration in the ignition zone.

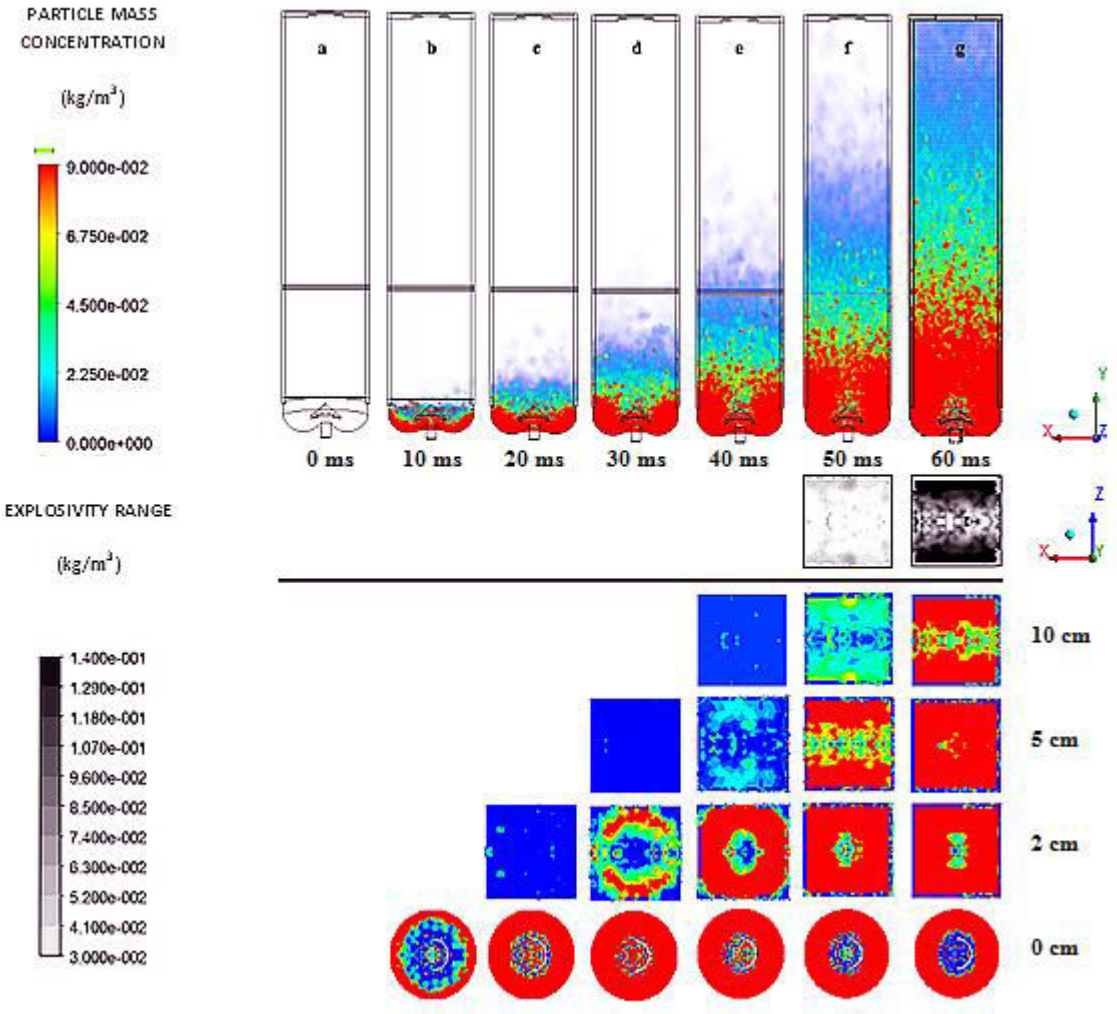

Figure 4.13. Aluminum concentration at different heights inside the modified Hartmann tube

The minimum explosive concentration (MEC) of the micrometric aluminum has been determined experimentally in the standardized 20 L sphere according to the operating specifications of the test method. The experimental test established that the MEC aluminum dust sample was 0.09 kg/m^3. Nevertheless, different values that range between 0.03 and 0.14 kg/m^3 have been reported for various aluminum dusts (Dufaud et al., 2010). For this reason, this study determined the time in which the MEC is reached at the ignition zone. The computational results established that this condition is achieved after 60 ms of dust dispersion. This fact implies that the ignition delay should be reduced for such powders but not below this value.

Furthermore, the computational results showed that the dispersion stages of aluminum dust do not have the same duration that the periods constituted for the wheat starch. The fast rising velocity and the agglomerates fragmentation in the bulk of the cloud showed that the major size reduction occurs during the first 40 ms of the dispersion process, which corresponds to the instability period of the organic powder. However, the stabilization is faster (10 ms) due to the placement of an important fraction of the dispersed solids at higher levels within the tube.

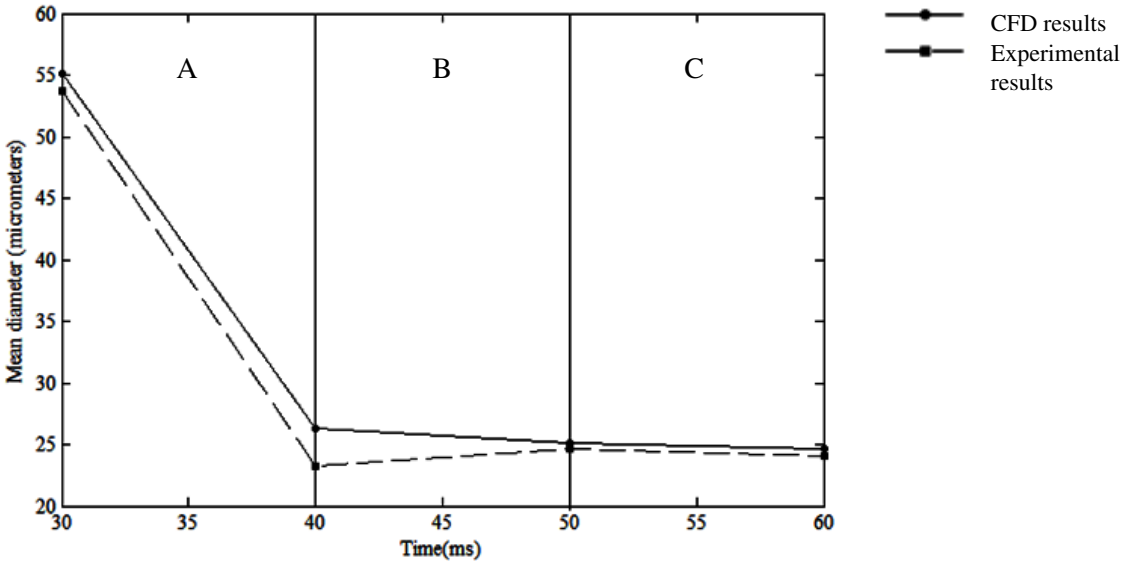

Figure 4.14. Mean diameter of 'Micro-Al 42' at the ignition sources location during the dispersion process A. Instability region B. Transition region C. Stability region.

These results allow concluding that the determination of the flammability parameters of powders with physical properties that facilitate their fluidization should be adaptable. At this point, the combination of simulations and experiments is recommended for every test of a combustible solid in order to consider the influence of its material properties (particle density, rigidity, shape factor, etc.) on the dust cloud development, and therefore, on the flammability parameters. Besides, the analysis of various dispersion conditions (notably pressures) or dispersion nozzles can be considered as an aspect of interest for a more accurate description of internal two-phase flows in such apparatuses.

4.1.6 Application to the determination of the minimum ignition energy of the micrometric aluminum and wheat starch

The last stage of the study of the dispersion process of the modified Hartmann tube envisages the main conclusions that can be determined from the experimental approach that was developed previously and this computational analysis. Table 4.4 lists the main conclusions that were determined for the variation of the height of the electrodes. Finally, it is verified that the position that is defined by the international standards is suitable for the development of a flammability test. Nevertheless, this position can be slightly adjusted for very fine powders of materials that can break up when the gas is injected at 7 barg.

Table 4.4. Commentaries about the modification of the height of the ignition sources

Height over the injection nozzle (cm)	Suitability of the position in the tube for a flammability test
2	This position is not recommended for a flammability test due to its high turbulence levels
5	This position is not recommended for a flammability test due to its high turbulence levels
10	The standard fixed value represents a compromise between the achievement of sufficient local concentrations and the fragmentation levels obtained by highly turbulent flows.
15	This height is only recommended for dusts that pose low variations of their size distribution and very high rising velocities (inertial effects).

Furthermore, Table 4.5 presents the recommendations proposed for the consideration of the gas pressurization as an adjustment variable of the modified Hartmann tube. The computational and experimental results of this study pose that this variable should be adapted in accordance with the physical properties of the powder in order to generate a dust cloud that provides a sufficient size reduction with the minimum turbulence level. Hence, the characterization of the dispersibility of the suspended combustible dust becomes necessary prior to the development of a flammability test.

Table 4.5. Ignition delays recommended for the reduced injection pressures

Injection pressure (barg)	Recommended ignition delay	Commentaries about the applicability
7	80 ms -120 ms	The dispersion conditions are appropriate. However, very fine powders would require the adjustment of the height of the electrodes
6	80 ms – 110 ms	The dispersion conditions are appropriate. However, very fine powders would require the small adaptation of the height of the electrodes.
5	80 ms - 100 ms	The dispersion conditions are appropriate. However, very cohesive powders would imply a short time span for the ignition delay
4	60 ms – 80 ms	This injection pressure is only recommended for non-cohesive powders with a small density.
3	---	This injection pressure is not recommended for a flammability test

Furthermore, the knowledge of the evolution of the transient conditions might also contribute to the reduction of the differences that are usually found between the ignitability of a dust cloud generated in an industrial facility and the ignitability determined in a laboratory test. This fact can be accomplished if the injection pressure and the ignition delay are modified to provide a temporary condition in the laboratory test that represents the other dust-air mixture. However, the flammability test is submitted to other factors that imply an uncertainty level in the implementation of the flammability parameters (e.g. cloud confinement, relative humidity, temperature, etc.). Nevertheless, this additional test could also be implemented in order to estimate the minimum ignition energy of a dust cloud under the normal operating conditions of a given industrial facility.

4.2 DESCRIPTION OF THE DUST DISPERSION IN THE 20 L SPHERE

This second part of the chapter analyzes the evolution of the two-phase flow within the 20 L sphere. Previously, the operating protocols of both flammability tests posed the similarities of the principles that dictate the generation of a combustible dust cloud in their corresponding apparatus. Indeed, there is an important correspondence since both tests envisage the injection of a finite amount of pressurized gas into a low pressure chamber. Therefore, the main approach that was posed for the modified Hartmann tube may be comparable with the one that was considered for the CFD simulations developed for the sphere. Nevertheless, there are some characteristics of the flow domain and the

boundary conditions that demanded the analysis of the dispersion process from a different perspective. For instance, the following remarks are listed to provide a better comprehension of the dissimilarities of the case studies:

- The initial pressure difference between the chambers is notably higher for the injection in the 20 L sphere (21bar-0.4bar) than in the modified Hartmann tube (8bar-1bar).
- The solids are placed in the dispersion chamber of the modified Hartmann tube whereas they are injected along with the pressurized gas in the 20 L sphere.
- As a result of the previous difference, the injection nozzle of the 20 L sphere is considered to be one of the factors of the particles fragmentation (Kalejaiye et al., 2010) whereas it is only a device installed for the gas distribution in the modified Hartmann tube.

Due to the specific characteristics of this flammability test, the basis of the CFD simulation of the 20 L sphere was envisaged from a different perspective. Unlike the modified Hartmann tube, the simulation of the sphere was not developed with a variable boundary. Rather than implementing a transient profile on the inlet face of the domain, the injection was modeled by connecting another body defined as a fluid. This additional body constitutes the canister that stores the pressurized gas prior to the development of the test.

The geometry of the flow domain was envisaged to evaluate the influence of the valve and the dispersion nozzle on the fragmentation of the dispersed agglomerates in the dust cloud. Evidently, this analysis could not have been performed with the other description since the dust is dosed into the sphere along with the pressurized gas. Moreover, the main purpose of this computational analysis was the determination of the influence of the injection nozzle and the operating conditions of the test on the evolution of the dust cloud. Hence, the CFD simulations were developed only with the micrometric wheat starch and not with aluminum.

Figure 4.15 presents the structure that was considered for the simulation of the dispersion process of a sample in the 20 L sphere. An important characteristic of the flow domain can be observed in the equatorial region of the dispersion sphere. The four cylindrical sections that are observed in the scheme correspond to the windows that were installed on the prototype (Figure 3.32) for the experimental data acquisition. Moreover, three internal elements were also considered for the definition of the flow domain. The fuses that are located at the top of the sphere for the placement of the ignition sources were represented by the two cylinders that are seen in the middle of the flow domain. In addition, the standard rebound nozzle (ASTM E1226 − 12a, 2012) was also represented at the bottom of the chamber. The injection valve was not considered rigorously for the definition of the geometry; hence it is represented by an elbow that is located at the base of the sphere.

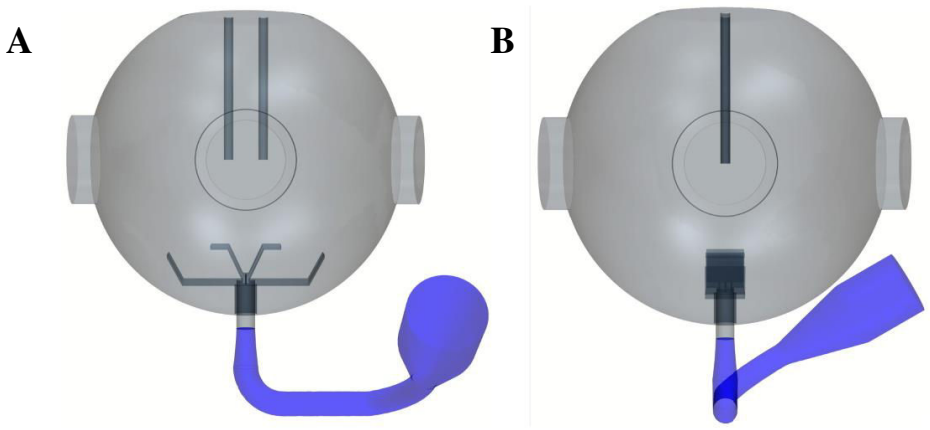

Figure 4.15. Flow domains of the modified 20 L sphere
(Gray: Dispersion sphere – Blue: Canister)
A. Front view B. Lateral view

Figure 4.16 presents a detailed description of the standard rebound nozzle. The representation of this device consists of the two plates that distribute the injected two-phase flow. Additionally, three internal holes are located between the upper plates whereas two big external holes are located in the middle of the base of the injection device. Unlike the modified Hartmann tube, the injection device was placed in the flow domain as a geometric subtraction rather than the addition of a solid body. This modification was considered in order to reduce the number of cells that would be simulated and thus achieve a lower computational cost.

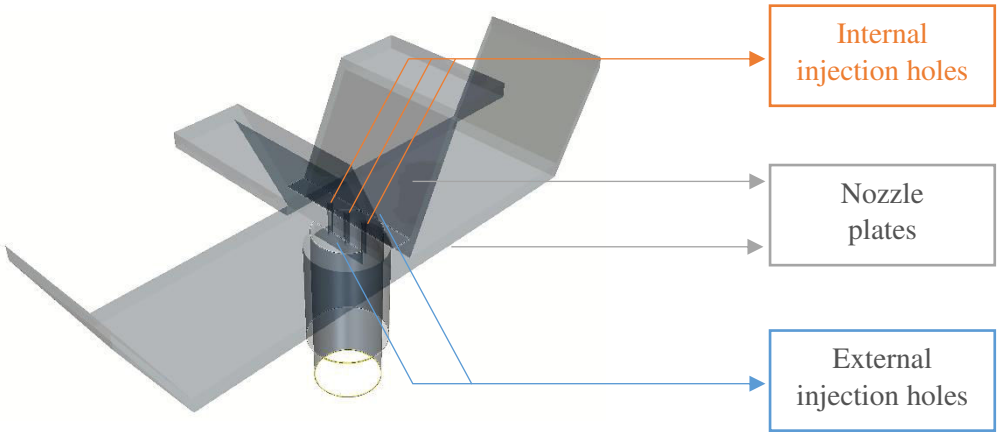

Figure 4.16. Representation of the standard rebound nozzle in the flow domain

Moreover, the computational analyses also considered the symmetric nozzle that was compared with the standard rebound nozzle in the previous chapter. The simulation of the two-phase flow developed with this device was performed to achieve a better comprehension of the dispersion process that was analyzed experimentally. For this purpose, the flow domain that is shown in Figure 4.17 was generated as a CAD model too. The geometry of this vessel was defined according to the same considerations that were discussed for the domain with the standard nozzle. Hence this domain is also composed by two bodies defined as fluid regions.

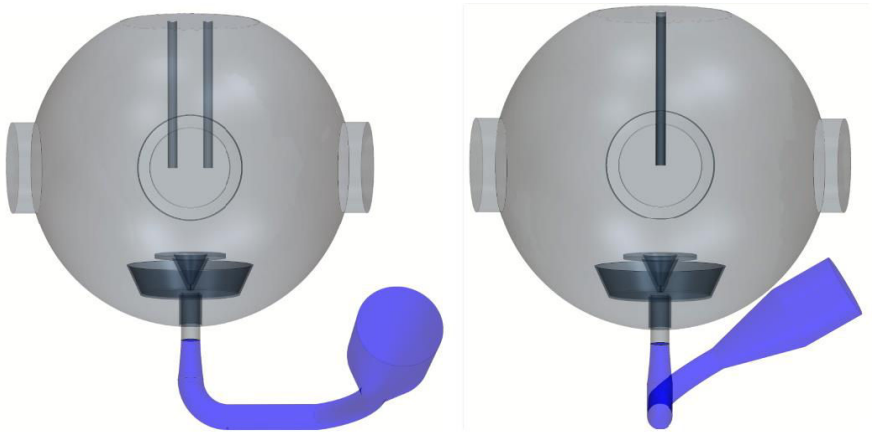

Figure 4.17. Flow domains of the modified sphere with the symmetric nozzle
(Gray: Dispersion sphere – Blue: Canister)
A. Front view B. Lateral view

Further details about the geometry of the symmetric nozzle are presented in Figure 4.18. The envisagement of this device as a revolution solid in the transversal plane of the standard nozzle generated only two injection holes in the geometry.

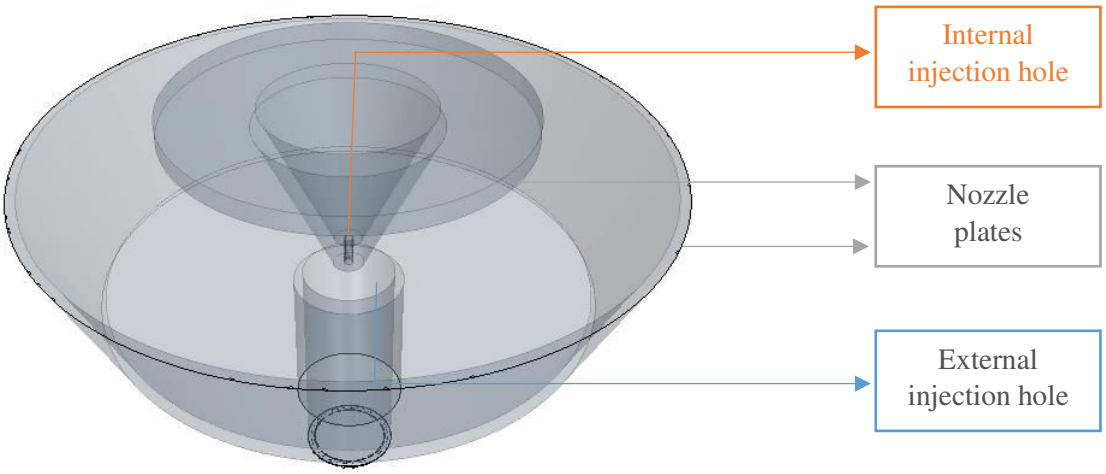

Figure 4.18. Representation of the standard rebound nozzle in the flow domain

4.2.1 Description of the mesh

The mesh of the 20 L sphere was generated with a method that differs from the one proposed for the modified Hartmann tube. The approach that was envisaged for this particular case was defined according to the advancing layer method that is available in the software STAR CCM+. This method is based on the generation of a mesh composed by polyhedral cells. This method was chosen due to the big volume of the dispersion chamber and the storage canister, which established that a tetrahedral division of the flow domain would imply the calculation of too many cells. On the contrary, a polyhedral mesh would be more suitable for a complex domain of this size because it can be generated with fewer finite-volumes and it can also provide a balanced solution with a quick mesh generation process (CD-Adapco, 2015).

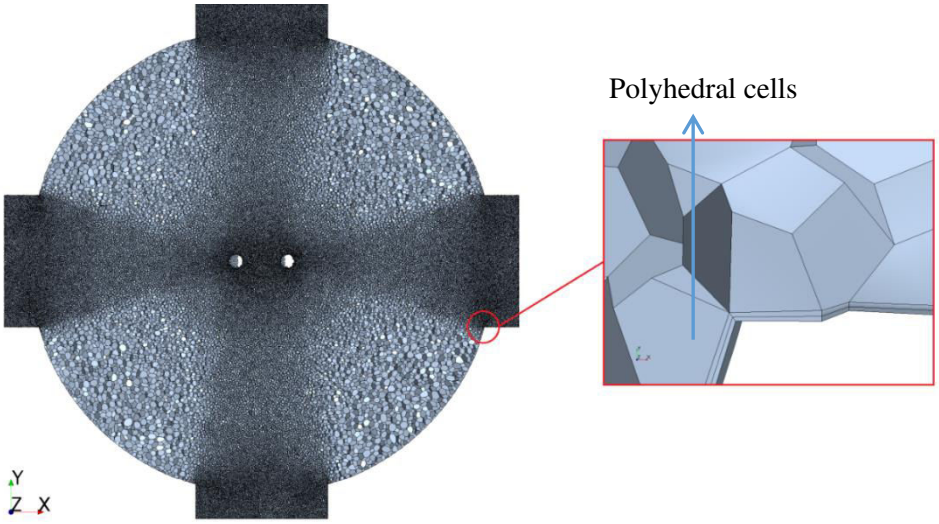

Figure 4.19. Implementation of the polyhedral cells method on the geometry of the 20 L sphere

The adjustment parameters of this method are listed on

Table 4.6. Initially, the refinements of the mesh were considered for the surroundings of the interface of the bodies and the injection nozzle. These regions were chosen after performing several tests that determined that the pressure changes at these locations are considerably relevant on the development of the flow in the zone located near the nozzle and the calculation stability. Afterwards, it was observed that the refinement of the cells situated near the visualization windows of the sphere was also important since there is an important change of momentum of the two phases in these regions.

Table 4.6. Parameters of the advancing layer method defined for the meshes of the 20 L sphere

PARAMETER	GEOMETRY WITH THE STANDARD REBOUND NOZZLE	GEOMETRY WITH THE SYMMETRIC NOZZLE
Maximum growth rate	1.3	1.3
Surface size (mm)	Minimum: 0.8 (Dispersion nozzle) Maximum: 16.0 (Separated cells)	Minimum: 0.75 mm (Dispersion nozzle) Maximum: 15.0 (Separated cells)
Number of cells	Sphere: 753,039 Canister: 9,935 Total: 762,974	Sphere: 787,839 Canister: 9,935 Total: 797,774
Number of faces	Sphere: 5,190,994 Canister: 59,188 Total: 5,250,182	Sphere: 5,427,774 Canister: 59,126 Total: 5,486,900

Finally, the mesh shown in Figure 4.20 was established for the description of the two-phase flows developed with the standard injection nozzle. Despite of the specific refinement, the number of cells is notably high. This fact represented a high computational cost for the CFD simulations. However, this refinement level was necessary to achieve the sufficient stability in the calculation during the initial stages of the dispersion process. Another important aspect that must be established about the grid relies on an aspect that has been neglected for the discretization of the flow domain. In fact, the constructed mesh is not dynamic, which implies that it does not adapt its geometry according to the conditions of the flow. For this reason, certain characteristics of the apparatus, such as the deformation of the injection device caused by the pressurized air, are not modeled in this study. This condition was omitted because it represented an inacceptable increase of the computational cost due to the necessity of a redefinition of the geometry and the mesh after every time step.

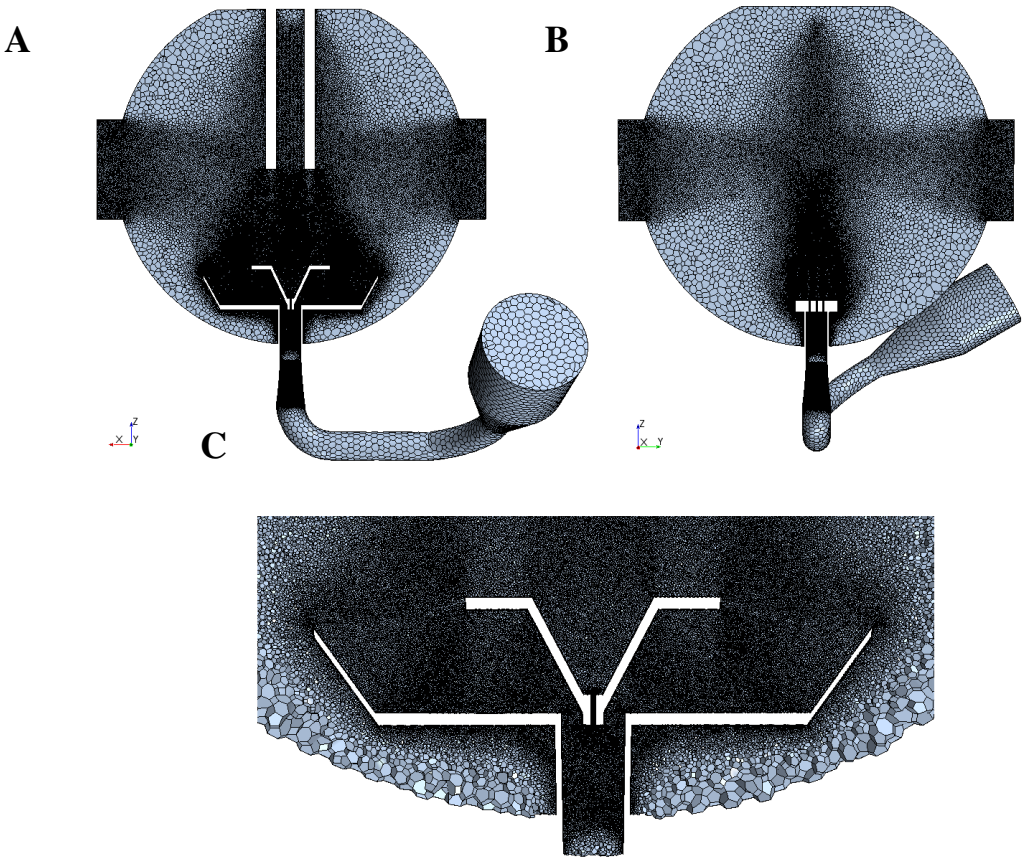

Figure 4.20. Mesh of the flow domain of the 20 L sphere with the standard rebound nozzle

A. Front view B. Lateral view C. Refinement near the injection nozzle

Furthermore, the same meshing method was implemented on the alternative geometry of the symmetric injection nozzle. The flow domain was divided into a more refined mesh due to the contact of the injected mixture with a larger solid surface.

Table 4.6 establishes that the mesh considered for this comparative case represented a considerable augmentation of the total number of cells despite of the definition of the refinements in the same regions of the standard case. These regions are shown in Figure 4.21, which presents the grid considered for the CFD simulations:

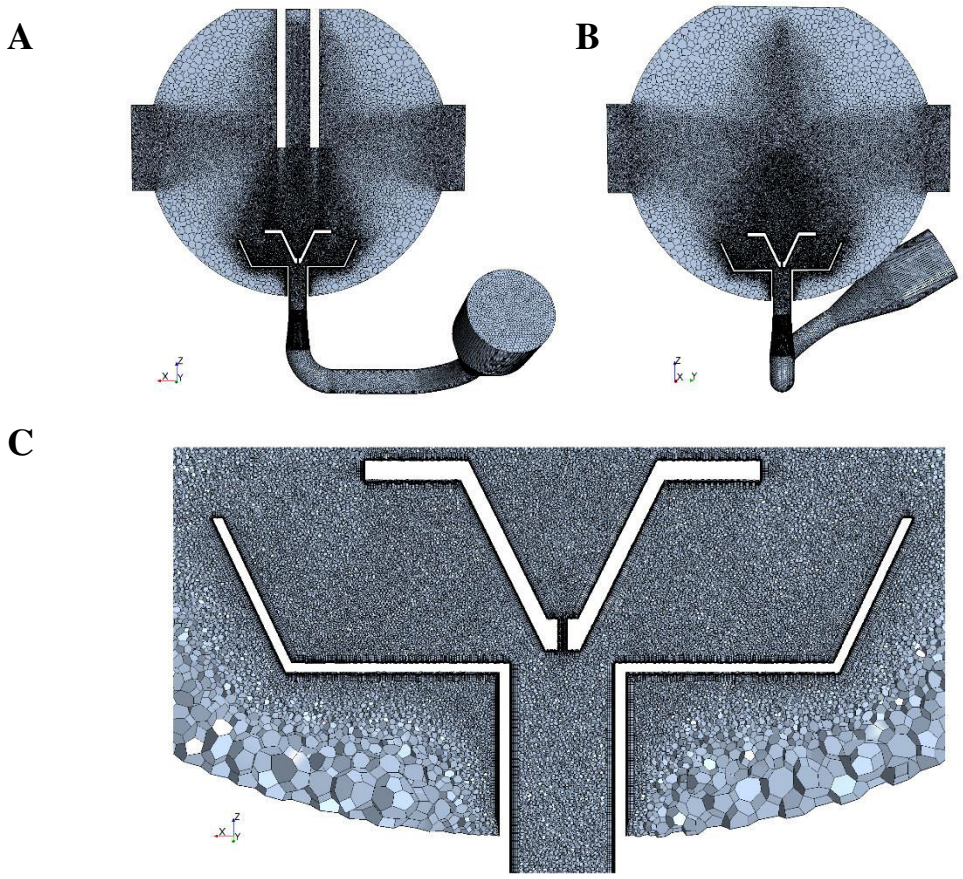

Figure 4.21. Mesh of the flow domain of the 20 L sphere with the symmetric nozzle
A. Front view B. Lateral view C. Refinement near the injection nozzle

4.2.2 Numerical parameters associated to the physics and the discretization

The calculation parameters of the CFD simulations developed for these analyses were defined with the same settings as for the modified Hartmann tube. In accordance with this statement, the evolution of the two-phase flow was analyzed with an implicit unsteady formulation. Therefore, the solver parameters were also defined according to the density-based approach after considering the interdependence among the density, energy and momentum. This relation arises from the transonic conditions caused by the adiabatic expansion of the dispersion gas.

The spatiotemporal discretization was set in the same fashion as in the previous computational study. Initially, the spatial discretization was defined with a hybrid scheme that blends the pure central differencing with the second-order upwind scheme due to the utilization of the Detached Eddy Simulation model for the evolution of turbulence. Thereafter, a second-order discretization was posed for the time integration of the conservation equations. However, the simulation topology demanded a

smaller time step to achieve the required convergence levels for the description of the phenomena within the 20 L sphere. Thus, the calculations were performed with a time step equal to 10^{-5} s and 15 iterations per time step.

Moreover, the Advection Upstream Splitting (AUSM) method was considered for the calculation of the convective terms associated to the cell. However, the algebraic multigrid method was specified in a different way with regard to the dispersion tube since a flexible formulation was established for all the flow variables. This modification was implemented in order to diminish the computational cost associated to the development of the calculation cycles of the AMG method. This flexible numerical solver was set to perform two sweeps per cycle. Thereafter, the Courant number was reduced from the default value (50) to 20 to reach rapidly a converged solution without compromising the calculation stability. Finally, the computation of the velocity field and the trajectories was performed with a server Intel Xeon X5650 with 12 processors of 2.66 GHz installed with a set of 48 GB of RAM. The calculation time required for the simulation of 100 ms of dust dispersion is approximately 6.5 days.

4.2.3 Initial and boundary conditions

This section briefly describes the initial values of the flow properties that were established for the flow domain according to the operating protocol defined on the international standards. These settings were defined in a similar way to the parameters of the modified Hartmann tube. However, this specification was developed in a more simple way since the canister was also simulated in this study and the momentum and energy balances were not contemplated to determine the flow of the injected gas.

A. *Boundary conditions*

Unlike the flow domain of the modified Hartmann tube, the 20 L sphere was conceived as a closed system. Thus, it is only composed by internal walls and there is no inlet or outlet condition in the geometry. All these internal walls have similar momentum specifications since they are defined with a no-slip condition for the gas flow and a reflect condition for the solid particles dispersed in the cloud (See section 4.1.2). Nevertheless, these walls are differenced by their thermal specifications. The dispersion chamber is covered by the cooling water that flows around the vessel surface; hence it was defined with as a boundary whose temperature is constant and equal to 300 K. On the contrary, all the other internal walls were defined as adiabatic walls.

B. *Initial conditions*

The initial conditions of the flow domain have been defined according to the operating protocol of the apparatus. In accordance with this statement, the two bodies are filled with air at the temperature of the environment (300 K). Moreover, the velocity field of the whole flow domain represents a quiescent amount of air. This fact implies that the velocity of the fluid and its initial turbulent kinetic energy are null.

Moreover, Figure 4.22 shows that there are only two initial conditions that differ in the two bodies. The first dissimilarity relies on their initial static pressure. The dispersion sphere is evacuated before the injection of the dust-air mixture until 0.4 bars whereas the storage canister is pressurized until 21 bars. This pressure difference causes the transonic flow that develops within the explosion chamber before the ignition of the cloud. Moreover, the solids are placed inside the canister as a surface injection in the same way that they were placed at the bottom of the modified Hartmann tube. For this

purpose, the whole internal surface of the body was set as the initial location of the 937,650 solid parcels.

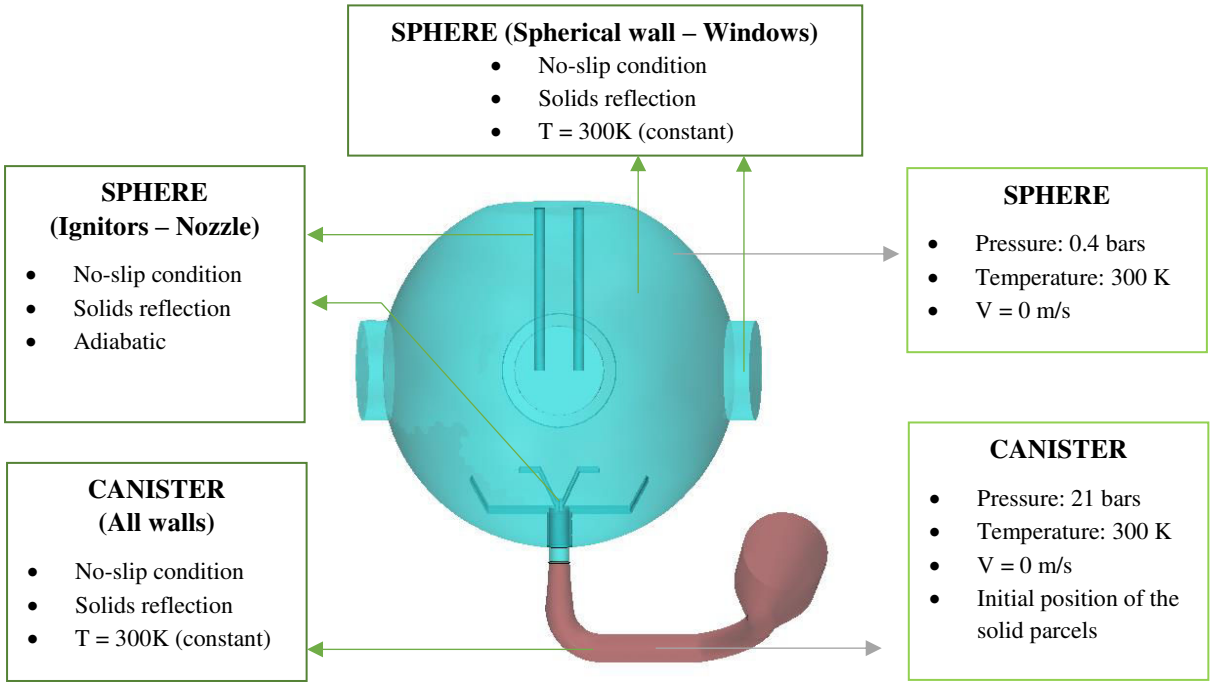

Figure 4.22. Initial and boundary conditions defined for the simulation of the dispersion process in the 20 L sphere
(Orange blocks: Boundary conditions – Green blocks: Initial conditions)

4.2.4 Results and comparison with the experimental approach

The dispersion process of the dust-air mixture generates the same behavior that was posed for the evolution of the dust cloud in the modified Hartmann tube. However, the evolution of the combustible cloud in the 20 L sphere defines different time intervals for the flow regimes that were indicated for the previous standardized apparatus. This condition demanded the description of the two-phase flow in two consecutive stages. Initially, the stage associated to the injection of the pressurized flow will present the characteristics that are influenced by the nozzle geometry as well as the major pressure difference. Thereafter, a second stage will describe the evolution of the mixture during a longer period of time in order to establish how the dispersion process affects the physical properties of the cloud. This subsequent analysis will dictate the operating parameters that will determine the most conservative information about the explosibility of the dust in the 20 L.

A. *First stage of injection of the pressurized flow (0- 10 ms)*

Initially, it can be seen in Figure 4.23 and Figure 4.24 that the two injection devices generate different conditions of the dispersion jets within the vessel. On the one hand, the geometry of the rebound nozzle establishes a jet that is mainly altered by the holes that compose the device and the only plates that contribute significantly to the shape of the jet are the top plates. On the other hand, the utilization

of the symmetric nozzle represented a major alteration of the initial trajectory of the injected flow since it is also significantly affected by the base plates. This fact implies that the standard rebound nozzle constitutes a smaller obstruction that may cause a reduced change of momentum in the two-phase flow.

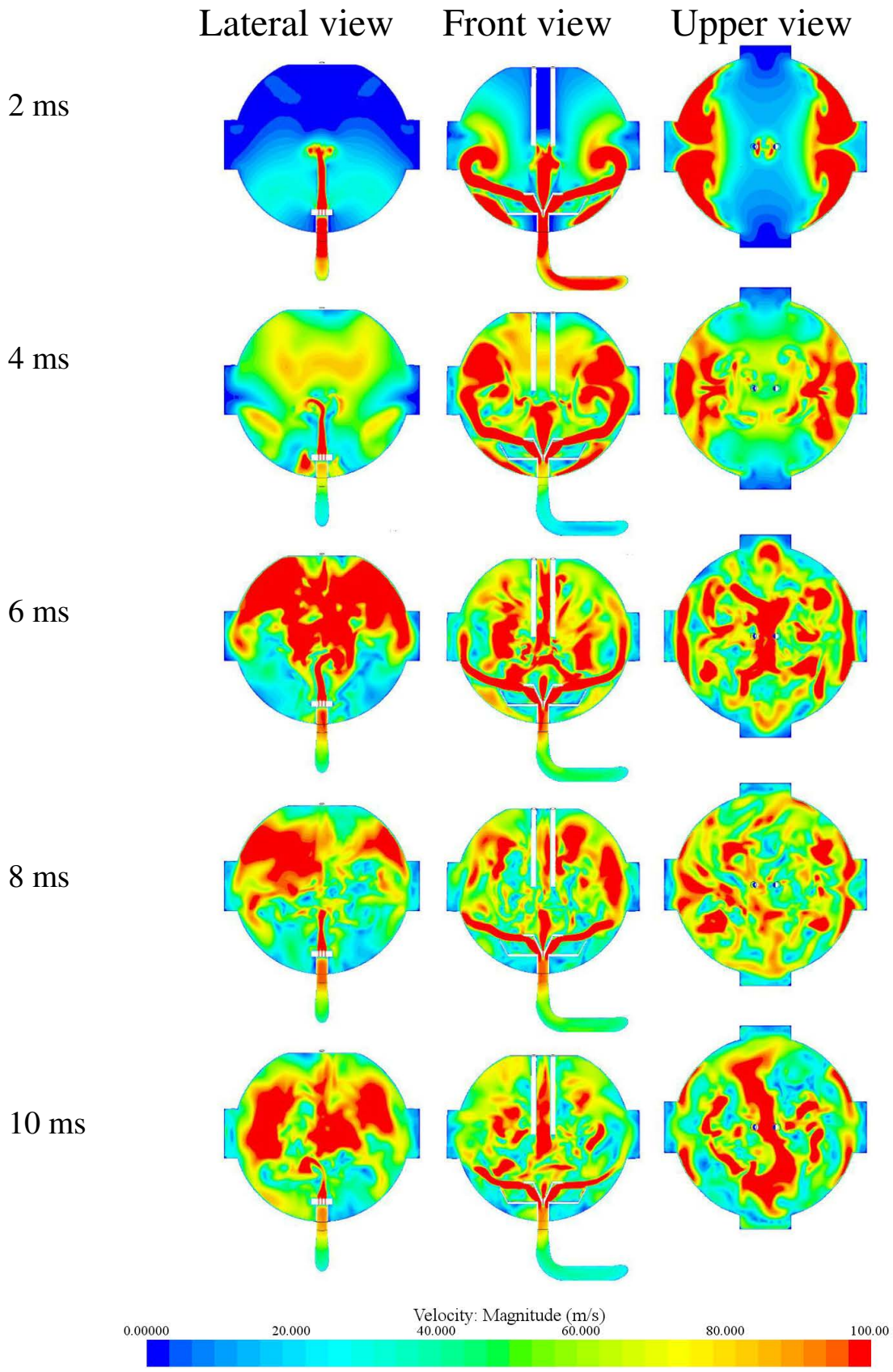

Figure 4.23. Velocity magnitude of the gas flow with an injection performed with the standard rebound nozzle

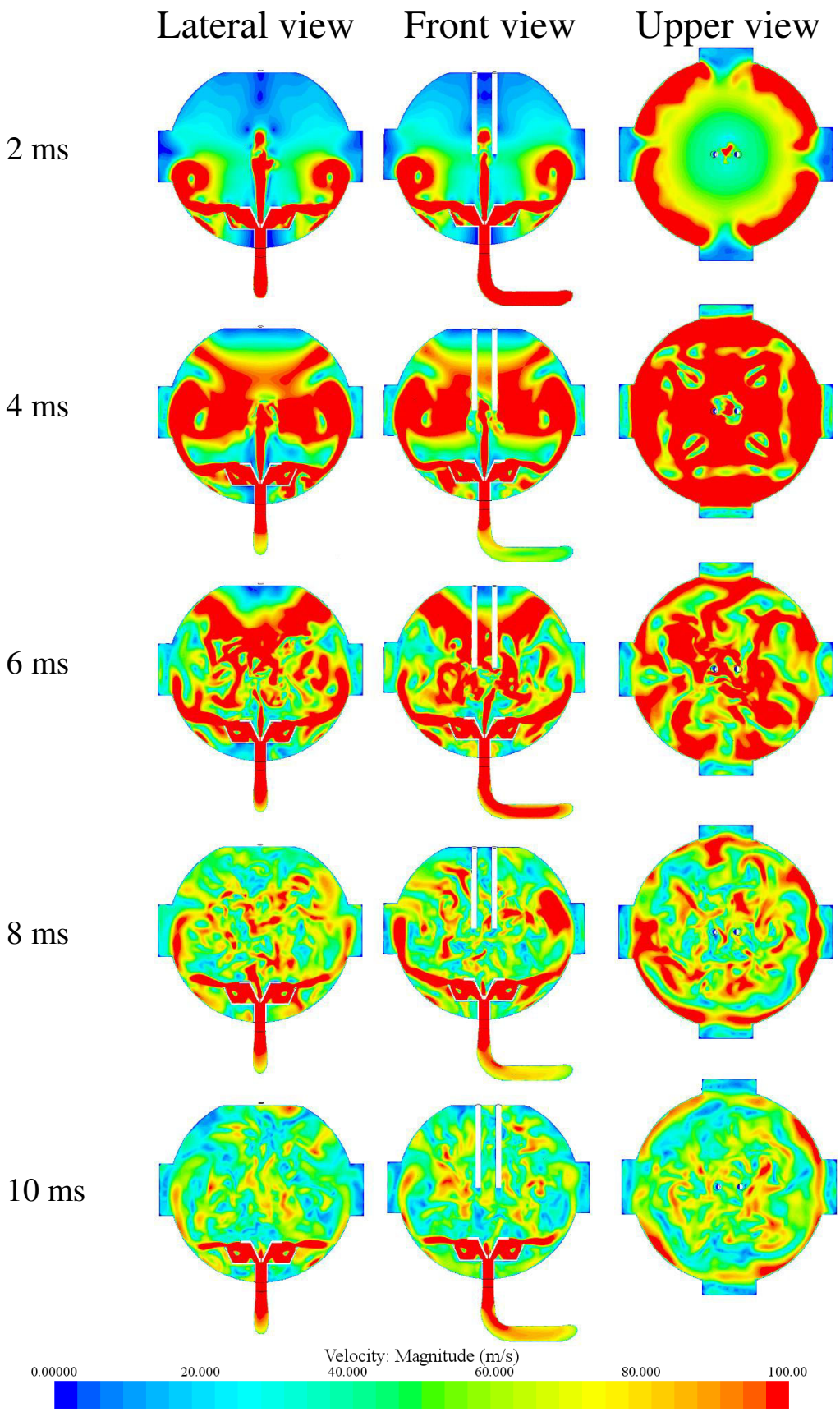

Figure 4.24. Velocity magnitude of the gas flow with an injection performed with the symmetric nozzle

The obstructions defined by the two nozzles established different profiles for the jets within the 20 L vessel. A comparison of the lateral view and the front view of the standard rebound nozzle (Figure 4.23) shows that the initial distribution of the gas flow is not homogeneous. The lateral view shows the flow that is attributed to the three internal injection holes whereas the front view shows how the most of the injected flow is directed towards the internal walls of the vessel. This condition constitutes the formation of two large vortex in the zones near the walls in the equatorial region of the sphere. These results correspond to the two rising fronts that were discussed in the previous chapter. During the first 8 ms of the dust dispersion, the vortex structures grow and rise due to the high mass flow that is caused by the high pressure difference between the canister and the dispersion chamber. Afterwards, the energy dissipation begins to reduce the size of these structures. Nonetheless, the injection of the pressurized gas lasts during a longer period of time as observed at the zones near the nozzle at 10 ms, which still have a high velocity.

On the contrary, the velocity field developed by the symmetric nozzle constitutes a different profile with regard to the standard injection system. The lateral and front views of Figure 4.24 do not have significant differences in the distribution of the injected gas flow, which implies more homogeneity of the dust cloud during the initial stage of dust dispersion. In addition, this distribution causes some variations in the vortex observed in the middle of the sphere since they have a toroidal shape due to the symmetric dose of the pressurized fluid. Moreover, the development of the internal jets with the symmetric nozzle causes higher velocities during the first 10 ms of dust dispersion. Therefore, it represents a faster dose of the dust-air mixture as well as higher turbulence levels during this initial stage of dispersion.

During the first 6 ms of the dispersion process, the symmetric nozzle poses a condition that approaches the assumption of the nominal concentration since it distributes the combustible dust homogeneously within the explosion chamber. The angles of the of the plates of this nozzle develop the expanded jets at upper heights and with larger sizes with regard to those generated by the standard device in the dispersion chamber. Consequently, the momentum loss of the two phases during this initial stage cannot be considered in the same way for the two injection systems. The symmetric nozzle constitutes an important collision at the top of the sphere that subsequently creates a downward flow. In addition, this nozzle is submitted to greater friction effects that are caused by the contact with the internal walls of the apparatus. For this reason, the collision at the top is not clearly evidenced for this injection system.

Furthermore, the previous chapter established how the collision of the two rising fronts generated by the standard rebound nozzle was the main factor on the segregation of the solid phase. The analysis of the upper view of the velocity field allows explaining this characteristic. The jets propagation towards the walls makes the velocity of the flow field increase from the walls to the center during the first 4 ms and create a transient region of high velocity in the region where the two jets rise. This fact causes the accumulation of the dispersed phase in the region where a drastic change in the direction of the streamlines is observed (Figure 4.25). Likewise, the symmetric nozzle increases the gas velocity from the walls to the center as well. However, this process is considerably faster for this dispersion nozzle because the velocity gradients are important in the whole region, which is not the case for the standard nozzle because it only defines the high velocity gradients in the central region of the sphere.

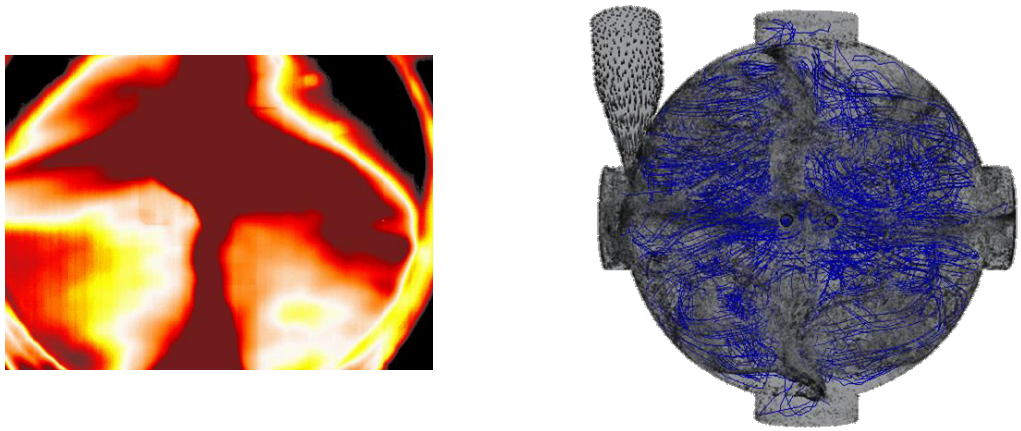

Figure 4.25. Distribution of the combustible dust and the gas flow after 10 ms of dust dispersion
A. Experimental image B. Streamlines and positions of the solid particles determined by CFD simulation

These conditions determine the moment in which the turbulence defined by the jets will constitute the chaotic behavior of the dust cloud. The segregation of the combustible dust is clearly defined when the gas flow is injected with high velocities and is widely dispersed when the internal pressure gradients promote the expansion of the injected gas within the vessel. For this reason, the symmetric nozzle reaches a chaotic behavior before the standard rebound nozzle, since it causes a wider distribution of the jets in the initial stages of dispersion. This fact also explains the experimental results discussed by Dahoe et al. (2001) who established that the standard perforated ring creates a great number of thin jets that dissipate before the jets formed with the rebound nozzle. These authors affirmed that the preferential direction of the flow and its high velocities are dictated by the geometry of the dispersion nozzle.

One of the major concerns on the development of a flammability test relies on the homogeneity assumption on the solids concentration of the dust cloud. For this reason, the influence of the geometry of the dispersion nozzle on the initial distribution of the solid phase must also be established with the comparison of the particle size distributions shown in Figure 4.26 and Figure 4.27. The computational results identify the particles segregation in the dispersion sphere. Initially, it is possible to evidence the initial lumps that were discussed in the DPIV analyses in the geometric center of the apparatus on the frames recorded after 2 ms of dust dispersion. At this moment, the central jets have similar characteristics for both injection devices since the solids fraction injected in the central holes is considerably low. Nevertheless, the lateral jets that collide at the top of the sphere after 4 or 5 ms of dust dispersion create rapidly the downward flow that collides subsequently with the central jet.

The evolution of the lateral jets is mainly dictated by the inertial effects of the gas flow. This condition is observed in the first instants of the dispersion process which shows that the highest elevation is achieved by the smallest particles. This condition was also determined numerically by Kosinski & Hoffmann (2007) who established that the fluidization of the dust particles in absence of external forces (e.g. magnetic fields) is mainly defined by the drag force exerted on the solids surface. In addition, the inertial effects are also clearly evidenced during the first 10 ms of the dispersion process, especially with the symmetric nozzle. The inferior view of Figure 4.26 and Figure 4.27 shows that the trajectories of the solid particles inside the sphere are slightly directed towards one of the sides of the chamber. This condition is observed because the storage canister is mounted on the right side of the apparatus. Therefore, the pressurized two-phase flow follows the path of least resistance and channels to one of the sides of the sphere (Mercer et al., 2001). In accordance with this statement, the complete uniformity of the dust cloud would require the montage of the canister just below the sphere.

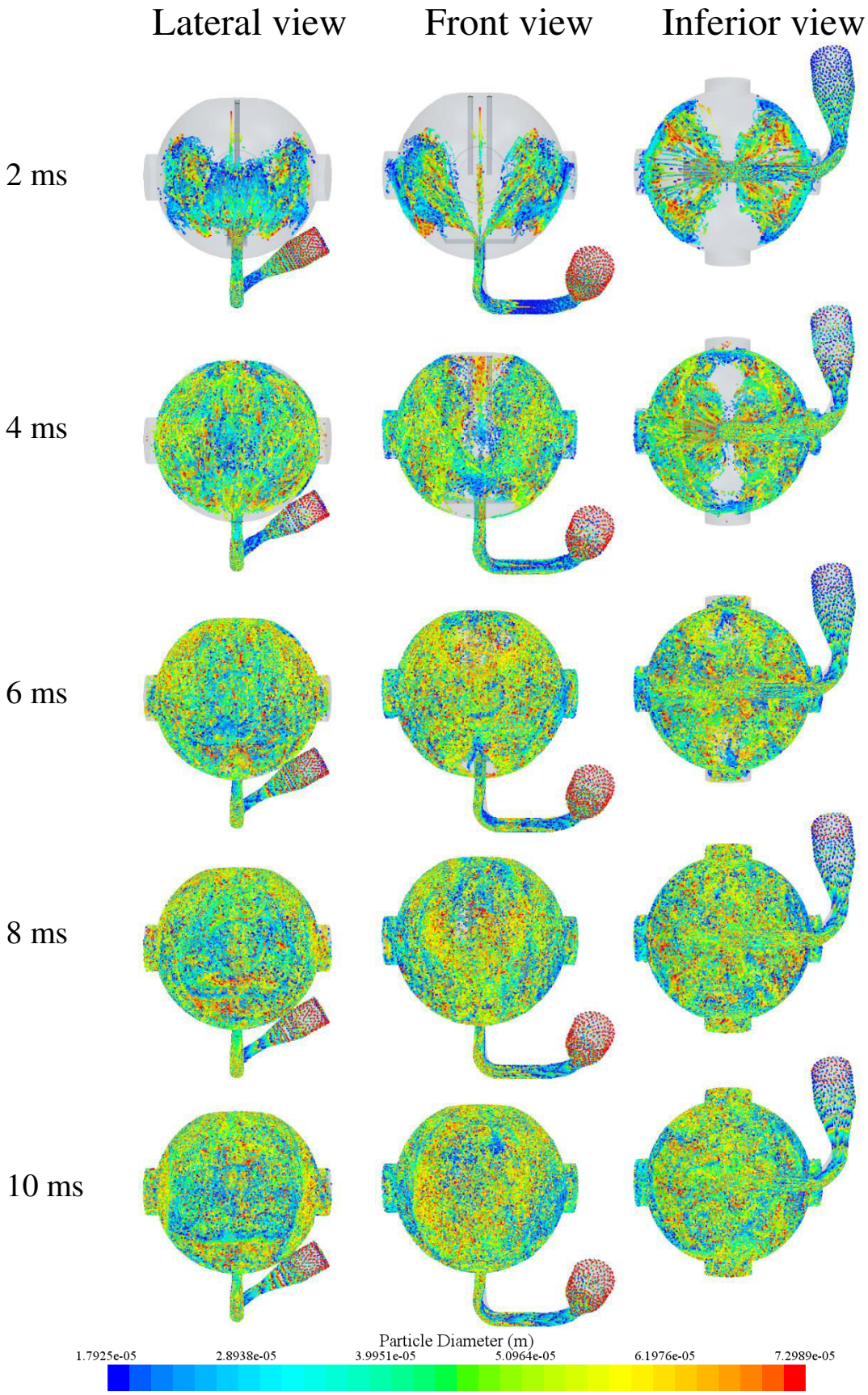

Figure 4.26. Particle size distribution of the combustible dust injected with the standard rebound nozzle

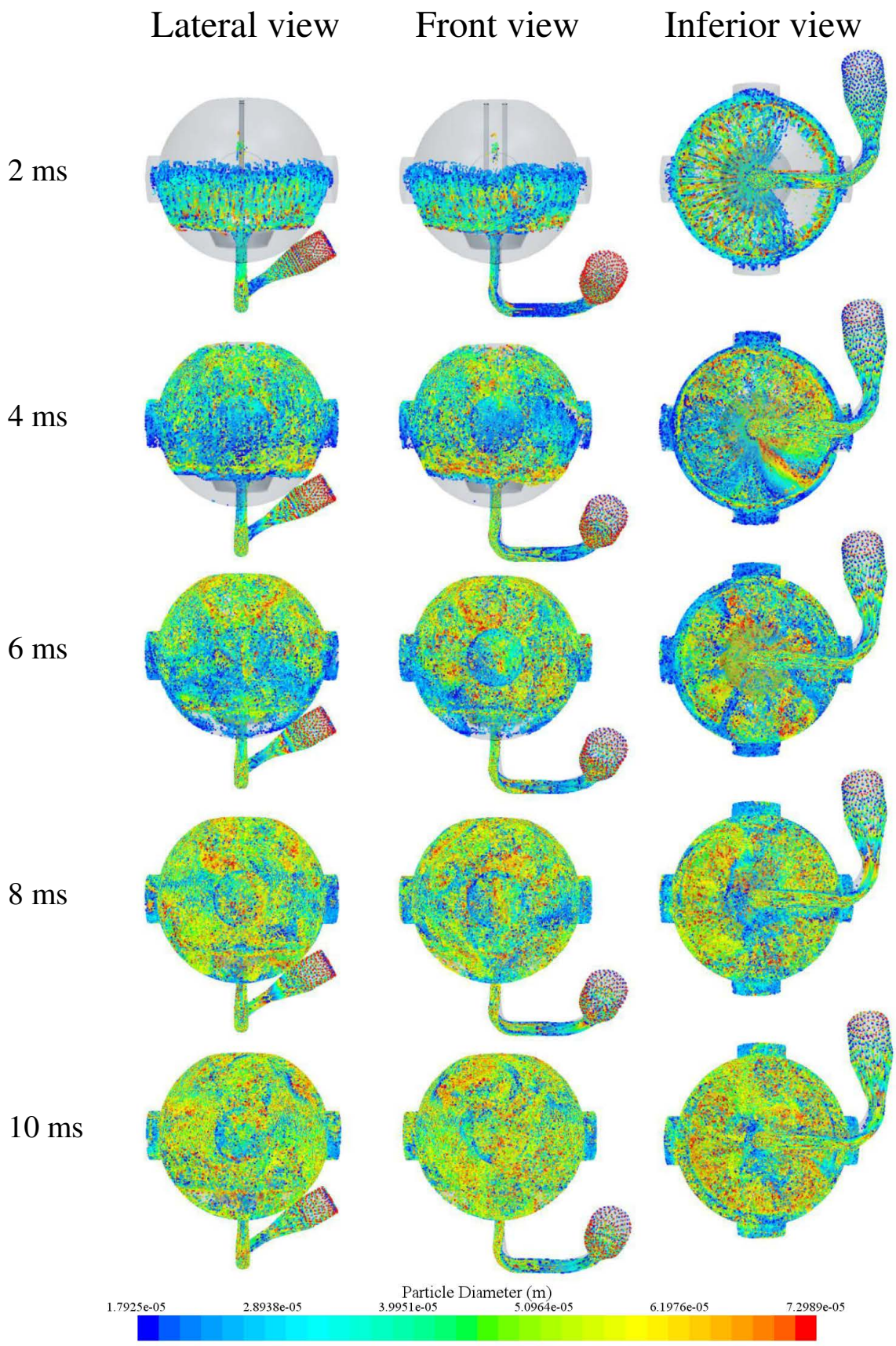

Figure 4.27. Particle size distribution of the combustible dust injected with the standard rebound nozzle

These facts pose the main aspects that must be considered for the selection of a dispersion nozzle for a flammability test. The quality of the solids mixing is enhanced when the symmetric nozzle is installed in the sphere but it would represent an important reduction of the concentration of cohesive powders when the weight of sample is too low due to the increased contact with the walls. For this reason, it is compulsory to establish how the velocity field and the dust concentration vary during the subsequent stages of the dispersion process. The following section analyzes the transient behavior of the dust cloud after the first 10 ms. The results of this analysis will evaluate not only the influence of the dispersion but also of the ignition delay on the conditions that affect the explosibility of the dust cloud.

B. *Evolution of the gas flow (10-100 ms)*

The previous section established that the injection of the dust-air mixture different injection nozzles will generate a different behavior during the first 10 ms of dust dispersion. These variations have a direct repercussion on the dynamics of the two-phase flows on the subsequent stages of dust dispersion. This section will discuss the influence of the geometry of the nozzle on the evolution of the dispersion process. Figure 4.28 presents the mean values of the velocity magnitude of the gas flow that were calculated for the two bodies that compose each flow domain:

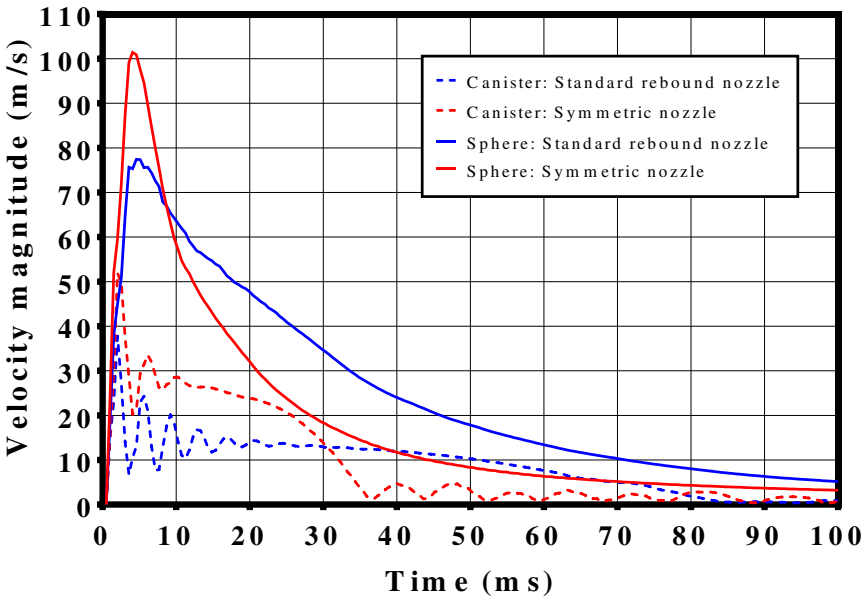

Figure 4.28. Mean velocity magnitude in the canister and the dispersion chamber of the 20 L sphere

The dose of pressurized air constitutes a continuous pressure increase in the dispersion sphere as the injection develops. This fact constitutes a transient behavior of the velocity magnitude of the fluid flow as it defines an increasing behavior during the first 6 ms and a decreasing tendency during the next stages of dust dispersion. This tendency is not similar for both cases since the velocity decay is more rapid with the symmetric nozzle. This condition constitutes a difference of 12 $m \cdot s^{-1}$ after the first 40 ms. This dissimilarity allows concluding that the sedimentation phenomenon will occur before with an injection performed with the symmetric nozzle. Moreover, the velocity magnitude in the pressurized canister presents the evolution of the injection during the dispersion process. During the first 15 ms, an oscillatory behavior in the storage canister. This condition is due to the high velocity fluctuations that are generated by the arrival of the jet to a quiescent field.

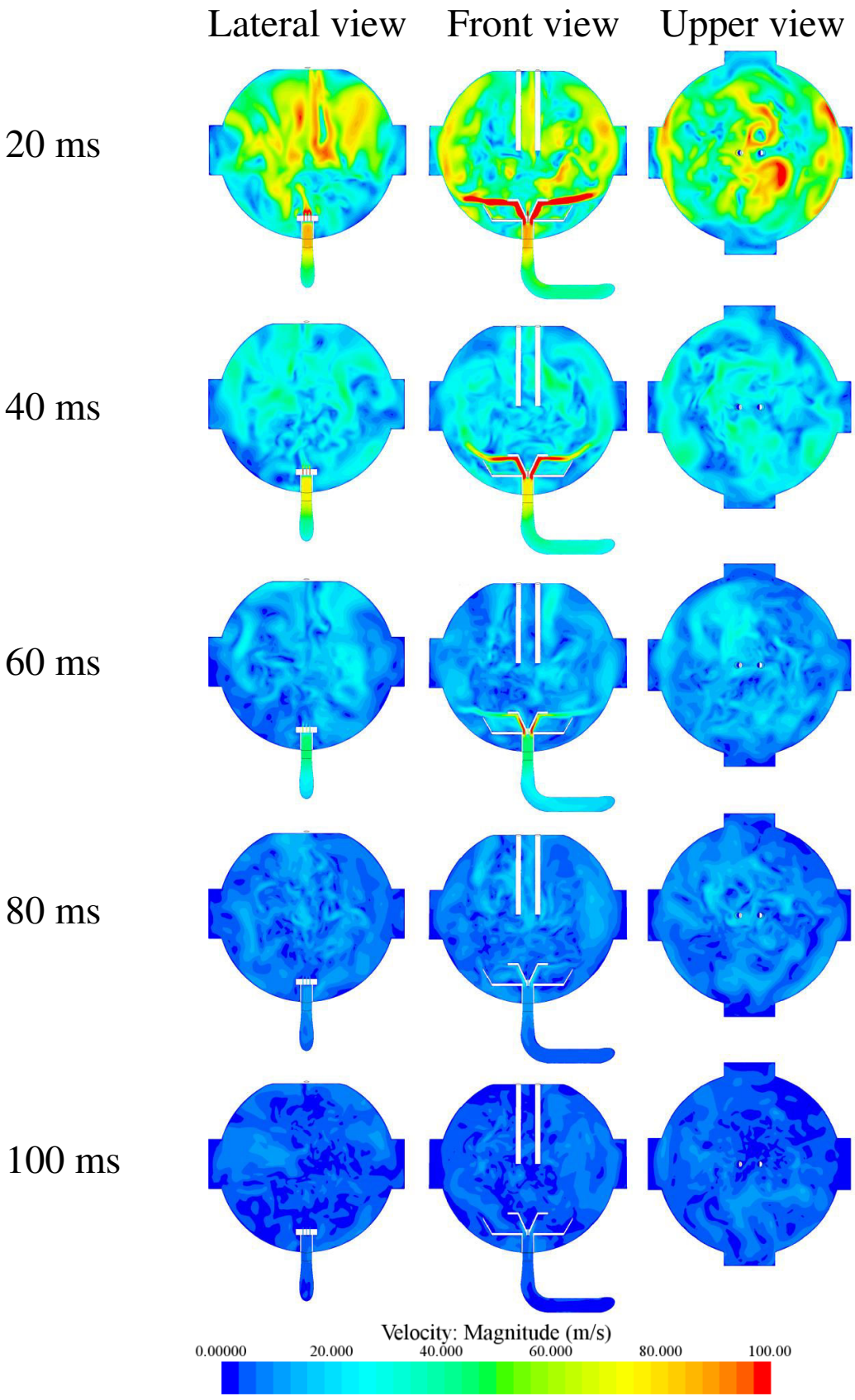

Figure 4.29. Velocity magnitude of the gas flow with an injection performed with the standard rebound nozzle

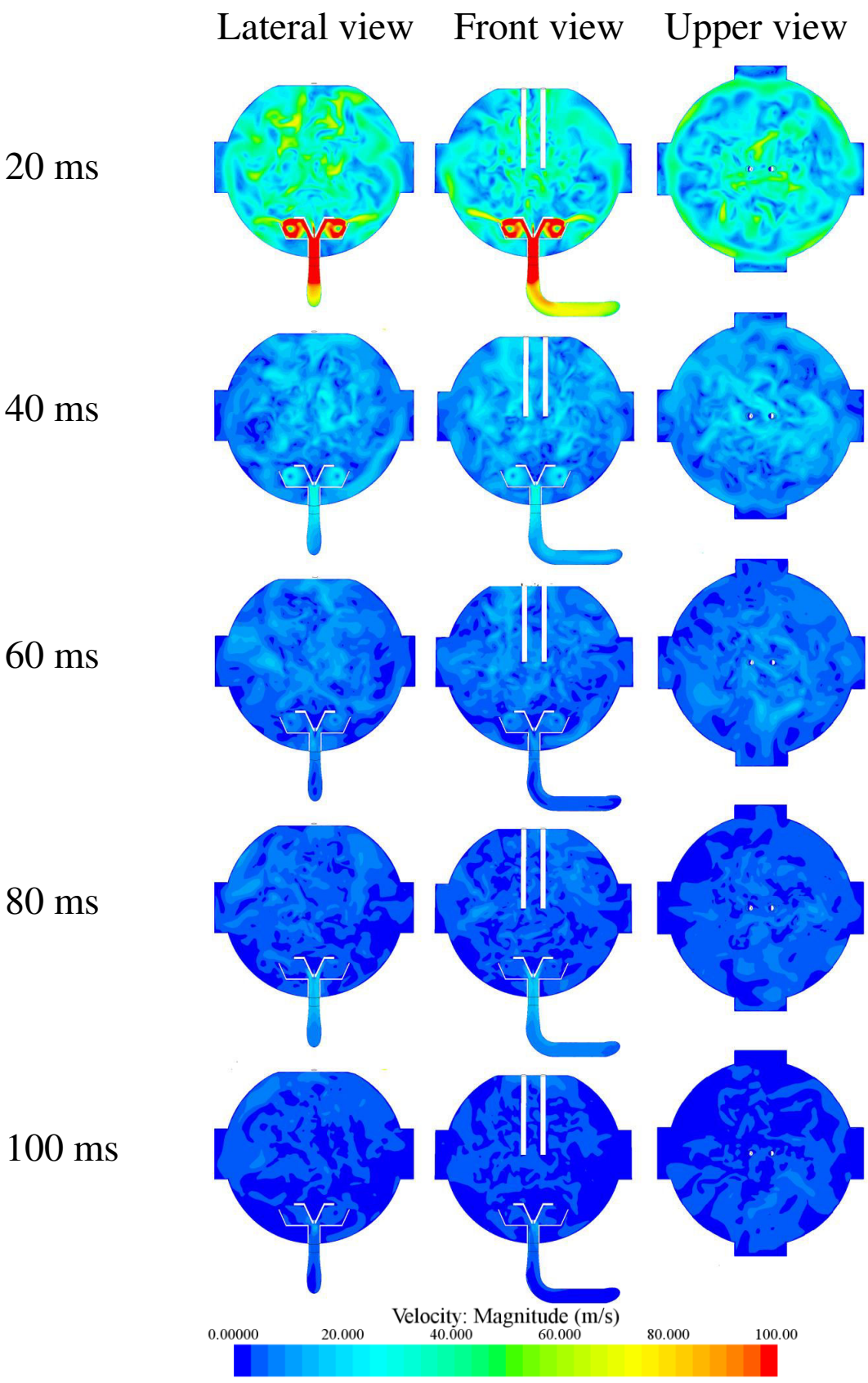

Figure 4.30. Velocity magnitude of the gas flow with an injection performed with the symmetric nozzle

Figure 4.29 shows that the high velocities at the outlet of the dispersion nozzle are sustained during the first 60 ms approximately. This condition verifies the experimental result obtained by Dahoe et al. (2001) who determined that this is the duration of the injection process. Similarly, Figure 4.30 establishes that the injection performed with the symmetric nozzle lasts 60 ms as well. Nonetheless, it constitutes a different velocity field because it achieves a faster energy dissipation due to the wider distribution of the jet. This fact constitutes a faster injection of the gas flow with this device with a higher velocity decay during the next stages of dust dispersion. Thereupon, the propagation of the jets from the walls to the center of the sphere shows that the random behavior of the gas flow is reached by the standard nozzle after 40 ms whereas the symmetric device generates this condition approximately 10 to 20 ms before.

Another remarkable difference of the velocity fields is observed in the injection zone of the dispersion sphere. Two vortex structures are formed between the plates of the symmetric nozzle due to the partial confinement generated by the angle of the low plates. This fact represents an additional factor for energy dissipation with the utilization of this injection device. On the contrary, the gas flow develops a linear jet with the standard rebound nozzle, whose strength decreases as the dispersion process evolves. Nevertheless, the results determine that the asymmetry that was identified in the early stages of dispersion becomes a determining factor only during the charge of the dust-air mixture because the velocity field is determined by the internal turbulence dissipation after it.

These characteristics of the two-phase flows developed by the two injection nozzles dictate the pressure increase in the 20 L sphere. Figure 4.31 shows a comparison of the pressure profiles constituted by the two injection nozzles with the pressure determined with the two pressure sensors of the test apparatus. The CFD simulations have a good agreement with the experimental data and determine a duration of the gas injection that is approximately 60 ms. This value is quite similar to the one determined by Dahoe et al. (2001). After this period, the pressure of the chamber remains stable until the ignition of the dust cloud.

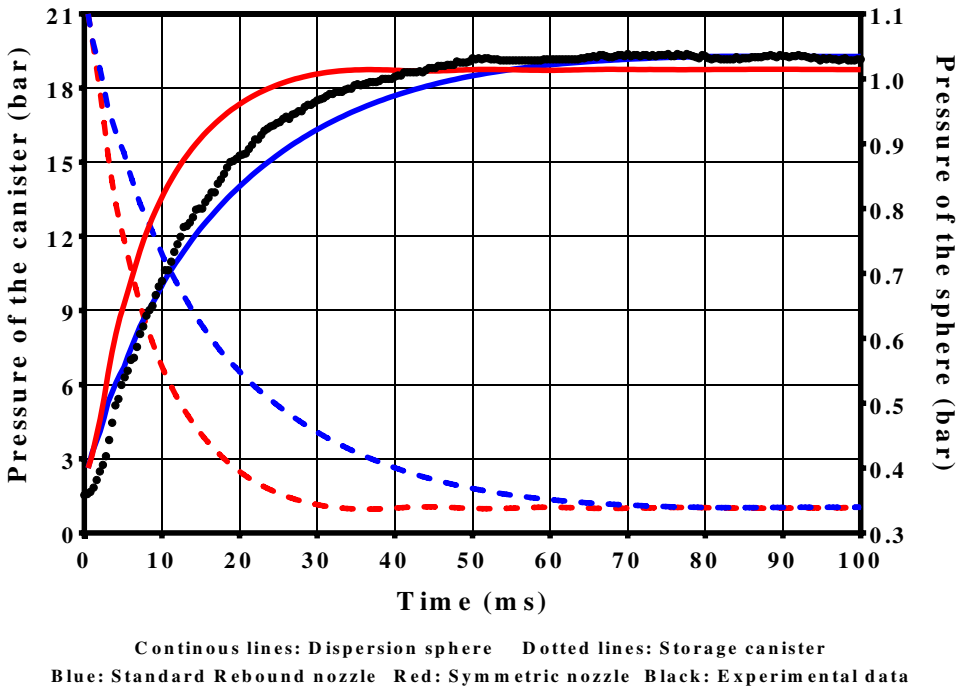

Figure 4.31. Comparison of the pressure profiles determined with the CFD simulations and the experimental data obtained with a test check

Furthermore, the dispersion process was divided in three different stages by Du et al. (2015). Initially, the DPIV analyses and the anemometry results of Dahoe et al. (2001) and Mercer et al. (2001) posed a tendency of the velocity magnitude that reaches a maximum value after 10 ms of dust dispersion that is followed by a continuous decrease of this variable. This decay will be sustained during the next 30 to 40 ms. This fast injection of dust particles defines the first stage of dispersion. Afterwards, the reduction of the injection changes drastically the rate of diminution of the velocity of the gas flow, which will define the second stage of the dispersion process, which is defined by the stabilization of the dust cloud. Finally, the sedimentation stage can be clearly identified after the first 100 ms. The stages pose different behaviors for the three velocity components of the gas flow in the dispersion sphere. These behaviors were determined with the analysis of the mean values of these variables in the dispersion chamber. These values are shown in Figure 4.32:

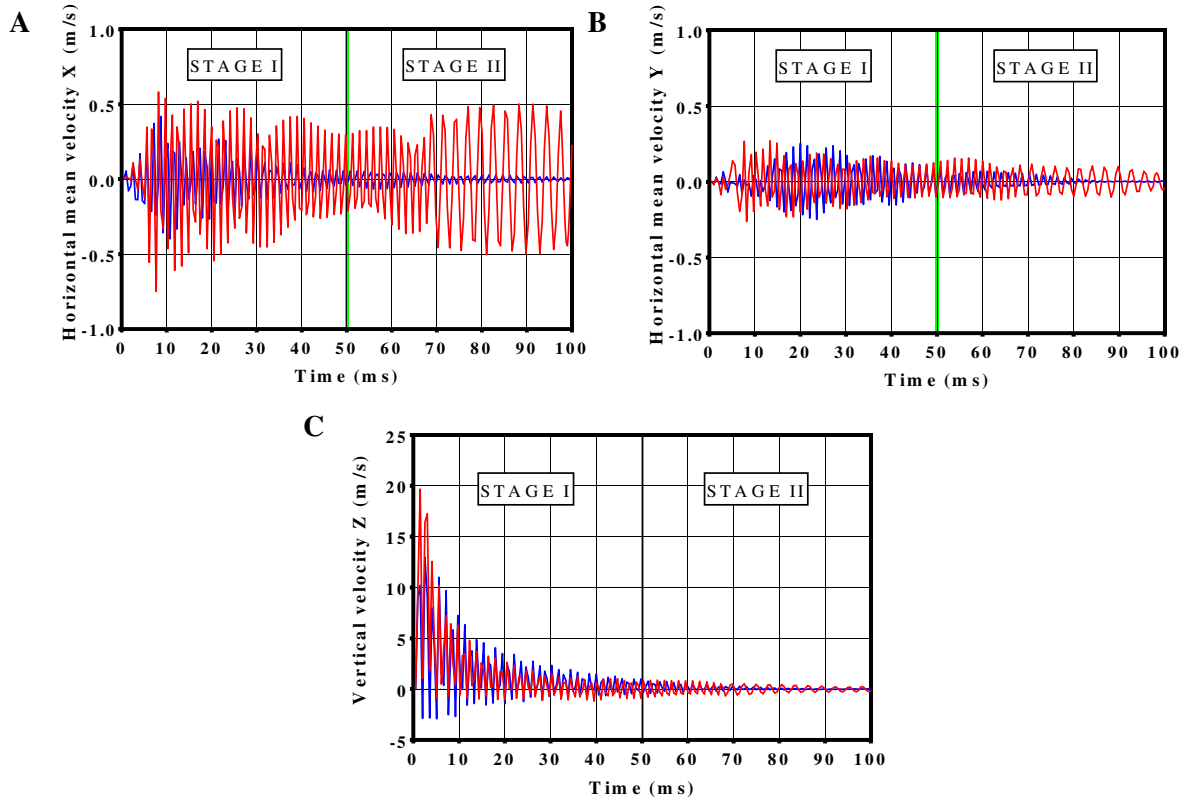

Blue: Standard rebound nozzle **Red: Symmetric Nozzle**

Figure 4.32. Mean values of the three components of the velocity field computed in the 20 L sphere A. Transversal (X-axis) B. Transversal (Z-axis) C. Axial (Y-axis).

The three components of the gas velocity have oscillatory behaviors that clearly show how the gas flow behaves during the first two stages of dispersion. The inertial effects observed by Mercer et al. (2001) explain why the velocity oscillations in the direction of the X-axis have a greater amplitude than the components in the direction of the Y-axis. The amplitudes of the horizontal components remain in the same order of magnitude during the whole process for the standard nozzle but not with the symmetric nozzle because of a higher energy dissipation. On the contrary, the vertical component (Figure 4.32C) shows the rapid decay that was discussed above during the first 40 ms as well as the subsequent stabilization. The final stage is not shown in the chart because the time scope of the CFD simulation did not comprise periods of time after 100 ms. Nevertheless, it is possible to affirm that the sedimentation of the solid particles is important after 80 ms.

Despite the variations of the dust concentration that are caused by the particles settlement, the selection of the ignition delay of a combustible dust cloud must not only be established by the sedimentation of the combustible dust. In fact, this parameter must also be set according to the variations of the turbulence levels. The computational results have shown that the computed velocity fields have various differences that constitute an important variation of the turbulence levels of the dust cloud. Thus, the ignition delays should not be the same if the injection nozzle is modified. For this reason, this analysis has also considered the variation of the turbulent kinetic energy in the two bodies that compose the flow domain of e CFD simulation. The mean value of this variable for the case studies considered are shown in Figure 4.33. This chart shows the same behavior that was observed by Di Benedetto et al., (2013). For each nozzle, the gas flow constitutes a rapid increase of the turbulence levels during the first milliseconds that is followed by a longer turbulence decay:

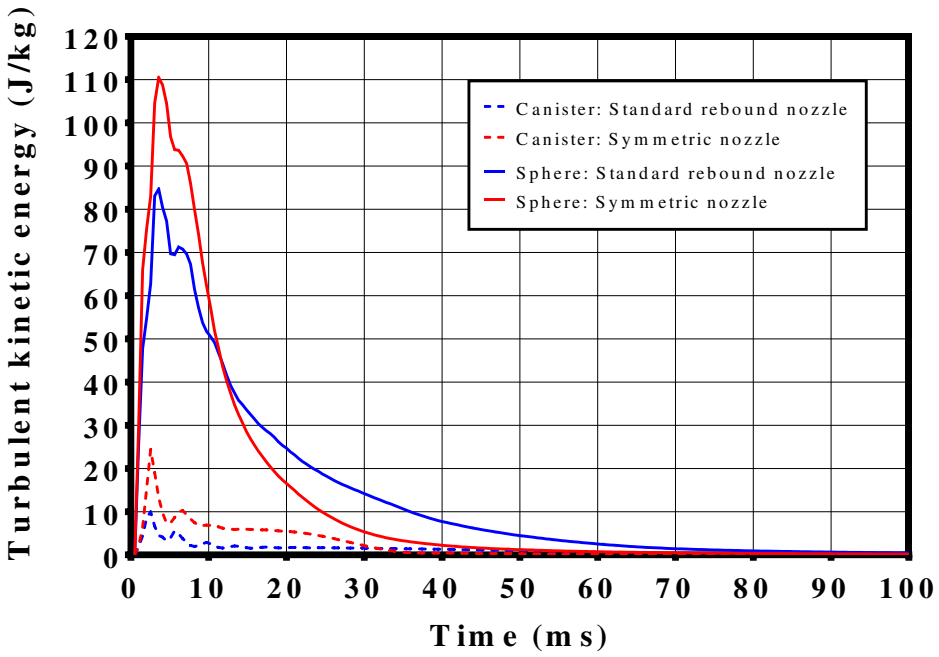

Figure 4.33. Evolution of the turbulent kinetic energy during the dispersion process

The experimental results obtained with fractional factorial design of the previous chapter showed that the standard rebound nozzle allowed acquiring more conservative information about the explosivity of the dust cloud (higher severity parameters). The comprehension of this experimental result is possible after considering the profiles shown in Figure 4.34 and Figure 4.35. The evolution of the turbulent kinetic energy is not similar with both injection devices. Indeed, the symmetric nozzle has dissipated the most of the turbulent kinetic energy after 40 ms whereas the standard nozzle keeps a mean turbulence level of 7.5 $J \cdot kg^{-1}$.This fact allows explaining some important characteristics of the cloud that were observed experimentally. For instance, the initial turbulence level is higher for the symmetric nozzle, which promotes the agglomerates fragmentation during the first 10 ms. However, the turbulence decay is faster for this device; hence it will promote the solids agglomeration at the late stages of dispersion. This condition agreed with the results of the granulometric tests, which showed that the utilization of the symmetric nozzle generated not only a greater reduction of the diameter d_{50} for the symmetric nozzle at the beginning of the dispersion process (Figure 3.49) but also the apparition of large agglomerates after 60 ms of dust dispersion (Figure 3.48).

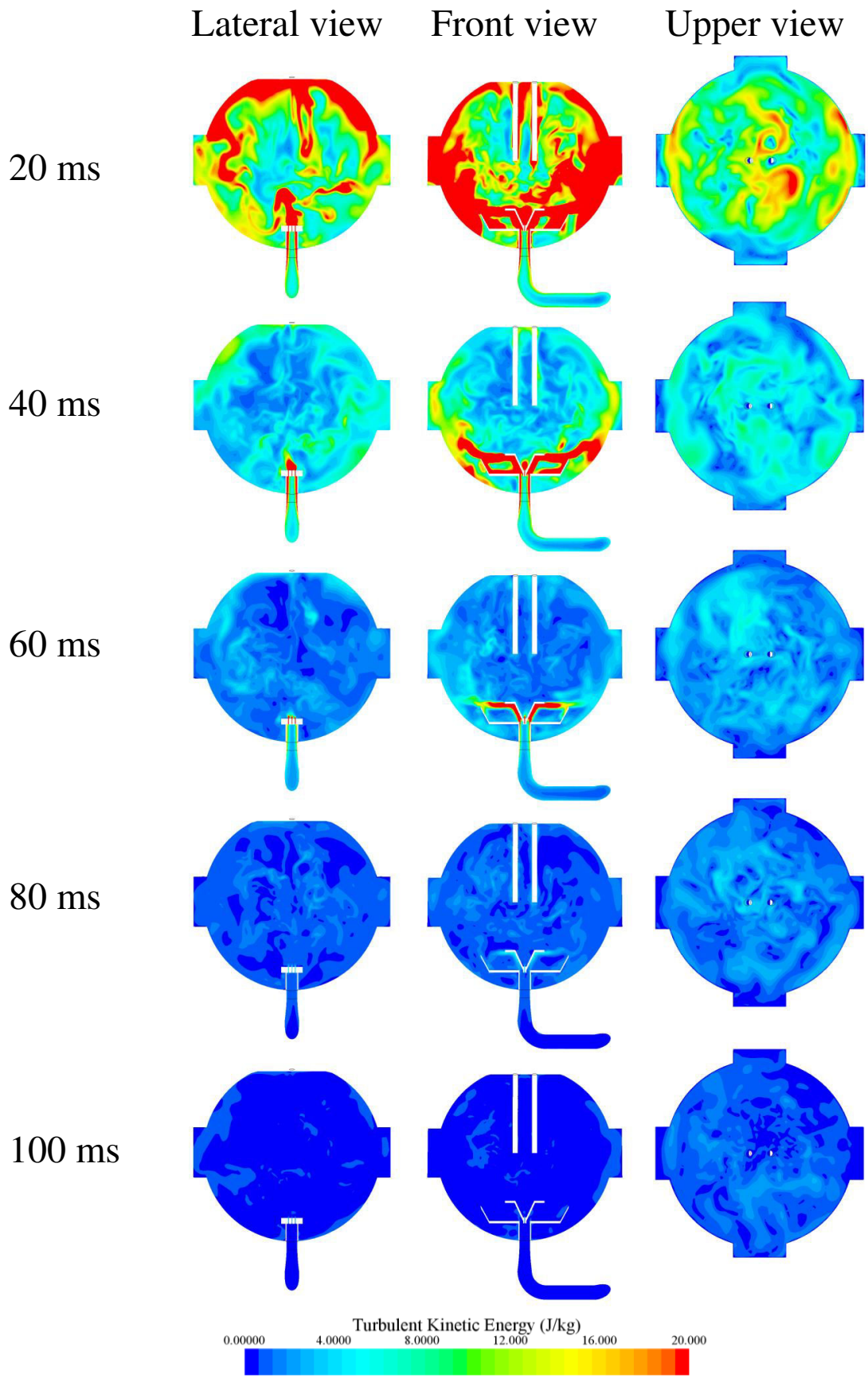

Figure 4.34. Turbulent kinetic energy of the gas flow with an injection performed with the standard rebound nozzle

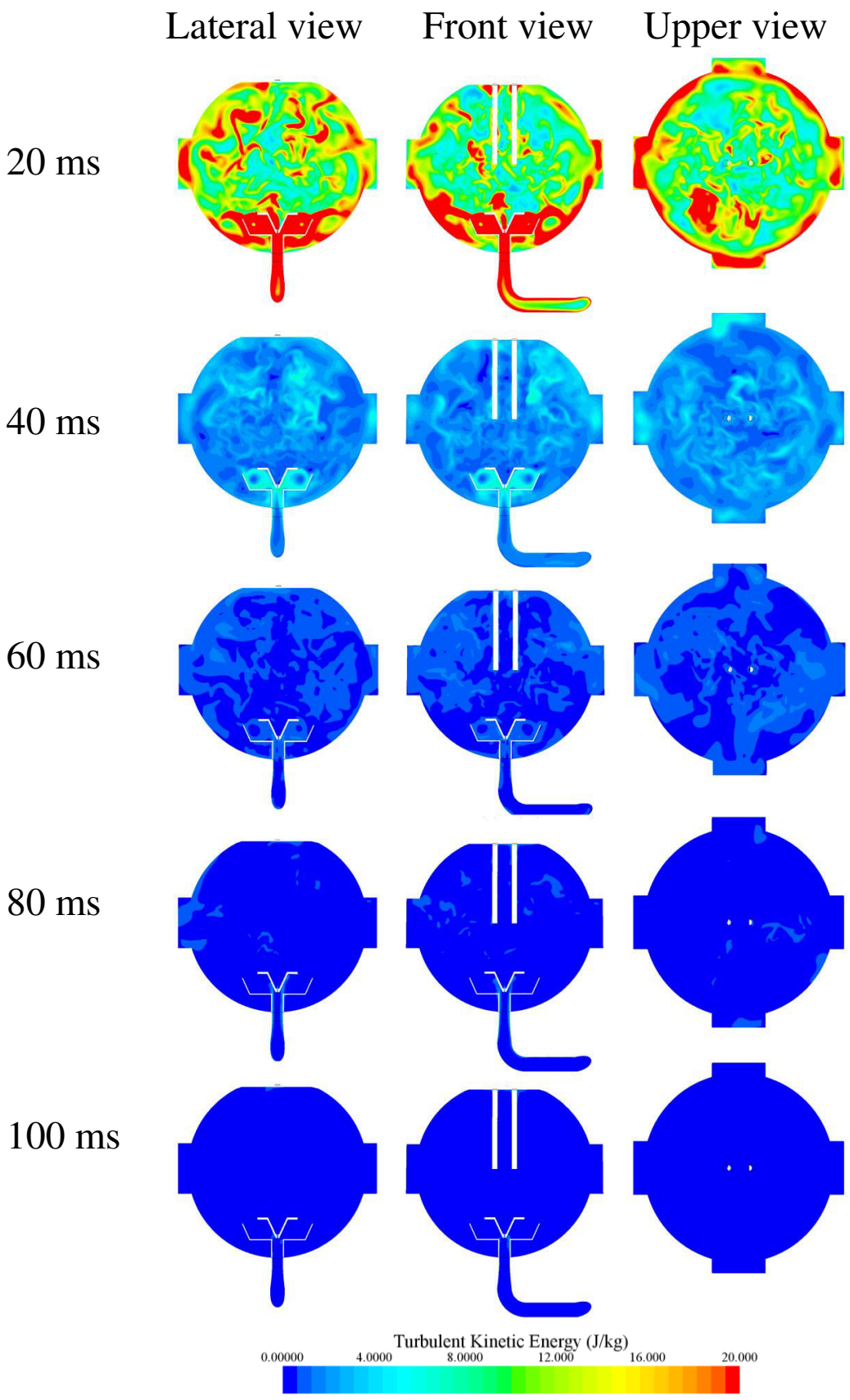

Figure 4.35. Turbulent kinetic energy of the gas flow with an injection performed with the symmetric nozzle

C. *Behavior of the dispersed phase at the geometric center of the sphere (10-100 ms)*

The evolution of the gas flow variables that were described above also determines the behavior of the combustible dust. For this reason, the last sections of this chapter analyze the behavior of the combustible dust in the region of major interest of the explosion chamber of the test apparatus, which is the ignition zone.

Previously, the characterization of the initial stage of the injection process showed that the combustible dust has a chaotic behavior that defines its distribution all over the sphere (Figure 4.26). This condition has constituted some basic considerations about the standard test method. For instance, the assumption of the uniformity of a turbulent dust cloud formed within the 20 L sphere allows estimating its minimum explosible concentration as the nominal concentration of a well-dispersed dust sample. However, the computation of the velocity field has shown that the dispersion conditions are defined by the injection nozzle. Thus, it is necessary to establish how the dispersed particles respond to the turbulence of the gas flow. For this analysis, a spherical region (diameter: 3 cm) was defined as the control volume in order to represent the zone where the ignition spark is formed.

Figure 4.36 shows the comparison of the dust concentration in the control volume that is obtained with each injection nozzle. On the one hand, the standard device clearly establishes temporary concentrations that differ significantly from the nominal concentration (0.03 kg/m^3). During the first 60 ms, the local concentration can be several times higher than the nominal value. This fact constitutes a higher ignitability of the dust cloud during certain moments because the high solids concentration favors the flame propagation without consuming the most of the energy provided by the ignitors (concentration below 0.75 kg/m^3). On the other hand, the symmetric nozzle distributes the combustible dust so that the concentration at the geometric center does not differ considerably from the nominal value. Hence, the ignitions are not submitted to great variations of the mass of the combustible powder near the ignitors and the uniformity assumption is more valid. Unfortunately, this distribution also implies a lower ignitability of the dust cloud.

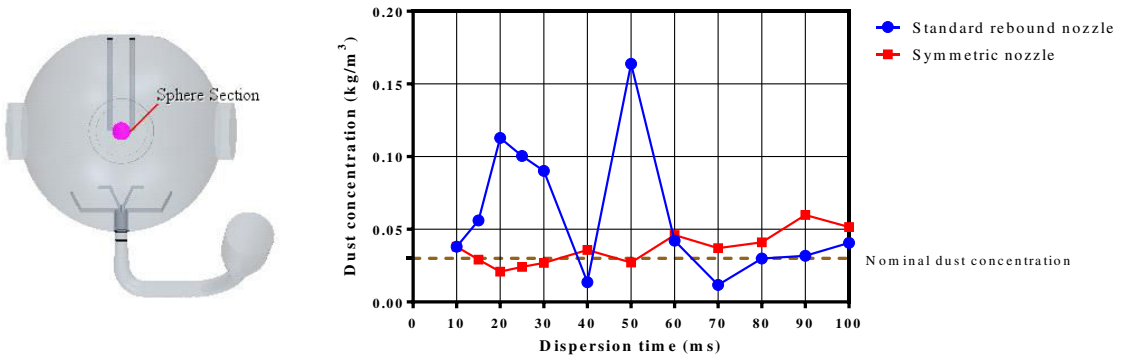

Figure 4.36. Variations of the dust concentration in a spherical region (diameter: 3 cm) located at the ignition zone of the 20 L sphere

Additionally, it is possible to identify a time period in which the concentrations established by the two nozzles are quite similar. After 80 ms of dust dispersion, the velocity of the gas flow has decreased to velocities below 20 m/s at the geometric center and the continuous displacement of the solid particles is lower. Hence, the fluctuations of the solids concentration decrease drastically and approach to the nominal value.

Furthermore, the DPIV analyses that were discussed in Section 3.6.4B allowed determining the variations of the turbulence levels at the geometric center of the 20 L sphere. This determination was accomplished

by tracking the particles seen in an interrogation window. This analysis was also developed with the tracking data that were obtained with the CFD simulations in order to compare the root-mean square (RMS) velocities of the solid particles dispersed with the two injection nozzles.

Figure 4.37 compares the root-mean square velocities of the particles located inside the spherical control volume during the dispersion process with the anemometry data obtained at the center of the sphere by Dahoe et al. (2001). The tendencies do not show a significant dissimilarity with the regard to the anemometry results. This condition can be explained after comparing the velocity fields of this region that are developed by each nozzle.

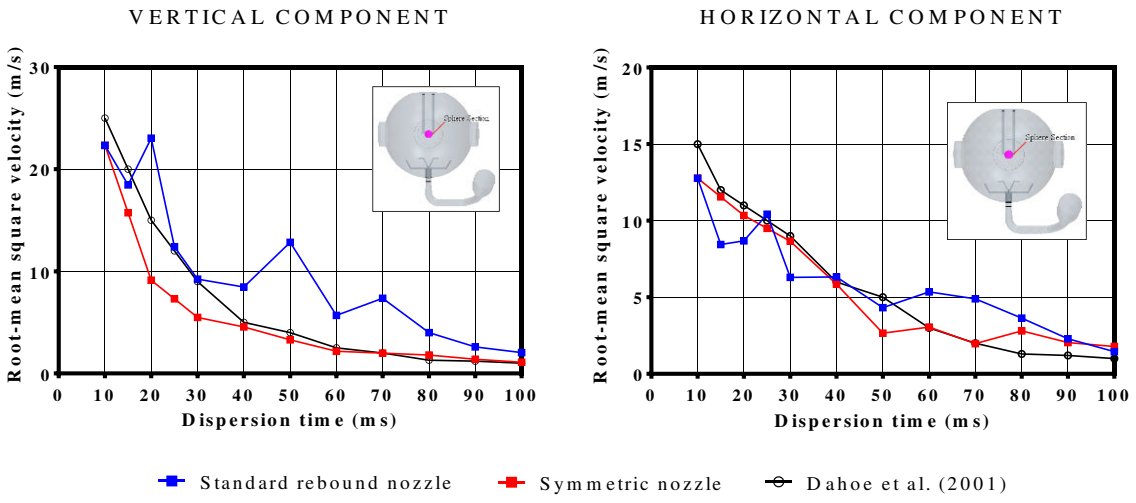

Figure 4.37. Comparison of the RMS velocity of the solid particles and the RMS of the gas flow determined by Dahoe et al. (2001) at the ignition zone of the 20 L sphere

The trajectories followed by the jets generated by the two injection nozzles favor their collision against the walls. This energy dissipation factor is complemented by the wall friction and the gas expansion. For this reason, the gas velocity in this region is quite similar for both cases since a great part of the turbulent kinetic energy has been dissipated previously. Moreover, the dispersed phase does not affect significantly the gas velocity due to its low concentration.

In accordance with this statement, the DPIV analyses can be considered as a valid tool for the characterization of the flow turbulence. For this reason, the turbulence decay tendencies that were determined with this experimental technique had a good agreement with the anemometry profiles established by Dahoe et al. (2001). Thus, the decay exponent calculated for the model shown in Equation 3.50 is 8.7% lower than that determined by anemometry. However, the absolute values of the RMS that were determined with the DPIV tests (Figure 3.46) are considerably low and do not correspond to the results of the CFD simulations or the anemometry data. This fact raises the possibility of a calibration error in the frames analyses. Nevertheless, the DPIV results have assessed properly the duration of the different stages of dust dispersion in the 20 L sphere.

D. *Variations of the particle size distribution in the 20 L sphere*

The continuous variations of the turbulence levels of the gas flow in the 20 L sphere modify the particle distribution due to the development of the mechanisms that were discussed in Section 2.1.5D. For this reason, the fragmentation of the combustible dust in the test apparatus with the standard rebound nozzle

was also considered in this computational approach. This analysis was performed by representing the dispersed phase as a set of particle clumps (Figure 4.38). Each clump is composed by three attached spherical particles. The size of the composing particles was adapted to generate 1324 particles adjusted to the size distribution determined by sedimentation analyses (Figure 3.5).

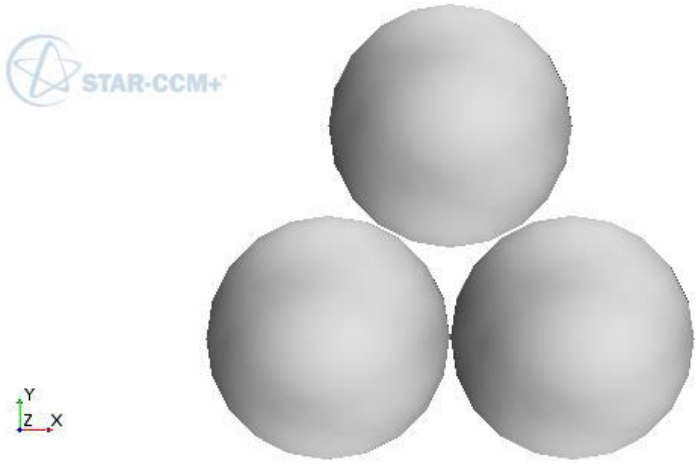

Figure 4.38. Representation of the wheat starch agglomerates

A dispersed agglomerate will fragment when a mechanical load provides the energy necessary to overcome the contact forces. This value corresponds to the maximum tensile and shear stresses defined for the simple failure model in the CFD simulation. These fragmentation stresses were estimated from the data provided by Schweiger & Zimmermann (1999) and Yilmaz et al. (2013). Thereafter, the stresses exerted on every dispersed clump were computed according to Equations 2.103 and 2.104 (Section 2.1.5D) and compared with the corresponding threshold values to establish if the dispersed agglomerates breakup. In the same way, the work of cohesion was defined from the experimental characterization of solids cohesion in starch granules developed by Rowe (1989).

In addition, the collision force of the soft-sphere model was computed according to the Hertz-Mindlin model. The collision force associated to this model was calculated with the coefficients of restitution defined in Section 4.1.4B. Finally, Table 4.7 lists the setting parameters set for the models of simple failure and linear cohesion model as well as the parameters required to calculate the contact force in the solid clumps:

Table 4.7. Numerical parameters set to define the solids fragmentation and agglomeration

PARAMETER	VALUE
Static friction coefficient	0.20
Normal restitution coefficient	0.25
Tangential restitution coefficient	0.20
Work of cohesion [W/m2]	117.4
Coefficient of rolling resistance	0.15
Maximum Tensile Strength [Pa]	23
Maximum Shear Strength [Pa]	19

The high computational costs of a CFD-DEM simulation developed with particle clumps restricted the analysis of the whole dispersion process. Thus, the fragmentation analysis was developed only for some specific times of the dispersion: 1, 20, 60 and 100 ms. These times are defined in different dispersion stages; hence their turbulence levels vary significantly. The analysis of these selected times allows

establishing how the fragmentation occurs during the initial injection (1 ms), the stages of high (20 ms) and low turbulence (100 ms) and at the standard ignition delay (60 ms). For each one of these moments of the dispersion process, a complementary simulation was developed with 5 time steps of 10^{-4} s in order to evaluate the variations of the particle size distributions of the injected clumps.

In accordance with this definition, four new simulations were developed from the pressure and velocity fields of the CFD simulation developed for the standard rebound nozzle. These moments represent not only time variations of the turbulence levels but also different spatial turbulence profiles. For this reason, the fragmentation of the solid agglomerates was analyzed by injecting the particle clumps in five different positions of the 20 L sphere (Figure 4.39). This definition represented an assumption in the fragmentation analysis since the PSD of the injected particle clumps was defined as the initial PSD of wheat starch that was determined with sedimentation analyses. Nonetheless, this comparative analysis established the influence of the local turbulence levels on the agglomerates fragmentation by establishing the same reference point for each simulation.

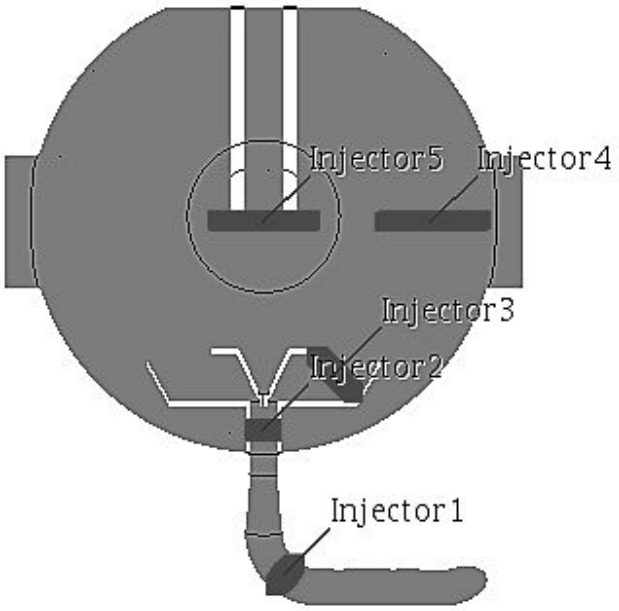

INJECTORS

1. Pressurized canister
2. Before the injection nozzle
3. After the injection nozzle
4. Equatorial plane (near the windows)
5. Geometric center of the sphere

Figure 4.39. Injection zones of the representative particle clumps

Figure 4.40 presents the comparison of the diameters d_{10}, d_{50} and d_{99} obtained with each injector for each instant considered in this analysis. In this way, it was possible to establish the influence of the local turbulence on the fine and coarse particles. Initially, the computational results show that the stabilization of the fragmented agglomerates is achieved after one or two time steps. This condition evidences the high tendency of the organic powder to breakup when it is dispersed in the 20 L sphere at conditions of high and moderate turbulence (1-60 ms). On the contrary, the clumps injected at 100 ms posed a negligible fragmentation level that generated a considerably low reduction of the diameter d_{99} and the increase of the diameter d_{10} after certain time steps. In addition, the last time step did not have a significant difference of the local variations of the PSD due to the low difference in the local turbulence within the sphere and the low number of particles. Evidently, a greater number of particles could have represented a greater agglomeration probability due to the collision of the dispersed solid particles.

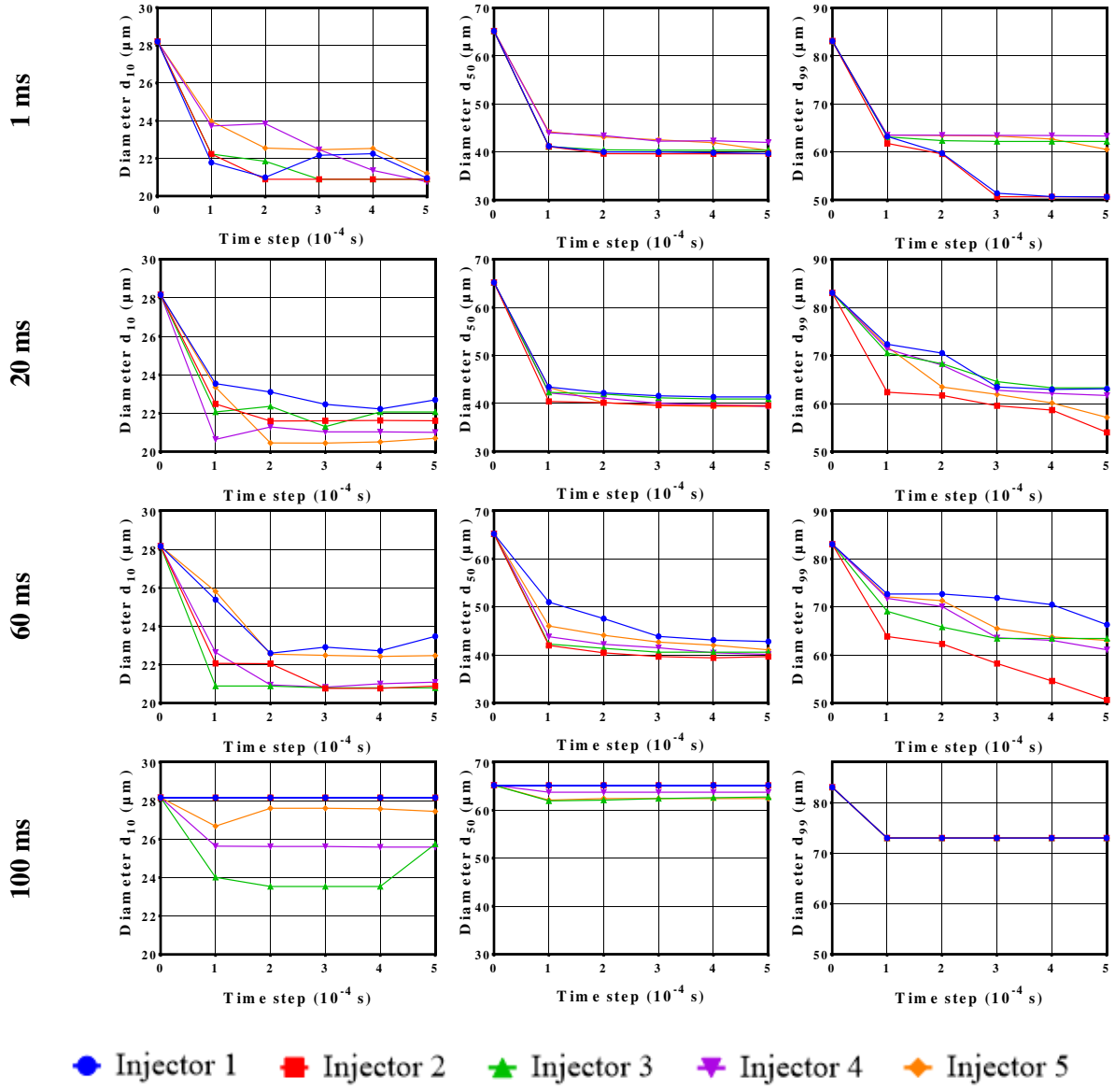

Figure 4.40. Variations of the PSD of the particle clumps injected in the five analyzed points

The analysis of the first three time steps describes how the development of the gas flow defines the fragmentation probability within the sphere. After 1 ms of dust dispersion, the diameter d_{99} shows that the greatest reduction of the size of the coarse agglomerates (39.0%) occurs in the location of the of the solenoid valve whereas a similar diminution is observed for the fine particles with all the injectors (25.6%). This condition is evidenced because the flow has only developed in the region where the valve is installed.

The dispersion process favors the dust fragmentation at the inlet of the nozzle and the center of the sphere when 20 ms have passed. The results establish that the diameter d_{10} has diminished 23.3% and the diameter d_{99} has decreased 35.0%. This condition can be explained after considering that the injected flow has reached a transonic state at the nozzle and the downward flow developed by the collision of the rising jets still maintains a high turbulent kinetic energy. However, the granulometric analyses determined a considerably smaller diameter d_{50} (Figure 3.49). Therefore, it is possible to establish that an agglomerate

breaks up through its whole trajectory followed within the dispersion sphere due to the different shear and tensile stresses exerted by the fluid flow. The contributions of the different zones of the test apparatus are determined by the transient conditions of the injection and expansion of the pressurized gas.

Furthermore, the final stage of the gas injection (60 ms) poses the major fragmentation levels of the particle clumps that were injected inside the sphere in two different places. The diameter d_{10} decreased 26.2% for the injector 3 whereas the diameter d_{99} decreased 39.0% for the injector 2. As discussed above, the reduction of the gas velocity in the flow domain begins at the end of the air injection. This fact reduces the drag force and the shear stress exerted by the fluid. For this reason, the highest fragmentation is observed in the surroundings of the standard rebound nozzle where the last fraction of injected gas gets into the spherical vessel.

In summation, the computational results agree with the experimental fragmentation analysis developed by Kalejaiye et al. (2010). They established that the grinding effect on dust particles can be mainly attributed to the combination of the injection valve and the dispersion nozzle. This affirmation is valid because the highest local turbulence levels are achieved in these regions due to their high pressure gradients. Nevertheless, the computational results also show that the fragmentation levels of the clumps placed with the injectors 4 and 5 do not differ significantly from those observed with the other injectors in the dispersion moments that were analyzed. This fact implies that the influence of the injection system on the dust fragmentation is not direct since it does not enhance significantly the agglomerates breakup by collision but determines the evolution of the turbulence of the gas flow.

4.2.5 Application to the determination of the explosibility parameters of the micrometric wheat starch

The previous sections have presented the computational description of the main features of the dust clouds formed with the standard rebound nozzle and the symmetric device. The analysis of these results complemented the characterization tests that were considered for the experimental approach. In this manner, this section presents the main aspects that should be taken into account for the development of a flammability test with the 20 L sphere when one of the injection nozzles that were characterized in this thesis is utilized.

The computational analyses have shown that it is possible to predict and describe the evolution of the variables that affect the flammability of a dust cloud when the physical properties of a combustible dust are specified along with the design and operating parameters of a standard test method. This fact allows establishing the most appropriate conditions to fluidize and ignite the dust sample and setting properly the ignition delay.

For the particular case of micrometric wheat starch, the experimental tests that were discussed in the previous chapter and the computational description that was discussed above have shown that the dynamics of the two-phase flow is not the same for the two injection systems that were characterized. These dissimilarity factors show the importance of adapting the operating conditions of a flammability test according to the combustible dust and the nozzle installed in the apparatus. In accordance with this statement, Table 4.8 presents a comparison of the most remarkable characteristics of the dust clouds formed with both nozzles:

Table 4.8. Comparison between the dispersion conditions developed by the standard rebound nozzle and the symmetric injection device

PARAMETER	STANDARD REBOUND NOZZLE	SYMMETRIC NOZZLE
Gas velocity	Two large jets (lateral) and a reduced jet (central) are generated during the injection.	A large expanded jet and a reduced jet (central) are generated during the injection.
	The injection of the pressurized gas lasts 60 ms approximately.	The injection of the pressurized gas lasts 10 to 20 ms less than the injection with the other nozzle.
	The initial velocities (0-10 ms) are slower but the gas flow maintains high velocities during a longer period of time.	This nozzle defines higher velocities during the first stage of dispersion but is characterized by a more rapid decrease of the gas velocity.
Pressure of the spherical vessel	The initial stage of dispersion establishes that the pressure with the symmetric nozzle is slightly greater. Nevertheless, this dissimilarity does not constitute a significant variation of the dispersion process because the final pressure is approximately 1 bar for both nozzles.	
Turbulence levels	This nozzle maintains a high turbulence level for a longer period of time (0-60 ms) but its maximum turbulence level is lower than that obtained with the other nozzle (84 J/kg).	This nozzle posed the highest turbulence peak (110 J/kg) but had a shorter period of high turbulence (0-40 ms).
Solids distribution	The dust-air mixture is injected towards the two of the lateral windows of the sphere. Thus, the heterogeneity of the mixture is considerably higher during the first 10 ms of dust dispersion	The dust-air mixture is injected towards the walls without a predominating direction. Thus, the nominal concentration is a more valid assumption for this nozzle.
	The dust concentration at the ignition has more fluctuations	The homogeneous distribution reduces the variations of the dust concentration
Particle size distribution	The reduction of the particle size distribution is lower with the utilization of this nozzle. However, the dust agglomeration is not clearly observed during the first 100 ms.	The initial turbulence levels are higher with this nozzle. Thus, the initial fragmentation is greater with this nozzle but the rapid turbulence and velocity decay promote the solids agglomeration and sedimentation after 80 ms.

The characteristics listed above allow concluding that the utilization of the symmetric nozzle is more limited than the standard device. This fact implies that the ignition delay for the new injection system should not be over 40 ms whereas the standard nozzle allows considering up to 80 ms. If the starch-air mixture is ignited before these limiting times, it is possible to consider a greater reduction of the size distribution and a turbulence level that enhances the homogeneity of the mixture.

In summation, the ignition delay of the starch dust cloud should be adapted for the 20 L sphere with same criterion that was posed for the modified Hartmann tube. The activation of the ignitors must correspond to the end of the transition stage in order to develop a combustion process under the most conservative conditions.

Nevertheless, these values are specific for the dust sample considered in this analysis (0.6 g of wheat starch with a specific PSD and moisture content). Indeed, the variations of the dust concentration and the

environmental conditions affect the evolution of the turbulence levels and the agglomeration rates as well. For this reason, the development of the characterization tests and simulations is suggested for future flammability tests performed with other dust samples. This fact will reduce the uncertainty of the experimental results of the flammability test and acquire the experimental data that determine the highest ignitability and severity of the dust cloud.

4.3 LIST OF VARIABLES

E	Potential energy of the system	[kJ·kmol^{-1}]
e_n	Coefficient of normal restitution	[-]
e_t	Coefficient of tangential restitution	[-]
k_n	Normal spring stiffness	[N·m^{-1}]
k_t	Tangential spring stiffness	[N·m^{-1}]
P_{inlet}	Pressure of the dispersion gas at the inlet boundary of the modified Hartmann tube	[Pa]
u_{pr}	Relative velocity between two colliding particles	[m·s^{-1}]

Greek symbols

δ	Maximum overlapping of two colliding particles	[-]
ϑ	Poisson's ratio	[-]
ρ	Fluid density	[kg·m^{-3}]
ρ_p	Particle density	[kg·m^{-3}]

4.4 REFERENCES

Alletto, M., & Breuer, M. (2012). One-way, two-way and four-way coupled LES predictions of a particle-laden turbulent flow at high mass loading downstream of a confined bluff body. *International Journal of Multiphase Flow*, *45*, 70–90.

Ansys Inc. (2009). ANSYS FLUENT 12.0 Theory Guide.

ASTM E789 - 95. (2001). Standard Test Method for Dust Explosions in a 1.2-Litre Closed Cylindrical Vessel. *Annual Book of ASTM Standards*, pp. 1–18.

ASTM E1226 − 12a. (2012). Standard Test Method for Pressure and Rate of Pressure Rise for Combustible Dusts. *Annual Book of ASTM Standards*, pp. 1–13.

Buffard, T., & Clain, S. (2010). Monoslope and multislope MUSCL methods for unstructured meshes. *Journal of Computational Physics*, *229*(10), 3745–3776.

Calvert, G., Hassanpour, A., & Ghadiri, M. (2013). Analysis of aerodynamic dispersion of cohesive clusters. *Chemical Engineering Science*, *86*, 146–150.

CD-Adapco. (2015). STAR-CCM+ Version 10.04, User Guide.

CEI IEC 1241-2-3 Ed. 1.0 b. (1994). Electrical apparatus for use in the presence of combustible dust - Part 2: Test methods - Section 3: Method for determining minimum ignition energy of dust/air mixtures. *Bureau Central de La Comission Electrotechnique Internationale*. Genève.

Cuervo, N., Murillo, C., Dufaud, O., Bardin-Monnier, N., Skali-Lami, S., Remy, J.-F., … Perrin, L. (2014). Combining CFD simulations and PIV measurements to optimize the conditions for dust explosion tests. *Chemical Engineering Transactions*, *36*, 259–264.

Dahoe, A. E., Cant, R. S., Pegg, M. J., & Scarlett, B. (2001). On the transient flow in the 20-liter explosion sphere. *Journal of Loss Prevention in the Process Industries*, *14*(6), 475–487.

Dahoe, A. E., Cant, R. S., & Scarlett, B. (2001). On the decay of turbulence in the 20-liter explosion sphere. *Flow, Turbulence and Combustion*, *67*(3), 159–184.

Deen, N. G., Van Sint Annaland, M., Van der Hoef, M. A., & Kuipers, J. A. M. (2007). Review of discrete particle modeling of fluidized beds. *Chemical Engineering Science*, *62*(1–2), 28–44.

Di Benedetto, A., Russo, P., Sanchirico, R., & Di Sarli, V. (2013). CFD simulations of turbulent fluid flow and dust dispersion in the 20 liter explosion vessel. *AIChE Journal*, *59*(7), 2485–2496.

Du, B., Huang, W., Liu, L., Zhang, T., Li, H., Ren, Y., & Wang, H. (2015). Visualization and analysis of dispersion process of combustible dust in a transparent Siwek 20-L chamber. *Journal of Loss Prevention in the Process Industries*, *33*, 213–221.

Dufaud, O., Traoré, M., Perrin, L., Chazelet, S., & Thomas, D. (2010). Experimental investigation and modelling of aluminum dusts explosions in the 20 L sphere. *Journal of Loss Prevention in the Process Industries*, *23*(2), 226–236.

Eckhoff, R. K. (2013). Influence of dispersibility and coagulation on the dust explosion risk presented by powders consisting of nm-particles. *Powder Technology*, *239*, 223–230.

Freireich, B., Litster, J., & Wassgren, C. (2009). Using the discrete element method to predict collision-scale behavior: A sensitivity analysis. *Chemical Engineering Science*, *64*(15), 3407–3416.

Helland, E., Occelli, R., & Tadrist, L. (2002). Computational study of fluctuating motions and cluster structures in gas–particle flows. *International Journal of Multiphase Flow*, *28*(2), 199–223.

Huilin, L., Shuyan, W., Jianxiang, Z., Gidaspow, D., Ding, J., & Xiang, L. (2010). Numerical simulation of flow behavior of agglomerates in gas–cohesive particles fluidized beds using agglomerates-based approach. *Chemical Engineering Science*, *65*(4), 1462–1473.

Ibsen, C. H. (2002). *An experimental and computational study of gas-particle flow in circulating fluidised reactors*. Aalborg University. Retrieved from http://library.certh.gr/libfiles/PDF/GEN-EKETA-1327-AN-EXPERIMENTAL-by-IBSEN-in-PHD-DK-PP-261-Y-FEB-2002.pdf

Jia, T., Zhang, Y., Chen, J. K., & He, Y. L. (2012). Dynamic simulation of granular packing of fine cohesive particles with different size distributions. *Powder Technology*, *218*, 76–85.

Kalejaiye, O., Amyotte, P. R., Pegg, M. J., & Cashdollar, K. L. (2010). Effectiveness of dust dispersion in the 20-L Siwek chamber. *Journal of Loss Prevention in the Process Industries*, *23*(1), 46–59.

Kosinski, P., & Hoffmann, A. C. (2007). An Eulerian–Lagrangian model for dense particle clouds. *Computers & Fluids*, *36*(4), 714–723.

Liou, M.-S. (2006). A sequel to AUSM, Part II: AUSM+-up for all speeds. *Journal of Computational Physics*, *214*(1), 137–170.

Liu, D., Bu, C., & Chen, X. (2013). Development and test of CFD–DEM model for complex geometry: A coupling algorithm for Fluent and DEM. *Computers & Chemical Engineering*, *58*, 260–268.

Mangwandi, C., Cheong, Y. S., Adams, M. J., Hounslow, M. J., & Salman, A. D. (2007). The coefficient of restitution of different representative types of granules. *Chemical Engineering Science*, *62*(1-2), 437–450.

Mercer, D. B., Amyotte, P. R., Dupuis, D. J., Pegg, M. J., Dahoe, A., de Heij, W. B. C., … Scarlett, B. (2001). The influence of injector design on the decay of pre-ignition turbulence in a spherical explosion chamber. *Journal of Loss Prevention in the Process Industries*, *14*(4), 269–282.

Murillo, C., Bardin-Monnier, N., Muñoz, F., & Dufaud, O. (2015). Application of CFD on the sensitivity analyses of some parameters of the modified Hartmann tube. *Journal of Loss Prevention in the Process Industries*.

Murillo, C., Dufaud, O., Bardin-Monnier, N., López, O., Munoz, F., & Perrin, L. (2013). Dust explosions: CFD modeling as a tool to characterize the relevant parameters of the dust dispersion. *Chemical Engineering Science*, *104*, 103–116.

Rao, P., & Medina, M. A. (2003). Evaluation of V and W multiple grid cycles for modeling one and two-dimensional transient free surface flows. *Applied Mathematics and Computation*, *138*(1), 151–167.

Rowe, R. C. (1989). Surface free energy and polarity effects in the granulation of a model system. *International Journal of Pharmaceutics*, *53*(1), 75–78.

Schweiger, A., & Zimmermann, I. (1999). A new approach for the measurement of the tensile strength of powders. *Powder Technology*, *101*(1), 7–15.

Versteeg, H., & Malalasekera, W. (2007). *An Introduction to Computational Fluid Dynamics: The Finite Volume Method* (2 edition). Harlow, England ; New York: Prentice Hall.

Wendt, J. F. (1992). *Computational Fluid Dynamics an Introduction*. Berlin, Heidelberg: Springer Berlin Heidelberg.

Yilmaz, M. T., Karaman, S., & Kayacier, A. (2013). Mathematical approach for two component modeling of salep–starch mixtures using central composite rotatable design: Part I. Physicochemical and steady shear properties. *Food Hydrocolloids*, *31*(1), 49–60.

CONCLUSION

This research study described the dynamics of the dust clouds formed in the standard setups developed to characterize the explosibility of combustible dusts. The applicability of the experimental results of these test methods in different contexts (mainly industrial) has constituted the development of standardization documents for the design and manipulation of these apparatuses. In this manner, the operating conditions of the setups are specified in various international standards (ASTM, ISO and IEC). However, the most remarkable uncertainty factor arises from the combustible dust itself. In fact, the physical and chemical properties of a dust sample dictate its fluidization characteristics as well as its reactivity; hence the definition of the same ignition conditions for different types of dust may not provide the most conservative information about the combustible dust.

This condition established the main objective of this thesis. This analysis intended to establish how some descriptive analyses can contribute to the determination of the most conservative information about the dust and enhance the repeatability and reproducibility of the flammability test. For this purpose, this study sought to answer the following question:

- Is it possible to describe the dispersion of a combustible dust within a standard apparatus to define the appropriate operating conditions of a flammability test by taking into account the phenomena that occur in the cloud?

The case studies of this study considered two of the standard setups: the modified Hartmann tube and the 20 L sphere. Thereafter, the descriptive analyses were performed with a metallic dust (aluminum) and an organic powder (wheat starch). The two standardized setups envisage the formation of a transient cloud by fluidizing a dust sample with a finite amount of pressurized gas. Thus, the initial description of the behavior of the mixture was focused on the variations of velocity and turbulence of the gas flow and the analysis of repercussions on the dispersed powder and the eventual propagation of a combustion flame.

The description of the gas flow was accomplished with a set of high-speed videos and Particle Image Velocimetry (PIV) analyses that were complemented with the computation of the velocity field with CFD simulations. The results identified the different three flow regimes that are developed within the two apparatuses due to the generation of unstable mixtures during a fixed time lapse:

- *High turbulence*: The pressurized gas is injected and creates a turbulent flow. This time lapse represented the lift of the dust samples. The development of the confined flow is determined by the geometry of the injection and the internal pressure gradients.
- *Stabilization:* The majority of the pressurized gas has already been injected and the fluctuations of the velocity field start to decrease.
- *Stable flow:* The gas flow tends to a quiescence state. This fact implies that the phenomenon of sedimentation dictates the behavior of the combustible dust.

The high-speed videos showed that the conditions of the dust particles in the mixture are also determined by the flow regimes of the dispersion gas. For instance, the high turbulence period showed a greater homogeneity of the mixture and the formation of some vortex structures in the regions around the dispersion nozzles that changed the trajectories of the dispersed particles. However, this period is also characterized by noticeable experimental uncertainties. On the contrary, the stability period is characterized by the low turbulence of the gas flow and the sedimentation of the coarse suspended particles but also by a good experimental reproducibility.

The direct response of the solid particles allowed proposing an alternative solution for the question mentioned above. In fact, the development of a granulometric analysis established the variations of the particle size distribution in a region of interest in order to know when the reduction of the particle size distribution constitutes the highest ignitability of the cloud. Evidently, the reader must think that this zone is defined at 10 cm for the modified Hartmann tube and the geometric center of the sphere (i.e. the position of the ignition sources), however, the comparison of the dispersion clouds of the analyzed dusts showed that the aluminum reaches higher rising velocities than the wheat starch during its fluidization. For this reason, the bulk of its cloud stabilizes at more elevated positions inside the modified Hartmann tube (over 12 cm). This condition was attributed to the higher fragmentation levels of the metallic powder and the different shape factors of the agglomerates of the two combustible dusts.

Additionally, the gas pressurization was modified in both vessels in a sensitivity analysis that was developed experimentally and with the CFD commercial codes available. The results showed that it is possible to define the duration and intensity of each one of the flow regimes be reducing the injection pressure. These facts allowed concluding that the positioning of the ignition sources in the modified Hartmann tube or the injection pressure of both apparatuses should be considered as adaptable parameters for the characterization of certain types of dusts. At this point, the CFD simulations can also become a useful tool for the development of the flammability tests since they help predicting the turbulence levels and the local dust concentrations at different positions of the test apparatuses in order to reduce the number of experimental assays.

Moreover, the granulometric analyses also showed that the periods of high fragmentation and agglomeration corresponded to the periods of the first and third flow regime. In this way, it was possible to establish the time period in which a dust cloud should be ignited by analyzing the evolution of the turbulence of the gas flow. In accordance with this discussion, the recommended ignition delay must correspond to the stabilization stage of the two-phase flow and, as a consequence, must be adjusted as a function of the powders physical properties. This setting allows initiating the combustion process with a great number of fine particles and moderate turbulence levels. In this manner, it will be possible to enhance the ignitability of the dust without considering great perturbations on the flame propagation.

The comparative analysis of the fluidization of the aluminum dust and the wheat starch established that the accurate definition of the stabilization period requires a detailed characterization of some physical properties of the dust such as its granulometry, density, hygroscopicity, etc. Nonetheless, the analyses performed with the two injection nozzles determined that the identification of the second flow regime must also consider other aspects such as the internal distribution of the gas flow during the injection and the geometry of the confinement vessel. In fact, the analysis of all these aspects provides a better comprehension of the different variations of the particle size distribution that were notably evidenced by Sanchirico et al. (2015).

The results obtained with the combination of the experimental descriptive tests with the computational approach showed that it is possible to consider some modifications of the operating parameters of the test apparatuses. The final recommendations for the adjustment of the manipulation settings for the characterization of the aluminum and starch samples of the case studies of this thesis are summarized in Table 4.4, Table 4.5 and Table 4.8. More generally, these recommendations can be considered in order to modify the existing procedures/standards.

Nonetheless, it is compulsory to remark that the values that were established in this study correspond to one of the multiple options that could have been analyzed. For instance, the increase of the mass of the solid samples and its repercussions on the variations of the size distribution and the momentum exchange

with the solid phase is an important characteristic that can be considered for further computational analyses. Moreover, other research subjects that can also be considered are listed below:

- Description of the dust cloud formed in other test apparatuses (for instance, the Godbert-Greenwald oven);
- Description of dense clouds formed inside the test apparatuses;
- Characterization of dust clouds composed by nanometric powders;
- Characterization of the combustion process through the further development of the computational approach (dust-air mixtures and hybrid mixtures: solid/solid or gas/solid).

The computational description of these types of mixtures might encounter some limitations that are usually associated to the phenomena described and the computational resources. For the particular cases of the dense clouds and the nanometric powders, a high number of particle interactions might be restrictive for the study of some systems of large length-scales. This fact resumes the discussion of the second chapter, which concluded that the detail level of the phenomena description will determine the most appropriate computational technique. Nevertheless, the CFD simulations have proven to be suitable for various scenarios associated to the characterization of the dust clouds formed inside the standardized laboratory equipment.

In summation, this thesis has proposed a methodology that is based on two complementary approaches that intend to constitute a preliminary phase of the flammability test. In this manner, the results obtained with these analyses will allow to develop a predictive model for the manipulation of the experimental setups in the short term. Afterwards, this methodology will promote the adaptation of the existing standards to define ab initio, by numerical simulation, the most conservative conditions for the quantification of the major risks associated to dust clouds.

APPENDIX A

PIVLAB ALGORITHMS IMPLEMENTED TO IMPROVE THE IMAGE QUALITY

- **Contrast limited adaptive histogram equalization (CLAHE):** This technique was developed to increase the readability of image data in medical studies. The main purpose of this image modification is focused on the exposure of the DPIV image. Furthermore, the uniformity of this variable is not achieved because the Gaussian distribution of the laser beam is not accomplished in all the regions of the picture (Thielicke, 2014). For this reason, CLAHE creates the intensity histogram of every image according to the local values of every subdivision.

  The analyses of the dust dispersion that were performed with the wheat starch were adjusted with the CLAHE technique on local subdivisions of 20 pixels. This fact provided an independent optimization of the image intensity that was considered to take into account the presence of solid particles in some regions with low intensity of the laser beam.

- **Intensity capping:** This technique is implemented to reduce the statistical errors of the correlation signal that are found in the correlation signal of non-uniform flows. This error comes from the analysis of tracer groups inside an interrogation window. This condition is based on the assumption of the same motion for all the particles. Indeed, the bright particles represent a more important contribution to the statistical values than the dark ones. For this reason, this filter establishes an upper limit for the greyscale. Hence all the values of the pixels that overcome a threshold value will be reduced. This intensity capping increases the probability of detecting valid vectors in 5.2 ± 2.5%.

- **Noise filter:** The noise in the DPIV images comes from the conversion of photons into an electric current within the image sensor. This issue is caused by the thermal noise of the integrated circuit of the image sensor. The effects associated to the noise in the images are reduced by performing a statistical estimation of the signal that corresponds to the clear image from the image received by the sensor. This estimation is performed according to the minimum mean-square error criteria and requires a good knowledge of the behavior of the signal expected (Umbaugh, 2005).

The implementation of the previous filters increased the particles density in the interrogation window. This fact allowed reducing the number of extrapolated vectors in the analyzed frames. An example of the image quality improvement is shown in Figure 3.10.

REFERENCES

Thielicke, W. (2014). *The Flapping Flight of Birds – Analysis and Application*. Rijksuniversiteit Groningen.

Umbaugh, S. E. (2005). *Computer Imaging: Digital Image Analysis and Processing*. CRC Press.